STUDIES ON THE MIXING IN A DENSITY-STRATIFIED SHEAR FLOW

by
Gregory Gartrell, Jr.

W. M. Keck Laboratory of Hydraulics and Water Resources
Division of Engineering and Applied Science
CALIFORNIA INSTITUTE OF TECHNOLOGY
Pasadena, California

Report No. KH-R-39 May 1979

STUDIES ON THE MIXING IN A DENSITY-STRATIFIED SHEAR FLOW

by

Gregory Gartrell, Jr.

Thesis Supervisor:

Norman H. Brooks
James Irvine Professor of
Environmental and Civil Engineering

Supported by
National Science Foundation
Grant Numbers GK35774X, ENG75-02985, ENG77-27398

Principal Investigator:

E. John List
Professor of Environmental Engineering Science

W. M. Keck Laboratory of Hydraulics and Water Resources
Division of Engineering and Applied Science
California Institute of Technology
Pasadena, California

Report No. KH-R-39 May 1979

ACKNOWLEDGMENTS

There are so many people to whom I owe so much, I feel I could write another volume the size of this one and still not thank everyone adequately. There are several friends who have been especially helpful over the last few years, and who have contributed to this work in many vital ways; I am sincerely grateful for the time, effort and friendship these people have offered me.

The two people to whom I owe the most are Professors Norman H. Brooks and E. John List. Dr. Brooks, my principal advisor on this project, suggested the topic and provided patient guidance and understanding as the work progressed. His warm sense of humor brightened countless days for me, and he always provided encouragement when it was needed.

Dr. List has been especially helpful. He has provided encouragement and friendship, and has always been willing to share a few moments to discuss new ideas and provide helpful insights. I owe more than I can ever repay to these two friends.

I would especially like to thank Elton Daly, whose special genius has never ceased to amaze me. No matter what needed to be built in the laboratory, Elton always had a better, simpler way to do it. He has been a close friend and an inspiration to me.

There are several other people who made valuable contributions to this work. I would like to thank Dr. Robert C.Y. Koh, who provided help in the data analysis and whose "MAGIC" language saved me hours of programming. I would also like to thank Professor Fred Raichlen, with whom I had many valuable discussions.

Professor Vito A. Vanoni deserves special thanks for the time and help he provided. His awesome dedication and vitality acted as a constant encouragement.

Joan Mathews typed a seemingly endless thesis, and retyped the corrected versions, a Sisyphean task. She provided friendship throughout the past years, and kind encouragement when it was greatly needed the last few weeks. I am truly thankful.

During the summer of 1977, I participated in the Geophysical Fluid Dynamics Program at the Woods Hole Oceanographic Institution. My visit there as a pre-doctoral fellow provided me with the opportunity not only to meet with many interesting and knowledgeable people, but also to take some time to reflect on this research and to hear fresh ideas. I returned from Woods Hole with a deeper understanding of the subject, and an enthusiasm that has stayed with me to this day. I would like to thank the Woods Hole Oceanographic Institution and the Geophysical Fluid Dynamics Program for the support they provided. I would also like to thank Professor George Veronis, who directed the program, and Professor Mårten T. Landahl, with whom I had many worthwhile discussions, and who taught me so much about the subject of turbulence.

No one can conduct an experimental program alone, and in this instance I had valuable help from Joe Fontana, Rich Eastvedt and Dave Byrum. The fine talents of Joe Fontana and Rich Eastvedt turned rough sketches into apparatus that not only worked as intended, but also looked like works of art. Dave Byrum provided help with the experiments, especially the photography, and did a magnificent job with more drawings

than he or I would ever care to see again.

I would also like to thank Phil Cormier, who helped take data and who, along with Dale Ota, helped in the data reduction. This research could never have been completed without the signal processor for the laser-Doppler system. Marc Donner designed and built the first working model. I would also like to thank Larry McClellan and Catharine van Ingen for their help.

There are several others who provided friendship, advice and assistance. I would especially like to thank Jim Pankow, Steve Wright, Phil Roberts, Jacques Lewalle and Jing-Chang Chen. I want to thank Mary Eichbauer for her love and encouragement and patience. I hope I can give as much as she continues with a task similar to this one.

I would like to thank the California Institute of Technology for providing facilities which made this study possible, and the National Science Foundation for providing financial support under Grants GK35774X, ENG75-02985, ENG77-27398; the Environmental Protection Agency under Grant T-900137; the National Institutes of Environmental Health Science under Training Grant 5T01 ES00004-15 and the Ford Motor Company Fund/Ford Energy Research Program.

This report was submitted on May 22, 1979 as a thesis for the degree of Doctor of Philosophy in Environmental Engineering Science at the California Institute of Technology.

ABSTRACT

The objective of this study was to examine in a fundamental way the mixing processes in a stably stratified shear flow. The results of the experimental program have yielded information on the nature of turbulence and mixing in density-stratified fluids. The results can be applied to such problems as the determination of the spreading and mixing rates of heated effluents discharged to lakes or the ocean, as well as to many geophysical problems.

An experimental investigation was made to measure the mixing in a two-layered density-stratified shear flow in a flume 40-meters long, with a cross-section of 110 cm wide by 60 cm deep. Both mean temperatures and the mean velocities of the two layers could be independently controlled, and steps were taken to ensure that the temperatures and velocities of the two layers remained nearly constant at the inlet. The relative density difference between the layers was 10^{-3} or less. A laser-Doppler velocimeter, designed for this study, allowed measurements of two components of velocity simultaneously, while a sensitive thermistor was used to measure the temperature. The temperature and velocity measurements were recorded and later analyzed.

The initial mixing layer which developed at the inlet was found to be dominated by large, two-dimensional vortex structures. When the flow was sufficiently stratified, these structures would collapse in a short distance and the flow would develop a laminar shear layer at the interface. It was found that the bulk-Richardson number $\frac{\Delta\rho}{\rho_o} g \ell_T^*/\Delta\bar{u}_o^2$, where ℓ_T^* is the maximum-slope thickness of the

temperature profile, attained a maximum value between 0.25 and 0.3 when the mixing layer collapsed.

Downstream, much less turbulent mixing took place in the stratified flows than homogeneous flows. The depth-averaged turbulent diffusivities for heat and momentum were often 30 to 100 times smaller in stratified flows than in homogeneous flows. The turbulence downstream was found to be dominated by large turbulent bursts, during which the vertical turbulent transport of momentum, heat and turbulent kinetic energy are many times larger than their mean values. It was found these bursts were responsible for most of the total turbulent transport of momentum, heat and turbulent kinetic energy, even though the bursts were found only intermittently.

The flux-Richardson number, R_f, in the flow was examined and found to be related to the local mean-Richardson number in many cases. When production of turbulent kinetic energy from the mean shear, $-\overline{u'v'}\,\frac{\partial \bar{u}}{\partial y}$, was the largest source of turbulent kinetic energy, it was found that $R_f < 0.3$, and when the flow was strongly stratified, $R_f < 0.2$. If the diffusion of turbulent kinetic energy $\frac{1}{2}\frac{\partial \overline{(u'^2 + v'^2)v'}}{\partial y} = \frac{\partial \overline{q^{*2}v'}}{\partial y}$ was the largest source of turbulent kinetic energy, then the flux-Richardson number often attained large values, and the quantity $-\frac{\overline{\rho'v'}}{\rho_o} g \Big/ \frac{\partial \overline{q^{*2}v'}}{\partial y}$ was found to be a more useful parameter than R_f. It was found that, in almost all cases, the rate at which the potential energy of the fluid increased due to turbulent mixing was much less than the estimated rate of viscous dissipation of turbulent kinetic energy.

TABLE OF CONTENTS

LIST OF FIGURES

LIST OF TABLES

NOMENCLATURE

A	constant
B	buoyant force per unit mass, $\frac{\rho - \rho_o}{\rho_o} g$
B_1	constant
D_1	constant
D_2	constant
E	$\overline{\frac{\partial q^2 v'}{\partial y}} \Big/ \overline{u'v'} \frac{\partial \bar{u}}{\partial y}$
E^*	$\overline{\frac{\partial q^{*2} v'}{\partial y}} \Big/ \overline{u'v'} \frac{\partial \bar{u}}{\partial y}$
F	$-\overline{B'v'} \Big/ \overline{\frac{\partial q^2 v'}{\partial y}} = R_f/E$
F^*	$-\overline{B'v'} \Big/ \overline{\frac{\partial q^{*2} v'}{\partial y}} = R_f/E^*$
G	$\rho_1 \rho_o^{-1/2}$ (Section 2.2, Equation 2.2.7)
I, I^*	conditional sampling functions (Section 6.5.3, Equations 6.5.3, 6.5.4)
K_u	Keulegan number, $\nu \frac{\Delta\rho}{\rho_o} g \Big/ \Delta U_o^3$
K_m	turbulent diffusivity of momentum, $-\overline{u'v'} \Big/ \frac{\partial \bar{u}}{\partial y}$
K_H	turbulent diffusivity of heat, $-\overline{v'T'} \Big/ \frac{\partial \bar{T}}{\partial y}$
L	path length of laser beam
L_c	conditional sampling level (Section 6.5.3, Equation 6.5.3)
L_p	conditional sampling level (Section 6.5.1, Equation 6.5.1)
N	Brünt-Vaisala frequency, $\left(\frac{-g}{\rho_o} \frac{\partial \bar{\rho}}{\partial y} \right)^{1/2}$
P	pressure

P_r^*	turbulent Prandtl number K_m/K_H
Q	total volumetric flow rate
Q_1	total volumetric flow rate of the upper layer
Q_2	total volumetric flow rate of the lower layer
R_b^*	bulk-Richardson number $\frac{\Delta\rho}{\rho_o} g\ell/\Delta U_o^2$
R_c	$\left(1 + \frac{2\overline{q^2}}{\overline{v'^2}} \frac{t_1}{t_2}\right)^{-1}$
R_c^*	$\left(1 + \frac{2\overline{q^{*2}}}{\overline{v'^2}} \frac{t_1}{t_2^*}\right)^{-1}$
Re	Reynolds number, $4R_h U/\nu$
R_f	flux-Richardson number $-\overline{B'v'} \Big/ \overline{u'v'} \frac{\partial \bar{u}}{\partial y}$
R_h	hydraulic radius, $w_f h/(w_f + 2h)$
Ri	Richardson number $-g \frac{\partial \rho}{\partial y} \Big/ \left(\frac{\partial u}{\partial y}\right)^2$
$\overline{Ri}$	mean-Richardson number $-g \frac{\partial \bar{\rho}}{\partial y} \Big/ \left(\frac{\partial \bar{u}}{\partial y}\right)^2$
S	surface slope of flow
T	temperature
T_o	constant, reference temperature
T_1	initial temperature of the upper layer
T_2	initial temperature of the lower layer
ΔT_o	$T_1 - T_2$
U	total mean flow speed, $Q/w_f h$
U_1	mean flow speed of the upper layer, $Q_1/w_f h_1$
U_2	mean flow speed of the lower layer, $Q_2/w_f h_2$

ΔU_o	$U_1 - U_2$
V	voltage
V_o	reference voltage
ΔV	estimated error in voltage measurements
c	phase speed of a wave
c_g	group velocity of a wave
$e_1, \ldots e_6$	constants (Section 2.4)
$\vec{e}_r$	unit vector in the direction of reference beam
$\vec{e}_s$	unit vector in the direction of scattering beam
f	friction factor
f	Section 2.2, amplitude of G
f_p	frequency
g	acceleration due to gravity, in the negative $y(x_2)$ direction
h	total flow depth
h_1	initial depth of the upper layer
h_2	initial depth of the lower layer, 30 cm
i(t)	current from photomultiplier tube
k	wave number
ℓ	length scale
ℓ_b	buoyancy length scale, $\Delta\bar{u}_o \dfrac{(\bar{u}_1 + \bar{u}_2)}{2} \Big/ \dfrac{\Delta\rho}{\rho_o} g$
ℓ_T	integral length scale for temperature (Equation 2.1.21)
ℓ_T^*	maximum-slope thickness of temperature profile (Equation 2.1.20)

ℓ_u^*	maximum-slope thickness of the velocity profile (Equation 2.1.19)
ℓ_δ	displacement thickness (Equation 5.1.1)
n	index of refraction
p	pressure, $\frac{\partial P}{\partial x_i} = \frac{\partial p}{\partial x_i} - \rho_o g \delta_{i2}$
p	probability density function
q^2	$\frac{1}{2}(u'^2 + v'^2 + w'^2)$
q^{*2}	$\frac{1}{2}(u'^2 + v'^2)$
t	time
$\overline{t_b}, \overline{t_b^*}$	mean period between bursts (Section 6.5.3)
t_1	$\overline{\rho'^2}/2\varepsilon\rho$
t_2	$\overline{q^2}/\varepsilon$
t_2^*	$\overline{q^{*2}}/\varepsilon^*$
t_3	$\overline{\rho' v'}/\varepsilon_{\rho v}$
u	velocity component in x-direction
u_e	entrainment velocity
u_i	velocity component in the i^{th} direction
$\overline{u}_1$	initial mean centerline speed of the upper layer
$\overline{u}_2$	initial mean centerline speed of the lower layer
$\Delta\overline{u}_o$	$\overline{u}_1 - \overline{u}_2$
u_*	shear velocity
v	velocity component in the y-direction
w	velocity component in the z-direction
w_f	flume width, 110 cm

x	distance in the horizontal direction of the mean flow
x_c	distance to the collapse of the large structure in the initial mixing layer
x_c^*	x_c/ℓ_b
x_i	distance in the i^{th} direction
y	distance in the vertical direction
z	distance in the horizontal direction, transverse to the mean flow
α	parameter in Equation 2.2.2
α^*	$d(\rho - \rho_o)/d(T - T_o)\big\vert_{\rho_o}$
γ	parameter, Section 2.2 $\alpha^2\gamma^2 = k^2 + \frac{\alpha^2}{4} - g\alpha/C^2$
δ_{ij}	Kronecker delta function
δ_ω'	$\frac{d(\ell_u^*)}{d\,x}$
ε	dissipation rate per unit mass of the turbulent kinetic energy, $\overline{q^2}$
ε^*	dissipation rate per unit mass for $\overline{q^{*2}}$
ε_ρ	dissipation rate for $\overline{\rho'^2}/2$
$\varepsilon_{\rho v}$	dissipation rate for $\overline{\rho' v'}$
η	fluid particle displacement (Section 2.2)
θ	$k(x - ct)$ (Section 2.2)
κ	thermal diffusivity
λ	wavelength of laser light, 632.8 nm
λ_m	$\Delta\overline{u}_o/(\overline{u}_1 + \overline{u}_2)$

μ	dynamic viscosity
ν	kinematic viscosity, μ/ρ
ν_D	Doppler frequency
$\Delta\nu_D/\nu_D$	relative error in Doppler frequency
ν_m	measured value of ν_D
ρ	fluid density
ρ_o	constant, reference density
ρ_1	perturbation in density, Section 2.2
$\frac{\Delta\rho}{\rho_o}$	initial relative density difference between the upper and lower layers (positive)
$\hat{\sigma}_p$	probable relative error in repeatability
$\hat{\sigma}_s$	systematic relative error
σ_u	σ_u'/u
σ_u'	error estimate for u
σ_v	σ_v'/u
σ_v'	error estimate for v
ϕ	amplitude of Ψ (Section 2.2)
$\Gamma,\Gamma^*,\tilde{\Gamma}$	time fraction for turbulent bursts (Section 6.5.3, Equations 6.5.1 - 6.5.8)
χ	dissipation rate for $\overline{T'^2}$
Ψ	stream function of perturbation wave (Section 2.2)
$\Phi_u,\Phi_v,\Phi_T(k)$	power spectral estimates for u', v' and T' where $\Phi = \frac{\bar{u}}{2\pi}\Phi^*$ and $k = 2\pi f_p/\bar{u}$
$\Phi^*(f_p)$	power spectral estimate in frequency domain

Σ_{uv}	standard deviation of u'v' record
Σ_{qv}	standard deviation of $q^{*2}v'$ record

SPECIAL NOTATION

prime (')	fluctuating part of a quantity (e.g. $u' = u - \overline{u}$)
overbar ($\overline{\ }$)	mean value of a quantity
$[\ \ ]_N$	normalization such that the mean is zero and the standard deviation is one
$<\ \ >$	conditionally sampled average (Section 6.5.3, Equations 6.5.1 - 6.5.8)

SUBSCRIPTS

i,j,k	integer indices
$(\ )_u$	unstratified case
$(\ )_s$	stratified case

CHAPTER 1

INTRODUCTION

Density-stratified shear flow problems are commonly encountered both in engineering practice and in geophysical studies. Yet, as with many fluid mechanics problems, they are not well understood. Part of the reason for this is that solutions for density-stratified shear flow problems often require some knowledge of the behavior of turbulence in fluids, at best a complicated and poorly understood matter. There are, however, a number of vital engineering problems which require knowledge on a fundamental level concerning the behavior of density-stratified shear flows in order that they might be intelligently solved.

Among these problems is that of the discharge of cooling water from power plants to lakes or the ocean. In such instances, a buoyant layer of warm water may form on the surface and slowly spread. The rate at which this layer of water drifts over and mixes with the cooler ambient water will depend upon, among other things, the density difference between the two layers, the shear at the interface, and the turbulence levels in the vicinity of the interface.

Another related problem is that of the discharge of sewage to the ocean; whether the sewage field rises to the surface or stays submerged, the ultimate turbulent mixing processes involve interactions with buoyancy forces. Similarly, the spread of smoke in a burning building, the circulation of water discharged into a power plant cooling pond, and the dispersion of air pollutants in an urban atmosphere are all

density-stratified shear flow problems. In addition, there are many geophysical stratified flow problems. These include atmospheric motions, the nature of oceanic currents, and the behavior of estuarine flows. There are also many problems related to mixing in lakes and reservoirs which involve density stratification.

The purpose of this study is to examine in detail the mixing which takes place in a two-layered density-stratified turbulent shear flow. The ultimate goal is to provide fundamental information on the nature of such flows in order that one might have a better understanding of them when approaching engineering problems.

As a major part of this study, an experimental investigation was conducted in order to measure the mixing in a density-stratified shear flow. Experiments were conducted in the 40-meter precision tilting flume in the Keck Hydraulics Laboratory. The flume was modified so that at the upstream end warm water entered the flume at one velocity from above a splitter plate, while cooler water entered at a slower velocity from below. At the downstream end, an adjustable splitter plate separated the upper and lower layers of water which were then returned to the inlet via separate return pipes with temperature control. Velocity measurements were made using a two-component laser-Doppler velocimeter, developed for this study, while temperature measurements were made with sensitive thermistors. The results of the measurements have yielded much new information on the nature of density-stratified flows.

In addition, density-stratified flows were considered in a

theoretical vein in order that the results of the experimental investigation might be more easily understood. Together, the theoretical and experimental investigations have answered a number of questions about the nature of density-stratified shear flow problems, but leave many more questions still unanswered.

Chapter 2 presents a review of some previous experimental and theoretical work related to density-stratified shear flows. In addition, new theoretical work is presented, including some work which was conducted by the author at the Geophysical Fluid Dynamics Program at the Woods Hole Oceanographic Institution.

Chapter 3 contains a discussion of the experimental apparatus. Included is a detailed description of the laser-Doppler velocimeter used in the study. (Appendix A contains a detailed description of the electronics used with the laser-Doppler velocimeter.)

In Chapter 4 the experimental procedure is described. Included are accounts of the calibration procedures of the various instruments and analyses of the measurement errors. Also included is a discussion on possible errors in velocity measurements caused by variations in the refractive index of the water in the density-stratified flows.

Chapter 5 contains a general description of the flow. Included are discussions on the inlet conditions and the boundary-generated turbulence. In addition, some results from flow visualization studies are presented.

In Chapter 6 the experimental results are presented. The chapter is divided into sections concerning the flow in the initial mixing

layer, the downstream flow over a smooth bed, the downstream flow over a roughened bed, and the organized structures found in the turbulent regions.

Chapter 7 contains a detailed discussion of the experimental results, and Chapter 8 gives the summary and the conclusions.

CHAPTER 2

THEORETICAL ANALYSIS AND REVIEW OF PREVIOUS WORK

2.0 Introduction

In this chapter previous theoretical and experimental studies on density-stratified shear flows are reviewed and some new analysis is presented. As discussed in Chapter 1, the bulk of this study concerns the experimental investigation of the mixing between a warm layer of water flowing over a colder layer. There are four basic regimes of mixing in this type of flow. The first regime is the initial two-dimensional mixing layer, which, given a sufficiently large buoyancy difference between the layers, can collapse to a laminar shear layer. If the mixing layer does not collapse, then downstream the fluid continues to mix due to boundary-generated turbulence, although it mixes at rates which are much lower than those found in homogeneous open-channel flows. This is the second mixing regime.

The third and fourth regimes are closely related and occur downstream if the mixing layer has collapsed. Shear stresses at the boundary of the flume may alter the velocity profile in such a way that a strong shear will exist across the stable interface. In addition, boundary-generated turbulence may produce internal waves at the interface. The waves may become unstable, because of the shear, and break, causing a gradual breakdown of the interface. This is the third regime. Finally, the boundary-generated turbulence may directly cause mixing at the bottom of the interface. In this case, the

turbulence "chips" away at the lower portion of the interface, without totally disrupting the interface.

The balance of this chapter considers theoretical analyses and experimental work which relate to these types of mixing processes. Of particular interest are studies relating to mixing layers and the nature of turbulence in density-stratified shear flows.

2.1 Equations of Motion and Pertinent Dimensionless Quantities

In this section, the pertinent equations of motion and the important dimensionless quantities are presented and discussed. For convenience, subscripted notation is used here; the variables and notation used are defined as follows: u_i denotes the fluid velocity in the x_i direction, and $(u_1,u_2,u_3) \equiv (u,v,w)$, while $(x_1,x_2,x_3) \equiv (x,y,z)$ where x is in the direction of the mean flow, y is in the vertical direction and z is in the lateral direction. An overbar (—) denotes an ensemble average and a prime (') denotes the usual fluctuating quantity. μ denotes the dynamic viscosity, ρ the density and $\nu \equiv \mu/\rho$, the kinematic viscosity; P denotes the pressure, T denotes temperature, and t denotes time.

2.1.1 Equations of Motion

The flow is assumed to be incompressible, hence, the continuity equation:

$$\frac{\partial u_i}{\partial x_i} = 0 \ . \qquad (2.1.1)$$

In addition, a linear equation of state, $\rho - \rho_o = \alpha^*(T - T_o)$, valid

for small temperature differences, is assumed, so that

$$\frac{\partial \rho}{\partial t} + u_i \frac{\partial \rho}{\partial x_i} = \kappa \frac{\partial^2 \rho}{\partial x_k \partial x_k} \tag{2.1.2}$$

where κ is the thermal diffusivity coefficient,

ρ_o is a reference density, and

T_o is a reference temperature.

The momentum (Navier-Stokes) equation is given by

$$\rho \left(\frac{\partial u_i}{\partial t} + u_k \frac{\partial u_i}{\partial x_k} \right) = - \frac{\partial P}{\partial x_i} - \rho g \delta_{i2} + \mu \frac{\partial^2 u_i}{\partial x_k \partial x_k} \tag{2.1.3}$$

where δ_{ij} is the Kronecker delta function, and g denotes the acceleration due to gravity (in the negative x_2 direction). Following the work of Phillips (1966), Equation 2.1.3 can be reduced to

$$\frac{\partial u_i}{\partial t} + u_k \frac{\partial u_i}{\partial x_k} = - \frac{1}{\rho} \frac{\partial p}{\partial x_i} - \frac{\rho - \rho_o}{\rho} g \delta_{i2} + \frac{\mu}{\rho} \frac{\partial^2 u_i}{\partial x_k \partial x_k} \tag{2.1.4}$$

where $$\frac{\partial P}{\partial x_i} = \frac{\partial p}{\partial x_i} - \rho_o g \delta_{i2} \quad \text{and}$$

ρ_o is a constant, reference density.

The Boussinesq assumption (in which it is assumed that $\rho \approx \rho_o$, a constant, except in the term involving the gravity force) is used and

$$\frac{\partial u_i}{\partial t} + u_k \frac{\partial u_i}{\partial x_k} = - \frac{1}{\rho_o} \frac{\partial p}{\partial x_i} - B \delta_{i2} + \nu \frac{\partial^2 u_i}{\partial x_k \partial x_k} \tag{2.1.5}$$

is obtained. Here B denotes the buoyant force per unit mass, $\frac{\rho-\rho_o}{\rho_o} g$.

From Equations 2.1.1 and 2.1.5, the following relationships can be derived (see Phillips (1966), Tennekes and Lumley (1972), Hinze (1959))

$$\frac{\partial \bar{u}_i}{\partial t} + \bar{u}_k \frac{\partial \bar{u}_i}{\partial x_k} = - \frac{1}{\rho_o} \frac{\partial \bar{p}}{\partial x_i} - \bar{B}\, \delta_{i2} - \frac{\partial \overline{u'_i u'_k}}{\partial x_k} + \nu \frac{\partial^2 \bar{u}_i}{\partial x_k \partial x_k} \quad , \tag{2.1.6}$$

$$\frac{\partial \bar{u}_i}{\partial x_i} = 0 \quad , \tag{2.1.7}$$

$$\frac{\partial \bar{B}}{\partial t} + \bar{u}_k \frac{\partial \bar{B}}{\partial x_k} + \frac{\partial \overline{B' u'_k}}{\partial x_k} = \kappa \frac{\partial^2 \bar{B}}{\partial x_k \partial x_k} \tag{2.1.8}$$

$$\frac{\partial \overline{u'_i u'_j}}{\partial t} + \overline{u'_k u'_j} \frac{\partial \bar{u}_i}{\partial x_k} + \overline{u'_i u'_k} \frac{\partial \bar{u}_j}{\partial x_k} + \bar{u}_k \frac{\partial \overline{u'_i u'_j}}{\partial x_k} + \frac{\partial \overline{u'_i u'_j u'_k}}{\partial x_k} =$$

$$- \left(\overline{u'_j \frac{\partial p'}{\partial x_i}} + \overline{u'_i \frac{\partial p'}{\partial x_j}} \right) \Big/ \rho_o - \left(\overline{u'_j B'} \delta_{2i} + \overline{u'_i B'} \delta_{2j} \right) - \frac{2}{3} \delta_{ij} \varepsilon \tag{2.1.9}$$

$$\frac{\partial \overline{B'^2}}{\partial t} + 2\overline{u'_k B'} \frac{\partial \bar{B}}{\partial x_k} + \bar{u}_k \frac{\partial \overline{B'^2}}{\partial x_k} + \frac{\partial \overline{B'^2 u'_k}}{\partial x_k} = - \frac{2 g^2 \varepsilon_\rho}{\rho_o^2} \tag{2.1.10}$$

and

$$\frac{\partial \overline{B'u'_i}}{\partial t} + \overline{B'u'_k}\ \frac{\partial \bar{u}_i}{\partial x_k} + \overline{u'_i u'_k}\ \frac{\partial \bar{B}}{\partial x_k} + \bar{u}_k \frac{\partial \overline{B'u'_i}}{\partial x_k} + \frac{\partial \overline{B'u'_i u'_k}}{\partial x_k} =$$

$$- \frac{1}{\rho_o}\ \overline{B' \frac{\partial p'}{\partial x_i}} - \overline{B'^2}\ \delta_{i2} - \frac{g\varepsilon_{\rho u}}{\rho_o} \qquad (2.1.11)$$

Here ε is the viscous energy dissipation rate per unit mass, ε_ρ is the dissipation rate for $\overline{\rho'^2}/2$ and $\varepsilon_{\rho u}$ is the dissipation rate for $\overline{\rho' u_i'}$.

Equations 2.1.6, 2.1.7, and 2.1.8 are the conservation equations for the mean quantities of momentum, mass and buoyancy for a Boussinesq flow. Equations 2.1.9 - 2.1.11 are conservation equations for second-order fluctuating quantities. For a detailed discussion of the terms in these equations, the reader is referred to Hinze (1959) or Tennekes and Lumley (1972).

From Equation 2.1.9, the conservation equation for turbulent kinetic energy is found to be

$$\frac{\partial \overline{q^2}}{\partial t} + \bar{u}_k \frac{\partial \overline{q^2}}{\partial x_k} + \frac{\partial \overline{q^2 u_k'}}{\partial x_k} = -\overline{u'_i \frac{\partial p'}{\partial x_i}}/\rho_o - \overline{u'_2 B'} - \overline{u'_i u'_k} \frac{\partial \bar{u}_k}{\partial x_i} - \varepsilon, \qquad (2.1.12)$$

where $$\overline{q^2} = \frac{1}{2}\ \overline{u_i' u_i'}.$$

These are the primary equations that are used in analysis of stratified shear flows.

2.1.2 Dimensionless Parameters

There are several important parameters which can be used

to describe density-stratified shear flows. One parameter is the Richardson number, Ri, which is defined as:

$$Ri = \frac{-g \frac{\partial \rho}{\partial y}}{\rho_o \left(\frac{\partial u}{\partial y} \right)^2} \qquad (2.1.13)$$

This quantity is useful in the analysis of laminar flows with wavelike perturbation; its usefulness in turbulent flows is open to question, since it is a rather difficult parameter to measure in a turbulent flow, and has both spatial and temporal fluctuations. The Richardson number is a stability parameter, for Miles (1961) and Howard (1961) have shown that a sufficient condition for an inviscid density-stratified shear flow to be stable is that the Richardson number be everywhere greater than 1/4.

A more commonly used parameter in a turbulent density-stratified shear flow is a mean-Richardson number defined as

$$\overline{Ri} = \frac{-g \frac{\partial \overline{\rho}}{\partial y}}{\rho_o \left(\frac{\partial \overline{u}}{\partial y} \right)^2} \quad . \qquad (2.1.14)$$

The general usefulness of this parameter, however, is not clearly established, at least to this author, in that a laminar flow with internal waves may have a large value of $\overline{Ri}$, while locally it may have values of Ri that are less than 1/4, and thus may become unstable. However, it is a parameter which gives a general description of the flow at a point, and may thus be useful as a parameter to consider

in the reduction of data.

The flux-Richardson number, defined as

$$R_f = \frac{\overline{B'v'}}{-\overline{u'v'}\,\frac{\partial \bar{u}}{\partial y}} \quad , \tag{2.1.15}$$

is the ratio of the vertical flux of buoyancy to the production of turbulent energy transferred by the Reynolds stresses from the mean flow. Both of these quantities are important terms in Equation 2.1.12.

Another dimensionless quantity which is often neglected is

$$E = \frac{\frac{\partial}{\partial y}\,\overline{q^2 v'}}{\overline{u'v'}\,\frac{\partial \bar{u}}{\partial y}} \quad , \tag{2.1.16}$$

the ratio of the gradient of the vertical flux of turbulent energy to the local production of turbulent energy. Again, both of these quantities come from Equation 2.1.12. This parameter can be rather important in some cases, particularly if the fluid is flowing over a roughened bed, where there can be an enormous production of turbulent energy. In this case, turbulent energy is transferred vertically from the bed by the vertical velocity; if there is no mean vertical flow, all the turbulent energy will be transferred away from the bed by the fluctuating vertical velocity, and $\overline{q^2 v'}$ is the measure of the vertical flux of turbulent energy. If E is large, then a term that would be more important than R_f is

$$F \equiv \frac{R_f}{E} = \frac{\overline{B'v'}}{-\frac{\partial}{\partial y}\overline{q^2v'}} \qquad (2.1.17)$$

which is a dimensionless quantity analogous to the flux-Richardson number.

Another Richardson number which is commonly used in the reduction of data is the bulk-Richardson number

$$R_b^* = \frac{\Delta\rho}{\rho_o} g\ell/U^2 \qquad (2.1.18)$$

where $\frac{\Delta\rho}{\rho_o} g$ is the buoyancy difference between two layers,

ℓ is an appropriate length scale of the problem, and

U is an appropriate velocity scale.

This parameter is, in fact, the inverse of the densimetric Froude number. The major problem with this parameter lies in the determination of the length and velocity scales; that which is an appropriate length scale in one problem may be inappropriate in another. This difficulty can make the comparison of results from different experiments a problem.

The Keulegan number, $\left(\nu \frac{\Delta\rho}{\rho_o} g\right)/U^3$, where U is an appropriate velocity scale, is formed by combining the Reynolds number, $Re \equiv U\ell/\nu$ and the bulk-Richardson number in such a way that the length scale ℓ is eliminated. Keulegan (1949) found this parameter to be useful in characterizing the mixing in a density-stratified flow, but Turner (1973) has

questioned the usefulness of this parameter, in that viscosity may not really be important. However, the Keulegan number may be useful in characterizing the initial mixing layer, for, in the idealized case, the mixing layer has no externally imposed length scale.

There are several measures of length scales in density-stratified flows which are useful. Length scales based on maximum gradients are useful in many flows, particularly flows with an interface. Two length scales defined using maximum gradients are

$$\ell_u^* = \Delta U_o \Big/ \left(\frac{\partial \overline{u}}{\partial y} \right)_{max} \tag{2.1.19}$$

and

$$\ell_T^* = \Delta T_o \Big/ \left(\frac{\partial \overline{T}}{\partial y} \right)_{max} \tag{2.1.20}$$

where ΔU_o is the initial difference in mean flow speeds between the two layers, and

ΔT_o is the initial temperature difference between the two layers.

Here, the maximum values of the gradients are taken to be local maxima. ℓ_u^* and ℓ_T^*, then, are local length scales which may be useful in forming parameters such as R_b^*.

An integral length scale which may also be useful is

$$\ell_T \equiv \frac{6}{(\Delta T_o)^2} \int_{-h}^{0} (T_1 - \overline{T})(\overline{T} - T_2)\, dy \tag{2.1.21}$$

where T_1 is the initial temperature of the upper layer, and T_2 is the initial temperature of the lower layer.

The coefficient of six is chosen so that $\ell_T = \ell_T^*$ for a linear temperature profile.

Another parameter which may be important is the turbulent Prandtl number, $P_r^* \equiv K_m/K_H$, where K_m is the turbulent diffusivity of momentum and K_H is the turbulent diffusivity of heat. Other important parameters may include $\overline{u'^2}/\bar{u}^2$, the usual measure of the relative turbulent intensity, although $\overline{v'^2}/\bar{u}^2$ may be more appropriate for stratified flows, since the vertical velocity fluctuations are ultimately responsible for much of the mixing.

2.2 Stability Considerations for Stratified Shear Flows

In some instances, a stratified shear layer may become unstable; in this situation internal waves may develop and break, resulting in substantial mixing. In this section, some aspects of the stability of stratified shear flows will be examined.

The stability of stratified shear flows has received a good deal of attention in the past. Taylor (1931) and Goldstein (1931) found stability curves for several inviscid cases. Miles (1961) and Howard (1961) showed that for inviscid flow, a sufficient condition for stability is that Ri be everywhere greater than 1/4. A review of much of the work done with stratified shear layers is given by Drazin and Howard (1966) and Thorpe (1973a).

Work on the stability of stratified shear layers has usually concentrated on finding neutral stability curves in the wave number-Richardson number plane. For free shear layers these curves often correspond to the curves where the wave celerity, c, of the disturbance vanishes. Neutral stability curves may not always coincide with the curve c = 0, however. Such a case was pointed out by Howard (1963); in these situations, the "principle of exchange of stabilities" does not hold and more complex methods are needed to determine the stability curves.

A situation which may occur is one in which a finite perturbation on the mean flow changes the flow in such a way that a secondary perturbation becomes unstable. Thus, one might expect a situation in which internal waves modify the flow in such a way that $Ri < 1/4$ locally, although not everywhere, thus allowing the local onset of instabilities. Woods (1968, 1969) felt that this phenomenon was responsible for the observed sudden onset of turbulence in stable layers.

Landahl (1972) has given criteria for the breakdown of a flow perturbed by a wavelike disturbance of finite amplitude. The basic idea behind his theory is that the primary disturbance modifies the flow in such a way that unstable secondary waves are focused at a location where they can suddenly attain large amplitudes (see Figure 2.2.1). The following conditions apply for a two-dimensional problem. The first condition is that the group velocity, c_g, of the secondary waves be equal to the phase speed, c, of the neutral primary wave. If

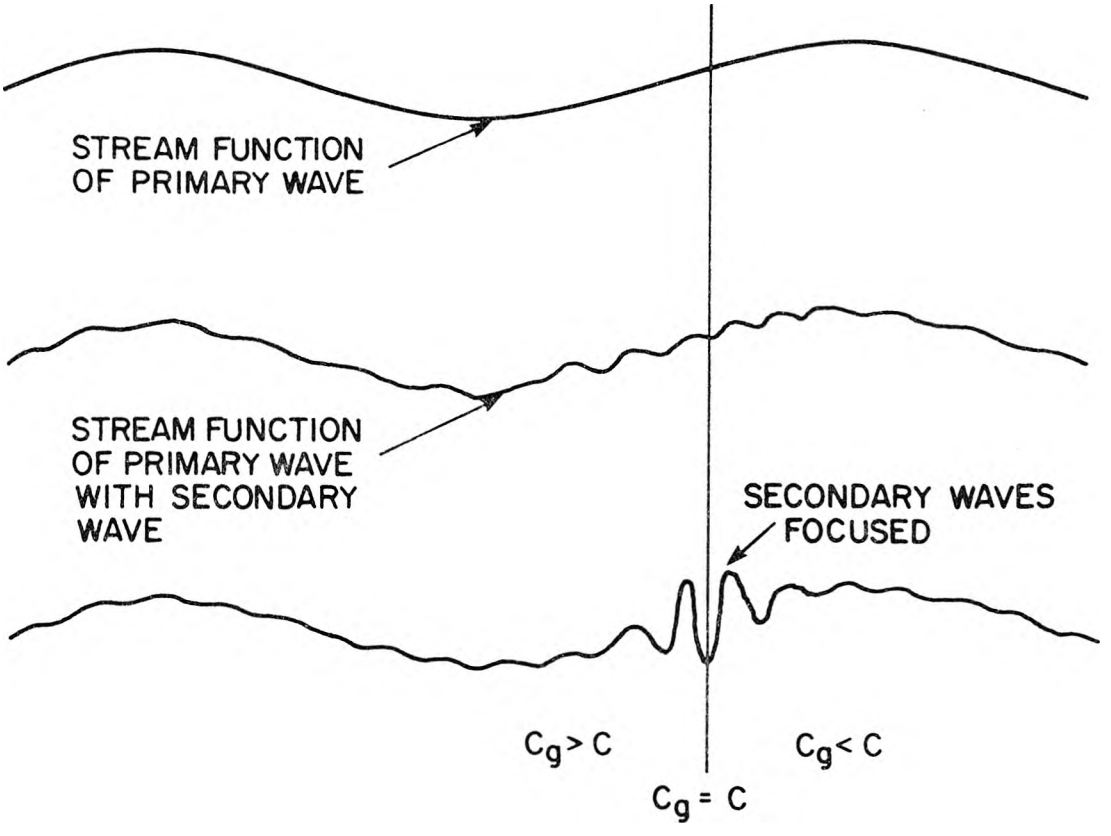

Figure 2.2.1 Breakdown of a flow due to focusing of a secondary disturbance.

Top: Stream function of primary disturbance to the mean flow.

Middle: Primary and secondary wave; group velocity c_g of secondary wave varies along the phase of the primary wave.

Bottom: Secondary wave is focused at the point where $c_g = c$ leading to breakdown.

the primary wave itself is unstable, then the condition is $c_g = -\frac{\partial c_g}{\partial t} \Big/ \frac{\partial c_g}{\partial x}$ where the derivatives are taken holding the wave number constant. The second condition for focusing of the waves is that the quantity $c_g - c$ decrease through the critical point where $c_g - c = 0$. If this condition holds, then waves close to the critical point will tend to move toward the critical point. For detailed discussions, see Landahl (1972) and Landahl and Criminale (1977).

The primary requirement that allows one to use Landahl's theory is that the wave number, k, of the secondary disturbance be much larger than that of the primary wave. Then, inhomogeneities in the fluid caused by the primary wave are small over one wavelength of the secondary wave. Landahl (1972) applied the theory to the sudden onset of turbulence in a boundary layer. Landahl and Criminale (1977) applied the theory to some simplified models of stratified shear flows, in particular, to flows which exhibited discontinuities in the density profile. Thorpe (1978a) considered the breaking of finite amplitude waves in a density-stratified shear flow. The photographs in his paper show properties that are remarkably similar to properties predicted by the theory of Landahl (1972) and Landahl and Criminale (1977). In particular, a series of his photographs show large waves which begin to break with the "appearance of thin laminae near the crest." However, shortly after this disturbance occurred on the primary wave, large amplitude instabilities (of the Kelvin-Helmholtz type) suddenly developed on a portion of the wave. Figure 12 of Thorpe's paper shows this quite well. Although more detailed measurements are required to demonstrate completely that the sudden breakdown to turbulence was caused by the

mechanism proposed by Landahl (1972), the theory and the experiment do match qualitatively, and the work by Landahl and Criminale (1977) does correctly predict the phase along the primary wave at which the breakdown occurs.

Work along lines similar to those of Landahl and Criminale (1977) was done by Gartrell (1977), and the basic results are presented here. This work was done under the supervision of M. T. Landahl in the Geophysical Fluid Dynamics program at the Woods Hole Oceanographic Institution.

The flow considered was a flow in which the density was a continuous function of depth; usually in a stability analysis discontinuous density profiles are assumed as they result in problems which are somewhat more tractable. The mean flow considered is given by

$$u_o = \begin{cases} 1, & y > 1 \\ 0, & |y| \leq 1 \\ -1, & y < -1 \end{cases} \tag{2.2.1}$$

and

$$\rho_o = \begin{cases} \hat{\rho}_o e^{-\alpha}, & y > 1 \\ \hat{\rho}_o e^{-\alpha y}, & |y| \leq 1 \\ \hat{\rho}_o e^{\alpha}, & y < -1 \end{cases} \tag{2.2.2}$$

Hence the density profile is continuous and the velocity profile is discontinuous (see Figure 2.2.2). The mean-Richardson number, $\overline{Ri}$, is defined here as $g\alpha/2$. The equations of motion for the inviscid flow are:

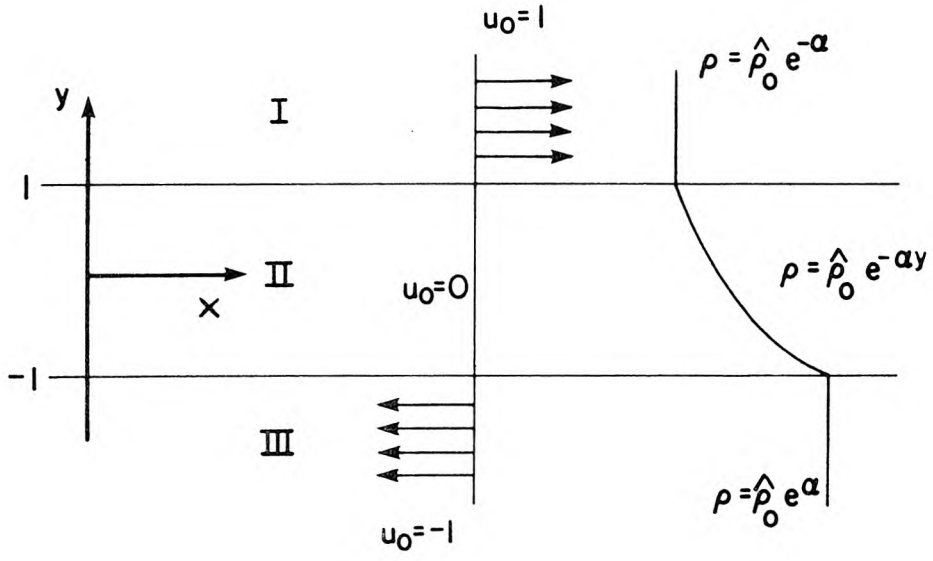

Figure 2.2.2 Velocity and density profiles assumed for wave breakdown model.

x-momentum $$\rho \frac{\partial u}{\partial t} + \rho u \frac{\partial u}{\partial x} + \rho v \frac{\partial u}{\partial y} = - \frac{\partial p}{\partial x} \qquad (2.2.3)$$

y-momentum $$\rho \frac{\partial u}{\partial t} + \rho u \frac{\partial v}{\partial x} + \rho v \frac{\partial v}{\partial y} = - \frac{\partial p}{\partial y} - \rho g \qquad (2.2.4)$$

continuity $$\frac{\partial u}{\partial x} + \frac{\partial v}{\partial y} = 0 \qquad (2.2.5)$$

incompressibility $$\frac{\partial \rho}{\partial t} + u \frac{\partial \rho}{\partial x} + v \frac{\partial \rho}{\partial y} = 0 \qquad (2.2.6)$$

Equation 2.2.6 requires that the density of a fluid particle remain constant as it moves. A stream function is introduced such that $u = u_o(y) + \frac{\partial \Psi}{\partial y}$ and $v = - \frac{\partial \Psi}{\partial x}$, where Ψ is the stream function of the primary wave perturbation; the density is given by $\rho = \rho_o(y) + \rho_1(x,y,t)$ where ρ_1 is the perturbation in the density. To facilitate the reduction of the equations, the transformations $\rho_1 = \rho_o^{1/2} G$ and $\Psi = \rho_o^{-1/2} \psi$ are made. Substituting the transformations into Equations 2.2.2 - 2.2.6, eliminating the pressure term and retaining only the first order perturbation quantities, one obtains

$$\psi_{yyt} + \psi_{xxt} + \psi_t \left(\frac{\left(\frac{\partial \rho_o}{\partial y} \right)^2}{4\rho_o^2} - \frac{1}{2} \frac{\frac{\partial^2 \rho_o}{\partial y^2}}{\rho_o} \right) + u_o \left(\psi_{xxx} + \psi_{yyx} \right) +$$

$$+ \psi_x u_o \left(\frac{\left(\frac{\partial \rho_o}{\partial y} \right)^2}{4\rho_o^2} - \frac{1}{2} \frac{\frac{\partial^2 \rho_o}{\partial y^2}}{\rho_o} \right) - \frac{1}{\rho_o} \frac{\partial}{\partial y} \left(\rho_o \frac{\partial u_o}{\partial y} \right) \psi_x - g G_x = 0 \qquad (2.2.7)$$

and

$$G_t + u_o G_x = \psi_x \frac{1}{\rho_o} \frac{\partial \rho_o}{\partial y} \qquad (2.2.8)$$

where the subscripts x, y, and t denote partial derivatives. Wavelike perturbation quantities in x and t are then assumed:

$$\psi = \phi(y) \exp(ik(x - ct)) \tag{2.2.9}$$

$$G = f(y) \exp(ik(x - ct)) \ . \tag{2.2.10}$$

Substituting these relations into Equations 2.2.7 and 2.2.8, one finds:

$$\phi'' - k^2\phi = 0, \quad f = 0 \text{ for } |y| > 1 \tag{2.2.11}$$

$$\phi'' - \phi(k^2 + \frac{\alpha^2}{4} - g\alpha/c^2) = 0, \ f = \frac{\alpha g}{c} \text{ for } |y| \leq 1 \ . \tag{2.2.12}$$

In addition, it is required that the fluid particle displacement, η, be continuous across the interfaces at $y = \pm 1$ and that the pressure also be continuous. Furthermore, it is required that the perturbation quantities vanish at $y = \pm\infty$.

Three cases may be distinguished, according to whether $\alpha^2\gamma^2 \equiv k^2 + \alpha^2/4 - g\alpha/c^2$ is equal to, less than, or greater than zero. If $\alpha^2\gamma^2$ is less than zero, $\phi(y)$ is wavelike in the y-direction; if $\alpha^2\gamma^2$ is greater than zero, $\phi(y)$ is exponential in character. Since these two cases are similar mathematically, they will be considered together, following an analysis for $\gamma^2 = 0$.

Case 1, $\gamma^2 = 0$

Here, the solutions are:

$$\phi \propto \exp(-k(y - 1)) \qquad y > 1 \tag{2.2.13a}$$

$$\phi \propto \exp(k(y + 1)) \qquad y < -1 \tag{2.2.13b}$$

$$\phi = (Ay + B_1) \qquad |y| \leq 1 \tag{2.2.13c}$$

Now η, the fluid particle displacement, is given by:

$$\eta = \Psi/(c - u_o) \tag{2.2.14}$$

For convenience, the solutions are written as:

$$\Psi_I = \delta_I(c-1)\exp(i\theta - k(y-1) + \alpha/2) \tag{2.2.15a}$$

$$\Psi_{II} = c(Ay + B_1)\exp(i\theta+\alpha y/2) \tag{2.2.15b}$$

$$\Psi_{III} = \delta_{III}(c+1)\exp(i\theta + k(y+1) - \alpha/2) \tag{2.2.15c}$$

$$\eta_I(1) = \delta_I\exp(i\theta + \alpha/2) \tag{2.2.16a}$$

$$\eta_{II} = (Ay + B_1)\exp(i\theta+\alpha y/2) \tag{2.2.16b}$$

$$\eta_{III}(-1) = \delta_{III}\exp(i\theta - \alpha/2) \tag{2.2.16c}$$

where the subscripts I, II and III refer to the regions $y > 1$, $|y| < 1$ and $y < -1$, respectively; where $\theta = k(x - ct)$ and both δ_I and δ_{III} are constant. The boundary conditions require

$$\eta_I(1) = \eta_{II}(1), \quad \eta_{II}(-1) = \eta_{III}(-1) \qquad \text{and}$$

$$(c-1)\frac{\partial\Psi_I(1)}{\partial y} = c\frac{\partial\Psi_{II}(1)}{\partial y}, \quad (c+1)\frac{\partial\Psi_{III}(-1)}{\partial y} = c\frac{\partial\Psi_{II}(-1)}{\partial y}$$

where the last two equations are obtained from the Bernoulli equation.

Applying the boundary conditions to (2.2.15) and (2.2.16) it is found that:

$$\delta_I = A + B_1 \text{ (continuity of } \eta \text{ at } y = 1) \tag{2.2.17a}$$

$$\delta_{III} = -A + B_1 \quad \text{(continuity of } \eta \text{ at } y = -1) \tag{2.2.17b}$$

$$-(c-1)^2\delta_I k = \frac{\alpha}{2} c^2(A+B_1) + c^2 A \quad \text{(continuity of pressure at } y = 1) \tag{2.2.17c}$$

$$(c+1)^2\delta_{III} k = \frac{\alpha}{2} c^2(B_1 - A) + c^2 A \quad \text{(continuity of pressure at } y = -1) \tag{2.2.17d}$$

In order to obtain nontrivial solutions, it is required that

$$c^4(k^2+k) + c^3(2\alpha k) + c^2(k - 2k^2 - 2\overline{Ri}) + k^2 = 0 \tag{2.2.18}$$

where the facts that $2\overline{Ri} = g\alpha$ and $\gamma^2 = 0$ have been used. This is the dispersion relation for $\gamma^2 = 0$.

Case 2, $\gamma^2 \neq 0$

The solutions for this case are:

$$\phi_I \propto \exp(-k(y-1)) \qquad y > 1 \tag{2.2.19a}$$

$$\phi_{II} = D_1 \exp(\alpha\gamma y) + D_2 \exp(-\alpha\gamma y) \qquad |y| < 1 \tag{2.2.19b}$$

$$\phi_{III} \propto \exp(k(y+1)) \qquad y < -1 \tag{2.2.19c}$$

Following the same procedure as in the previous case, one finds

$$\Psi_I = (c-1)\delta_I \exp(i\theta - k(y-1) + \alpha/2) \tag{2.2.20a}$$

$$\Psi_{II} = c(D_1 e^{\alpha\gamma y} + D_2 e^{-\alpha\gamma y}) \exp(i\theta + \alpha y/2) \tag{2.2.20b}$$

$$\Psi_{III} = (c+1)\delta_{III} \exp(i\theta + k(y+1) - \alpha/2) \tag{2.2.20c}$$

$$\eta_I(1) = \delta_I \exp(i\theta + \alpha/2) \tag{2.2.21a}$$

$$\eta_{II} = (D_1 e^{\alpha\gamma y} + D_2 e^{-\alpha\gamma y}) \exp(i\theta + \alpha y/2) \tag{2.2.21b}$$

$$\eta_{III}(-1) = \delta_{III}\exp(i\theta - \alpha/2) \qquad (2.2.21c)$$

The boundary conditions require:

$$\delta_I = D_1 e^{\alpha\gamma} + D_2 e^{-\alpha\gamma} \qquad \text{(continuity of } \eta \text{ at } y = 1) \qquad (2.2.22a)$$

$$\delta_{III} = D_1 e^{-\alpha\gamma} + D_2 e^{\alpha\gamma} \qquad \text{(continuity of } \eta \text{ at } y = -1) \qquad (2.2.22b)$$

$$-k\delta_I(c-1)^2 = c^2\alpha(D_1 e^{\alpha\gamma}(\tfrac{1}{2}+\gamma) + D_2 e^{-\alpha\gamma}(\tfrac{1}{2}-\gamma)) \qquad \text{(continuity of pressure, } y = 1) \qquad (2.2.22c)$$

$$k\delta_{III}(c+1)^2 = c^2\alpha(D_1 e^{-\alpha\gamma}(\tfrac{1}{2}+\gamma) + D_2 e^{\alpha\gamma}(\tfrac{1}{2}-\gamma) \qquad \text{(continuity of pressure at } y = -1) \qquad (2.2.22d)$$

Again, for non-trivial solutions, the dispersion relation is obtained:

$$\tanh(2\alpha\gamma)[c^4(2k^2) + 2\alpha k c^3 - c^2(2k^2 + 2\overline{Ri}) + k^2] + 2\alpha\gamma k[c^4 + c^2] = 0 \qquad (2.2.23)$$

If $|\alpha\gamma| \ll 1$ then Equation 2.2.23 reduces to

$$2\alpha\gamma[c^4(2k^2 + k) + (2\alpha k)c^3 + c^2(k - 2k^2 - 2\overline{Ri}) + k^2] \approx 0 \qquad (2.2.24)$$

where the approximation $\tanh\varepsilon \approx \varepsilon$ for $|\varepsilon| \ll 1$ has been used. Equation 2.2.23 then reduces to Equation 2.2.17 when $|\alpha\gamma|$ approaches zero.

For the case that γ^2 is real and negative, the amplitudes of the perturbation quantities are wavelike in the region of non-zero density gradient. Equation 2.2.22b, in this case, is of the form

$$D_1 a = -D_2 a^* \qquad (2.2.25)$$

where the * superscript denotes the complex conjugate. This implies that $|D_1| = |D_2|$. In addition, if it is required that at $y = 0$,

$\eta_{II} = b \exp i\theta$ where θ may include an arbitrary phase and b is real, then $D_1 + D_2$ is real (from Eq. 2.2.21b) and, therefore, $D_1 = D_2^*$. This means that the amplitude of Ψ_{II} is wavelike in the y-direction, but the waves are standing waves. Hence, waves travel only in the x-direction.

By setting γ^2 to zero and using Equation 2.2.18, which is the dispersion relation for this case, curves in the wave number-Richardson number plane can be found which separate the regions for the different types of solutions. Equation 2.2.18 can be rewritten as:

$$(c^2 - 1)^2 k^2 + kc^2(c^2 + 2\alpha c + 1) - \frac{c^4 \alpha^2}{2} = 0$$

with

$$\overline{Ri} = \frac{c^2}{2}\left(k^2 + \frac{\alpha^2}{4}\right) \quad .$$

Then, c can be used as a parameter to find the values of k and Ri. Two branches are found, one for $c < 1$ and the other for $c > 1$. These are shown in Figure 2.2.3 for the case where $\alpha = 10^{-3}$. These curves correspond to one root of the quadratic equation for k. The other root corresponds to $k < 10^{-6}$ and can be neglected for the purposes of this discussion. The regions of wavelike amplitudes of the perturbation are shown on Figure 2.2.3.

As stated previously, the conditions leading to breakdown of the flow by secondary waves are that the secondary waves be unstable and of much smaller scale than the primary wave, and that the group velocity of the secondary waves be equal to the phase velocity of the neutral primary wave. The group velocity of an unstable wave generated by shear at an interface, where the velocity of the fluid is discontinuous,

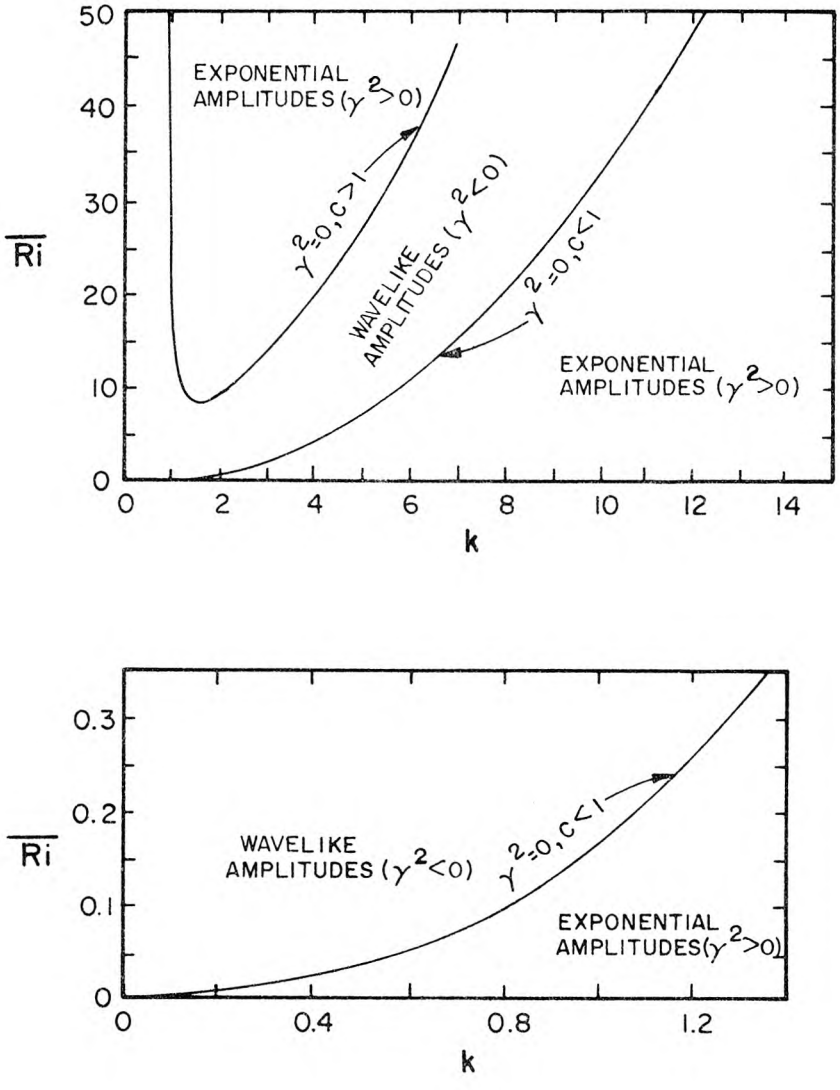

Figure 2.2.3 Regions for the various types of solutions of Equation 2.2.12, for $\alpha = 0.001$. Curves correspond to $\gamma^2 = 0$ (linear amplitudes).

is given by the mean of the velocities on either side of the interface (cf. the Kelvin-Helmholtz problem). Therefore, the group velocities of the secondary waves at the interfaces are given by:

$$c_g(1) = \frac{1}{2}\left(1 + \frac{\partial \Psi_I(1)}{\partial y} + \frac{\partial \Psi_{II}(1)}{\partial y}\right) = \frac{1}{2} + u_m^+ \qquad (2.2.26)$$

$$c_g(-1) = \frac{1}{2}\left(-1 + \frac{\partial \Psi_{III}(-1)}{\partial y} + \frac{\partial \Psi_{II}(-1)}{\partial y}\right) = -\frac{1}{2} + u_m^- \qquad (2.2.27)$$

Substituting the results for the stream functions, one finds that

$$u_m^+ = -\eta_I k(c-1)(1-\frac{1}{2c}) \qquad (2.2.28)$$

$$u_m^- = \eta_{III} k(c+1)(1+\frac{1}{2c}) \qquad (2.2.29)$$

These relations hold for all values of γ. Therefore, for breakdown to occur at the upper interface, it is required that

$$c_g = c = \frac{1}{2} - \eta_I k(c-1)(1-\frac{1}{2c})$$

or

$$c(c-\tfrac{1}{2}) = -\eta_I k(c-1)(c-\tfrac{1}{2}) \ . \qquad (2.2.30)$$

For the lower interface the requirement is

$$c(c+\tfrac{1}{2}) = \eta_{III} k(c+1)(c+\tfrac{1}{2}) \qquad (2.2.31)$$

If $c \neq \pm \frac{1}{2}$, then the requirements are

$$c_b^+ = \frac{\eta_I k}{1+\eta_I k} \tag{2.2.32a}$$

and

$$c_b^- = \frac{\eta_{III} k}{1-\eta_{III} k}$$

where c_b^+ and c_b^- are used to denote the phase speeds of the primary wave which are required for breakdown to occur on the upper and lower interfaces, respectively.

As k becomes small, this condition approaches that found by Landahl and Criminale (1977) for the Kelvin-Helmholtz problem.

The conditions that $c = 1/2$ or $c = -1/2$ correspond to cases where $u_m^+ = 0$ or $u_m^- = 0$. In either of these cases, secondary waves are trapped but not focused. Using the dispersion relation (Eq. 2.2.23) one can find values of k and $\overline{Ri}$ for the case that $c = 1/2$. These curves are plotted in Figure 2.2.4 for $\alpha = 10^{-3}$ and for a range of values of k and $\overline{Ri}$. These curves indicate wave numbers of primary waves, for given values of $\overline{Ri}$, at which secondary waves can be trapped, leading to breakdown. It is to be noted that, because of the factor involving tanh, there are multiple values of $\overline{Ri}$ for a given wave number k, when γ^2 is negative. In addition, it is noted that when $c = 1/2$, the condition for breakdown on the lower interface is

$$\eta_{III} = \frac{1}{3k} \tag{2.2.33}$$

Since it is required that the wavelength of the primary wave be smaller than the density interface thickness, (say, less than 1/2 the interface thickness), k is at most 2π. (Recall that the density interface extends from +1 to -1, therefore the unit length is 1/2 the density interface

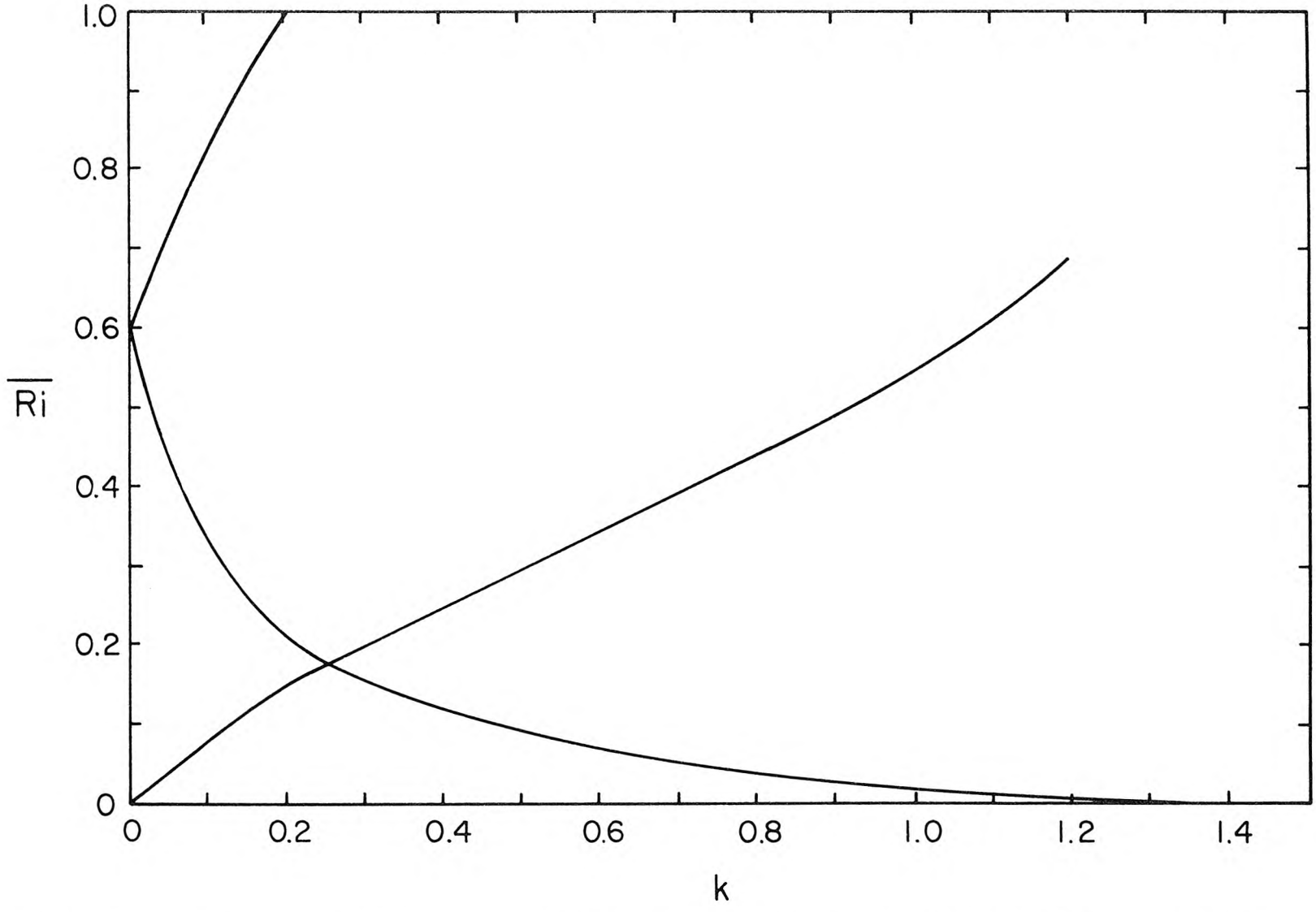

Figure 2.2.4 Wave trapping condition ($c = 1/2$) for $\alpha = 0.001$. Note multiplicity of solutions, and that wave trapping can occur at large values of $\overline{Ri}$.

thickness.) Therefore, η_{III} must be greater than 0.05. For $k < 1/3$, η_{III} must be greater than 1, a deflection which is clearly outside the range permitted by the small perturbation assumption. However, it is fair to say that when $1/3 < k < 2\pi$, and $c = 1/2$, secondary waves can be focused, leading to breakdown, on the lower interface, while at the same time secondary waves are trapped on the upper interface. A similar result is true when $c = -1/2$.

The main result is, then, that a density-stratified shear flow may become unstable and break down, *even when the mean-Richardson number is large.* The periodic nature of the solutions, for this case with a continuous density profile, leads to this somewhat surprising conclusion. The nature of the breakdown is not well predicted by this simple model; it is not clear from the theory that the breakdown will lead to the onset of turbulence throughout the interfacial region or just locally at the edges. At any rate, one would expect to find that an otherwise stable layer can suddenly become unstable locally, with turbulent mixing the result.

2.3 Turbulent Mixing with Buoyancy Effects

In this section, several relationships are presented which characterize the turbulent mixing in a fluid with a stable density-stratification. The derivations presented, which are based on the work by Ellison (1957), indicate relationships between the flux-Richardson number, R_f, the quantity $\overline{v'\rho'}/\sqrt{\overline{v'^2}}\sqrt{\overline{\rho'^2}}$, and the mean-Richardson number $\overline{Ri}$.

Ellison (1957) used Equations 2.1.10, 2.1.11 and 2.1.12 to derive the relationship

$$\frac{K_H}{K_m} = \frac{\overline{q^2}\ \overline{v'^2}(1 - R_f/R_c)}{\overline{u'v'}^2 (1 - R_f)^2 \frac{t_2}{t_3}} \qquad (2.3.1)$$

where

$$R_c \equiv \left(1 + \frac{2\overline{q^2}}{\overline{v'^2}} \frac{t_1}{t_2}\right)^{-1}$$

$$t_1 = \overline{\rho'^2}/2\varepsilon_\rho$$

$$t_2 = \overline{q^2}/\varepsilon$$

$$t_3 = \overline{\rho'v'}/\varepsilon_{\rho v} \quad \text{and}$$

K_m/K_H is the previously defined turbulent Prandtl number.

Ellison neglected horizontal gradients and "the diffusion terms like $\frac{\partial \overline{u'\rho'^2}}{\partial z}$," as well as pressure terms and considered the system to be in a steady state. Ellison (1957) pointed out that Equation 2.3.1 indicates that there is a critical value of $R_f = R_c$, where K_H/K_m goes to zero and estimated this value to be 0.15 or less. In making this estimate, he assumed $t_1/t_2 = 1$ and used values of $\overline{q^2}$ measured in neutral conditions.

Arya (1972) pointed out that while Ellison's theory predicts that K_H/K_m monotonically decreases to zero with increasing stability, his data indicate that it approaches a constant non-zero value as R_f approaches a critical value. However, Arya's data only show K_H/K_m as a function of R_f over a range of $0 < R_f < 0.06$. The data of Ellison and Turner (1960) show K_H/K_m as a function of $\overline{Ri}$; they found K_H/K_m decreasing to much smaller values than Arya (1972), but still not to zero, even at $R_f \approx 0.15$.

While Ellison (1957) assumed t_1/t_2 was constant, Arya (1972) in fact found that the quantity increased with increasing values of R_f. Arya then proposed a model in which the conservation equation for $\overline{u'v'}$ was used with Equation 2.1.12, and the term $\overline{p' \frac{\partial u'}{\partial y}}$ was retained. He found a critical value of R_f between 0.15 and 0.25.

In both these analyses, the term $\frac{\partial \overline{q^2 v'}}{\partial y}$ was neglected. However, there are some situations in which this term is relatively large. If one considers the flow of a stably stratified fluid over a rough boundary, then there will be a substantial production of turbulent energy at the boundary. The turbulent flux of turbulent energy away from the boundary is given by the term $\overline{q^2 v'}$; the gradient of this quantity gives the rate of decrease of turbulent energy at a point. If one considers the turbulent energy balance at a point well above the rough bed, where the velocity gradient may be small, then the term $-\frac{\partial \overline{q^2 v'}}{\partial y}$ may very well be of the same order or larger than the production term $-\overline{u'v'} \frac{\partial \bar{u}}{\partial y}$, and the turbulent flux of turbulent energy may well dominate Equation 2.1.12.

Equation 2.3.1, then, is rederived here without neglecting the term $\frac{\partial \overline{q^2 v'}}{\partial y}$. By neglecting horizontal gradients, and pressure correlation terms, and assuming a steady state as before, one reduces equations 2.1.10, 2.1.11, and 2.1.12 to

$$\overline{v'\rho'} \frac{\partial \bar{\rho}}{\partial y} + \varepsilon_\rho = 0 \quad , \tag{2.3.2}$$

$$\overline{u'v'} \frac{\partial \bar{u}}{\partial y} + \frac{\partial \overline{q^2 v'}}{\partial y} + \frac{\overline{v'\rho'} g}{\rho_o} + \varepsilon = 0, \quad \text{and} \tag{2.3.3}$$

$$\overline{v'^2} \frac{\partial \bar{\rho}}{\partial y} + \frac{\overline{\rho'^2} g}{\rho_o} + \varepsilon_{\rho v} = 0 \quad . \tag{2.3.4}$$

Here, $\overline{v}$ and $\overline{w}$ are assumed to be zero. Following the procedure of Ellison (1957), one finds "after a little algebra,"

$$\frac{K_H}{K_m} = \frac{\overline{q^2}\ \overline{v'^2}(1 - R_f/R_c + E)}{\overline{u'v'}^2 (t_2/t_3)(1 - R_f + E)^2} \tag{2.3.5}$$

where $$E = \frac{\partial \overline{q^2 v'}}{\partial y} \Big/ \overline{u'v'}\ \frac{\partial \overline{u}}{\partial y}$$

and all other terms are defined as in Equation 2.3.1.

One immediately sees the effect of retaining the term $\frac{\partial}{\partial y}\ \overline{q^2 v'}$; the new critical value of R_f is now

$$R_f\Big|_{crit} = (1+E) \Big/ \left(1 + \frac{2\overline{q^2}}{\overline{v'^2}}\ \frac{t_1}{t_2}\right) = (1+E)R_c \ . \tag{2.3.6}$$

Equation 2.3.5 can also be rewritten as

$$\overline{Ri} = \frac{R_f\ \frac{t_2}{t_3}\ \overline{u'v'}^2\ (1 - R_f + E)^2}{(1 - R_f/R_c + E)\ \overline{q^2}\ \overline{v'^2}} \ . \tag{2.3.7}$$

Thus, even at large values of $\overline{Ri}$, indicating stable flows, one would expect to find a non-zero value of K_H, and, hence R_f, if the quantity E is sufficiently large. If E is zero (Ellison's equation) then the R_f can approach the value R_c, but never reach it except as $\overline{Ri} \to \infty$. Here, with $E \neq 0$, R_f can attain larger values.

Following Ellison again, the relationship for $\overline{v'\rho'} \,/\, (\overline{v'^2}\ \overline{\rho'^2})^{1/2}$ is found to be:

$$\frac{\overline{v'\rho'}^2}{\overline{v'^2}\ \overline{\rho'^2}} = \frac{1 - R_f/R_c + E}{2\,\frac{t_1}{t_3}\,(1 - R_f + E)} \quad . \tag{2.3.8}$$

For large values of E, $\overline{v'\rho'} / (\overline{v'^2}\ \overline{\rho'^2})^{1/2}$ has nearly the same value here as in the limiting neutral case found by Ellison, as would be expected, since $E \gg 1$ and $E \gg R_f$ imply that buoyancy effects are small. In addition, as $R_f \to (1+E)R_c$, the vertical flux of buoyancy would vanish.

Although Equations 2.3.7 and 2.3.8 are more general than Ellison's equations, they are certainly more difficult to use, because an understanding of the term $\overline{\frac{\partial q^2 v'}{\partial y}} \Big/ \overline{u'v'}\ \frac{\partial \bar{u}}{\partial y}$, as well as dissipation rates, is required. However, if there is a significant source of turbulence away from the point of measurement, then this term must be taken into account.

It is fairly obvious that a laminar flow with a stable value of $\overline{Ri}$ will not mix unless it is perturbed in some way. If waves in the laminar flow cause local instabilities so that mixing occurs, then the production term $-\overline{u'v'}\ \partial\bar{u}/\partial y$ will dominate the mixing process. If, however, external turbulence is generated, the diffusion term $\partial\overline{q^2 v'}/\partial y$ will dominate the mixing process unless the turbulence also causes local instabilities in the mean flow, in which case both terms will be important.

One may also find that in some portions of a density-stratified flow E is a significant factor, while in other portions it is insignificant. An example might be a strongly stratified flow over a rough bed. Below the laminar interfacial layer E may be important, while within the laminar layer it may not be. In such a case one would

expect R_f to approach a critical value near the laminar region. Then, as the interfacial region is crossed, both E and R_f would decrease. Hence, one might expect to find a range of values of $\overline{Ri}$ in this flow for which R_f approaches a critical value and then goes to zero (since K_H/K_m vanishes when $E \to 0$ and $R_f \to R_c$) as the turbulent-laminar interface is crossed.

When buoyancy effects are relatively small in a flow, then one might expect K_H/K_m to remain near unity if E is large, regardless of $\overline{Ri}$. In this case R_f may take on large values, much larger than R_c. Hence, the retention of the term $\frac{\partial \overline{q^2 v'}}{\partial y}$ in Equation 2.3.3 seems to be important if there is a source of turbulence in the flow. Equations 2.3.7 and 2.3.8 will be used in later analysis of experimental data.

2.4 Spectral and Other Properties of Turbulent Flows

In this section, properties of turbulent flows which one would expect to find in a density-stratified shear flow are examined. In particular, the spectral characteristics of density-stratified shear flows are discussed as are some properties of coherent structures in turbulent shear layers. The two-dimensional mixing layer is not considered here, as it is discussed in Section 2.6.

2.4.1 Spectral Considerations

As has been well established in past work (e.g. Gibson and Schwarz (1963)), the (-5/3) power law of Kolmogoroff (1941) works surprisingly well in spectral considerations of turbulent flow. From Kolmogoroff's theoretical work, one expects to find in a homogeneous turbulent velocity field a domain of wave numbers (the inertial subrange), in

which the power spectrum, $\Phi(k)$, of the velocity fluctuations behaves as $k^{-5/3}$. Kolmogoroff's argument was that the dissipation rate of turbulent energy, ε, was important in this range, and with dimensional arguments, one finds

$$\Phi(k) = e_1 \varepsilon^{2/3} k^{-5/3} \tag{2.4.1}$$

where e_1 is a constant. For large wave numbers, viscous effects are important, so that again by dimensional arguments, Equation 2.4.1 should be valid for a range of wave numbers

$$k < e_2 (\varepsilon/\nu^3)^{1/4} \quad .$$

For a one-dimensional spectrum, e_1 and e_2 are found to be about 0.5 and 0.1 respectively (Gibson, Vega and Williams (1974), Gibson and Schwarz (1963)).

In the inertial subrange, the spectrum of scalar quantities, such as temperature, should also follow the (-5/3) power law (Corrsin (1951), Obukhov (1949)). In this case, Gibson and Schwarz (1963) have found

$$\Phi_T(k) = e_5 \chi \varepsilon^{-1/3} k^{-5/3} \tag{2.4.3}$$

where χ is the dissipation rate for $\overline{T'^2}$ (related to ε_ρ, the dissipation rate for $\overline{\rho'^2}/2$) and e_5 is a constant approximately equal to 0.4 (Gibson and Schwarz (1963), Kaimal *et al.* (1972)) but it may be as high as 1.2 in some stratified flows (Gibson *et al.* (1970)).

As pointed out by Batchelor (1959) the spectrum of scalar fields, such as temperature, may have a domain of wave numbers above the inertial subrange in which the molecular diffusive properties of the scalar are

important. In this case Batchelor found

$$\Phi_T = e_3 \chi \left(\frac{\nu}{\varepsilon}\right)^{1/2} k^{-1} \qquad (2.4.4)$$

where e_3 is a constant. Gibson *et al.* (1970) found this viscous-convective subrange for wave numbers greater than about $(\varepsilon/\nu^3)^{1/4}/30$.

In a density-stratified fluid, there may exist a domain of wave-numbers where buoyancy, rather than dissipation, dominates the flow (Turner (1973), Gibson *et al.* (1974), Williams and Gibson (1974)). In this subrange one would expect the important parameters to be the wave number and the Brunt-Vaisala frequency, $N = \left(\frac{-g\ \partial\bar{\rho}/\partial y}{\rho_o}\right)^{1/2}$. As discussed by Turner (1973) this leads to a power spectrum of the form

$$\Phi = e_4 N^2 k^{-3} \qquad (2.4.5)$$

where e_4 is a constant. This range would be valid for wave numbers less than the value $e_6(N^3/\varepsilon)^{1/2}$; Gibson *et al.* (1974) found that e_6 is near unity. Turner (1973) points out that this "buoyancy subrange" should be found in a region where turbulence from an external source is mixing the fluid, so that there is an energy transfer through the spectrum. Turner argues that one would not expect to find this subrange in a region where breaking internal waves are the dominant cause of mixing. Thus, in a two-layered density-stratified shear flow in which turbulence is produced at a lower boundary, one would expect to find the "buoyancy subrange" at the bottom of the interface, where buoyancy forces dominate the flow, but mixing also occurs because of the boundary-generated turbulence. (It should be pointed out that Lumley (1964)

also found the form of Equation 2.4.5 in considering the spectrum of "nearly inertial turbulence in a stably stratified fluid." Lumley's derivation required locally inertial turbulence and with this assumption he found a spectral form on the complete buoyancy-inertial subrange. See also Phillips (1966, p. 232) for a discussion.)

In an internal wave field, the power spectrum of temperature or velocity fluctuations is likely to be highly dependent upon the way in which the waves are produced. Garrett and Munk (1972) proposed a model of the scales for internal waves which indicates that $\Phi \propto k^{-p}$. The factor p, however, must be determined experimentally. Recent measurements of the spectra of temperature fluctuations in the ocean by Eriksen (1978) indicate that p is in the neighborhood of 2 to 2.5; the large range of values is probably indicative of the fact that the nature of the production of internal waves is important.

In summary, there are several patterns of behavior of the power spectra of velocity and temperature fluctuations in a density-stratified shear flow. In an internal wave field, one would expect to find Φ behaving like k^{-p} where $p \approx 2$. In a turbulent region, Φ and Φ_T should behave like k^{-3} in the "buoyancy subrange," and $k^{-5/3}$ in the inertial subrange. Φ_T should behave like k^{-1} in the viscous-convective subrange.

2.4.2 Coherent Structures in Turbulent Fields

Since it has now been well established that large coherent structures exist in turbulent shear flows, a few comments will be made on their possible effects in a density-stratified shear flow. Here,

the primary concern is with boundary-generated turbulence; the nature of the free shear layer is discussed in Section 2.6. For reviews of recent work in this area, one is referred to Willmarth (1975) and Laufer (1975).

An important feature of large turbulent structures is that they are identifiable and that a significant fraction of the total mixing which occurs in a turbulent flow, occurs as a direct result of the large turbulent structures (Lu and Willmarth (1973), Willmarth (1975), Wallace *et al.* (1977)). The work of Wallace *et al.* (1977) indicates that the structures can be identified with properly programmed computers. Wallace *et al.* observed the time history of u' at a point and noticed a general pattern consisting of a long period of slow deceleration followed by a relatively sudden acceleration. This pattern can be recognized in many velocity signals measured in laboratories (Wallace *et al.* (1977); Laufer (1975), Figure 9 taken from Sunyach (1971); Thomas (1977)). Lu and Willmarth (1973) found that a large fraction (over 75% of the total momentum flux) occurs during bursts in the boundary layer. It is, then, quite apparent that large structures play a major role in the mixing processes in a turbulent shear flow.

Because the large structures are responsible for a large amount of the mixing, one might expect that they are equally responsible for a large fraction of the flux of turbulent kinetic energy. Thus, the presence of structures might be detected in time histories of quantities such as q^2v' and q^2u'.

The effect of these structures on the mixing in stratified flows is difficult to surmise. The mixing might be found to be intermittent, and to correspond to turbulent bursts. On the other hand, the bursts may produce large internal waves which simply propagate away or propagate and later break. In this latter case, the turbulent heat flux may not be well correlated with the presence of turbulent bursts. Furthermore, the nature of the structures may be altered by the presence of buoyant forces. These ideas, presented in a qualitative manner here, are discussed in more detail in Chapters 6 and 7.

2.5 Integral Balances

In this section, integral balances of heat (or buoyancy), momentum and some turbulent quantities, which will be useful in later analysis of data, are presented. These balances are derived by the integration over the vertical coordinate of Equations 2.1.6 through 2.1.12. The following assumptions are made. First the flow is assumed to be steady and two-dimensional; hence, derivatives in time and in the lateral (z) coordinate vanish. The mean velocity in the lateral coordinate (w) is assumed to be zero. Fluctuating quantities and the mean vertical velocity are assumed to vanish at the free surface. Second derivatives in the streamwise direction are also neglected. Integrals are taken from a fixed depth to the free-surface, which is assumed to be free of surface waves.

When integrated, the continuity equation (2.1.7) becomes

$$\frac{\partial}{\partial x}\int_{-y_o}^{0} \overline{u}\, dy - \overline{v}(-y_o) = 0 \qquad (2.5.1)$$

where $-y_o$ is a fixed depth beneath the free-surface. The x-momentum equation (2.1.6) becomes

$$\frac{\partial}{\partial x}\int_{-y_o}^{0}(\bar{u}^2+\frac{\bar{p}}{\rho_o}+u'^2)dy = \bar{u}\,\bar{v}\Big|^{-y_o}+\overline{u'v'}\Big|^{-y_o}+$$

$$+\nu\left(\frac{\partial\bar{u}}{\partial y}(0)-\frac{\partial\bar{u}}{\partial y}(-y_o)\right). \qquad (2.5.2)$$

Here $\bar{v}$ is not assumed to vanish except at the free-surface.

The heat (or buoyancy) equation (2.1.8) becomes

$$\frac{\partial}{\partial x}\int_{-y_o}^{0}\bar{u}\,\bar{B}\,dy = \bar{B}\,\bar{v}\Big|^{-y_o}+\overline{B'v'}\Big|^{-y_o} \qquad (2.5.3)$$

The final equations to be considered here are the conservation equations for turbulent kinetic energy (2.1.12) and temperature (or buoyancy) fluctuations (2.1.10). These become, upon integration

$$\frac{\partial}{\partial x}\int_{-y_o}^{0}(\overline{q^2}\,\bar{u}+\overline{q^2u'})dy+\int_{-y_o}^{0}(\overline{v'B'}+\varepsilon)dy = \qquad (2.5.4)$$

$$\overline{q^2}\,\bar{v}\Big|^{-y_o}+\overline{q^2v'}\Big|^{-y_o}-\frac{1}{\rho_o}\int_{-y_o}^{0}\left(\overline{u'\frac{\partial p'}{\partial x}}+\overline{v'\frac{\partial p'}{\partial y}}\right)dy-\int_{-y_o}^{0}\overline{u'v'}\,\frac{\partial\bar{u}}{\partial y}\,dy\ ,$$

and

$$\frac{\partial}{\partial x}\int_{-y_o}^{0}(\overline{B'^2}\,\bar{u}+\overline{B'^2u'})dy = \overline{B'^2}\,\bar{v}\Big|^{-y_o}+\overline{B'^2v'}\Big|^{-y_o}-$$

$$2\int_{-y_o}^{0}(\overline{v'B'}\,\frac{\partial\bar{B}}{\partial y}+\varepsilon_\rho)dy\ , \qquad (2.5.5)$$

where $\overline{u'v'}\,\frac{\partial \bar{u}}{\partial y}$ is assumed to dominate turbulent energy production and $\overline{u'B'}\,\frac{\partial \bar{B}}{\partial x}$ is assumed to be small compared to $\overline{v'B'}\,\frac{\partial \bar{B}}{\partial y}$. These integral conservation equations are used in later analysis of the experimental data.

2.6 Initial Mixing Layer

In this section, the two-dimensional mixing layer will be discussed briefly. This topic is of some importance to this study, since a two-dimensional mixing layer was produced at the inlet of the flume used in the experimental work.

The two-dimensional mixing region has been studied in great detail in the past (Liepmann and Laufer (1947), Wygnanski and Fiedler (1970), Winant and Browand (1974), Brown and Roshko (1971, 1974), Koop (1976), Dimotakis and Brown (1976)); the mean velocity profiles and mean turbulent quantities (fluctuating velocities and higher moments) have been well documented by Liepmann and Laufer (1947) and Wygnanski and Fiedler (1970). More recently, the two-dimensional mixing layer has been found to be dominated by two-dimensional vortices (Brown and Roshko (1974), Winant and Browand (1974)). Koop (1976) has studied the mixing layer at low Reynolds numbers, with buoyancy effects. Dimotakis and Brown (1976) have studied the mixing layer, and particularly the large vortex structures, at high Reynolds numbers.

The work of Koop (1976) is of particular interest since buoyancy was important in his experiments. Koop used a small open channel flume (10 cm by 10 cm in cross-section). Salt and fresh water, initially separated by a splitter plate, entered his flume through a contraction

section. The velocity differences between the two layers were in the range of 4 to 10 cm/s; the relative density differences were in the range of about 0.004 to 0.034. Koop found that the vortex structure, which developed in the experiments with small initial Richardson number (which was based upon the value of ℓ_u^* at the inlet of the test section), collapsed and the flow approached a laminar state downstream. From dimensional arguments, the collapse distance x_c should be proportional to $\frac{1}{2}(U_1 + U_2)(U_1 - U_2)/\frac{\Delta\rho}{\rho_o} g$, where U_1 and U_2 are the mean velocities of the upper and lower layers, respectively, and $\frac{\Delta\rho}{\rho_o}$ is the relative density difference between the layers. Koop took the collapse distance to be the distance at which the bulk-Richardson number (based on the maximum-slope thickness of the density profile) reached its maximum value, and found $x_c^* \equiv x_c \frac{\Delta\rho}{\rho} g / \frac{1}{2}(U_1 + U_2)(U_1 - U_2) \approx 6$. From his photographs, however, the vortices appear to begin to collapse at a dimensionless distance somewhat less than 6 or 7, indicating that some mixing occurs during the collapse process. In addition, Koop found that the bulk-Richardson number after the collapse was around 0.32. His results were basically in agreement with the work of Thorpe (1973b) and Baddour and Chu (1977). Koop did not measure the vertical velocity, and consequently was unable to measure momentum and heat fluxes directly. Thus, there are many aspects of the dynamics of the collapse process about which one can only speculate.

Thorpe (1973b) also made measurements of the growth and collapse of vortices in a two-dimensional mixing layer. However, Thorpe's experiments had two counter-flowing layers, and the vortices developed

in time, rather than in space and time as in a mixing layer from a splitter plate. As was pointed out by Koop (1976), the vortices which developed in the experiments of Thorpe were skew-symmetric, while in Koop's experiments the vortices were initially asymmetric, and grew from the low speed side to the high speed side. (Koop (1976) pointed out that the solution from linear stability theory, for a spatially growing homogeneous shear layer, is asymmetric with respect to the centerline.) The asymmetry in the initial development of the shear layer is very likely responsible for the asymmetric profile of $\sqrt{\overline{\rho'^2}}$ that Koop found. From the photographs the vortices are seen growing largely toward the high speed side, with a rather sharp, but "wavy," line between the mixing layer and the fluid on the low speed side. There is little wonder that the fluctuations of ρ quickly fall to zero on the low speed side, while they slowly fall off on the high speed side.

There is another aspect of mixing layers which is interesting. Thorpe (1973b) found that the ratios of the length scales for the velocity profile and the density profile (ℓ_u^*/ℓ_T^* in the present notation) in the interface were in the range of 1.1 to 1.4 after collapse. Chu and Vanvari (1976) also found the ratio of the length scales, ℓ_u^*/ℓ_T^*, to be greater than one downstream. Koop (1976) found that in some cases the ratio increases to as much as six far downstream ($x \frac{\Delta\rho}{\rho} g / \frac{1}{2} (U_1 + U_2)(U_1 - U_2) > 40$), although in the region of the collapse (and shortly after it), Koop's data indicate that the ratio is slightly greater than one. It would appear then, that the

velocity profile changes more drastically than the temperature (or buoyancy) profile during the collapse, but this is not surprising. Up to the point of collapse (where it appears that ℓ_u^*/ℓ_T^* is near unity from the data of Koop (1976) and Chu and Vanvari (1976)) the vortex structure is largely responsible for the mixing processes and one might expect only small differences in the mixing processes for momentum and heat. During and after the collapse, pressure and viscous forces may play a large role in the transfer of momentum. (Pressure forces certainly play a large role before the collapse, as can be seen from the difference in the symmetries of the profiles of buoyancy and velocity fluctuations).

Dimotakis and Brown (1976) made measurements in a homogeneous mixing layer. They concluded that the amalgamation of vortices was responsible for mixing in the shear layer and that the entrainment process, in which outside fluid is pulled into the vortices, was an almost distinct process from the fine scale mixing process. Thus, the mixing process in the shear layer can be described as, first, an entrainment process, in which outside fluid is "rolled" into the vortices, and then a mixing process as vortices coalesce. Ultimately, if buoyancy effects cause the layer to collapse, there is a final mixing as fluid particles move toward their positions of neutral buoyancy.

2.7 A Review of Experiments on Mixing in Density-Stratified Shear Flows

2.7.1 Entrainment Rates in Stratified Fluids--Shear Flow Experiments

In the past twenty years, a variety of experiments have been conducted to determine mixing rates in density-stratified shear

flows. For the most part, the experiments have involved large initial values of the bulk-Richardson number. Usually, an attempt is made to find a mixing rate or an entrainment rate as a function of a bulk-Richardson number. In this section, the major findings of some of these experiments are discussed.

Keulegan (1949) observed mixing in stratified flows and found that the parameter $\nu \frac{\Delta\rho}{\rho} g/U^3$, now referred to as the Keulegan number, was significant, for when this parameter fell below a critical value, he observed that waves in the flow began to break. The Keulegan number is, in fact, formed by combining the Reynolds number with the Froude number (the inverse of the bulk-Richardson number) in such a way that the length scale is removed. Turner (1973) points out that viscosity really may not be that important, and in view of the small range of Reynolds numbers in Keulegan's experiments, it is difficult to determine viscous effects.

Ellison and Turner (1959) conducted several experiments to determine mixing rates between a thin moving layer of fresh water and a deep quiescent layer of salt water. Defining the entrainment velocity u_e as the gradient of the volume flux per unit width of the buoyant fluid ($\frac{d}{dx} U_1 h_1$ where U_1 is the mean speed and h_1 is the depth of the buoyant layer), Ellison and Turner found that u_e/U_1 was proportional to $U_1^2/g \frac{\Delta\rho}{\rho_o} h_1 = R_b{}^{*-1}$.

This inverse relationship between the bulk-Richardson number and entrainment rate has been found in a variety of experiments. This result is somewhat physically pleasing in that it implies that the rate of gain of potential energy is directly proportional to power input into

the system. As will be seen later in this discussion, this inverse relationship is not always found, and whether the entrainment rate is proportional to R_b^{*-1} or $R_b^{*-3/2}$ or some other power of R_b^* is open to question.

Lofquist (1960) found results similar to those of Ellison and Turner for the flow of a thin layer under a deep buoyant layer. R_b^* varied from about 1.5 to about 50 in Lofquist's experiments, compared to 0.1 to about 0.8 in the experiments of Ellison and Turner (1959). However, Lofquist used an initial value of the bulk-Richardson number in presenting his results, while Ellison and Turner used a local value.

Kato and Phillips (1969) applied a shear stress to the surface of a linearly stratified fluid in an annular ring and again found the entrainment rate, u_e/u_*, to be proportional to the inverse of a bulk-Richardson number, this time based on the shear velocity u_* and the depth of the mixed layer. The reason for the dependence on the depth of the mixed layer is not altogether obvious, unless one considers that the turbulence generated at the surface must travel that distance to the interface. (One would expect to find the turbulence levels decreasing with the distance from the generation point.) The data are rather scattered, but there does appear to be a general trend to $u_e/u_* \propto R_b^{*-1}$ for $12 < R_b^* < 400$.

Moore and Long (1971) measured the buoyancy flux in a two-layered stratified shear flow, and found that the dimensionless vertical buoyancy flux, $\overline{B'v'}/2\Delta U \frac{\Delta\rho}{\rho_o} g$, where $2\Delta U$ and $\Delta\rho$ were the respective differences between the velocities and densities in the two layers, was proportional to the inverse of a bulk-Richardson number, $R_H^* = H\Delta\rho/\rho_o(2\Delta U)^2$, where 2H was the depth of the apparatus (each layer)

being of depth H). In addition, they presented data which indicate that there is a linear relationship between the bulk-Richardson number based on the layer depth and a bulk-Richardson number, R_L^*, based on a measure of the interface thickness (actually, the distance over which the velocity gradient was approximately linear). Their values of R_H^* varied from 0.7 to 61.5, while R_L^* varied from 0.44 to 4.1, and the relationship between the two Richardson numbers is not perfect. There is, however, a linear trend, and while the data are scattered, it would indicate that the dimensionless buoyancy flux is also inversely proportional to R_L^*, a somewhat more pleasing variable than one based on the total depth of the system.

Moore and Long also demonstrated that their dimensionless buoyancy flux was proportional to an entrainment velocity, so that their results were comparable to other studies in which the entrainment rate was found to be proportional to the inverse of the bulk-Richardson number. Furthermore, Moore and Long concluded that this inverse relationship was valid for a wide variety of conditions if the bulk-Richardson number was less than about five.

Pedersen (1974) conducted experiments similar to those of Ellison and Turner (1959) and found that the entrainment rate was proportional to R_b^{*-1}, where R_b^* is based on the depth of the thin upper layer. In addition, Chu and Vanvari (1976) found the entrainment rate in an experiment similar to that of Ellison and Turner (1959) to fall much faster with increasing R_b^* than did Ellison and Turner, although it is difficult to determine a power-law relationship from their data.

For the most part, experiments with shear tend to indicate that an entrainment rate is proportional to the inverse of a bulk-Richardson number. However, physically different scales for length and velocity have been used in the experiments, leading one to suspect that the results may be, in part, fortuitous. Results of experiments discussed in the next section will bear this out, particularly in the case of the experiments of Kato and Phillips (1969) which were perhaps the most extensive of those discussed in this section.

2.7.2 Entrainment Rates in Stratified Flows-- Oscillating Grid Experiments

Turner (1968) examined the mixing across a density interface in a stirred tank. Unlike the previously mentioned experiments, no mean shear was involved in these measurements. Turner found that the mixing rate was proportional to R_b^{*-1} for thermally stratified water, but when salt was used to stratify the water, the mixing rate fell to $R_b^{*-3/2}$, for $R_b^* > 7$. The rate was the same for $R_b^* < 7$ and the power law was between -1 and -1.5. Turner's bulk-Richardson number was based on the stirring frequency and an unknown turbulent length scale. It is interesting to note that Moore and Long found that the relationship between the mixing rate and the bulk-Richardson number was the same whether heat or salt was used to stratify the system. However, when a mean shear is present in the system, an additional mixing process is involved, since turbulence produces waves which cusp at the interface and wisps of fluid are broken off from the cusps by the mean shear.

In order to "calibrate" the stirred tank, Thompson and Turner (1975) measured turbulence levels in the tank used by Turner (1968).

Horizontal velocity fluctuations were measured and they found that the horizontal velocity fluctuations were proportional to $y^{-3/2}$ where y was the vertical distance from the oscillating grid stirrer. They were, however, unable to find a general relationship between the generated turbulent energy and the frequency, stroke length and geometry of stirrer, but were able to use the results to recalculate Turner's (1968) results in terms of dimensionless variables. Because they found a linear relationship between the horizontal turbulent fluctuations at a point and the stirring frequency, the relationship between the mixing rate and bulk-Richardson number was the same as determined by Turner (1968) using arbitrary length scales.

This leaves, however, the annoying -3/2 power law found by Turner (1968) for salt stratified systems. Long (1975) considered this problem and pointed out that on dimensional grounds, the turbulent velocity in a stirred tank was proportional to the frequency of oscillation of the stirrer only in the homogeneous case. Furthermore, he showed that a weak dependence of $\sqrt{\overline{u'^2}}$ on the bulk-Richardson number ($\sqrt{\overline{u'^2}} \propto R_b^{*-1/6}$) would change the -3/2 power found by Turner to a -1 power. Long's discussion leaves the -1 power law found in the thermally stratified experiments of Turner to be explained by the small Peclet number of those experiments. Still, when R_b^* is less than seven in Turner's experiment (corresponding to high Peclet numbers for either stratification), the power law can be chosen anywhere in the range of -1 to -1.5.

However, Hopfinger and Toly (1976) measured turbulent fluctuations in a stirred tank, but included measurements near a density interface. They found that, contrary to the expectations of Long (1975), the

turbulent velocity fluctuations were independent of the presence of the interface. Hence, the -3/2 power law seems to be general for high Peclet numbers in stirred tank experiments.

Long (1975) also observed that the flux-Richardson number may not, in many cases, be an important quantity. Obviously, in stirred-tank experiments with no mean shear, $R_f = \infty$, but turbulence still exists. Long suggests that instead of using the term $-\overline{u'v'}\,\frac{\partial \bar{u}}{\partial y}$ in the definition of R_f, a term like $\overline{u'^3}/\ell$, where ℓ is a length scale of the turbulence, is more appropriate, in that such a term might incorporate all turbulence generation, transport (such as $\frac{\partial}{\partial y}\,\overline{q^2 v'}$) and dissipation rates. At any rate, it seems apparent both from experimental observations and from examination of Equation 2.1.12 that the turbulence properties at the interface are the important parameters and not necessarily the turbulence properties far from the point of interest.

Linden (1975) used the same apparatus as used by Turner (1968) and Thompson and Turner (1975) to determine the energy loss due to internal waves. Several experiments were made, some with a sharp density gradient between two mixed layers and some with an interface separating a mixed layer and a linearly stratified layer. His main conclusions were, first, that the mixing rate was proportional to the *rate of input of turbulent kinetic energy at the interface*, and <u>not</u>, in general, to the rate of supply of kinetic energy at the top of the mixed layer, and second, that energy loss by internal waves can cause a reduction in mixing. His first conclusion seems to mean that relationships found between bulk quantities involving, for example, the total depth of the

mixed layer, may be more a matter of good luck than a matter of relating physically meaningful quantities, particularly for experiments in which a parameter used in the analysis was not varied.

Linden's second main conclusion indicates that some energy was lost to internal waves in the experiments of Kato and Phillips (1969). Kantha (1975) and Kantha, Phillips and Azad (1977) conducted experiments similar to those of Kato and Phillips (1969) except that they used homogeneous layers above and below the density interface, thus eliminating the energy losses by internal waves in the constant density gradient layer of the experiments of Kato and Phillips. Using a bulk-Richardson number based on the shear velocity at the surface (where a stress was applied) and the depth of the mixed layer, Kantha found no simple power law relationship between the entrainment rate and R_b^*. The mixing rates found by Kantha were higher than those found by Kato and Phillips, indicating the ability of the linear density-gradient to transmit energy in internal waves, and they found that the entrainment rate might be proportional to R_b^{*-1} for $90 < R_b^* < 400$, although the data are very scattered. Over the whole range of measurements ($30 < R_b^* < 1000$), there was no simple power law relationship. Their explanation was that different effects dominate the local mixing at different Richardson numbers, as was evident from some of their visual observations.

Thus, one is left with a rather confusing picture. While some investigations find the mixing rate to be proportional to R_b^{*-1}, (a somewhat physically pleasing result) there is enough evidence that this is not a general relationship to suggest that relating local mixing

processes to bulk fluid quantities may be a futile (and certainly frustrating) effort. The large scatter in the data certainly reinforces this opinion.

2.7.3 Turbulent Diffusivities in Stratified Flows

Kullenberg (1977) measured entrainment rates in the field under conditions in which the wind shear stress at the surface of the body of water was large. Kullenberg found that the entrainment rate was proportional to the inverse of a bulk-Richardson based on the shear velocity, u_*, and the depth of the mixed layer. However, Kullenberg also calculated K_H/K_m and found that $K_H/K_m \propto \overline{Ri}^{-1}$. Kullenberg was unable to relate K_H/K_m to the bulk-Richardson number, or the entrainment rate to $\overline{Ri}$. In addition, Kullenberg's measurements of K_H/K_m as a function of $\overline{Ri}$ are consistent with those of Thorpe (1973b).

One difficulty arises here, however, in that Kullenberg's (and Thorpe's) measurements imply that for $\overline{Ri} > 0.1$, $R_f \approx 0.05$, a much lower value than found by Ellison and Turner (1960). Arya and Plate (1969) found in boundary layer measurements in a wind tunnel, that K_H/K_m varied only slightly with $\overline{Ri}$ or R_f, for $\overline{Ri} < 0.1$, but that $R_f \approx 0.06$ at $\overline{Ri} = 0.1$. The measurements of Kullenberg extended over a range of values of $\overline{Ri}$ from 0.05 to over 10; in contrast, Ellison and Turner (1960) found R_f in the range of 0.1 to 0.2 for $\overline{Ri}$ between 0.1 and 1. Part of the difficulty here can be explained by the fact that Kullenberg calculated K_m from an empirical relationship involving the wind speed over the surface and the values of K_m thus obtained are apparently surface values, while K_H is calculated from the dispersion of dye in the mixed layer.

As has been demonstrated already, turbulence properties at the top of a mixed layer are not necessarily related to turbulence properties below.

At any rate, there is some evidence (Thorpe (1973b), Ellison and Turner (1960), Lofquist (1960)) that K_H/K_m decreases rapidly with $\overline{Ri}$, while the measurements of Arya and Plate (1969) show K_H/K_m approximately constant. The resolution of this may well be found in Equation 2.3.5, which indicates that K_H/K_m depends not only on $\overline{Ri}$ but also on $E \equiv \frac{\partial}{\partial y} \overline{q^2 v'} \Big/ \overline{u'v'} \frac{\partial \bar{u}}{\partial y}$. In particular, Equation 2.3.5 shows that if E is small, then K_H/K_m will go to zero as R_f approaches the value R_c. It appears, then, that when turbulence is generated outside the region of interest (at a free surface or solid boundary, for example) then the turbulent flux of turbulent kinetic energy may be an important parameter, and may not be neglected.

In summary, it appears that a knowledge of turbulence properties in a density-stratified flow is required in order to relate bulk properties of the flow to mixing rates. When one assumes that the mixing rate at an interface (a local process) is related to bulk flow conditions, one is essentially assuming a straightforward and simple transfer of energy by turbulence. As pointed out by List (1978, private communication) to assume the former is, in essence, to assume that a simple closure based on bulk flow conditions is valid for turbulence models. If a simple closure based on the bulk flow properties exists, it has thus far eluded many researchers. Thus, it appears that bulk fluid properties alone are insufficient to describe mixing processes in a stratified fluid and that more detailed knowledge of turbulence properties is required.

2.7.4 Qualitative Observations of Stratified Flows

In this section, stratified flows are considered from a somewhat more qualitative point of view. In particular, visual observations and gross features of the flow will be considered.

Schiller and Sayre (1973) measured mean speeds and temperatures in an open-channel density-stratified flow. They described several features of the flow which are of interest here. First of all, Schiller and Sayre found that secondary currents which were obvious in the homogeneous flow, were not present in the stratified flow. The secondary circulation consisted of a number of cells of streamwise vortices; it was apparent that the buoyancy of the thin surface layer inhibited the vertical velocity to such a degree that the secondary circulation was unable to develop. Furthermore, the secondary circulation moves slow fluid from the boundaries to the surface of the channel; hence, one would expect the velocity at the surface to increase when the flow is stratified. This was, in fact, found to be the case by Schiller and Sayre, who also predicted this on the basis of a somewhat simplified model of a stratified, open-channel flow.

French (1978) reported measurements in an open-channel density-stratified flow and found that the velocity of the surface decreased with stratification, with flow conditions otherwise held constant. French's measurements were made in a channel 40 cm wide, with depths of flow from 37 cm to 48 cm, while the experiments of Schiller and Sayre (1973) were made in a flume 76 cm wide, with depths of flow from 7.6 cm to 15.2 cm, so the wall effects were probably much greater in

French's experiments. French predicted that the surface velocity would decrease with increasing stratification with a simplified theory, but he assumed $\overline{\rho' v'} = k^2 y^2 \frac{\partial \bar{u}}{\partial y} \frac{\partial \bar{\rho}}{\partial y}$ in his model, which, of course, implies that turbulent heat transfer is in the wrong direction. When the correct sign is added, the theory then predicts that the surface velocities will increase, contrary to French's measurements, but in agreement with those of Schiller and Sayre. Wall effects are very likely responsible for the discrepancy.

Csanady (1978) examined the velocity measurements of Lofquist (1960) and found that turbulent flow near a laminar density interface behaves much as flow near a solid boundary. In particular, Csanady was able to identify a viscous sublayer and a logarithmic buffer layer between the interface and the homogeneous layer. The results can vary, of course, due to the nature of internal waves at the interface, and due to the amount of mixing that takes place, but the nature of Csanady's results suggests that processes near solid boundaries and density interfaces may be similar.

The nature of turbulent mixing processes near and in a density interface is a subject of interest, and recent work by several investigators has produced some interesting observations. Woods (1968, 1969) observed instabilities in the thermocline in the Mediterranean Sea which led to turbulence and mixing. The instabilities were clearly of the Kelvin-Helmholtz type and occurred intermittently in regions of high density gradient. Woods (1968) concluded that the heat flux in the thermocline was controlled by the frequency of the formation of

turbulent patches through the Kelvin-Helmholtz instability. Woods (1969) characterized the mixing process as one in which Kelvin-Helmholtz instability leads to a patch of turbulence which entrains fluid until the local Richardson number is of order unity. The turbulence then decays to a thick laminar layer, which is slowly thinned by the action of weak turbulence in deep layers of low density gradient on either side of the mixed "sheet." As the sheet thins, the gradients across it increase and eventually the process is repeated. Thus, in Woods' analysis, ambient turbulence has only a secondary effect.

Thorpe (1978b) placed a string of thermistors in Loch Ness under stable conditions and found large turbulent billows, apparently arising from Kelvin-Helmholtz type instabilities. The billows he found had a vertical scale of several meters with a wavelength on the order of ten to twenty meters. Thorpe concluded that, on the basis of estimated diffusivities in the region where the billows were found, the Kelvin-Helmholtz instabilities play an important role in mixing in the ocean.

Wyatt (1978) studied films of the experiment carried out by Kantha, Phillips and Azad (1977) to determine the nature of the mixing processes at a density interface. There appear to be two basic types of mixing processes which can be seen near an interface; the two types are probably related and have been described by many investigators (Kato and Phillips (1969), Keulegan (1949), Moore and Long (1971)). The first type is usually seen at larger values of $\overline{Ri}$. In this case it appears that a turbulent eddy, or burst, hits the interface and deforms it in such a way that the crest of the newly formed internal

wave sharpens. Eventually, a wisp of fluid is broken off of the crest and mixed in the surrounding fluid and the internal wave relaxes. The second process involves billowing and breaking of smaller waves and is usually seen at lower values of $\overline{Ri}$. These two processes are not mutually exclusive, in that turbulent fluctuations can deform the interface in such a way that, in addition to wisps of fluid breaking from wave crests (or troughs) local instabilities along the phase of the waves can develop and cause mixing. Likewise, it appears probable that turbulence is largely responsible for the initial development of small waves which billow and break in low $\overline{Ri}$ interfaces. Wyatt (1978) examined interfacial mixing with these processes in mind.

There are several important results which Wyatt found from her investigations. Concentrating mainly on the "billowing" waves rather than the "wisping" waves, Wyatt found that the length scales of the Kelvin-Helmholtz type instabilities did not scale with the depth of the mixed layer above the interface. Again, this would indicate that local properties of turbulence are more important in determining mixing rates than bulk-flow properties.

In addition, Wyatt found that the instabilities were intermittent. The driving mechanism in the experiment was a shear stress applied to the surface of the fluid; it may well be that the resulting turbulence occurred in bursts. The bursts of turbulence would hit the interface and deform it slightly or simply increase the local shear rate for a short period of time, leading to the observations of intermittent Kelvin-Helmholtz type instabilities.

In summary, observations of stratified flows indicate that gross

features of flows can be drastically changed by relatively small stratifications (Schiller and Sayre (1973), Csanady (1978)). In addition, much of the mixing in interfacial regions appears to be the result of local shear instabilities, caused initially by externally generated turbulence, which do not scale well with bulk flow properties. This latter observation again leads to the conclusion that mixing processes are characterized by local turbulence properties, and not necessarily bulk flow properties.

CHAPTER 3

EXPERIMENTAL APPARATUS

3.0 Experimental Objective

The primary objective of this investigation was to determine experimentally the mixing properties of a two-layered density-stratified shear flow over a wide range of conditions. Several parameters were varied including the temperature difference (hence, density difference) and velocity difference of the two layers, as well as the turbulence level of the flow. The Keulegan number at the flume inlet was varied from zero (corresponding to zero density difference) up to about 0.3 (corresponding to a small velocity difference). In the first series of experiments, detailed temperature measurements were made at several cross sections along the flume. Later, vertical profiles of two velocity components and the temperature were measured at points along the centerline of the flume. The velocity and temperature measurements were recorded digitally and later processed to determine, among other things, the respective mean and fluctuating quantities, as well as the turbulent fluxes of heat and momentum. From these data, the mixing and friction in a density-stratified shear flow were determined over as wide a range of conditions as the apparatus permitted. A description of the experimental apparatus follows.

3.1 Flume Characteristics

Experiments were conducted in the 40-meter precision tilting flume

in the Keck Hydraulics Laboratory. The flume is 40 meters in length and has a cross section of 110 cm wide and 61 cm deep. The flume has been described in detail by Vanoni *et al.* (1967).

As shown in Figure 3.1.1, the flume has two separate pumps and return pipes. Originally, these two return lines were designed to be used separately, the 10 hp pump for low flows and the 30 hp pump for high flows. In this study, the flume was modified so that both pumps could be used simultaneously, the smaller for returning the upper layer water, and the larger for the lower layer. A second downstream hopper (Figure 3.1.2) was constructed of fiberglass and placed inside the existing downstream hopper. The fiberglass hopper was connected to the inlet pipe of the 10 hp pump by means of a flexible rubber boot allowing the flume to be tilted. The existing hopper was connected to the inlet of the 30 hp pump.

Figure 3.1.2 shows the two hoppers. A splitter plate constructed of fiberglass and plywood was installed in the last 2.4 meters of the flume. The plate had a flexible connection with the fiberglass hopper so that the vertical position of its upstream end could be adjusted. The side edges of the splitter plate were sealed tightly to the flume walls with a rubber seal. Thus, water leaving the flume above the splitter plate was returned through the 10 hp pump and the rest was returned through the 30 hp pump.

The inlet to the flume was also modified, as shown in Figure 3.1.3. The water returning through the 10 hp pump was brought through the wall of the inlet box and through a dividing wall. The dividing

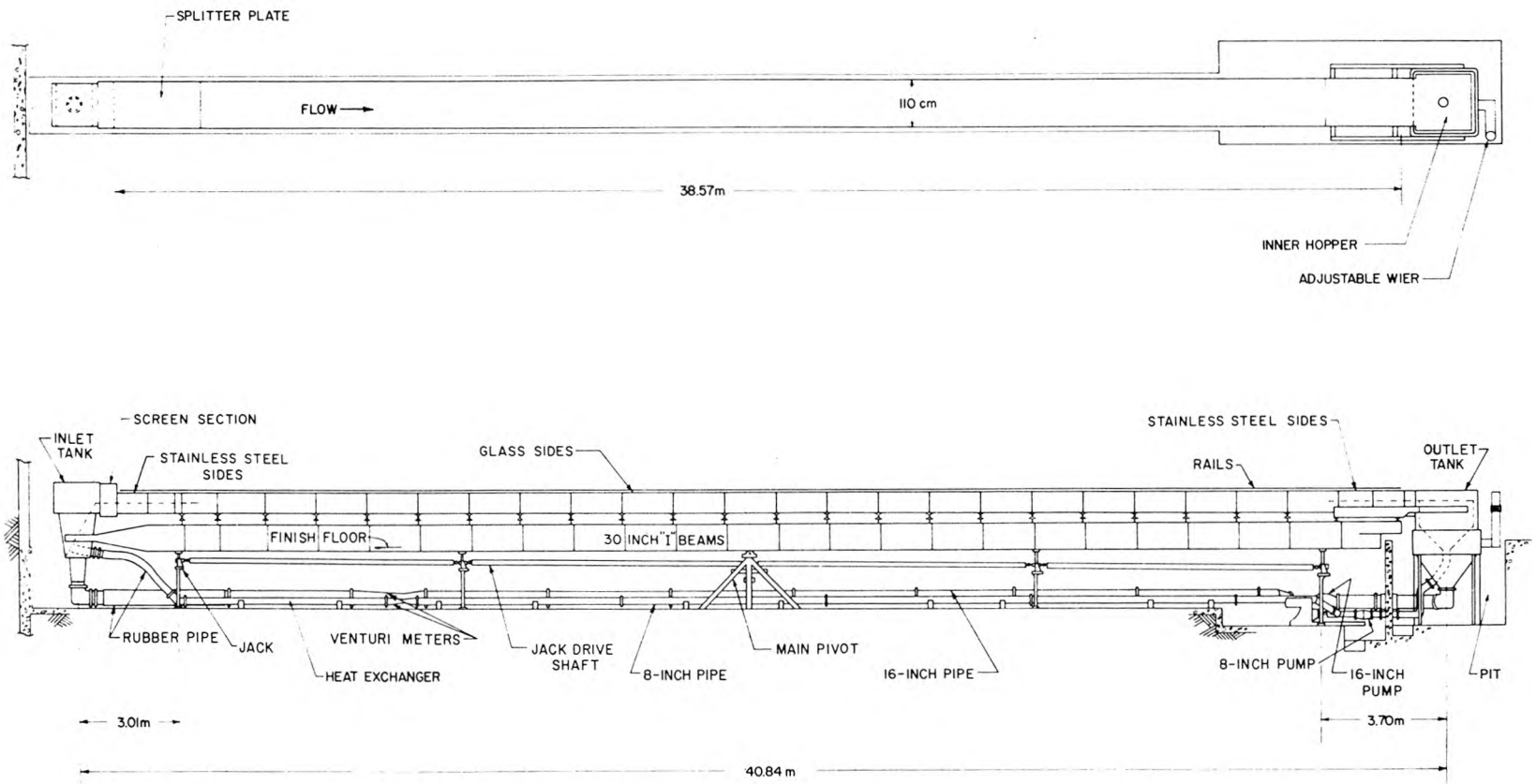

Figure 3.1.1 40-m flume used in experiments. Note splitter plates and separate return pumps for upper and lower layers.

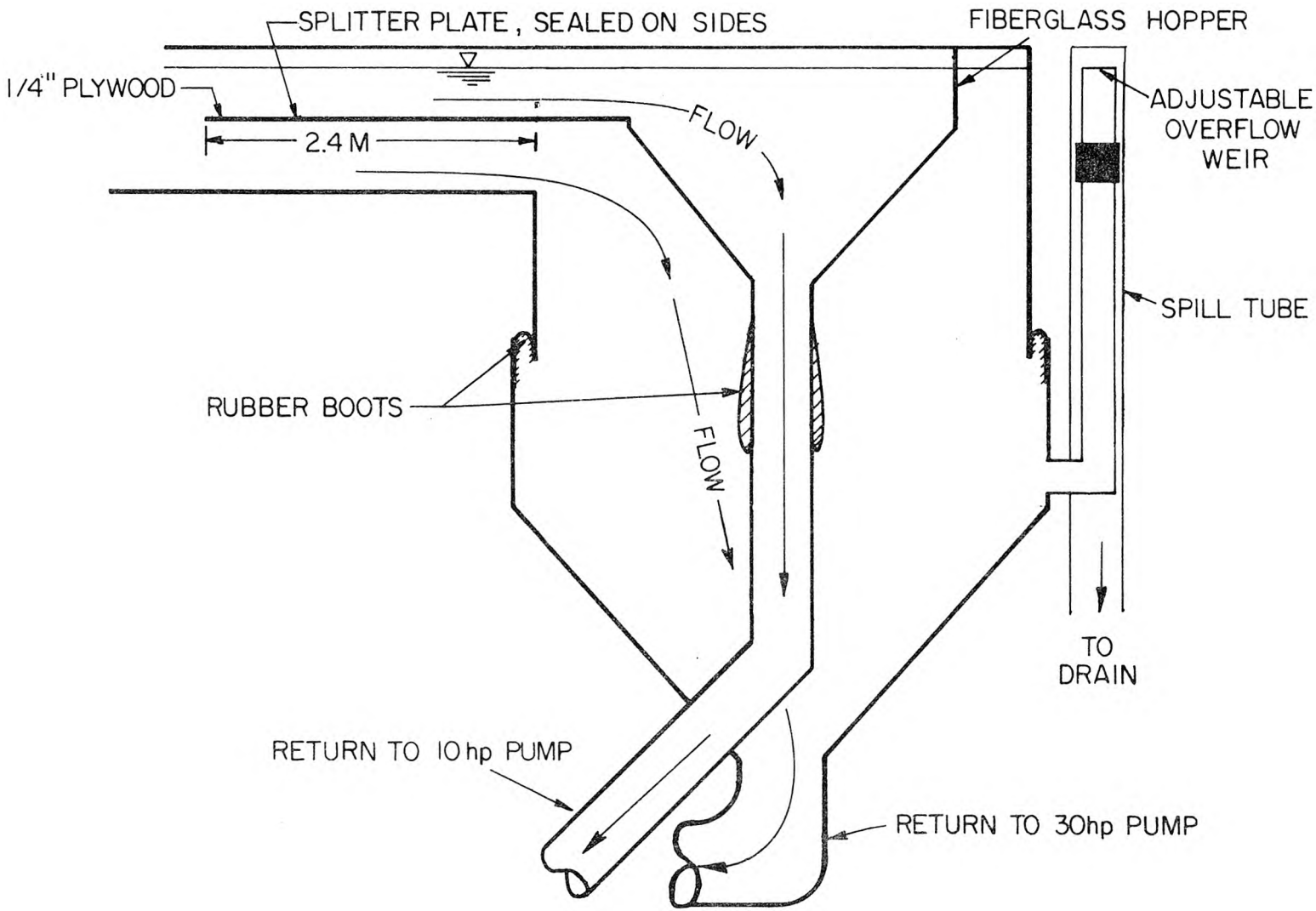

Figure 3.1.2 Flume outlet hoppers.

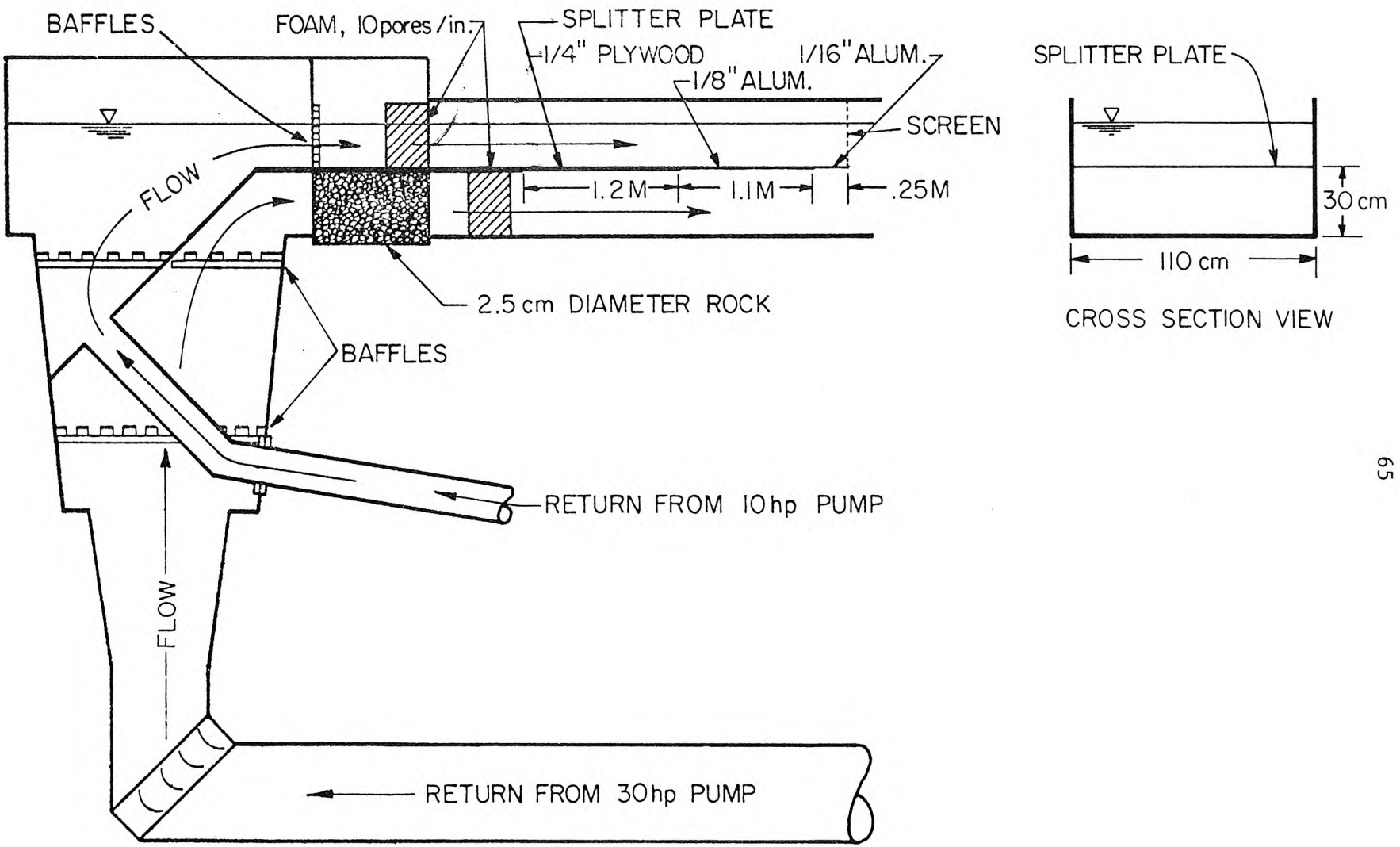

Figure 3.1.3 Flume inlet hopper and splitter plate.

wall was constructed of 1/2 in. plywood and fiberglass. The water returning through the 30 hp pump entered the flume below the dividing wall. The flow in both layers passed through a series of wood baffles and then turned the corner into the flume. The water in the lower layer passed through a section containing rocks with a mean diameter of about 2.5 cm and then through a 20 cm section of polyurethane foam (Scott Industrial Foam). The foam, which has about four pores per centimeter, greatly reduced the turbulence level in the water and produced a remarkably uniform flow.

The upper layer also passed through a 20 cm section of polyurethane foam as it entered the main channel. Both layers then traveled about 4 m before reaching the end of the splitter plate, which spanned the full width of the flume.

The splitter plate was about 4 m long, measuring from the section containing rocks. The first 1.4 m was constructed from 1/2 in. plywood and fiberglass, and the next 1.2 m used 1/4 in. plywood. Following the 1/4 in. plywood was a 1.1 m section of 1/8 in. (3.2 mm) aluminum plate, followed by a 25 cm section of 1/16 in. (1.6 mm) aluminum plate. The splitter plate was sealed along the flume walls and the trailing edge of the splitter plate was set approximately 30 cm above the flume bottom.

Finally, a vertical screen (14 x 18 x .011 galvanized window screen) was attached to the end of the splitter plate. The screen served two purposes. One was to support the splitter plate and prevent it from sagging in the middle, and the other was to improve

the flow in the upper layer. The screen had a tendency to flatten the velocity profile and reduce the size of the wake following the splitter plate.

It was found that the minimum discharge through the 30 hp pump was much larger than desired. Consequently, an orifice plate with a 12.5 cm diameter hole was placed in the return pipe (diameter of 40 cm) following the 30 hp pump. The discharges from the two pumps were measured with the existing Venturi meters installed in the return lines.

3.2 Heating and Cooling of the Water

Since the primary objective of this study was to investigate density-stratified shear flows, a method was needed to vary the densities of the two layers. It was determined that the addition of salt to increase the density of the lower layer would be impractical, for two reasons. First, corrosion would have been a problem because most of the flume is constructed of steel. Second, maintaining a constant density difference between the two layers for long periods in a recirculating flow is difficult when salt is used for stratification. The only remaining practical choice was to heat the upper layer.

Saturated steam at 50 psi (3.5×10^6 dyne/cm^2) was available in the laboratory. A heat exchanger was constructed from six 20 foot (6.1 m) lengths of 5/8 in. (1.6 cm) diameter copper tubing. The tubing was arranged in an hexagonal array and installed in a section of the return pipe following the 10 hp pump. The maximum heating rate with this system was about 120 kW.

Since the lower layer was heated slightly because of the mixing

which took place over the reach of the flume, a method was devised to cool the lower layer water before it returned to the flume inlet. A 4 in. (10.2 cm) vertical pipe was attached to the flume drain line (see Figure 3.1.2). The end of the pipe was open and the vertical elevation of the pipe end could be adjusted. Before an experiment, the lower layer was heated to about 27°C; then through the course of an experiment cold tap water was introduced through a hose into the downstream hopper near the inlet pipe to the 30 hp pump. The vertical pipe was adjusted so that the flume depth was as desired; as cold water (approximately 16°C) ran into the hopper, an equal volume of warm flume water ran out over the end of the vertical pipe. The end of the pipe had a sharpened edge, so that it was essentially a round, sharp-crested weir. With this method, the temperature difference at the inlet of the lower layer seldom varied by more than 0.04°C and the depth of the water never varied by more than 0.06 cm over an eight hour period.

Because the experiments were conducted with water heated to temperatures above that of the laboratory, a rather large amount of heat loss occurred from evaporation off the water surface. To reduce this heat loss, the flume was covered with polyethylene sheets. The sheets were attached to wooden frames which were placed on top of the glass sides. The air space between the polyethylene and the water quickly became saturated with water vapor, as was evident from the condensation on the polyethylene and the flume walls, and greatly reduced the heat loss from the flume.

3.3 Temperature Measurements

Thermistors were used to measure temperature in all experiments, and the characteristics of the two types used are given in Table 3.3.1. The glass bead thermistors were used in initial experiments to make general temperature measurements and the small, fast-response thermistors were used to make more detailed measurements.

Table 3.3.1 Thermistor characteristics.

Type	Head Diameter	Dissipation Constant Still Water	Response Time Moving Water	Resistance at 25°C
Small Bead Fenwall Elect. GA 51MC1	0.35 mm	0.75 mW/°C	20-25 ms	~200 kΩ
Glass Bead Veco 32A1	2.3 mm	(unknown)	~1 s	~2.5 kΩ

A glass bead thermistor is shown in Figure 3.3.1. The thermistor is approximately 2.3 mm in diameter by 10 mm long and is mounted in a stainless steel tube. The thermistor formed one side of a bridge circuit, shown in Figure 3.3.2. The resistors used in the circuit were precision metal-film resistors and an operational amplifier (Texas Instruments, SN741) was used to reduce the output impedance of the signal. The output signal had a response of about 50 mV/°C.

The glass-bead thermistors were used in a vertical rake of eight shown in Figure 3.3.3, and in a horizontal rake of ten thermistors, shown in Figure 3.3.4. Both rakes were mounted on carriages so that

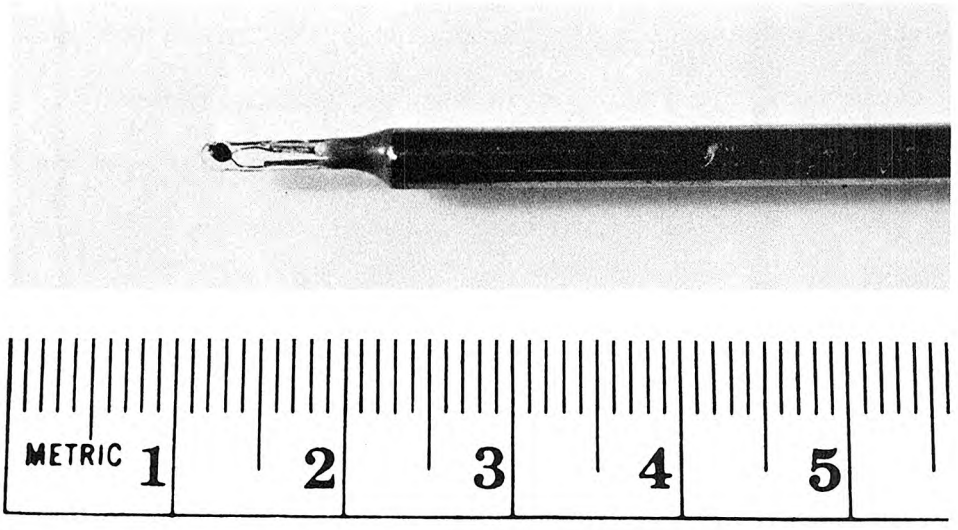

Figure 3.3.1 Photograph of a glass-bead thermistor.

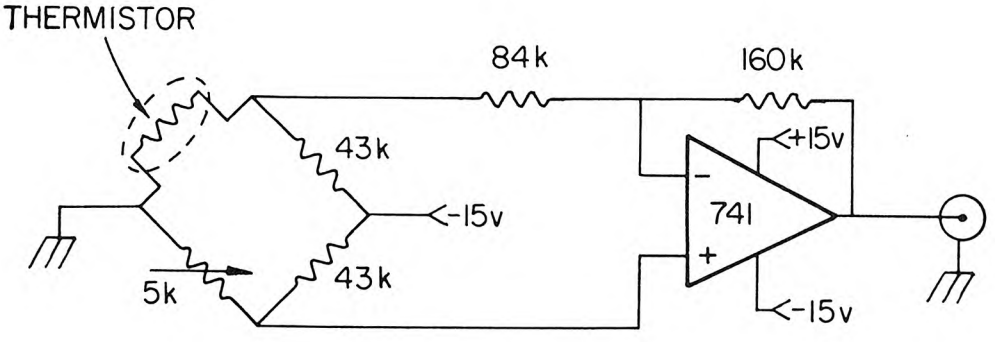

Figure 3.3.2 Glass-bead thermistor circuit.

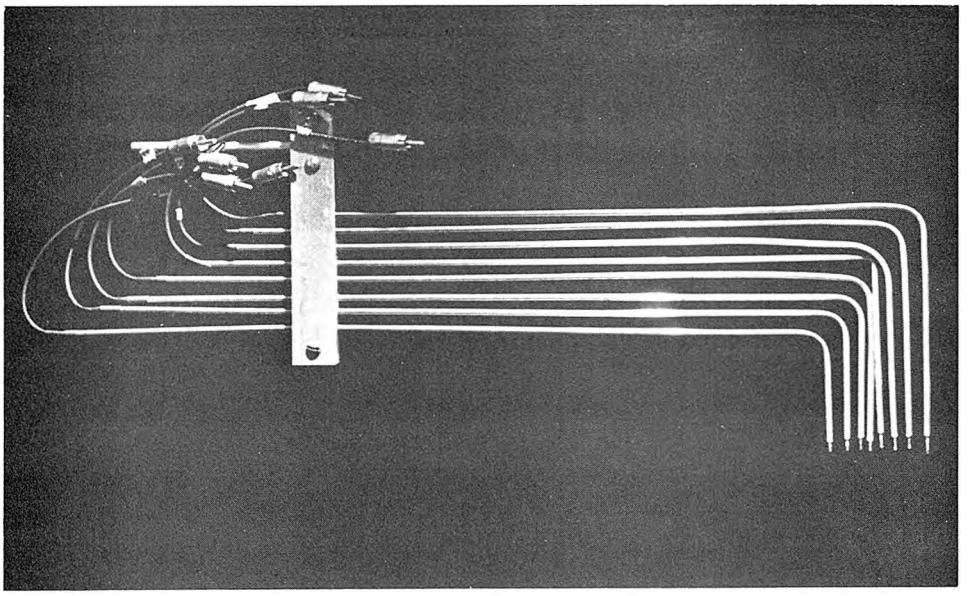

Figure 3.3.3 Photograph of the rake of eight glass-bead thermistors.

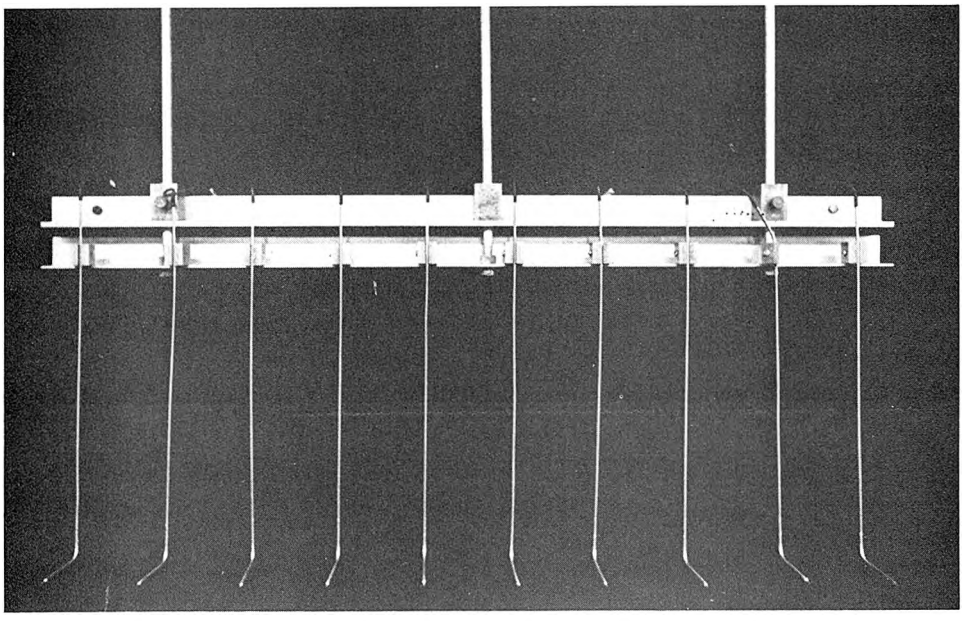

Figure 3.3.4 Photograph of the horizontal array of ten glass-bead thermistors.

they could be moved to any location along the reach of the flume. In addition, both could be raised and lowered. Hence, cross-sectional temperature measurements could be made with the probes.

A fast-response thermistor is shown in Figure 3.3.5. This thermistor has a diameter of about 0.35 mm and was mounted in a stainless steel tube. The thermistor formed one side of a bridge circuit shown in Figure 3.3.6, and a dual operational amplifier (Texas Instruments, SN558) was used to buffer, amplify and low-pass filter the signal from the bridge. All resistors used in the circuit were precision metal-film or wire-wound resistors. The current through the thermistors was approximately 3.8 μa, hence they dissipated approximately 2.2×10^{-3} mW. Using the dissipation constant from Table 3.3.1, it was found that the internal self-heating of the thermistors was approximately 0.003°C.

The signals from the fast-response thermistors were low-pass filtered, with a cutoff frequency at about 100 Hz; the filter had a roll-off of about 6 dB per octave. The amplified signal response was about 1.5 V/°C, and the output of the circuit could be offset so that the zero-level output would correspond to a convenient temperature level. The entire circuit was mounted in a small aluminum box and attached to the thermistor probe to eliminate noise inherent with long cables.

The response time of the thermistors was measured by suddenly plunging the thermistor into warm water (a simulation of a step-function of temperature change) and sampling the output signal at about 1000 Hz with the laboratory data acquisition system (see Section

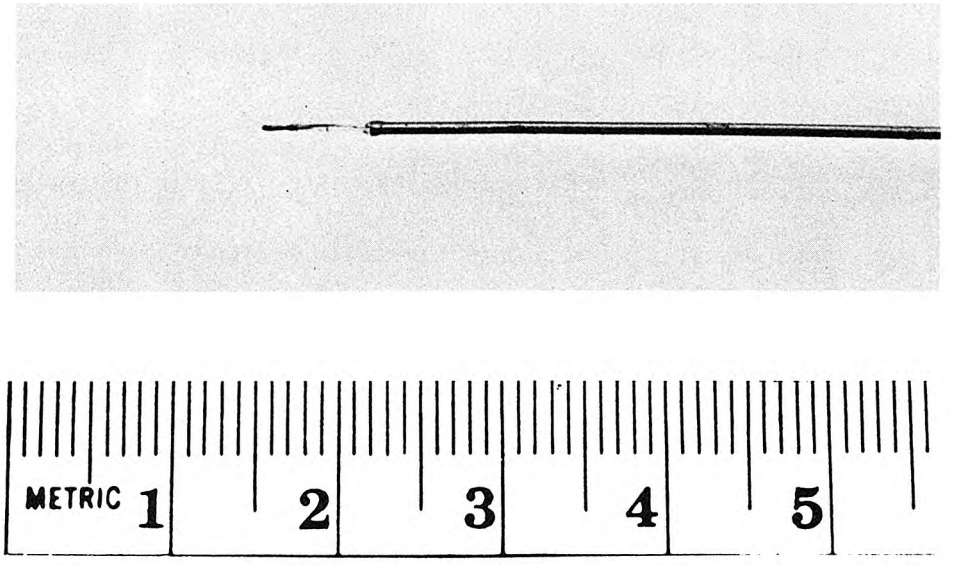

Figure 3.3.5 Photograph of a fast-response thermistor.

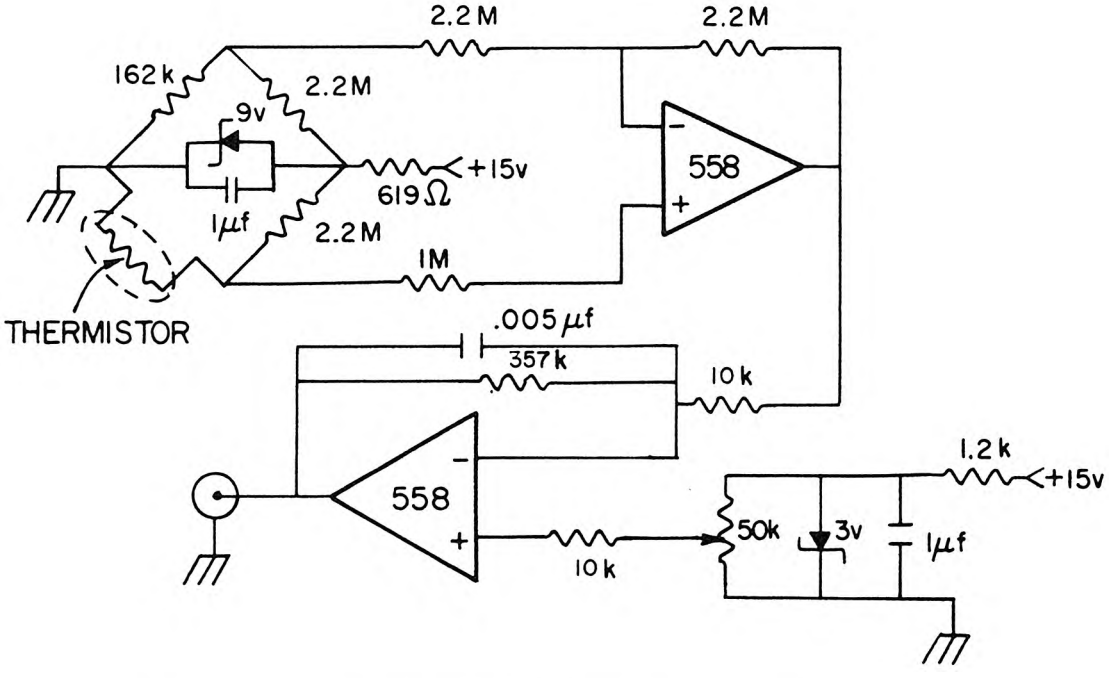

Figure 3.3.6 Fast-response thermistor circuit.

3.6). The response time, which is defined here as the time for the signal to reach 63% of its final value, was about 18 ms for the fast-response thermistors and about one second for the others. The transfer function, shown in Figure 3.3.7, was calculated from the ratio of the power spectrum of the thermistor output to the power spectrum of a Heaviside function, and indicates that the -3 dB point is at 10 Hz.

The root-mean-square noise level in the fast-response thermistors was less than 1 mV (corresponding to less than 10^{-3} °C) measured when the probe was in moving water of a constant temperature. The drift was less than 10 mV over an extended period, giving the thermistors an accuracy of better than 0.01°C. The noise level and drift of the glass bead thermistors gave an accuracy of about 0.04°C.

3.4 Velocity Measurements

In this study, a two-dimensional laser-Doppler velocimeter (LDV) system was used to make velocity measurements. The reference beam method, shown schematically in Figure 3.4.1 for a one-dimensional measurement, was used in the system. Only the essentials of laser-Doppler velocimetry will be discussed here; for a detailed explanation, the reader is referred to Durst *et al.* (1976) and Watrasiewicz and Rudd (1976).

In using the reference beam method, a laser beam is split and the two resulting beams are focused to a point. One of the beams, the reference beam, is very much dimmer than the other beam and is directed into a photodetector. The second beam is usually quite intense, and is referred to as the scattering beam. When a small particle in the

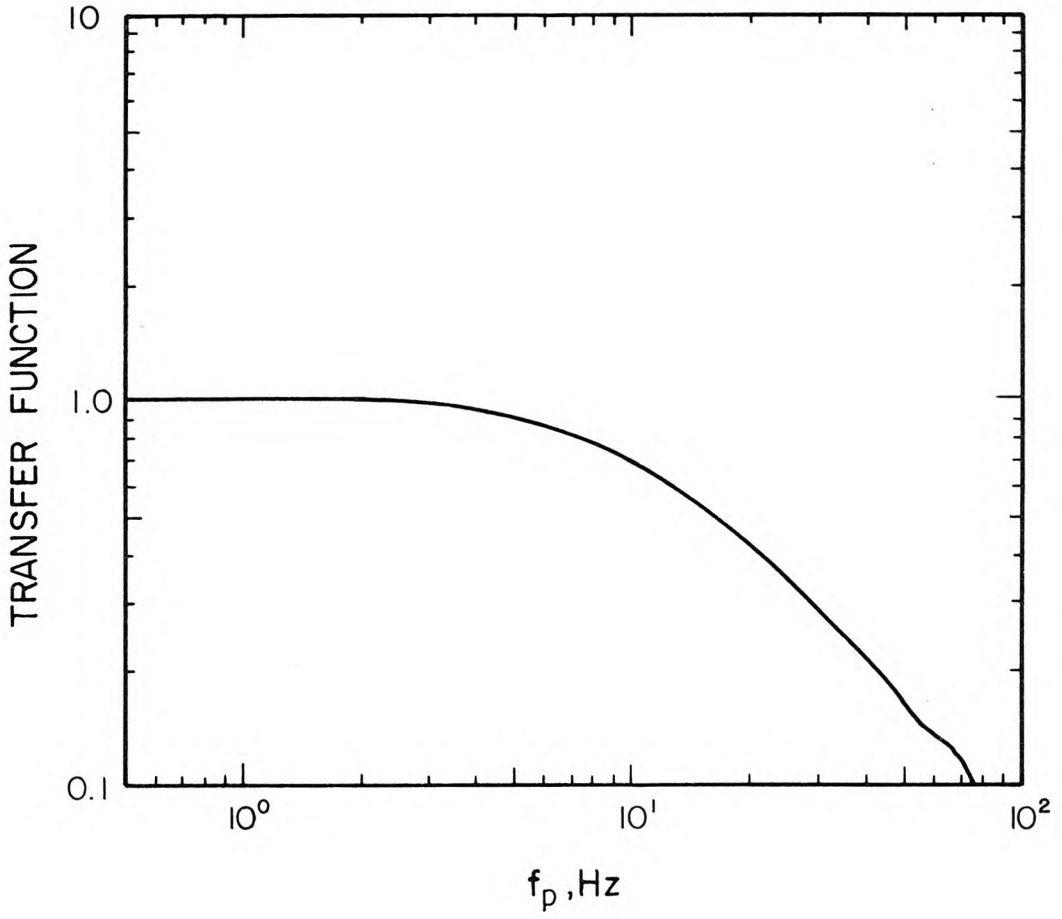

Figure 3.3.7 Transfer function for fast-response thermistor.

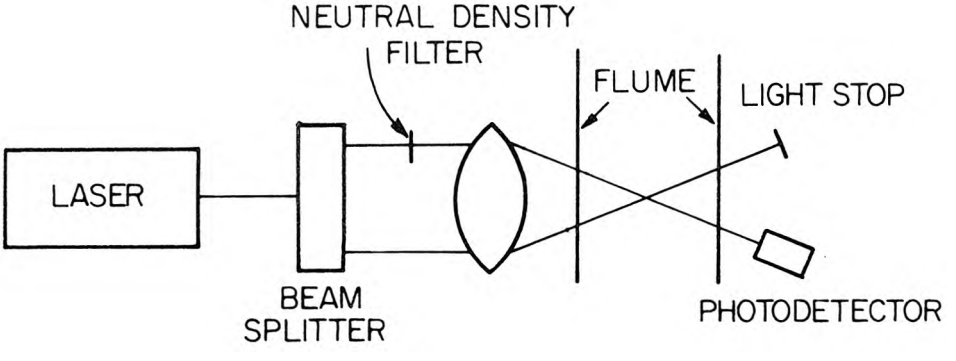

Figure 3.4.1 Reference beam system for laser-Doppler velocimetry.

fluid crosses the intersection of the two beams, it will scatter a small amount of light from the scattering beam into the photodetector. The light from the reference beam and the scattered light produce a current from the photodetector which has an amplitude:

$$i(t) = A(t) \cos \nu_D t + C(t) \tag{3.4.1}$$

where

t is the time,

A(t) and C(t) are functions which will, in general, depend upon the intensities of the two beams and the optical properties of the particle, and

ν_D is the Doppler frequency.

The quantity ν_D can be expressed as

$$\nu_D \approx n \vec{u} \cdot (\vec{e}_r - \vec{e}_s)/\lambda \tag{3.4.2}$$

where

$\vec{e}_s$ is the unit vector in the direction of the scattering beam,

$\vec{e}_r$ is the unit vector in the direction of the reference beam,

n is the index of refraction of the medium,

$\vec{u}$ is the particle velocity, and

λ is the wavelength of the laser light in a vacuum.

Here, the speed of the particle $|\vec{u}|$ is assumed to be small compared to the speed of light, c, and terms on the order of $|\vec{u}|^2/c^2$ are neglected.

The system designed and built for this study is shown in Figure 3.4.2. The laser source was a Spectra-Physics Model 120, 5 mW, Helium-Neon laser. The laser light first passed through a beam splitter, which produced two parallel beams of light, one of which had an intensity of about ninety per cent of the incoming beam, the other about five per cent. The dimmer of these beams passed through a radial diffraction grating which produced a vertical diffraction pattern.

The diffraction grating (manufactured by Dynamics Research Corporation) was a disk with a diameter of 7.5 cm and had 2048 equally spaced radial lines. The disk was mounted on the shaft of a synchronous motor (Hurst Corporation) which could rotate at 900 revolutions per minute. If ν_o is the frequency of the incident light, then the frequency of the k^{th}-order diffracted light has a frequency

$$\nu_k = \nu_o \pm MNk \tag{3.4.3}$$

where

N is the rotational speed of the diffraction grating,

M is the number of lines on the diffraction grating,

k is the diffraction order.

Thus, the rotating diffraction grating provides a convenient method for optically shifting the frequency of laser light (Stevenson (1970)).

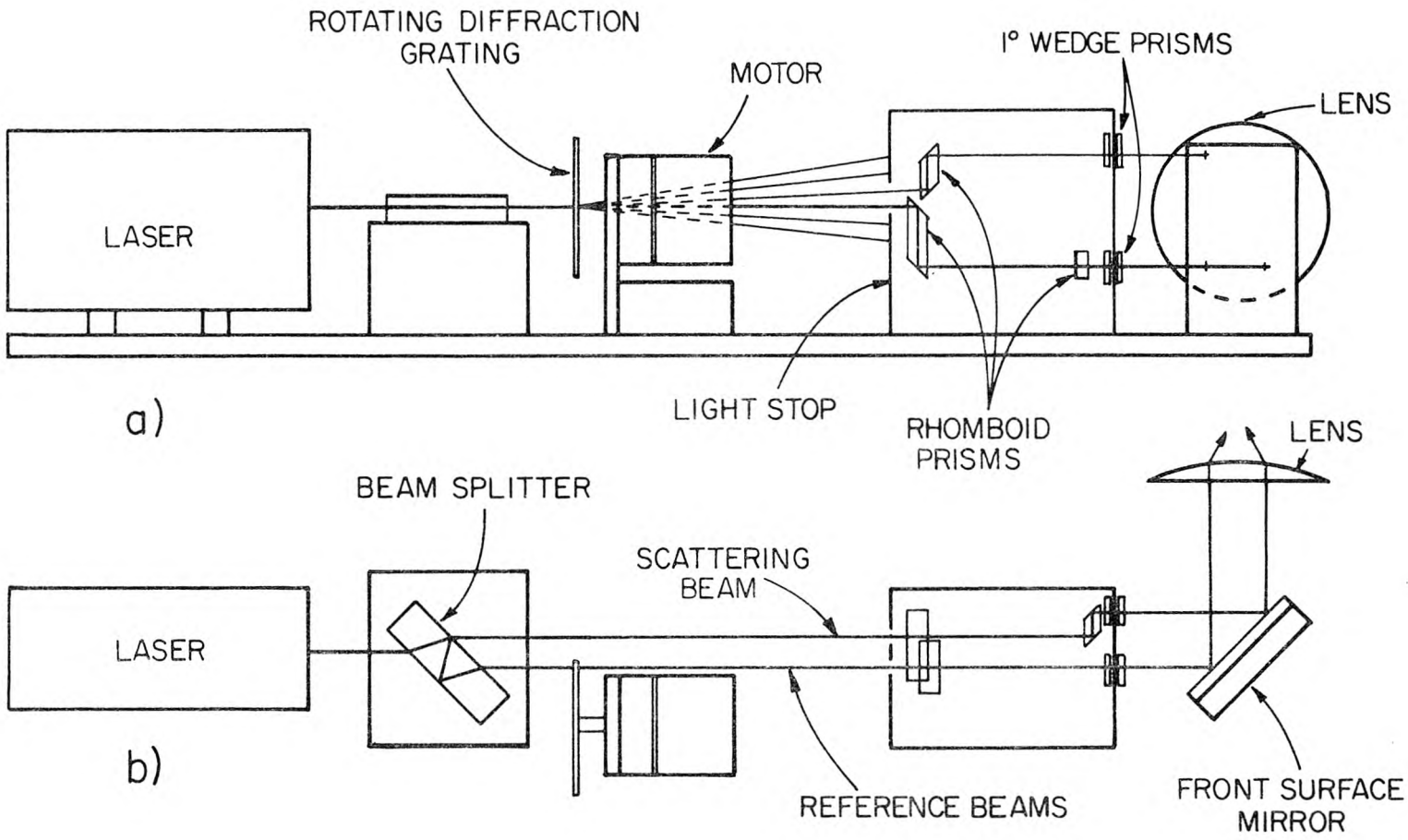

Figure 3.4.2 Optical arrangement for laser-Doppler velocimeter; a) elevation, b) plan view.

A light block followed the diffraction grating so that only the intense, undiffracted beam, and the zeroth and first-order diffracted beams passed to the rest of the optics. Following the light block, several rhomboid prisms were used to separate the beams. The intense, undiffracted beam (which became the scattering beam) and the first-order diffracted beam each passed through a separate pair of one-degree wedge prisms. Each wedge prism could be rotated independently, thus allowing fine adjustments to be made on the directions of the two beams. Finally, the three beams were turned ninety degrees by a front surface mirror and focused by a lens. The transmitting optics are shown in Figure 3.4.3.

Opposite the transmitting optics were two photomultiplier tubes (RCA 8645), into which the two reference beams were directed. In front of the photomultiplier tubes were band pass filters which reduced the amount of extraneous light entering the photodetectors.

The beams were aligned in the following manner. The optics were all firmly attached to a 1/2 in. (1.25 cm) thick jig plate and the plate was adjusted so that the zeroth order diffracted beam (reference-beam 1) was level. Then the two wedge prisms, through which the first-order diffracted beam (reference-beam 2) passed, were rotated until reference-beam 2 was parallel with reference-beam 1. The scattering beam was made parallel with the reference beams in a similar fashion. The directions of the beams were measured by shining the beams on a wall approximately nine meters from the transmitting optics and using a transit to determine the relative locations and directions of the

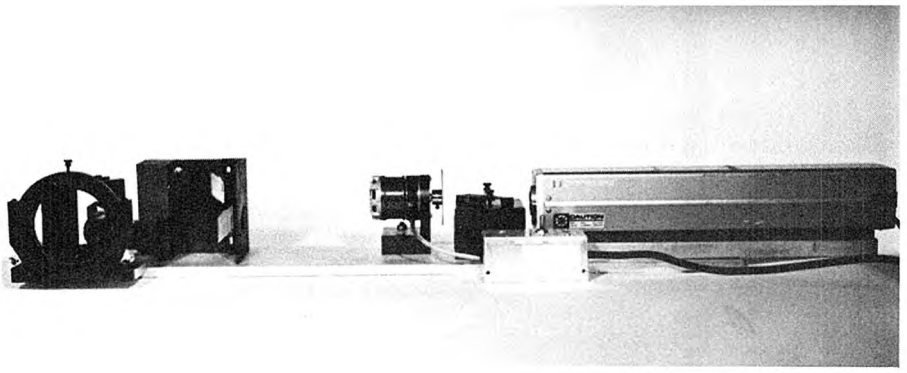

a)

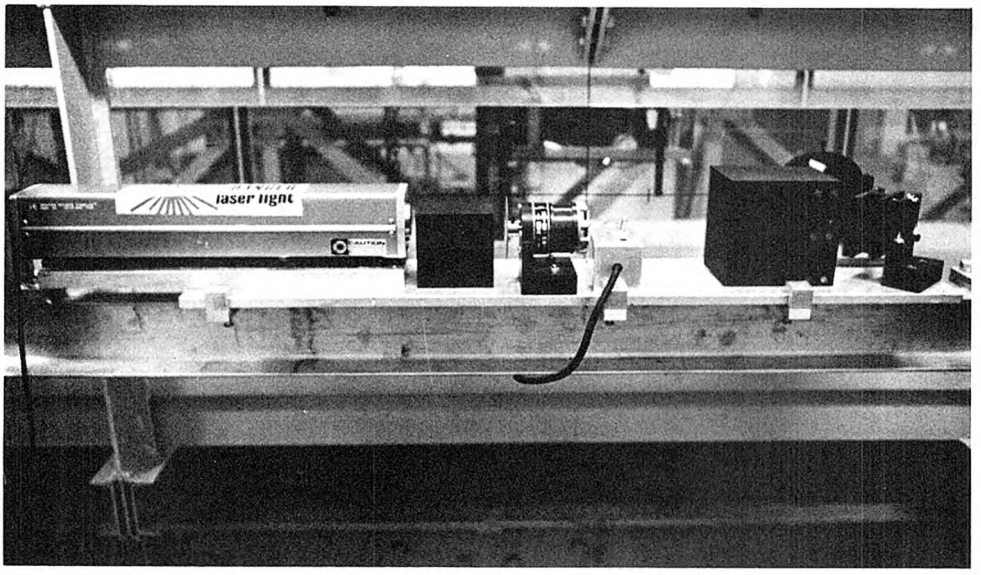

b)

Figure 3.4.3 Photograph of the transmitting end of the laser-Doppler velocimeter. a) View from the receiving side. b) View of the optics on the carriage with the flume in the background.

beams. The coordinates of the beams are given in Figure 3.4.4.

After the beams were made parallel, the 9.5 cm diameter, optically coated lens was installed. The lens was adjusted so that the optical center of the lens aligned with the center of the circle determined by the triangle of light beams. Thus, the light beams all lay on a right cone, whose base was the circle determined by the three beams, and focused to a point. The angles of the beams and the focal length of the lens were then measured using the transit.

The Doppler frequency (Equation 3.4.1) can be expressed as

$$\nu_D = 2nu_\perp \sin \frac{\phi}{2} / \lambda \qquad (3.4.4)$$

where

ϕ is the angle between the reference and scattering beams at the beam intersection, and

$u_\perp$ is the component of $\vec{u}$ in the direction of $(\vec{e}_r - \vec{e}_s)$.

The angle ϕ was measured for both reference beams and the respective quantities of $\nu_D/u_\perp$ were determined. These are listed in Table 3.4.1, along with the fluid velocity directions measured when the system is aligned such that the beams enter the flume in the normal direction to the flume walls and the beams are horizontal before they pass through the lens. The error estimates are based on probable measurement errors.

At the exit of the laser, the light beam is approximately 0.65 mm in diameter (measured at the $1/e^2$ intensity points); and the beam divergence is approximately 0.0017 radians. Using these values, the

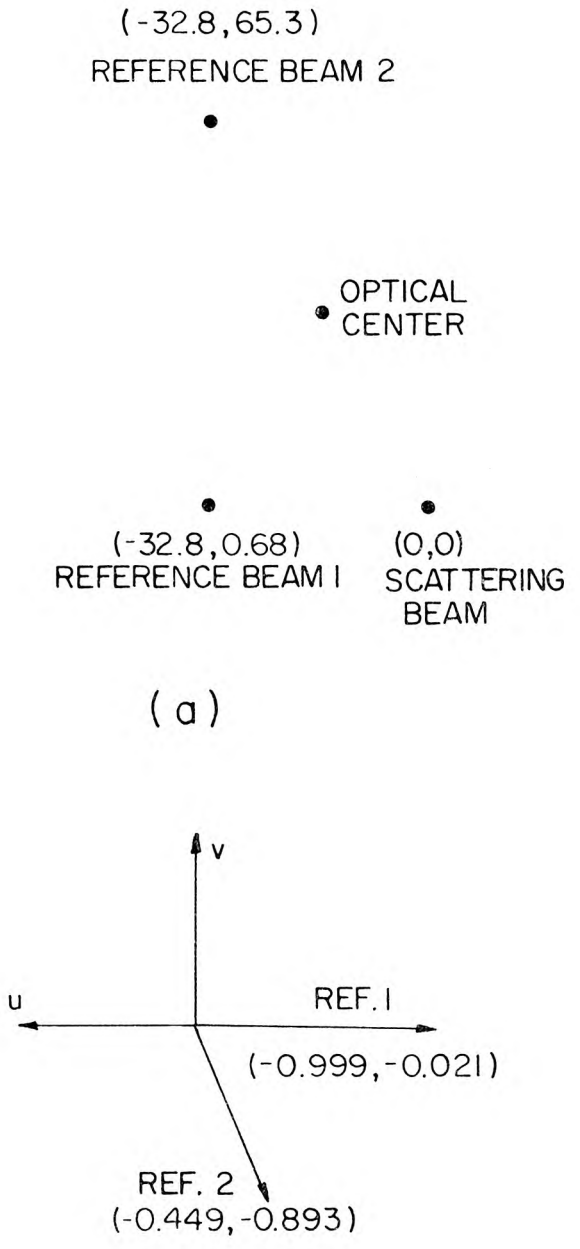

Figure 3.4.4 a) Relative position of laser beams prior to focusing.
b) Velocity components measured with the laser-Doppler system.

Table 3.4.1 Laser-Doppler Velocimeter Data.

Reference Beam	Scattering Angle ϕ Radians	$\nu_D/u_\perp$ cm^{-1}	Estimated Error cm^{-1}	Measurement Direction[1] (unit vectors)	Estimated Errors in Unit Vector Directions[2]
1	0.0576	908.8	±4.6	(-0.9998,-0.0209,0)	±(0.0001,0.0044,0.0044)
2	0.1284	2022.	±5.0	(-0.4492,-0.8934,0)	±(0.0018,0.0011,0.0044)

[1] (x,y,z) = (direction along mean flow, vertical, lateral).

[2] First two components based on measurement errors, last component based on possible alignment errors in mounting apparatus on carriage.

beam diameters at the focal volume were estimated to be about 0.28 mm and the total length of the intersection of the beams in the focal volume was estimated to be 1.28 cm. The maximum number of fringes crossed by a particle moving horizontally through the beam intersection was about 44. The estimates were obtained using the formulae given by Durst *et al.* (1976).

The transmitting optics were mounted on one side of a special carriage (see Section 3.5). Two photomultiplier tubes (RCA 8645) with band pass light filters were mounted on the carriage on the side of the flume opposite the transmitting optics. Each photomultiplier tube was aligned so that one reference beam fell on its light sensitive surface.

Typical amplified and filtered signals from the photomultiplier tubes are shown in Figures 3.4.5 - 3.4.9. Figures 3.4.5 and 3.4.6 show the signals when various beams are blocked. These signals indicate the noise levels from the photomultiplier tubes. Figure 3.4.7 shows the signals with the scattering beam blocked. Note especially here the lack of a Doppler signal in the photograph. Since the two reference beams are of extremely low intensity, very little light is scattered from one reference beam along the path of the other. Figures 3.4.8 and 3.4.9 show the laser-Doppler signals of the two reference beam systems. All photographs were taken under identical flow conditions, with the mean velocity at the beam focal volume at about 10 cm/sec, and with the same gain across the amplifiers.

Initially, it was believed that the frequency of one of the

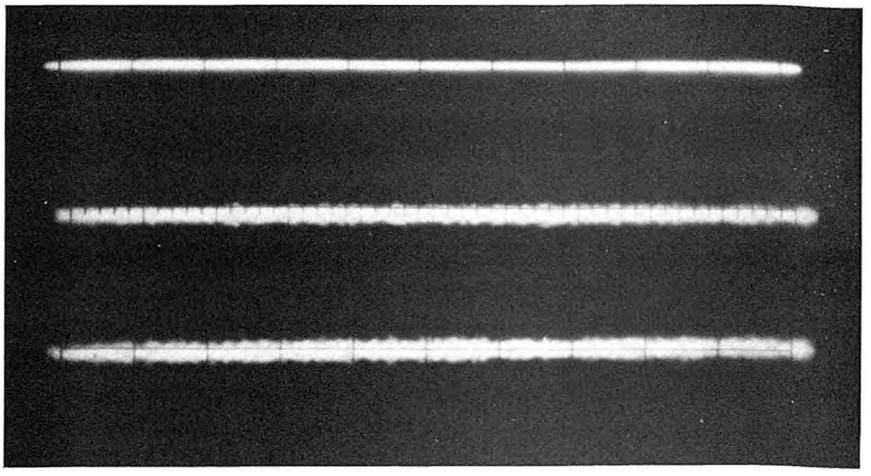

Figure 3.4.5 Oscilloscope traces of outputs from channel 1 of the laser-Doppler system. Scales: vertical 0.5 V/div., horizontal 2 ms/div.
Top: all beams blocked.
Middle: with reference beam blocked, scattering beam on.
Bottom: reference beam 1 on, scattering beam blocked.

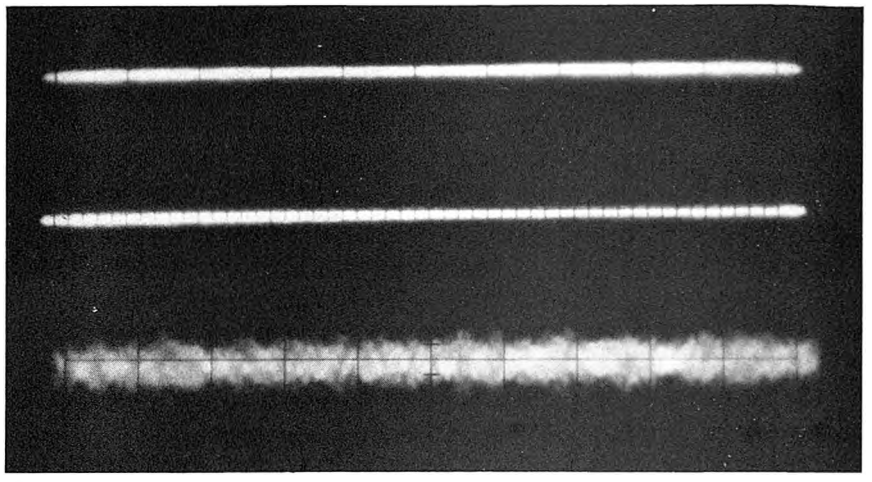

Figure 3.4.6 Oscilloscope traces of outputs from channel 2 of the laser-Doppler velocimeter. Scales: vertical 0.5 V/div., horizontal 2 ms/div.
Top: all beams blocked.
Middle: reference beams blocked, scattering beam on.
Bottom: reference beam 2 on, scattering beam blocked.

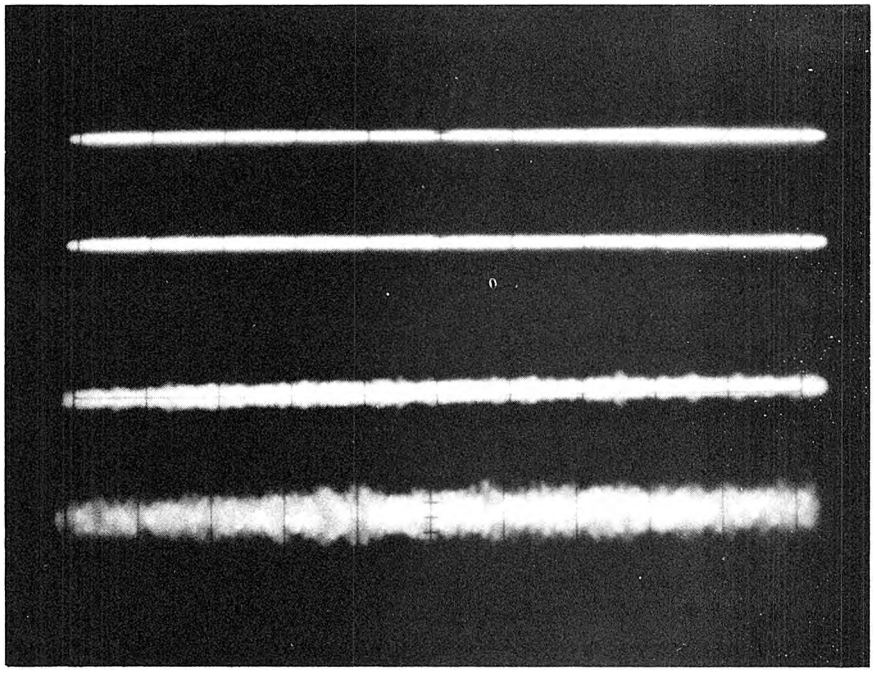

Figure 3.3.7 Oscilloscope traces of outputs from the laser-Doppler velocimeter. Scales: vertical 0.5 V/div., horizontal 2 ms/div.
Top traces: all beams blocked.
Bottom traces: scattering beam blocked; upper is channel 1, lower is channel 2.

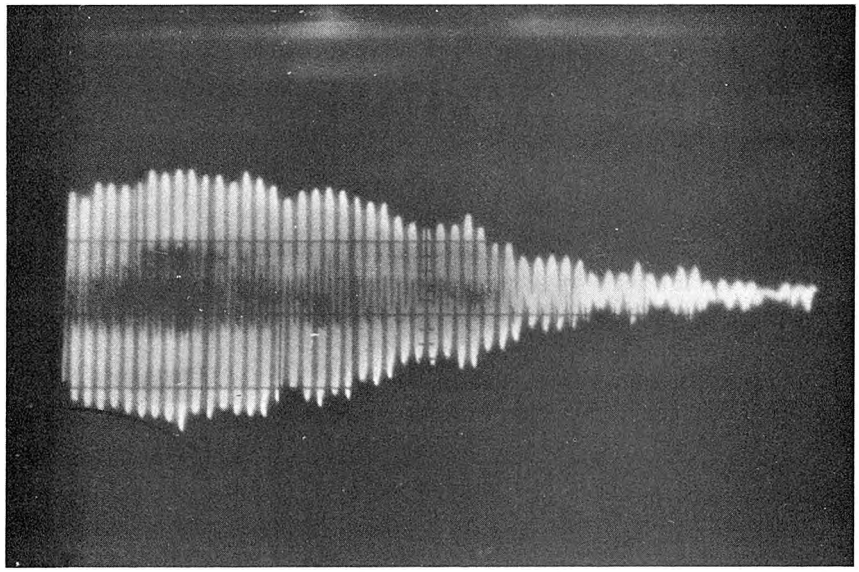

Figure 3.4.8 Oscilloscope trace of the output of channel 1 from the laser-Doppler velocimeter. All beams on; scale: vertical 0.5 V/div., horizontal 0.5 ms/div.

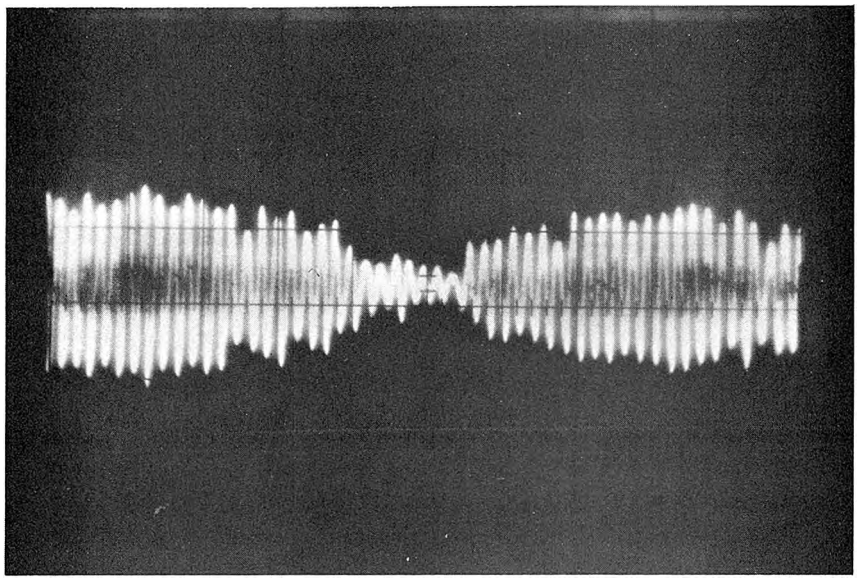

Figure 3.4.9 Oscilloscope trace of the output of channel 2 from the laser-Doppler velocimeter. All beams on; scale: vertical 0.5 V/div., horizontal 0.5 ms/div.

reference beams should be shifted so that the measured frequencies from the two systems would be substantially different. When the system was designed, the amount of light that would be scattered from one reference beam into the path of the other was not known; if a significant amount was scattered between the two beams, the resulting ambiguous Doppler signal could be electronically filtered if the two beams had different frequencies. In addition, there are some applications where frequency shifting is absolutely necessary. However, it was found that the amount of light scattered between the two reference beams was small enough to create no significant noise (see Figures 3.4.5 - 3.4.7) and no frequency shifting was used in this study.

The laser signals were processed with a counter system developed for this project. The system is described in detail in Appendix A. Basically, the system amplifies and filters the signals, then determines when a Doppler burst appears in the signal (corresponding to the passage of a particle through the focal volume). When the system detects a Doppler signal, the period of the Doppler frequency is timed with a 10 MHz clock and the system then gives either a binary number or a voltage output, both of which are proportional to the period of the Doppler frequency.

3.5 Laser-Doppler Carriage

A special carriage for the laser-Doppler velocimeter was designed and built to facilitate the velocity measurements. The carriage is shown in Figure 3.5.1. The carriage rested on three legs (made from standard four-inch steel H-beams) and straddled the flume. Two legs

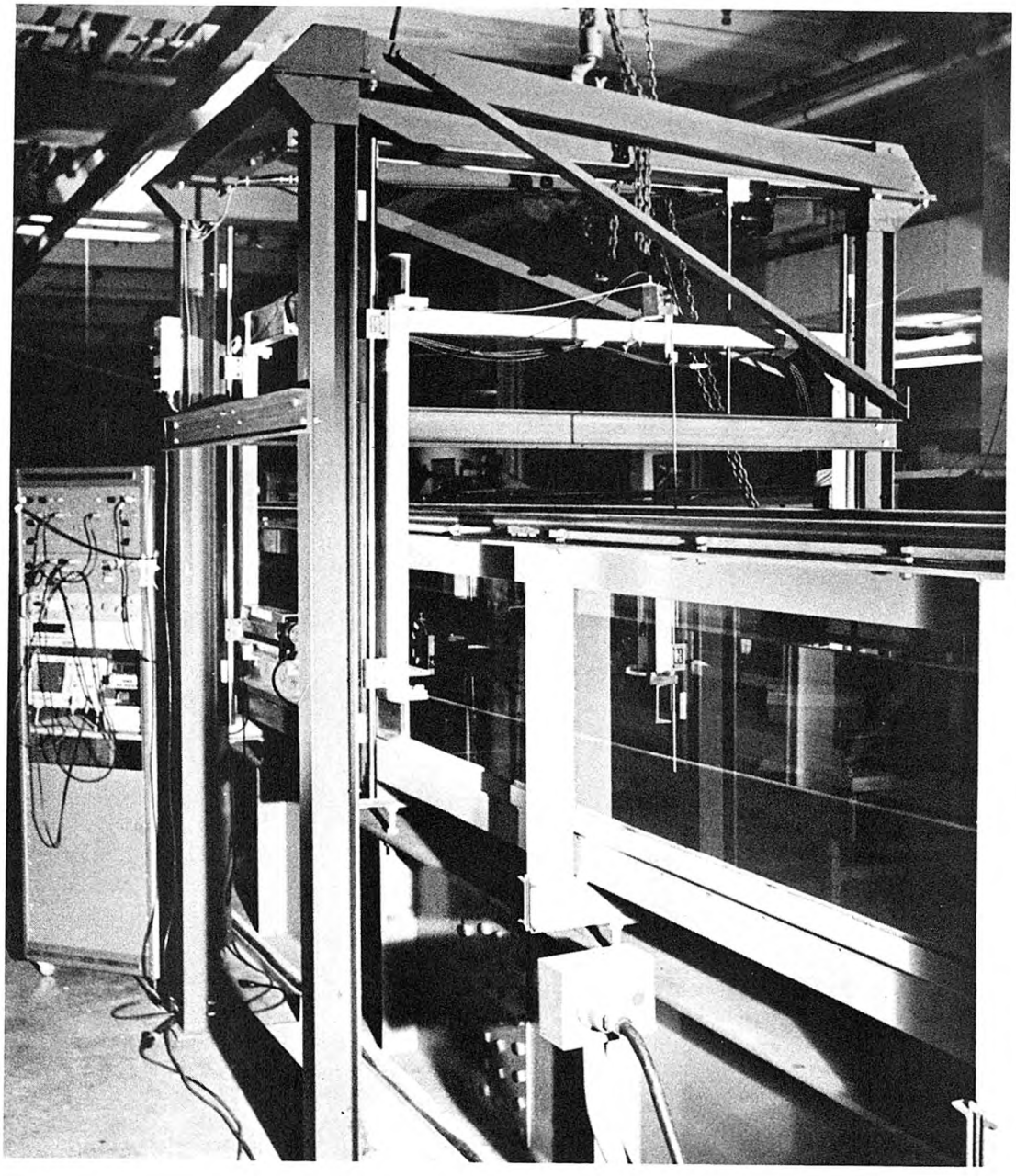

Figure 3.5.1 Photograph of the three-legged laser-Doppler velocimeter carriage as it straddles the flume.

on one side of the flume were braced together with a four-inch H-beam at the top and four-inch standard steel channel at the middle and bottom. The third leg on the opposite side of the flume was connected to the other legs with a six-inch H-beam at the top and several additional braces.

Each leg had a precision rail running vertically on the side facing the flume. An inner carriage, which rode on these parallel rails, was supported by two screw jacks which were attached to the six-inch H-beam. Two linear bearings attached each vertical leg of the inner carriage to the precision rails. Thus, the whole inner carriage could be raised and lowered smoothly by the two screw jacks, which were driven by an electric motor.

The laser optics were mounted on one side of the carriage (as shown in Figure 3.5.1) and the photomultipliers were mounted on the opposite side. Thus, velocity profiles could be made by simply raising and lowering the inner carriage; no readjustment of the optical system was necessary. A precision scale was attached to the inner carriage so that the relative vertical position of the carriage could be accurately determined. The scale was graduated in millimeters and had a vernier which allowed the position to be read to the nearest 0.1 millimeter.

The entire carriage could be raised off the floor of the laboratory and moved along the reach of the flume by means of an overhead winch. The winch rolled along the existing I-beam attached to the laboratory ceiling along the flume centerline. Because of the stiffness designed

into the carriage, the deflections of the members were small when the carriage was moved and no optical realignment was necessary after moving, except for a very slight readjustment of the photomultiplier tubes. The photomultiplier tubes were not rigidly fastened to the carriage, but could rotate slightly about one axis; sometimes when the carriage was moved, vibration caused the photomultiplier tubes to move out of alignment. In addition, slight imperfections in the laboratory floor caused slight misalignment. To facilitate alignment of the carriage, a galvanized angle iron was attached firmly to the floor parallel with the flume. The two-legged side of the carriage butted firmly against this angle iron when the carriage was placed on the ground, ensuring that the beams always entered the flume normal to the walls.

3.6 Data Acquisition System

All measurements were made with the laboratory Analog-to-Digital Data Acquisition System (Digital Data Systems). The system is described in detail by Okoye and Raichlen (1969), and Okoye (1970). The system can take up to eight analog inputs and samples and digitizes the input voltages at a rate set on the front panel or by an external trigger source. The digitized voltages are packed on magnetic tape in such a way that the precision of the instrument is one part in two-thousand, full scale. However, it was found that on the ±10V range used in the experiments, the precision of the instrument was about 0.02V.

The input impedance of the system is so low that buffers were

installed before the inputs to the system multiplexer. The buffers, shown in Figure 3.6.1 are simple voltage followers made from operational amplifiers (Texas Instruments, SN741). The buffers raised the input impedance of the system to about 1 megohm.

Data written on the magnetic tape were retrieved and processed at the Booth Computing Center initially with an IBM 370/168 digital computer, and later with an IBM 370/3032 digital computer.

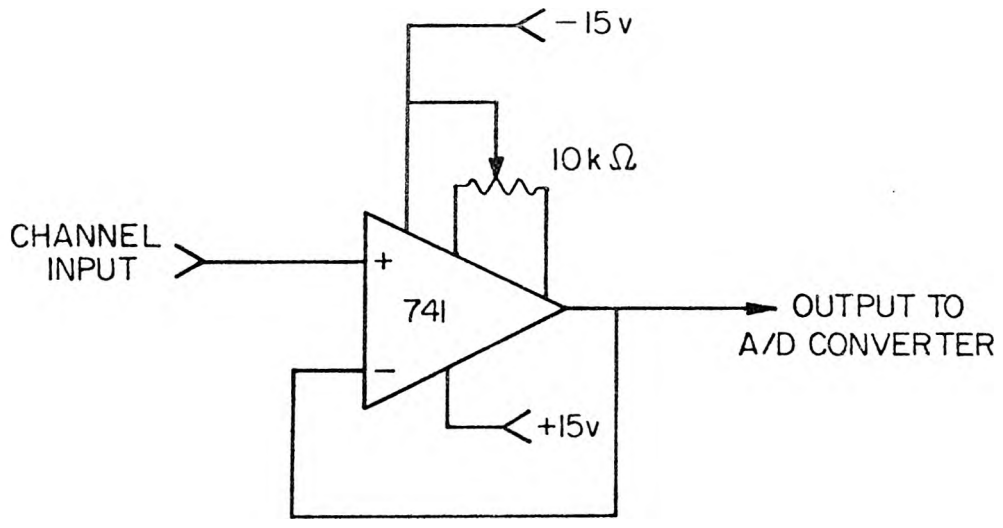

Figure 3.6.1 Buffer circuit for A/D converter.

CHAPTER 4

EXPERIMENTAL PROCEDURE

4.0 Introduction

In this chapter the details for calibration and usage of the experimental apparatus are given, and the experimental procedures are described. In addition, sources of possible errors are discussed. Finally, the acquisition and subsequent reduction of the data are detailed.

4.1 Instrument Calibration and Usage

4.1.1 Thermistors

All the thermistors used in this study were individually calibrated. The thermistors were placed in a constant temperature bath and connected to the identical cables and associated circuitry (see Section 3.3) that were used in experiments. The bath temperature was read to ± 0.02°C with a mercury thermometer graduated in 0.1°C intervals. The voltages from the thermistors were digitized and recorded on magnetic tape (see Section 3.6) and later processed. A second-order polynomial was fit in the least-squares sense to the calibration data. Typical calibration curves along with the calibration data are shown in Figures 4.1.1 and 4.1.2.

In order to correct for possible drift between experimental runs, the calibrations were checked each time an experiment was performed. Usually, at least two, and often several points were checked. Typically it was found that the glass-bead thermistor outputs would drift

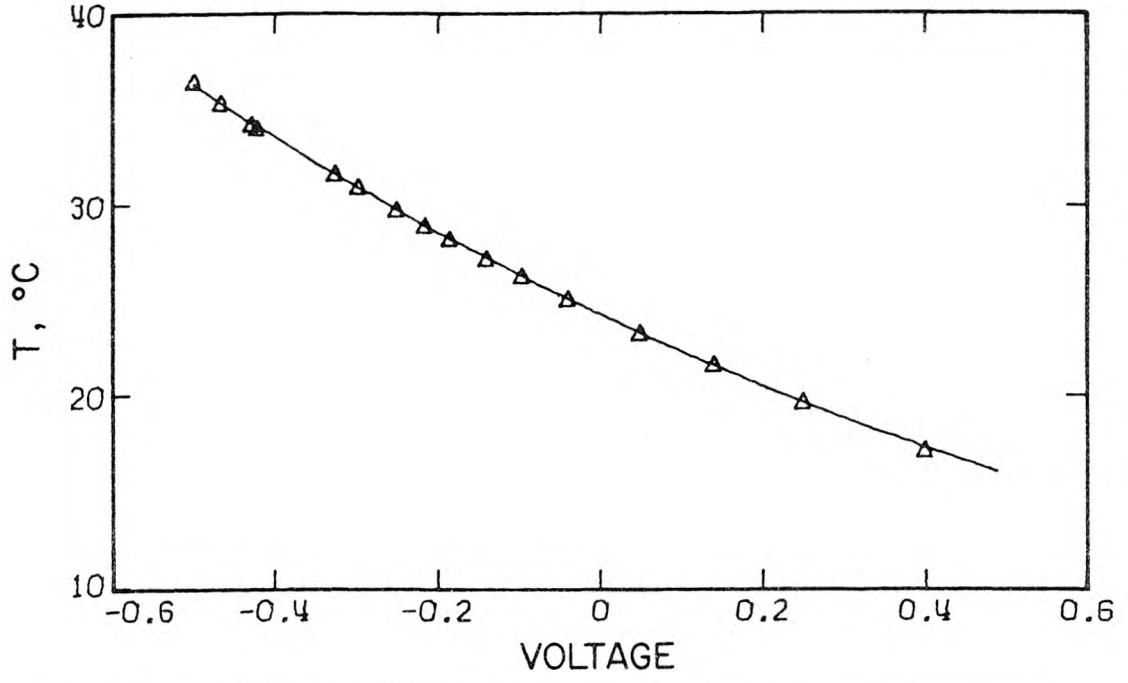

Figure 4.1.1 Typical calibration curve for glass-bead thermistor. Points are measured calibration data, curve is best fit.

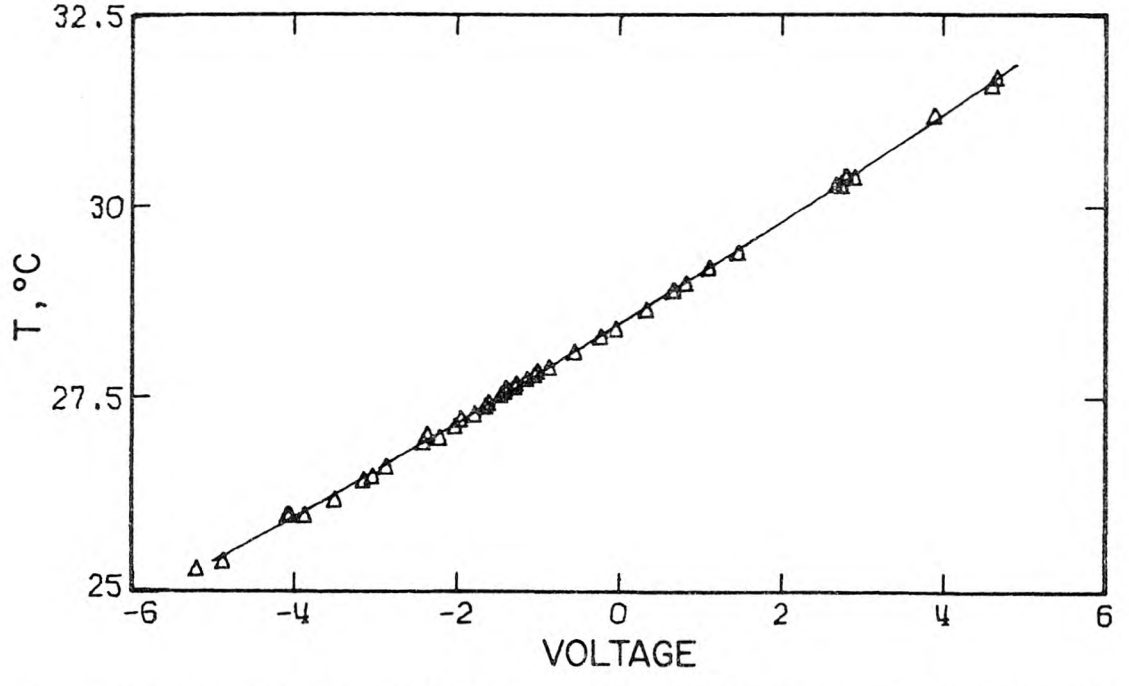

Figure 4.1.2 Typical calibration curve for fast-response thermistor. Points are measured calibration data, curve is best fit.

slightly between experiments and that a correction could be made by adjusting the leading constant of the calibration polynomial (i.e., adding a small constant to the polynomial). The drift was found to be due in large part to the long cables connecting the thermistors to the associated electronics and, in particular, the connections themselves. Since the glass-bead thermistors have a resistance of about 2kΩ at 25°C, small changes in the resistance of the cables and connectors could have a significant effect. Usually the changes amounted to a shift in the calibration of a few hundredths of a degree Celsius. This problem was eliminated with the fast-response thermistors by attaching the electronics to the probe itself, eliminating the long cables between the thermistor and its associated electronics. The fast-response thermistors were found to drift on the order of 0.01°C between experiments, which is the order of drift experienced during a typical experiment.

The absolute accuracy of the temperature measurements is believed to be about 0.2°C. The combination of signal noise and drift gives a precision of about 0.03°C for the glass-bead thermistors and about 0.01°C for the fast-response thermistors. Because of the roundoff error of the data acquisition system (see Section 3.6) the precision of the fast-response thermistors was about 0.013°C.

4.1.2 Laser-Doppler Velocimeter Calibrations

The counter systems used to determine the velocities from the laser-Doppler velocimeters were calibrated before each experimental run. First, the maximum and minimum velocities to be measured were

estimated. The corresponding maximum and minimum frequencies were determined, using the data from Table 3.4.1, and the output from the counters was offset so that the output voltage range for the frequencies to be encountered was in the measurement range of the Analog-to-Digital (A/D) data acquisition system. Finally, several continuous sinusoidal signals were fed into the counters and the output voltages were recorded. Usually, about ten different frequencies were used to calibrate the counters. The calibration frequencies were checked using a separate counter (General Radio, Model 1192-B), which counted the number of zero-crossings of the input signal over a one or ten second interval. The input signal frequency was then determined to an accuracy of better than one part in 5000.

The counter systems gave an output voltage proportional to the period of the Doppler frequency; consequently, a function of the form

$$\nu_D = A/(V - V_o) \tag{4.1.1}$$

was fit in the least-squares sense to the calibration data. Here, ν_D is the Doppler frequency, V is the output voltage, and V_o and A are constants determined in the least-squares fit. The fluid velocity in the vertical direction and the horizontal direction along the mean flow could then be determined using the data in Table 3.4.1.

4.1.3 Error Analysis for the Laser-Doppler System

This section contains a discussion of several sources of error inherent in the laser-Doppler system that was used in the study. Here probable error is defined such that the measured value of a

quantity will differ from the true value by the probable error less than 50% of the time.

Large particles in the flow can cause significant measurement errors, since larger particles may not follow the fluid trajectories. Particles with a diameter smaller than about 15μm are required for measuring turbulence (in water) with significant power at a frequency of 1 kHz (Durst *et al.*, 1976). The size distribution of particles in the flume water was measured (Hunt, 1978) and is shown in Figure 4.1.3. There are essentially no particles above 5μm; above that size the flume water size distribution coincides with filtered water. Hence, it is believed that the scattering particles were small enough that they essentially followed the fluid trajectories and therefore no significant measurement errors resulted from this source.

Errors in the velocity measurements can come from several other sources. One source is the inability of the counter system to distinguish two signals of slightly different frequency (see Appendix A). This error is estimated to be

$$\frac{\Delta\nu_D}{\nu_D} \approx 1.6 \times 10^{-6} \frac{\nu_m}{k-1} \qquad (4.1.2)$$

where $\Delta\nu_D/\nu_D$ is the relative error in the frequency measurement,

ν_m is the measured frequency in Hertz,

k-1 is the number of periods timed by the counter.

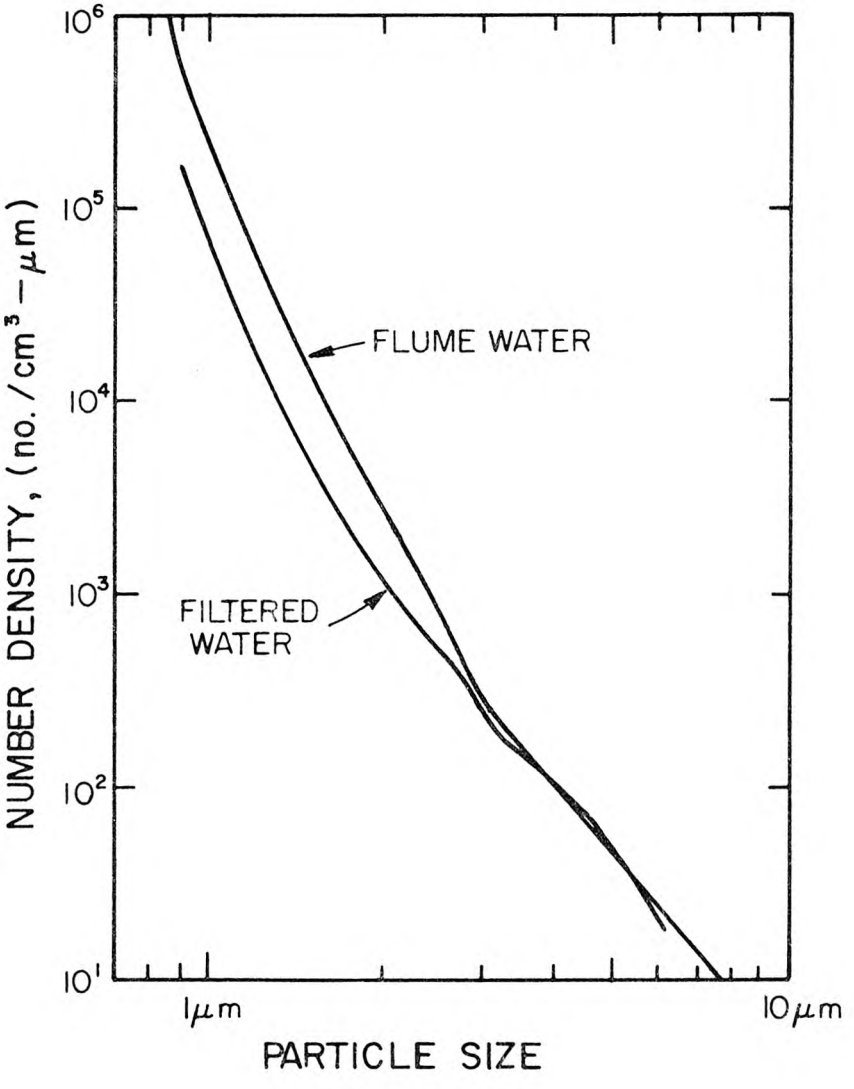

Figure 4.1.3 Measured size distribution of particles in the flume water, compared with filtered water; from Hunt (1978).

The maximum number of Doppler periods in a signal burst from the laser-Doppler system was about forty, but the counters were usually set to time twenty to twenty-five periods. The number of zero-crossings counted was chosen to be so large as to ensure that the particles crossed the beams near the center of their intersection, but not so large as to substantially reduce the data rate or require a low threshold setting to maintain a reasonable data rate. (A low threshold setting resulted in erroneous measurements, if the threshold was set so low that the counter system could not distinguish noise from a signal burst.) For the frequencies measured, $\Delta\nu_D/\nu_D$ was found to be less than 0.002.

A second source of error resulted from the digitizing of the analog output of the counter system. It was found that the laboratory data acquisition system (see Section 3.6) had a precision of 0.02 V in the ±10V range used in the measurements. The outputs from the counters were amplified and offset before being sampled by the A/D converter in order to utilize as much of the ±10V range as possible, thus minimizing the effect of this error. From Equation 4.1.1, it is found that the relative error is

$$\frac{\Delta\nu_D}{\nu_D} = \frac{\Delta V}{A}\,\nu_m \qquad (4.1.3)$$

where ΔV is the estimated error in the voltage measurement.

The value of A, which depends on the number of zero-crossings counted,

was typically greater than 1.4 x 10^5 V/s; the relative error of $\Delta\nu_D/\nu_D$ was less than 1.4 x 10^{-7} ν_m. The total relative error resulting from the inherent precision of the counter system and the digitizing process was

$$\frac{\Delta\nu_D}{\nu_D} < 1.6 \times 10^{-7} \nu_m \qquad (4.1.4)$$

where ν_m is the measured frequency in Hertz.

Since this error is a random error, it is a factor in determining the precision of the measurements.

There were also several sources of systematic errors which resulted from errors in measuring the exact locations and directions of the laser beams and thus affected the accuracy of the computed velocity components. The data and their estimated errors used in determining the velocity components from the measured frequencies are given in Table 3.4.1, along with the directions of the two velocity components that were measured. From the measured frequencies ν_1 and ν_2, the orthogonal velocity components u and v were determined from the equations

$$u = \frac{a\nu_1}{A_1} + \frac{b\nu_2}{A_2} \qquad (4.1.5a)$$

and

$$v = \frac{c\nu_1}{A_1} + \frac{d\nu_2}{A_2} \qquad (4.1.5b)$$

where a, b, c, d, A_1 and A_2 are given in Table 4.1.1 along with their respective probable errors. Using the data in Table 4.1.1 and Equations 4.1.4 and 4.1.5, the probable errors in the accuracy of the measured

Table 4.1.1

Data for Equations 4.5.1a and 4.5.1b

Symbol	Value	Probable Error	Units
a	-1.011	0.0053	
b	0.0236	0.0050	
c	0.5082	0.0033	
d	-1.131	0.0057	
A_1	908.8	4.6	cm^{-1}
A_2	2022.	5.0	cm^{-1}
ν_D	5-20	$0.00016\nu_D^2$	kHz

values of u and v can be obtained. It is found that

$$\sigma_u \equiv \frac{\sigma_u'}{u} = 0.008 + 1.48 \times 10^{-4}|u| \qquad (4.1.6a)$$

and

$$\sigma_v \equiv \frac{\sigma_v'}{u} = 0.005 + 1.05 \times 10^{-4}|u| \qquad (4.1.6b)$$

where σ_u' and σ_v' are the error estimates for u and v respectively, and

u is given in cm/s.

Here it has been assumed that $\nu_1 \approx \nu_2$, which is a reasonable assumption since, if v is zero, then

$$\nu_1 = 908.8u \qquad (4.1.7a)$$

and

$$\nu_2 = 908.2u \qquad (4.1.7b)$$

and if $|v|$ is u/10, then

$$\nu_1 = 913.5u \qquad (4.1.8a)$$

and

$$\nu_2 = 1088u \quad . \qquad (4.1.8b)$$

(The fact that $\nu_1 \approx \nu_2$ when v is zero was a coincidence which resulted from the beam locations, the actual focal length of the lens and luck.) Furthermore, Equation 4.1.7a has been assumed in order to obtain Equations 4.1.6.

The constant terms on the right-hand side of Equations 4.1.6 resulted from errors in the measurements of the alignment of the laser

beams. Consequently, these errors affect only the absolute accuracy of the velocity measurements; they do not affect the precision or repeatability of the measurements. The terms on the right-hand side of Equations 4.1.6 which involve $|u|$ come from errors in measuring the frequencies ν_1 and ν_2, and affect the precision of the instrument. The values of σ_u and σ_v are at most 0.011 and 0.007, respectively, for the highest values of u encountered in the flume (about 20 cm/s).

To realize the effects of these errors on the measured quantities, consider the following. Let $\hat{v}_i$ be the i^{th} measurement of the vertical velocity and let v_i be the true value of this same velocity. Then

$$\hat{v}_i = v_i + \hat{\sigma}_s u_i + \hat{\sigma}_p u_i r_i \qquad (4.1.9)$$

where u_i is the i^{th} true value of the horizontal velocity,

$\hat{\sigma}_s$ is the relative systematic error,

$\hat{\sigma}_p$ is the probable relative error in repeatability, and

r_i is a Gaussian distributed random number with zero mean value and a standard deviation such that the probability that $-1 \leq r_i \leq 1$ is 0.5.

From Equation 4.1.9 it is seen that the measured value $\hat{v}_i$ differs from the true value by two quantities, one of which is a systematic bias in the measurement, the other a random component. If there are N

measurements of $\hat{v}_i$, and if N is sufficiently large, then the estimated mean will be (assuming an unbiased ensemble)

$$\frac{1}{N}\sum_{i=1}^{N}\hat{v}_i \approx \overline{v} + \hat{\sigma}_s\overline{u} \tag{4.1.10}$$

where $\overline{v}$ is the true mean vertical velocity, and

$\overline{u}$ is the true mean horizontal velocity.

Thus the measured mean will be in error by at least $\hat{\sigma}_s\overline{u}$, regardless of sampling errors.

Removing the measured mean from the measured values, one obtains

$$\hat{v}_i' \equiv \hat{v}_i - \frac{1}{N}\sum_{i=1}^{N}\hat{v}_i = v_i' + \hat{\sigma}_s u_i' + \hat{\sigma}_p u_i r_i \tag{4.1.11}$$

where $v_i' \equiv v_i - \overline{v}$ and

$u_i' \equiv u_i - \overline{u}$.

Thus the <u>probable</u> error in a measurement of the fluctuating component of the vertical velocity can be estimated by $\hat{\sigma}_p\overline{u} + (\hat{\sigma}_s + \hat{\sigma}_p)\sqrt{\overline{u'^2}}$. The values of $\hat{\sigma}_s$ and $\hat{\sigma}_p$ can be estimated from Equation (4.1.6b); for the vertical velocity component, $|\hat{\sigma}_s| < 0.005$ and $\hat{\sigma}_p = 1.1 \times 10^{-4}|u|$, where u is given in cm/s. Using an estimate of $0.2\overline{u}$ for the value of $\sqrt{\overline{u'^2}}$, one finds that the relative probable error is

$$\frac{|\hat{v}_i' - v_i'|}{\overline{u}} < 0.0008 + 0.00014\ |\overline{u}| \tag{4.1.12}$$

with $\bar{u}$ again given in cm/s. In a similar fashion, the errors can be estimated for the measured values of u. Table 4.1.2 lists the probable errors in measuring the velocity components for a range of horizontal speeds. The errors for quantities such as $u - \bar{u}$ and $v - \bar{v}$ must be considered when calculating quantities such as $\overline{u'v'}$.

The laser carriage was moved several times during the course of an experiment, so it was possible that the beams did not enter the flume in exactly the same direction at each measurement location due to the nonuniformity of the laboratory floor. For this reason, the direction of the laser beams was checked at each measurement location. It was found that the direction of the beams changed only slightly from one position to another, and the error from the resulting misalignment has been incorporated in the previous analysis. It was found, however, that the error resulting from misalignment of the carriage was somewhat smaller than the estimated error in the beam direction measurements.

4.1.4 Venturi Meters

The flow rates through the two return circuits were measured with the existing Venturi meters (laboratory numbers Q-6 and Q-39). Before any experiments were begun, the Venturi meters were removed and cleaned, as a small amount of corrosion had taken place over the years since their initial installation. The Venturi meters were calibrated when the flume was initially brought into operation, and the calibration curves used are shown in Figures 4.1.4 and 4.1.5.

Table 4.1.2

ESTIMATED PROBABLE ERRORS FOR VELOCITY MEASUREMENTS
(in cm/s)

Mean Horizontal speed ($\bar{u}$, cm/s)	Measured Quantities					
	u	$\bar{u}$	$u-\bar{u}$	v	$\bar{v}$	$v-\bar{v}$
5	0.05	0.04	0.01	0.03	0.03	0.01
7	0.07	0.06	0.02	0.05	0.04	0.01
10	0.11	0.08	0.03	0.07	0.05	0.02
15	0.18	0.12	0.06	0.12	0.08	0.04
20	0.26	0.16	0.10	0.17	0.10	0.07

Note: $\sqrt{\overline{u'^2}}$ is assumed to be $0.2\bar{u}$. In practice, $\sqrt{\overline{u'^2}}$ was found to be $0.15\bar{u}$ or less; therefore, these estimates are likely to be too high. These estimates do not include sampling errors.

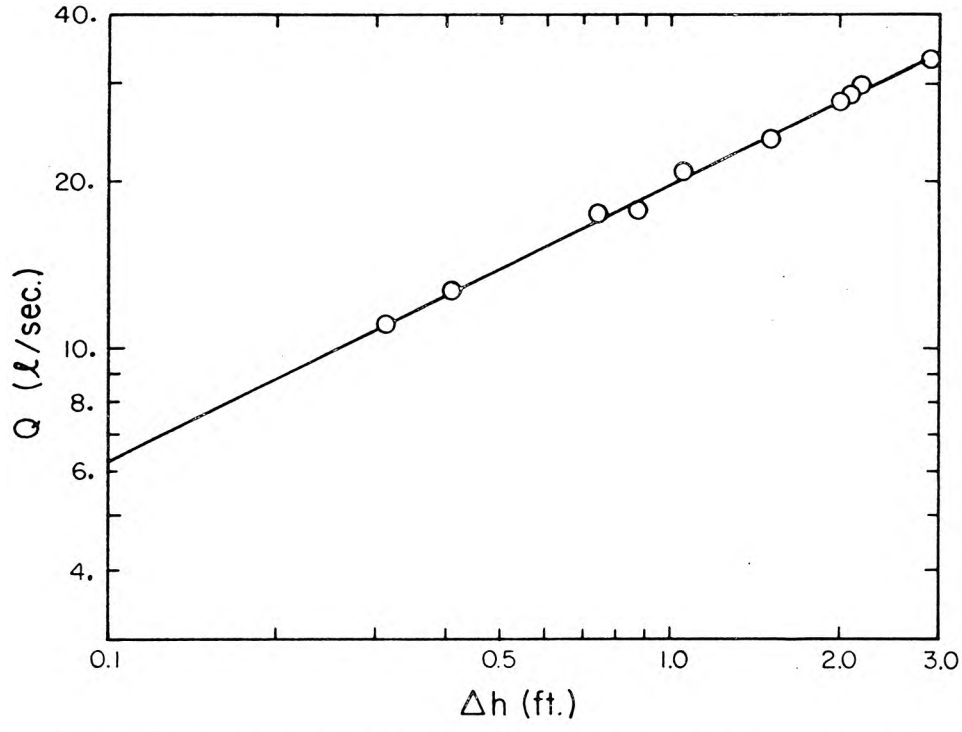

Figure 4.1.4 Flow rate calibration curve for Venturi meter Q-6.

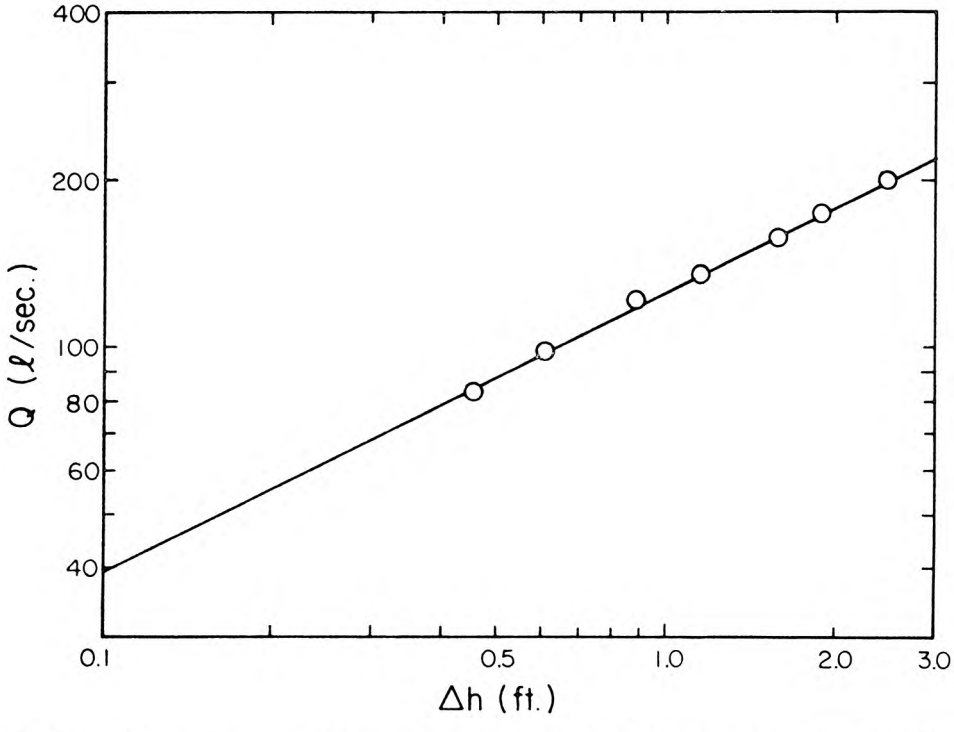

Figure 4.1.5 Flow rate calibration curve for Venturi meter Q-39.

The head difference was measured with a water manometer, which could be read to the nearest 0.03 cm (0.001 ft). This gives an absolute error in the precision of the measurements of the mean speeds of 0.2/U for the upper layer and 0.8/U for the lower layer, where U is the measured value of the mean flow speed (in cm/s) in the respective layers.

4.1.5 Depth and Slope Measurements

Point gages were used to measure the depth of water in the flume and to determine the slope of the water surface. The gages can be read to the nearest 0.01 cm and it was found that the repeatability of the gages was about 0.02 cm. Since the floor of the flume varied slightly over the reach of the working section, the probable error in the depth measurements was about 0.2 cm.

The surface slope of the flow was determined using the still water surface as a reference. The slope was determined by measuring the relative height of the water surface between two points separated by 31.00 meters. Thus, the accuracy of the surface slope measurements was 6.5×10^{-6}.

4.1.6 Density Measurements

Water densities were calculated from tables (Handbook of Chemistry and Physics, 1975) using the measured temperatures. The tables give densities for "ordinary water" at various temperatures, along with the thermal expansion coefficients. The flume water was tap water and had a salinity of about 0.5 parts per thousand. Hence some error is introduced because of the salinity. However, since the

relative density differences are the important quantities, and not the absolute densities, it is felt that the resulting error is slight.

4.2 Boundary Heat Losses

As mentioned in Section 3.2 the water in the flume was heated to a temperature several degrees Celsius above the air temperature in the laboratory. The flume was covered with polyethylene sheets to reduce evaporation; however, some heat was still lost by conduction through the walls and bed of the flume, as well as through the covered surface.

In order to determine the amount of heat lost from the flume water, the following experiments were made. The flume water was heated several degrees above room temperature (to a temperature typical of those used in experiments) and thoroughly mixed. In one case, the water was allowed to stand still, and the temperature was measured at many locations along the flume after a period of time. In another case, the flume water was recirculated continuously and the temperature measured at one point over a long period of time. (The reason for recirculating the water was that thermal stresses which developed in the glass walls when the water was hot and quiescent occasionally caused windows to break.)

For the purposes of this study, only heat losses in the working section caused measurement errors. Other heat losses during an experiment were compensated for by the flume heating and cooling system. Therefore, heat loss measurements made with the flume water recirculating, which include additional losses through hopper walls and pipes, should be considered as an upper bound for the losses in the working section.

It was assumed that the rate of change of water temperature was proportional to the difference between the flume water temperature and the laboratory air temperature. Hence,

$$\frac{\Delta T_a(t)}{\Delta T_b} = e^{-k_h t} \qquad (4.2.1)$$

where $\Delta T_a(t)$ is the temperature difference between water and air

ΔT_b is the initial temperature difference,

t is the time, and

k_h is a constant.

The value of k_h was found to be about 0.03 hr^{-1} ; only a slight difference in k was found in the two measurement methods. Typically, ΔT_b was about 6°C, and the mean velocity was usually 10 cm/s or greater. Thus, over the thirty meter reach of the working section, one would expect to find a 0.015°C drop in the mean flume temperature. For any particular case, the expected temperature drop would be

$$\frac{\Delta T_a}{\Delta T_b} = \exp(-8.3 \times 10^{-6}\ x/U) \qquad (4.2.2)$$

where x is the location along the flume in cm, and

U is the mean speed of the flow in cm/s.

Since the precision of the temperature measurements is on the order of

the temperature drop due to heat loss, it would be hard to notice the effect directly during a typical experiment. In some cases, however, the mean flow speed was low (6 cm/s) and in other cases ΔT_b was large (10°C); either of these cases would cause somewhat larger heat losses.

In summary, the maximum temperature drop over the working section of the flume was less than 0.03°C; in most cases, it was less than 0.02°C. It is believed that this amount of heat loss had little dynamic effect on the overall flow, but must certainly be taken into account in any type of heat balance.

4.3 Experimental Procedure

In this section, the procedure for a typical experimental run is described. The following sections describe some of the problems with the data collection and the subsequent analysis.

Before beginning an experimental run, the water in the flume was heated to about 28°C, which was about three or four degrees above the laboratory air temperature. Next, the upper layer was heated until the required temperature difference between the two layers was achieved. The mean velocities of the two layers were then set and the flow was allowed to come to equilibrium.

During the first several hours as the flow approached equilibrium, slight adjustments in the steam flow rate and the cold water flow rate were usually made to achieve the required temperature difference. The flow was then allowed to continue for several hours (at least eight) before the measurements were made.

During the period in which measurements were made (usually eight

to ten hours) the temperatures of the upper and lower layers at the end of the splitter plate were measured every twenty to thirty minutes. Usually, the temperature difference between the layers did not vary more than about 0.04°C from the mean temperature difference. The experiments with the largest variations over the eight-hour period had larger temperature differences, and the variation was almost always less than two per cent of the temperature difference; in most cases, the variation was much less than two per cent.

The absolute temperatures of the two layers usually drifted about 0.15°C over the course of an experiment. This drift was taken into account in the data analysis, particularly in producing contour plots of the mean temperature in the flume. The temperature drift was slow, however, due in part to the large mass of water involved.

The discharges in both the upper and lower layer circuits were measured several times during an experiment, and were found to vary only slightly, if at all. In general, the discharges varied less than one per cent over an eight-hour period.

Finally, the slope of the water surface and the water depth were measured several times during an experiment. The total depth of the flume stayed constant to within a millimeter over an eight-hour period, while the slope always remained constant to within the accuracy of the point gages.

4.4 Errors in Velocity Measurements Due to Thermal-Optical Effects

One potentially serious problem with the laser-Doppler system is that it is sensitive to changes in the refractive index of the fluid

medium. If the refractive index of the fluid is changing in time, then the beams change direction and errors may result. Since the refractive index of water varies with the water temperature, problems can arise in measuring velocities in thermally stratified flows.

In almost all the experiments in which the laser-Doppler system was used, the temperature difference between the two layers was less than 3°C. When the measurements were made close to the splitter plate, where the spatial and temporal gradients of temperature were largest, the temperature difference was usually kept below 2°C. Since the relative change in refractive index of the flume water was about $-9.2 \times 10^{-5}/°C$, the small temperature differences helped to minimize the errors resulting from the refractive index fluctuations.

In this section, possible measurement errors resulting from changes in the refractive index of the flume water will be examined.

4.4.1 Effects of the Mean Temperature Gradient

A mean temperature gradient in the flow will cause the laser beams to refract as they travel to the focal volume. This means that the location of the focal volume, and the relative direction of the beams will differ from the homogeneous case. The errors caused by the beam deflection due to a mean temperature gradient will be examined in this section.

Except for the region close to the splitter plate (less than 50 cm from the end), the mean temperature gradients in the vertical direction were generally less than about 0.2°C/cm. In passing from the glass walls to the beam intersection, the laser beams traversed

a vertical distance of about 2.5 cm and a horizontal distance of about 55 cm. If one assumes a constant temperature gradient of 0.5°C/cm in the vertical direction, so that the relative refractive index gradient is -4.6×10^{-5}/cm, then the deflection of the beams can be calculated using Fermat's principle of least time (or, equivalently, Snell's Law). After a somewhat tedious calculation, it was found that the focal volume moved about 0.07 cm vertically and a negligible amount (relative to the length of the focal volume) in the horizontal direction, perpendicular to the flume axis. If one beam was assumed to pass through a sharp interface with a 0.5°C temperature jump, then the beam intersection was calculated to move less than 0.03 cm vertically and about 0.5 cm in the horizontal direction, perpendicular to the flume axis. Since typical mean temperature gradients were smaller than 0.5°C/cm, it is reasonable to assume that these values give an upper bound for the change in the position of the focal volume. Thus, in considering velocity data that are taken in a region of strong temperature gradient, one must keep in mind that the vertical location at which the data are taken may have been in error by less than 0.07 cm and that the horizontal location may have deviated from the center of the flume by less than 0.5 cm. In general, the deviations were much less than these values, and they are not considered to be serious errors.

The mean temperature gradient also caused a change in the angles at which the beams intersect; however, it also caused a change in the wavelength of the laser light. Since the Doppler frequency is directly proportional to the product of the sine of the half-angle of the beam

intersection and the index of refraction of the medium (Equation 3.4.4), the changes in the intersection angles and the wavelength of the light were somewhat self-compensating (recall Snell's Law). They were not totally self-compensating, since the intersection angle is dependent upon the integral effect of the refractive index changes along the beam path, whereas the light wavelength at the intersection depends only on the refractive index at the intersection. With the assumption of a constant temperature gradient of 0.5°C/cm, the quantity $\nu_D/u_\perp$ (from Equation 3.4.4) was calculated to change a negligible amount from the homogeneous case; with the assumption of a sharp temperature jump of 0.5°C as before, $\nu_D/u_\perp$ was calculated to change by less than 1 per cent from the homogeneous case. Again, these assumptions give the worst case.

A change in the beam directions also changes the components of velocity that are measured. The total error in the velocity measurements due to the beam angles changing (using the previous assumptions for the temperature gradient) is estimated to be less than 1.5 per cent of the mean horizontal velocity. Since this is an error based on the mean deviation of the beams it affects the accuracy of the measurements, hence, the mean quantities would be in error by, at most, 1.5 per cent of the mean horizontal velocities; the errors in the fluctuating quantities would be in error by at most 1.5 per cent of their values. (This is similar to the error analysis in Section 4.1.2.) Again, these errors, though small, must be kept in mind when data from regions of high temperature gradients are considered.

4.4.2 Errors Due to Fluctuations in the Refractive Index

Probably the most serious error caused by refractive index changes, and certainly the most difficult to characterize quantitatively, is the error caused by the motion of the beams. When the beams were moving because of refractive index fluctuations, an apparent velocity was measured which was the true velocity of the fluid added to the relative motion of the beam intersection. Since the beams traveled some distance to the beam intersection, and because the fluctuations were three-dimensional, one would expect that the relative motion of the beam intersection would be completely uncorrelated with the true fluid velocity at the intersection. While observing the motion of the beams after passing through the interface, one observes that they tend to "dance" around in a random fashion in an area that is perhaps as much as ten times the cross-sectional area of the beam itself. One would expect that this "dancing" would result in velocity measurements which contained the true velocity plus noise.

Buchhave, George and Lumley (1979) have considered the effect of refractive index fluctuations on the velocity signal from a laser-Doppler velocimeter. They assumed that the spectrum of the refractive index fluctuations was proportional to $k^{-5/3}$ (where k, the wave number of the fluctuations, is $2\pi f_p/\bar{u}$), and found the spectrum, $\Phi(k)$, of the velocity signal from the laser-Doppler velocimeter to be proportional to $L^3U^2\overline{T'^2}k^{4/3}$, where L is the path length of the beams, U is a velocity scale and $\overline{T'^2}$ is the mean-square value of the temperature fluctuations.

It was sometimes found in this study that $\Phi_T(k)$, the spectrum of the temperature fluctuations, was proportional to k^{-3}, which would indicate

that buoyancy effects dominated the flow (see Section 2.4.1). If one assumes that the spectrum of the refractive index fluctuations is proportional to k^{-3}, then following the same method of Buchhave *et al.* (1979) one finds that Φ is proportional to $\frac{-g}{\rho_o}\frac{\partial\bar{\rho}}{\partial y} L^3U^2\overline{T'^2}$, and independent of k. One difficulty in either case is that the spectra of u', v' and T' are proportional to $k^{-5/3}$ (or k^{-3}) for a small range of wave numbers. The assumptions are not valid for small or large wave numbers, and the theory developed by Buchhave *et al.* is not easily solved if the spectrum of the refractive index fluctuations is much more complex than a simple power law.

On the basis of these findings, it is expected that the noise from the refractive index changes should be seen primarily at the higher wave numbers. Furthermore, the motion of the beams would certainly cause an increase in the root-mean-square values of the velocity fluctuations. The behavior of the spectrum of the noise, however, should be strongly influenced by the behavior of the turbulence (or internal wave) spectrum.

To check these ideas, velocity measurements were made for two flows, one with constant temperature, the other similar except that the upper layer was 2.3°C warmer than the lower layer. The total depths were 45.1 cm, and the splitter plate was located 15.1 cm from the surface. The mean speed of the upper layer was about 12 cm/s at the splitter plate, while it was 8 cm/s in the lower layer. Measurements were made one meter from the end of the splitter plate, a distance at which it was felt that buoyancy effects on the flow with the large temperature difference would be relatively small. In fact, the large structure in the turbulent mixing layer was observed to begin to collapse at about two meters from the splitter plate.

Figures 4.4.1 through 4.4.4 show the results of the measurements. In Figure 4.4.1, the mean horizontal velocity profiles are compared; Figure 4.4.2 shows the profiles of the root-mean-square values of the fluctuations in the horizontal and vertical velocities. Figure 4.4.3 compares the profiles of the vertical momentum flux per unit mass. Finally, Figure 4.4.4 shows the profiles of the root-mean-square values of the temperature fluctuations.

The first thing to be noticed from the graphs is the large temperature fluctuations (Figure 4.4.4) in the mixing layer for the stratified case. The mean temperature gradient in this region was as large as 0.48°C/cm; thus one might expect the refractive index fluctuations to affect the velocity measurements substantially. This is not the case, however, even though the beams were observed to wobble a good deal.

The profiles of $\bar{u}$, $\sqrt{\overline{u'^2}}$, $\sqrt{\overline{v'^2}}$, and $-\overline{u'v'}$ are nearly identical for both cases except in the lower portion of the mixing region. In the lower portion of the mixing region, there is a slight difference between the measured values in the two cases.

If one assumed that a change in the mean refractive index gradient caused smaller values of $\bar{u}$ in the stratified case, then one would expect that $\sqrt{\overline{u'^2}}$ and $\sqrt{\overline{v'^2}}$ would also decrease. In fact, if the beam angle did change because of a change in the refractive index, then one would expect that the ratios $\bar{u}_s/\bar{u}_u$, $\sqrt{\overline{u'^2_s}}/\sqrt{\overline{u'^2_u}}$ and $\sqrt{\overline{v'^2_s}}/\sqrt{\overline{v'^2_u}}$ would be the same at any vertical location. (Here the subscript u and s denote the unstratified case and stratified case respectively.) These values are not the same, however, as $\bar{u}_s/\bar{u}_u$ varies from 1.0 to 0.91, while

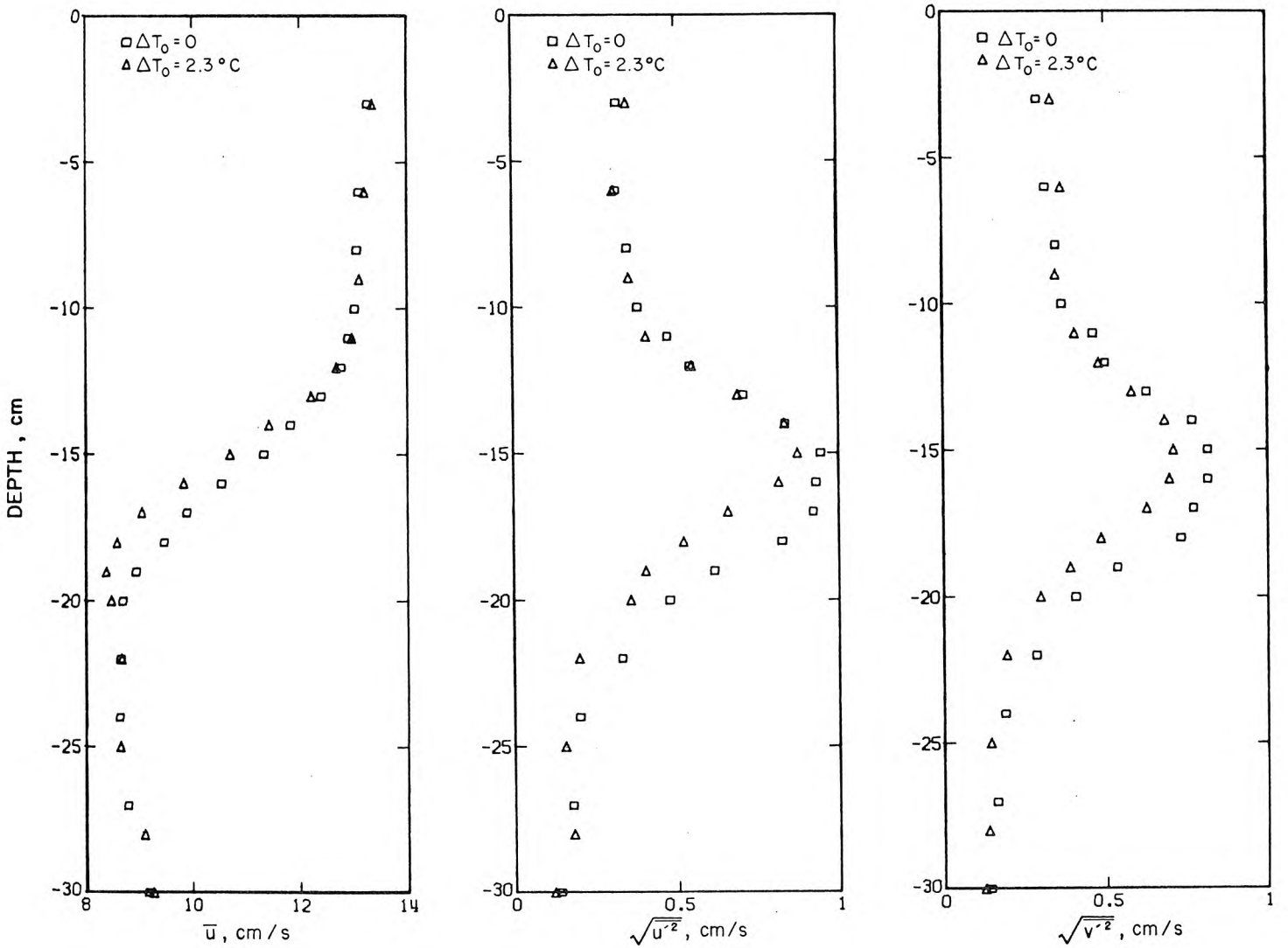

Figure 4.4.1 Comparison of mean velocity profiles.

4.4.2a Comparison of r.m.s. values of horizontal velocity fluctuations.

4.4.2b Comparison of r.m.s. values of vertical velocity fluctuations.

Comparison of measurements, made 1 meter from the splitter plate, between a homogeneous flow and a flow with ΔT_o = 2.3°C.

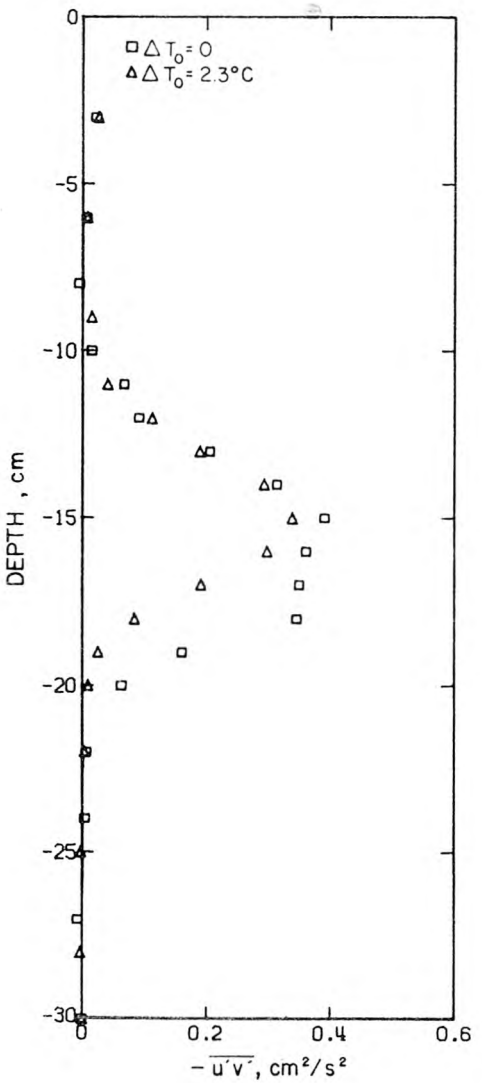

Figure 4.4.3 Comparison of Reynolds stress ($-\overline{u'v'}$) profile.

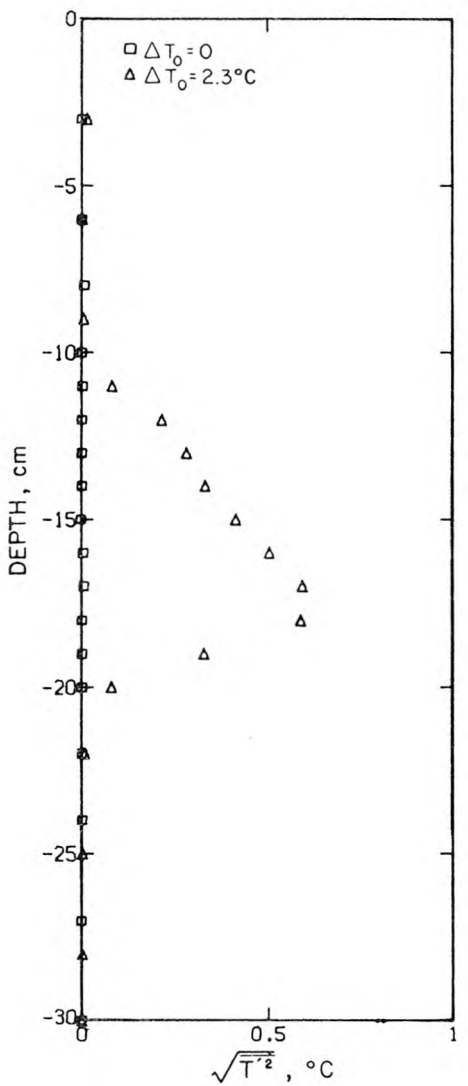

4.4.4 Comparison of r.m.s. values of temperature fluctuations.

Comparison of measurements, made 1 meter from splitter plate, for a case with homogeneous flow, and a similar case with ΔT_o = 2.3°C.

$\sqrt{\overline{u'^2_s}}/\sqrt{\overline{u'^2_u}}$ varies from 1.0 to 0.62 and $\sqrt{\overline{v'^2_s}}/\sqrt{\overline{v'^2_u}}$ varies from 1.0 to 0.65. If anything, $\sqrt{\overline{u'^2_s}}/\sqrt{\overline{u'^2_u}}$ should be larger than $\bar{u}_s/\bar{u}_u$, since the beam wobble should increase $\sqrt{\overline{u'^2_s}}$ while leaving $\bar{u}_s$ unaffected; this is not observed.

Furthermore, all profiles are very similar for both cases to a depth of about 14 cm from the surface, yet the temperature gradient at this depth was 0.19°C/cm and the temperature fluctuations were quite substantial. It must be remembered that two of the beams entered the flume about 2.5 cm <u>below</u> the measurement location; thus when the measurement was made at 14 cm, two beams entered at 16.5 cm and were affected by refractive index changes between 16.5 cm and 14 cm. Thus the smaller values of $\bar{u}$ in the stratified case are not caused by refractive index changes but by buoyancy effects.

Since the velocity gradient is larger in the stratified case it seems that the amount of mixing has been reduced by buoyancy effects. In fact, this is apparent from the profiles of the velocity fluctuations, and in particular, from the profile of $-\overline{u'v'}$. Since the laser beams were observed to wobble, there certainly must have been some noise level which appears in the values of $\sqrt{\overline{u'^2}}$ and $\sqrt{\overline{v'^2}}$. However, $\sqrt{\overline{u'^2}}$ and $\sqrt{\overline{v'^2}}$ are nearly identical for both cases down to a depth of 14 cm, even though the beams had passed through the region of highest temperature fluctuations to make measurements at 14 cm. Since the $\bar{u}$ and $-\overline{u'v'}$ profiles are similar down to 14 cm as well, it appears that the noise level is so small compared to the velocity fluctuations, that its effect is not seen; surely, the values of $\sqrt{\overline{u'^2}}$ and $\sqrt{\overline{v'^2}}$ would increase

because of the noise, while $-\overline{u'v'}$ would decrease, but this is not observed.

Further evidence that the noise from the beam wobble is small is seen in Figures 4.4.5 and 4.4.6. These figures compare the power spectra, Φ^*, of the velocity fluctuations in the mixing layer for the two cases. Figure 4.4.7 shows smoothed spectra, from which the spectral trend is seen more easily. One can see that the spectra are nearly identical for both cases. If the noise from the beam wobble were large enough to cause substantial errors in the velocity measurements, then it would certainly appear in the power spectra, but this is not observed here.

There were, however, some cases in which the noise from the beam wobble was apparent. Figure 4.4.8 shows power spectra for temperature and velocity fluctuations measured far downstream (24 m from the splitter plate) in a flow in which the interface was laminar. The initial temperature difference in this case was 3.5°C and the initial velocity difference was 4 cm/s. The fluctuations in this region were caused by internal waves. One would expect that the spectra of the velocity and temperature fluctuations would be similar in either a laminar region, such as this one, or in a region where the temperature effects are so small that the temperature is essentially a tracer. One can see that the spectra are quite similar in the low frequency end. At the high frequency end, there is apparently white noise in the velocity spectra.

In contrast, Figure 4.4.9 shows power spectra for the same experiment, but made in the interface at a distance of 4.7 m from the splitter plate. The velocity fluctuations were much larger at this location,

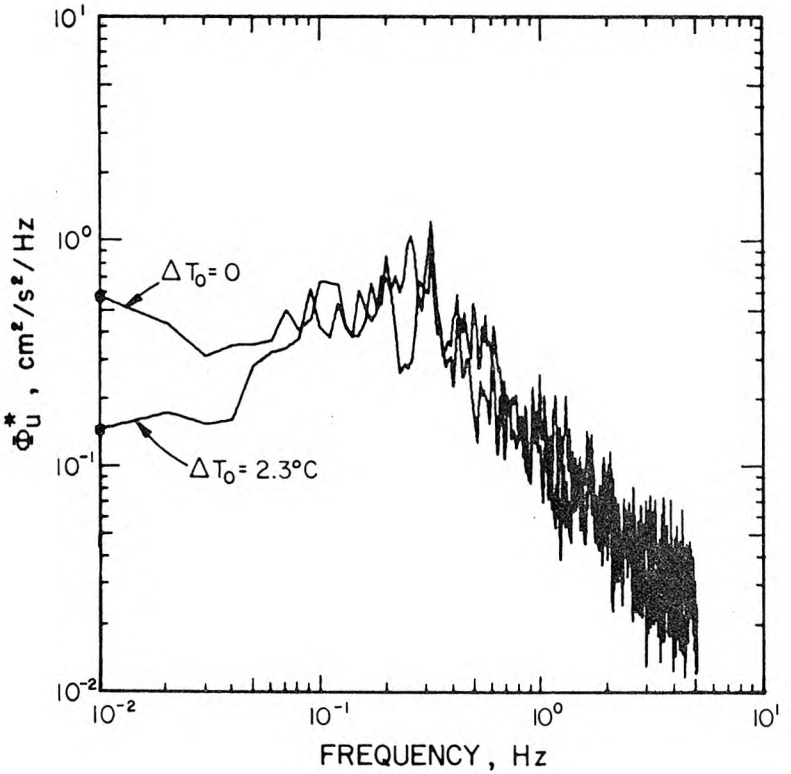

Figure 4.4.5 Comparison of power spectral estimates of u' for a flow with $\Delta T_o = 0$ and a flow with $\Delta T_o = 2.3°C$. Measurements made in mixing layer, 1 meter from splitter plate, and 13 cm below surface.

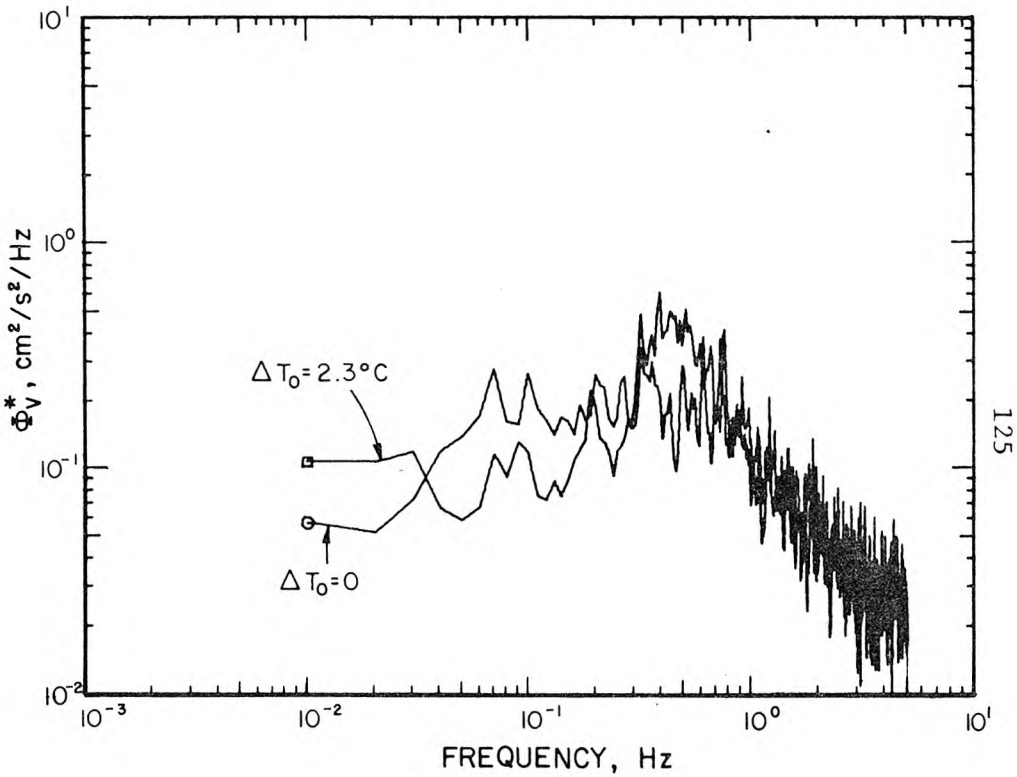

Figure 4.4.6 Comparison of power spectral estimates for v'; same conditions as in Figure 4.4.5.

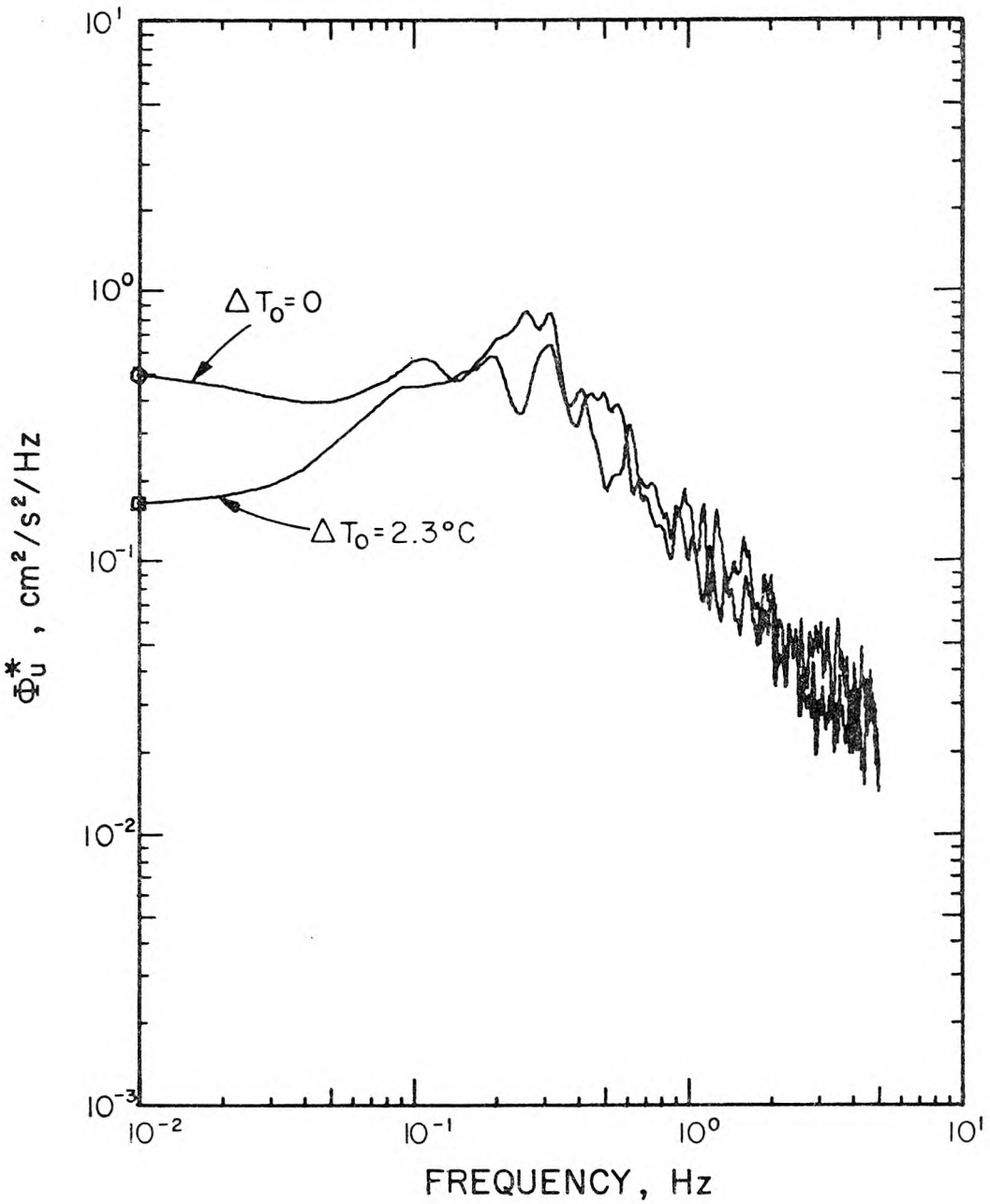

Figure 4.4.7 Comparison of smoothed power spectral estimates of u', same conditions as in Figure 4.4.5.

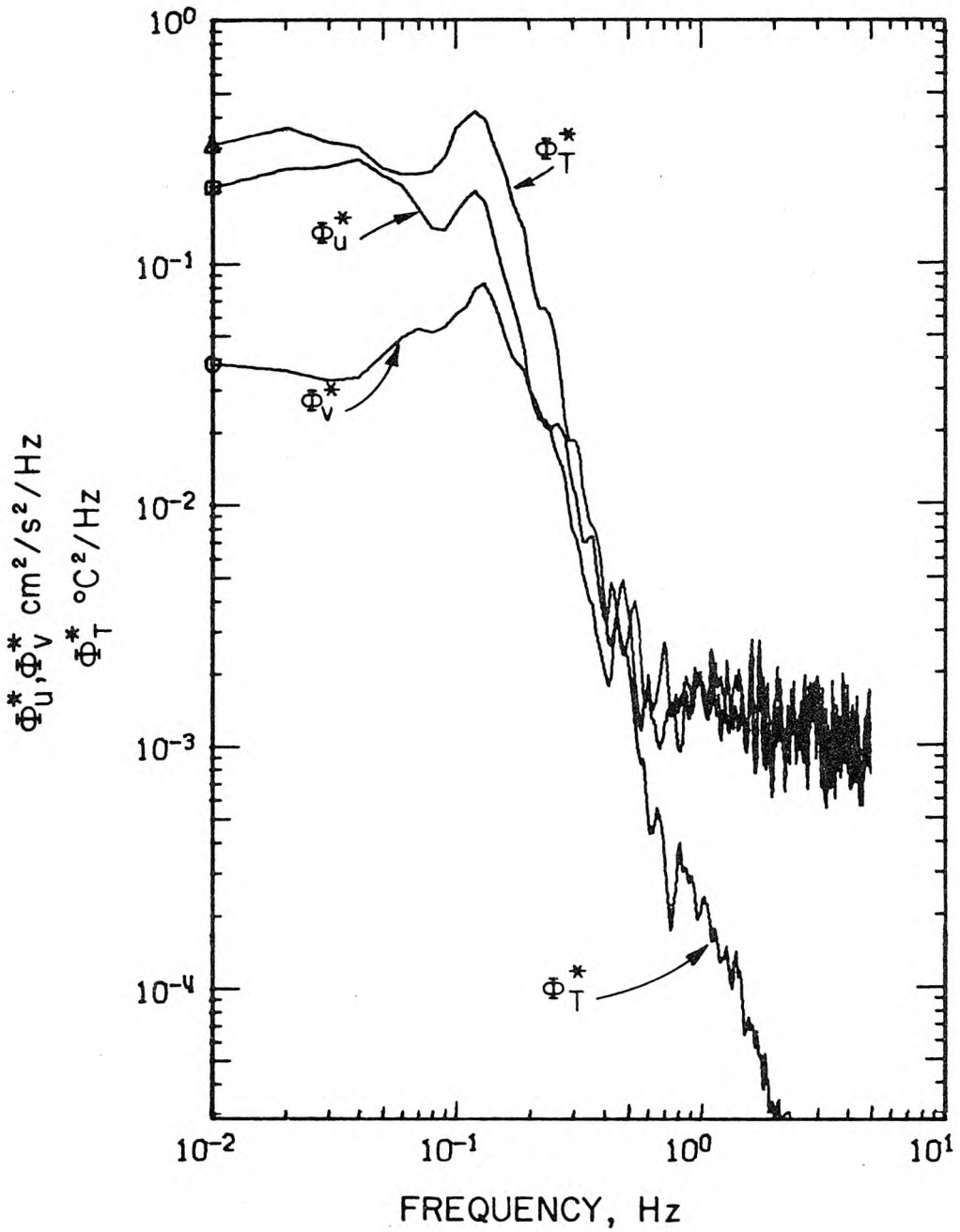

Figure 4.4.8 Power spectral estimates of u', v', and T' for a measurement in a region of large temperature gradient ($\partial\overline{T}/\partial y = 0.43\,°C/cm$) and low velocity fluctuations. Note noise in u' and v' signals, due to refractive index changes.

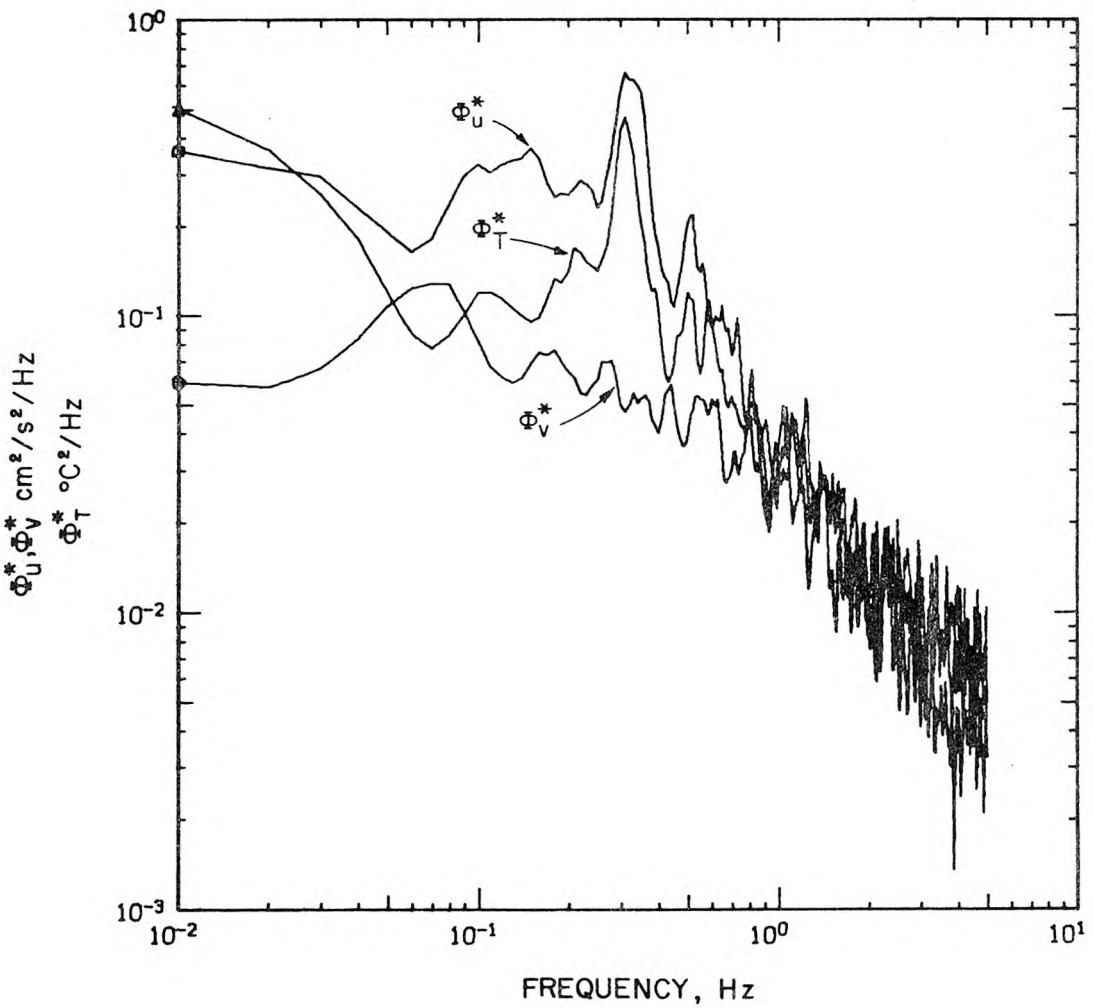

Figure 4.4.9 Power spectral estimates of u', v', and T' for a measurement in a region of large temperature gradient ($\partial\overline{T}/\partial y$ = 0.3°C/cm) and large velocity fluctuations. Note absence of noise in u' and v' signals.

as the effects of the mixing layer turbulence were still apparent; the flow was nearly laminar, but the internal wave amplitudes were large. At this location, however, both the mean temperature gradient and the root-mean-square value of the temperature fluctuations were similar to the values in the interface 20 m downstream (0.43°C/cm and 0.28°C, respectively, downstream, compared to 0.3°C/cm and 0.39°C upstream). The main difference between the flows in the two locations was the magnitude of the velocity fluctuations.

From the power spectra measured at these two locations, it appears that when the temperature difference is large and the velocity fluctuations are sufficiently small, then the noise from the refractive index changes can be significant. In the case considered here, $\sqrt{\overline{T'^2}}$ was about 0.28°C and $\partial\overline{T}/\partial y$ was about 0.43°C/cm; when the root-mean-square values of the velocity fluctuations were lower than about 0.2 cm/s, the effect of the beam wobble was noticeable.

It seems that the noise level appears in the power spectrum with a power of about 2×10^{-3} $(cm/s)^2/Hz$ for this case. Integrating this level over the frequency range measured means that the noise level accounts for about 10^{-2} $(cm/s)^2$ of the mean-square velocity fluctuations. Thus, for the measured value of $\sqrt{\overline{u'^2}}$ to be in error by at most 5 per cent of the true value, the true value of $\sqrt{\overline{u'^2}}$ must be at least 0.3 cm/s. This limit on the true value of $\sqrt{\overline{u'^2}}$ for accurate measurements applies, of course, only to those cases in which the measurements are made in a region with high temperature fluctuations, as in the case considered.

To demonstrate that this noise level is due to temperature fluctuations and not other noise, Figure 4.4.10 is presented. This figure

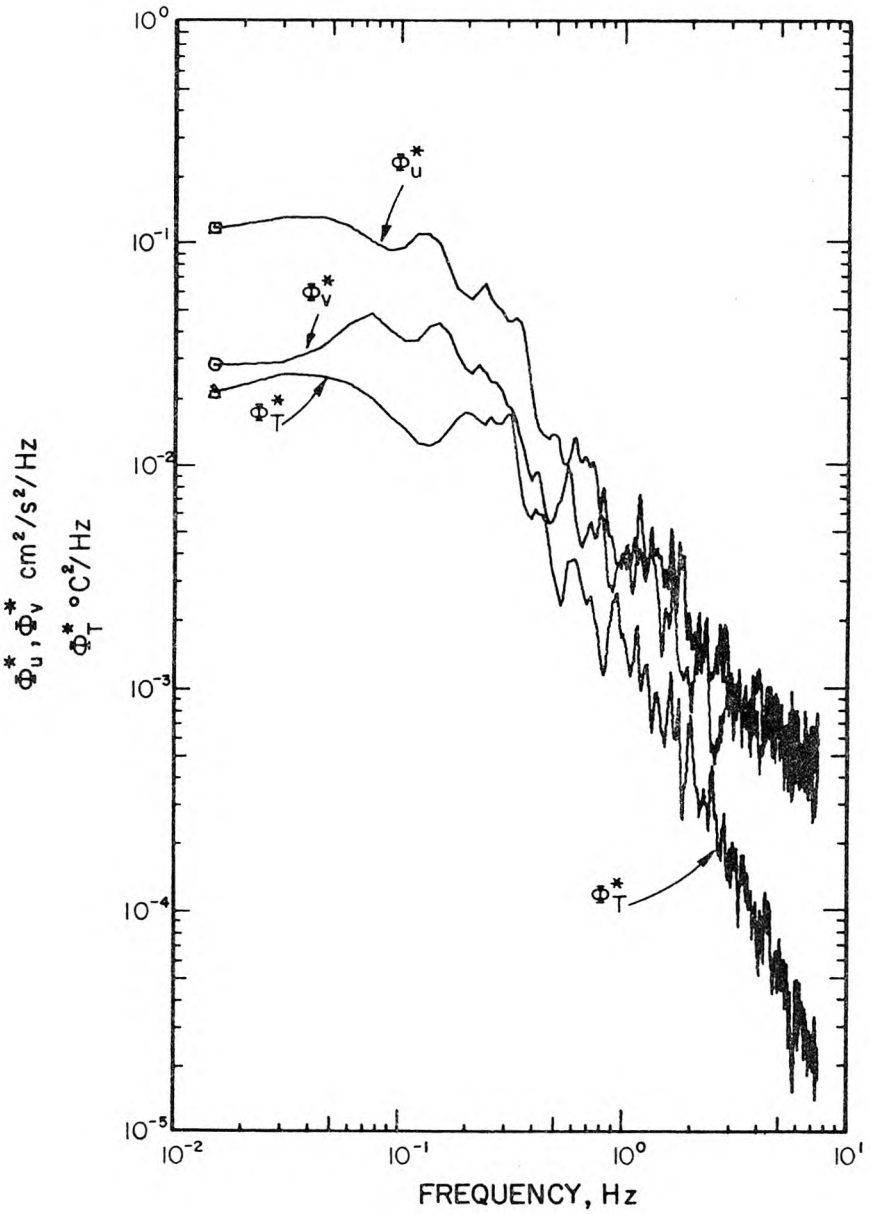

Figure 4.4.10 Power spectral estimates of u', v' and T' for a measurement in a region of low temperature gradient ($\partial\overline{T}/\partial y = 0.05°C/cm$) and low velocity fluctuations.

shows power spectra of temperature and velocity fluctuations for a case where both the temperature and velocity fluctuations were small. The power spectra of the velocity fluctuations go below the level of 2×10^{-3} $(cm/s)^2/Hz$ and no white noise level is apparent. The conclusion here is that although the velocity fluctuations were quite small, the measurements were not affected by refractive index changes as they, too, were small.

The conclusion that must be drawn from these data is that if the velocity fluctuations are sufficiently small and the temperature (hence, refractive index) fluctuations are sufficiently large, then the velocity measurements may be in error. For the experiments conducted in this study, the contribution to the variance of the velocity fluctuations from the refractive index fluctuations will, in general, be less than 10^{-2} $(cm/s)^2$, as this value comes from an experiment with a much larger than usual temperature stratification. But even in this case, the noise level from the beam wobble was not apparent except in the laminar interface.

The last problem, that of signal dropouts due to the beam wobble (caused by the beams failing to cross when they were in motion), was not a particularly serious problem. When the dropouts became excessively large at a location, data were not collected there. Thus, in some cases, measurements could not be made because of the high dropout rate.

For the most part, the refractive index changes were not a serious problem; in those few cases in which they were a problem, the problem was easily detected and, if it were possible to make measurements (such as in the laminar interface), corrections to the measurements could be

made. These corrections, as well as other data processing techniques are discussed in the next section.

4.5 Data Analysis

In this section, the methods of data analysis used in the study are detailed. In addition, some problems in the data analysis are discussed.

It is important to note that the data from a laser-Doppler velocimeter are not a continuous record but a series of data from measurements made over discrete intervals. Typically, a velocity measurement was made over a period of about 2 ms (for a particle moving at about 10 cm/s) and there was a typical interval of about 10 ms between the end of one measurement and the beginning of the next. Thus the typical data rate was in the neighborhood of about 80 measurements per second. (This rate could be adjusted somewhat by adjusting the threshold level on the counter system.)

In some instances, however, the data rate fell below this level. The cause was invariably due to changes in the refractive index of the water. If the data rate became low enough (below about 20 measurements per second) the dropouts usually became too long and measurements were not made in these circumstances. This was, however, an infrequent problem.

Since it was found that most of the turbulent energy was in the very low frequencies below 15 Hz, the data rate from the laser-Doppler velocimeters was five to ten times faster than was needed to make useful measurements. This was not always the case; for example, the initial

mixing layer contained some turbulent energy in higher frequencies. In general, however, most of the turbulent energy was contained in large structures which appear in the lower frequencies.

Before making a measurement, the outputs of the laser-Doppler systems were observed on an oscilloscope to determine the data rate from the laser-Doppler counters and to estimate the frequency of the velocity fluctuations. The data sampling rate was then set so that it was faster than the frequencies of the large scale motions but at most one-half of the data rate of the counters. In this way there was little possibility of sampling the counter outputs more than once without a new measurement having been made. Then, following the method proposed by Dimotakis (1976), the velocity of the fluid at the measurement point is estimated from the data record and unbiased means can be obtained.

Dimotakis' method requires that the data be sampled at a rate large compared to the frequency of the large velocity fluctuations and that the time between measurements be known. Then, averages can be made using trapezoidal approximations to time integrals. This method was employed to estimate mean quantities.

It was found that record lengths of at least one minute were required to obtain good estimates of the mean values of u, the horizontal component of velocity, v, the vertical component of velocity and T, the temperature. Record lengths of two minutes were required to obtain good estimates of the mean-square values of fluctuating quantities, and three to six minutes of data were required to obtain good estimates for

cross-correlation coefficients. These values were obtained empirically by recording data for a long period of time and comparing the mean values obtained from short time periods with the mean values obtained from the whole record.

It was also found that good estimates of mean quantities could be obtained from very low sampling rates if the record covered a sufficiently long period of time. Thus the mean value obtained for, say, the horizontal velocity component is essentially the same if the data record is a series of measurements taken at fifteen samples per second for one minute or two samples per second for seven minutes. It was found in some instances, however, that to obtain good estimates of cross-correlation coefficients the data rate had to be at least three samples per second and the record length at least four minutes. The circumstance which required this was the situation in which the cross-correlation coefficient was, in absolute value, less than about 0.2. Since this circumstance was not known *a priori*, the length of the data record for each point was in the neighborhood of four to seven minutes. In addition, the sampling rate was usually in the neighborhood of ten to thirty samples per second. Typically, the data records for the two velocity components and the temperature each contained about three to five thousand measurements.

In most instances, velocity profiles were usually made at about six locations along the flume. Each profile consisted of measurements at about twenty points. The vertical locations of the measurement points were chosen so that the density of points was greater in regions of

large vertical gradients. By observing the outputs of the laser-Doppler counters and the thermistor, one was able to make a rough estimate of the mean values at a point; measurement points were then selected based on the changes in the various signals. Thus, the density of measurement points in the initial mixing layer was much greater than outside the mixing layer. The average time to make one profile was about ninety minutes.

Measurement locations along the flume were selected so that changes along the reach of the flume could be well documented. Selection of the locations took a bit of trial and error, but it was found that measurements every four meters was sufficient for the far field, while much smaller intervals were required in the initial mixing region.

In some cases, corrections were made to the data. One situation where corrections have been applied are in heat balances and in contour maps of isotherms. The measurements were made over a period of eight to ten hours, and during this period, some drift in the flume temperature was usually observed. The drift in absolute temperature was usually on the order of 0.15°C, while the drift in the initial temperature difference was much less. In making heat balances, the temperature profiles were adjusted for the small changes in the inlet conditions, which were measured periodically. It is clearly noted in subsequent sections when this has been done.

The other cases in which corrections have sometimes been made are the situations where the velocity records contain noise due to refractive index changes. These situations occurred when the flow at the interface

was laminar. In some cases, the noise was removed by digitally filtering the data records. An example is shown in Figure 4.5.1. This case is the same as used in Figure 4.4.8; the flow is laminar, but interfacial waves are present. The temperature record is quite smooth, while the velocity record exhibits the high frequency noise which is evident in the power spectra shown in Figure 4.4.8. Figure 4.5.2 shows a digitally filtered velocity record, which appears to be more nearly similar to the temperature record, as one would expect in a laminar region. In any event, when filtered data are used in calculations, it is always noted, and the results obtained with unfiltered data are also presented. In some cases, however, it is felt that the filtered data represent the true situation more correctly than the unfiltered.

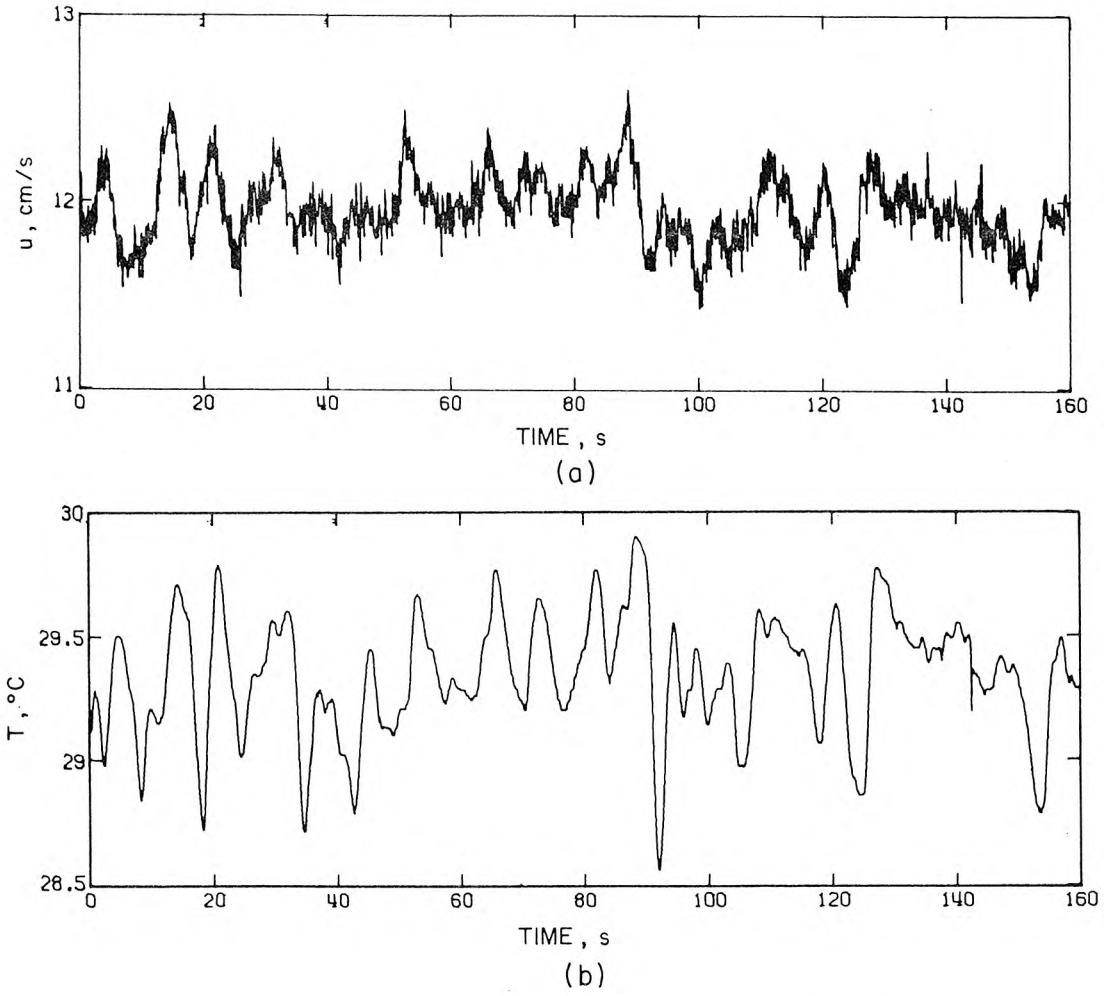

Figure 4.5.1 Time-record of (a) u and (b) T in a laminar region of high temperature gradient. Note high frequency noise due to refractive index changes. Power spectral estimates of these records are shown in Figure 4.4.8.

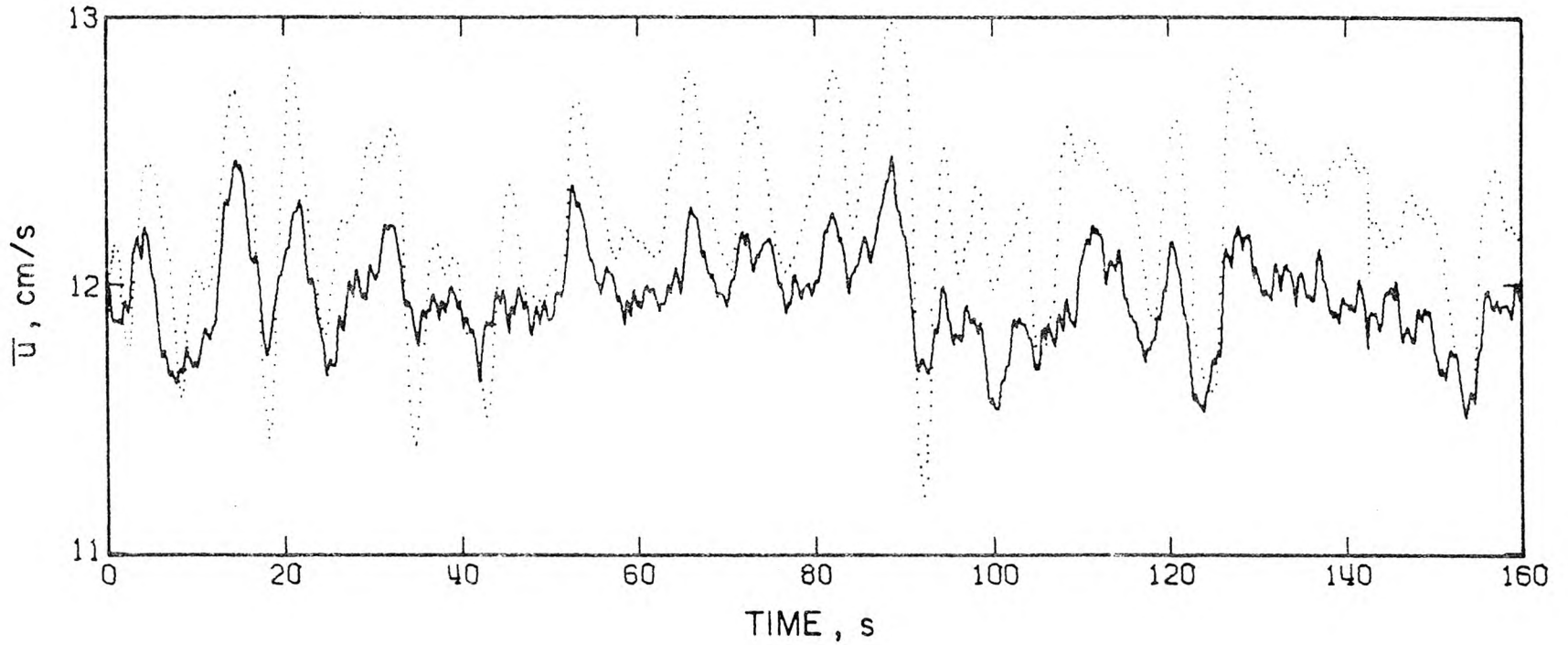

Figure 4.5.2 Low-pass filtered record of u (from Figure 4.5.1a). Note similarity of filtered u signal and unfiltered T signal (shown here with dotted trace).

CHAPTER 5

GENERAL DESCRIPTION OF THE FLOW

5.0 Introduction

In this chapter, a general description of the flows encountered in the experiments is given whereas more quantitative descriptions are given in the subsequent chapters. Here the inlet conditions and the boundary effects are described in detail, and then a qualitative picture of the flow is presented.

Basically, the flow began with a mixing layer, which collapsed to a laminar layer if the density difference between the layers was sufficiently large relative to the given initial velocity difference. A substantial shear often persisted through the laminar layer. Downstream, further mixing took place under certain circumstances. In some cases, the turbulence generated at the boundaries slowly "chipped" away at the edges of the interface. In other cases, the interface became unstable and began to mix slowly. In either event, an energy input (in this case, bed-generated turbulence) was required for mixing to continue. Without an external input, the instabilities caused some mixing and then decayed.

5.1 Inlet Conditions

In this section, the flow conditions at the flume inlet are described. Although the flume inlet did not have a contraction section to reduce turbulence levels, straighten the flow, and reduce the size of boundary layers, it did have sections of polyurethane foam in the inlet

which greatly reduced the turbulence levels and produced a very uniform flow. However, there was still a substantial boundary layer on either side of the splitter plate which resulted in a wake at the end of the splitter plate. In addition, the turbulence levels at the inlet were somewhat larger than would have been desirable. Discussions of the wake size, the turbulence levels, and temperature profiles at the inlet follow, along with discussions of their possible effects on the flow development.

5.1.1 Splitter Plate Wake

Figure 5.1.1 shows a profile of the mean horizontal velocity component, $\overline{u}$, as a function of the depth. The profile was taken 10 cm downstream from the end of the splitter plate, which was located 15 cm below the water surface. The mean speed of the upper layer was 18.7 cm/s (somewhat larger than used in most experiments) while the lower layer mean speed was 12.7 cm/s; the temperatures of the two layers were identical. The velocity defect in Figure 5.1.1 near -15 cm is a result of the boundary layer on the splitter plate; this wake is quickly washed out when there is a sufficiently large velocity difference between the two layers, as can be seen in Figure 5.1.2. The velocity profile shown in this figure was measured 20 cm from the splitter plate, for the same case as the profile shown in Figure 5.1.1; the velocity defect is just barely apparent. The large mean speed of the upper layer resulted in the slight shear in the upper portion of the flow. This was not apparent when the mean speed of the upper layer was less, as was typical of most experiments.

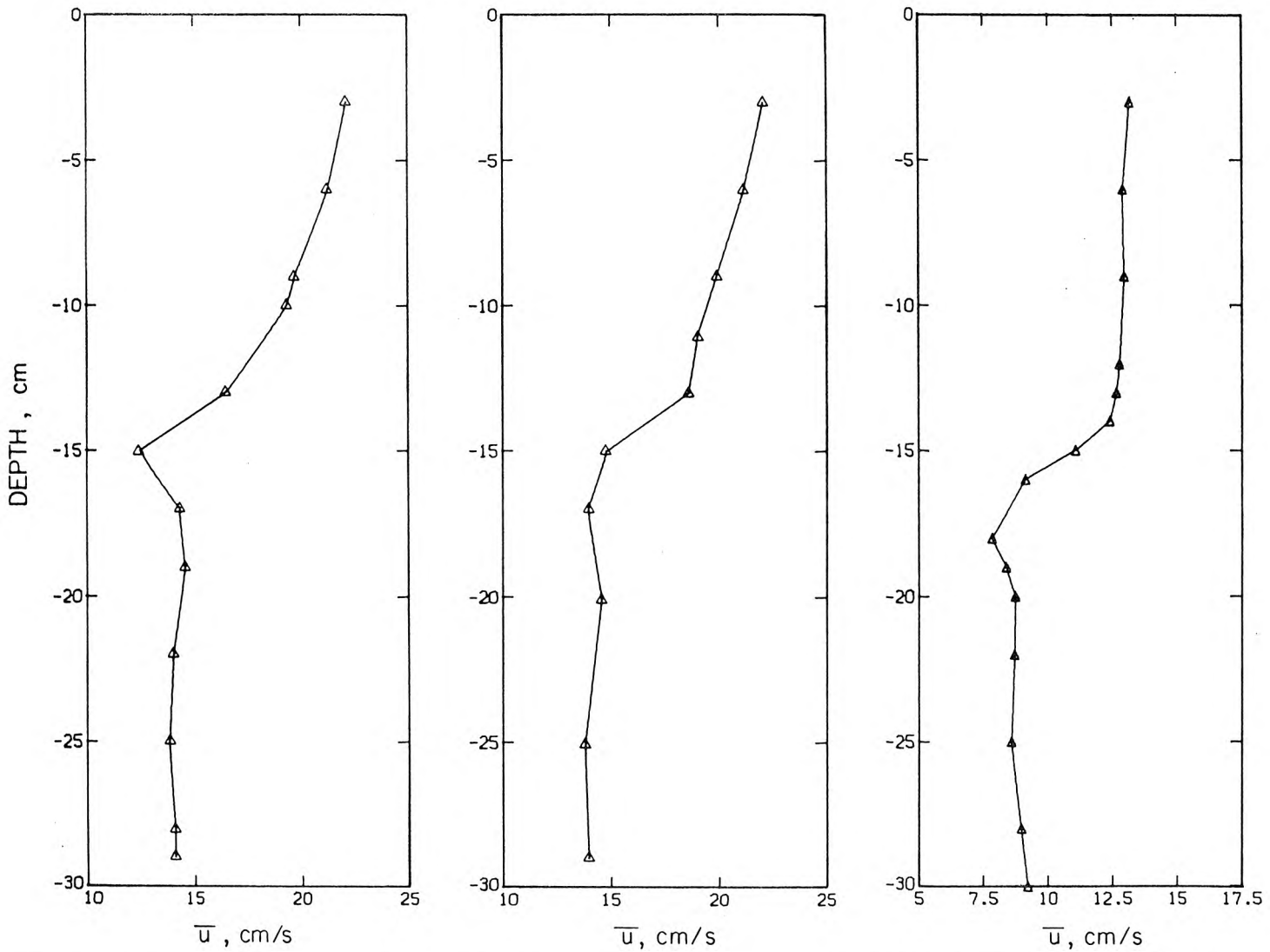

Figure 5.1.1 Profile of $\overline{u}$ measured 10 cm from the splitter plate. $U_1 = 18.7$ cm/s, $U_2 = 12.7$ cm/s, $\Delta T_o = 0$.

5.1.2 Profile of $\overline{u}$ measured 20 cm from the splitter plate. Same case as in Figure 5.1.1.

5.1.3 Profile of $\overline{u}$ measured 20 cm from the splitter plate. $U_1 = 11.8$ cm/s, $U_2 = 8.2$ cm/s, $\Delta T_o = 0$.

Note: Points are measured values, lines are linear interpolations. Velocity scales are offset from zero.

Figure 5.1.3 also shows a profile of $\bar{u}$ measured 20 cm from the splitter plate for a case where the mean speed of the upper layer, U_1, was 11.8 cm/s and the mean speed of the lower layer, U_2, was 8.2 cm/s. Here, the velocity profile is much more uniform in the upper layer than in Figure 5.1.1, and the velocity defect is still apparent, although it was nearly nonexistent 50 cm from the splitter plate, as the wake from the splitter plate was quickly destroyed by the mixing layer which developed. As would be expected, the larger the velocity difference between the two layers, the sooner the wake was destroyed.

For the cases in which there was a density difference between the layers as well as a velocity difference, the wake was not quickly destroyed if the initial shear was not sufficiently large. Figure 5.1.4 shows a velocity profile measured 40 cm from the splitter plate in a case where U_1 was 12.6 cm/s, U_2 was 10.2 cm/s and the temperature difference between the layers was 1.5°C ($\Delta\rho/\rho = 4.3 \times 10^{-4}$). A slight velocity defect is apparent, and it was still apparent at 80 cm from the splitter plate. The small velocity difference in this case, coupled with the density difference, was not sufficient to "wash out" the wake rapidly. In other cases, where the velocity difference was larger, the wake was rapidly destroyed.

In some cases, experiments were conducted with very little velocity difference between the two layers. In the cases which also had a substantial density difference, the wake was apparent far downstream. The turbulence in the wake of the splitter plate was quickly suppressed by buoyancy effects and a laminar layer developed

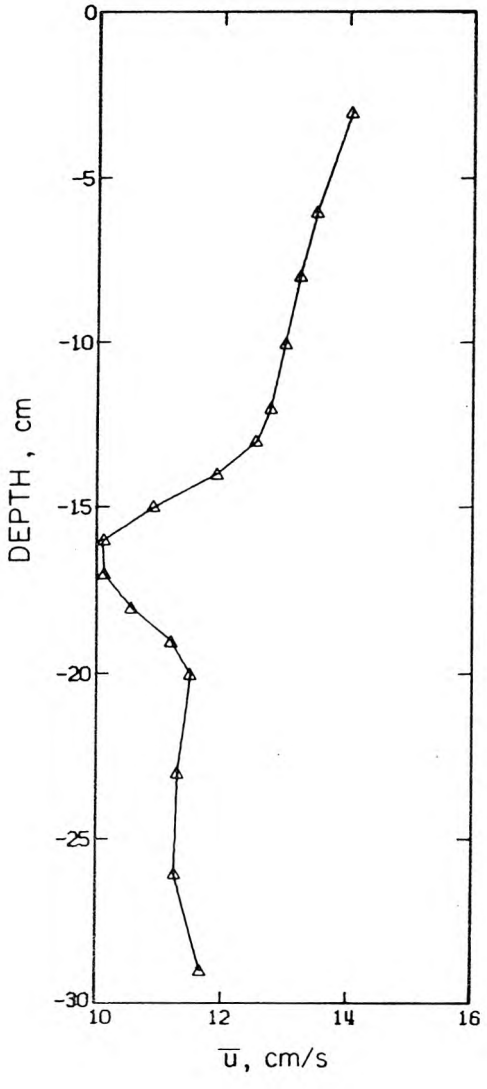

Figure 5.1.4 Profile of $\overline{u}$ measured 40 cm from the splitter plate. $U_1 = 12.6$ cm/s, $U_2 = 10.5$ cm/s, $\Delta T_o = 1.5°C$ ($\Delta\rho/\rho_o = 4.3 \times 10^{-4}$).

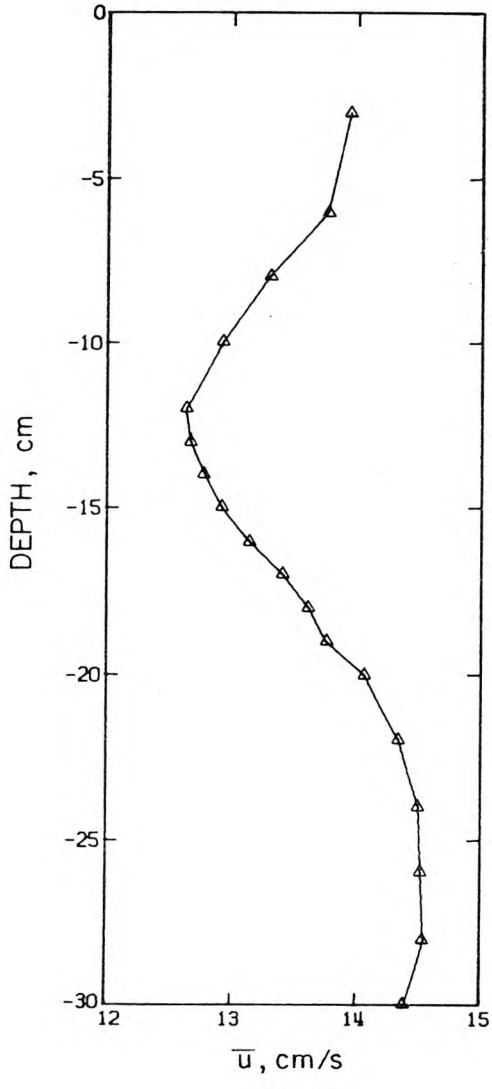

5.1.5 Profile of $\overline{u}$ measured 4.7 m from the splitter plate. $U_1 = 11.9$ cm/s, $U_2 = 12.5$ cm/s, $\Delta T_o = 1.4°C$ ($\Delta\rho/\rho_o = 4.2 \times 10^{-4}$).

Note: Points are measured values, lines are linear interpolation. Velocity scales are offset from zero.

at the interface. The velocity defect then persisted in the interface far downstream. Figure 5.1.5 shows an example of this; here U_1 was 11.9 cm/s, U_2 was 12.5 cm/s and the initial temperature difference, ΔT_o, was 1.4°C ($\Delta\rho/\rho_o = 4.2 \times 10^{-4}$). The velocity defect from the wake is still apparent at 4.7 m from the splitter plate.

A measure of the thickness of the wake when ΔU_o is zero can be given by the displacement thickness, defined here as

$$\ell_\delta = \int \left(1 - \frac{\overline{u}}{U}\right) dy \qquad (5.1.1)$$

where $U = U_1 = U_2$. Measurements made about 10 to 15 centimeters from the splitter plate indicate that ℓ_δ was about one centimeter. This value gives a rough estimate of the size of the wake. Figures 5.1.6 and 5.1.7 show photographs of dye streaks at the flume inlet. In Figure 5.1.6, the velocity difference between the two layers is close to zero, while in Figure 5.1.7, the upper layer has a mean speed of 6 cm/s faster than the lower layer. The photographs give an indication of the size of the wake from the splitter plate and of the shape of the velocity profiles.

The wake certainly had an effect on the downstream flow when there was a density difference between the two layers and no velocity difference; however, the mixing which occurred near the splitter plate when there was a sufficiently large velocity difference greatly reduced the influence of the wake on the flow far downstream. Evidence produced in Section 5.3 shows that the wake in fact had little effect on the mixing layer as well, for the large two-dimensional structure found in

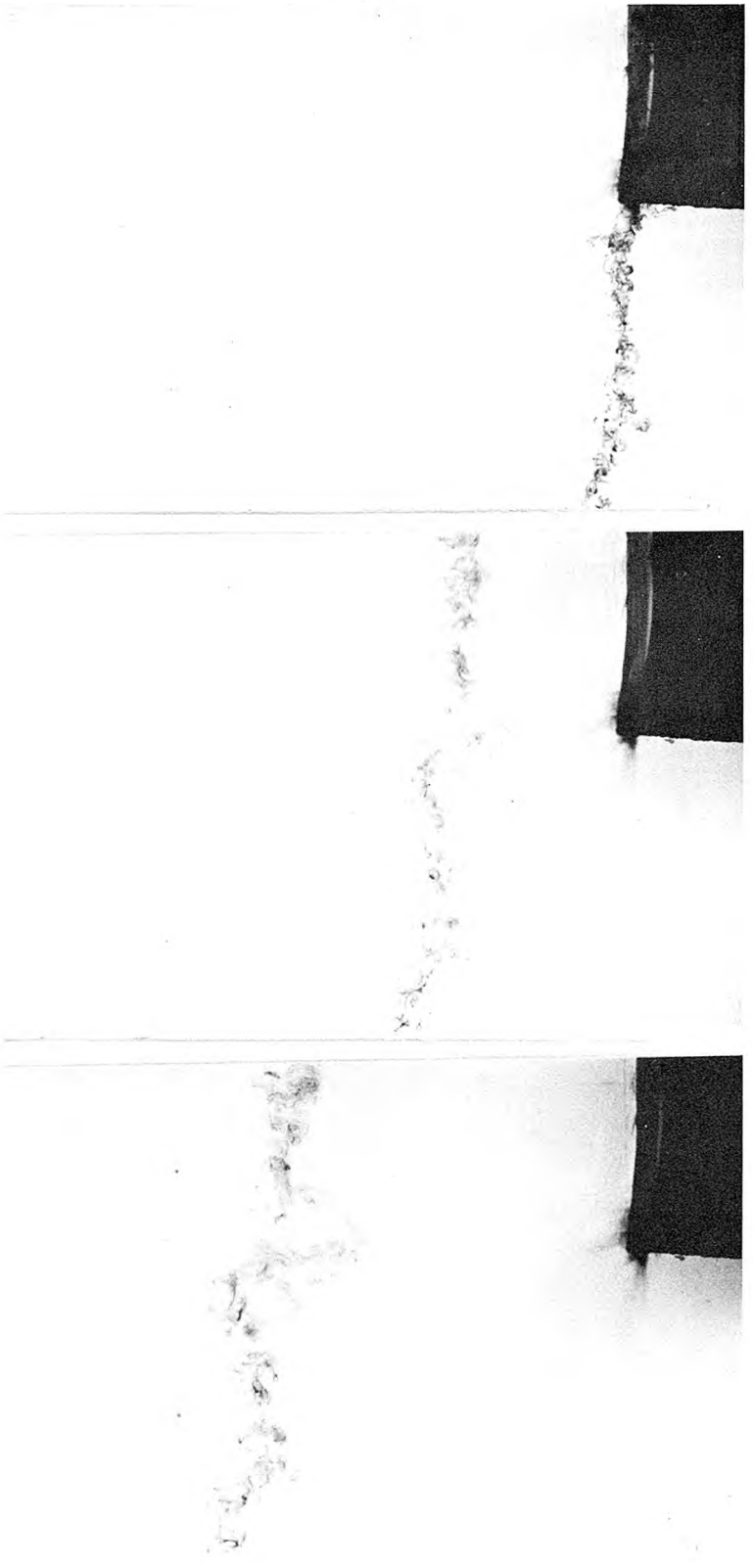

Figure 5.1.6 Three successive photographs of a single dye streak at the flume inlet. $\Delta U_o \approx -0.5$ cm/s, $\Delta\rho/\rho_o = 0$.

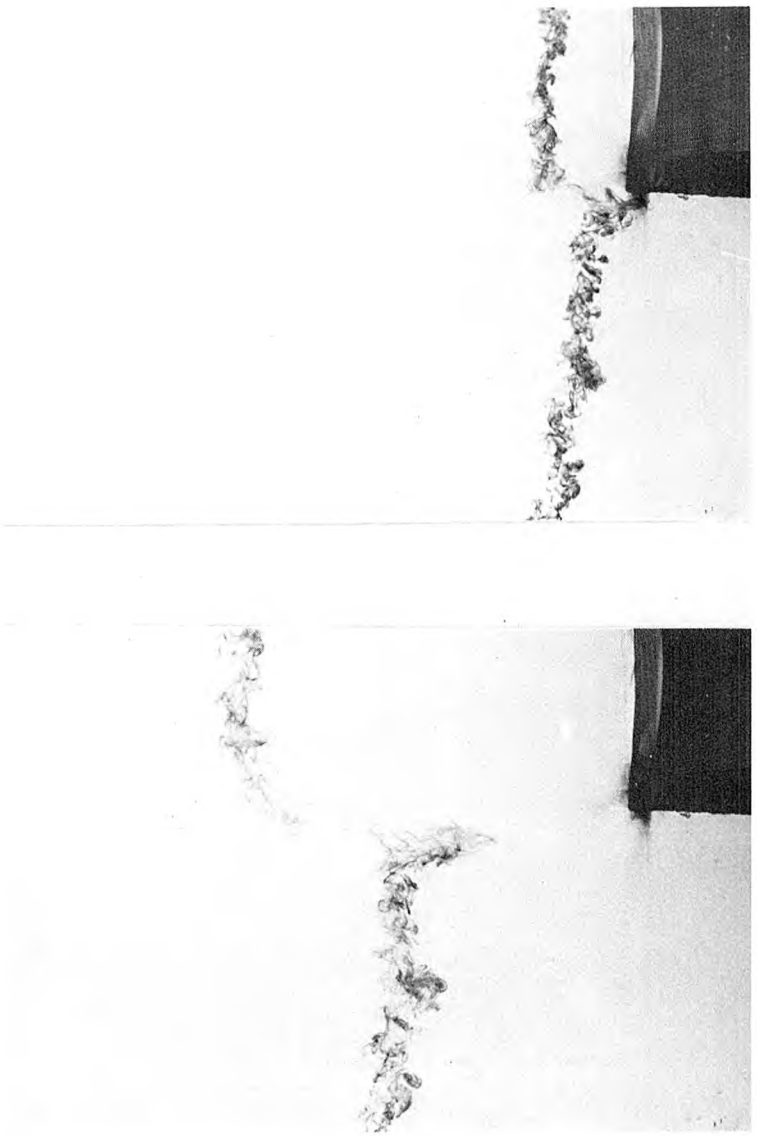

Figure 5.1.7 Two successive photographs of a single dye streak at the flume inlet. $\Delta U_o \approx 6$ cm/s, $\Delta\rho/\rho_o = 0$.

mixing layers by Brown and Roshko (1974), Winant and Browand (1974), Dimotakis and Brown (1976), and others, was found here as well.

5.1.2 Inlet Turbulence Levels and Flow Uniformity

The typical root-mean-square values of the velocity fluctuations at the inlet ranged from one to three per cent of the local mean velocity. Figure 5.1.8 shows profiles of $\sqrt{\overline{u'^2}}$, $\sqrt{\overline{v'^2}}$ and $\sqrt{\overline{u'^2}}/\bar{u}$ measured 20 cm from the splitter plate; the corresponding mean velocity profile for this case is given in Figure 5.1.3. One can see that the turbulent intensity is fairly constant within the regions above and below the mixing layer, which is near y = -15 cm. Typically, it was found that the turbulence intensity was about 2.5 per cent of the local mean velocity in the upper layer and about 1.5 per cent of the local mean velocity in the lower layer, with slightly higher values (up to 0.5 per cent higher) nearer the splitter plate (excluding the mixing layer).

Figure 5.1.9 shows a profile of $-\overline{u'v'}$ for the same case considered in Figures 5.1.3 and 5.1.8. Outside of the mixing layer, the values of $-\overline{u'v'}$ are very nearly zero; since $\sqrt{\overline{u'^2}}$ and $\sqrt{\overline{v'^2}}$ are not zero, one must conclude that the vertical and horizontal velocity fluctuations are not correlated at the inlet away from the mixing layer. This is not unexpected, since the vertical velocity gradient away from the mixing layer (above and below) is very small.

The laser-Doppler velocimeter used in the experiments was capable of making measurements only along the centerline of the flume; hence, detailed velocity measurements over the cross-section of the inlet could not be made. The uniformity of the flow was checked using dye

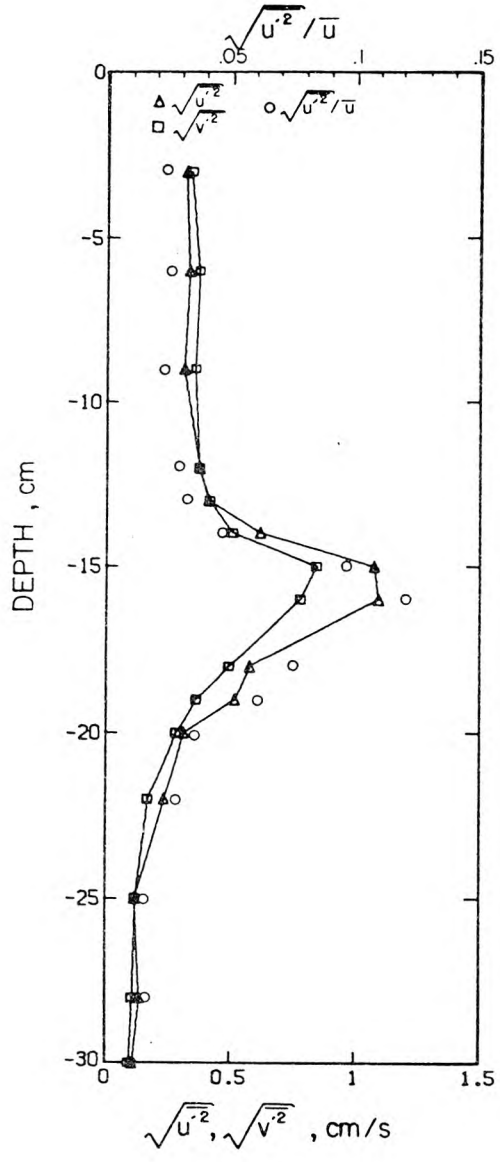

Figure 5.1.8 Profiles of $\sqrt{\overline{u'^2}}$, $\sqrt{\overline{v'^2}}$ and $\sqrt{\overline{u'^2}}/\overline{u}$, measured 20 cm from the splitter plate for the same case as shown in Figure 5.1.3.

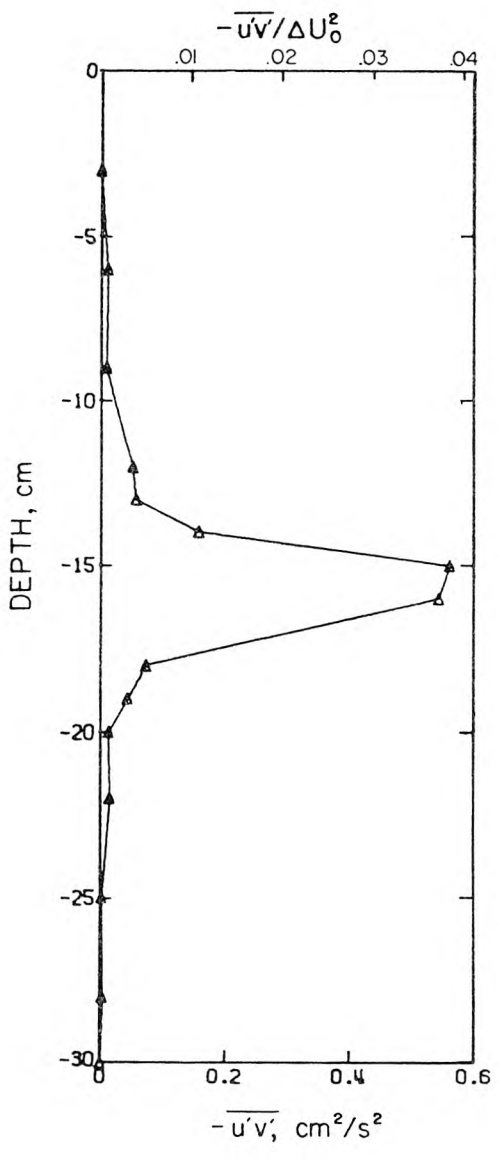

5.1.9 Profile of $-\overline{u'v'}$ measured 20 cm from the splitter plate, for the same case shown in Figure 5.1.3.

streaks, and the flow distribution was found to be remarkably uniform in the lateral direction. The use of polyurethane foam in the inlet had an astounding effect on the flow, producing a very flat velocity profile across the channel at the inlet. Dye streaks indicated a boundary layer about 5 cm thick at either wall, with a flat profile across the middle 100 cm of the flume. Figure 5.1.10 shows photographs of dye streaks across the flume channel at the inlet. The photographs were taken a few seconds after the dye was placed in the flume, and from the photos, one can see the boundary layers on the walls.

5.1.3 Inlet Temperature Profile

Because the splitter plate was made of aluminum, which conducts heat quite well, the temperature profile at the end of the splitter plate was not an exact step-function for the cases in which there was a temperature difference in the two layers. Figure 5.1.11 shows profiles of the mean temperature and temperature fluctuations measured on the centerline of the flume at the exact end of the splitter plate. The temperature profile has a rapid change at the splitter plate, but the gradient of the mean temperature is a continuous function. Defining a length scale, ℓ_T, for the temperature gradient as:

$$\ell_T = \frac{6}{\Delta T_o^{\,2}} \int_{-h}^{0} (T_1 - \overline{T}(y))\ (\overline{T}(y) - T_2)\,dy \qquad (5.1.2)$$

where y is the vertical coordinate,

T_1 is the mean temperature of the upper layer (away from the splitter plate),

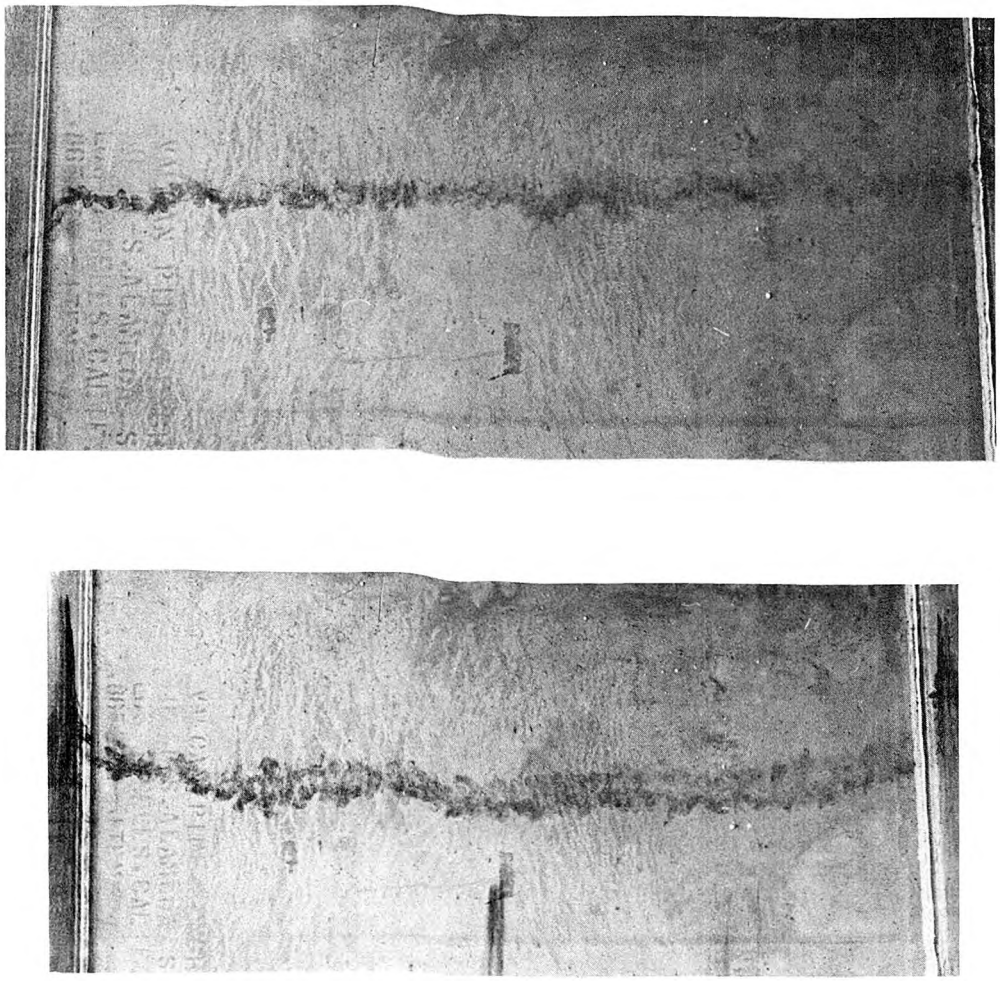

Figure 5.1.10 Photographs of dye streaks across the width of the flume at the inlet. Dye was injected at the end of the splitter plate, which coincides with the upper edges of the photographs. Upper photograph shows dye streak which was injected in the upper layer of flow, lower photograph shows dye streak in the lower layer of flow.

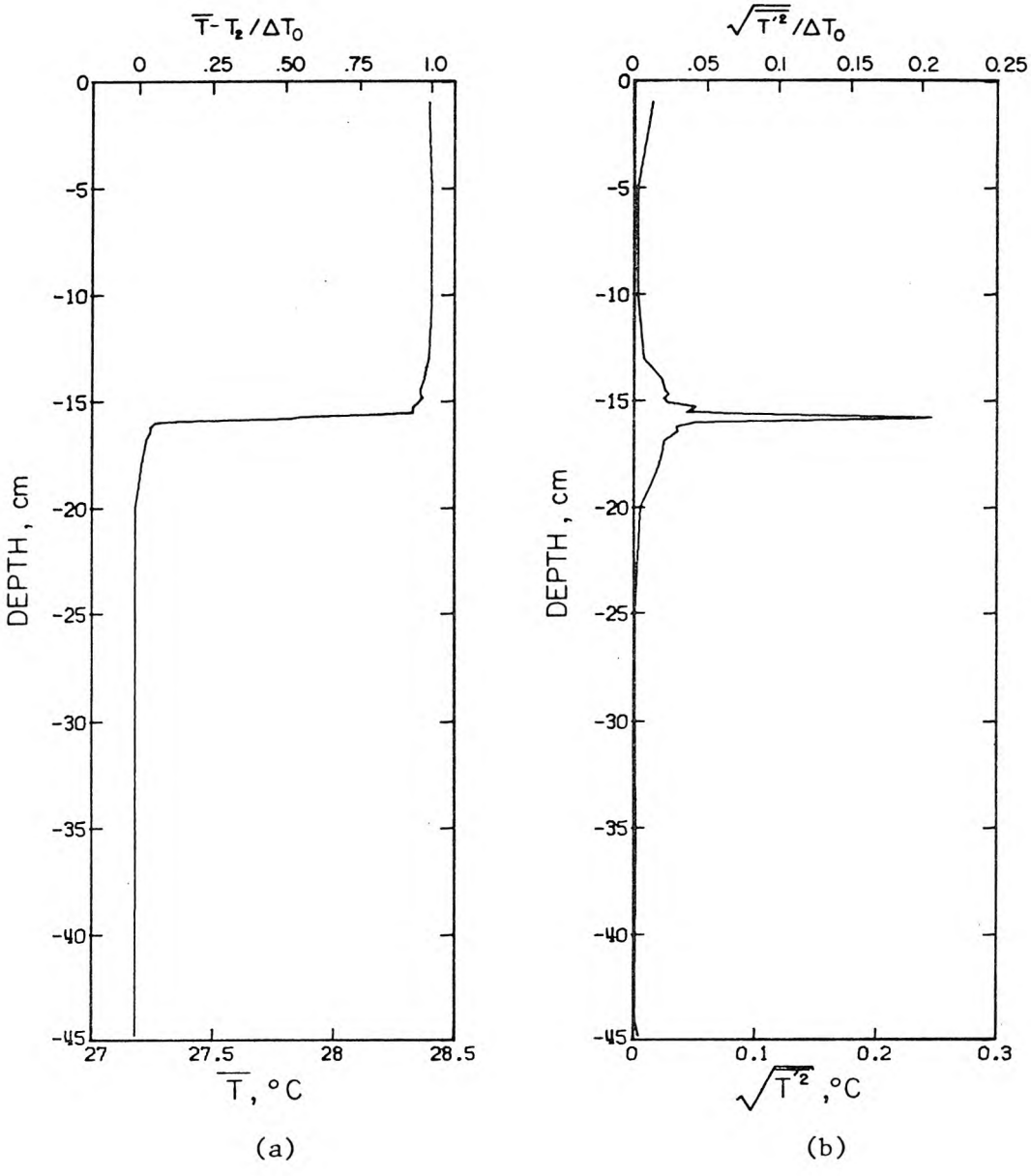

Figure 5.1.11 Profiles of (a) the mean temperature and (b) the r.m.s. temperature fluctuations at the splitter plate. $\Delta T_o = 1.2°C$.

T_2 is the mean temperature of the lower layer (away from the splitter plate),

$\Delta T_o \equiv T_1 - T_2$, and

h is the total depth,

then one finds for this profile that $\ell_T = 0.66$ cm. Using the maximum slope thickness (Equation 2.1.20), one finds $\ell_T^* = 0.45$ cm. These values, then, are length scales for the temperature (and hence, density) effects at the inlet.

It was found that the temperature field at the inlet was quite uniform across the flume. Figure 5.1.12 shows a contour plot of isotherms at the inlet for a case in which the temperature difference between the layers was about 1.7°C and both layers had a mean speed of about 9 cm/s. As can be seen from the figure, the temperature of the water is quite uniform across the inlet. One would expect that the fluid near the walls would be somewhat cooler than the fluid near the center of the flume. The water in the flume was in this case, as in most cases, about five to seven degrees warmer than the air temperature. However, the walls are glass, a relatively poor heat conductor and radiator and, in this case, the water 0.2 cm from the wall was about 0.02°C cooler than the water near the center of the channel, and about 0.01°C cooler than the water 5 cm from the wall. It is expected that this slight transverse temperature gradient would have a negligible effect on the dynamics of the whole system.

In performing these experiments, one would like to have flat velocity and temperature profiles in the upper and lower layers with

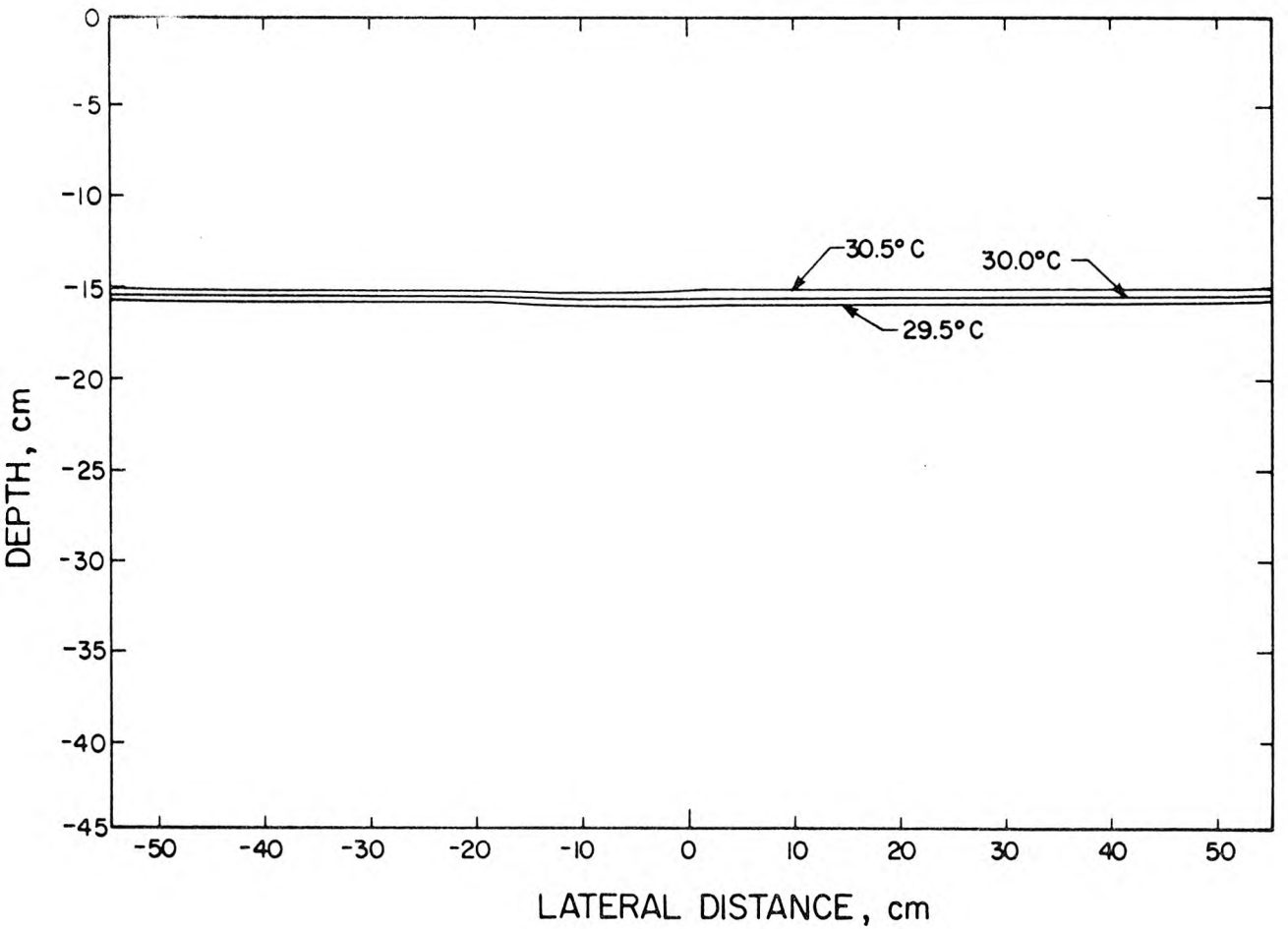

Figure 5.1.12 Plots of isotherms at the end of the splitter plate. ΔT_o = 1.7°C, T_1 = 30.8, T_2 = 29.1, U = 9 cm/s, h = 45.3 cm. Splitter plate was located 15.3 cm below water surface (y = 0).

sharp discontinuities at the splitter plate, and a straight flow with a negligibly small turbulence level. In this case, these things were not all possible, and one is left with the problem of determining their respective effects on the flow downstream. The flow at the inlet was quite straight, primarily due to the polyurethane foam in the inlet. The wake from the splitter plate was substantial, but it did not prevent the development of large two-dimensional vortices in the mixing layer. The wake did, however, result in a small velocity defect far downstream when ΔU_o was near zero and ΔT_o was greater than zero.

The high turbulence level of about one to three per cent of the local mean velocity undoubtedly caused additional mixing in the mixing layer; the velocity and temperature profiles must have been smoother downstream than they would have been with lower turbulence levels at the inlet. Furthermore, the additional mixing no doubt had an effect upon the dynamics of the large scale turbulent structure in the mixing layer, particularly when there was a density difference between the two layers. Thus while the inlet conditions were quite good, they were not perfect and this fact is taken into account in the subsequent discussions of the data.

5.2 Bottom Roughness and Boundary-Generated Turbulence

When the initial experiments were conducted, the channel had no artificial roughness. The bottom of the flume is made of stainless steel plate and each section is quite flat, although there are small changes in the elevation of the flume bottom up to about 0.2 cm between sections, due to small misalignments. The walls of the flume were made

of plate glass which was hydrodynamically smooth, except at the joints, where there are often slight depressions due to shrinkage of the sealant.

For the most part, the depth of the water during the experiments was about 45 cm; thus the hydraulic radius, R_h, was about 24.8 cm. The overall mean speed of the flow, U, varied from about 6 cm/s to 15 cm/s, so the Reynolds number $Re \equiv 4R_h U/\nu$ for the total flow varied from about 0.75×10^5 up to 1.85×10^5. Usually the Reynolds number was in the range of 1.1×10^5 to 1.5×10^5.

The average shear stress of the walls and bottom on the flow was determined by measuring the slope of the water surface. The shear velocity, u_*, was then determined from the equation

$$u_* = \sqrt{R_h g S} \qquad (5.2.1)$$

where g is the acceleration due to gravity, and

S is the slope of the water surface.

The average friction factor, f, was determined from the equation:

$$f = 8\, u_*^2/U^2 \quad . \qquad (5.2.2)$$

The average value of f for the flume with no artificial roughness was found to be 0.012 with a standard deviation of 0.01 for a range of Reynolds numbers from 1.17×10^5 to 1.5×10^5. The mean value of 0.012 puts the friction factor below the smooth curve on a Moody diagram, but this is not surprising, given the spread of data. Typically, the surface slopes were about 10^{-5}, but the accuracy of the slope measurements was

6.5×10^{-6}. Even using a high value of 0.01 cm for the average roughness of the glass and steel boundaries, one would expect the flume to be nearly hydraulically smooth. Using the standard Moody diagram for friction factors, one finds the value f = 0.017 for a hydraulically smooth channel with a Reynolds number of 1.3×10^5 (Davis and Sorensen (1969)).

Measurements of the Reynolds stress, $-\rho \overline{u'v'}$, were made in several experiments and the friction factor was computed from these measurements. The value of the shear stress at the bottom, τ_w, was computed using the values of $-\overline{u'v'}$ measured at several locations. A typical profile of $\overline{u'v'}$ is shown in Figure 5.2.1 for a case with negligible initial shear and no initial temperature difference. The measurements were made to a depth of y = -30 cm and the flume bottom was at y = -45 cm. For a uniform, two-dimensional, open channel flow, one would expect $\overline{u'v'}$ to be a linear function of the depth below the surface. Here, $\overline{u'v'}$ is very nearly zero to a depth of about -17 cm and then starts to rapidly decrease. (The values of $-\overline{u'v'}$ are small in the upper region because the velocity profile, shown in Figure 5.2.3, is very nearly flat in that region.) The shear stress at the bed was found by linear extrapolation of the measured values of $-\overline{u'v'}$ in the lower portion of the flow; for Figure 5.2.1 the extrapolated value of $-\overline{u'v'}$ at the bed was 0.45 cm^2/s^2. The friction factor for this case was then calculated from the average value of the shear stress along the bottom. For this particular case, the bed friction factor computed in the above manner is 0.018, while the overall friction factor computed from the surface slope measurement is 0.02 (compared to an average value for all experiments of 0.012). The

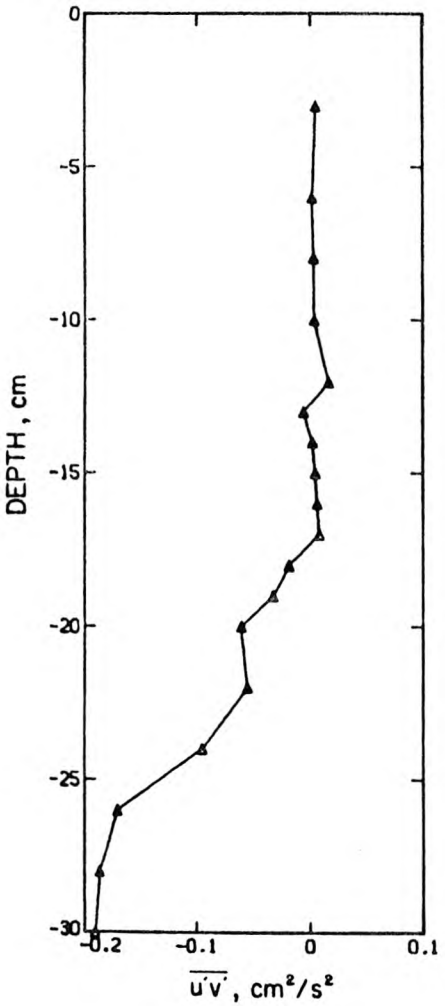

Figure 5.2.1 Profile of $\overline{u'v'}$ measured 21.5 m from the splitter plate. U = 12.1 cm/s, $\Delta T_o = 0$.

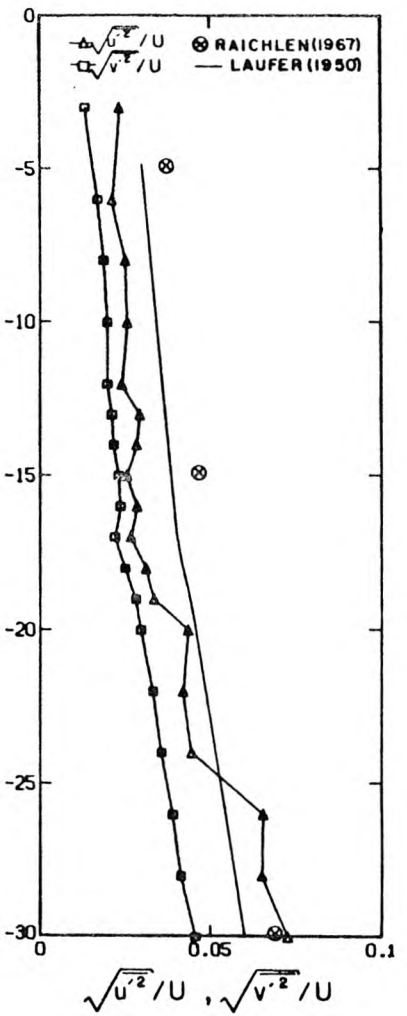

5.2.2 Profiles of $\sqrt{\overline{u'^2}}/U$ and $\sqrt{\overline{v'^2}}/U$ for the same case shown in Figure 5.2.1. Data of Laufer (1950) and Raichlen (1967) shown for comparison.

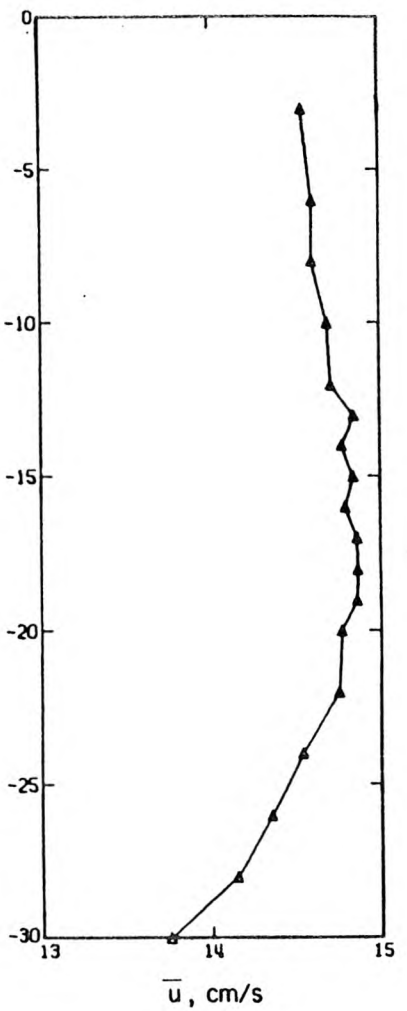

5.2.3 Profile of $\overline{u}$ for the same case shown in Figure 5.2.1.

Reynolds number was 1.5×10^5, and the smooth channel friction factor for this value is 0.0166.

Turbulence levels far downstream are shown in Figure 5.2.2 for the same flow conditions as in Figure 5.2.1. The measurements were made 21.5 m from the splitter plate; U_1 was 12.0 cm/s and U_2 was 12.2 cm/s. The overall Reynolds number of the flow was 1.51×10^5. The mean velocity profile for this case is shown in Figure 5.2.3. It is apparent from this figure that the flow does not have the logarithmic profile characteristic of a wide open channel flow. This is not unexpected, as the width of the channel is only 2.44 times as large as the depth. The velocity profile does have a maximum below the surface, as is typical for deep open channel flows. An indicator of the sensitivity of the laser-Doppler system is the fact that in the upper region of the flow, where the velocity gradient is negative, though small in absolute value, the corresponding values of $\overline{u'v'}$ are positive, as would be expected.

Figure 5.2.2 also shows the data of Laufer (1950) for a two-dimensional channel flow with a Reynolds number of 6.2×10^4 based on the maximum of the mean local velocities. The velocity fluctuations are normalized with U, the mean flow velocity. In the upper portion of the flow, the turbulence levels were somewhat lower in the present study than were measured by Laufer for the two-dimensional channel, while in the lower portion of the flow, the turbulence levels were comparable. Several values of turbulence levels measured by Raichlen (1967) in an open-channel flow at a Reynolds number of 9×10^4 are also shown for comparison. The comparison here is not made to show that

the flow in the present study was completely two-dimensional, as it certainly was not, but to show that the turbulence levels in the flume were not dissimilar to other types of channel flows.

Figure 5.2.4 shows the power spectral estimates of the velocity fluctuations at several depths for the same case as shown in Figures 5.2.1 - 5.2.3. The spectra are all similar at the higher wave numbers, regardless of depth, and the spectral estimates decay like $k^{-5/3}$ for the domain of wave numbers measured, as one would expect for the inertial subrange. Here, the wave number, k, is defined as the frequency of the fluctuation, in radians per second, divided by the mean local velocity, $\bar{u}$.

After conducting several experiments with a small initial density difference between the two layers, it became apparent that the turbulence levels in the flume were insufficient to cause appreciable mixing downstream. Further experiments were conducted with the floor of the flume roughened. Initially, the flume bottom was roughened by spreading bricks in a regular fashion over a section of the flume. Later the bricks were replaced with large, irregular rock. In both cases, the turbulence levels in the flume were substantially increased.

In the first set of experiments in which the flume was roughened, cement bricks 10 cm wide by 20 cm long and 5 cm high were cut in half to make pieces 10 cm by 10 cm by 5 cm and were placed in the flume in a regular fashion. Figure 5.2.5 shows the regular array in which the bricks were placed. The bricks covered 10 per cent of the flume floor in the section in which they were placed, starting at 4.5 m from the

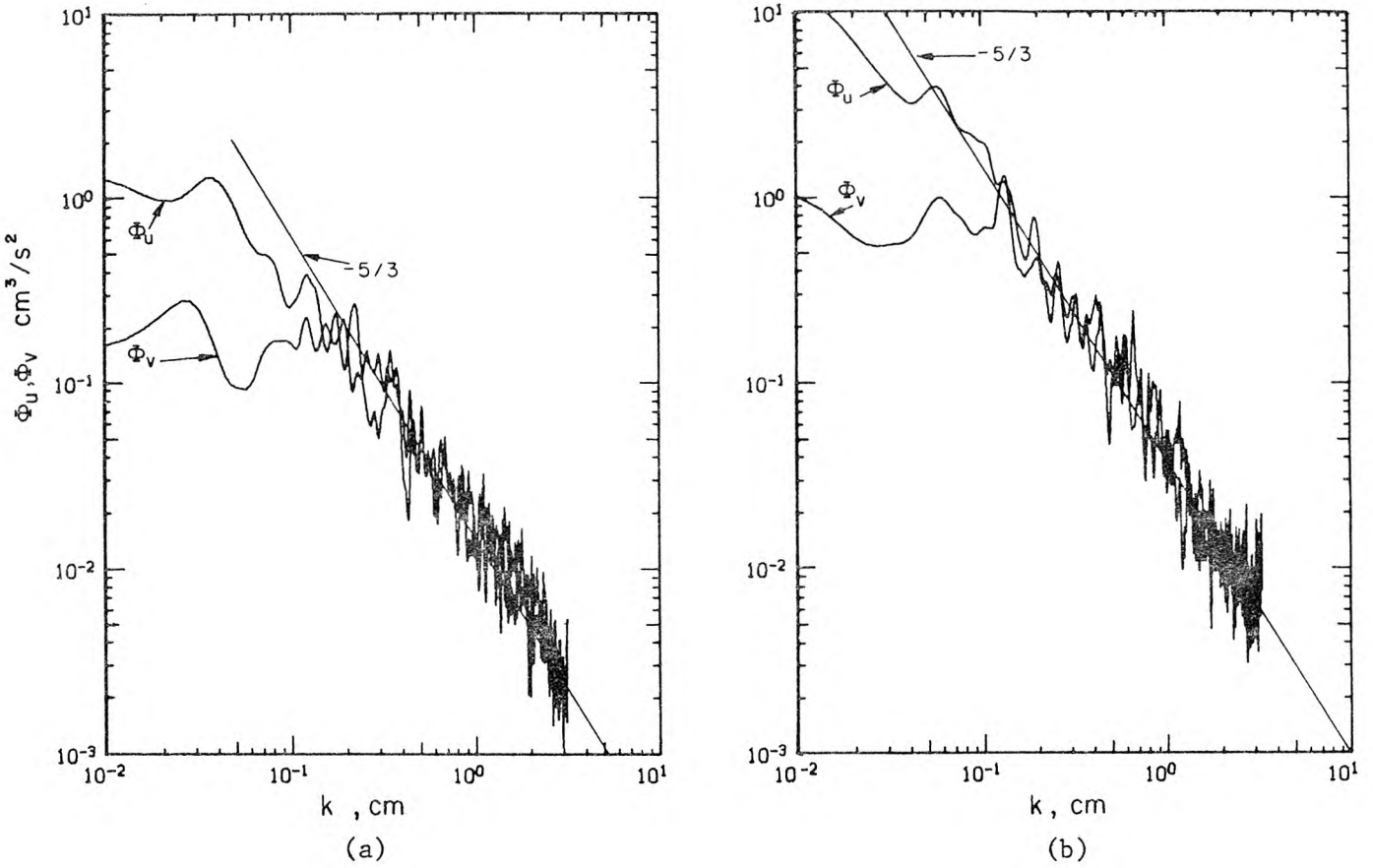

Figure 5.2.4 Power spectral estimates for u' and v' for the same case shown in Figure 5.2.1. (a) Measured 18 cm below the free surface. (b) Measured 28 cm below the free surface.

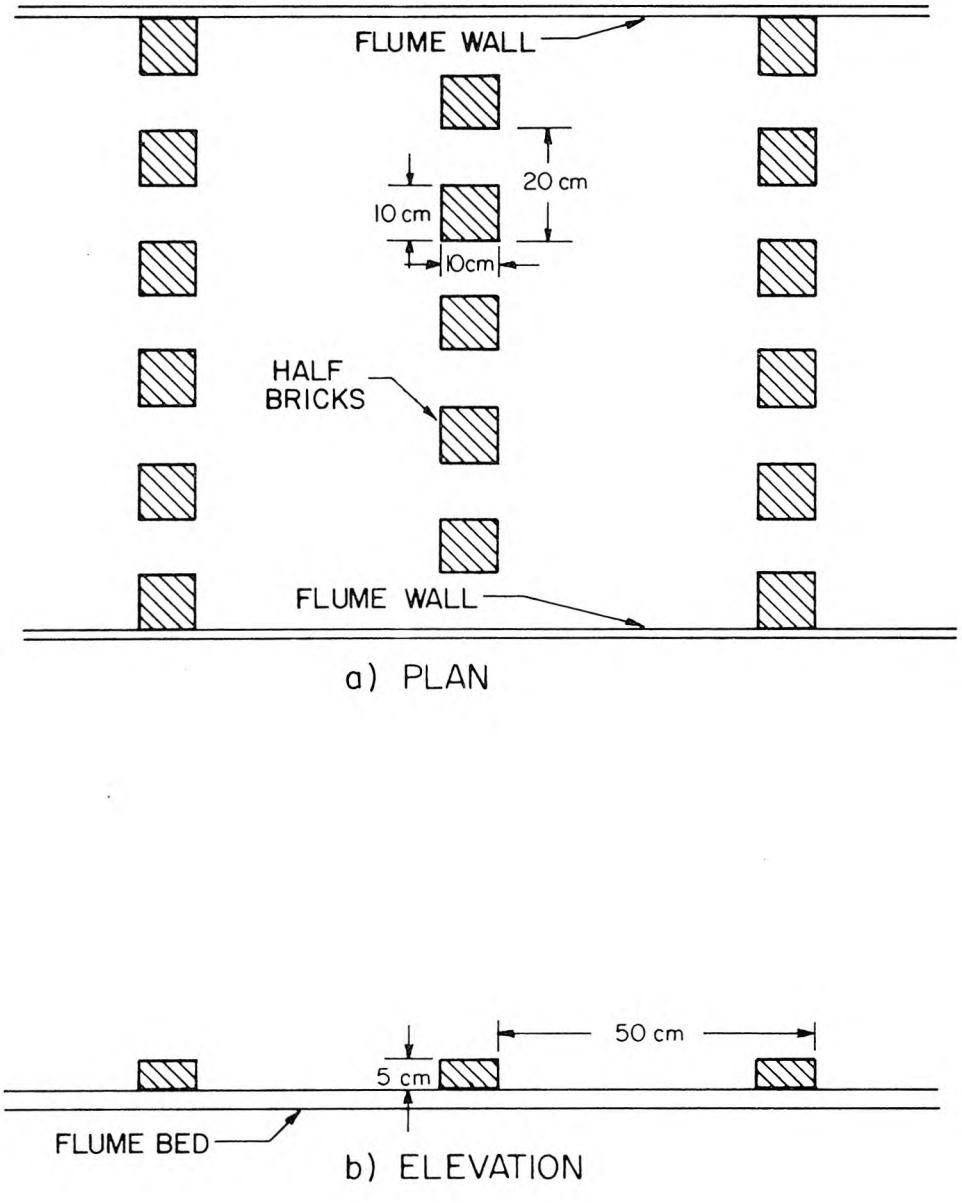

Figure 5.2.5 Arrangement of bricks on the flume bed for brick-roughened experiments.
(a) plan view (b) elevation

splitter plate and continuing downstream for 20 m. The initial 4.5 m was left smooth to allow the initial mixing layer to develop and, in some cases, collapse to a laminar layer undisturbed. In two experiments, the section of bricks was reduced to 10 m long, to study the relaxation process in the interface after instabilities developed. The spacing of the bricks was selected so that there was no obvious bias to the flow that would result in a secondary flow downstream and so that the bed shear stress was maximized (Koloseus and Davidian (1966)).

The friction factor for the flume with the brick roughness elements was measured as before. The average, overall friction factor for the whole flume with a 20 m section of the brick roughness elements was 0.046, with a standard deviation of 0.01, for a range of Reynolds numbers of 10^5 to 1.8×10^5. Using the method of side-wall correction proposed by Johnson (1942) and modified by Vanoni and Brooks (1957), the friction factor for the brick-roughened bed was calculated to be 0.095 ± 0.01. This value is an average over the roughened portion of the bed and includes the development of the fully rough turbulent flow at the beginning of the roughened section. The equivalent sand-grain roughness of the brick-roughened portion of the bed was 13 ± 2 cm.

From the measured values of $\overline{u'v'}$ for several cases with a range of Reynolds numbers from 10^5 to 1.8×10^5, an average friction factor of 0.075, with a standard deviation of 0.03, was calculated for the brick-roughened section of the flume. This value agrees fairly well with the value calculated above from the surface slope, and using the side-wall correction method.

Figures 5.2.6 - 5.2.8 show profiles of $\bar{u}$, $\sqrt{\overline{u'^2}}$, $\sqrt{\overline{v'^2}}$ and $\overline{u'v'}$ for a case with the brick-roughened section in the flume, but otherwise similar to the case shown in Figures 5.2.1 - 5.2.3. There are some striking differences between the two cases, aside from the greatly increased turbulence intensity. The mean speed of the flow is substantially greater in the upper portion of the flow for the case with the brick-roughened bottom. This is attributed to the fact that the roughened bottom greatly reduced the speed near the flume bottom. The profiles are otherwise similar, except that the turbulent quantities are much greater in the brick-roughened case.

Figure 5.2.9 shows spectral estimates of the velocity fluctuations for the same case considered in Figures 5.2.6 - 5.2.7. These power spectra are quite similar in shape to the ones shown in Figure 5.2.4. Thus, the brick-roughened section of the flume increased the turbulence intensity in the flume, but did not greatly alter the spectral characteristics of the turbulence.

The final set of experiments was conducted with the flume bed roughened with angular, crushed white rock with a nominal size range of 2.5 cm to 5 cm. The rock was first washed to remove the fines and then hand packed one layer thick on the flume bed. Figure 5.2.10 shows a section of the bed covered with the rock. The rocks initially covered a 10 m section, starting 4.5 m from the splitter plate, and was later extended to a 20 m section. The mean height of the rocks above the flume bed was 2.5 cm with a standard deviation of 1.25 cm.

In a manner similar to that described previously, the average Darcy

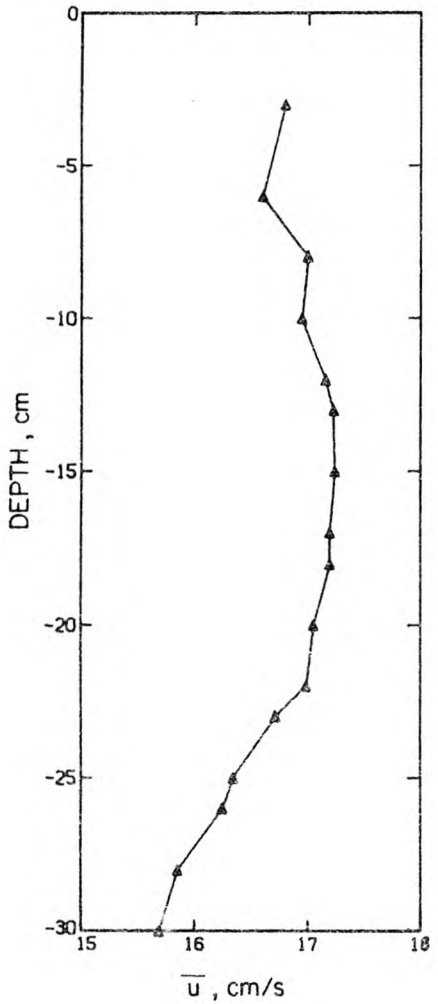

Figure 5.2.6 Profile of $\overline{u}$ for brick-roughened flow measured 24 m from the splitter plate. $U = 12.2$ cm/s, $\Delta T_o = 0$.

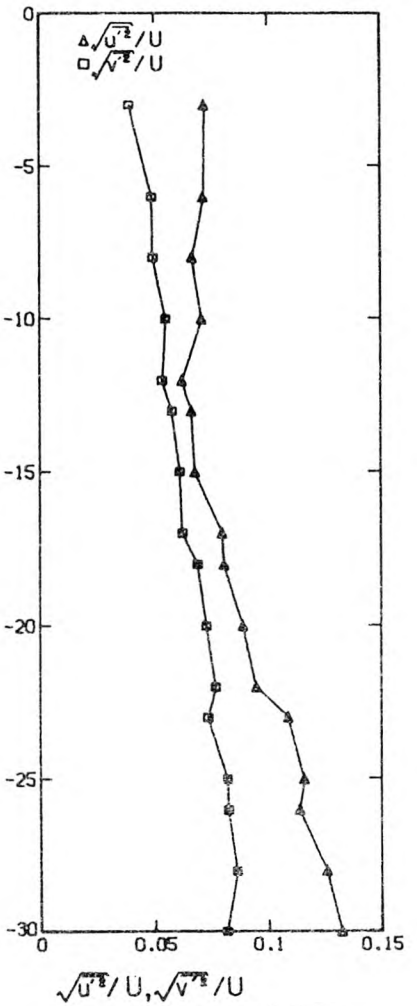

5.2.7 Profiles of $\sqrt{\overline{u'^2}}/U$, $\sqrt{\overline{v'^2}}/U$ for the same case as shown in Figure 5.2.6.

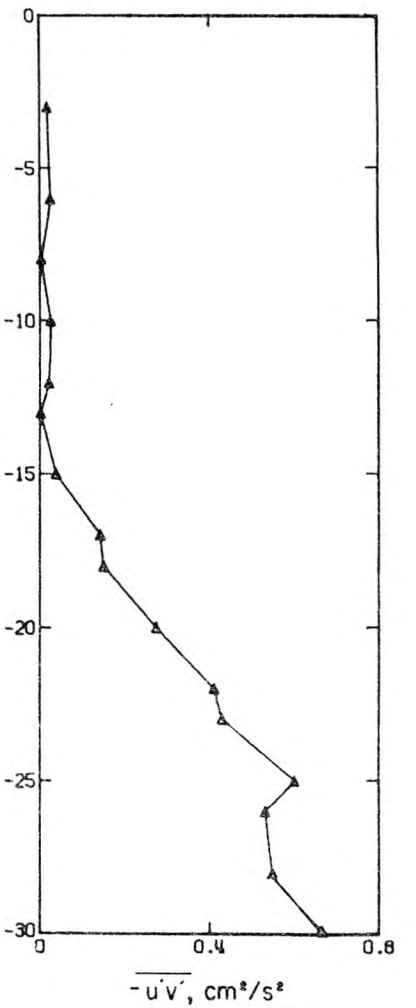

5.2.8 Profile of $-\overline{u'v'}$ for the same case as shown in Figure 5.2.6.

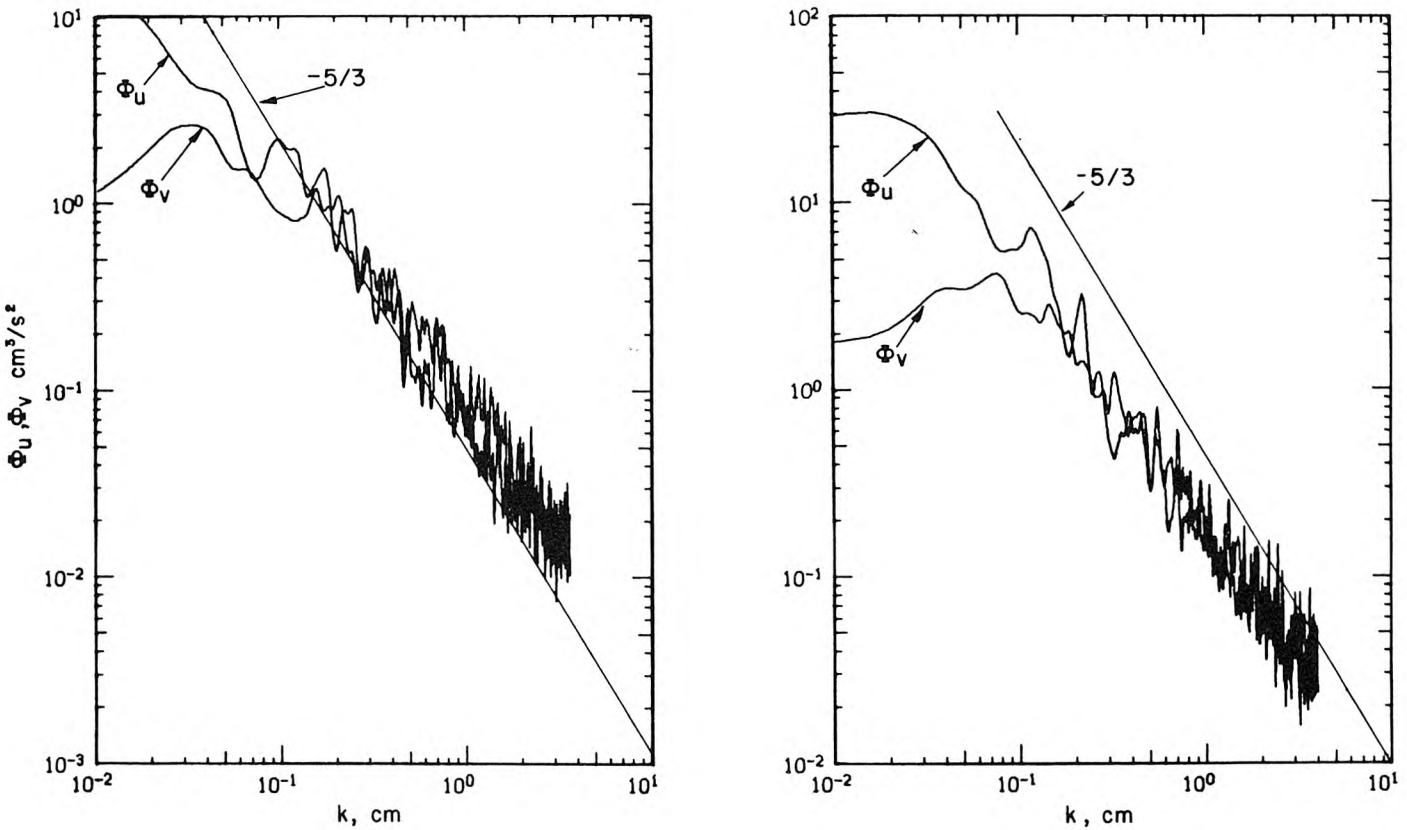

Figure 5.2.9 Power spectral estimates for u' and v' for the same case as shown in Figure 5.2.6. (a) Measured 17 cm below the free surface. (b) Measured 30 cm below the free surface.

Figure 5.2.10 Section of the flume bed roughened with rocks.

friction factor for the rock-roughened bed was calculated to be 0.066, with a standard deviation of 0.01, from surface slope measurements. The equivalent sand-grain roughness was 6 cm. The average friction factor calculated from profiles of $-\overline{u'v'}$ was found to be 0.07, with a standard deviation of 0.03. These values include the effect of the decreased water depth over the rocks.

Figures 5.2.11 - 5.2.13 show profiles of $\bar{u}$, $\sqrt{\overline{u'^2}}$, $\sqrt{\overline{v'^2}}$ and $-\overline{u'v'}$ for a flow over the rock-roughened bed, but otherwise similar to the flow shown in Figures 5.2.1 - 5.2.3. The mean velocities are somewhat larger here than in the case with the brick-roughened bed (shown in Figure 5.2.6); this is partly due to the decreased depth of flow over the rocks. Consequently, the gradients and turbulence levels are somewhat higher near the bed for the rock-roughened case.

Figure 5.2.14 shows the spectral estimates of the velocity fluctuations for this same case. These spectra are quite similar to the spectra obtained for the smooth bed and brick-roughened cases, and again show the $k^{-5/3}$ dependence in the higher wave numbers.

5.3 Qualitative Flow Description I - The Mixing Layer

In this section, a qualitative description of the initial flow development is given. Detailed quantitative descriptions are presented in Chapters 6 and 7.

In the experiments which had an initial velocity difference between the two layers, a mixing layer formed directly off the splitter plate. The most striking features of the mixing layer were the large two-dimensional vortical structures which developed in the flow. These have

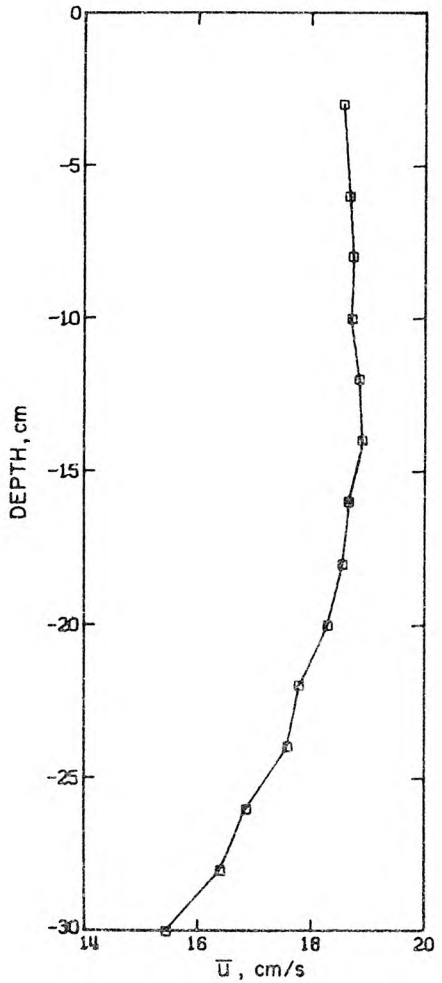

Figure 5.2.11 Profile of $\bar{u}$ for a rock-roughened case measured 24 m from the splitter plate. $U = 12.5$ cm/s, $\Delta T_o = 0$.

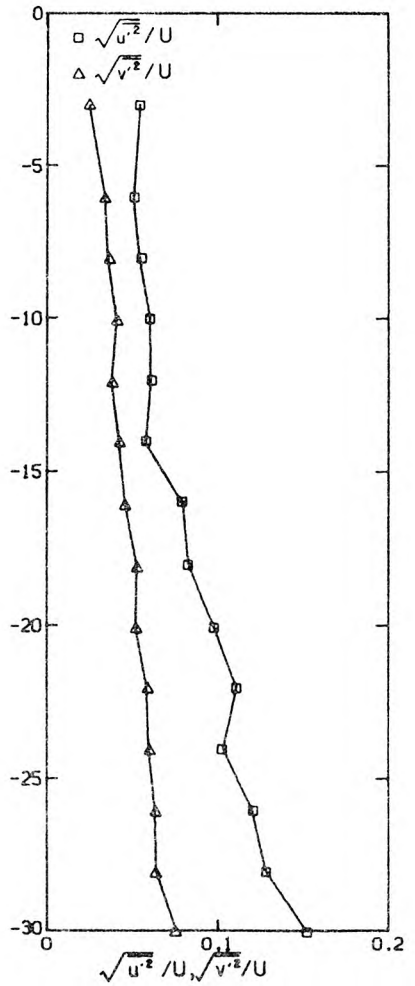

5.2.12 Profiles of $\sqrt{\overline{u'^2}}/U$ $\sqrt{\overline{v'^2}}/U$ for the same case shown in Figure 5.2.11.

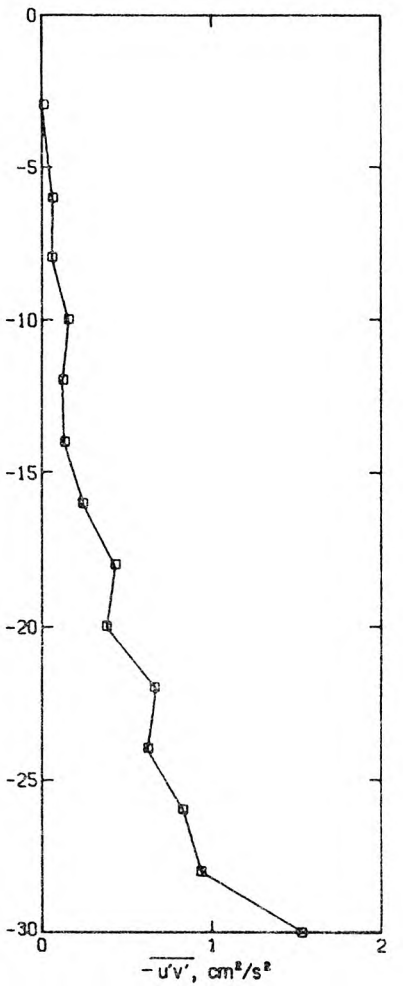

5.2.13 Profile of $-\overline{u'v'}$ for the same case shown in Figure 5.2.11.

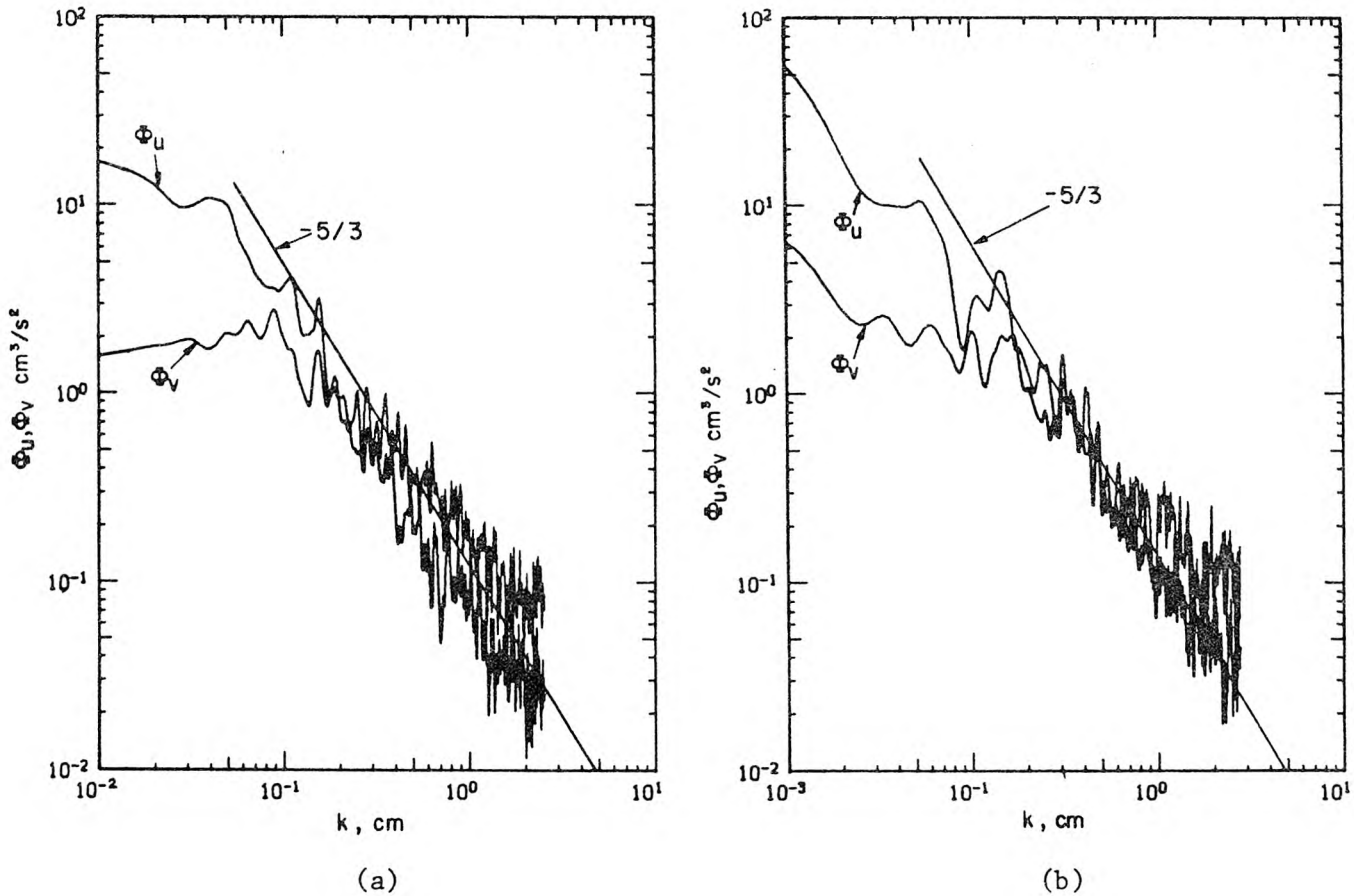

Figure 5.2.14 Power spectral estimates of u' and v' for the same case as shown in Figure 5.2.11. (a) Measured 18 cm below the free surface. (b) Measured 26 cm below the free surface.

of course, been observed previously (Brown and Roshko (1974); Winant and Browand (1974)) and it was expected that they would be seen here. There are, however, several aspects of the mixing layer that will be discussed here.

A typical flow is shown in Figure 5.3.1 where the overall channel Reynolds number of the flow was about 6×10^4 and the velocity difference was 4.4 cm/s between the two layers. In this photograph, dye had been injected into the flow a few centimeters upstream from the end of the splitter plate.

The initial portion of the mixing layer just downstream of the splitter plate sometimes became three-dimensional for a short distance, in the sense that the large vortices which developed did not always persist completely across the flume. The three-dimensionality at higher Reynolds numbers seemed to be caused by a combination of the velocity defect which developed from the splitter plate wake, and the high turbulence levels at the inlet. Large eddies were still observed in this region, and appeared to be responsible for much of the mixing which occurred in this region.

Further downstream, however, the large, two-dimensional structure appeared if the initial velocity difference was sufficiently large. "Sufficiently large" in this instance usually meant about three or four centimeters per second. While the inlet turbulence and the wake off of the splitter plate tended to inhibit the development of the two-dimensional structure, it did not prevent it from eventually developing.

Figure 5.3.2 shows an example of the development of the large,

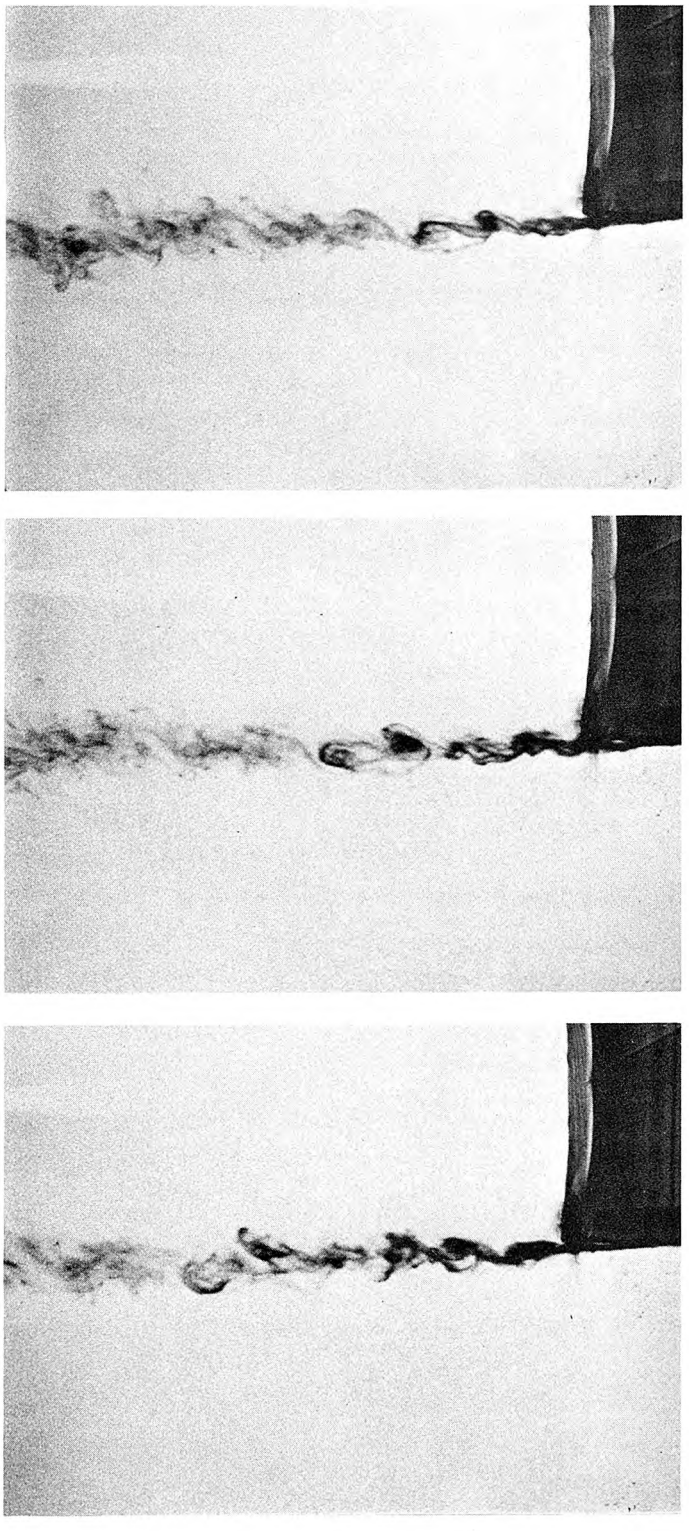

Figure 5.3.1a Three successive photographs of a dye streak at the flume inlet. $\Delta U_o \approx 4.4$ cm/s, $\Delta\rho/\rho_o = 0$. Center of photographs is at x = 0.3 m.

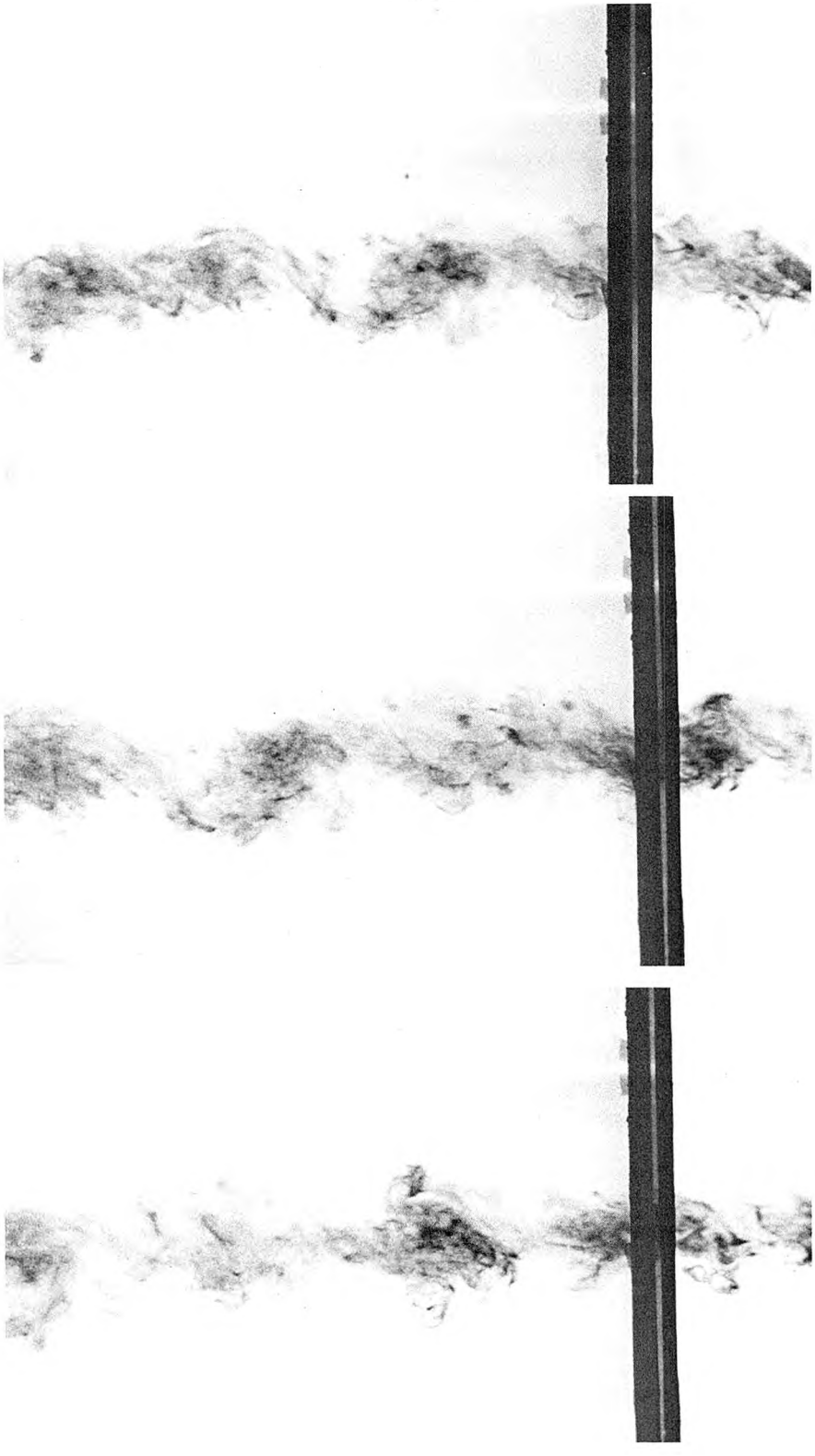

Figure 5.3.1b Three successive photographs of a dye streak downstream of the inlet. Same flow conditions as in Figure 5.3.1a, ΔU_o = 4.4 cm/s, $\Delta\rho/\rho_o$ = 0. Center of photographs is at x = 1.05 m.

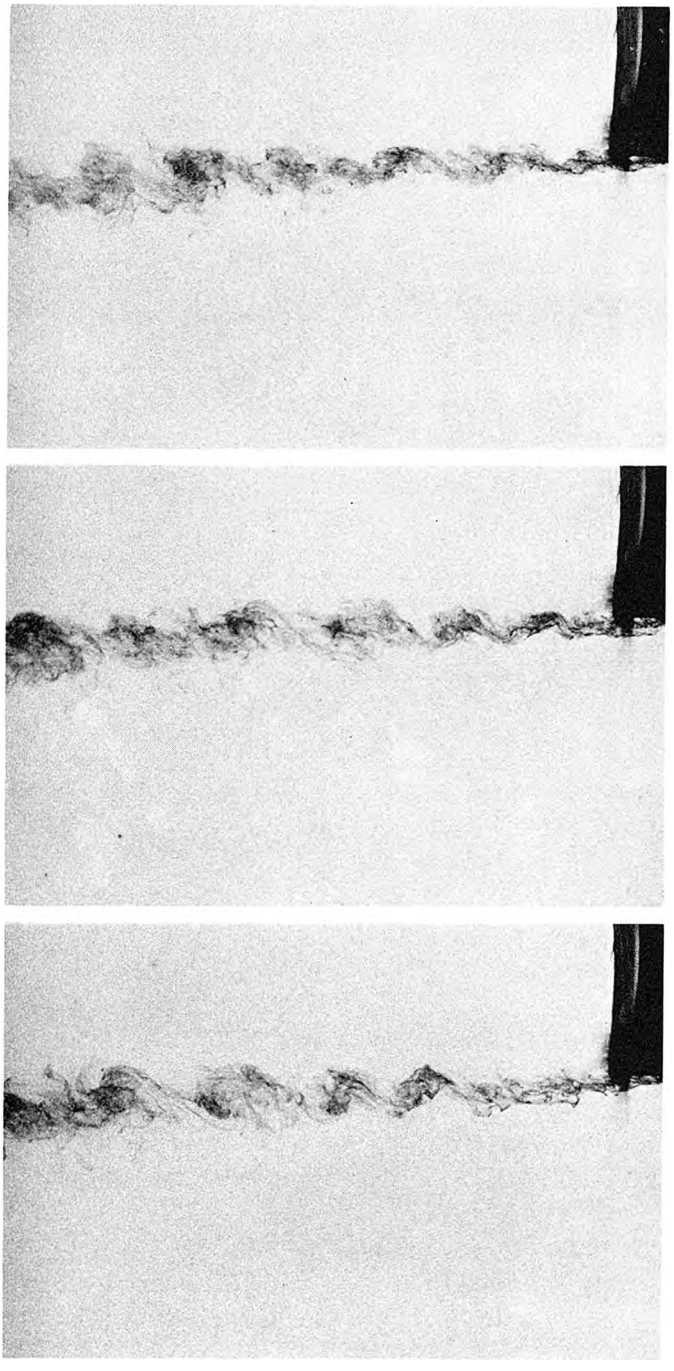

Figure 5.3.2a Three successive photographs of a dye streak injected at the flume inlet. ΔU_o = 6 cm/s, $\Delta\rho/\rho_o$ = 0. Center of photographs is at $x \cong 0.3$ m.

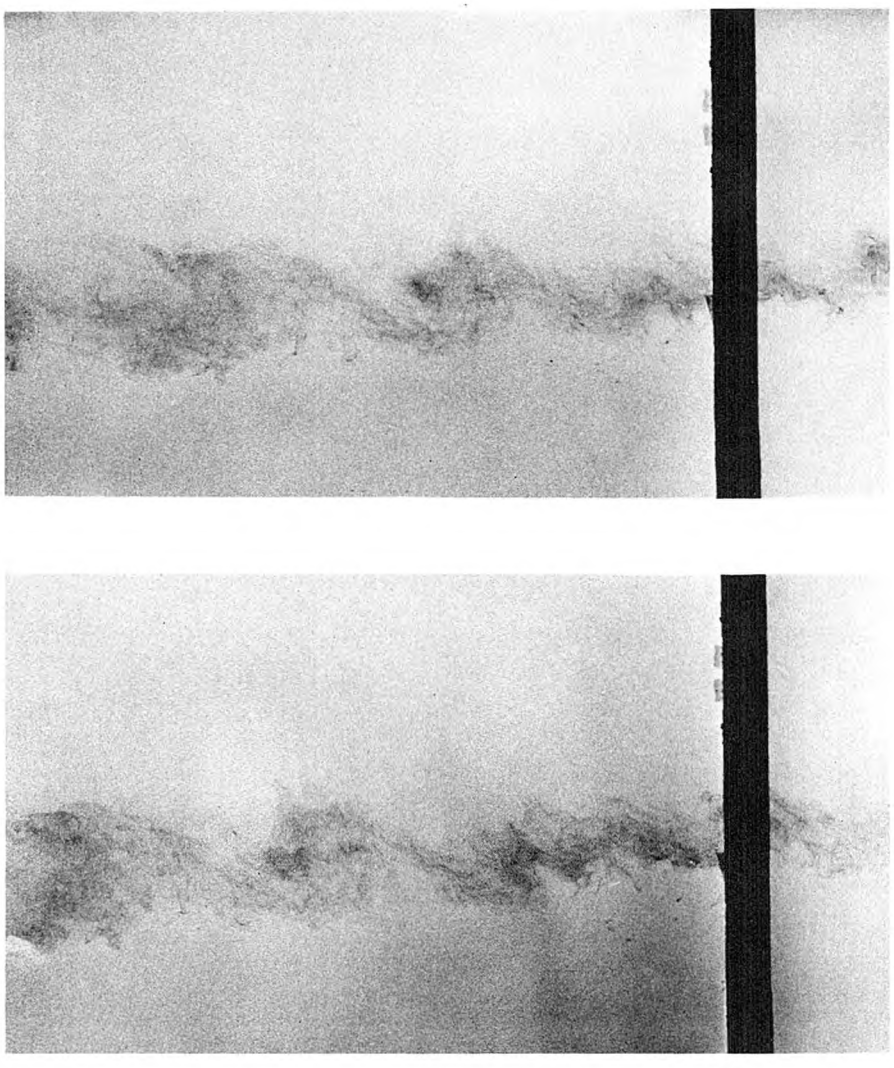

Figure 5.3.2b Two successive photographs of a dye streak downstream of the inlet. Same flow conditions as in Figure 5.3.2a, ΔU_o = 6 cm/s, $\Delta\rho/\rho_o$ = 0. Center of photographs is at x = 1.05 m.

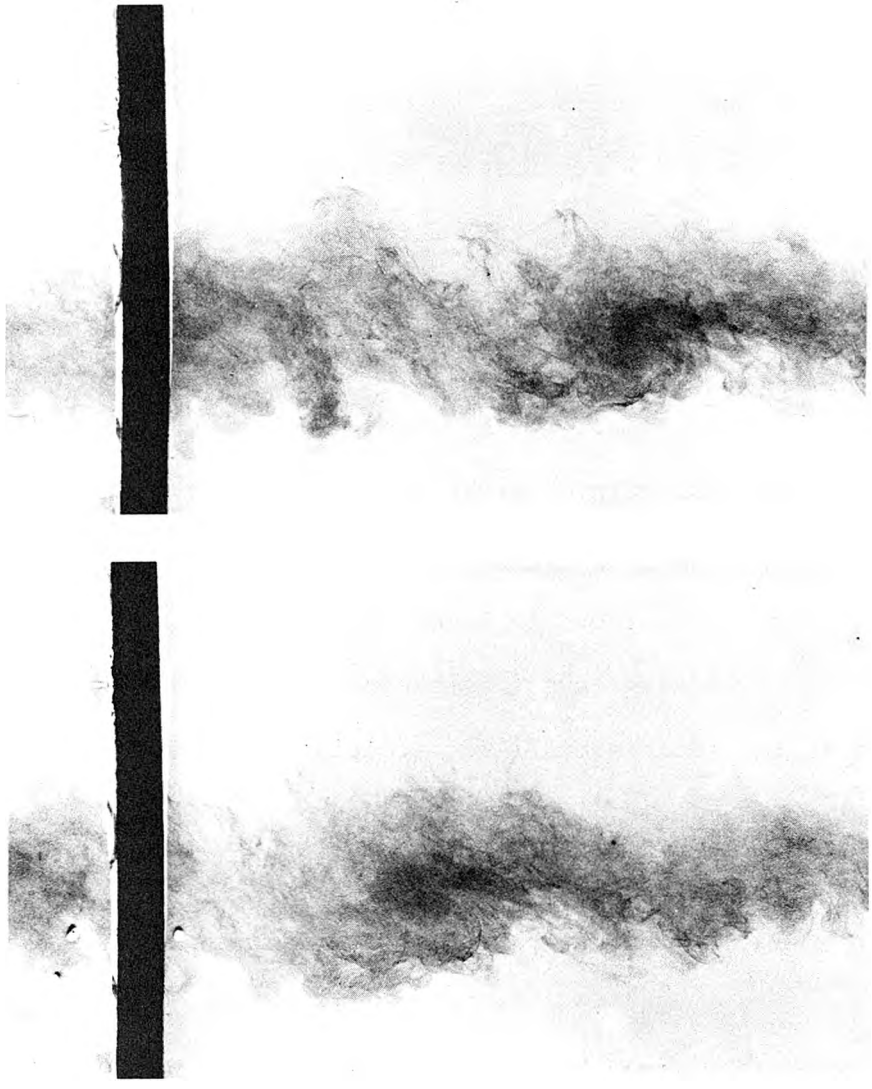

Figure 5.3.2c Photographs of a dye streak downstream of the inlet. Same flow conditions as in Figure 5.3.2a, ΔU_o = 6 cm/s, $\Delta\rho/\rho_o$ = 0. Center of photographs is at x = 1.8 m.

two-dimensional structures. In these photographs, dye had been injected into the flow a few centimeters upstream of the splitter plate. The upper layer had a mean speed of 13 cm/s and the lower layer had a mean speed of 7 cm/s. The large two-dimensional structure can be seen developing about 50 cm from the end of the splitter plate.

Chandrsuda *et al.* (1978) reported instances in which a two-dimensional mixing layer broke down into "fully three-dimensional turbulence." Exactly what the authors meant by "fully three-dimensional turbulence" is not totally clear, but presumably it allows large structures in the mixing layer, as these were observed by Chandrsuda. However, the authors did find situations in which the two-dimensional structure developed clearly three-dimensional properties. The authors state, however, they believe that if the two-dimensional structure is to persist, low turbulence levels are required in the free streams. The authors do not state how low a turbulence level is sufficiently low, but explicitly imply "a two-stream mixing layer fed from a high-quality contraction" is necessary.

In this study, a high-quality contraction in the inlet was not available, nor any contraction, for that matter; the flow entered the working section from a 4 m long straight section (see Figure 3.1.3). The turbulence levels were quite high at the inlet, as much as 3.0 per cent of the local mean velocity, and there was a substantial wake off of the splitter plate. Nevertheless, large two-dimensional structures were observed to develop in the mixing layer.

It is not easy to resolve the differences between the observations

in this study and those reported by Chandrsuda *et al.*[1] However, some of the conclusions of Chandrsuda *et al.* are not based on direct evidence, but are inferred from other evidence. The authors do not explicitly state, for example, how high the free-stream turbulence level must be to result in a fully three-dimensional turbulent mixing layer. Their own observations are based largely on a single-stream mixing layer (one side stationary), in which the turbulence level on the still side is difficult to measure, or even define. They also found that the two-dimensional structure was destroyed when a turbulence grid was placed in one of the free streams of a two-stream experiment, but they do not state what the turbulence level was. There is no doubt that if the free streams are sufficiently disturbed, be it by highly intermittent turbulence, a wake off the splitter plate or buoyancy effects, the the two-dimensional mixing layer may break down or fail to develop.

In this study, it was found that if the velocity difference between the two layers was small, on the order of two centimeters per second, then the wake from the splitter plate disrupted the development of the two-dimensional structure. Chandrsuda *et al.* point out that Pui and Gartshore (1977) found similar results. However, it was also found in this study that *if the velocity difference was sufficiently large, the two-dimensional structure developed downstream despite the fact that close to the splitter plate there was clearly three-dimensional turbulence.* The large vortical structures that developed were two-dimensional in the sense that the main structure was uniform across the flume, but small scale three-dimensional turbulence was clearly

[1]A recent publication, by Wygnanski *et al.* (1979), J. Fluid Mech., Vol. 93, pp. 325-336, supports the findings of the present study in this regard.

contained inside the vortices. The turbulence was three-dimensional in the small, but the main vortical structure appeared to be strongly two-dimensional. As the velocity difference increased, the two-dimensionality of the structure was enhanced.

From the observations of the mixing layer in this study, along with the measurements of the turbulence levels at the inlet, it appears that, while the two-dimensional vortical structure in the mixing layer can be disrupted if disturbances in the flow are sufficiently large, it takes somewhat larger disturbances than Chandrsuda *et al.* imply in their conclusions. It is clear from this study that despite the lack of laminar boundary layers and low-turbulence levels at the end of the splitter plate the large two-dimensional vortical structures appeared in the mixing layer. Whether or not the large structure eventually breaks down due to the three-dimensional small scale turbulence within the structures could not be determined in this study; the structures were observed to grow and pair until they were so large (up to 25 cm in diameter several meters from the splitter plate) that they were clearly influenced by the presence of the free surface. It does not seem appropriate to speculate upon subsequent evolution of the structures without supporting evidence.

Previously, it was mentioned that buoyancy effects could destroy the large structure in the mixing layer. This has been observed by, among others, Thorpe (1971, 1973b) and Koop (1976). In fact, buoyancy effects were found to destroy all turbulence in the interface, if the initial density difference were sufficiently large, and downstream only internal waves remained as a trace of the previous disturbance.

Figure 5.3.3 shows photographs of the collapse of the mixing layer due to buoyancy effects; the process is similar to the process seen in the photographs of Thorpe (1973b) and Koop (1976), although here the Reynolds number is much higher, and the initial turbulence levels are greater.

Basically, the initial development of the mixing layer appeared to be the same whether or not there was a density difference between the layers. The vortices grew and amalgamated, but when the initial density difference was sufficiently large, they eventually reached a point where they no longer had sufficient energy to overcome buoyancy forces. In some cases, two adjacent vortices attempted to pair, but could not quite complete the process. (In general, when two vortices pair, the trailing vortex rolls over the top of the leading vortex (when the upper layer is moving faster) and engulfs a good deal of fluid in the process.) During the collapse, it appeared that buoyant forces, produced as the vortices attempted to engulf fluid, prevented amalgamation. The two vortices then slowly flattened as the mean shear stretched them out.

The collapse process began and ended not at fixed points, but over a region. At times, a lone vortex would continue to roll slowly for a short distance down the flume, with a collapsing layer leading and trailing it, until that vortex eventually collapsed. Often one would observe a series of large vortices slowly flatten, without attempting a final amalgamation, and collapse. Because the mean shear stretched the vortices as they collapsed, they appeared to get

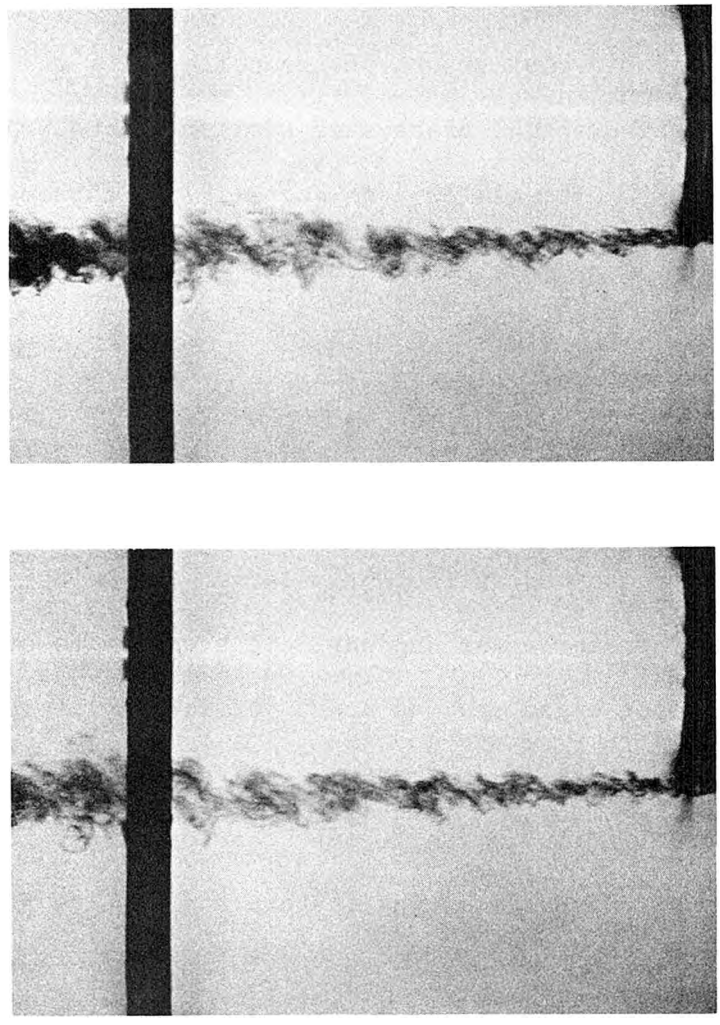

Figure 5.3.3a Successive photographs of a dye streak at the flume inlet. ΔU_o = 6 cm/s, ΔT_o = 2.0°C, $\Delta\rho/\rho_o = 0.6 \times 10^{-3}$. Center of the photographs is at x = 0.3 m.

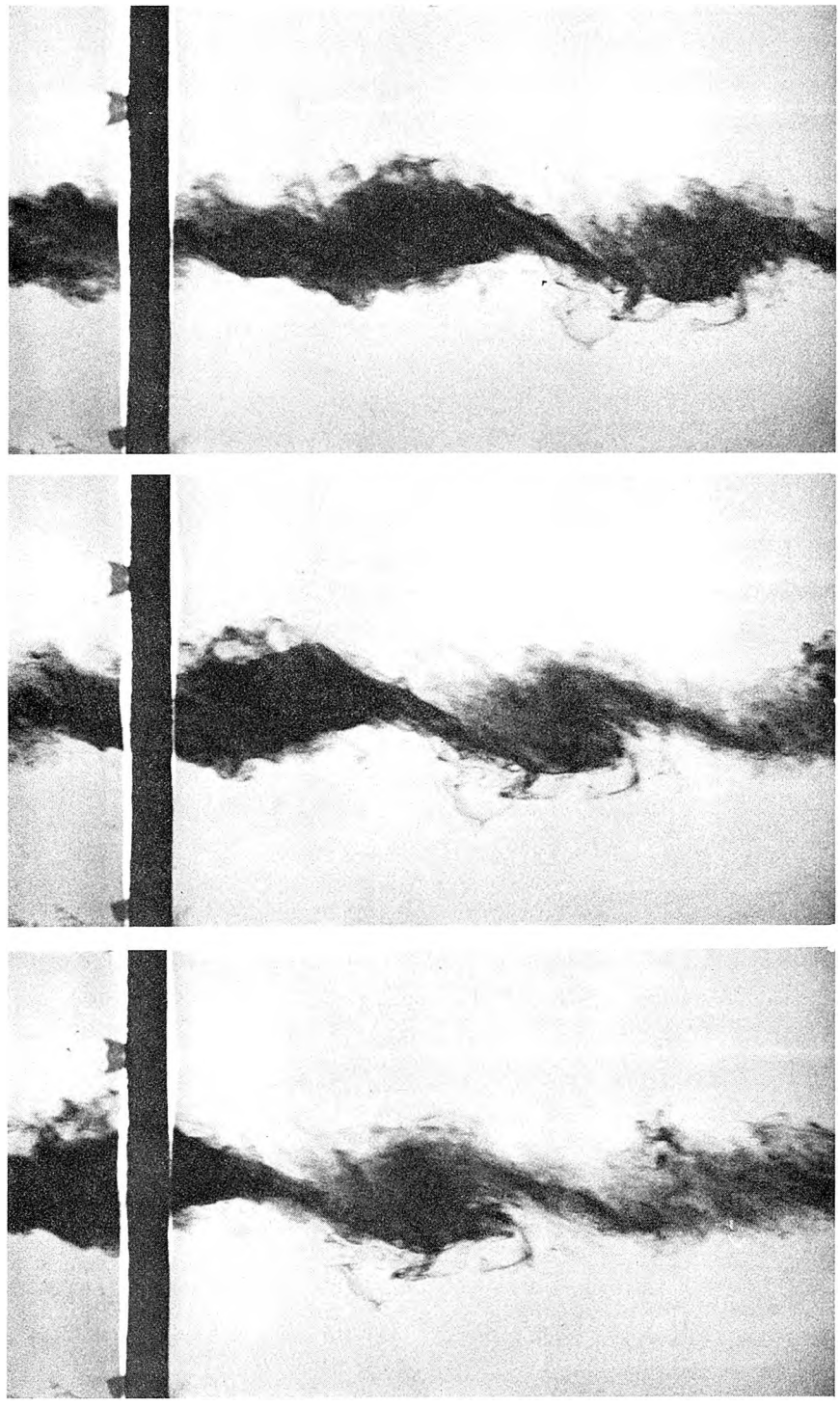

Figure 5.3.3b Successive photographs of a dye streak downstream of the flume inlet. Same flow conditions as in Figure 5.3.3a, ΔU_o = 6 cm/s, ΔT_o = 2°C, $\Delta\rho/\rho_o = 0.6 \times 10^{-3}$. Center of photographs is at x = 1.8 m.

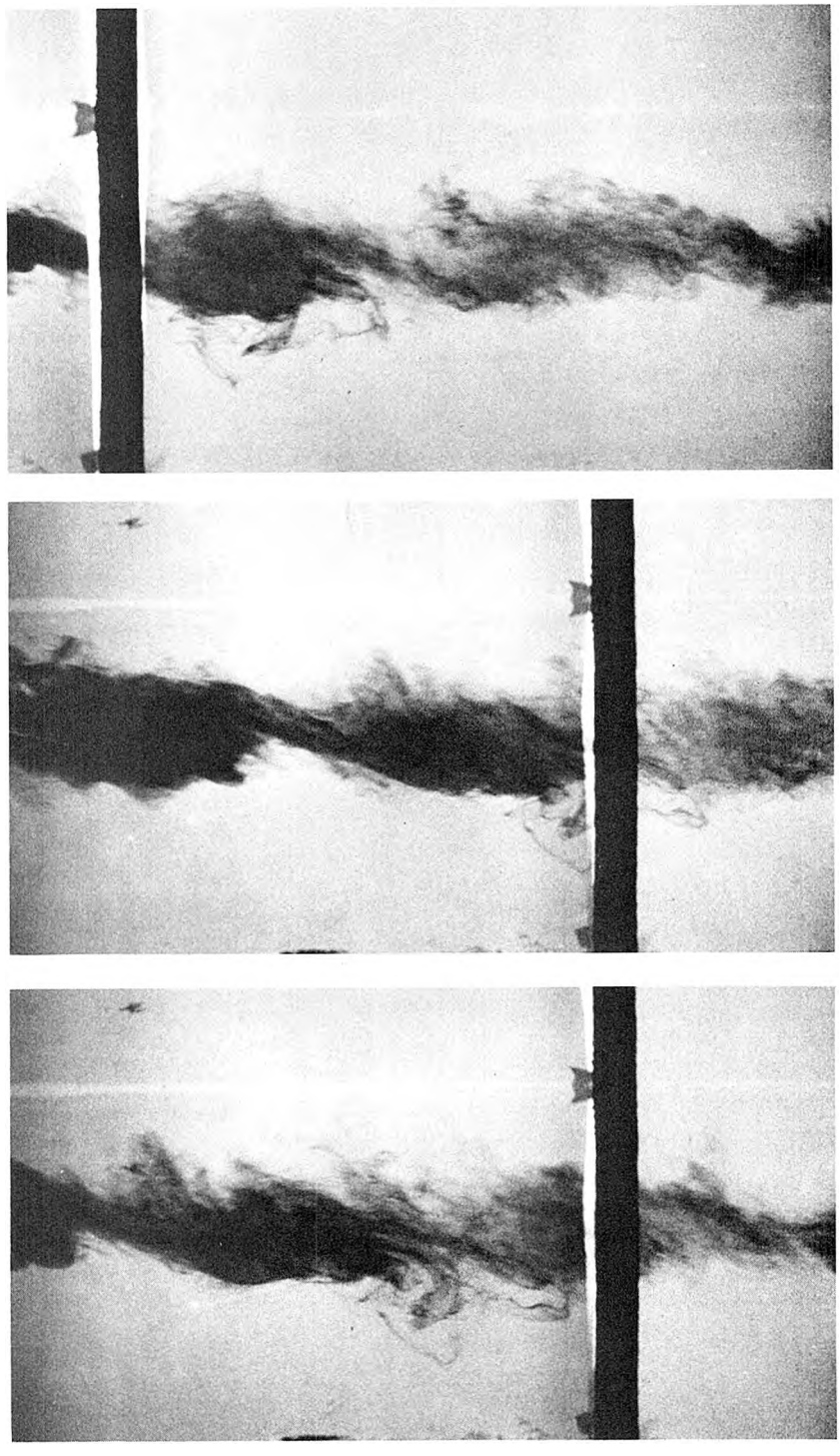

Figure 5.3.3c Continuation of the series of photographs of Figure 5.3.3b. Center of upper photograph is at x = 1.8 m, lower two at x = 2.6. Dark vortex in center of upper photograph is the same one seen in the center of the middle and left of center in the bottom.

"squashed" in the process, and what was once a round, healthy vortex shortly became a long thin filament of fluid (as visualized with dye). The point at which a particular vortex collapsed seemed to depend not only upon its own history (that is, its "size") but also upon the history of its neighbors (their "size" and separation), so that the collapse process took place over a distance, and neither definitely began nor definitely ended at given positions for given inlet conditions. A more quantitative discussion of the collapse process is given in Chapters 6 and 7.

5.4 Qualitative Flow Description II--Downstream Mixing and Instabilities

In this section a qualitative description of the flow downstream of the initial mixing region is given. Two distinct states of flow were observed: in some cases, the initial density difference was so large that a laminar region of flow developed; in other cases, with very small initial density differences, no laminar region developed, and significant mixing was always observed throughout the flow field. In this latter case, the flow was not strikingly different from the cases with no initial density difference, except that the mixing and turbulent intensities were reduced. This type of flow is, however, best described quantitatively, and further discussion of it is presented in Chapters 6 and 7.

If a laminar region developed in the flow field, then further mixing between the two layers was greatly reduced. It was found that if the turbulence level in the lower layer was sufficiently low (which

was the case when the flume bed was smooth), then the laminar interface persisted downstream to the end of the flume. The interface between the two layers had an abundance of internal waves, which resulted from the initial flow development region as well as from the turbulence generated at the solid boundaries. However, mixing was greatly reduced and only a few, small waves were observed to become unstable and break, and these all at the lower boundary of the interface. The fact that the interface between the two layers was laminar did allow a substantial shear to persist at the interface. Evidence of this shear can be seen in Figure 5.4.1, which shows a photograph of dye streaks in the flume about 15 m from the splitter plate. The initial temperature difference in this case was 2.0°C ($\Delta\rho/\rho_o = 0.6 \times 10^{-3}$) and the initial velocity difference was about 4 cm/s. The dye streaks were made by injecting a solution of dye through a thin tube ($\sim$0.1 cm O.D.) while rapidly pulling the tip of the tube from the flume bed to the surface. Thus, the turbulence generated as the dye solution jetted out of the tube is evident in photographs and accounts for the fact that the streaks are on the order of a centimeter or two in width. The strong, laminar shear layer is quite evident in the photograph.

Figure 5.4.2 shows a series of photographs taken under the same conditions as the photograph shown in Figure 5.4.1. Here, dye was injected continuously for about thirty seconds at the splitter plate, and then photographed as it passed by 15 m downstream. The streak is greatly elongated, a result of the shear. The dye in the upper portion is diffuse because of the mixing which took place in the initial mixing

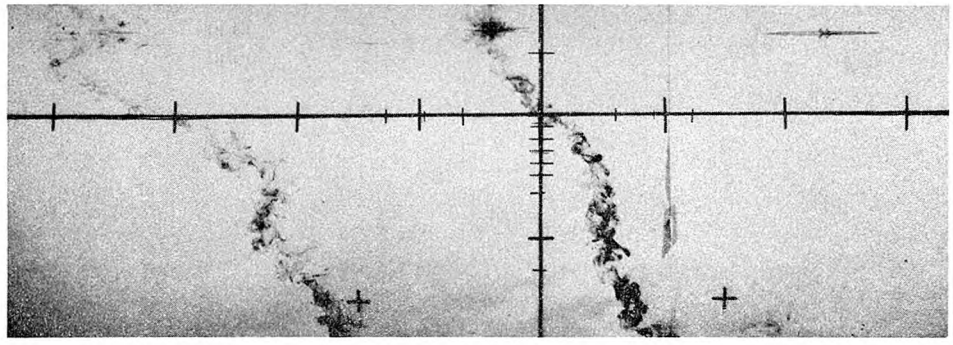

Figure 5.4.1 Photograph of two dye streaks injected into the flume a few seconds apart. ΔU_o = 4 cm/s, ΔT_o = 2°C, $\Delta\rho/\rho_o$ = 0.6 x 10^{-3}, smooth bed. Photograph taken at x = 15 m.

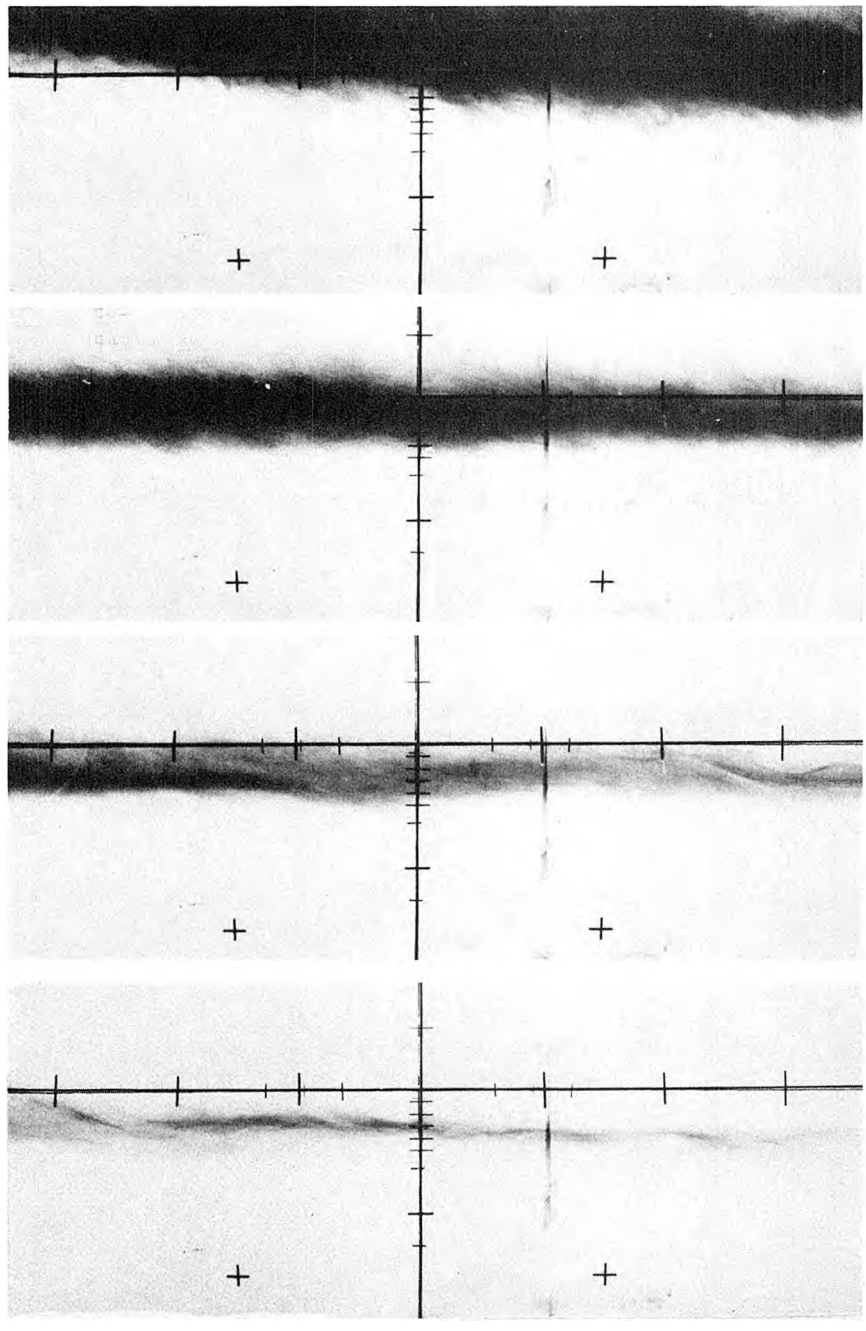

Figure 5.4.2 Successive photographs taken at x = 15 m of a dye streak which was injected into the flume at the inlet. Same flow conditions as in Figure 5.4.1, ΔU_o = 4 cm/s, ΔT_o = 2.0°C, $\Delta\rho/\rho_o = 0.6 \times 10^{-3}$.

layer which developed off of the splitter plate. The mixing layer collapsed to a laminar shear layer and little mixing was taking place at the location the photographs were taken. Some internal waves can be seen in the lower portion of the interface, but in this case they were, for the most part, stable and little mixing was observed.

A more extreme example is shown in Figures 5.4.3 and 5.4.4, which show photographs of dye streaks in a very stratified flow ($\Delta T_o = 5.5°C$, $\frac{\Delta\rho}{\rho_o} = 1.8 \times 10^{-3}$, $\Delta U_o = 4$ cm/s). A strong laminar shear layer is evident in Figure 5.4.3, and internal waves can be seen in the dye streak in Figure 5.4.4.

In contrast to these photographs is that of Figure 5.4.5 which shows dye streaks in a similar, but homogeneous flow. In this photograph, no sharp, persistent shear layer is apparent; however, it is apparent that the turbulent mixing is greater in this case, as the dye streaks smear out more rapidly than in the stratified flows.

When the flume bed was roughened, much more mixing took place downstream. If the laminar interface was sufficiently sharp (that is, on the order of a few centimeters thick or less), then large waves were often observed to develop on the interface. These waves had a wavelength on the order of 30 to 70 cm, and appeared to be unstable in the sense that they grew in amplitude. The waves appeared to originate from turbulent bursts growing from the roughened bed. Often, one would observe a rather flat and smooth dye streak suddenly bulge upward, apparently as a turbulent burst hit it. In many cases, these large waves would break; in other cases, the waves would develop but

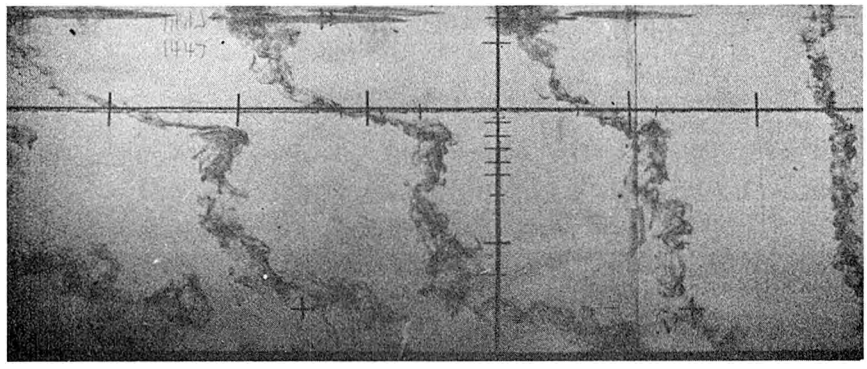

Figure 5.4.3 Photograph of several dye streaks injected a few seconds apart. ΔU_o = 5 cm/s, ΔT_o = 5.0°C, $\Delta\rho/\rho_o = 1.8 \times 10^{-3}$, smooth bed photographs taken at x = 15 m.

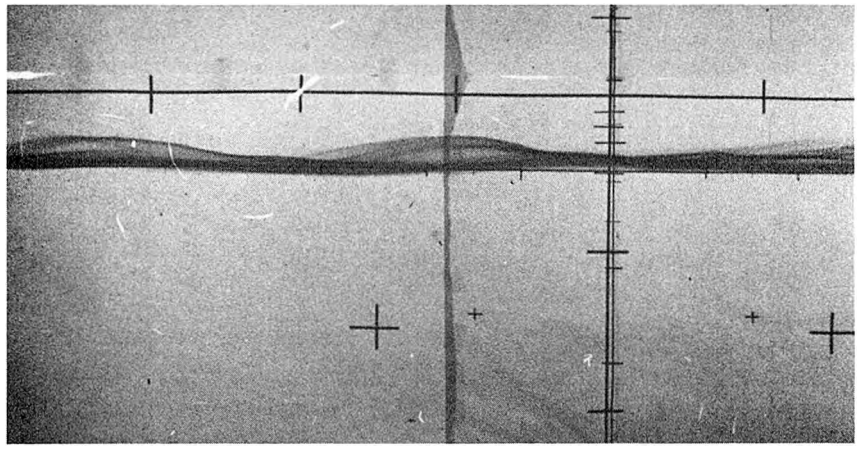

Figure 5.4.4 Photograph taken at x = 15 m of a dye streak which was injected into the flume at the inlet. Same flow conditions as in Figure 5.4.3.

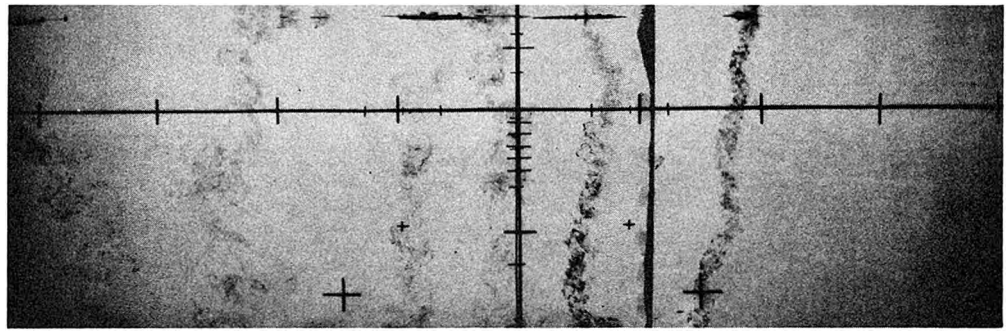

Figure 5.4.5 Photograph of several dye streaks injected a few seconds apart at x = 15 m. Homogeneous flow, but otherwise similar to the flow conditions in Figure 5.4.1.

propagate away without breaking. However, in some cases, instabilities developed on these large waves which resulted in a breakdown of the interface. As the amplitude of the long waves grew to 5 or 6 cm, waves of smaller wavelength were sometimes observed to grow and break along the large waves. Usually, after one small wave began to break, many in the neighborhood would develop and break, causing some relatively strong local mixing.

Figure 5.4.6 shows photographs of a dye streak which had been injected into the flume at the splitter plate. In this case, the initial temperature difference was 2.0°C, there was no initial velocity difference, and the flume was roughened with rocks. One can see a series of waves of short wavelength breaking on a large wave of much greater wavelength in this photograph. This type of instability is qualitatively similar to the breakdown processes described by Landahl (1972) and Landahl and Criminale (1977), which are discussed in Section 2.2. Usually when this type of instability was observed, it was found to occur quite suddenly, and in a very short time one small wave would develop and begin to break, and then many other small waves would develop and break in close proximity to the first.

When a large wave broke, as shown in the photographs in Figure 5.4.7, the trough of the wave was often seen to form a cusp, and the cusp was subsequently observed to break off and mix away from the wave. Similar types of instabilities have been observed previously (Koop (1976), Browand and Winant (1973), Keulegan (1949) and others). After the tip of the cusp broke off, the remaining trough would recede and the wave would continue to travel along the interface. The formation of a cusp often

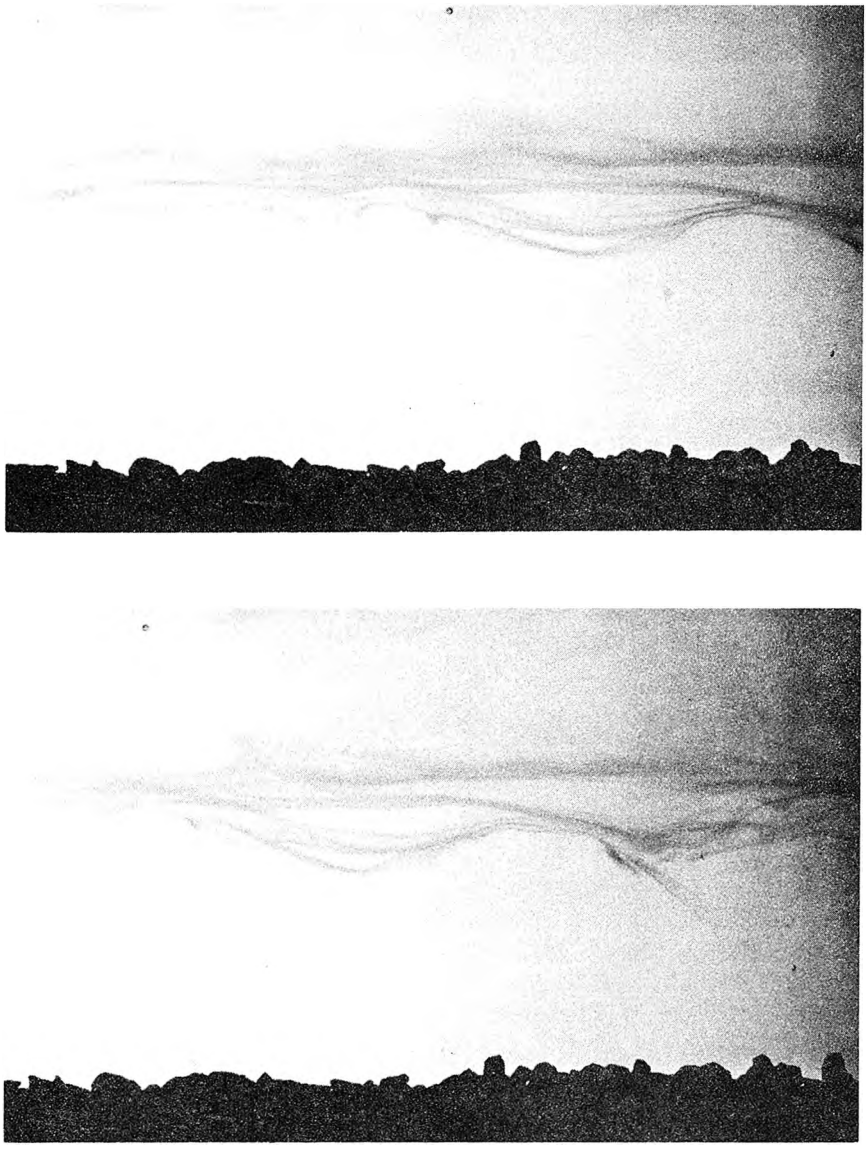

Figure 5.4.6 Photographs taken at x = 20 m of a dye streak in a stratified flow over a roughened bed. Photographs show small waves breaking on a larger internal wave. $\Delta U_o = 0$, $\Delta T_o = 2.0°C$, $\Delta\rho/\rho_o = 0.6 \times 10^{-3}$.

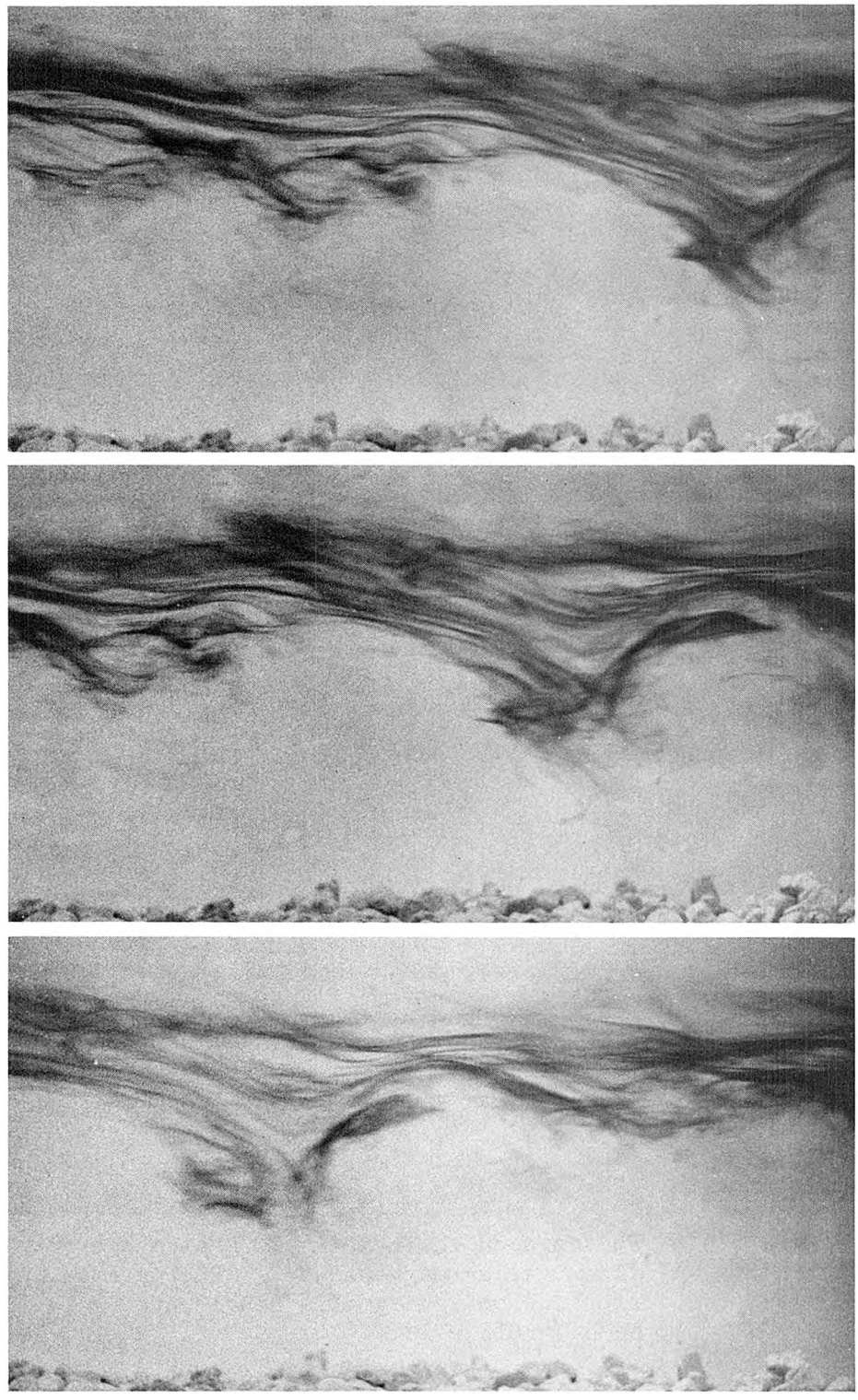

Figure 5.4.7 Successive photographs of a large wave breaking in a stratified flow over a roughened bed. $\Delta U_o = 0$, $\Delta T_o = 2.0°C$, $\Delta\rho/\rho_o = 0.6 \times 10^{-3}$. Center of photographs is at x = 20 m.

preceded (and perhaps caused) other instabilities in its neighborhood, but this was not always the case.

In cases where the initial velocity difference was large, but the density difference was sufficiently large so that a laminar layer resulted, then a rather thick interface developed. In these cases, the downstream mixing was the result of small three-dimensional waves breaking near the bottom of the interface. The turbulence essentially "chipped" away at the interface, as it caused small local instabilities. Again, the instabilities were local and intermittent, but large amplitude deformations of the entire interface were not observed. Instead, turbulent bursts appeared to "dent" the lower portion of the interface, and cause local mixing without disrupting the entire flow.

Figure 5.4.8 shows a series of photographs of this process. The photographs show a dye streak, 20 m downstream from the splitter plate, where it was initially injected into the flow. The initial temperature difference was 3.0°C ($\Delta\rho/\rho_o = 0.9 \times 10^{-3}$), the initial velocity difference was 4.0 cm/s and the bed was roughened with rocks. The photograph shows small waves breaking at the bottom of the interface. This process was different from the processes which involved large scale waves on the interface. In both cases, it seems likely that the interfacial shear was a factor in the mixing, as the small waves were seen to curl over in a fashion not unlike Kelvin-Helmholtz billows, although the processes were highly three-dimensional. However, when the interface was thick, large waves did not really seem to dominate the mixing process. Rather, the breaking of smaller waves which developed seemed to be responsible for much of the mixing.

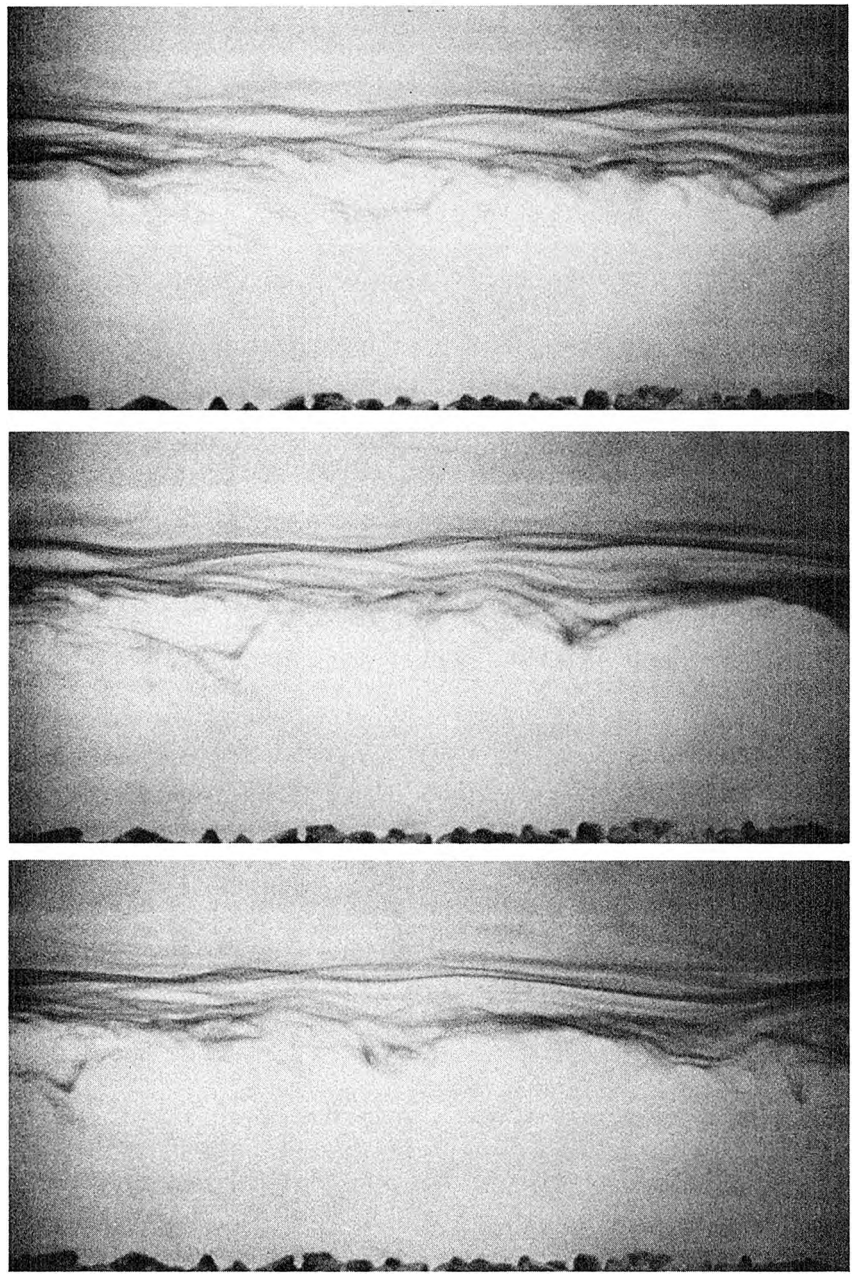

Figure 5.4.8a Successive photographs of small waves breaking at the bottom of the interfacial region in a stratified flow. ΔU_o = 5 cm/s, ΔT_o = 3.0°C, $\Delta\rho/\rho_o$ = 0.9 x 10^{-3}. Photographs taken at x = 20 m, bed was roughened with rocks.

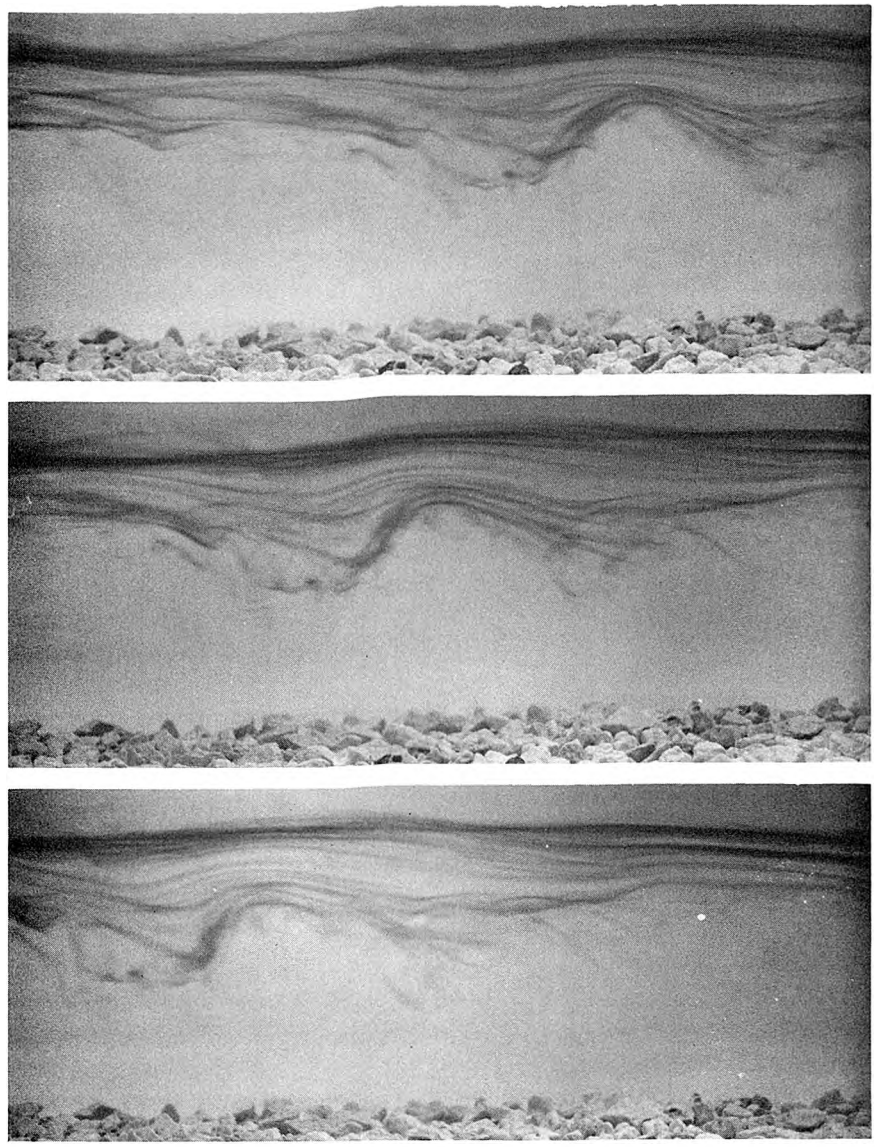

Figure 5.4.8b Successive photographs of large internal waves in the interface of a stratified flow. Same flow conditions as in Figure 5.4.8a: ΔU_o = 5 cm/s, $\Delta\rho/\rho_o = 0.9 \times 10^{-3}$. Photographs taken at x = 20 m, bed was roughened with rocks.

This is not to imply that large waves cannot develop when the interface is thick, however, for when the interface is thick as characterized by the region of a substantial vertical temperature gradient, it usually extends nearly to the surface. Thus the presence of the surface no doubt influences the large scale processes at the interface. Thus, it is felt that a very broad interface will experience the large scale wave development if the depths of the mixed regions above and below are sufficiently deep. The experiments in which it was likely that the close proximity of the surface to the thick interface might have prevented large waves from developing are still interesting in that they yield information on a mixing process which essentially "chips away" at a portion of the interface rather than disrupting the whole interfacial layer.

It is important to note that the interface did not become unstable at one point and then remain turbulent downstream. Rather, the wave development and breaking was intermittent, and often a developing instability would result in local turbulent mixing, which subsequently damped out far downstream. As the interface became more deformed and the characteristics of the mean flow properties changed, the mixing events appeared more frequently and the nature of these events often changed to some degree. For example, as the interface thickened, one could see more mixing off of the bottom portion of the interface, though the mixing was still not a continuous process, but again appeared to be intermittent with many small waves forming cusps and breaking.

As a final note in this discussion, the uniformity of the flow downstream was examined by injecting dye streaks across the flume width.

Figure 5.4.9 shows photographs of such streaks a few seconds after they were introduced into the flume. One can see that the velocity profile is rather flat across the middle portion of the flume. As velocity measurements were made only on the centerline of the flume, this photograph is presented as evidence that there were no large lateral mean velocity gradients in the center of the channel.

In the initial series of experiments, temperature measurements were made at several cross-sections of the channel, so that plots of isotherms could be made. In general, the isotherms were quite flat across the channel, as were the contours of temperature fluctuations. In particular the isotherms did not tend to broaden near the walls which would indicate that the stratification was reducing the turbulence generation at the walls to such an extent that there was little wall-generated mixing occurring. While the walls certainly had an effect on the flow development when the flow was homogeneous, it appeared their effects were smaller where the flow was stratified. Furthermore, when the flume bed was roughened, the relative effects of the wall-generated turbulence were very much smaller than the bed-generated turbulence, even in homogeneous flows. It should be noted that most of the major results in the following chapters come from measurements in the initial mixing layer where the wall effects were unimportant, or from measurements in the downstream flow over roughened beds, where the bed-generated turbulence dominated the flow.

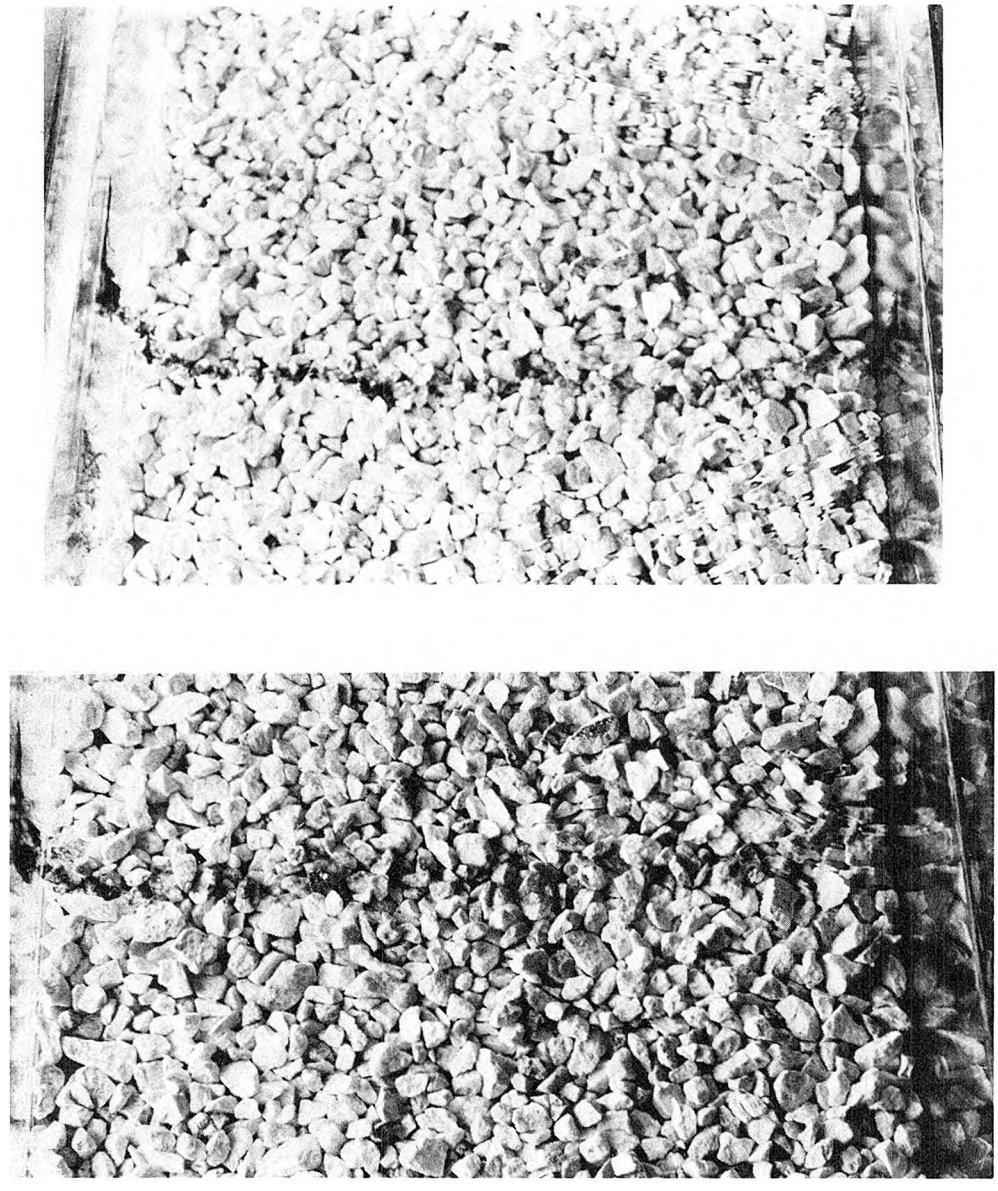

Figure 5.4.9 Photographs of horizontal dye streaks across the flume channel at x = 20 m. U = 9.0 cm/s, bed was roughened with rocks. Upper photograph, homogeneous flow, lower, $\Delta\rho/\rho_o = 0.6 \times 10^{-3}$.

CHAPTER 6

PRESENTATION OF EXPERIMENTAL RESULTS

6.0 Introduction

In this chapter the experimental results of this study are presented. Chapter 7 contains further discussion of the results.

Section 6.1 details the range over which parameters were varied in the experiments. Section 6.2 deals with the results of measurements made in the initial mixing layer. In Section 6.3, there is a discussion of the results from measurements made downstream of the initial mixing layer when the flume bed was smooth, while in Section 6.4 the downstream flow over the roughened bed is considered. Finally, Section 6.5 deals with the large, coherent structures found in the turbulent flow and their effects on the mixing processes.

6.1 Experimental Parameters

Complete information regarding the experimental parameters and initial data of the experiments is given in Tables 6.1.1 through 6.1.4. The information in these tables is explained as follows:

Column 1: the identification number for the experimental run.

Column 2: the initial difference between the mean flow speeds of the two layers, $\Delta U_o = U_1 - U_2$, in cm/s.

Column 3: the initial difference between the mean temperatures of the two layers, $\Delta T_o = T_1 - T_2$, in °C.

Column 4: the total depth of flow h, in cm (upper layer depth is $h_1 = h - 30$).

Table 6.1.1 Parameters for experiments with homogeneous flow.

Experiment Number	ΔU_o cm/s	ΔT_o °C	h cm	U_1 cm/s	U_2 cm/s	U cm/s	$\frac{\Delta\rho}{\rho_o} \times 10^3$	Re x 10^{-3}	Ku	bed[1]	Measurement Locations m
B-3	6.0	0	44.5	18.7	12.7	14.7	0	166	0	smooth	0.1,0.2,0.5,1.0,2.5, 4.7,10,20
B-4	-0.2	0	45.0	12.0	12.2	12.2	0	139	0	smooth	4.7,9.,12,16,20,21.4
B-5	3.6	0	45.2	11.8	8.2	9.3	0	107	0	smooth	0.2,0.5,1.0,1.5,2.0
C-1	-0.3	0	45.1	12.1	12.4	12.2	0	139	0	b.r. 4.5-24.5	20,24
C-4	6.4	0	45.3	14.0	7.6	9.8	0	112	0	b.r. 4.5-24.5	4.7,9,12,16,20,24
C-5	0.4	0	45.3	9.4	9.0	9.2	0	106	0	b.r. 4.5-14.5	4.7,9,12,16,20,24
D-1	1.0	0	45.1	10.1	9.1	9.4	0	108	0	r.r. 4.5-14.5	4.7,9,12,16,20,24
D-2	6.4	0	45.1	14.1	7.7	9.8	0	112	0	r.r. 4.5-14.5	4.7,9,12,16,20,24
D-3	-0.9	0	45.2	11.9	12.8	12.5	0	143	0	r.r. 4.5-24.5	24
D-4	1.8	0	45.0	10.2	12.0	8.9	0	101	0	r.r. 4.5-24.5	2.7,9,12,16,20,24
D-5	6.7	0	44.9	14.1	7.4	9.6	0	109	0	r.r. 4.5-24.5	4.7,9,12,16,20,24

[1] b.r. = brick-roughened, r.r. = rock-roughened; numbers indicate flume section (in m) which was roughened.

Table 6.1.2 Mixing layer experiments.

Experiment Number	ΔU_o cm/s	ΔT_o °C	h cm	U_1 cm/s	U_2 cm/s	U cm/s	$\frac{\Delta\rho}{\rho_o} \times 10^3$	Re x 10^{-3}	Ku x 10^3	bed	Measurement Locations m
BH-9	2.1	1.55	45.3	12.6	10.5	11.0	0.43	132	0.25	smooth	0.1,0.4,0.8,1.6, 2.25,3,4.7
BH-10	3.8	1.60	45.3	12.2	8.4	9.6	0.44	113	0.06	smooth	0.45,0.9,1.8,2.5, 3.5,4.7
BH-11	5.6	1.50	45.4	13.9	8.3	10.2	0.40	119	0.02	smooth	0.5,1,2,3,4.7
BH-12	3.7	2.33	45.2	11.8	8.1	9.4	0.69	114	0.01	smooth	1,1.5,2,3,4.7

Table 6.1.3 Smooth bed experiments, downstream measurements.

Experiment Number	ΔU_o cm/s	ΔT_o °C	h cm	U_1 cm/s	U_2 cm/s	U cm/s	$\frac{\Delta\rho}{\rho_o} \times 10^3$	Re x 10^{-3}	Ku x 10^3	bed	Measurement Locations m
BH-3	5.5	1.80	45.6	16.5	11.0	12.9	0.48	148	.026	smooth	0.5,1,2.5,4.7,10,20
BH-6	-0.6	1.36	45.1	11.9	12.5	12.4	0.42	156	15	smooth	4.7,9,12,16,20,21.4
BH-7	-0.4	0.70	45.0	11.9	12.3	12.2	0.18	136	24	smooth	4.7,9,12,16,20,21.4
BH-8	-0.5	2.05	45.2	11.8	12.3	12.1	0.58	144	39	smooth	4.7,9,12,16,20,21.4
BH-13	3.8	2.15	45.1	11.9	8.1	9.4	0.63	112	0.09	smooth	4.7,9,12,16,20
BH-14	5.7	1.31	45.2	13.9	8.2	10.2	0.37	119	0.02	smooth	4.7,9,12,16,20,24
BH-15	5.4	2.45	45.2	13.7	8.3	10.1	0.73	125	0.04	smooth	4.7,9,12,16,20,24
BH-16	3.9	3.50	45.0	11.9	8.0	9.3	1.04	113	0.14	smooth	4.7,9,12,16,20,24
BH-17	6.1	2.15	45.3	13.9	7.8	9.9	0.61	121	0.22	smooth	4.7,9,12,16,20,24

Table 6.1.4 Roughened bed experiments, downstream measurements.

Experiment Number	ΔU_o cm/s	ΔT_o °C	h cm	U_1 cm/s	U_2 cm/s	U cm/s	$\frac{\Delta\rho}{\rho_o} \times 10^3$	Re x 10^{-3}	Ku x 10^3	bed[1]	Measurement Locations m
CH-1	-0.2	2.45	45.1	9.3	9.5	9.0	0.70	112	--	b.r. 4.5-24.5	4.7,9,12,16,20,24
CH-2	0.4	2.35	45.0	6.3	5.9	6.1	0.65	71	117	b.r. 4.5-24.5	4.7,9,12,16,20,24
CH-3	4.6	2.67	45.2	12.3	7.7	9.2	0.79	115	0.06	b.r. 4.5-24.5	4.7,9,12,16,24
CH-4	6.4	0.81	45.2	14.3	7.9	10.0	0.24	125	0.007	b.r. 4.5-24.5	4.7,9,12,16,20,24
CH-5	0.2	2.18	45.3	9.4	9.2	9.2	0.69	122	--	b.r. 4.5-14.5	4.7,9,12,16,20,24
DH-1	0.9	1.67	45.1	10.0	9.1	9.4	0.49	120	4.9	r.r. 4.5-14.5	4.7,9,12,16,20,24
DH-2	6.4	1.90	45.1	14.0	7.6	9.7	0.63	131	0.02	r.r. 4.5-14.5	4.7,9,12,16,20,24
DH-3	0.9	0.70	45.2	9.9	9.0	9.3	0.21	116	2.2	r.r. 4.5-14.5	4.7,9,12,16,20,24
DH-4	0.8	0.70	45.4	9.8	9.0	9.2	0.21	116	3.4	r.r. 4.5-24.5	4.7,9,16,20,24
DH-5	6.8	0.61	45.2	14.3	7.5	9.8	0.18	125	0.005	r.r. 4.5-24.5	4.7,9,12,16,20,24
DH-6	1.9	1.61	45.1	10.1	8.2	8.9	0.50	114	0.59	r.r. 4.5-24.5	4.7,9,12,16,20,24
DH-7	6.5	1.67	45.0	14.0	7.5	9.6	0.53	127	0.02	r.r. 4.5-24.5	4.7,9,12,16,20,24

[1] b.r. = brick-roughened, r.r. = rock-roughened; numbers indicate flume section (in m) which was roughened.

Column 5: the mean speed of the upper layer flow, $U_1 = Q_1/h_1 w_f$, in cm/s, where w_f, the flume width, is 110 cm.

Column 6: the mean speed of the lower layer flow, $U_2 = Q_2/h_2 w_f$, in cm/s where h_2, the lower layer depth, is 30 cm.

Column 7: the mean speed of total flow, $U = (Q_1 + Q_2)/hw_f$, in cm/s.

Column 8: the initial relative density difference $\Delta\rho/\rho_o$ (x 1000) between the two layers.

Column 9: the overall Reynolds number (x 10^{-3}) of the flow, where $Re = 4R_h U/\nu$. (ν was based on the mean flow temperature which ranged from 23°C to 31°C.)

Column 10 the Keulegan number of the flow at the inlet, where $K_u = \Delta\rho g\nu/\rho_o \Delta U_o^3$.

Column 11 the flume bed characteristics; b.r. indicates brick-roughened section, r.r. indicates rock-roughened. Station numbers indicate the roughened section (in m) of the flume bed.

Column 12 the distances from the splitter plate (in m) at which measurements were made.

6.2 Experimental Results from Measurements in the Initial Mixing Layer

In this section the results from measurements made in the initial mixing layer are presented. Details on the initial conditions of the mixing layer experiments are given in Tables 6.1.1 and 6.1.2. Further discussions on the initial mixing layer, and comparisons with the work of others, are given in Section 7.1.

There are several parameters and length scales which are used

frequently in this section, and they are defined here. Length scales are ℓ_u^*, the maximum-slope thickness of the velocity profile and defined by Equation 2.1.19; ℓ_T^*, the maximum-slope thickness of the temperature profile and defined by Equation 2.1.20; and ℓ_b a buoyancy length scale, defined by

$$\ell_b = \frac{1}{2} (\bar{u}_1 + \bar{u}_2) \Delta\bar{u}_o / \frac{\Delta\rho}{\rho_o} g \qquad (6.2.1)$$

where $\bar{u}_1$ is the mean centerline speed of the upper layer,

$\bar{u}_2$ is the mean centerline speed of the lower layer, and

$\Delta\bar{u}_o = \bar{u}_1 - \bar{u}_2$.

In addition, ℓ_T, an integral length scale based on the temperature profile and defined by Equation 2.1.21, is used.

Because of the boundary layers on the walls, the flume bed and the splitter plate, the measured mean velocities on the centerline differed slightly from the overall mean flow speeds which were calculated from the flow rates measured with the Venturi meters. The centerline values of the mean velocity (averaged over depth) are important when considering the flow in the mixing layer and are listed in Table 6.2.1 for the experiments in which the measurements were made in the initial mixing layer. In addition, Table 6.2.1 contains the values of the buoyancy length scale, ℓ_b, and a dimensionless parameter, $\lambda_m \equiv \Delta\bar{u}_o/(\bar{u}_1 + \bar{u}_2)$.

Dimensionless parameters of interest here include $(y - y_o)/(x - x_o)$,

Table 6.2.1 Centerline mean flow speed for mixing layer experiments.

	Mean Flow Speed cm/s			Mean Centerline Speed cm/s			ℓ_b =	λ_m =
Experiment Number	U_1	U_2	ΔU_o	$\bar{u}_1$	$\bar{u}_2$	$\Delta \bar{u}_o$	$\frac{1}{2}(\bar{u}_1 + \bar{u}_2)\Delta u_o / \frac{\Delta\rho}{\rho_o} g$, cm	$\Delta \bar{u}_o / (\bar{u}_1 + \bar{u}_2)$
B-5	11.8	8.2	3.6	13.0	8.7	4.3	∞	0.20
BH-9	12.6	10.5	2.1	13.4	11.5	1.9	56	0.08
BH-10	12.2	8.4	3.8	12.7	9.3	3.4	87	0.15
BH-11	13.9	8.3	5.6	16.5	8.8	7.7	247	0.30
BH-12	11.8	8.1	3.7	13.2	8.7	4.5	73	0.21

where y_o is defined as the point at which $(\overline{u} - \overline{u}_2)/\Delta\overline{u}_o = 0.5$ and x_o is the virtual origin of the mixing layer. In addition, several Richardson numbers are used, including $(\overline{Ri})_{min}$, the minimum value of the mean-Richardson number $\overline{Ri}$, defined by Equation 2.1.14, and several bulk-Richardson numbers, defined by $\frac{\Delta\rho}{\rho_o} g\ell/\Delta\overline{u}_o^2$, where ℓ represents one of the previously mentioned length scales.

6.2.1 Profiles of the Mean Horizontal Velocity

Figure 6.2.1 shows the normalized velocity profiles from several experiments. The virtual origin, x_o, is determined from the growth rate of the mixing layer and is discussed in Section 6.2.3. The value of y_o is defined to be the position at which $(\overline{u} - \overline{u}_2)/\Delta\overline{u}_o$ is 0.5. Values of x_o are given in Table 6.2.2, which appears in the discussion on growth rates in Section 6.2.3.

Figure 6.2.1 is presented primarily to indicate the degree of similarity in the velocity profiles. In particular, the velocity profiles measured in flows with a density difference are all quite similar to each other; the profiles made in the homogeneous flow are also similar to each other, but not to the profiles of inhomogeneous flows. In fact, it is apparent that there is a bit less shear in the homogeneous case, indicating a faster growth rate and more mixing. Table 6.2.1 shows that the value of $\lambda_m = \Delta\overline{u}_o/(\overline{u}_1 + \overline{u}_2)$ is quite similar for the cases shown in Figure 6.2.1. The parameter λ_m has been shown to be related to the growth rate of the mixing layer (see Brown and Roshko (1974)), and one might therefore expect the growth rates for these cases to be similar. As will be seen in later discussions, the

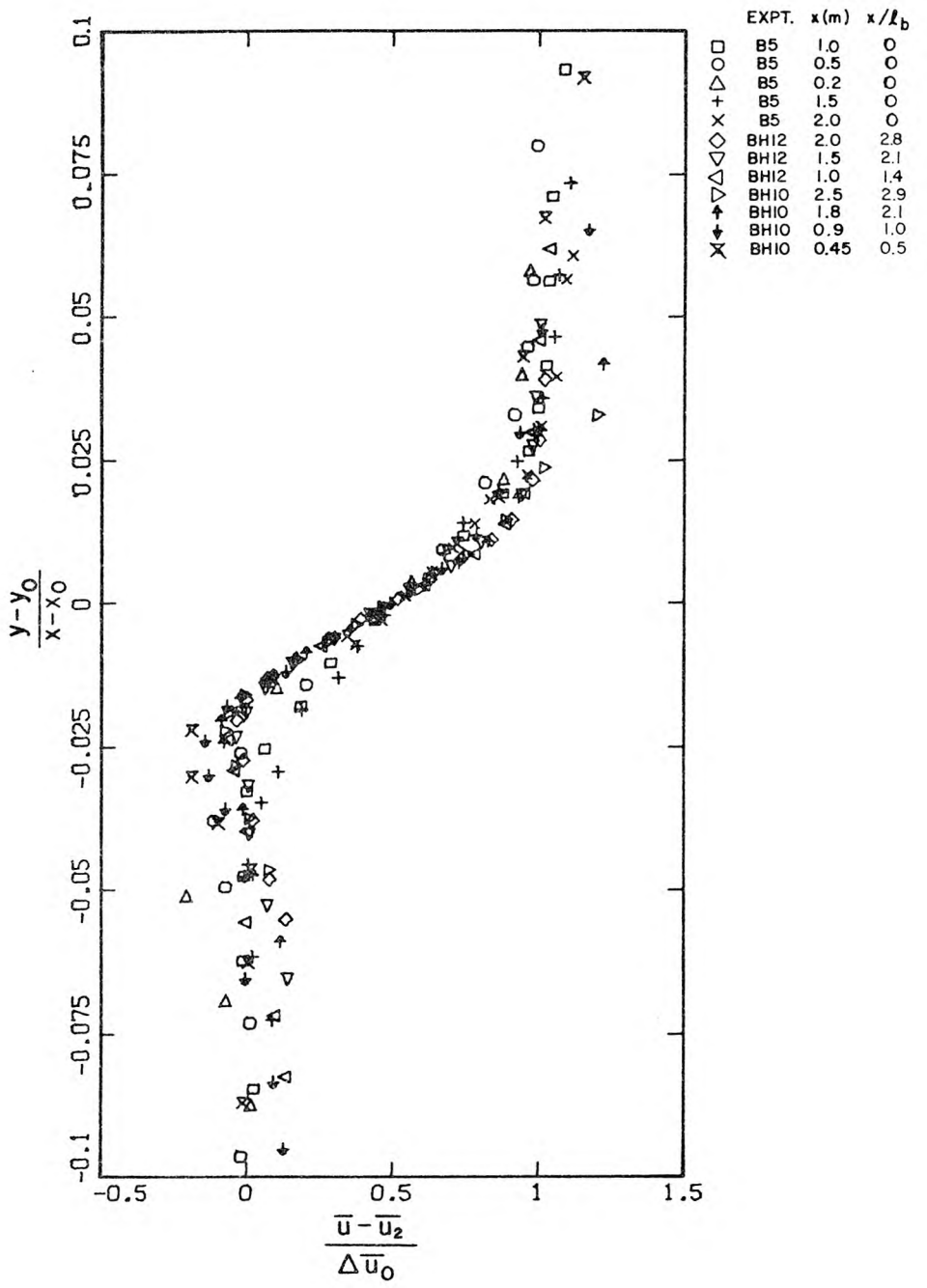

Figure 6.2.1 Profiles of the normalized mean horizontal velocity in the initial mixing layer. Symbol key gives: symbol, experiment number, downstream location of the measurement in meters and x/ℓ_b.

buoyancy forces in the stratified flows reduce the turbulent fluxes of heat and momentum, and this reduction is responsible for the increased shear in the stratified cases.

The wake from the splitter plate is also apparent in Figure 6.2.1, at $(y - y_o)/(x - x_o) \approx -0.025$. The velocity defect is larger for smaller values of x, as expected, and at a given x, it is larger for larger values of $\Delta\rho/\rho_o$; this indicates, again, that buoyancy forces inhibit the mixing processes.

Figure 6.2.2 shows additional normalized velocity profiles for several stratified flows measured at locations where x/ℓ_b was greater than four. In fact, as is discussed in Section 6.2.4, the mixing layer begins to collapse visually when x/ℓ_b attains the value of about 1.8. When x/ℓ_b is four or more, $\frac{\Delta\rho}{\rho_o} g\ell_T^*/\Delta\bar{u}_o^2$ approaches a constant value of about 0.25. These profiles, then, show the velocity during and after the collapse of the mixing layer. Figure 6.2.2 also shows the pre-collapse profiles from Figure 6.2.1 for comparison. It is easily seen that the normalized gradient increases slightly after the collapse process begins. This will be discussed in detail later (Section 7.1), but the reason that the normalized gradient increases is in part due to the destruction of the two-dimensional vortices, and the resulting reduced growth rate of the mixing layer.

The fact that the wake is more apparent in the profiles in Figure 6.2.2 than in the pre-collapse profiles is mainly due to the data from one experiment (BH9) in which the mean velocity difference was only 1.9 cm/s, so the wake had a greater influence on the flow development in that case. Thus, some of the increase in the normalized gradient

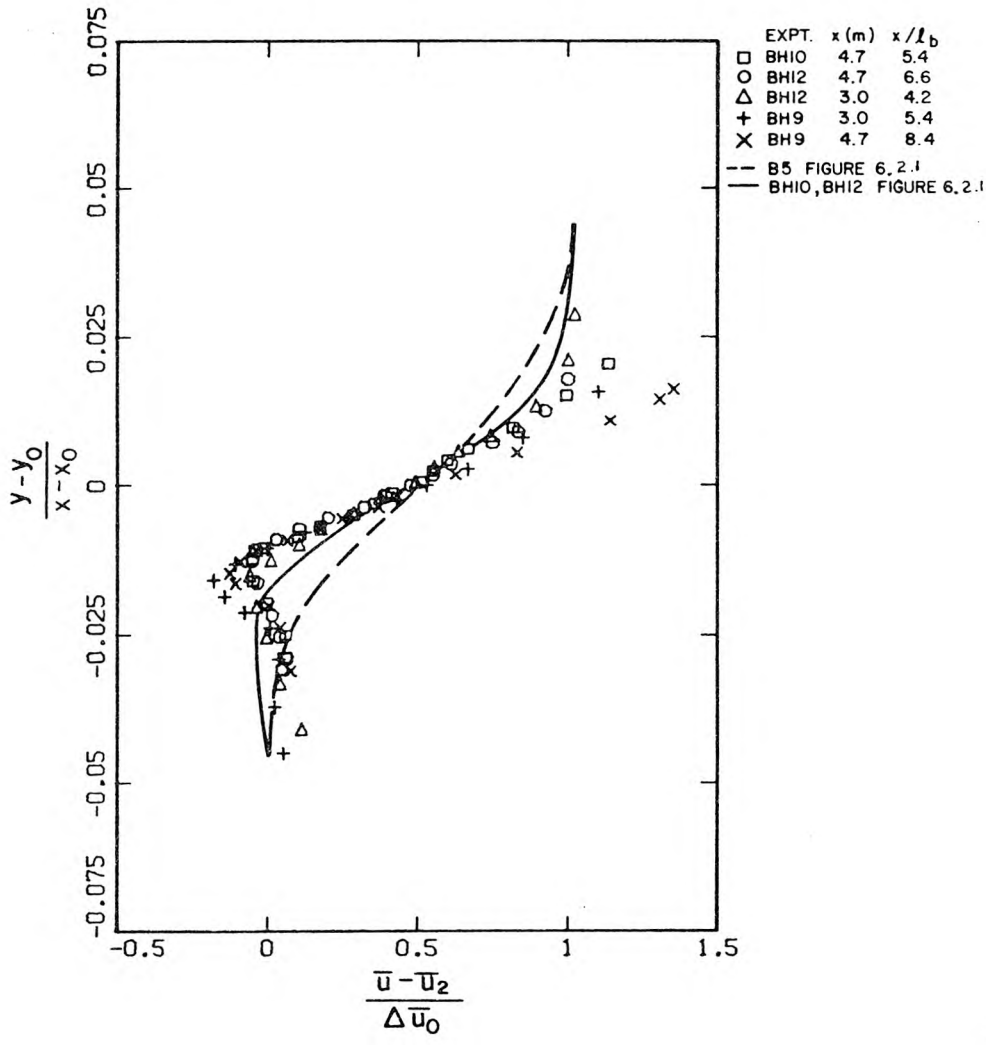

Figure 6.2.2 Profiles of the normalized mean horizontal velocity, for measurements made at $x/\ell_b > 4$. Lines indicate profiles from Figure 6.2.1 for comparison. Symbol key gives: symbol, experiment number, downstream location of the measurement in meters and x/ℓ_b.

that appears to be due to the collapse is, in fact, due to the more substantial wake in a few of the profiles (those from Experiment BH9). However, profiles from Experiments BH10 and BH12 are shown in both Figure 6.2.1 and Figure 6.2.2, and the profiles from these experiments are the basis for the observation of the increase in the normalized gradient during the collapse of the mixing layer.

6.2.2 Profiles of the Mean Temperature

Figure 6.2.3 shows normalized profiles of the mean temperature, for the same cases as shown in Figure 6.2.1. Two of the profiles (those from Experiment BH10 with $x/\ell_b = 1.0$ and 0.5 respectively) differ slightly from the others; this is probably due to the effect of the splitter plate wake on the mixing layer, as these profiles were taken at smaller values of x/ℓ_b than the others. The other profiles show a high degree of similarity, but the most striking thing about the profiles is that they are very asymmetric. There is a very sharp "corner" in the temperature profiles near $(y - y_o)/(x - x_o) = -0.025$, but the normalized mean temperature makes a smooth transition to unity for $(y - y_o)/(x - x_o) > 0$. This type of asymmetric profile has been observed by others (Koop (1976), Brown and Roshko (1974)) and will be discussed in more detail in Section 7.1. The asymmetric shape is, in part, a result of the nature of the two-dimensional vortex structures which make up the mixing layer.

Figure 6.2.4 shows normalized profiles of the mean temperature for values of x/ℓ_b greater than four, for the same cases as shown in Figure 6.2.2. Again, the profiles from Experiment BH9 probably reflect the larger effect of the splitter plate wake.

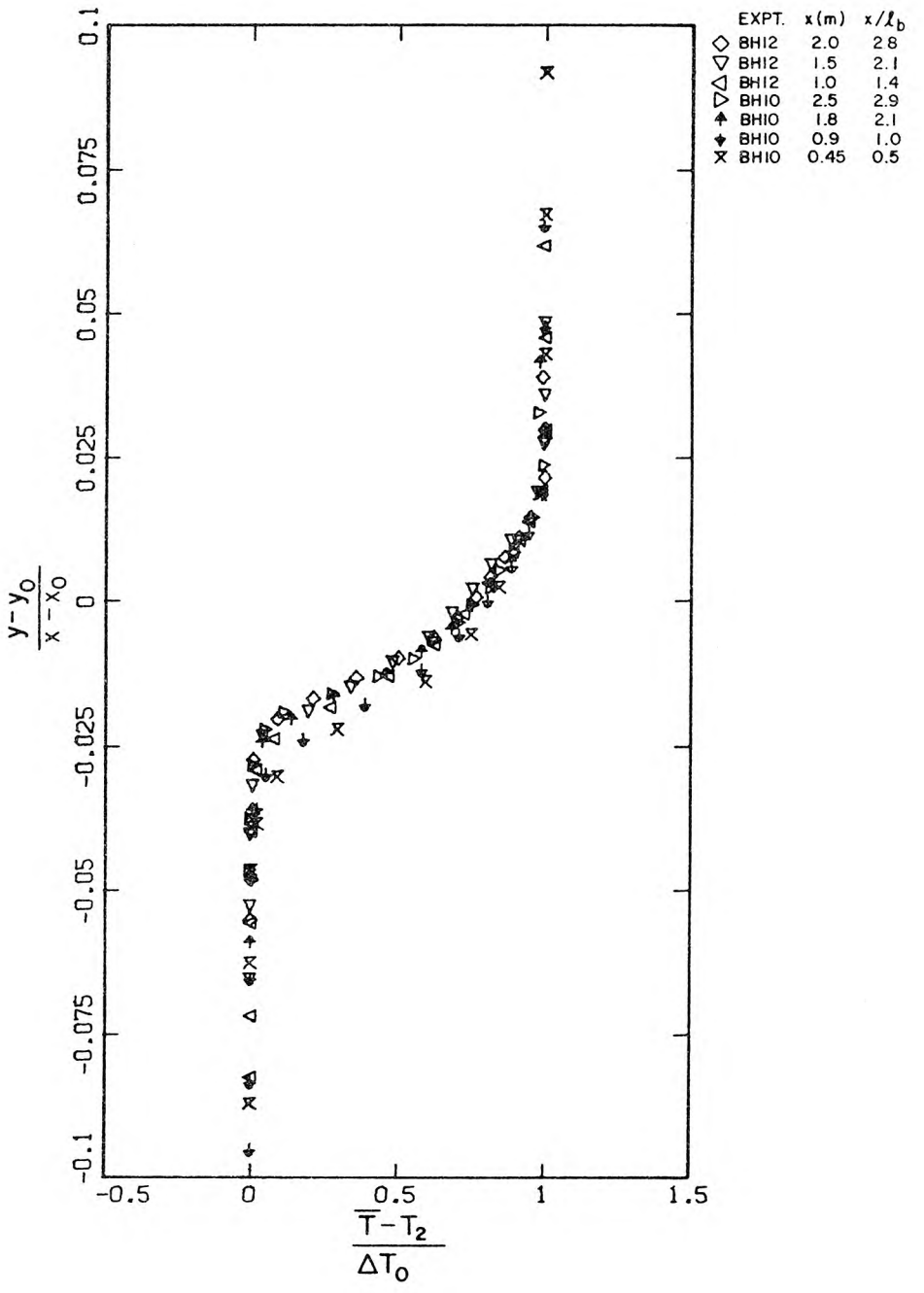

Figure 6.2.3 Profiles of the normalized mean temperature, for measurements made at $x/\ell_b < 3$. Symbol key gives: symbol, experiment number, downstream location of the measurement in meters and x/ℓ_b.

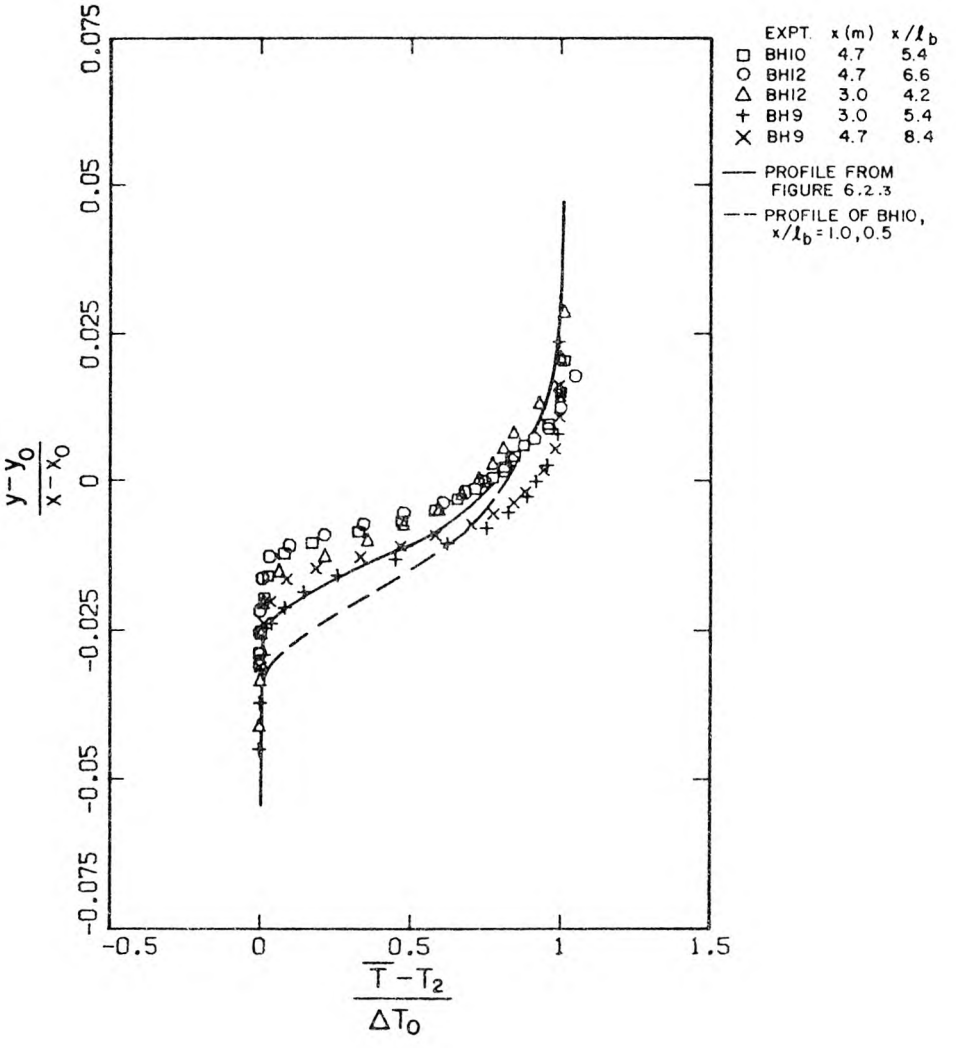

Figure 6.2.4 Profiles of the normalized mean temperature, for measurements made at $x/\ell_b > 4$. Lines indicate profiles from Figure 6.2.3 for comparison. Symbol key gives: symbol, experiment number, downstream location of the measurement in meters and x/ℓ_b.

As was the case with the velocity gradient, the normalized temperature gradient increases during the collapse of the mixing layer. In fact, Figure 6.2.4 shows that the gradient increases slightly for a given experiment, as x/ℓ_b increases. As is shown in Section 6.2.3, the thickness of the mixing layer, ℓ_T^*, becomes approximately constant when the layer collapses, while ℓ_u^* continues to increase, although at a reduced rate. Thus, when the normalized profiles are plotted against $(y - y_o)/(x - x_o)$, they are quite sensitive to changes in the rate at which the thickness of the mixing layer increases.

6.2.3 Growth Rates and Length Scales in the Mixing Layer

There are several length scales upon which growth rates of mixing layers can be determined. Since the maximum slope thickness of the velocity profile, ℓ_u^* (Equation 2.1.19), has been commonly used in the past and appears to be a reasonable choice physically, that length scale is used here. However, other length scales are important in these experiments and they, too, will be discussed in this section.

Figure 6.2.5 shows plots of ℓ_u^* (in cm) as a function of downstream distance x (in cm) for the five mixing layer experiments. As can be seen from the graphs, ℓ_u^* varies approximately in a linear fashion with downstream distance in the homogeneous case. However, ℓ_u^* seems to be a linear function of x for the inhomogeneous cases only near the splitter plate (actually for smaller values of x/ℓ_b) and farther downstream the rate of growth decreases. The decrease in the rate of growth is due to the collapse of the mixing layer.

A line was fit in the least-squares sense to the points in the

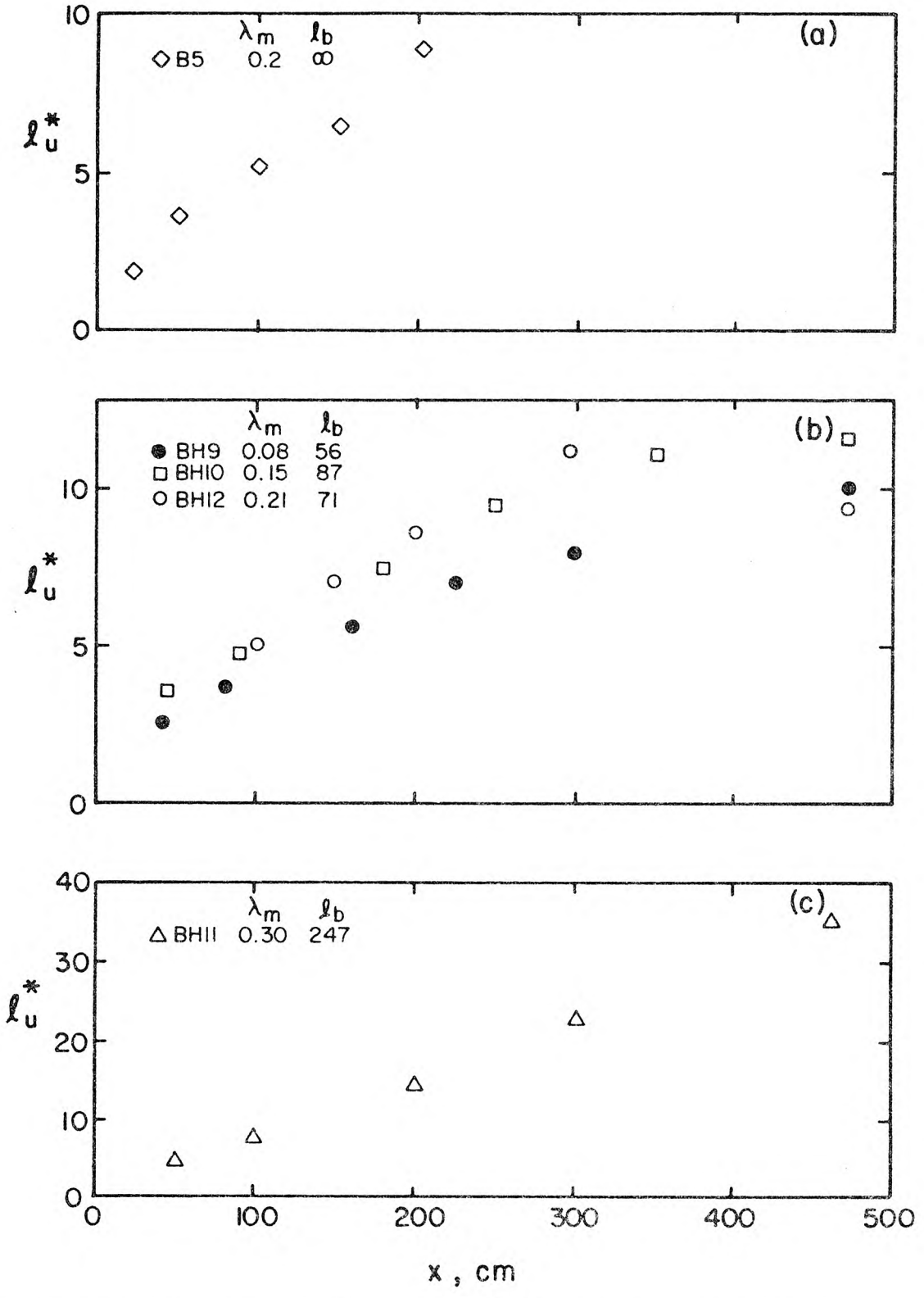

Figure 6.2.5 Maximum-slope thickness, ℓ_u^* (in cm) plotted against distance, x (in cm), from the splitter plate for the mixing layer experiments. Symbol key gives: symbol, experiment number, $\lambda_m = \Delta\bar{u}_o/(\bar{u}_1 + \bar{u}_2)$, ℓ_b (in cm).

region which appeared to have a linear growth (all but the farthest downstream points in the inhomogeneous cases) in order to determine the growth rates. Table 6.2.2 lists the growth rates $\delta_\omega' = \frac{d\ell_u^*}{d(x-x_o)}$, and the values of the virtual origin x_o for the various experiments. Included in Table 6.2.2 are the values of δ_ω' from the relationship $\delta_\omega' = 0.181\ \lambda_m$ given in Brown and Roshko (1974). The measured and predicted values agree fairly well, and all the values fall within the scatter band of previously measured values upon which the above relationship is based.

Table 6.2.2 Mixing layer growth rates.

Experiment No.	δ_ω'	x_o	x_o/ℓ_b	λ_m	$0.181\ \lambda_m = \delta_\omega'$ (Brown and Roshko, 1974)
B5	0.035	-35	0	0.20	0.036
BH9	0.023	-78	-1.4	0.08	0.014
BH10	0.029	-79	-0.91	0.15	0.028
BH11	0.069	-20	-0.08	0.30	0.054
BH12	0.030	-85	-1.2	0.21	0.038

The rather large values of x_o are due to the initial wake from the splitter plate. The graphs in Figure 6.2.5 indicate that ℓ_u^* at $x = 0$ (the end of the splitter plate) lies between 1.2 cm and 2.5 cm, with higher values arising from the experiments in which the buoyancy forces were more influential. Despite the wake, the growth rates here are not dissimilar to those measured by other investigators, and as was pointed out in Section 5.3, large two-dimensional vortices were observed in the mixing layer.

The maximum-slope thickness of the temperature profile is also of importance in the density-stratified cases. Values of ℓ_T^*/ℓ_b are plotted against x/ℓ_b in Figure 6.2.6. The main feature of this graph is the near-linear growth until x/ℓ_b is about 2, after which the growth rate declines. The reduction in the growth rate appears to be much more dramatic for the temperature length scale ℓ_T^* than for the velocity length scale ℓ_u^*. To show this more clearly, ℓ_T^*/ℓ_u^* is plotted against x/ℓ_b in Figure 6.2.7. As x/ℓ_b increases, ℓ_T^*/ℓ_u^* can be seen to gradually decrease, indicating that ℓ_u^* increases faster than ℓ_T^*. This is not surprising, in that heat is transferred almost entirely by turbulent mixing processes, whereas momentum is not only transferred by turbulent mixing, but by pressure forces and, as the mixing layer collapses, to some extent by viscous forces.

The usefulness, then, of ℓ_T^* becomes more apparent from Figures 6.2.6 and 6.2.7, in which the change in ℓ_T^* with x seems to indicate quite well the region in which the mixing layer is growing "normally" and the region in which it is collapsing to a laminar shear layer. On the other hand, ℓ_u^* is not as sensitive to the collapse of the mixing layer as ℓ_T^*. It is also interesting to note that, because of the asymmetry in the temperature profiles, ℓ_T^* and ℓ_u^* are not found at the same value of $(y - y_o)/(x - x_o)$. Whereas the maximum value of $\partial\overline{u}/\partial y$ is found near $(y - y_o)/(x - x_o) = 0$, the maximum value of $\partial\overline{T}/\partial y$ is found near $(y - y_o)/(x - x_o) = -0.02$, as can be seen in Figures 6.2.1 - 6.2.4.

Finally, the integral length scale ℓ_T, defined by Equation 2.1.21,

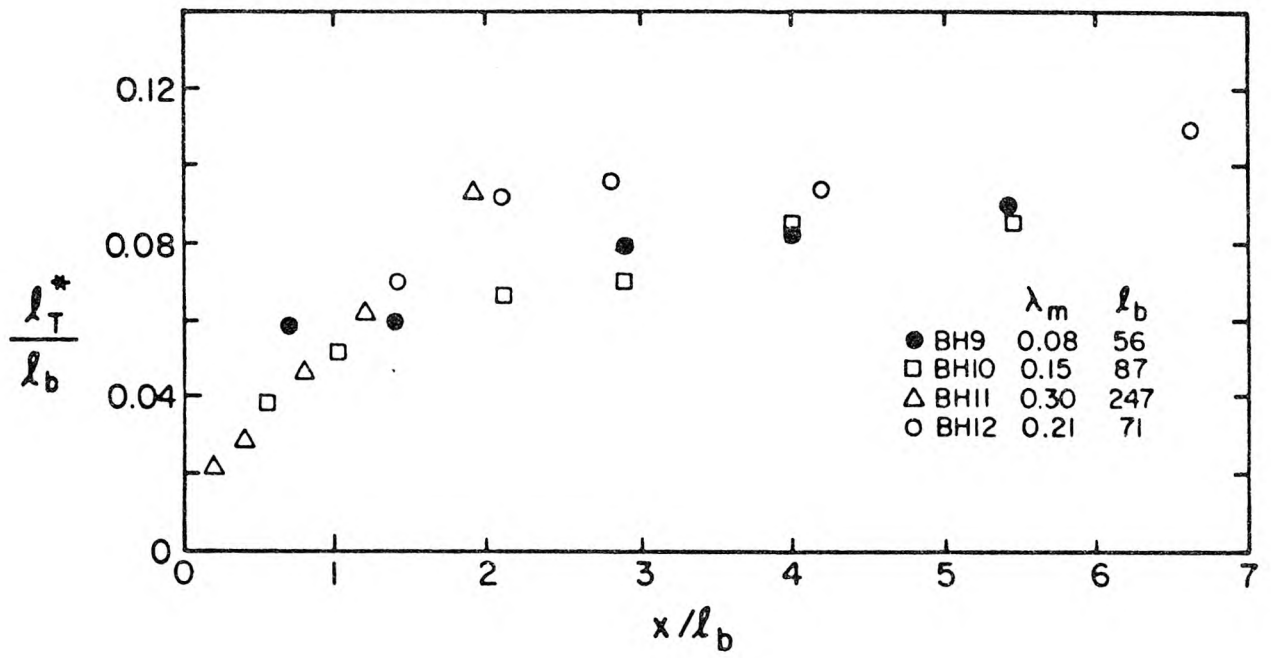

Figure 6.2.6 Normalized maximum-slope thickness, ℓ_T^*/ℓ_b, of the temperature profile plotted against x/ℓ_b. Symbol key gives: symbol, experiment number, λ_m, and ℓ_b (in cm).

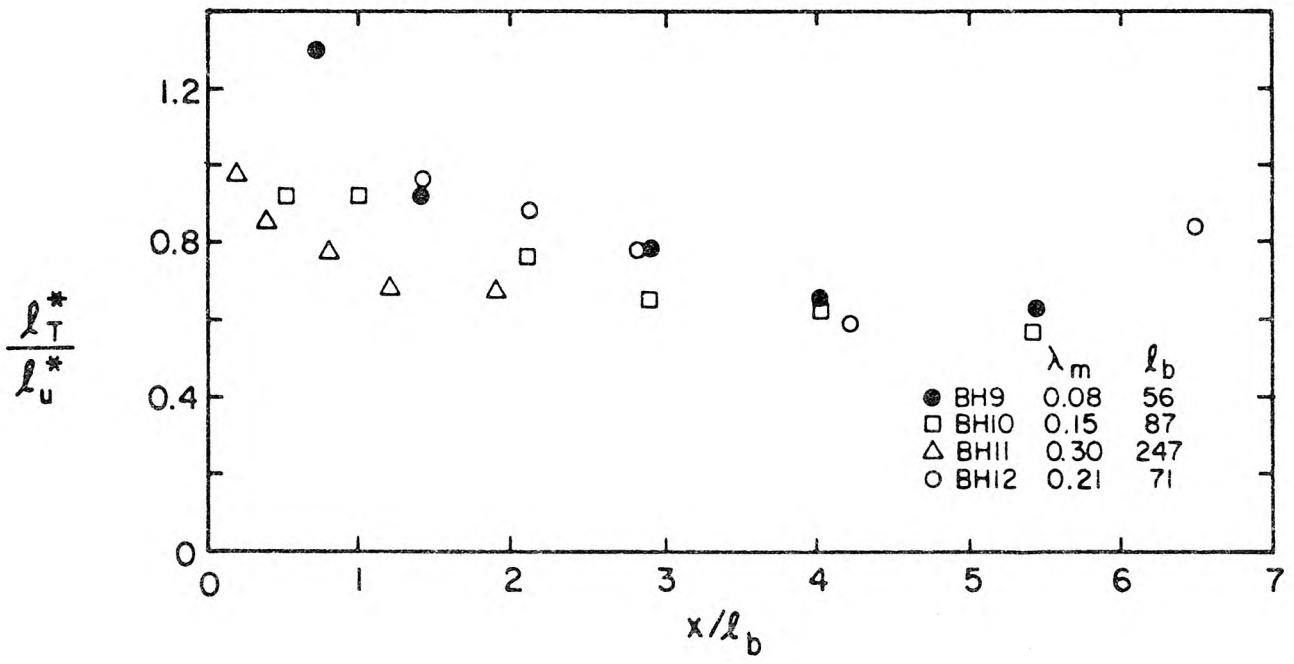

Figure 6.2.7 Ratio of the maximum-slope thickness of the temperature profile to the maximum-slope thickness of the velocity profile, plotted against x/ℓ_b. Symbol key gives: symbol, experiment number, λ_m, and ℓ_b (in cm).

was examined and found to be closely related to the length scale ℓ_T*. The ratio ℓ_T/ℓ_T* was found to have a mean value of 1.5 with a standard deviation of 0.3. The fact that these two length scales are related is not surprising in light of the similarity of the temperature profiles. Whether one is more useful than the other in describing the flow is not clear, since one length scale reflects a purely local situation and the other a depth-averaged situation. One can imagine a variety of different profiles all with identical values of ℓ_T and ℓ_T*. Because of the simplicity of its determination, ℓ_T* is preferred here, but ℓ_T is probably just as good a choice for a length scale of the temperature profile.

6.2.4 Collapse of the Mixing Layer

As was discussed in a qualitative manner in Section 5.3, the mixing layer was observed to collapse to a laminar shear layer provided that the initial density difference was sufficiently large. A number of experiments were conducted in which the collapse process was observed visually. Dye was injected into the mixing layer and the two-dimensional vortices were then observed. The average distance at which the vortices began to collapse was noted.

About thirty experiments of this type were conducted. The Keulegan number, $\left(\frac{\Delta\rho}{\rho_o} g\nu\right)/\Delta U_o{}^3$, for these experiments varied from 8×10^{-6} to 4×10^{-4}, $\frac{\Delta\rho}{\rho_o}$ varied from 2×10^{-4} up to 10^{-3} and $\Delta U_o/(U_1 + U_2)$ varied from 0.1 to 0.3. (Note that the mean flow speeds are used here, as no velocity measurements were made.) The data indicate that the quantity $2 \frac{\Delta\rho}{\rho_o} g x_c/(U_1 + U_2)\Delta U_o$ is about 1.8, where x_c is the distance from the splitter plate at which the vortices begin to collapse. This distance

cannot be determined very precisely, since not all vortices begin to collapse at the same place, and it is a subjective judgment as to when the collapse begins. Note also that the quantity $(U_1 + U_2)\Delta U_o$ involves overall mean speeds, and these are slightly less than centerline speeds (see Table 6.2.1). The value 1.8, then, should not be taken as an absolute measure of the dimensionless distance at which the collapse process begins, but only as a very approximate measure. The value of 1.8 does agree with the data in Figure 6.2.6, which indicate that the collapse begins approximately at $x/\ell_b = 2$.

Koop (1976) and Thorpe (1973b) have shown that some Richardson numbers seem to be important parameters when considering the collapse process, and these are examined in some detail here. Figure 6.2.8 shows values of $(\overline{Ri})_{min}$ plotted against x/ℓ_b, where $(\overline{Ri})_{min}$ is the minimum value of $\overline{Ri}$ measured in the mixing layer at any particular location downstream. In this graph $(\overline{Ri})_{min}$ is seen to rise to a value in the neighborhood of 0.25 to 0.3 at $x/\ell_b = 6$. The value of $(\overline{Ri})_{min}$ appears to be still increasing at $x/\ell_b = 6$, and this is not surprising. As was shown in Section 6.2.3, ℓ_T^* approaches a maximum value during the collapse, while ℓ_u^* continues to increase. This indicates that the velocity profile continues to change (causing $\frac{\partial \overline{u}}{\partial y}$ to decrease) while the temperature (hence, density) profile remains fairly constant. As can be seen in Figure 6.2.8, the rate of increase in $(\overline{Ri})_{min}$ decreases with x/ℓ_b.

Figure 6.2.9 shows a bulk-Richardson number, $\frac{\Delta\rho}{\rho_o} g\ell_u^*/\Delta\overline{u}_o^2$, plotted against x/ℓ_b. Here, $\frac{\Delta\rho}{\rho_o} g\ell_u^*/\Delta\overline{u}_o^2$, is seen to increase to between 0.35

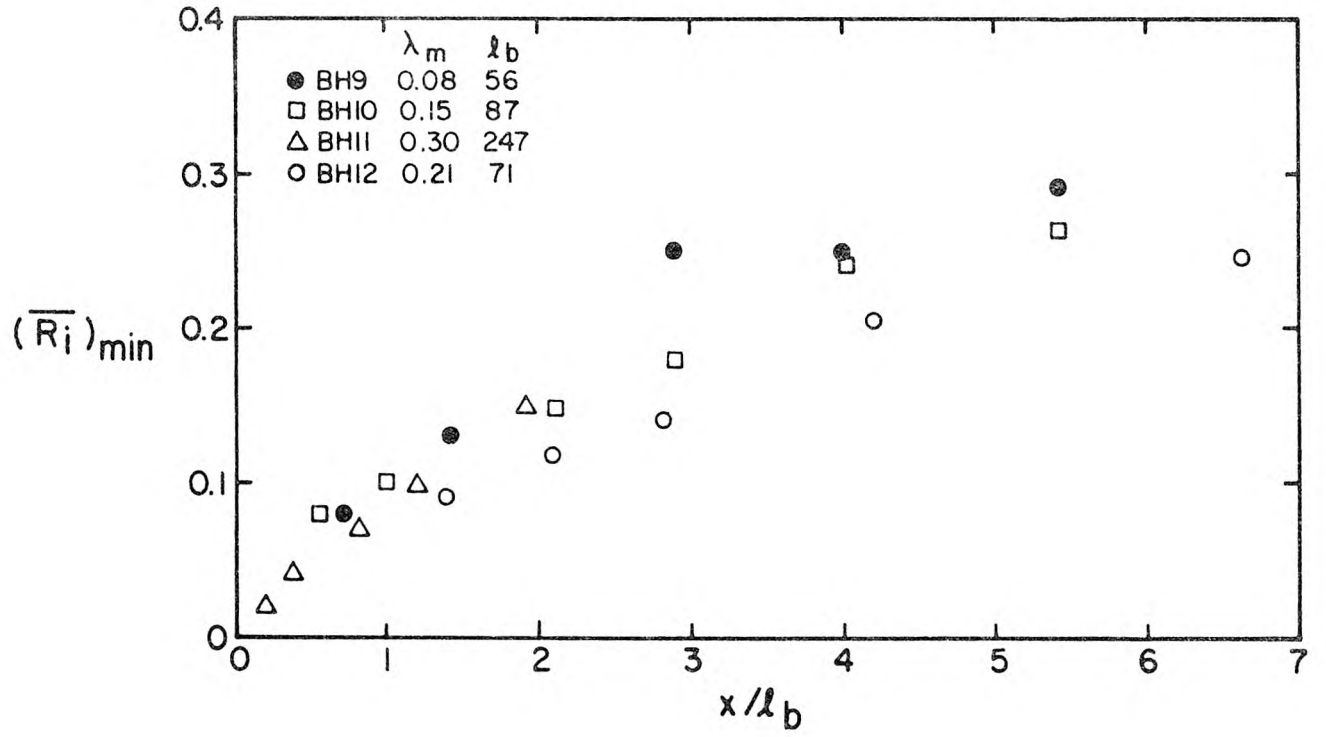

Figure 6.2.8 Local minimum value of $\overline{Ri}$ plotted against x/ℓ_b. Symbol key gives: symbol, experiment number, λ_m, and ℓ_b (in cm).

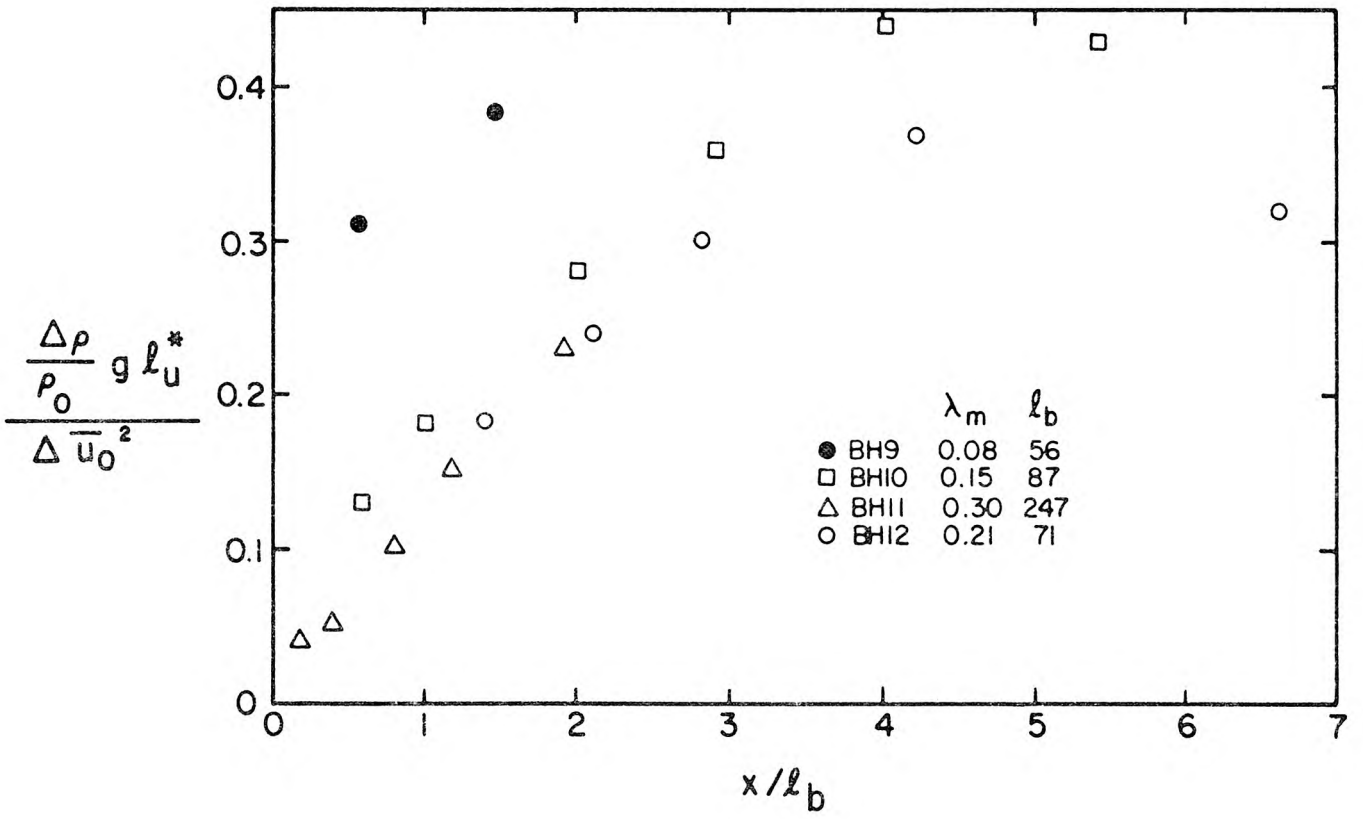

Figure 6.2.9 Bulk-Richardson number based on ℓ_u* plotted against x/ℓ_b. Symbol key gives: symbol, experiment number, λ_m, and ℓ_b (in cm).

and 0.45, and it appears that this bulk-Richardson number is continuing to increase. This is expected, of course, since ℓ_u^* continues to increase well after the collapse process has begun. The quantity ℓ_T^*, however, was seen to be influenced strongly by the collapsing of the mixing layer.

Figure 6.2.10 shows the bulk-Richardson number, $\frac{\Delta\rho}{\rho} g \ell_T^* / \Delta\bar{u}_o^2$ plotted against x/ℓ_b. The graph indicates that as the layer collapses, the bulk-Richardson number based on ℓ_T^* approaches a value between 0.25 and 0.3, and this is a rather significant result.

Data from Experiment BH9 indicated that at $x/\ell_b = 0.7$, the bulk-Richardson number based on ℓ_T^* was already 0.4, while the bulk-Richardson number based on ℓ_u^* was about 0.3. Furthermore, ℓ_T^*/ℓ_b was observed to increase only slightly for $x/\ell_b > 0.7$, indicating that the layer had begun collapsing upstream of $x/\ell_b = 0.7$, the location of the measurement made closest to the splitter plate in that experiment. In addition, the velocity profiles indicate that the splitter plate wake had a large influence on the flow development for this experiment, because of the small velocity difference. For these reasons, the data from Experiment BH9 may be somewhat anomalous, and should be regarded with caution when mixing layers are being considered.

Bulk-Richardson numbers such as $\frac{\Delta\rho}{\rho_o} g \ell_u^{*2} / \Delta\bar{u}_o^2 \ell_T^*$, were also calculated, but shed little additional light on the matter. The above mentioned bulk-Richardson number has been used by Thorpe (1973b), who found that it approached a value of about 0.32 after the collapse of the mixing layer. Using Thorpe's reported mean value of ℓ_u^*/ℓ_T^*, one

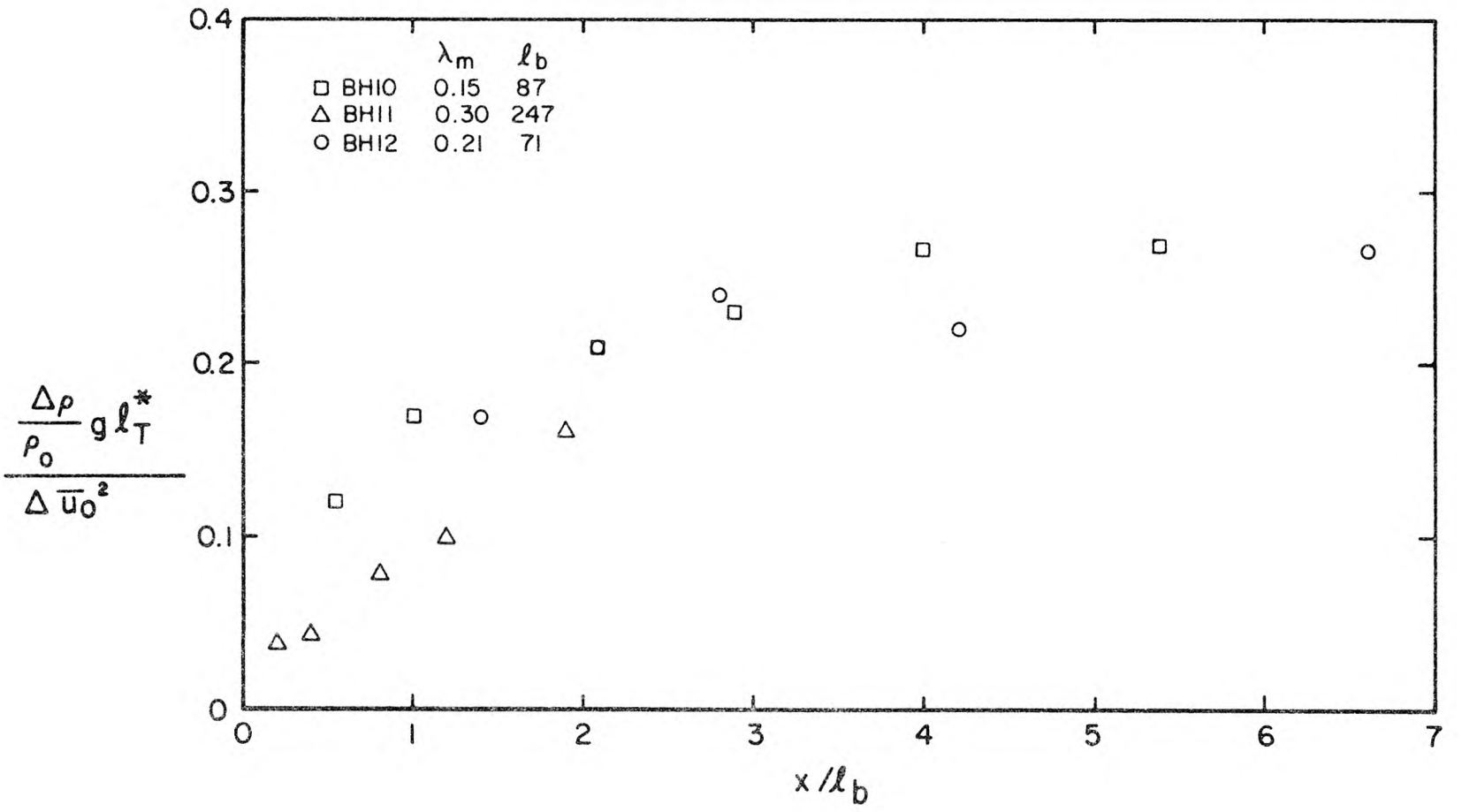

Figure 6.2.10 Bulk-Richardson number based on ℓ_T^* plotted against x/ℓ_b. Symbol key gives: symbol, experiment number, λ_m, and ℓ_b (in cm).

finds that $\frac{\Delta\rho}{\rho_o} g\ell_T^*/\Delta\bar{u}_o^2$ approaches a value of 0.24 in his experiments, in good agreement with the results presented here.

Thorpe's experiments, however, were conducted with two counter-flowing currents, unlike the present study. Consequently, the temperature profiles (as well as the two-dimensional vortex structures) were antisymmetric with respect to the flow centerline ($y = y_o$) in his experiments, unlike the asymmetric temperature profiles (and vortex development) characteristic of mixing layers developing spatially from a splitter plate. Thus, in Thorpe's experiments, $\left(\frac{\partial\bar{u}}{\partial y}\right)_{max}$ and $\left(\frac{\partial\bar{T}}{\partial y}\right)_{max}$ are found at the same location, whereas in this study (and others like it), these two quantities do not occur at the same location. Consequently, the use of ℓ_u^{*2}/ℓ_T^* as a length scale may not be very physically significant in this present study.

In summary, then, as the mixing layer collapses to a laminar shear layer, $\frac{\Delta\rho}{\rho_o} g\ell_T^*/\Delta\bar{u}_o^2$ approaches a value between 0.25 and 0.3. On the other hand, it appears that the velocity profile continues to change during and after the collapse of the mixing layer, so that $(\overline{Ri})_{min}$ and bulk-Richardson numbers based on ℓ_u^* continue to change as x increases. Finally, visual observations indicate that the collapse process begins at about $2x_c \frac{\Delta\rho}{\rho_o} g/\Delta U_o(U_1 + U_2) = 1.8$; this agrees well with measurements of ℓ_T^*, which indicate that the flow starts to collapse at $x/\ell_b = 2$.

6.2.5 Profiles of $\sqrt{\overline{u'^2}}$, $\sqrt{\overline{v'^2}}$ and $\sqrt{\overline{T'^2}}$

Figure 6.2.11 shows vertical profiles of $\sqrt{\overline{u'^2}}/\Delta\bar{u}_o$ for the same cases shown in Figure 6.2.1. These profiles were taken at values of x/ℓ_b up to 2.9, and therefore they largely reflect pre-collapse

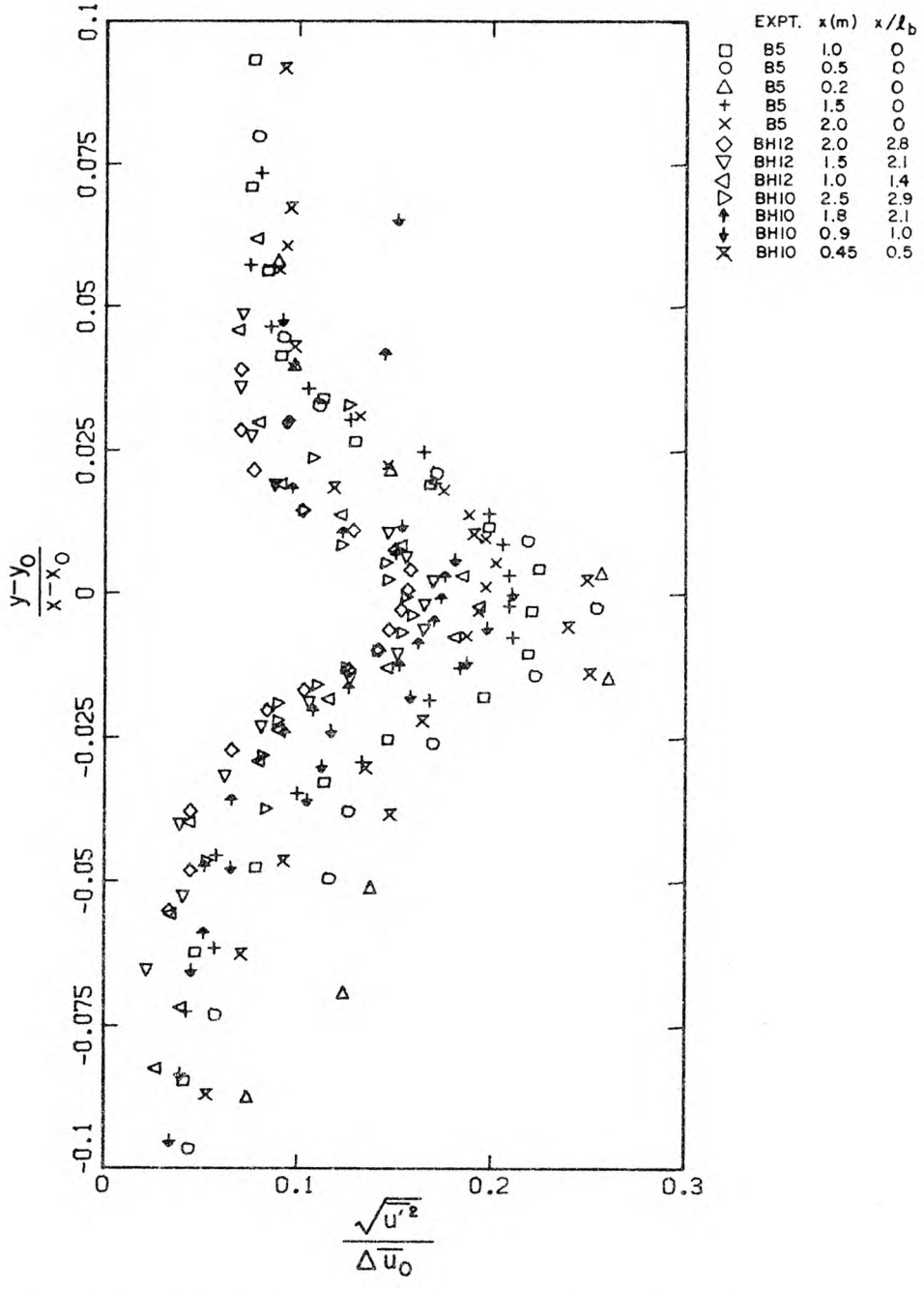

Figure 6.2.11 Profiles of normalized, r.m.s. values of the horizontal velocity fluctuations. Symbol key gives: symbol, experiment number, downstream location of measurement in meters and x/ℓ_b.

profiles. The main feature to be noted in these profiles is that within the mixing layer $\sqrt{\overline{u'^2}}/\Delta\bar{u}_o$ is smaller in the density-stratified cases than in the unstratified cases. Furthermore, the values of $\sqrt{\overline{u'^2}}/\bar{u}_o$ at a fixed value of $(y - y_o)/(x - x_o)$ are seen to decrease with x in the stratified cases, whereas in the homogeneous case, they remain nearly constant. (Wygnanski and Fiedler (1970) also found that $\sqrt{\overline{u'^2}}/\bar{u}_o$, $\sqrt{\overline{v'^2}}/\bar{u}_o$ and $\sqrt{\overline{u'^2}}/\bar{u}_o$ were nearly constant with x for a homogeneous mixing layer.) The profiles are otherwise quite similar, as can be seen more clearly in Figure 6.2.12, which shows the quantity $\left\{\sqrt{\overline{u'^2}} - (\sqrt{\overline{u'^2}})_{min}\right\}\Big/\left\{(\sqrt{\overline{u'^2}})_{max} - (\sqrt{\overline{u'^2}})_{min}\right\}$ plotted against $(y - y_o)/(x - x_o)$ for the same data shown in Figure 6.2.11. The profiles of $\sqrt{\overline{u'^2}}$ normalized in this manner appear to be quite similar within the mixing layer. This is not unexpected since the mixing layers are comprised of growing two-dimensional vortices which initially appear to be similar regardless of the presence of density stratification.

The non-zero values of $\sqrt{\overline{u'^2}}/\Delta\bar{u}_o$ above and below the mixing layer are due to the turbulence levels at the inlet. As can be seen in Figure 6.2.11, the free-stream values of $\sqrt{\overline{u'^2}}$ are as much as one-half of the maximum values of $\sqrt{\overline{u'^2}}$ found in the mixing layer. Nevertheless, contrary to the conclusions of Chandrsuda *et al.* (1978) which are discussed in Section 5.3, the mixing layer was observed to develop large two-dimensional vortices.

Figure 6.2.13 shows values of $\sqrt{\overline{v'^2}}/\bar{u}_o$ plotted against $(y - y_o)/(x - x_o)$, for the same cases shown in Figure 6.2.11. Again, the profiles appear to be similar, but the values of $\sqrt{\overline{v'^2}}/\bar{u}_o$ measured

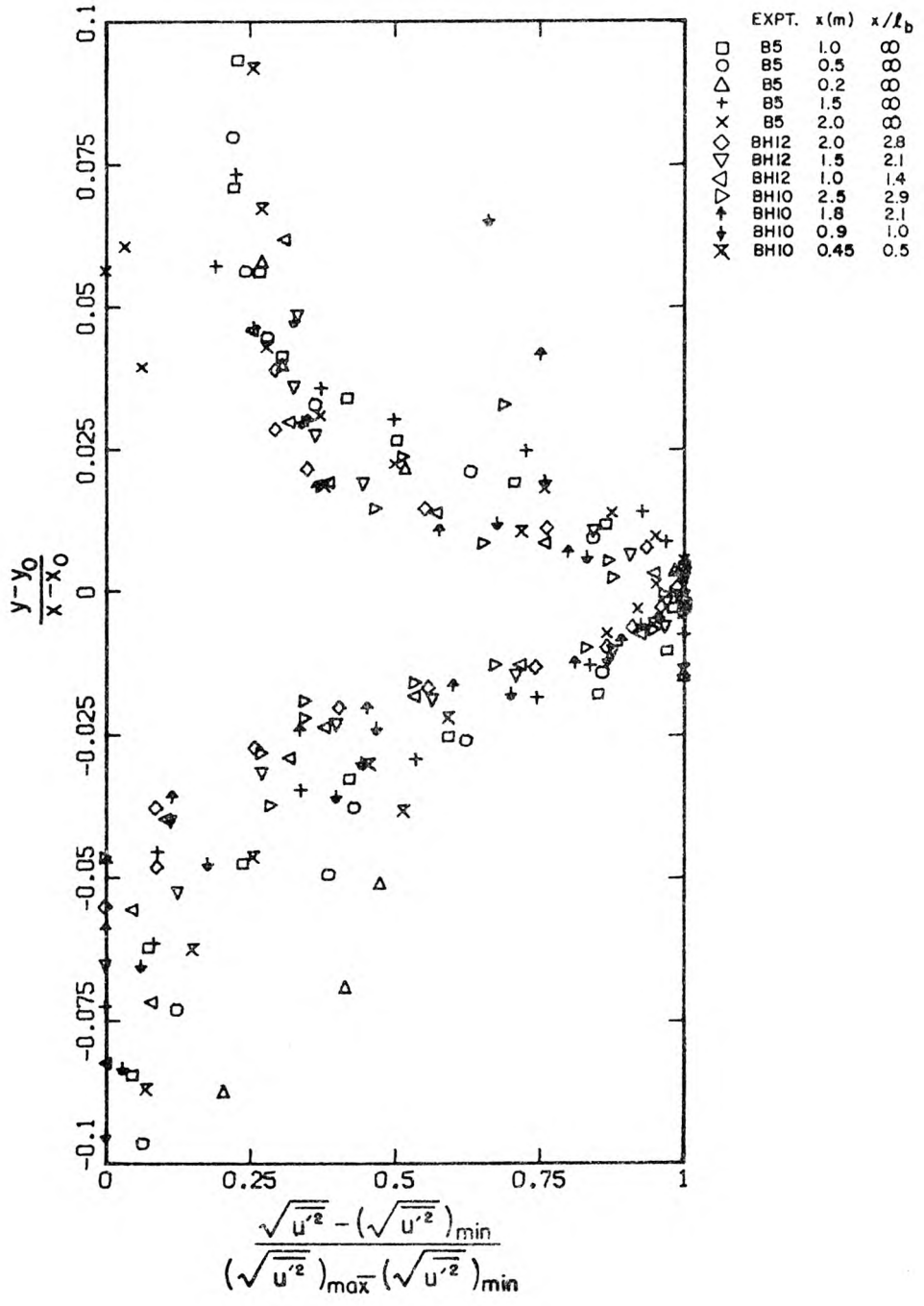

Figure 6.2.12 Profiles of the r.m.s. values of the horizontal velocity fluctuations, normalized to their local maximum values. Symbol key gives: symbol, experiment number, downstream location of measurement in meters and x/ℓ_b.

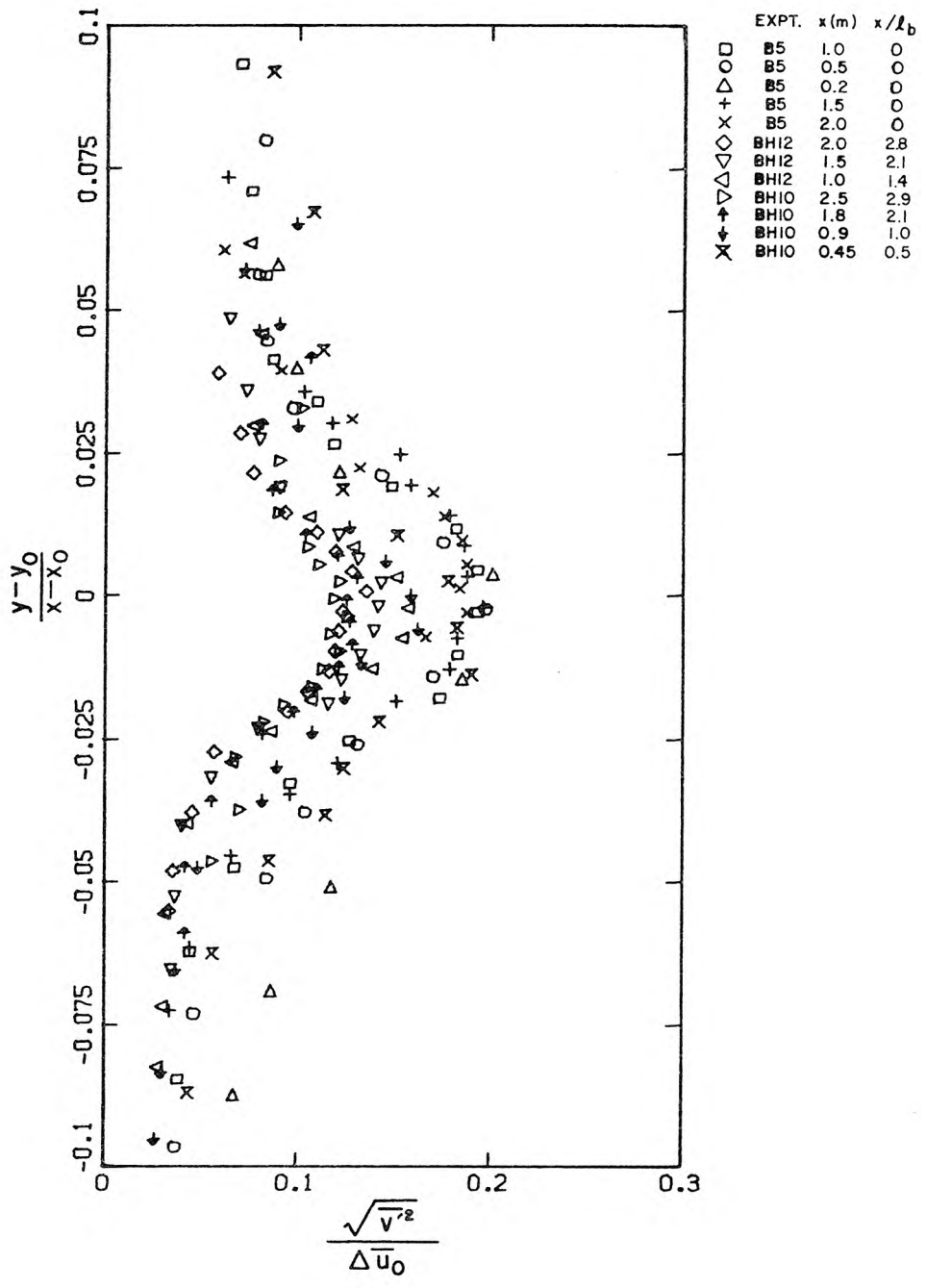

Figure 6.2.13 Profiles of normalized, r.m.s. values of the vertical velocity fluctuations. Symbol key gives: symbol, experiment number, downstream location of measurement in meters and x/ℓ_b.

in the stratified cases decrease with x, as was seen to be the case for $\sqrt{\overline{u'^2}}/\bar{u}_o$. Figure 6.2.14 shows $\left\{\sqrt{\overline{v'^2}} - (\sqrt{\overline{v'^2}})_{min}\right\}\Big/\left\{(\sqrt{\overline{v'^2}})_{max} - (\sqrt{\overline{v'^2}})_{min}\right\}$ plotted against $(y - y_o)/(x - x_o)$ for the same data shown in Figure 6.2.13. Again, there is a high degree of similarity in the profiles.

Figure 6.2.15 shows values of $\sqrt{\overline{T'^2}}/\Delta T_o$ plotted against $(y - y_o)/(x - x_o)$, for the same cases that are shown in Figures 6.2.11 - 6.2.14, excluding, of course, the homogeneous cases. These profiles are very nicely similar when plotted in this fashion, but unlike profiles of $\sqrt{\overline{u'^2}}/\Delta\bar{u}_o$ and $\sqrt{\overline{v'^2}}/\Delta\bar{u}_o$, the profiles of $\sqrt{\overline{T'^2}}/\Delta T_o$ are not symmetric with respect to $(y - y_o)/(x - x_o) = 0$. In fact, the position of the maximum value of $\sqrt{\overline{T'^2}}/\Delta T_o$ appears closely related to the position of the maximum value of $\frac{1}{\Delta T_o}\frac{\partial \bar{T}}{\partial y}$ (see Figure 6.2.3). The reason for the asymmetric profile of $\sqrt{\overline{T'^2}}/\Delta T$ is probably related to the asymmetric development of the mixing layer and is discussed in more detail in Section 7.1.

After the collapse of the mixing layer, there is no longer similarity of the profiles of turbulence intensities. Figure 6.2.16 shows $\sqrt{\overline{u'^2}}/\Delta\bar{u}_o$ plotted against $(y - y_o)/(x - x_o)$ for the cases shown in Figure 6.2.2. Figure 6.2.17 shows $\sqrt{\overline{v'^2}}/\Delta\bar{u}_o$ for the same cases. Again the profiles from Experiment BH9 were probably influenced by the splitter plate wake and may be anomalous. There is a trend toward smaller values of $\sqrt{\overline{u'^2}}/\Delta\bar{u}_o$ and $\sqrt{\overline{v'^2}}/\Delta\bar{u}_o$ with increasing values of x/ℓ_b, excluding the data from Experiment BH9. In addition, the profiles appear to be somewhat similar in shape, and there appears to be some asymmetry in the profiles. $\sqrt{\overline{u'^2}}/\Delta\bar{u}_o$ and $\sqrt{\overline{v'^2}}/\Delta\bar{u}_o$ decline more rapidly

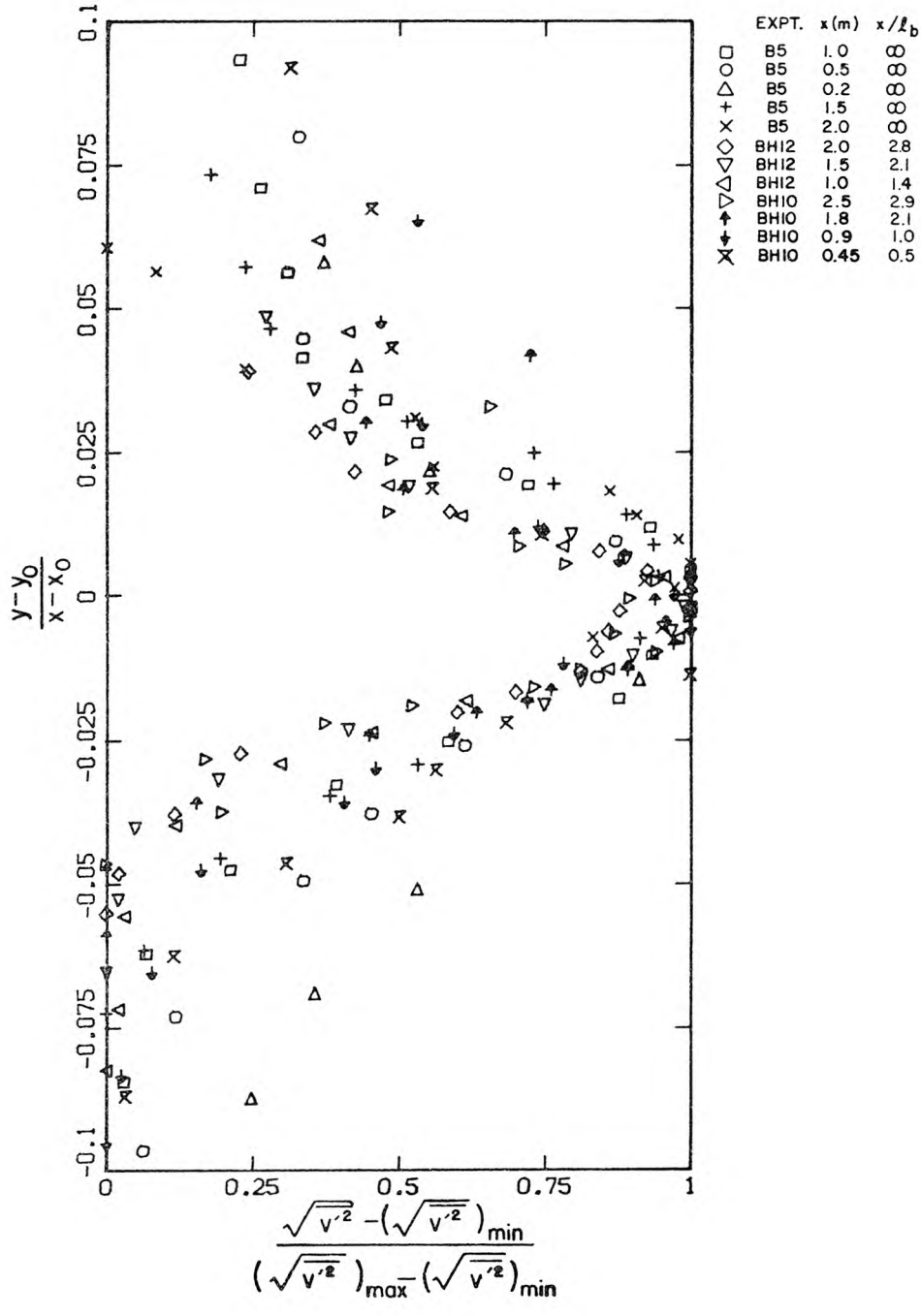

Figure 6.2.14 Profiles of the r.m.s. values of the vertical velocity fluctuations, normalized to the local maximum values. Symbol key gives: symbol, experiment number, downstream location of measurement in meters and x/ℓ_b.

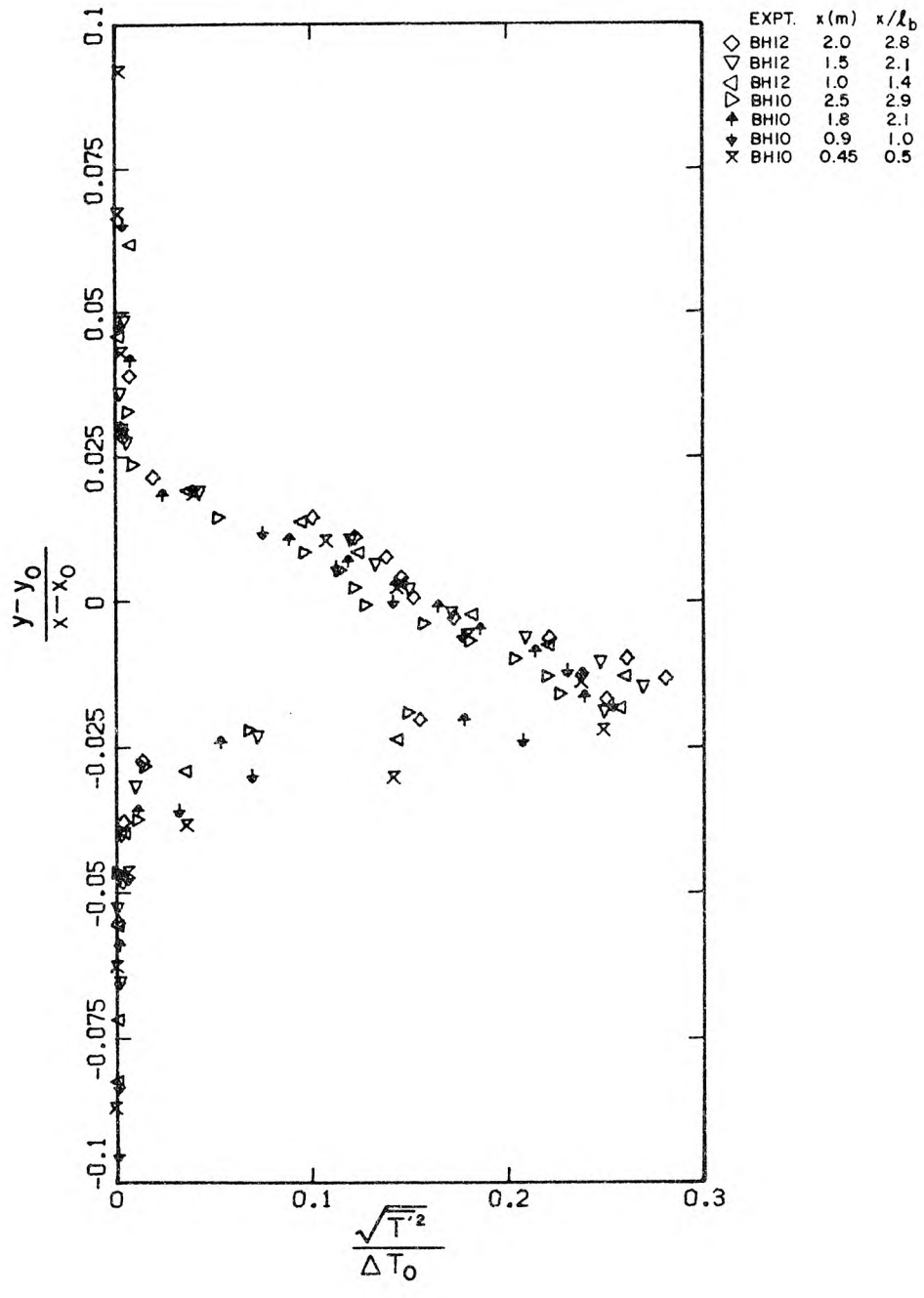

Figure 6.2.15 Profiles of normalized, r.m.s. values of the temperature fluctuations. Symbol key gives: symbol, experiment number, downstream location of measurement in meters and x/ℓ_b.

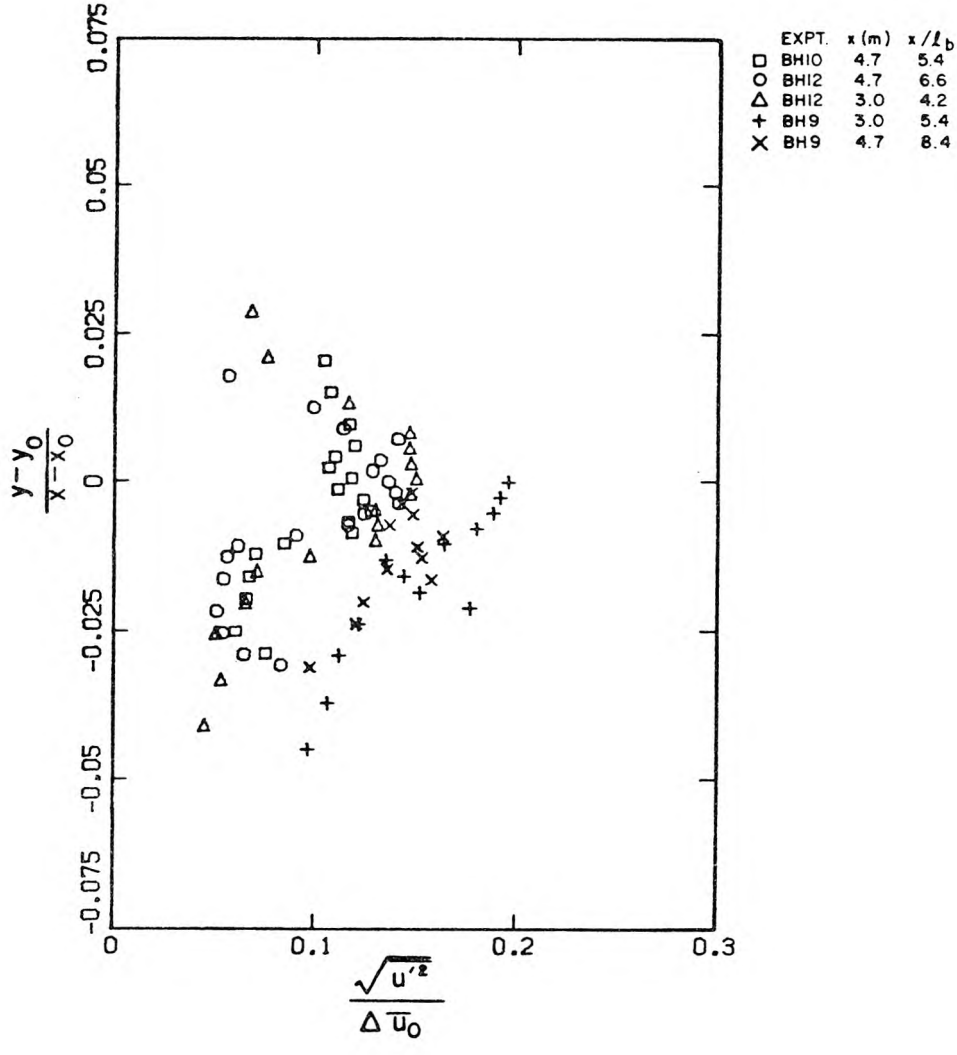

Figure 6.2.16 Profiles of normalized, r.m.s. values of the horizontal velocity fluctuations, for measurements made at $x/\ell_b > 4$. Symbol key gives: symbol, experiment number, downstream location of measurement in meters and x/ℓ_b.

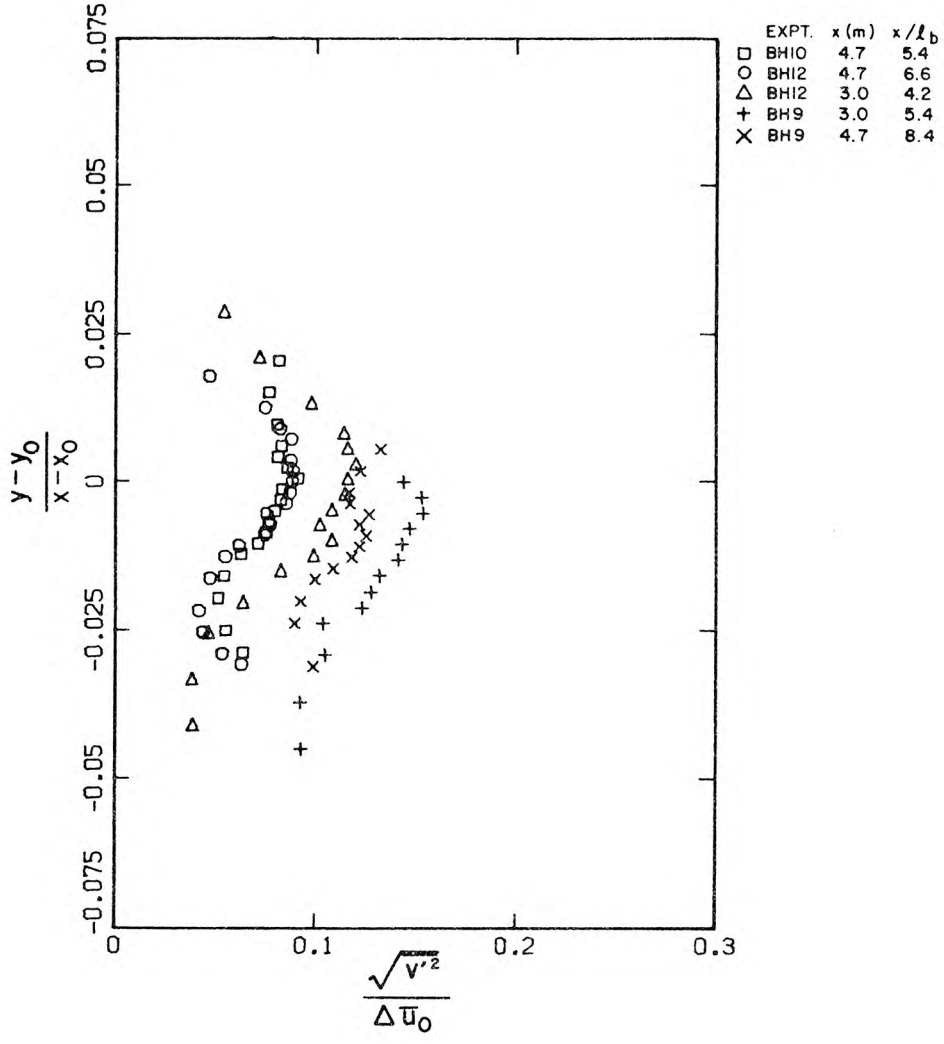

Figure 6.2.17 Profiles of normalized, r.m.s. values of the vertical velocity fluctuations, for measurements made at $x/\ell_b > 4$. Symbol key gives: symbol, experiment number, downstream location of measurement in meters and x/ℓ_b.

near $(y - y_o)/(x - x_o) = -0.01$, which coincides with the maximum slope of the temperature profile (Figure 6.2.4), than they do for $(y - y_o)/(x - x_o) > 0$, and this is probably the result of buoyancy forces.

Figure 6.2.18 shows profiles of $\sqrt{\overline{T'^2}}/\Delta T_o$ plotted against $(y - y_o)/(x - x_o)$ for the cases considered in Figures 6.2.16 and 6.2.17. These profiles appear to be somewhat more consistent than those of the velocity fluctuations. The profiles from Experiment BH9 have maximum values somewhat smaller than the others and seem to be shifted down from the others; otherwise, the profiles are quite similar, and again exhibit the asymmetry seen in Figure 6.2.15. However, the maximum values of the profiles in Figure 6.2.18 are somewhat less than those in Figure 6.2.15 and the region of substantial temperature fluctuations ($\sqrt{\overline{T'^2}}/\Delta T_o > 0.03$) is somewhat reduced in the profiles of Figure 6.2.18.

6.2.6 Profiles of Turbulent Flux Quantities

Figure 6.2.19 shows values of $-\overline{u'v'}/\Delta\bar{u}_o^2$ plotted against $(y - y_o)/(x - x_o)$ for the same cases as presented in Figure 6.2.1. As was the case with the turbulent velocity fluctuations, the stratified flows exhibit somewhat smaller values of $-\overline{u'v'}/\Delta\bar{u}_o^2$ than the unstratified cases at a given distance from the splitter plate. The profiles otherwise exhibit a high degree of similarity, as is seen more clearly in Figure 6.2.20, which shows profiles of $-\overline{u'v'}$ normalized to their local maximum values. The maximum value of the profiles is found near $(y - y_o)/(x - x_o) = 0$, which is not unexpected considering the nature of the mean velocity profile (Figure 6.2.1) and the symmetry found in

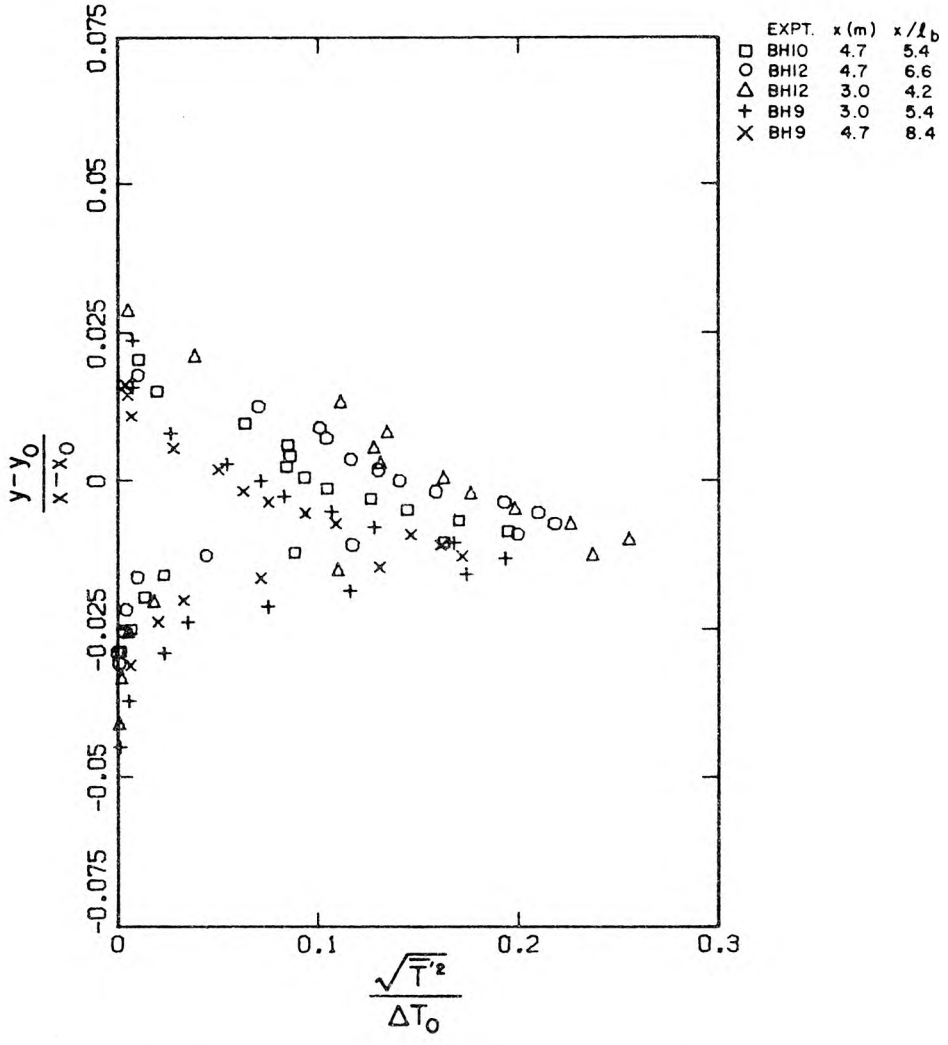

Figure 6.2.18 Profiles of normalized, r.m.s. values of the temperature fluctuations, for measurements made at $x/\ell_b > 4$. Symbol key gives: symbol, experiment number, downstream location of measurement in meters and x/ℓ_b.

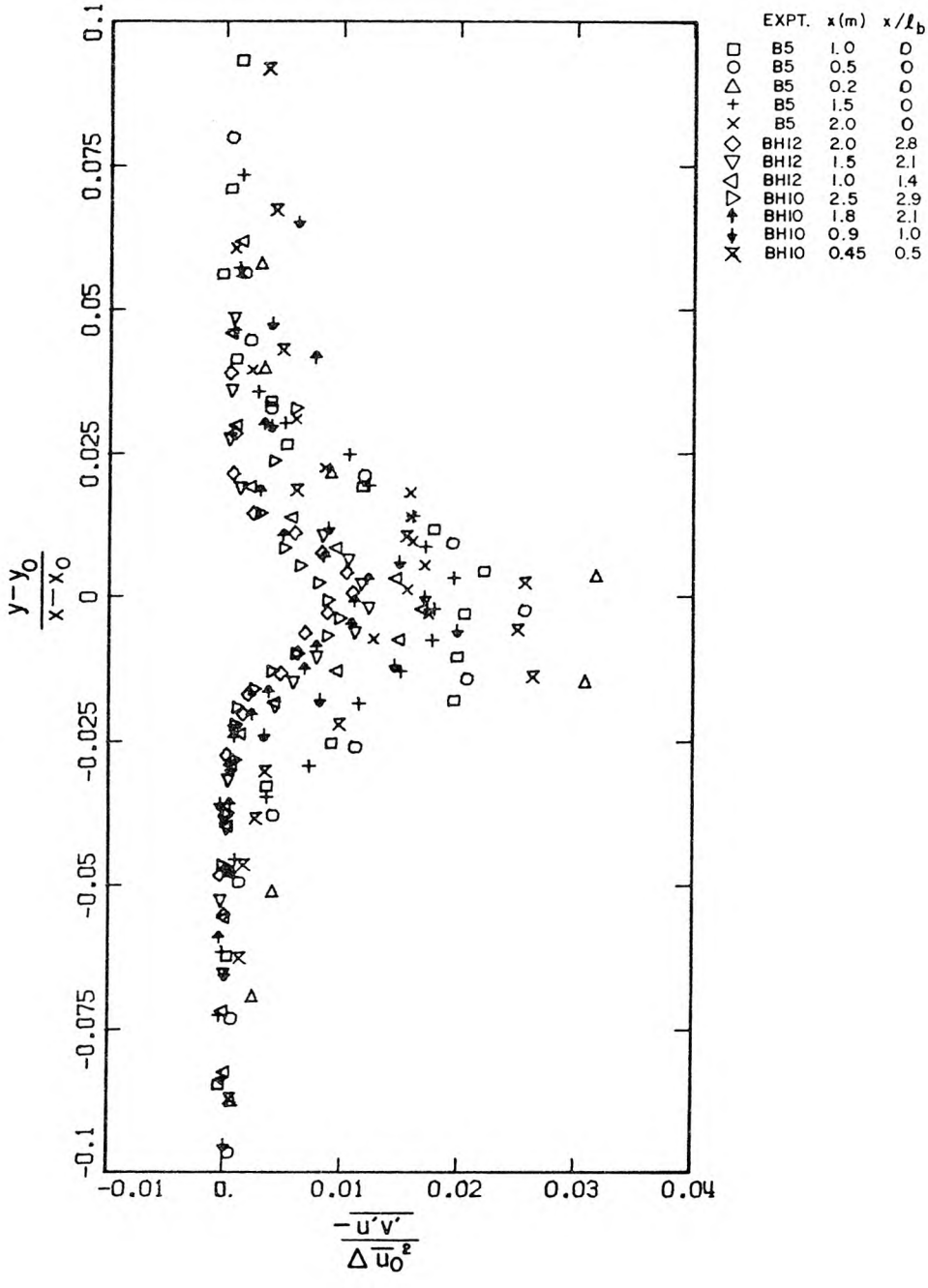

Figure 6.2.19 Profiles of $-\overline{u'v'}/\Delta\overline{u}_o^2$, measured at $x/\ell_b < 3$. Symbol key gives: symbol, experiment number, downstream location of measurement in meters and x/ℓ_b.

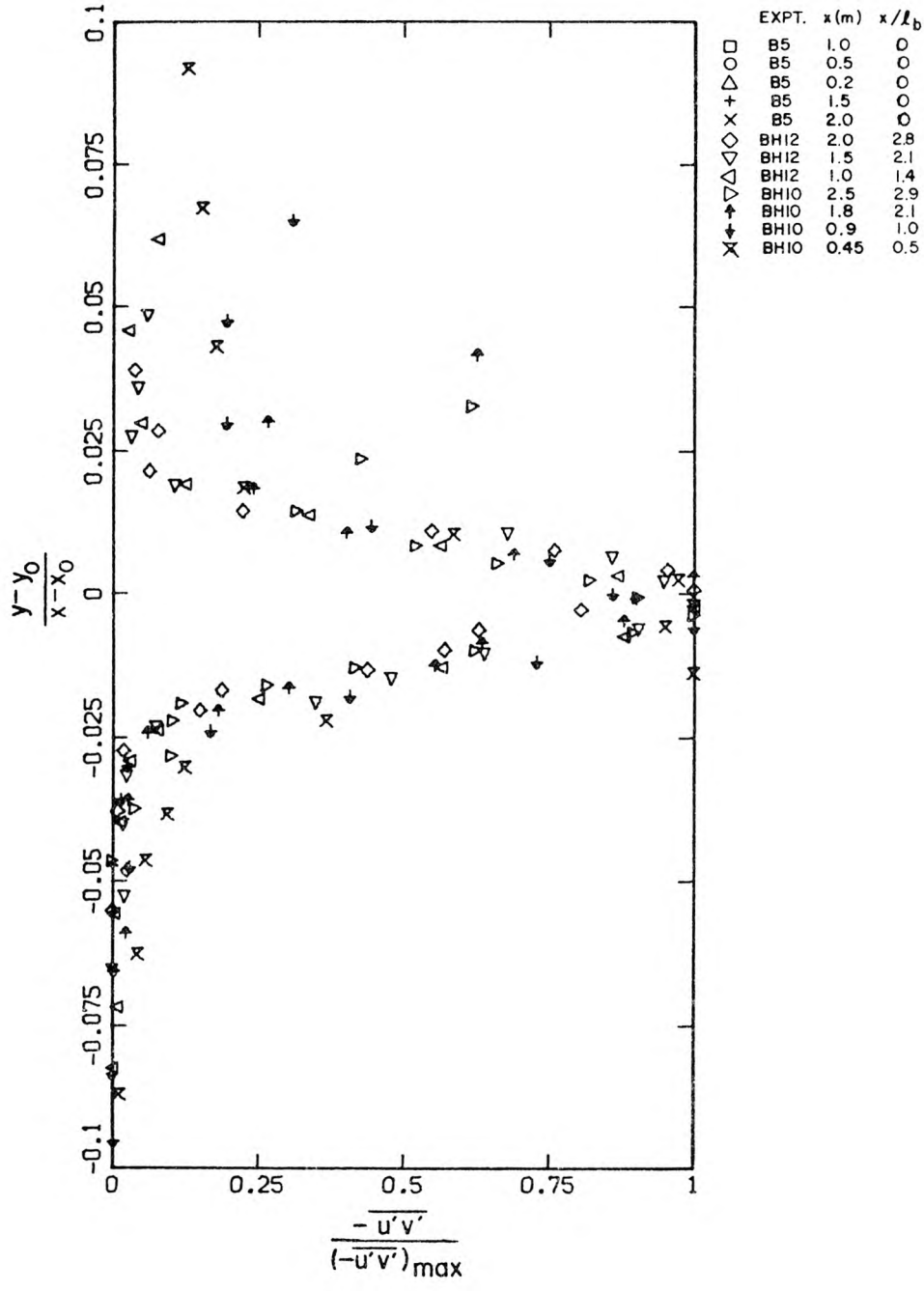

Figure 6.2.20 Profiles of $-\overline{u'v'}$ normalized with the local maximum for the same data as shown in Figure 6.2.19. Symbol key gives: symbol, experiment number, downstream location of measurement in meters and x/ℓ_b.

the profiles of $\sqrt{\overline{u'^2}}/\Delta\bar{u}_o$ and $\sqrt{\overline{v'^2}}/\Delta\bar{u}_o$ (Figures 6.2.11 - 6.2.14), measured at the smaller values of x/ℓ_b. It is also interesting to note that, although $\sqrt{\overline{u'^2}}$ and $\sqrt{\overline{v'^2}}$ are rather substantial away from the mixing layer (Figures 6.2.11 and 6.2.13), $-\overline{u'v'}$ is near zero away from the mixing layer.

The correlation coefficients between u' and v' are shown in Figure 6.2.21 for the same data shown in Figure 6.2.19 and 6.2.20. When plotted this way, the data are more scattered, but there are some general trends. In the middle of the mixing layer, the values of $-\overline{u'v'}/\sqrt{\overline{u'^2}}\sqrt{\overline{v'^2}}$ are around 0.5 ± 0.1, and there does not seem to be much difference between the stratified and unstratified cases.

Figure 6.2.22 shows values of $-\overline{v'T'}/\Delta\bar{u}_o\Delta T_o$ plotted against $(y - y_o)/(x - x_o)$, again for smaller values of x/ℓ_b. As with $-\overline{u'v'}$, the values of $-\overline{v'T'}$ away from the mixing layer are very nearly zero, as expected. There does seem to be a trend toward smaller values of $-\overline{v'T'}/\Delta\bar{u}_o\Delta T_o$ with larger values of x/ℓ_b, but the data are too scattered to draw firm conclusions on this. The data are quite similar, as can be seen in Figure 6.2.23, which shows profiles of $-\overline{v'T'}$ normalized to their local maximum values. The maximum values are found when $(y - y_o)/(x - x_o)$ is between zero and -0.02, which is in the neighborhood of, but slightly above, the location of the maximum gradient of the mean temperature profile (Figure 6.2.3).

The correlation coefficients $-\overline{v'T'}/\sqrt{\overline{v'^2}}\sqrt{\overline{T'^2}}$, shown in Figure 6.2.24, are smaller and somewhat less scattered than the correlation coefficients between u' and v' (Figure 6.2.21). The maximum values of

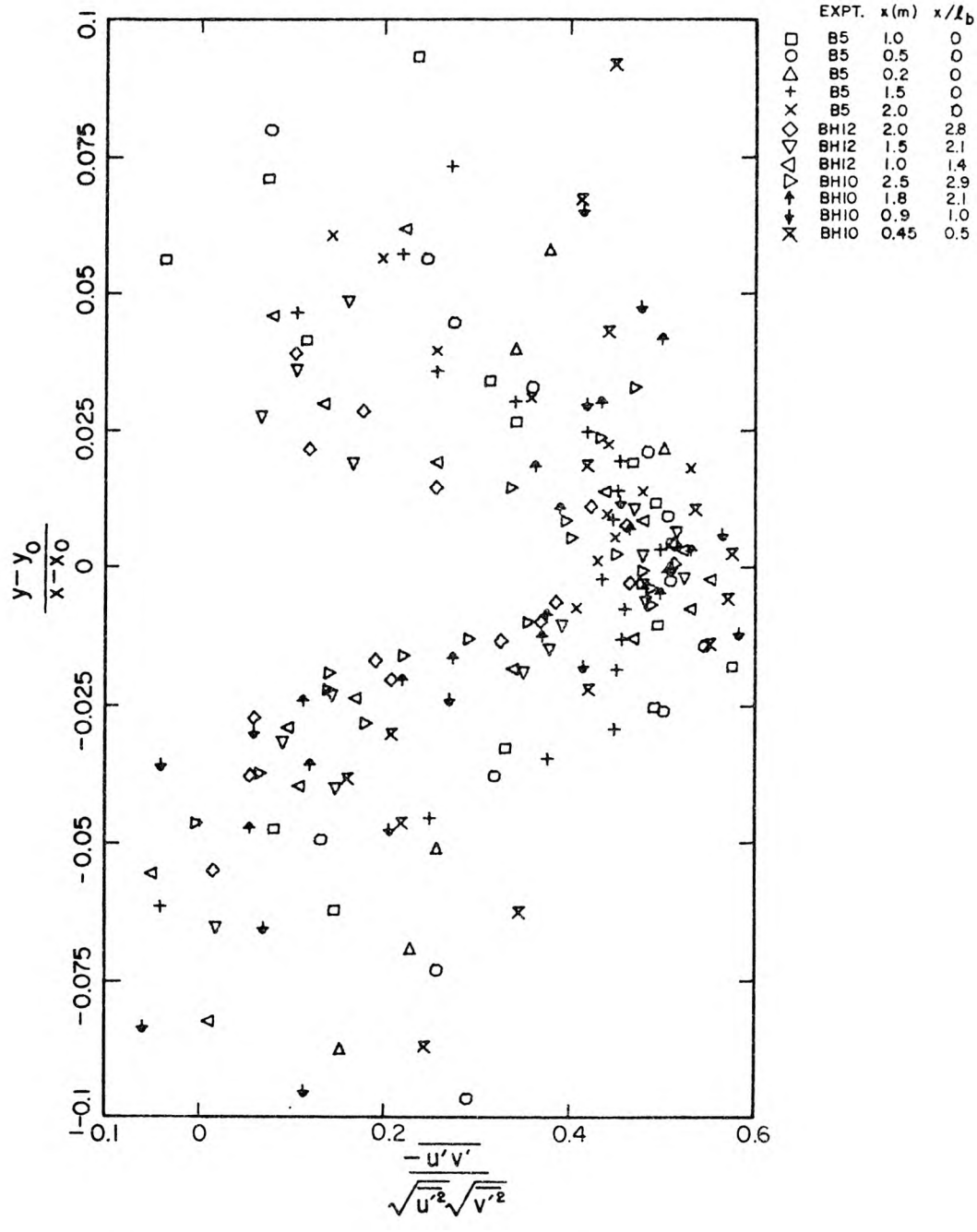

Figure 6.2.21 Profiles of the negative correlation coefficient, $-\overline{u'v'}/\sqrt{\overline{u'^2}}\sqrt{\overline{v'^2}}$ for the same data as shown in Figure 6.2.19. Symbol key gives: symbol, experiment number, downstream location of measurement in meters and x/ℓ_b.

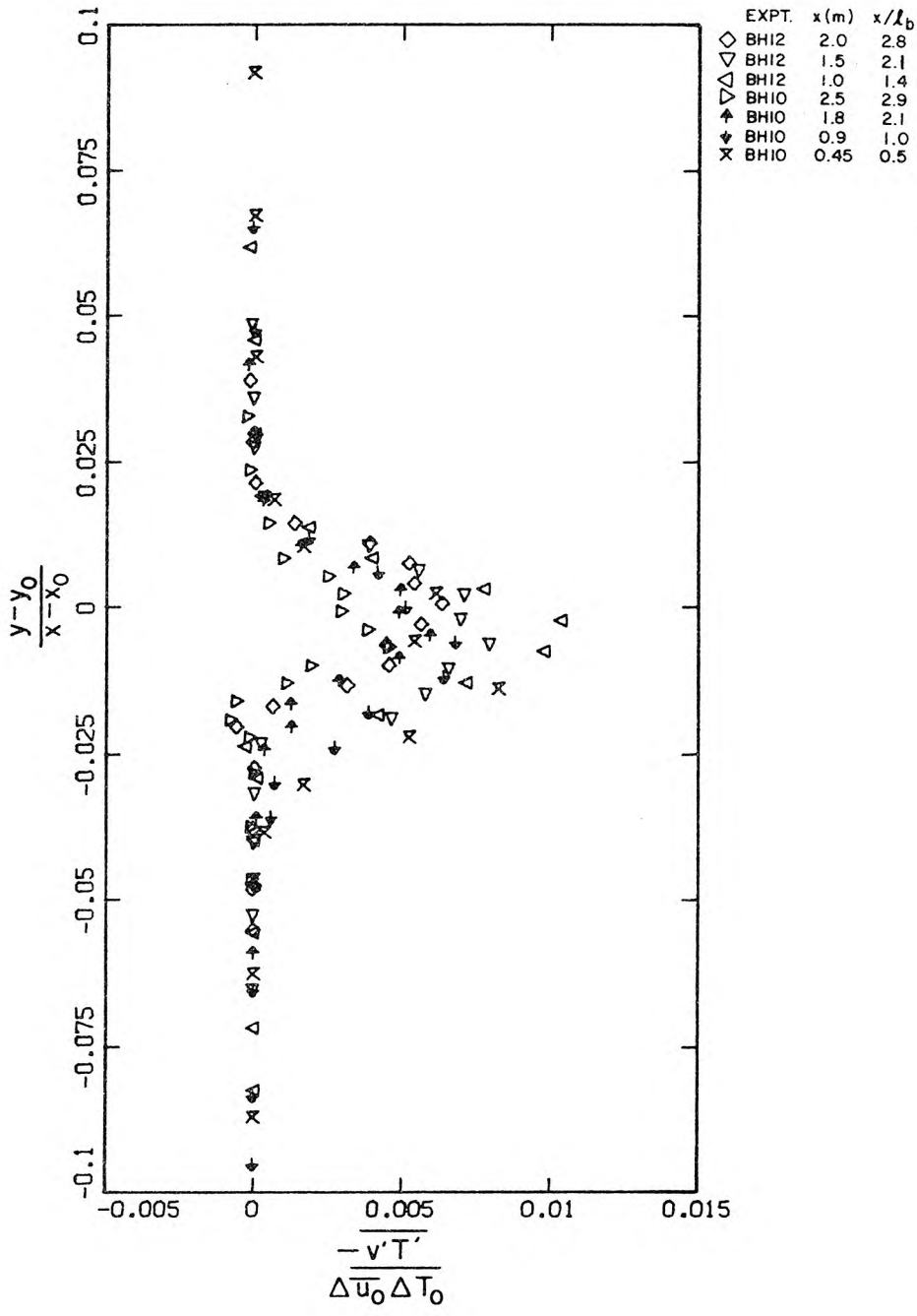

Figure 6.2.22 Profiles of $-\overline{v'T'}/\Delta u_o \Delta T_o$ for measurements made at $x/\ell_b < 3$. Symbol key gives: symbol, experiment number, downstream location of measurement in meters and x/ℓ_b.

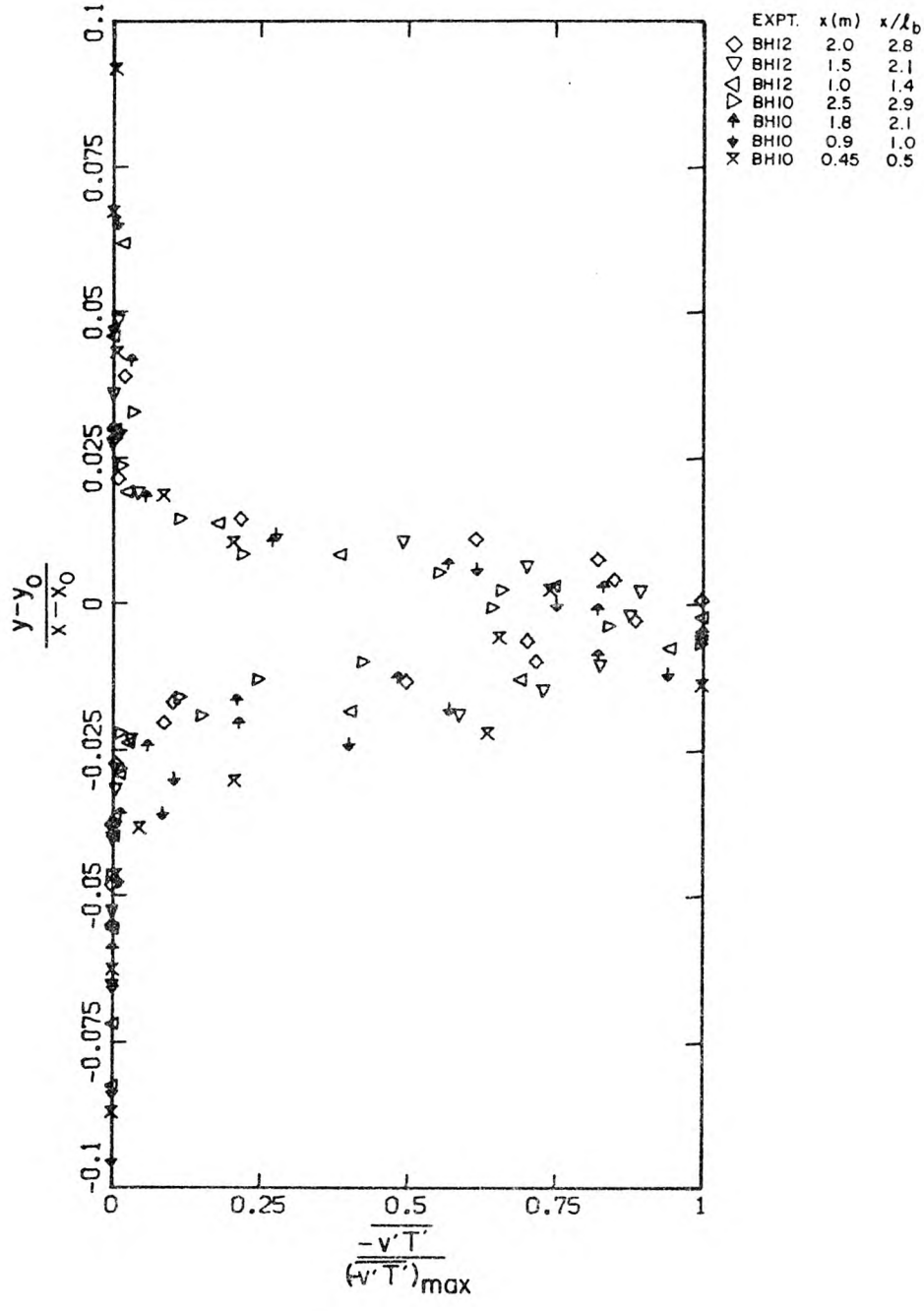

Figure 6.2.23 Profiles of $-\overline{v'T'}$ normalized to the local maximum for the same data as shown in Figure 6.2.22. Symbol key gives: symbol, experiment number, downstream location of measurement in meters and x/ℓ_b.

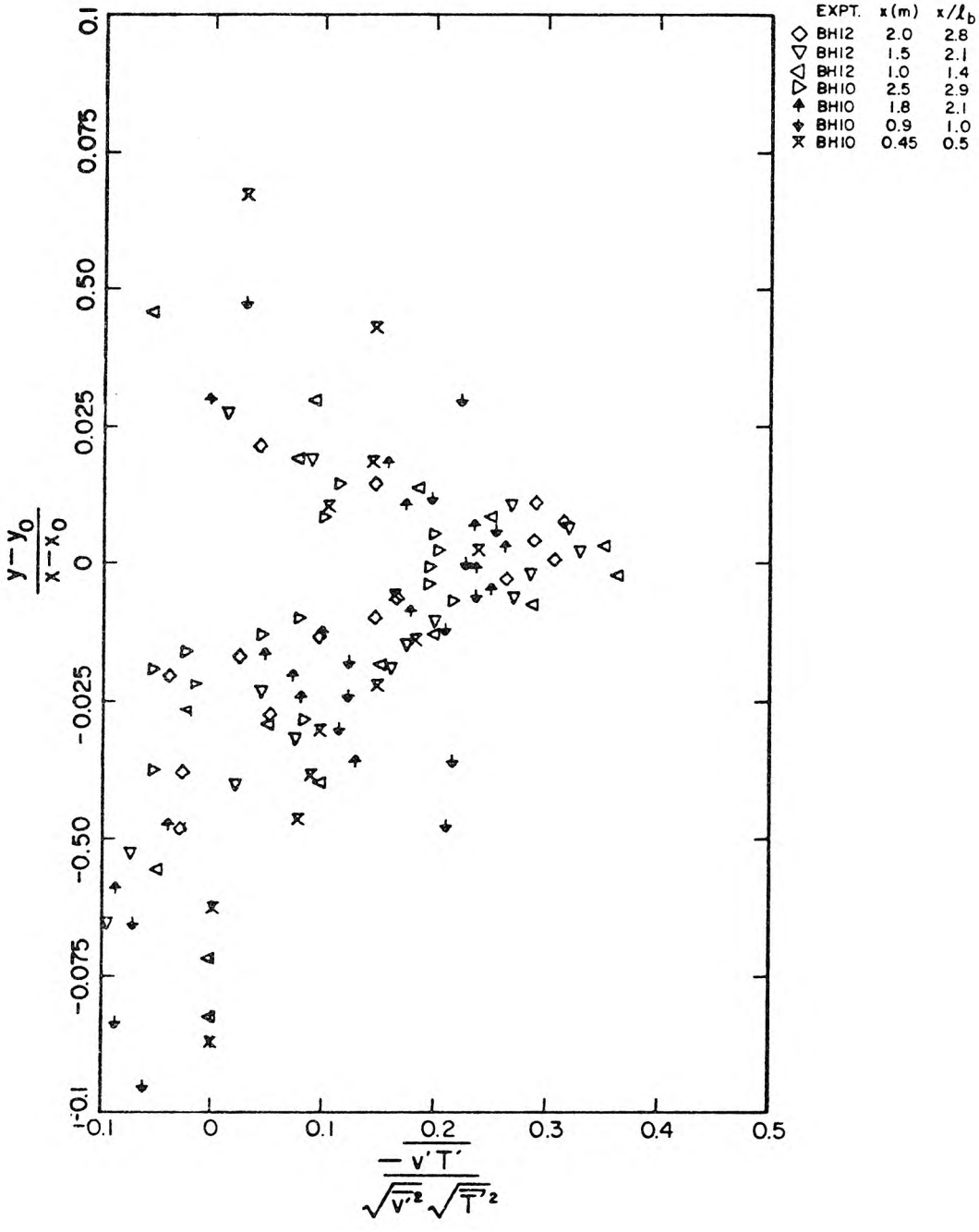

Figure 6.2.24 Profiles of the negative correlation coefficient, $-\overline{v'T'}/\sqrt{\overline{v'^2}}\sqrt{\overline{T'^2}}$ for the same data as shown in Figure 6.2.22. Symbol key gives: symbol, experiment number, downstream location of measurement in meters and x/ℓ_b.

$-\overline{v'T'}/\sqrt{\overline{v'^2}}\sqrt{\overline{T'^2}}$ are about 0.3, and there does not appear to be much of a trend with x/ℓ_b.

As the mixing layer collapses farther downstream, the mixing is substantially reduced, as can be seen in Figure 6.2.25, which shows profiles of $-\overline{u'v'}/\Delta\bar{u}_o^2$ for $x/\ell_b > 4$. Again, the data from Experiment BH9 may be anomalous, but it appears that there are some general trends. Besides the smaller values of $-\overline{u'v'}/\Delta\bar{u}_o^2$ downstream, there seems to be a reduction in the values of $-\overline{u'v'}/\Delta\bar{u}_o^2$ near $(y - y_o)/(x - x_o) = -0.01$. This would correspond to the region of highest mean temperature gradient (Figure 6.2.4). The correlation coefficients for these data, shown in Figure 6.2.26, again reveal maximum values of $-\overline{u'v'}/\sqrt{\overline{u'^2}}\sqrt{\overline{v'^2}}$ between 0.4 and 0.5. This would indicate that the main cause of the reduction in $-\overline{u'v'}/\Delta\bar{u}_o^2$ is a reduction in the turbulence intensities, and not a change in the correlation between u' and v'.

Figure 6.2.27 shows profiles of $-\overline{v'T'}/\Delta\bar{u}_o\Delta T_o$ for $x/\ell_b > 4$. The most interesting feature of these profiles is the region near $(y - y_o)/(x - x_o) = -0.01$ where $-\overline{v'T'}/\Delta\bar{u}_o\Delta T_o$ is negative, indicating a transfer of heat *against* the mean temperature gradient. The values of $\overline{v'T'}/\sqrt{\overline{v'^2}}\sqrt{\overline{T'^2}}$ in this region were as high as 0.15; for the number of data points (typically 2000 to 4000), the probability that the correlation coefficient between v' and T' was positive due to sampling error alone is very small. A positive correlation between v' and T' in the lower part of the *collapsing* mixing layer was found in many other experiments in which measurements were made at the end of the collapsing mixing layer, and this was the only region in which a statistically

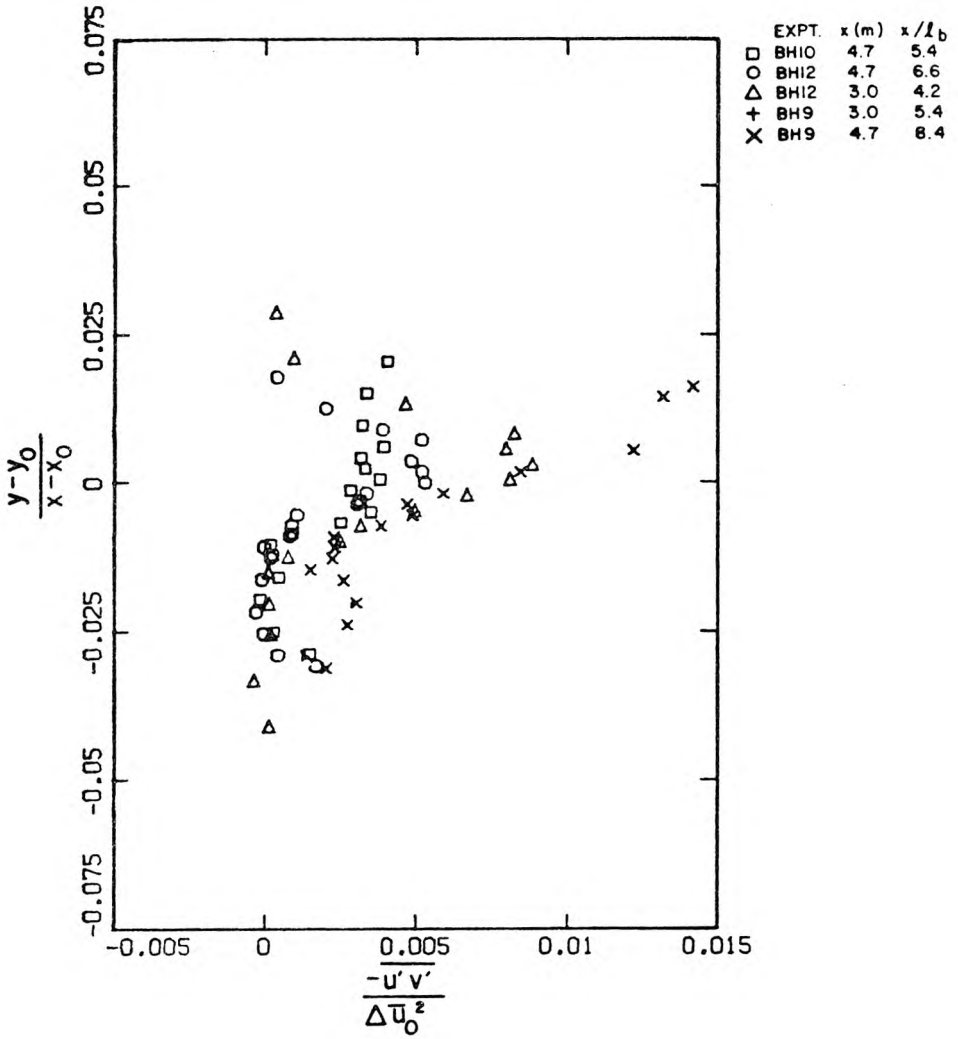

Figure 6.2.25 Profiles of $-\overline{u'v'}/\Delta\bar{u}_o^2$ measured at $x/\ell_b > 4$. Symbol key gives: symbol, experiment number, downstream location of measurement in meters and x/ℓ_b.

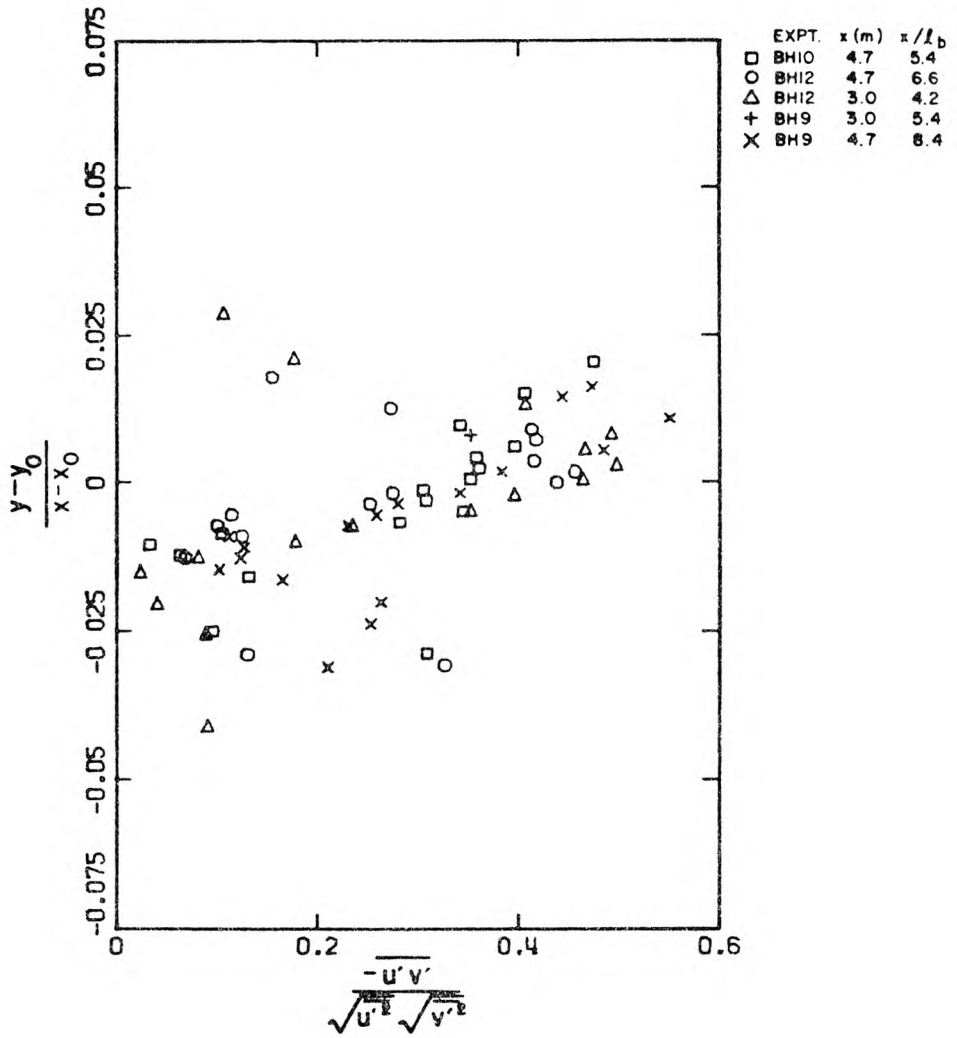

Figure 6.2.26 Profiles of the negative correlation coefficient, $-\overline{u'v'}/\sqrt{\overline{u'^2}}\sqrt{\overline{v'^2}}$, for the same data as shown in Figure 6.2.25. Symbol key gives: symbol, experiment number, downstream location of measurement in meters and x/ℓ_b.

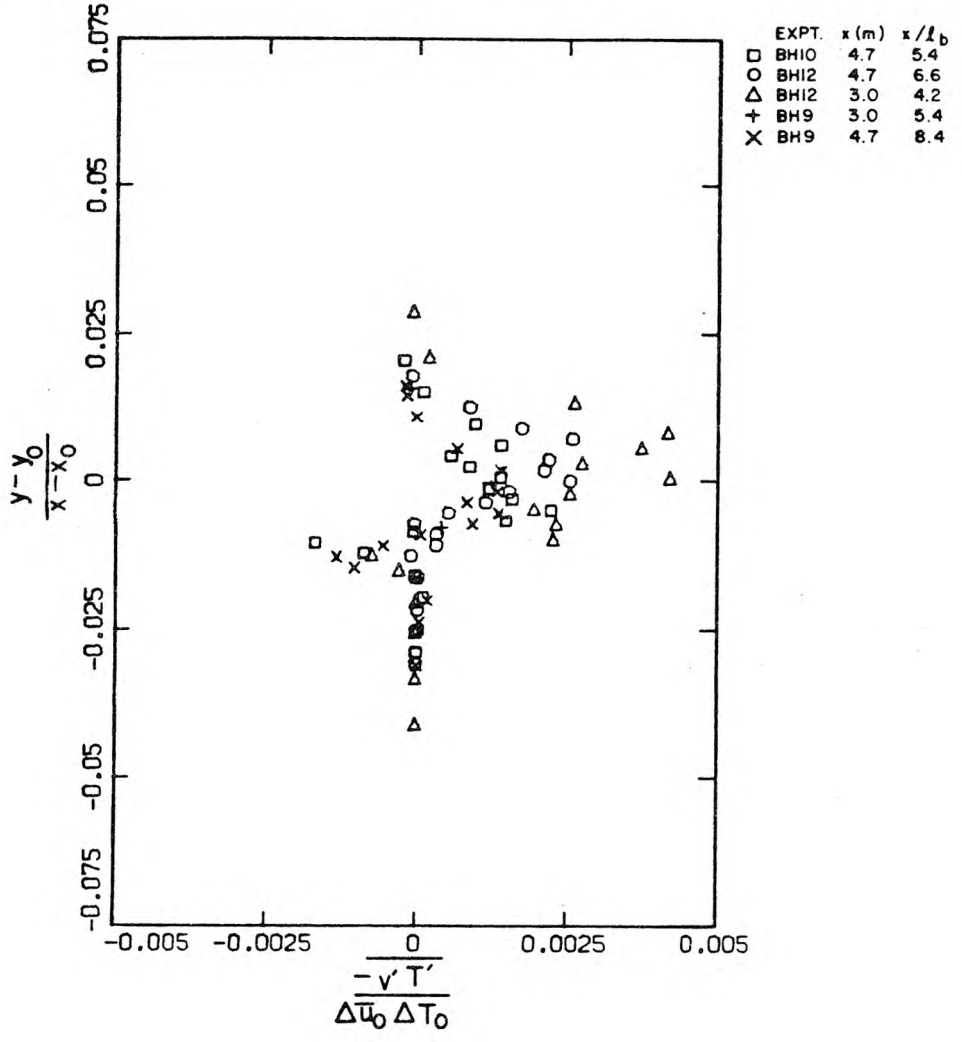

Figure 6.2.27 Profiles of $-\overline{v'T'}/\Delta\bar{u}_o\Delta T_o$ measured at $x/\ell_b > 4$. Symbol key gives: symbol, experiment number, downstream location of measurement in meters and x/ℓ_b.

significant positive correlation between v' and T' was found. This is a somewhat surprising result and is no doubt related to the decrease in the growth rate of the collapsing mixing layer, and to the collapse process. This phenomenon is discussed in more detail in Section 7.1.

Finally, profiles of turbulent fluxes of turbulent kinetic energy are presented in Figures 6.2.28 and 6.2.29. Figure 6.2.28 shows profiles of $\frac{1}{2}\ \overline{(u'^2 + v'^2)u'}$, the horizontal flux and Figure 6.2.29 shows profiles of the vertical flux, $\frac{1}{2}\ \overline{(u'^2 + v'^2)v'}$. The data in both cases are somewhat scattered, and attempts to find normalizations which would result in similarity among the respective profiles were unsuccessful. There are, nevertheless, features which are interesting.

As one might expect, the profiles exhibit some degree of anti-symmetry with respect to $(y - y_o)/(x - x_o) = 0$. Figure 6.2.28 indicates that the mean turbulent flux of turbulent kinetic energy is upstream on the high speed side of the flow and downstream on the low speed side, while Figure 6.2.29 indicates it is up on the high speed side (i.e., in the positive y-direction) and down on the low speed side. Away from the mixing layer, the mean turbulent flux of turbulent energy is near zero. One is reminded that the gradient of $\frac{1}{2}\ \overline{(u'^2 + v'^2)v'}$ is an important term in the conservation equation for turbulent kinetic energy; here, $\frac{1}{2}\ \partial\overline{(u'^2 + v'^2)v'}/\partial y$ is generally positive in the middle of the mixing layer, indicating a loss of turbulent kinetic energy from this region by means of turbulent diffusion.

6.2.7 Probability Density Functions of Fluctuating Quantities

In this section a few features of the probability density

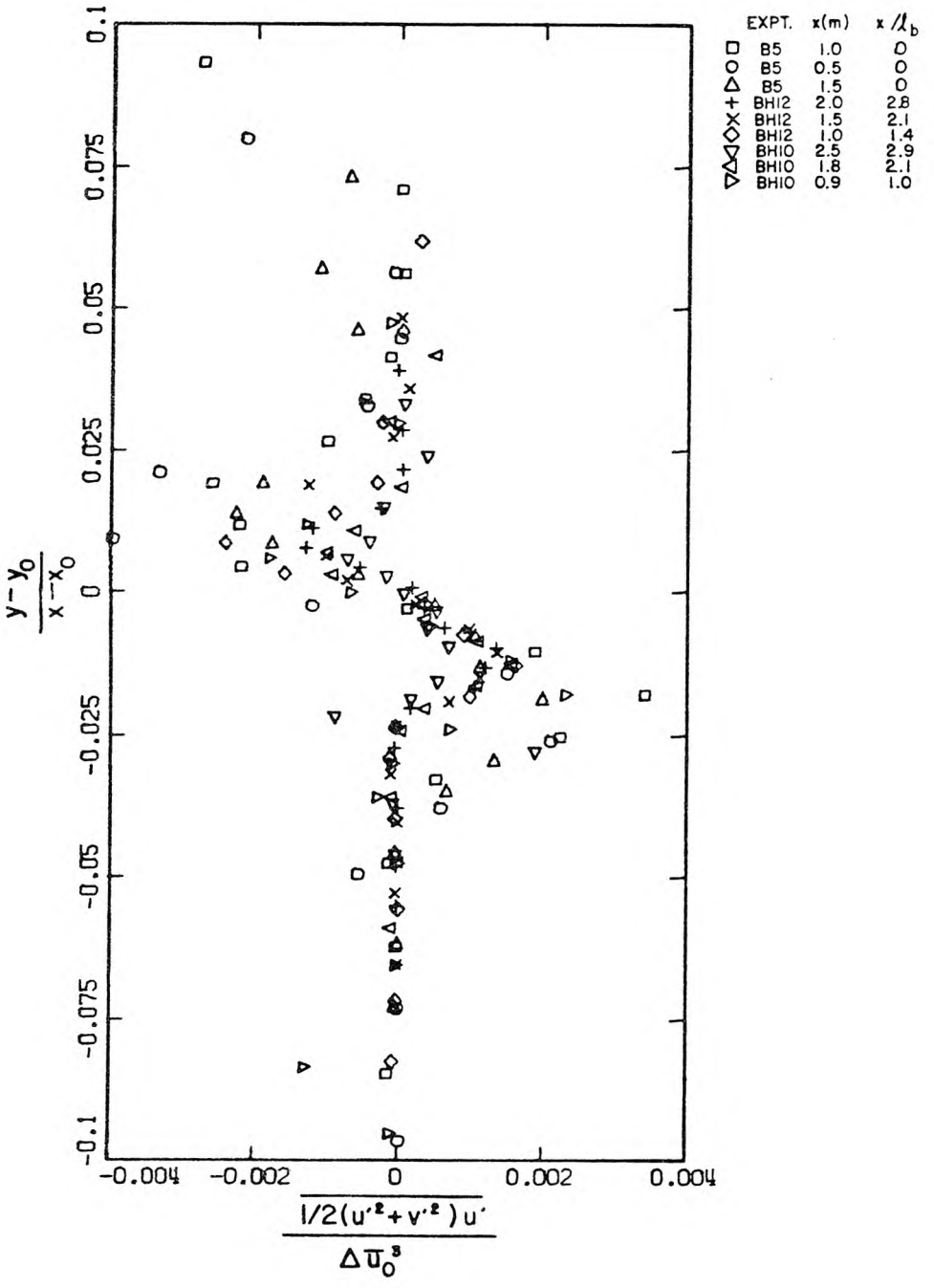

Figure 6.2.28 Profiles of the turbulent, horizontal flux of turbulent kinetic energy, measured at $x/\ell_b < 3$. Symbol key gives: symbol, experiment number, downstream location of measurement in meters and x/ℓ_b.

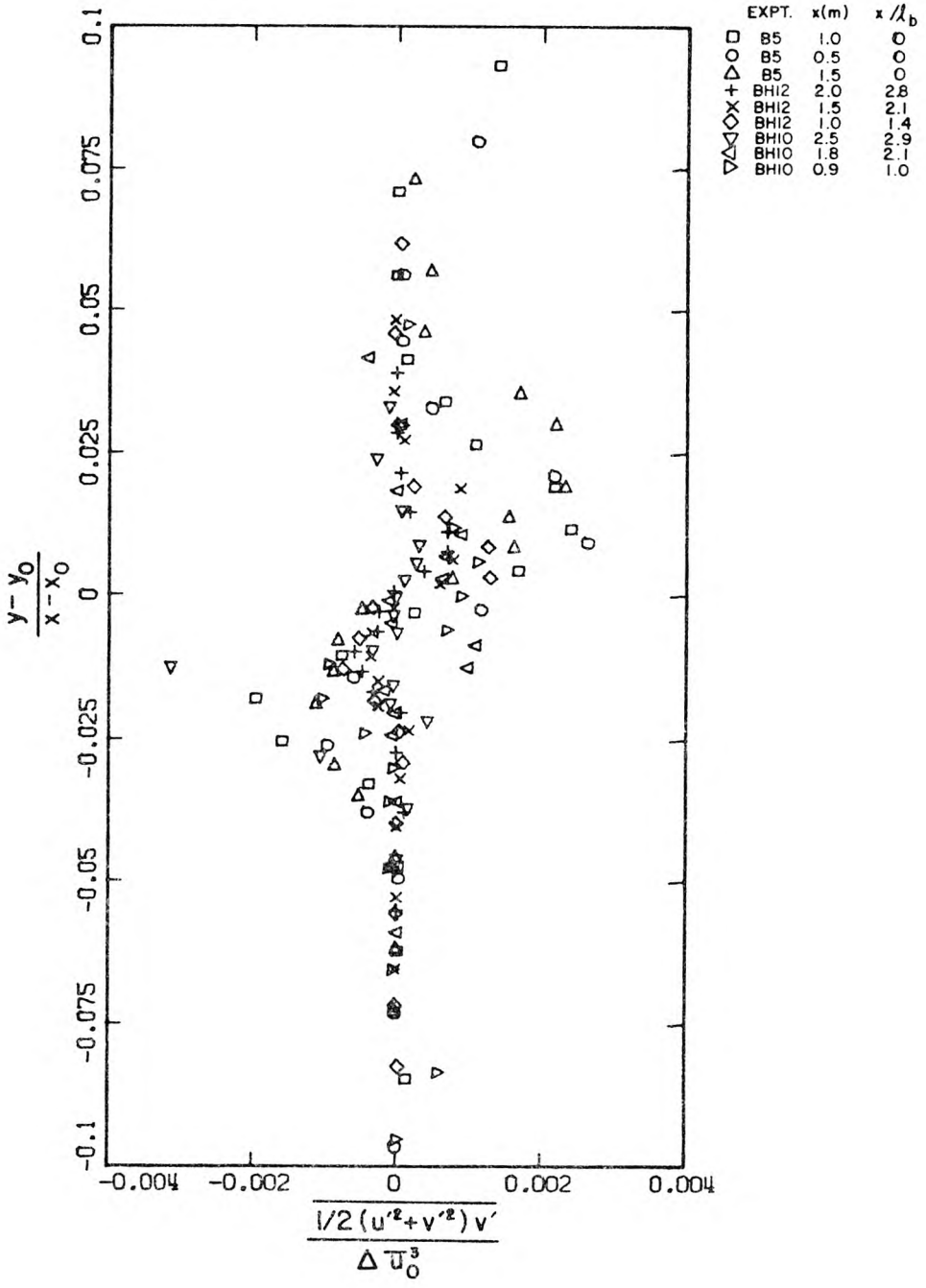

Figure 6.2.29 Profiles of the turbulent, vertical flux of turbulent kinetic energy, measured at $x/\ell_b < 3$. Symbol key gives: symbol, experiment number, downstream location of measurement in meters and x/ℓ_b.

functions for u', v', u'v' and v'T' are discussed in order to help explain the mixing processes in the mixing layer. The probability density functions shown are taken from a few particular cases, but they are representative of the probability density functions found along the mixing layer.

Figure 6.2.30 shows the variation with depth in the probability density functions for $v'/\Delta\bar{u}_o$, using data taken at $x/\ell_b = 0.5$ from Experiment BH10. The main features of this plot are the symmetry around $v' = 0$, and the lack of a significant number of extreme values. These are typical features of a probability density function for v' taken in the mixing layer. In addition, it is typical that the probability density functions near the middle of the mixing layer ($(y - y_o)/(x - x_o) = 0$) are somewhat broader than those away from the mixing layer, as would be expected.

Figure 6.2.31 shows the variation with depth in the probability density function for $u'/\Delta\bar{u}_o$, using data taken at x = 0.5 m, from Experiment B5. This figure exhibits similar gross features as found in the probability density functions for v'. In general, little difference was found between the general features of probability density functions of v' and those of u', or between stratified and unstratified cases.

Somewhat more interesting are the probability density functions for u'v' and v'T'. Probability density functions for $u'v'/\Delta\bar{u}_o^2$ are shown in Figures 6.2.32 and 6.2.33 for the same cases considered in Figure 6.2.30 and Figure 6.3.31, respectively. In all these figures the non-zero values at the extreme left (or right) edge indicate the

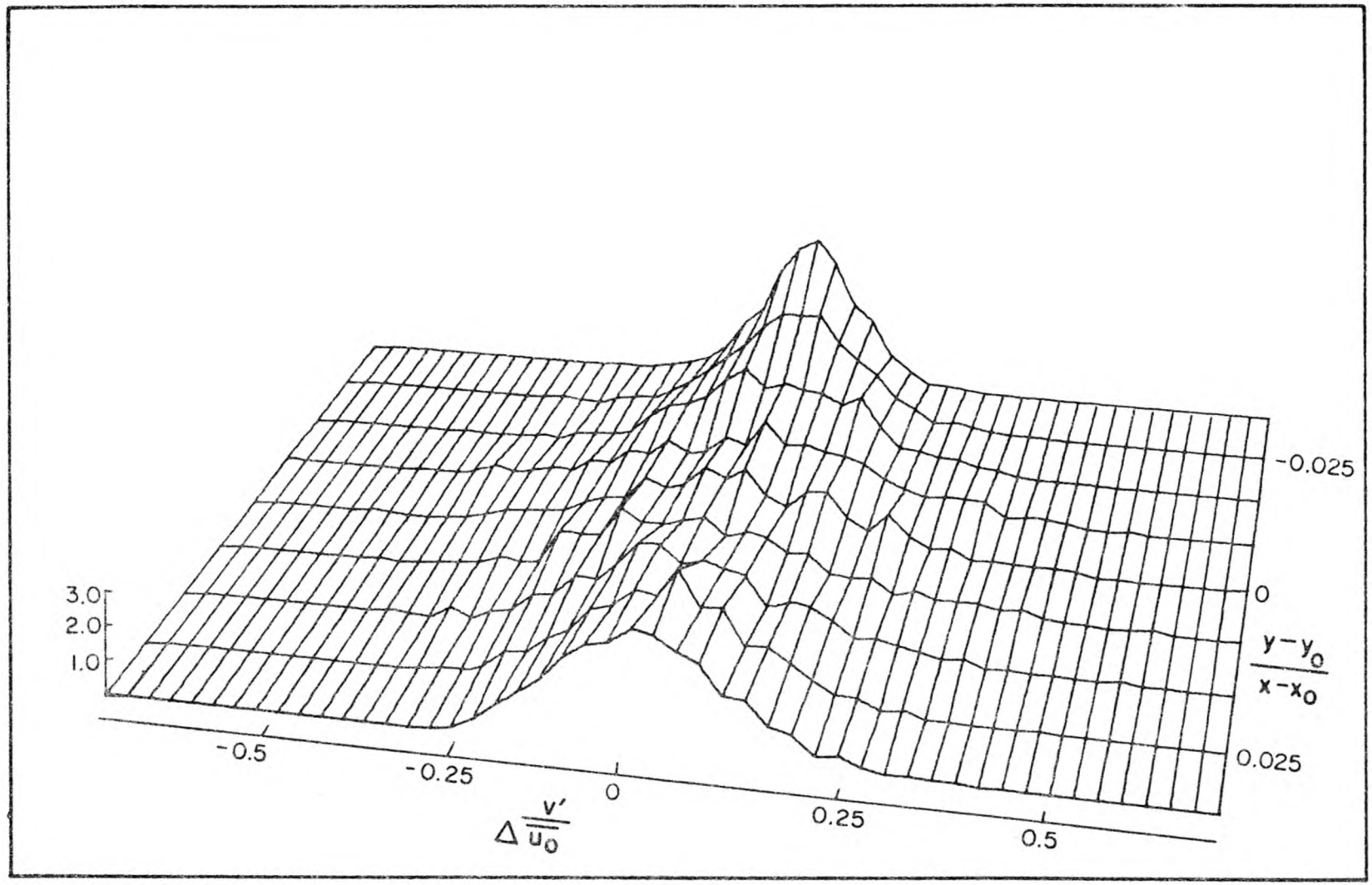

Figure 6.2.30 Variation with depth of the probability density functions for $v'/\Delta\overline{u}_o$. Measurements from Experiment BH10, $x = 45$ cm, $x/\ell_b = 0.5$.

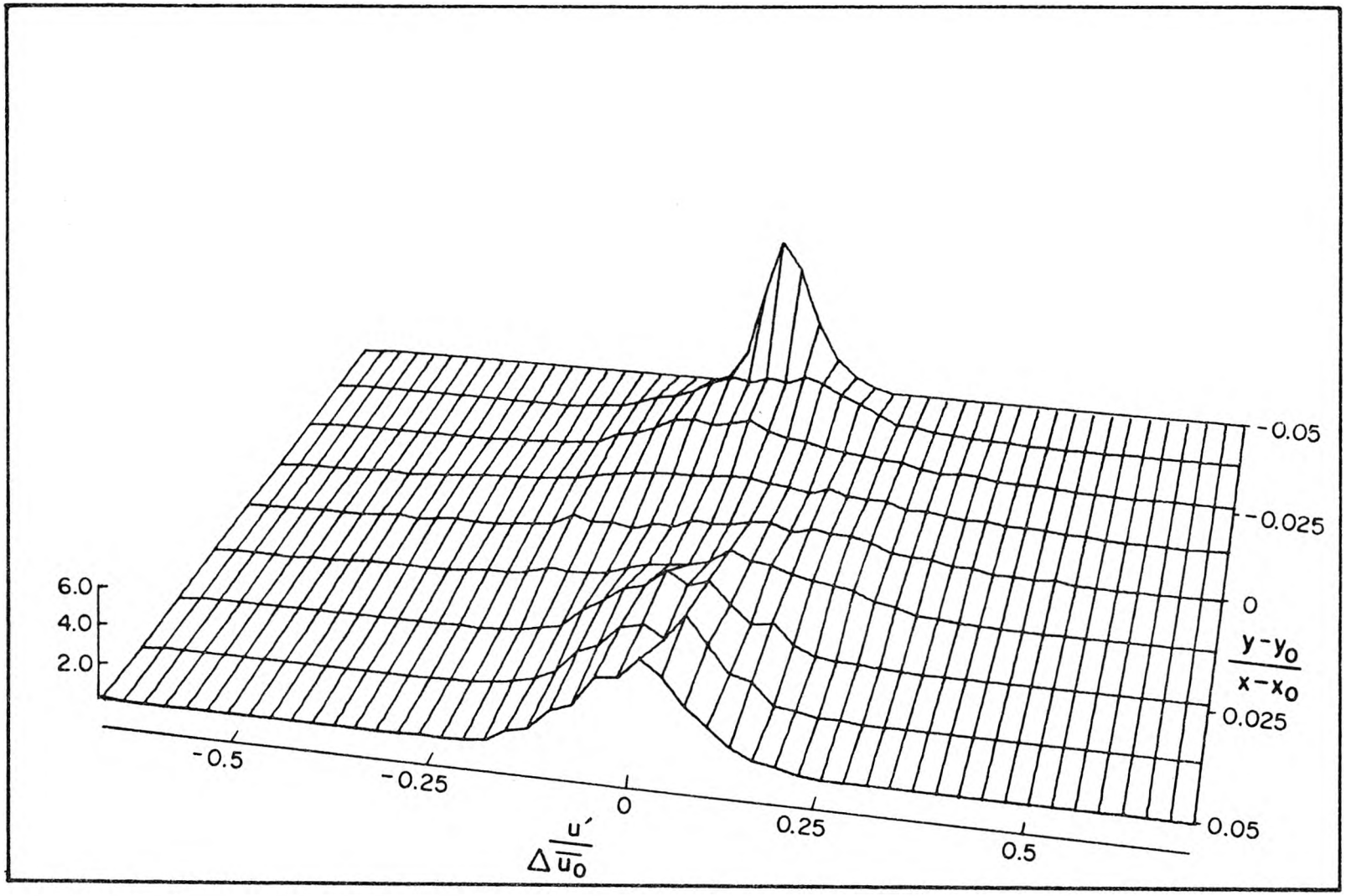

Figure 6.2.31 Variation with depth of the probability density functions for $u'/\Delta\overline{u}_o$. Measurements from Experiment B5, $x = 50$ cm, $x/\ell_b = 0$.

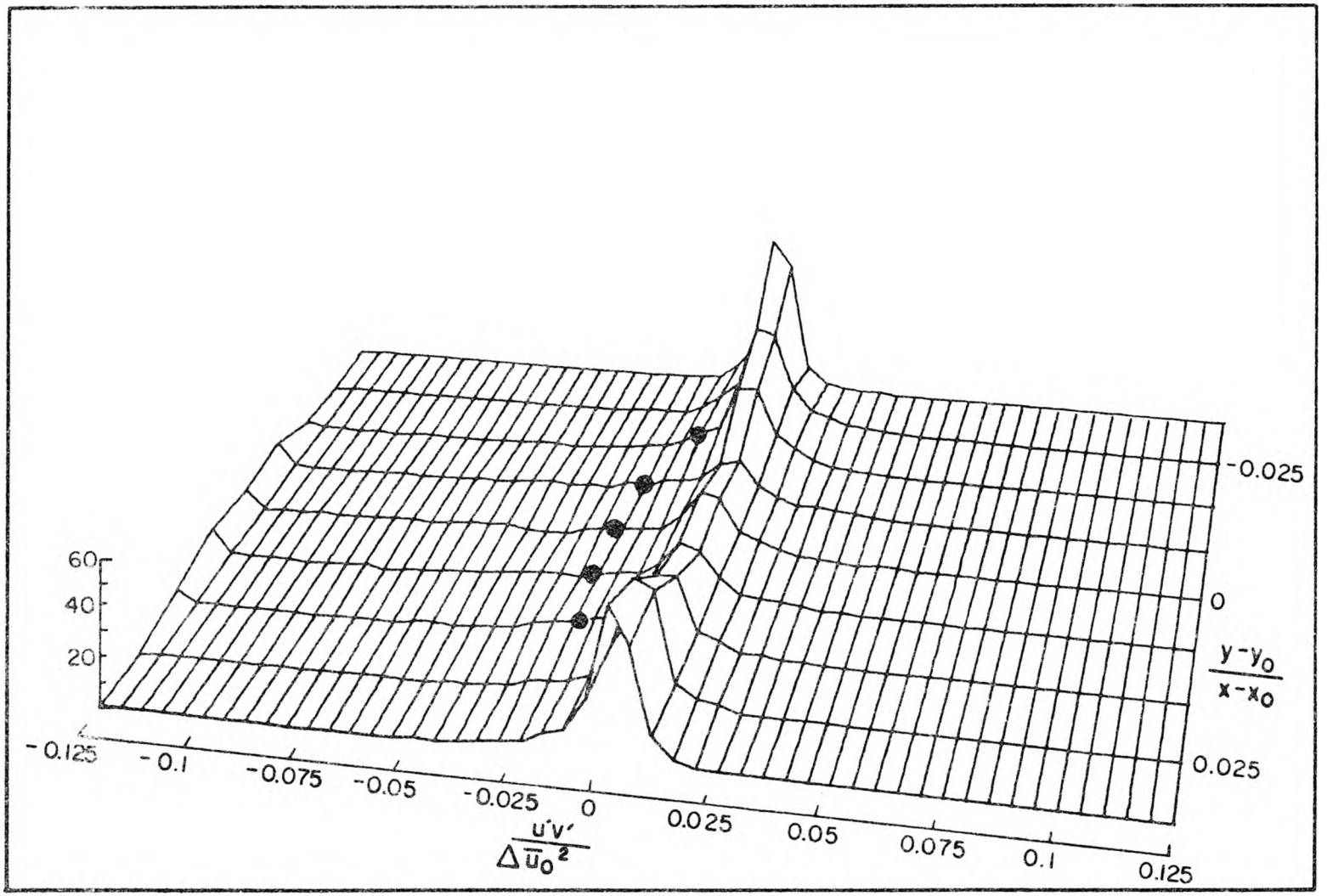

Figure 6.2.32 Variation with depth of the probability density functions for $u'v'/\Delta\bar{u}_o^2$. Measurements from Experiment BH10, $x = 45$ cm, $x/\ell_b = 0.5$; darkened circles indicate local values of $\overline{u'v'}/\Delta\bar{u}_o^2$.

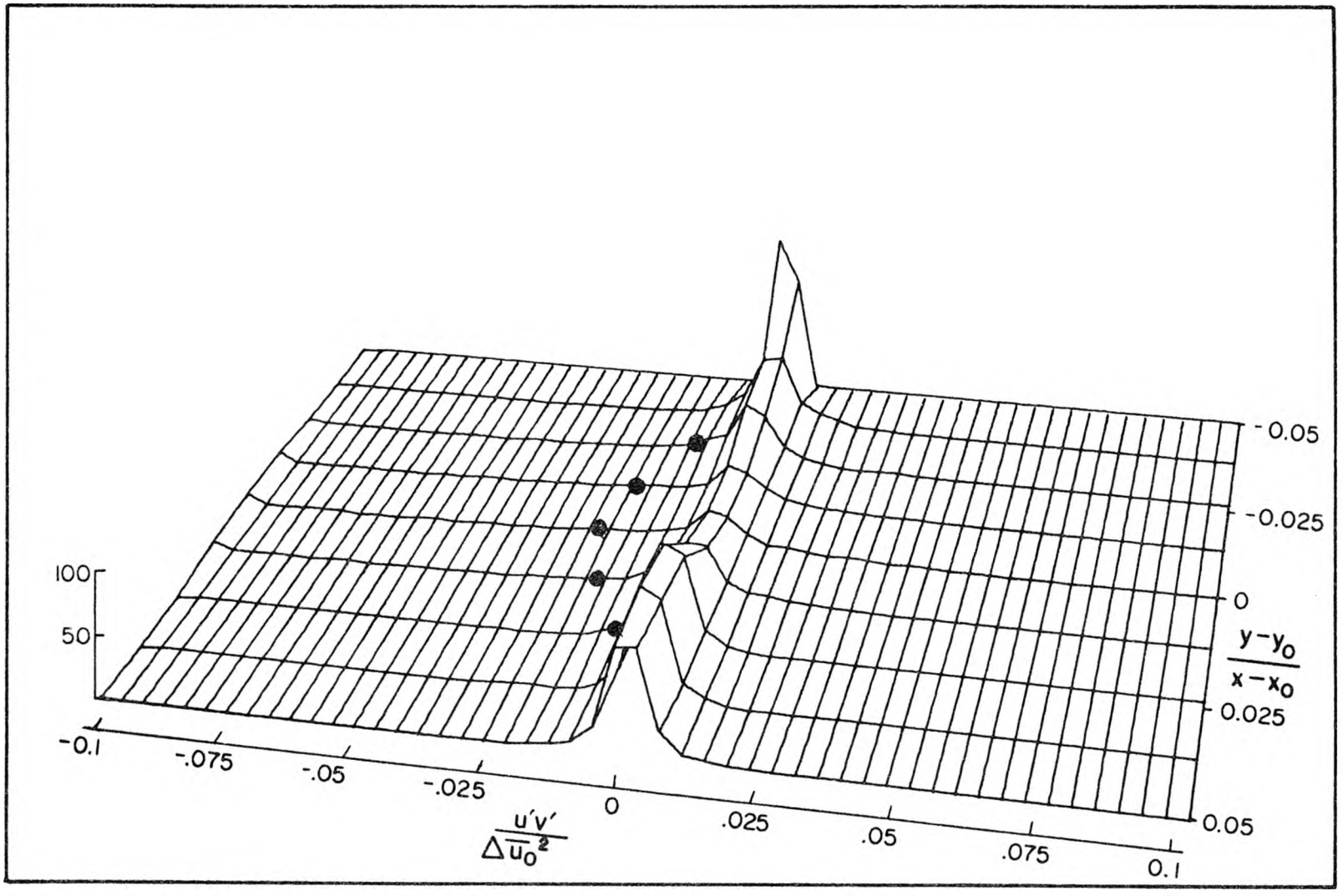

Figure 6.2.33 Variation with depth of the probability density functions for $u'v'/\Delta\overline{u}_o^2$. Measurements from Experiment B5, $x = 50$ cm, $x/\ell_b = 0$; darkened circles indicate local values of $\overline{u'v'}/\Delta\overline{u}_o^2$.

probability of finding values less than (or greater than) the value indicated. Thus, above or below the mixing layer u'v' is almost always near zero, while in the mixing layer, u'v' is often near zero, but for a significant amount of time, u'v' is considerably less than zero. In fact, Figure 6.2.32 indicates that for six per cent of the time, u'v' exceeds its mean value by a factor greater than five. Because it is clear from the two figures that u'v' is very often near zero in the mixing layer, one might suspect that the non-zero mean value of u'v' results almost entirely from the extreme values, with the mean of the remaining values near zero. In fact, this is found to be the case, and this result is discussed in more detail in Section 6.5.

A similar result was found for v'T', as is shown in Figure 6.2.34, which presents probability density functions of $v'T'/\Delta\bar{u}_o\Delta T_o$, for the same case considered in Figures 6.2.30 and 6.2.32. The gross features of the probability density functions for v'T' are quite similar to those of u'v', and again the mean value of v'T' results almost exclusively from the extreme values.

Similar results are found in the collapsing region of the mixing layer. Figures 6.2.35, 6.2.36 and 6.2.37 show probability density functions for v', u'v' and v'T', respectively, all measured at $x/\ell_b = 5.4$. Figure 6.2.35 again shows the symmetry of the probability density functions for v', and the lack of a significant number of extreme values. As can be seen in Figures 6.2.36 and 6.2.37, both u'v' and v'T' again have a large number of extreme values. However, Figure 6.2.37 indicates there is a significant number of both positive

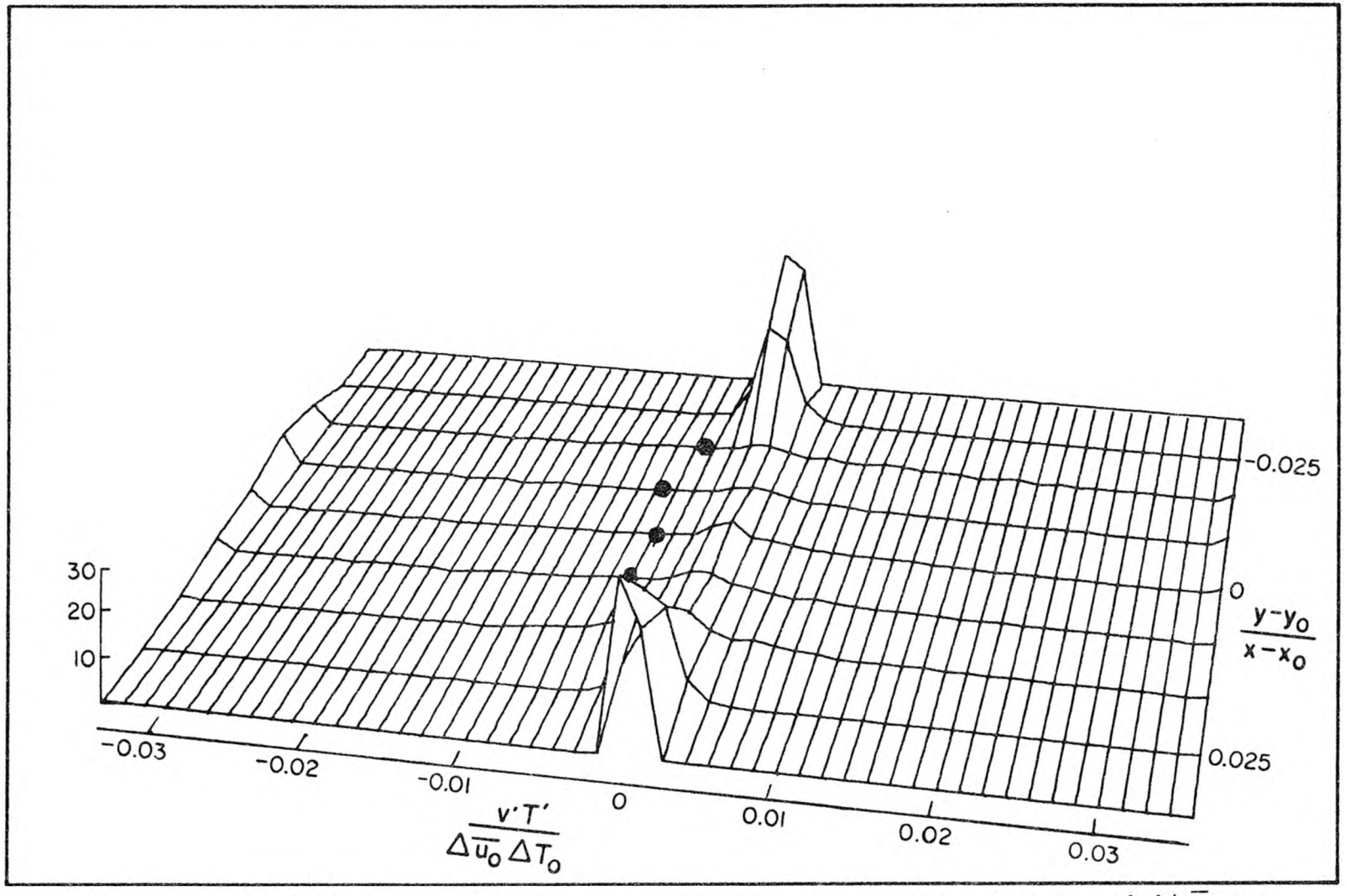

Figure 6.2.34 Variation with depth of the probability density functions for $v'T'/\Delta\overline{u}_o\Delta T_o$. Measurements from Experiment BH10, $x = 45$ cm, $x/\ell_b = 0.5$; darkened circles indicate local values of $\overline{v'T'}/\Delta u_o\Delta T_o$.

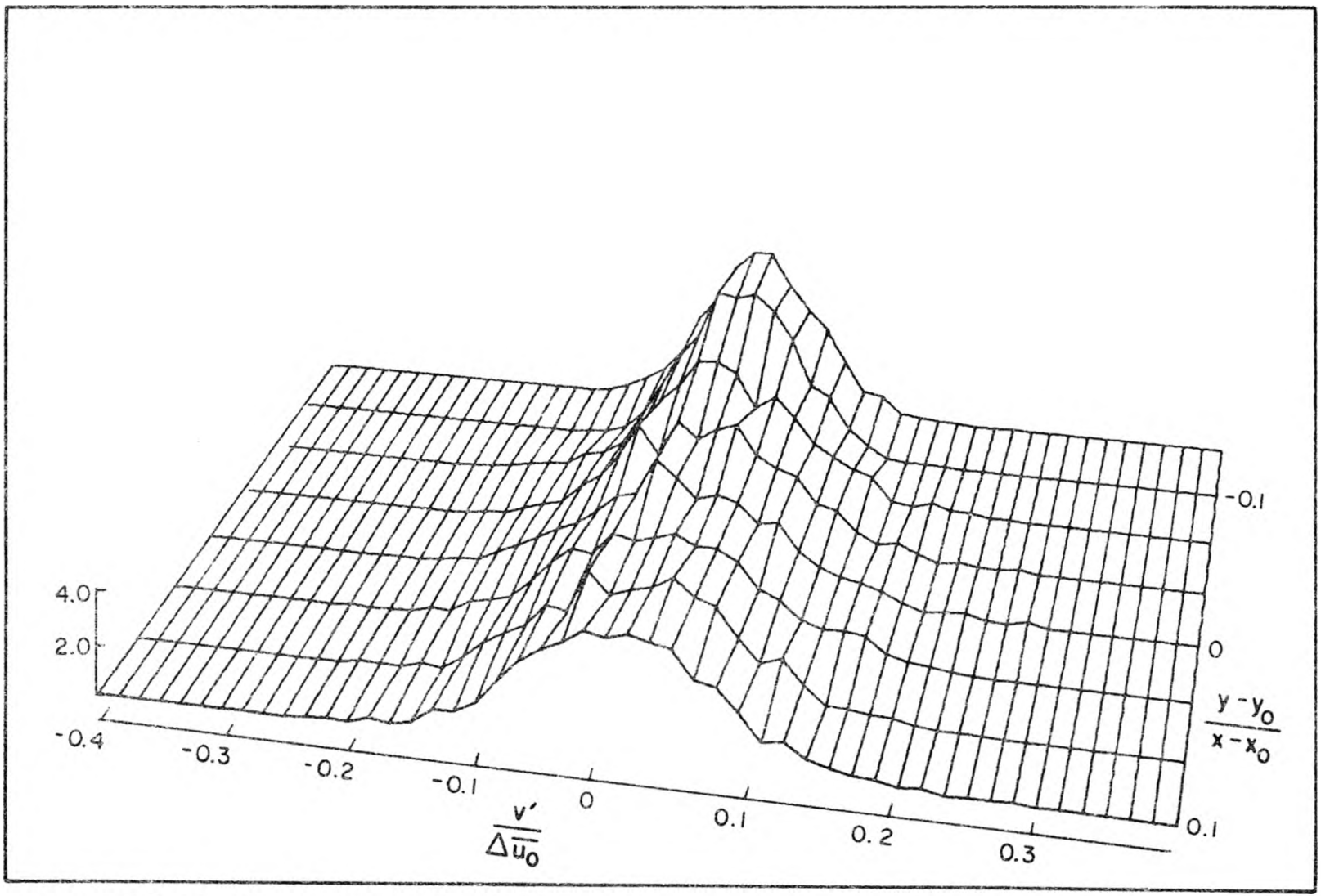

Figure 6.2.35 Variation with depth of the probability density functions for $v'/\Delta u_o$. Measurements from Experiment BH10, $x = 4.7$ m, $x/\ell_b = 5.4$.

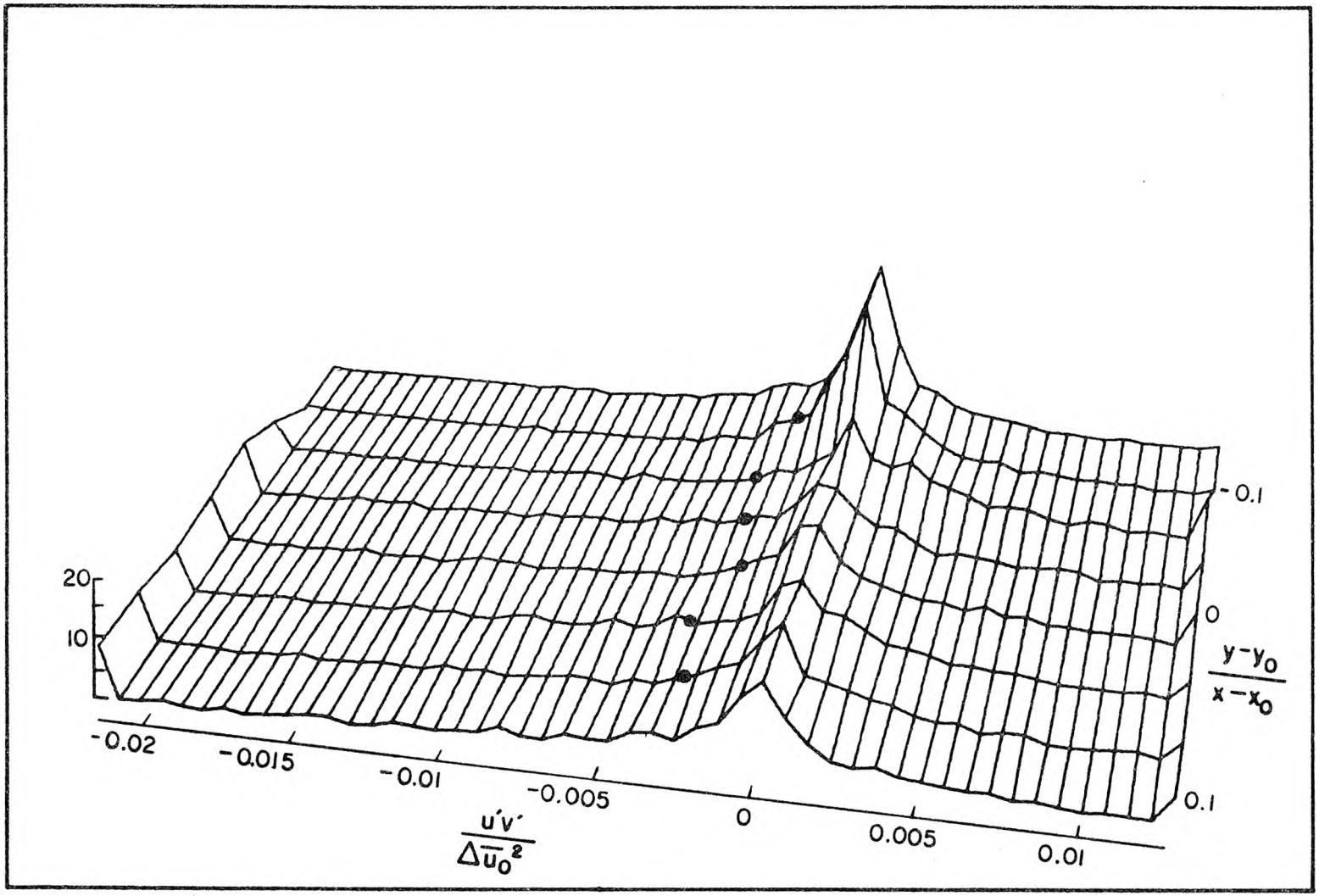

Figure 6.2.36 Variation with depth of the probability density functions for $u'v'/\Delta\bar{u}_o^2$. Measurements from Experiment BH10, $x = 4.7$ m, $x/\ell_b = 5.4$; darkened circles indicate local values of $\overline{u'v'}/\Delta\bar{u}_o^2$. Values at the ends of the scales indicate fraction of measurements greater than (or less than) the range of $u'v'/\Delta\bar{u}_o^2$ shown.

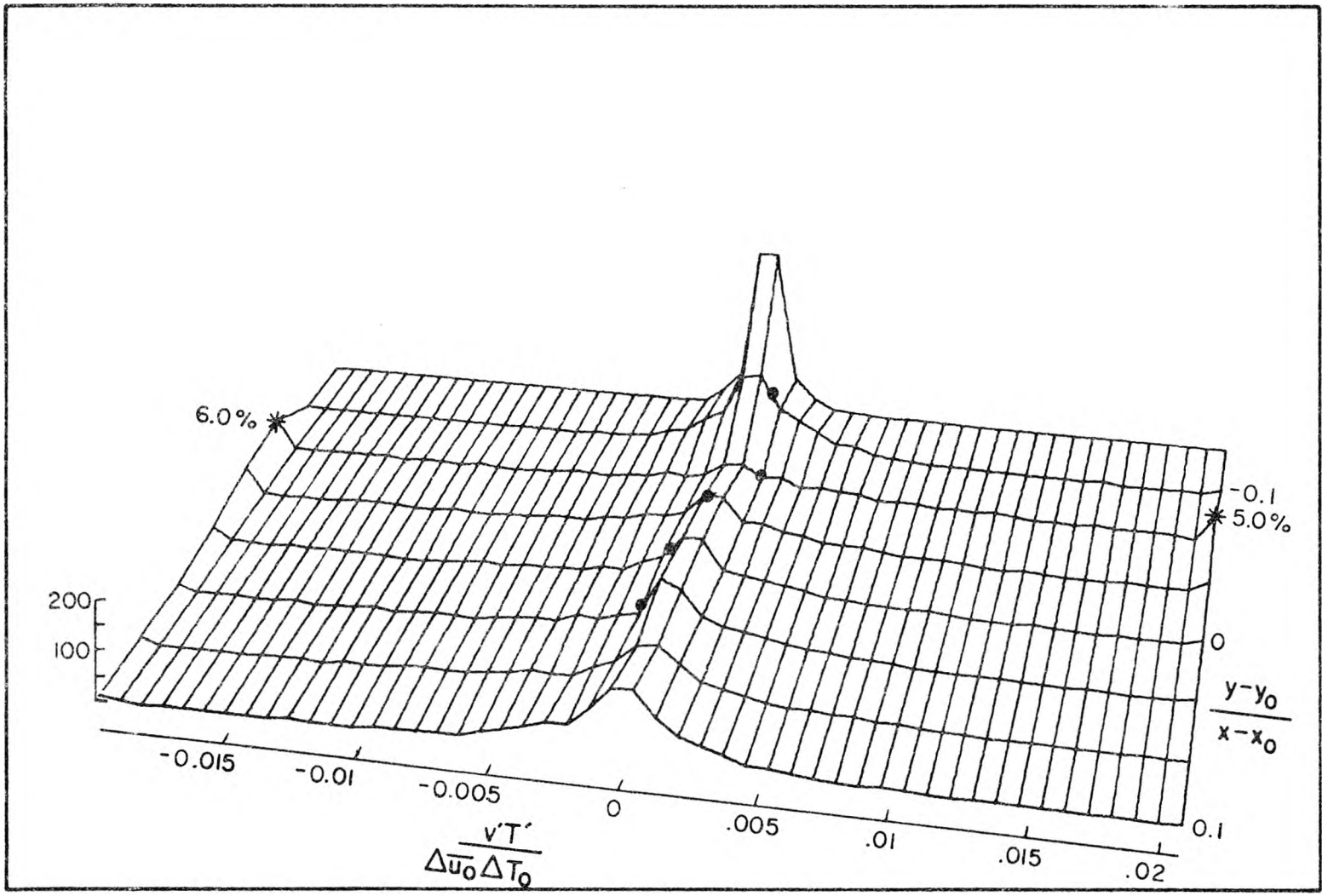

Figure 6.2.37 Variation with depth of probability density functions for $v'T'/\Delta\bar{u}_o\Delta T_o$. Measurements from Experiment BH10, $x = 4.7$ m, $x/\ell_b = 5.4$; darkened circles indicate local values of $\overline{v'T'}/\Delta\bar{u}_o\Delta T_o$. Values at the ends of the scales indicate the fraction of measurements greater than (or less than) the range of $v'T'/\Delta\bar{u}_o\Delta T_o$ shown.

and negative values of $v'T'$. Thus, it seems that there are periods during the collapse process in which a significant amount of heat transfer against the mean temperature gradient occurs.

This latter result is not surprising when one considers that the mixing layer is a series of vortices which are rolling up fluid from both the high speed and low speed sides of the flow. If the fluid in a vortex is not fully mixed before the collapse begins, then one would expect to find a significant fraction of positive values of $v'T'$, since there would be unmixed cold and warm fluid in the vortex which would return to equilibrium elevations. This process very likely results in the negative values of $-\overline{v'T'}$ found in a small region of the collapsing mixing layer (see Figure 6.2.27).

The fact that the net mixing is a result of extreme events occurring in a small fraction of the total time is a rather significant result. It would seem to suggest that the dynamics of the mixing process may not be easily modeled without a rather detailed understanding of this process. As is shown in Section 6.5, this result is not unique to the initial mixing layer; even more extreme instances of intermittency in the mixing processes were found far downstream of the initial mixing layer region of the flow.

6.2.8 Power Spectral Estimates of Fluctuating Quantities

In this section the power spectra of u', v' and T' are considered. Only a few representative cases are considered here, and only general features of the spectra are discussed.

In this section, and others in which power spectra are considered,

the power spectra for u', v' and T' are denoted by $\Phi_u(k)$, $\Phi_v(k)$ and $\Phi_T(k)$, where k is the wave number. The power spectra computed from a time series are denoted by $\Phi^*(f_p)$; Φ and k are then computed with the relationships

$$k = 2\pi f_p/\bar{u} \tag{6.2.2}$$

$$\Phi = \frac{\bar{u}}{2\pi}\Phi^* \tag{6.2.3}$$

where $\bar{u}$ is the mean speed of the fluid at the point of measurement. Usually, a time record was divided into four pieces, the power spectral estimates were found for each piece, and the spectral estimates were then averaged. In this way, the noise in the estimates was reduced and the trend more easily seen.

The power spectra found in the mixing layer were similar in many respects whether or not the flow was stratified. In addition, the spectra measured in the collapsing layer seemed not to differ significantly from spectra measured in the pre-collapse mixing layer.

Figure 6.2.38 and 6.2.39 show power spectra measured in the mixing layers of an unstratified case and a stratified case. There are several features to be noted. First, there appears to be a slight reduction in the power of the stratified case (Figure 6.2.39) compared to the unstratified case (Figure 6.2.38) at the high wave number end. The stratified case seems to exhibit the (-5/3) power of the inertial subrange, whereas the unstratified case falls off a little more slowly. This was generally found to be the case in the mixing layer; it seems likely that buoyancy forces are responsible. (It was found that

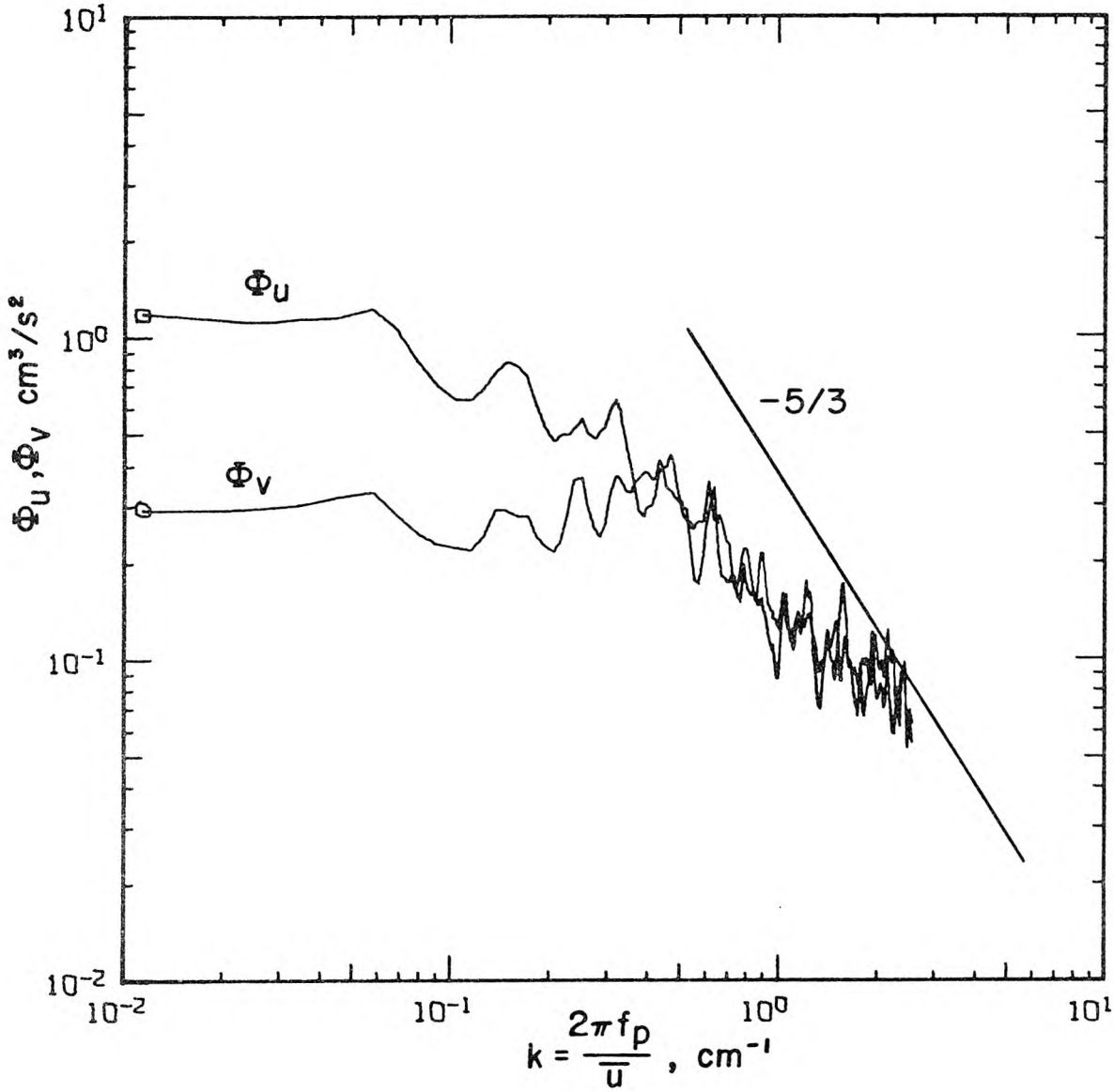

Figure 6.2.38 Power spectral estimates for u' and v' measured in the homogeneous mixing layer at x = 0.5 m and $(y - y_o)/(x - x_o)$ = 0.021; Experiment B5.

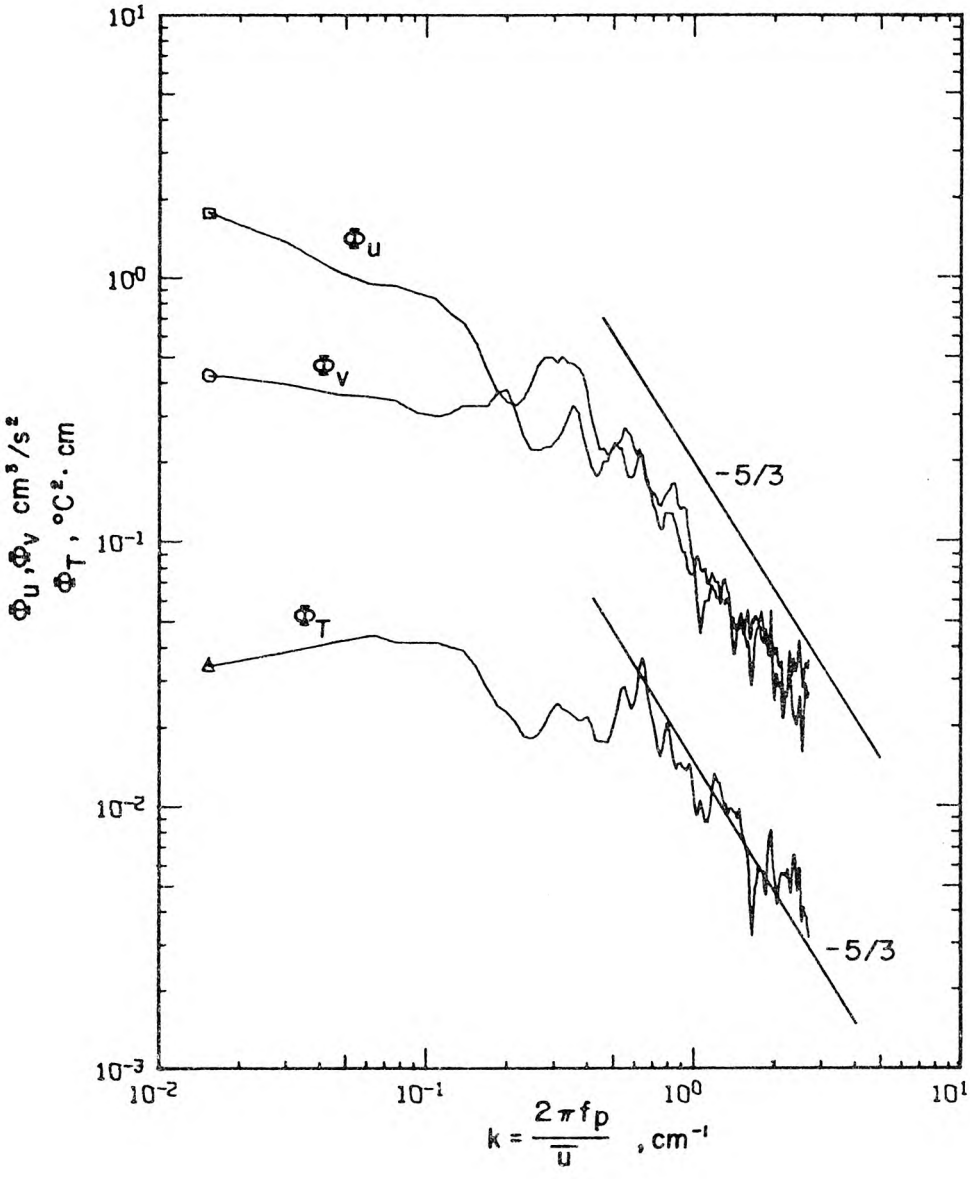

Figure 6.2.39 Power spectral estimates for u', v' and T' measured in a stratified mixing layer at x = 0.45 m and $(y - y_o)/(x - x_o)$ = 0.01; Experiment BH10.

photographing the vortex structures was somewhat easier when the flow was stratified, and this was clearly due to the suppression of turbulent mixing in the small scales. In particular, it appeared that the inlet turbulence was damped to some degree by the buoyancy forces.) Usually, it was found that the spectra at the low wave numbers were similar; however, it appeared that the power in the larger scales was reduced in the stratified cases but the data are too scattered to confirm any trend.

Another feature of the spectra is the similarity between the different spectra of the same flow, particularly those of u', v' and T' at the high wave numbers. Though the similarity between Φ_T and Φ_u is not excellent in Figure 6.2.39, it was found that Φ_T and Φ_u or Φ_v were, in general, very similar, particularly at the higher wave numbers. A good example of this is presented in Figure 6.2.40, which shows spectra of u', v' and T' in a stratified mixing layer ($x/\ell_b = 2.1$, $(y - y_o)/(x - x_o) = -0.02$). In this figure, Φ_v and Φ_T are similar over all wave numbers, while Φ_u, Φ_v and Φ_T are all similar at the higher wave numbers.

6.2.9 Integral Balances

In this section a discussion on the efficacy of integral balances to determine mixing rates is presented. The equations under consideration are those given in Section 2.5, particularly Equations 2.5.1, 2.5.2 and 2.5.3, as all the terms in these equations, except the pressure term, were measured directly in the mixing layer.

Table 6.2.3 lists the measured quantities for one experiment, from which the terms in Equations 2.5.1 - 2.5.3 can be calculated.

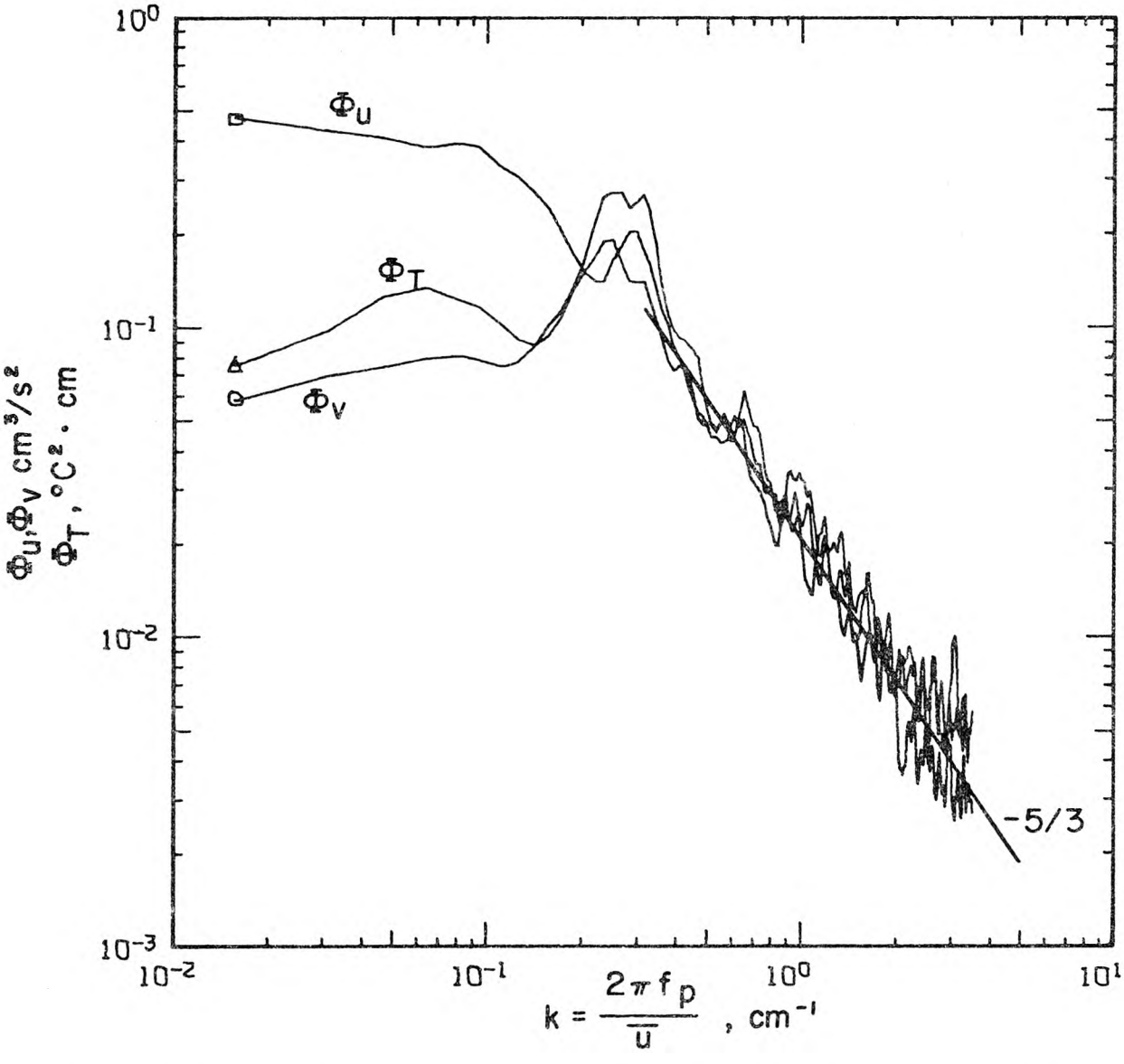

Figure 6.2.40 Power spectral estimates of u', v' and T' measured in a stratified mixing layer at x = 1.8 m and $(y - y_o)/(x - x_o)$ = -0.02, Experiment BH10.

Table 6.2.3 Measured quantities for integral balances of mass, momentum and buoyancy. Experiment BH12.

1	2	3	4	5	6	7	8
x, cm	$\int_{y_1}^{y_2} \overline{u}\, dy$ cm^2/s	$\int_{y_1}^{y_2} \overline{u}^2\, dy$ cm^3/s^2	$\int_{y_1}^{y_2} \overline{u'}^2\, dy$ cm^3/s^2	$-\overline{u'v'}\Big\|_{y_1}^{y_2}$ cm^2/s^2	$\nu \frac{\partial \overline{u}}{\partial y}\Big\|_{y_1}^{y_2}$ cm^2/s^2	$\int_{y_1}^{y_2} \overline{u}\,\overline{B}\, dy$ cm^3/s^3	$-\overline{B'v'}\Big\|_{y_1}^{y_2}$ cm^2/s^3
100	154	1971	2.9	-0.315	-0.006	95.6	-0.031
150	152	1929	2.9	-0.235	-0.005	93.8	-0.022
200	151	1905	3.0	-0.170	-0.004	92.6	-0.017
300	150	1882	3.4	-0.128	-0.004	88.1	-7.9×10^{-3}
470	146	1789	3.5	-0.054	-0.003	81.5	-0.0035

Note $y_1 = -15$ cm, $y_2 = -3$ cm, measured from the free surface.

Calculations of this type were made for all cases, and the one presented here is a typical example. The value of the initial temperature difference, ΔT_o, was observed to drift slightly over the nine hours during which measurements were made but the drift was less than ± 1 per cent of ΔT_o. The values of T_1 and T_2 also changed slightly during the experiment (although they changed in such a way that the drift in ΔT_o was small) and this slight drift has been taken into account in calculating the quantity $\overline{B} = g \frac{\rho - \rho_o}{\rho_o}$. The integration was taken over the interval from $y_1 = -15$ cm to $y_2 = -3$ cm, as measured from the free surface; thus, the integrated values include about one-half of the mixing layer. In this discussion, the symbol $\int$ shall denote the definite integral, $\int_{y_1}^{y_2}$.

The mass balance (Equation 2.5.1) is considered first. The value of $\overline{v}\Big|_{y_1}^{y_2}$ can be estimated from the change in $\int \overline{u} dy$ with the distance x. Overall, the average value of $\overline{v}\Big|_{y_1}^{y_2}$ is found to be about -0.02 ± 0.005 cm/s, far below the accuracy limit of the laser-Doppler system (see Table 4.1.2 with $10 < \overline{u} < 14$). In fact, the average measured value of $\overline{v}\Big|_{y_1}^{y_2}$ was about -0.15 ± 0.1. Thus, the value of $\overline{v}\Big|_{y_1}^{y_2}$ calculated from the integral of the measured value of $\overline{u}$ is probably more accurate than the directly measured value, simply because the accuracy of the laser-Doppler velocimeter was about 0.1 cm/s. However, Equation 2.5.1, which was used to calculate $\overline{v}\Big|_{y_1}^{y_2}$, was derived under the assumption that $\frac{\partial \overline{w}}{\partial z}$ was negligible; because of the accuracy of the measurements, and the fact that w was not measured, there is no accurate way to check the validity of this assumption. While $\overline{u}$ was observed to be quite uniform across

the flume (see Section 5.1, and Figure 5.1.10) a small secondary flow could possibly result in a non-negligible value of $\frac{\partial \overline{w}}{\partial z}$. However, because the flow was quite uniform and because density stratification tends to suppress secondary circulations (Schiller and Sayre (1973)), it is believed that $\frac{\partial \overline{w}}{\partial z}$ was negligible compared to $\frac{\partial \overline{u}}{\partial x}$ and $\frac{\partial \overline{v}}{\partial y}$.

The momentum balance (Equation 2.5.2) includes one term, $\frac{\partial}{\partial x}\int \frac{\overline{p}}{\rho_o}\, dy$, which was not measured. With this term aside for the moment, the other terms can be considered. From Column 3 of Table 6.2.3, it is seen that $\frac{\partial}{\partial x}\int \overline{u}^2\, dy$ is about -0.46 ± 0.10 cm^2/s^2. By comparison, the term $\frac{\partial}{\partial x}\int \overline{u'^2}\, dy$ is negligible, as would be expected. The average value of $-\overline{u'v'}\Big|_{y_1}^{y_2}$ is about -0.15 cm^2/s , while the average value of $\nu \frac{\partial \overline{u}}{\partial y}\Big|_{y_1}^{y_2}$ is about -0.004 cm^2/s^2. Using the previously calculated value of -0.02 for $\overline{v}\Big|_{y_1}^{y_2}$ and assuming $\overline{v}(y_2) = 0$, $\overline{u}\,\overline{v}\Big|_{y_1}^{y_2}$ is found to be -0.21 cm^2/s^2. Thus, the imbalance in Equation 2.5.2 is about -0.10 cm^2/s^2. One can easily see the problems which arise when one attempts to find mixing rates from integral balances. For example, the value of $\overline{u'v'}$ estimated from the momentum balance in this case would be considerably different from the measured value. This is due in large part to the propagation of errors. With integral balances, one is forced to use the difference between too large values to estimate a small value, and the result is evident from the example. It is obvious that one must be extremely cautious when considering data in which mixing rates are computed from integral balances.

This is equally true for the balance of mean buoyancy (Equation 2.5.3). From Column 7 of Table 6.2.3, $\frac{\partial}{\partial x}\int \overline{u}\,\overline{B}\, dy$ is estimated to be

-0.04 ± 0.01 cm^2/s^3. Using the computed value for $\bar{v}\Big|_{y_1}^{y_2}$ as before, $\bar{v}\,\bar{B}\Big|_{y_1}^{y_2}$ is estimated to be -0.009 cm^2/s^3. The average measured value of $\overline{B'v'}$ is -0.012 cm^2/s^3 which results in an imbalance of about -0.018 cm^2/s^3. Similar results were obtained for other cases.

It is apparent that, unless measurements are extremely accurate, integral balances are rather useless for obtaining mixing rates. Increased difficulties are encountered if some terms are not measured. A good example of this would be an attempt to balance the conservation equation for turbulent kinetic energy (Equation 2.5.4); in this study, the dissipation rate ε was not measured, but it is the dominating term of Equation 2.5.4. Furthermore, there are several terms which have been neglected in the derivation of Equations 2.5.1 - 2.5.5, and as the neglected terms were not measured, there is no way to quantify exactly their effects.

Thus it is concluded that, while integral balances are helpful in obtaining a gross validation of the experimental method, extreme accuracy in the measured values is required in order to obtain dependable results.

6.2.10 Turbulent Energy Exchange

In this section the main results of the measurements in the initial mixing layer are presented with reference to the discussion on the exchange of turbulent kinetic energy (Section 2.3), and include results which involve relationships between $\overline{B'v'}$, $-\overline{u'v'}\,\frac{\partial \bar{u}}{\partial y}$, ε and $\overline{Ri}$.

In Section 2.3, a relationship between $\overline{Ri}$, R_f and E was derived (Equation 2.3.7) for a three-dimensional turbulent flow. In this study,

the component w of the velocity vector was not measured, so that in order to check the measured results against Equation 2.3.7, some assumptions must be made about the third velocity component. However, in order to avoid making any assumptions, the experimental results are retained in their two-dimensional form, and Equation 2.3.7 will be re-derived for a two-dimensional case. In fact, the two-dimensional case is identical in form to the three-dimensional case. Taking Equation 2.1.9 for two dimensions, and using the same assumptions that were used to derive Equation 2.3.3, one finds

$$\overline{u'v'}\,\frac{\partial \bar{u}}{\partial y} + \frac{\partial \overline{q^{*2}v'}}{\partial y} + \overline{B'v'} + \varepsilon^* = 0 \qquad (6.2.4)$$

where $q^{*2} = \frac{1}{2}(u'^2 + v'^2)$. The quantity ε^* is the dissipation rate, reduced for two dimensions. (For an isotropic turbulent flow, one might expect that $\varepsilon^* = 2/3\ \varepsilon$.) From Equation 6.2.4, it is found that

$$\overline{Ri} = \frac{R_f \frac{t_2^*}{t_3} \overline{u'v'}^{\,2} (1 - R_f + E^*)^2}{(1 - R_f/R_c^* + E^*)\,\overline{q^{*2}}\,\overline{v'^2}} \qquad (6.2.5)$$

where

$$R_c^* = \left(1 + \frac{\overline{2q^{*2}}}{\overline{v'^2}} \frac{t_1}{t_2^*}\right)^{-1},$$

$$R_f = -\overline{B'v'} \Big/ \overline{u'v'}\,\frac{\partial \bar{u}}{\partial y}$$

$$t_2^* = \overline{q^{*2}}/\varepsilon^* \qquad \text{and}$$

$$E^* = \frac{\partial}{\partial y} \overline{q^{*2} v'} \Big/ \overline{u'v'} \frac{\partial \bar{u}}{\partial y} \quad .$$

This relationship is identical in form to Equation 2.3.7.

In this study, the dissipation rates ε^*, ε_ρ and $\varepsilon_{\rho v}$ were not measured directly. Hence, only the basic features of Equation 6.2.5 can be checked directly with the data. The quantities ε^*, ε_ρ and $\varepsilon_{\rho v}$ can be estimated from the measurements, however, and can be compared to estimates of ε and ε_ρ obtained from power spectra of u', v' and T'. With these estimates, Equation 6.2.5 can be examined in more detail. In this section, however, only the experimental relationships between the pertinent parameters such as R_f, $\overline{B'v'}/\varepsilon^*$ and $\overline{Ri}$ are presented, and a detailed discussion of Equation 6.2.5 is presented in Section 7.2.

Figure 6.2.41 presents the measured values of R_f plotted against $\overline{Ri}$ for the mixing layer experiments. The figure shows only data measured within the mixing layer itself and includes data from the collapsing mixing layer as well as the pre-collapse mixing layer. The values of E^* for these data were, for the most part, between -0.3 and 0.2, with most of the values near -0.2.

The main feature of the figure is that most of the points are bounded by the lines $R_f = 0.2$ and $R_f = \overline{Ri}$, the latter boundary indicating that K_H/K_m is less than unity for most of the data. (Recall that $R_f = \overline{Ri}\ K_H/K_m$.) Although the data are scattered, there does seem to be a trend which would indicate that, for the mixing layer, the maximum value of R_f is in the neighborhood of 0.2.

There also appears to be a slight trend towards an increase in R_f

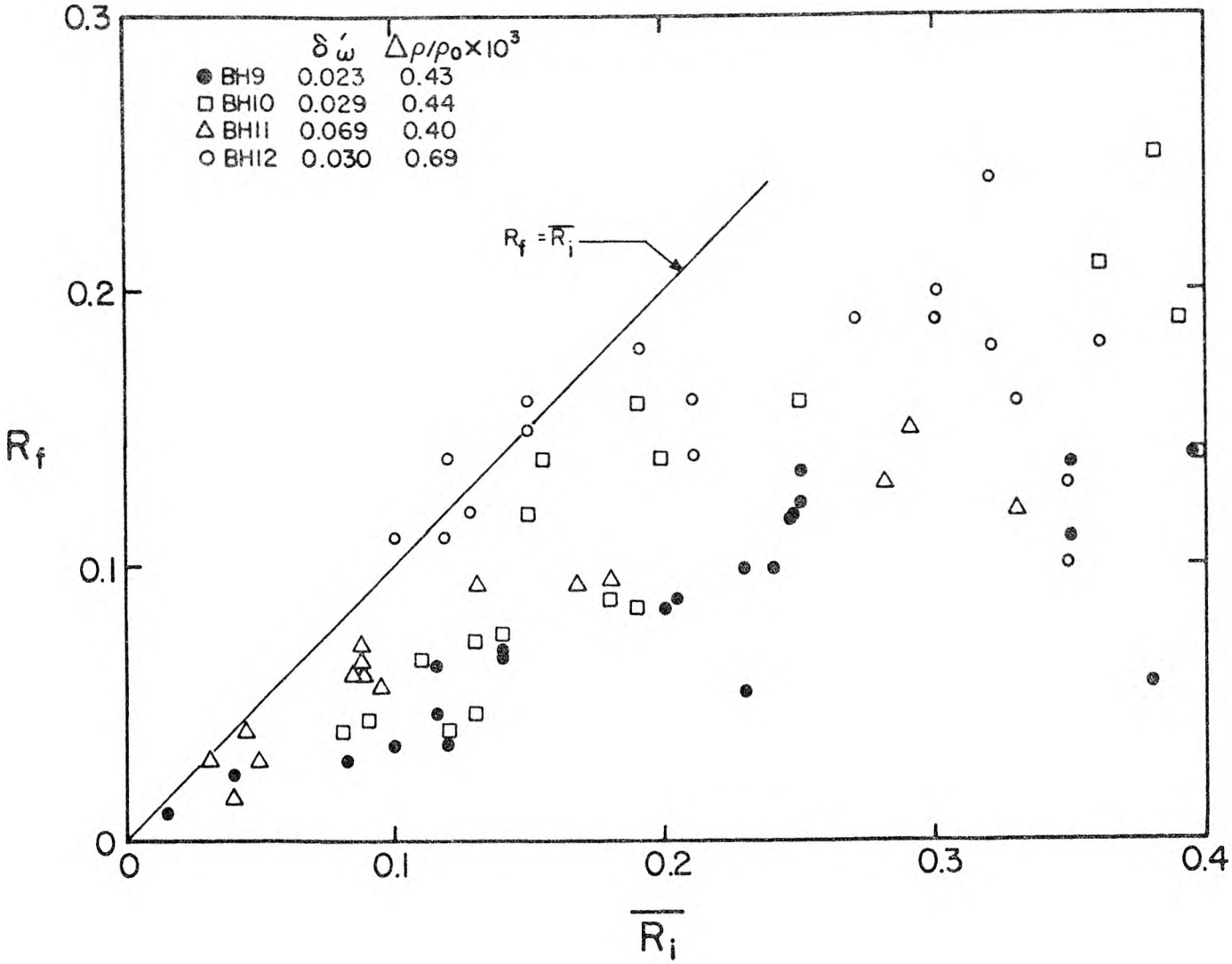

Figure 6.2.41 Values of the flux-Richardson number plotted against the local mean-Richardson number for measurements made within the mixing layer. Symbol key gives: symbol, experiment number, measured growth rate of the mixing layer and the initial relative density difference.

with an increase in δ_ω' and $\Delta\rho/\rho_o$ for a given value of $\overline{Ri}$. This would not be unexpected, since the mixing layers are qualitatively similar, regardless of the degree of stratification. Thus, an increase in the spreading rate, all other things being equal, would accompany an increase in the mixing rates (that is, $\overline{\rho'v'}$ and $-\overline{u'v'}$) and a decrease in $\frac{-\partial\overline{\rho}}{\partial y}$ and $\frac{\partial\overline{u}}{\partial y}$. The net effect would be a slight increase in R_f and a slight decrease in $\overline{Ri}$. Because the buoyancy effects were seen to have relatively minor effects on the initial portion of the mixing layer, one would expect that a slight increase in $\Delta\rho/\rho_o$ would cause a slight increase in both R_f and $\overline{Ri}$. (In essence, it is argued that small increases in the buoyancy forces cause only slight changes in the initial vortex development, and that, to some degree, the temperature difference can be considered to be a passive tracer. Of course, this is not strictly true, otherwise the mixing layer would not collapse to a laminar shear layer, but one might expect $\overline{\rho'v'}$ and $\frac{\partial\overline{\rho}}{\partial y}$ to scale at least weakly with $\Delta\rho/\rho_o$ in the initial mixing layer.) Although the data are scattered, they do indicate trends toward slight increases in R_f with increases in the values of δ_ω' and $\Delta\rho/\rho_o$.

Figure 6.2.42 presents a significant result of this study. This figure shows the values of $\overline{B'v'}/\varepsilon^*$ plotted against $\overline{Ri}$ where, again, both parameters were measured within the mixing layer. As mentioned previously, ε^* was not measured directly; in this instance, it was calculated from the measured quantities using the relationship:

$$\varepsilon^* = -\overline{B'v'} - \overline{u'v'}\frac{\partial\overline{u}}{\partial y} - \frac{\partial\overline{q^{*2}v'}}{\partial y} - \overline{u}\frac{\partial\overline{q^{*2}}}{\partial x} \qquad (6.2.6)$$

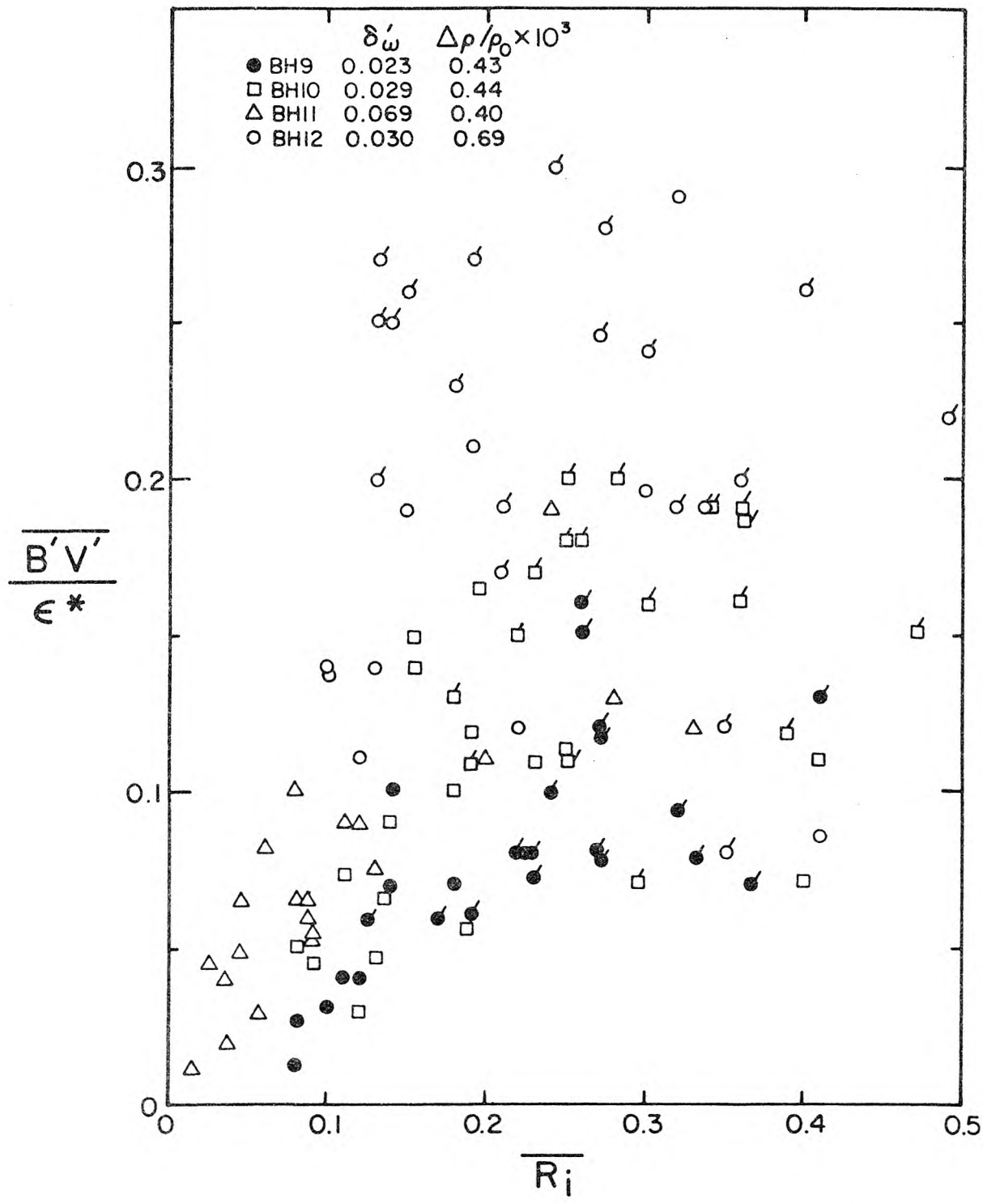

Figure 6.2.42 Values of $\overline{B'v'}/\varepsilon^*$ plotted against the local mean-Richardson number for measurements made within the mixing layer. Symbol key gives: symbol, experiment number, measured growth rate of the mixing layer and the initial density difference. Flags on symbols indicate data for which $x/\ell_b > 2.5$.

The terms on the right-hand side were found to be the significant contributors in the two-dimensional form of Equation 2.1.12. The quantity $\frac{\partial \overline{q^{*2}}}{\partial x}$ was not measured directly, but calculated from the change in the profiles of $\overline{q^{*2}}$ with the distance x along the flume.

In the mixing layer, $-\overline{u'v'}\,\frac{\partial \bar{u}}{\partial y}$ was by far the largest term, as would be expected in a region of strong shear. Typically, E^* was found to be about -0.2, R_f less than 0.2, and $-\overline{B'v'}/\,\bar{u}\,\frac{\partial \overline{q^{*2}}}{\partial x}$ between 0.3 and 1.2. This latter term reflects the reduction of $\sqrt{\overline{u'^2}}$ and $\sqrt{\overline{v'^2}}$ with x as discussed in Section 6.2.5.

It is interesting that the rate at which $\overline{q^{*2}}$ was reduced (that is, $-\bar{u}\,\frac{\partial \overline{q^{*2}}}{\partial x}$) was often much greater than the rate at which the potential energy per unit mass was increased, especially in the middle of the mixing layer near $(y - y_o)/(x - x_o) = 0$. Although $\bar{u}\,\frac{\partial \overline{q^{*2}}}{\partial x} / \overline{u'v'}\,\frac{\partial \bar{u}}{\partial y}$ was generally between 0.15 and 0.7 in the stratified flows, it was less than 0.05 in the homogeneous flows. It seems clear then that the stratification has resulted in the large rate of reduction of $\overline{q^{*2}}$, but the process is clearly not a simple exchange of turbulent kinetic energy, as $-\overline{B'v'}\,/\,\bar{u}\,\frac{\partial \overline{q^{*2}}}{\partial x}$ was usually less than one (and much less than one near $(y - y_o)/(x - x_o) = 0$). In Section 7.1 there is further discussion of this point.

The data in Figure 6.2.42 indicate that in the mixing layer the dissipation rate by far exceeds the rate of increase of potential energy. There are several other trends which can be seen in Figure 6.2.42. The data of a particular experiment tend to rise to a maximum value of $\overline{B'v'}/\varepsilon^*$ near $\overline{Ri} = 0.25$ and then decline. (The data for which $x/\ell_b > 2.5$

are marked with a flag to indicate the measurements made in the collapsing layer; these data are generally associated with higher values of $\overline{Ri}$.) Thus it appears that $\overline{B'v'}/\varepsilon^*$ rises until the mixing layer begins to collapse, then tends to decline as a laminar shear flow is developed. The data also indicate that, for a given value of $\overline{Ri} < 0.25$, $\overline{B'v'}/\varepsilon^*$ increases with both $\Delta\rho/\rho_o$ and δ_ω', as does R_f.

The results shown in Figure 6.2.42 are significant in that they indicate the inefficiency of turbulent mixing when small buoyancy forces are present. Of the total energy available to raise the potential energy of the system, most is apparently dissipated by viscous forces. It seems rather astounding that very small buoyancy forces can cause the turbulent mixing layer to collapse to a laminar state, and yet most of the energy available for mixing was dissipated, while very little of the energy available was used to increase the potential energy of the system. Furthermore, the system is at its highest efficiency (that is, $\overline{B'v'}/\varepsilon^*$ is highest) while it is collapsing, but the actual values of $\overline{B'v'}$ and ε^* are relatively low during the collapse process.

At this point, the quantity ε^* will be examined to some degree, because it was not measured directly and is a rather important quantity in this analysis. One method of checking the value of ε^* calculated from the data and Equation 6.2.6 is to compute ε from the power spectra of u'. As was discussed in Section 2.4, the spectrum $\Phi_u(k)$ should be proportional to $\varepsilon^{2/3}$ in the inertial subrange. Using Equation 2.4.1 and the spectral estimates of u', the value of ε can be estimated.

Strictly speaking, Equation 2.4.1 is valid only for isotropic turbulence which certainly is not found in a two-dimensional mixing layer, not to mention a density-stratified mixing layer. Nevertheless, ε (for the three-dimensional equation) can be estimated in this manner, and can be compared to ε^* (for the two-dimensional equation) in order to get an idea as to the relationship between ε and ε^*.

For the homogeneous mixing layer, it was found that $\varepsilon/\varepsilon^* \approx 0.98$ where ε was calculated from measured estimate of $\Phi_u(k)$, and Equation 2.4.1 with $e_1 = 0.5$, and ε^* was the calculated sum of $-\overline{u'v'}\,\frac{\partial \bar{u}}{\partial y}$ and $-\frac{\partial \overline{q^{*2}v'}}{\partial y}$. It was found that $\bar{u}\,\frac{\partial \overline{q^{*2}}}{\partial x}$ was small near $y - y_o = 0$, where these measurements were made. The fact that $\varepsilon/\varepsilon^*$ was close to unity is somewhat surprising at first glance. However, from Equations 2.3.3 (or 2.1.12) and 6.2.4 it is seen that $\varepsilon^* = \varepsilon + \frac{1}{2}\frac{\partial \overline{w'^2v'}}{\partial y}$. Therefore, if the values of ε calculated from the power spectra are valid estimates of the dissipation rate, then it would seem that $\frac{\partial \overline{w'^2v'}}{\partial y}$ is a small quantity in the two-dimensional mixing layer, as was found by Wygnanski and Fiedler (1970). In fact, as will be seen in Section 6.5, the quantity $q^{*2}v'$ is for the most part very nearly zero, except during very short, intermittent periods in which it attains extremely high values. The mean value of $q^{*2}v'$ is, in fact, often found to be an order of magnitude less than its standard deviation, and sometimes two orders of magnitude less than its peak values. Thus, the small values of $\overline{q^{*2}v'}$ are a result of very short periods in which $q^{*2}v'$ is extremely large coupled with long periods when $q^{*2}v'$ is near zero. In the two-dimensional mixing layer (not the ideal case, but the case under investigation in this

study) one might expect that w' and v' are never as well correlated as u' and v' are, and that as a consequence $\overline{w'^2v'}/\overline{q^{*2}v'}$ is typically a small quantity. Hence, it would not be unusual in these circumstances to find $\frac{1}{2}\frac{\partial\overline{w'^2v'}}{\partial y}$ to be small compared to ε, which leads to the conclusion that $\varepsilon \approx \varepsilon^*$.

The value of ε was also calculated for the density-stratified cases and it was found that $\varepsilon/\varepsilon^* \approx 0.91$, though the data are somewhat scattered, as the standard deviation was 0.3. Comparing Equations 2.3.3 (or 2.1.12) and 6.2.4 it is found that $\varepsilon^* = \varepsilon + \frac{1}{2}\frac{\partial\overline{w'^2v'}}{\partial y} + \frac{\overline{u}}{2}\frac{\partial\overline{w'^2}}{\partial x}$ for the density-stratified cases. Here $\frac{\partial\overline{w'^2}}{\partial x}$ may not be neglected, as was the case for the homogeneous flow. (Wygnanski and Fiedler (1970) found little variation in $\overline{u'^2}$, $\overline{v'^2}$ and $\overline{w'^2}$ with x in the homogeneous mixing layer near $y = y_o$; in this study, $\overline{u'^2}$ and $\overline{v'^2}$ were found to vary little with x in homogeneous flows, but not in stratified flows; it is likely that $\overline{w'^2}$ also varied with x in stratified flows.)

If $\frac{\partial\overline{w^2}}{\partial x}$ is comparable in size to $\frac{1}{2}\frac{\partial\overline{q^{*2}}}{\partial x}$, and if $\frac{1}{2}\frac{\partial\overline{w'^2v'}}{\partial y}$ is again negligible, then using typical values of $\frac{\partial q^{*2}}{\partial x}$ and ε^*, one finds $\varepsilon/\varepsilon^* \approx 1.1$; thus, it seems as though the values of ε computed from the power spectra (assuming isotropy) are low by about twenty per cent in this instance. Nevertheless, it is gratifying that ε computed from the power spectra agrees as well as it does with the values of ε^* calculated from the averaged data.

In summary, the data in Figure 6.2.42 indicate that the exchange of turbulent kinetic energy to potential energy is an inefficient process in the stratified mixing layer. The data further indicate that,

in the mixing layer, $\overline{B'v'}/\varepsilon^*$ rises to a maximum value when $\overline{Ri}$ is about 0.25 and then declines; by contrast R_f rises to about 0.2 as the mixing layer collapses and does not appear to decline. Finally, the value of ε^* found in the homogeneous mixing layer appears likely to be close to the value of ε, the three-dimensional dissipation rate. The value of ε^* found in the stratified mixing layer appears to be about ten per cent less than ε; it also appears that the value of ε found from power spectral estimates in the density-stratified mixing layer may be smaller than the true value by about twenty per cent.

6.2.11 Summary of Results for the Initial Mixing Layer

The most significant results of the mixing layer studies are presented in Figures 6.2.41 and 6.2.42, which indicate that R_f has a maximum value of about 0.2 in the stratified mixing layer, and that $\overline{B'v'}/\varepsilon^*$ rises to a maximum mean $\overline{Ri} = 0.25$ and then decreases as the mixing layer collapses. Furthermore, it was found that buoyancy effects caused a reduction in $\overline{q^{*2}}$ at a rate which generally exceeded the rate of increase of potential energy, $\overline{B'v'}$.

The collapse of the mixing layer was examined in detail, and it was found visually that the mixing layer began to collapse when $2\frac{\Delta\rho}{\rho_o} gx/(\bar{u}_1 + \bar{u}_2)\Delta\bar{u}_o \approx 2.0$. Furthermore, it was found that as the layer collapsed, the parameter $\frac{\Delta\rho}{\rho_o} g \ell_T^*/\Delta\bar{u}_o^2$ approached a value between 0.25 and 0.3 (Figure 6.2.6), but the maximum-slope thickness of the velocity profile, ℓ_u^*, continued to increase slowly (Figures 6.2.5 - 6.2.7).

Probability density functions indicate that for the most part,

u'v' and v'T' are very nearly zero, and that the non-zero means are a result of short periods in which $|u'v'|$ and $|v'T'|$ attain extremely large values (Figures 6.2.32 - 6.2.37). In addition, periods in which v'T' attained large positive values were found in the collapsing layer (Figure 6.2.37), indicating periods of heat transfer against the mean temperature gradient. Finally, similarity profiles were found for $\overline{u}$ and $\overline{T}$ (Figures 6.2.1 - 6.2.4); it was found that the profiles of $\overline{T}$ (and those of $\sqrt{\overline{T'^2}}$) were asymmetric with respect to the centerline of the mixing layer (Figures 6.2.3, 6.2.4, 6.2.15).

6.3 Experimental Results from Measurements Made in the Downstream Flow Over a Smooth Bed

In this section the results from measurements made in the downstream flow over a smooth bed are presented. Details on the initial conditions of these experiments are given in Tables 6.1.1 and 6.1.3.

Vertical profiles of mean quantities which are presented in this section are shown as a function of y/h, where h is the total flow depth and y is the vertical coordinate with a zero level arbitrarily defined as the vertical coordinate of the splitter plate (that is, 30 cm above the flume bed). Therefore, the normalized coordinate of the bed is $y/h \approx -0.67$, while that of the surface is $y/h \approx -0.33$. The velocity scale used for normalization is U, the overall mean flow speed, and the temperature scale used is ΔT_o, the initial temperature difference between the two layers. The profiles which are presented show measured values; lines between points are linearly interpolated.

6.3.1 Profiles of Mean Velocity and Temperature

Because of the large number of variables involved, such as x/ℓ_b, K_u, Re and y/h, the downstream profiles of the mean velocity and temperature did not lend themselves to convenient, similarity descriptions as was the case for the mixing layer profiles. There are, however, several features of the mean profiles which are interesting and clearly show the strong stabilizing effect of small density differences in an open-channel flow. These measurements are presented mainly to aid in the general understanding of the nature of density-stratified shear flows, and not to lead into a universal description for stratified flows.

Figures 6.3.1 and 6.3.2 show profiles of the normalized mean velocity for three cases (Experiments BH6, BH7 and B4) in which the values of $\Delta\rho/\rho_o$ were 4.2×10^{-4}, 1.8×10^{-4} and 0.0, respectively, but other flow parameters were nearly the same (see Tables 6.1.1 and 6.1.3). Figure 6.3.1 shows the results of measurements made 4.7 m from the splitter plate. While all three profiles reflect the slightly lower mean speed in the upper layer compared to the lower layer, the two profiles with the non-zero density difference dramatically reflect the reduced mixing which is a direct result of the buoyancy forces. The wake from the splitter plate is clearly evident in both of these cases; in fact, the stronger the stratification, the more noticeable the wake.

In all three of these cases the velocity difference between the layers was small, so that the mixing at the interface was essentially

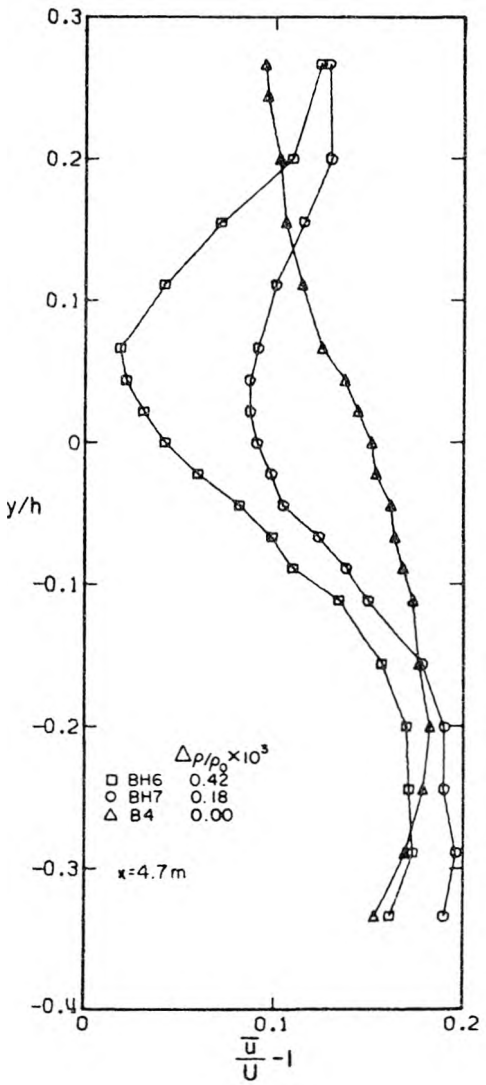

Figure 6.3.1

Profiles of the mean velocity, measured 4.7 m downstream of the splitter plate, for flows with different initial stratifications. Symbol key gives: symbol, experiment number, and $\Delta\rho/\rho_o \times 10^3$. $y/h = 0$ corresponds to the level of the splitter plate (30 cm above the flume bed).

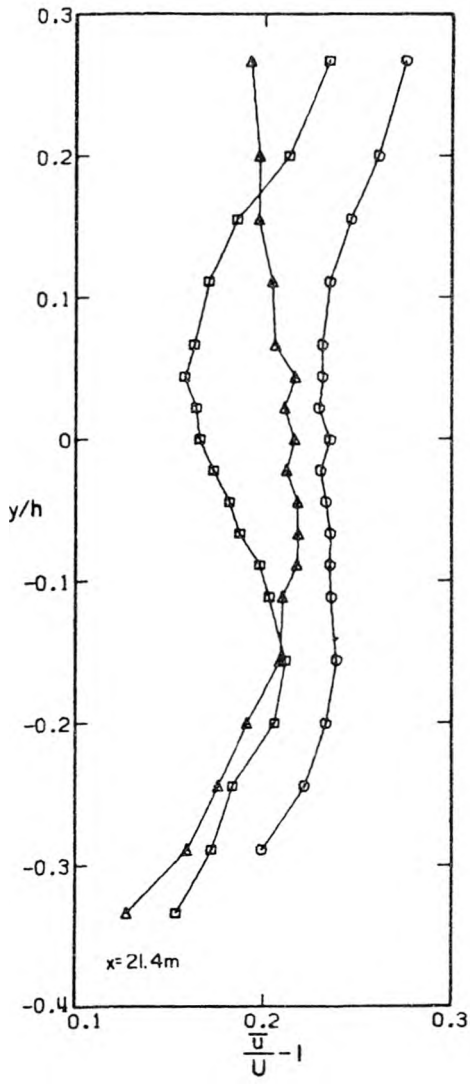

Figure 6.3.2

Mean velocity profiles, measured 21.4 m downstream of the splitter plate for the same flows shown in Figure 6.3.1. Symbols are as in Figure 6.3.1.

the result of the turbulent wake from the splitter plate and the inlet turbulence; the mixing which did occur was, of course, much less than would be found in a mixing layer in which ΔU_o was substantial. However small, the mixing in the homogeneous case was sufficient to reduce the velocity defect substantially compared to the stratified cases.

Figure 6.3.2 shows profiles measured 21 m downstream of the splitter plate for the same cases as shown in Figure 6.3.1. The velocity defect from the splitter plate is easily seen in the profile of the most stratified case, and it still exists, though to a lesser degree in the weakly stratified case. The profile for the homogeneous case shows an entirely different character, in that there is a slightly negative velocity gradient in the upper portion of the flow. This is typical of homogeneous flows in open-channels with moderate aspect ratios (here $h/w_f = 0.41$), for secondary circulations bring slow fluid near the walls to the upper middle portion of the channel. As was discussed in Section 2.7.4, density stratification inhibits the development of secondary circulation, and this may result in an increase in the shear.

The mean temperature profiles for these cases are shown in Figures 6.3.3 and 6.3.4. The temperature profiles measured 4.7 m from the splitter plate, presented in Figure 6.3.3, show distinct homogeneous regions above and below the interfacial region in which a temperature gradient exists. Downstream the profiles for the two cases are still different. The case with the larger density difference (Experiment BH6, with $\Delta\rho/\rho_o = 4.2 \times 10^{-4}$) exhibits an interfacial region separating relatively mixed regions (recall that the flume bed lies at $y/h = -0.666$),

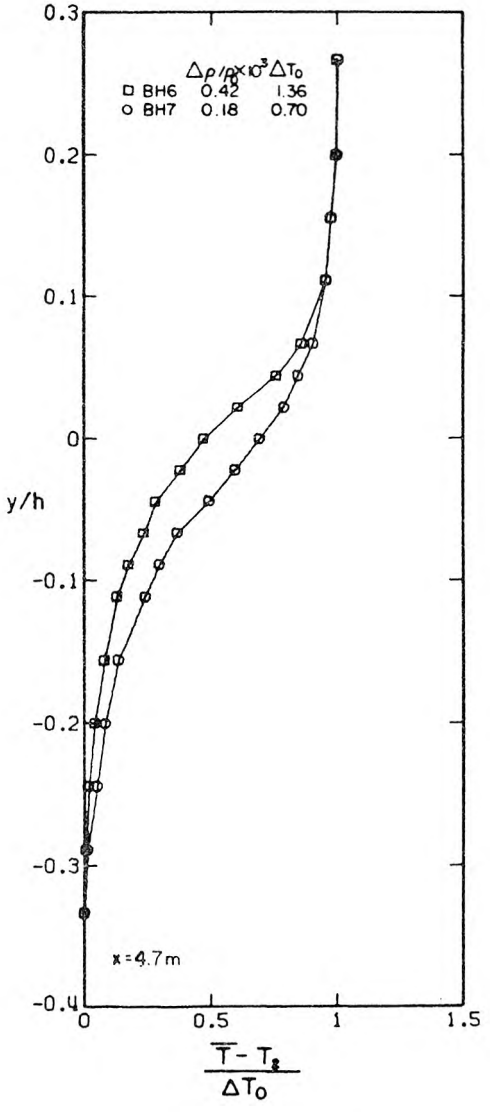

Figure 6.3.3

Profiles of the mean temperature, measured 4.7 m downstream of the splitter plate, for the stratified flows shown in Figure 6.3.1. Symbol key gives: symbol, experiment number, $\Delta\rho/\rho_o \times 10^3$, and ΔT_o(°C). $y/h = 0$ corresponds to the level of the splitter plate.

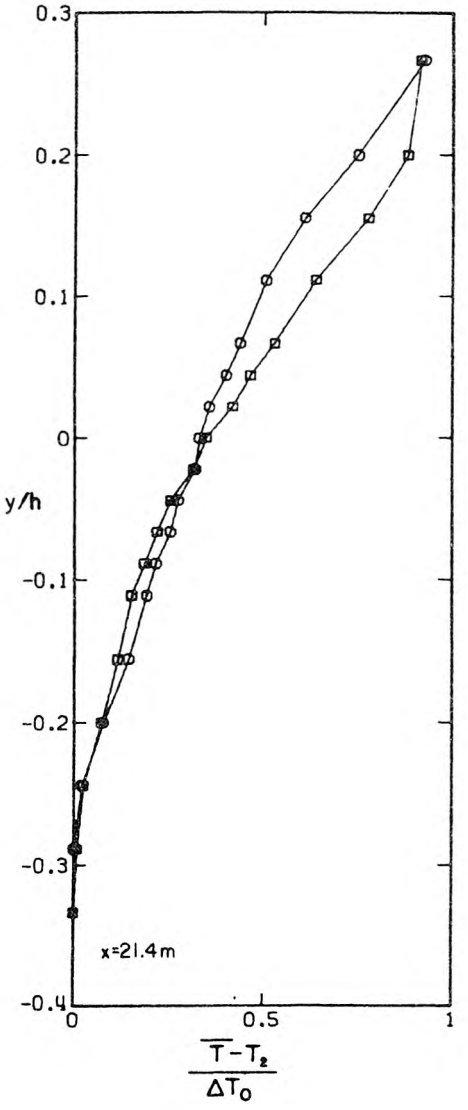

Figure 6.3.4

Mean temperature profiles, measured 21.4 m downstream of the splitter plate, for the same flows shown in Figure 6.3.3. Symbols as in Figure 6.3.3.

while the other case (Experiment BH7, $\Delta\rho/\rho_o = 1.8 \times 10^{-4}$) exhibits a gradually increasing mean temperature gradient with y/h with no apparent inflection in the profile, which indicates that the boundary-generated turbulence was able to break up the weaker interface. Still, the wake from the splitter plate was apparent in both flows at this downstream location (Figure 6.3.2).

When there was a substantial initial shear, the basic results were essentially the same: an increase in the stratification resulted in reduced mixing and a greater shear. Figures 6.3.5, 6.3.6 and 6.3.7 show profiles for two stratified flows with initial shear. The first two of these figures clearly show the stabilizing effect of density stratification, as the flow with the greater initial density difference exhibits greater shear both upstream (Figure 6.3.5) and downstream (Figure 6.3.6), despite the fact that the other flow had a slightly larger initial velocity difference.

Figure 6.3.7 shows the downstream temperature profiles for these cases; the profile of one case (Experiment BH15, $\Delta\rho/\rho_o = 7.3 \times 10^{-4}$) is interesting in that it still exhibits the asymmetric shape that was apparent in temperature profiles in the initial mixing layer (see Figure 6.2.3). Apparently the stratification in this case was so strong that little mixing occurred downstream, and the shape of the temperature profile was largely preserved. In the other case shown, the mixing was sufficient to result in a rather smooth temperature profile.

An extreme example is shown in Figure 6.3.8 which presents a mean

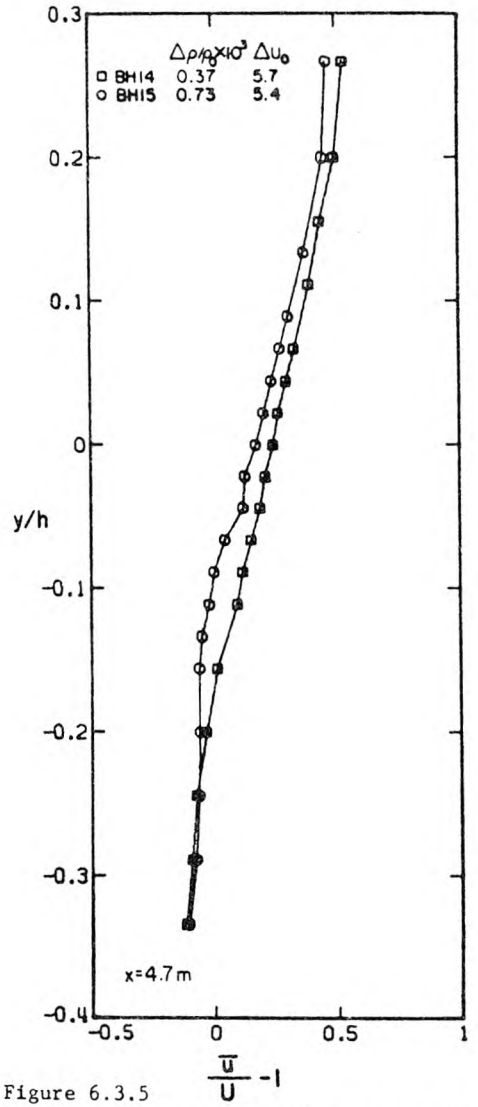

Figure 6.3.5 Profiles of mean velocity, measured at x = 4.7 m, for stratified flows with initial shear. Symbol key gives: symbol, experiment number, $\Delta\rho/\rho_o \times 10^3$, ΔU_o (cm/s).

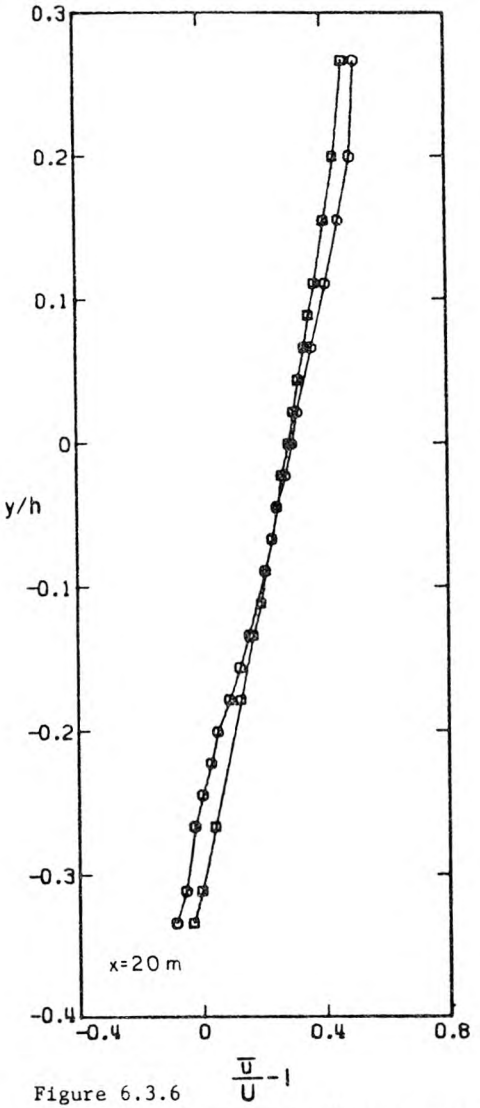

Figure 6.3.6 Profiles of mean velocity, measured at x = 20 m, for the same flows as in Figure 6.3.5. Symbols as in Figure 6.3.7.

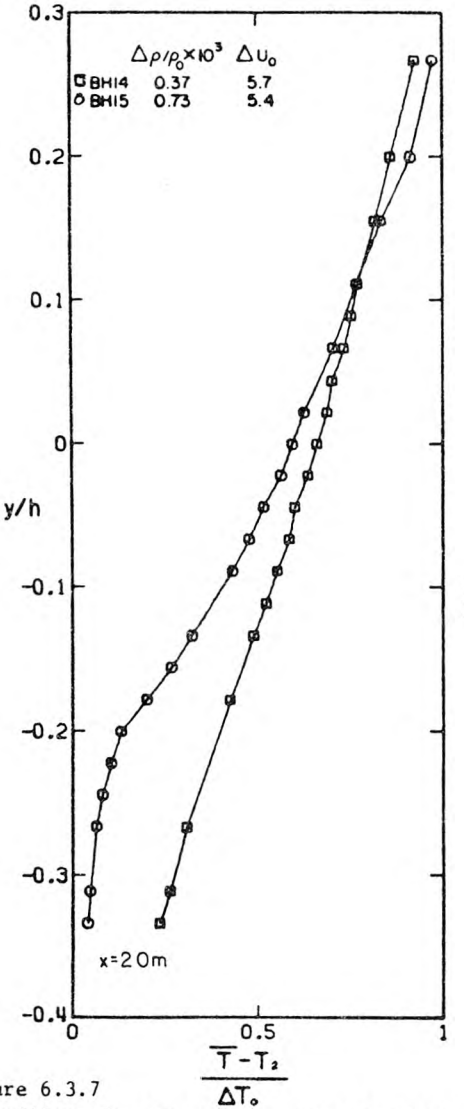

Figure 6.3.7 Profiles of mean temperature, measured at x = 20 m, for the same cases shown in Figure 6.3.6. Symbol key gives: symbol, experiment number, $\Delta\rho/\rho_o \times 10^3$, ΔU_o (cm/s).

velocity profile measured 24 m from the splitter plate for a stratified flow with $\Delta\rho/\rho_o = 1.04 \times 10^{-3}$ and $\Delta U_o = 3.9$ cm/s. A strong laminar shear layer was observed to develop after the collapse of the mixing layer; this shear layer is clearly evident in Figure 6.3.8, even at a distance of 24 m from the splitter plate. The mean temperature profile for this case is shown in Figure 6.3.9 and this profile indicates that the regions of large temperature and velocity gradients coincide, as might be expected. Thus, it is seen that the buoyancy forces were so strong in this instance that a laminar layer with a strong shear was able to persist in the flow.

From these examples, one can easily see the large effect of a small density stratification on a turbulent flow. In fact, because the flow was so well stabilized by small density differences, it became apparent that unless more turbulence was generated at the boundaries, there would be very little mixing which could be measured. For this reason, the flume bed was roughened and two additional series of experiments were conducted, the primary results of which are presented in Section 6.4.

6.3.2 Profiles of $\sqrt{\overline{u'^2}}$, $\sqrt{\overline{v'^2}}$ and $-\overline{u'v'}$

The profiles of the root-mean-square values of the velocity fluctuations also show the strong stabilizing effects of density stratification. Figures 6.3.10, 6.3.11 and 6.3.12 show profiles of $\sqrt{\overline{u'^2}}/U$, $\sqrt{\overline{v'^2}}/U$ and $\frac{-\overline{u'v'}}{U^2}$ for the same cases shown in Figures 6.3.1 and 6.3.3. The fact that larger values of $\sqrt{\overline{u'^2}}$ and $\sqrt{\overline{v'^2}}$ are found in the upper portion of the flow in the most stratified case (Experiment BH6) is

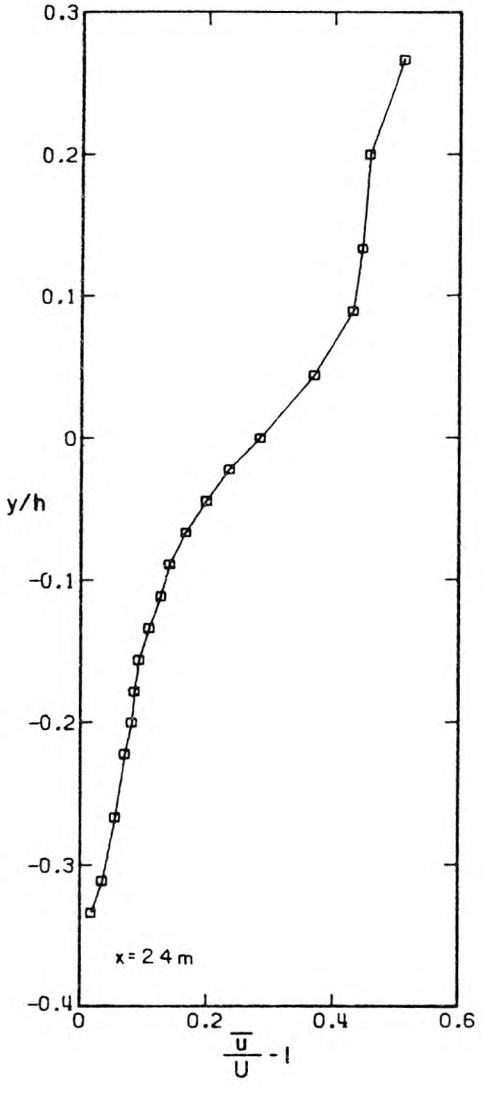

Figure 6.3.8

Profile of mean velocity of a highly stratified flow measured at x = 24 m. Experiment BH16, $\Delta\rho/\rho_o$ = 1.04×10^{-3}, ΔU_o = 3.9 cm/s.

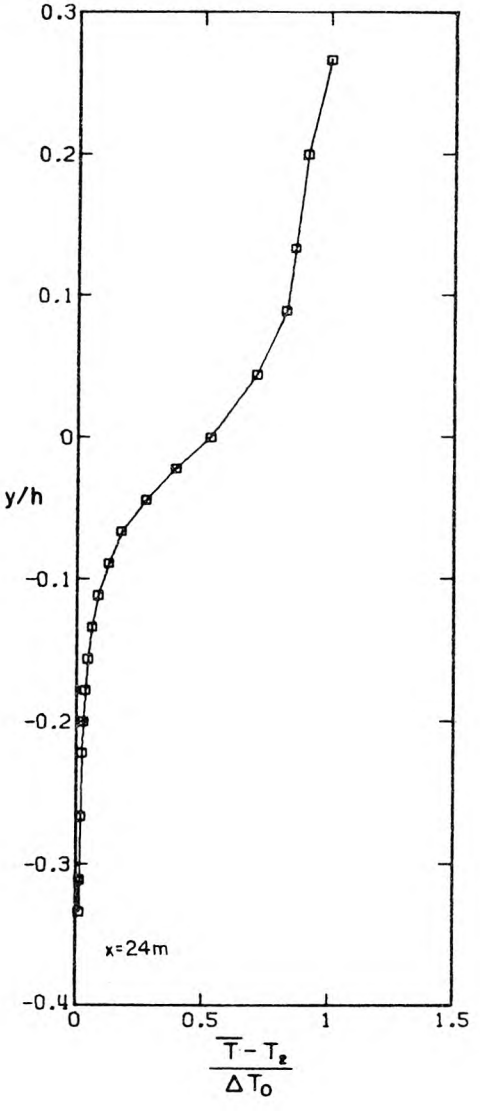

Figure 6.3.9

Profile of the mean temperature measured at x = 24 m, for the same case as in Figure 6.3.8, Experiment BH16, ΔT_o = 3.50°C.

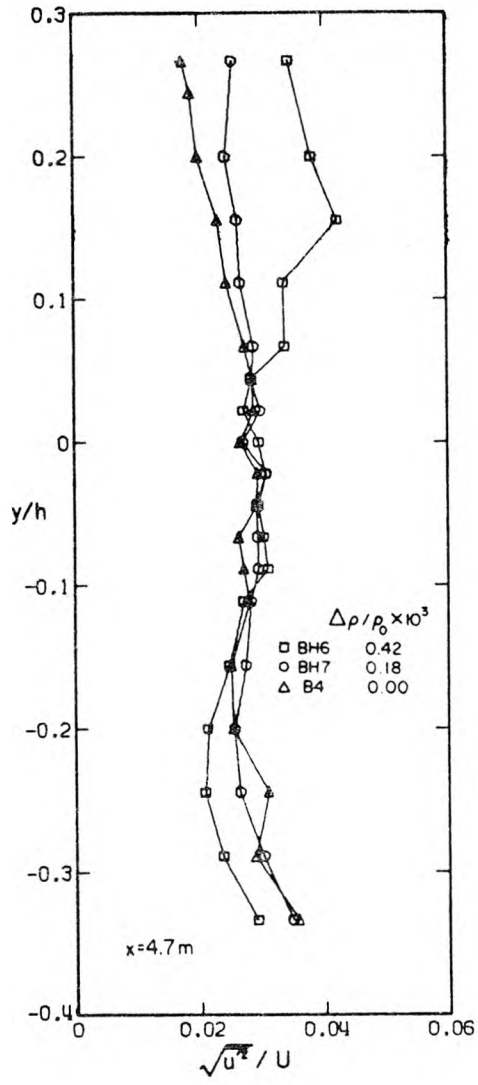

Figure 6.3.10
Profiles of $\sqrt{\overline{u'^2}}/U$, measured at x = 4.7 m, for the same flows in Figure 6.3.1. Symbol key gives: symbol, experiment number, $\Delta\rho/\rho_o \times 10^3$.

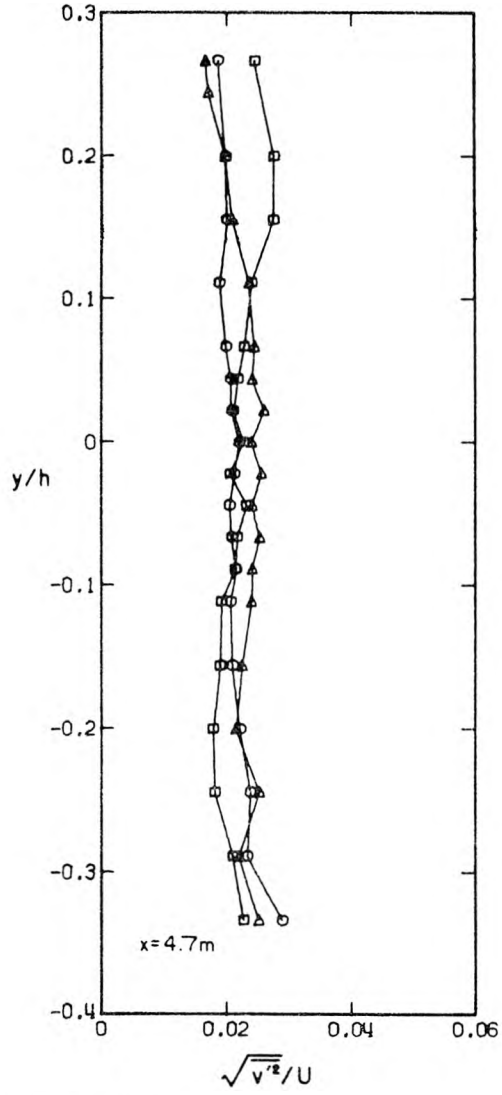

Figure 6.3.11
Profiles of $\sqrt{\overline{v'^2}}/U$, measured at x = 4.7 m, for the same flows considered in Figure 6.3.1 and 6.3.10. Symbols as in Figure 6.3.10.

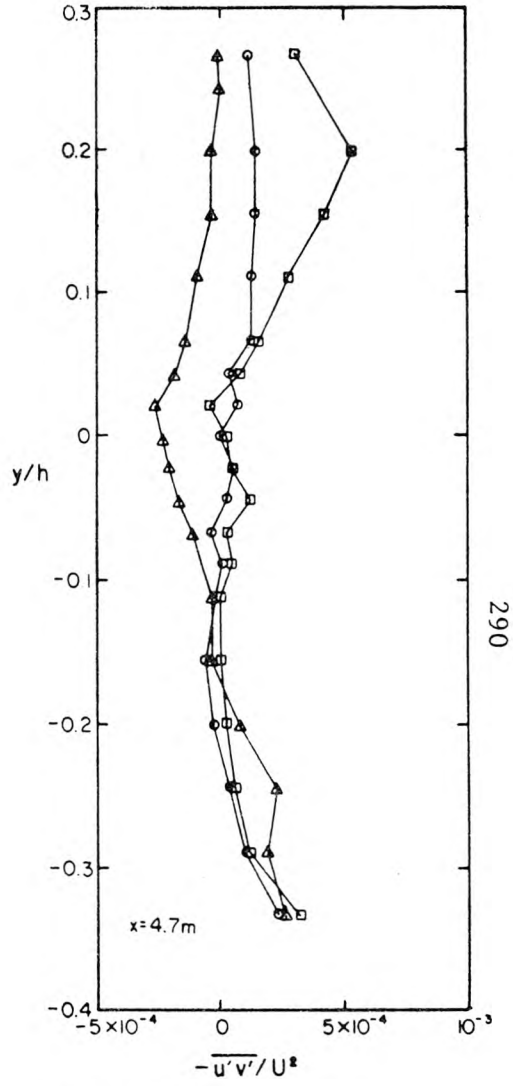

Figure 6.3.12
Profiles of $-\overline{u'v'}/U^2$, measured at 4.7 m for the same flows considered in Figure 6.3.1. Symbols as in Figure 6.3.10.

attributed to turbulence generated by the stronger shear in this region (Figure 6.3.1). Furthermore, the values of $|\overline{u'v'}/U^2|$ are much larger in the stratified case than the homogeneous case (Figure 6.3.12) in the upper portion of the flow, and this too is attributed to the difference in shear. (In fact, $-\overline{u'v'}$ is negative for $y/h > -0.2$ in the homogeneous case shown, due to the fact that $\frac{\partial \bar{u}}{\partial y}$ is also negative in this region.)

In the middle portion of the flow, $\sqrt{\overline{u'^2}}/U$ is nearly the same for all cases, while $\sqrt{\overline{v'^2}}/U$ is smaller in the stratified cases, which indicates the effects of buoyant forces. Furthermore, $-\overline{u'v'}/U^2$ is near zero in this region for the stratified cases which, when one considers that the velocity gradients are mostly non-zero in this region, indicates not only that the turbulent diffusivities are reduced but also that the velocity fluctuations are probably a result of internal waves (for which $\overline{u'v'}$ is zero) rather than turbulence.

Figures 6.3.13 - 6.3.15 show downstream measurements of $\sqrt{\overline{u'^2}}/U$, $\sqrt{\overline{v'^2}}/U$ and $-\overline{u'v'}/U^2$ for the same cases considered in Figures 6.3.2 and 6.3.4. Again $\sqrt{\overline{u'^2}}/U$ and $\sqrt{\overline{v'^2}}/U$ are smaller in the stratified cases throughout the flow, while the values of $-\overline{u'v'}/U^2$ indicate reduced mixing in the lower portion of the stratified flows compared to the homogeneous flows. In the upper portion of the flow, $-\overline{u'v'}/U^2$ is very nearly zero in all cases; the slightly negative gradient of $\bar{u}$ in the homogeneous case results in slightly negative values of $-\overline{u'v'}$. The increase in $\sqrt{\overline{u'^2}}/U$, $\sqrt{\overline{v'^2}}/U$ and $-\overline{u'v'}/U^2$ in the lower portion reflects the generation of turbulence at the flume bed.

These results were typical of all the flow measurements made

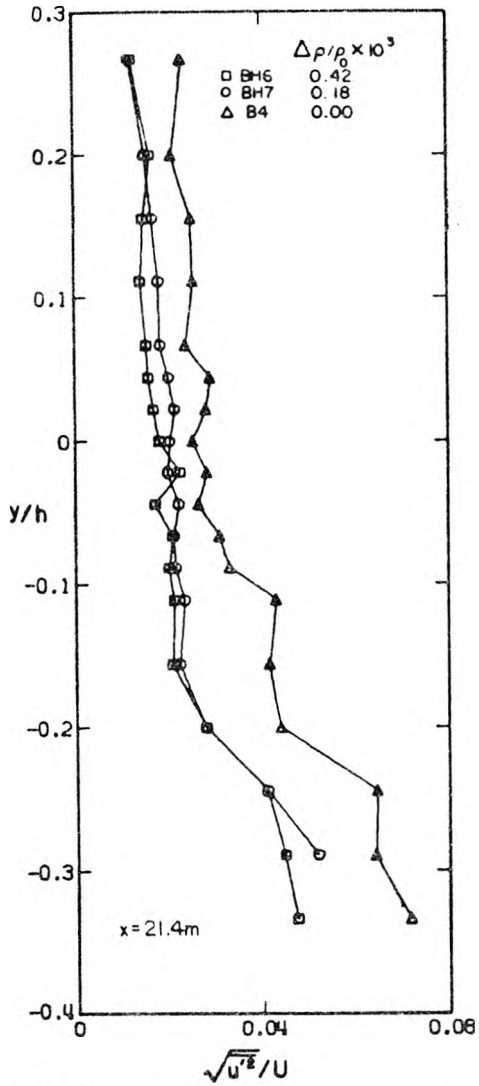

Figure 6.3.13
Profiles of $\sqrt{\overline{u'^2}}/U$ measured at x = 21.4 m, for the same cases considered in Figure 6.3.2. Symbol key gives: symbol, experiment number, $\Delta\rho/\rho_o \times 10^3$.

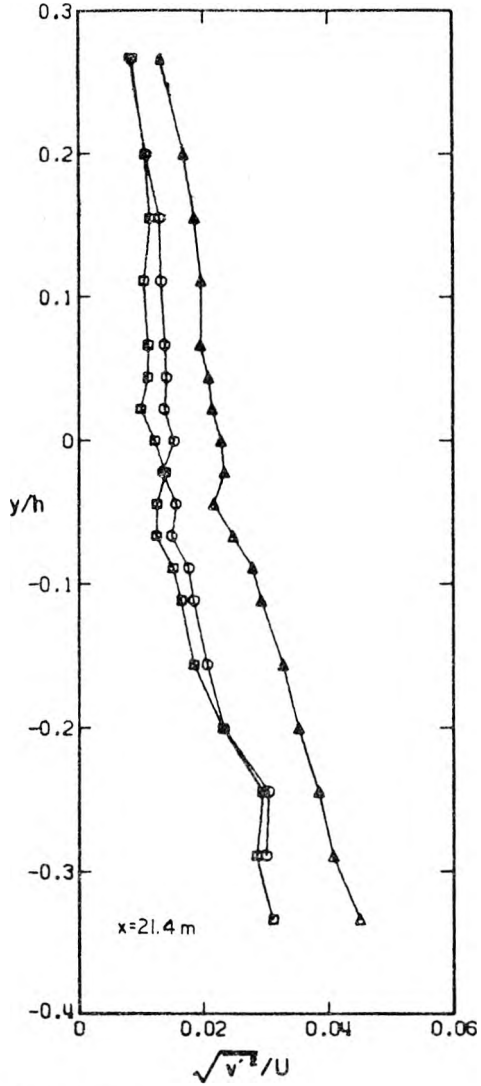

Figure 6.3.14
Profiles of $\sqrt{\overline{v'^2}}/U$ measured at x = 21.4 m for the same cases considered in Figure 6.3.2 and 6.3.13. Symbols in Figure 6.3.13.

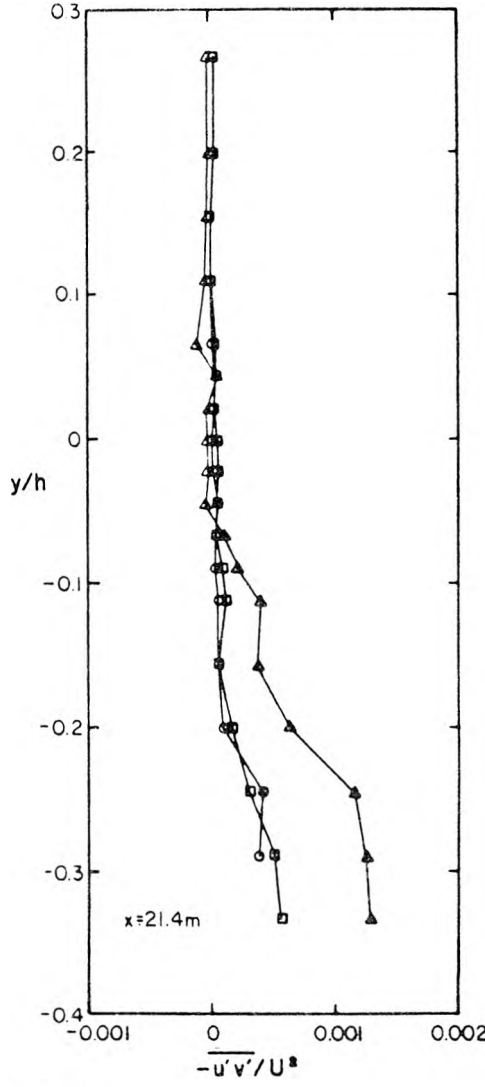

Figure 6.3.15
Profiles of $-\overline{u'v'}/U^2$ measured at x = 21.4 m for the same cases considered in Figure 6.3.2 and 6.3.13. Symbols are in Figure 6.3.13.

downstream. Further evidence is shown in Figures 6.3.16 and 6.3.17, which show profiles of $\sqrt{\overline{v'^2}}/U$ and $-\overline{u'v'}/U^2$ for the same cases shown in Figure 6.3.6. Here, a substantial shear is evident (Figure 6.3.6), which was a result of the initial velocity difference. The case shown with the smaller initial density difference (Experiment BH14) was not observed to develop a laminar layer, but continued to mix slowly all the way down the flume. This is evident in both Figure 6.3.16, which shows that the values of $\sqrt{\overline{v'^2}}/U$ are much higher in this case than in the more stratified case, and in Figure 6.3.17, which shows that non-zero values of $-\overline{u'v'}/U^2$ are found throughout this flow, as opposed to the more stratified case in which $-\overline{u'v'}$ is very nearly zero in the upper portion. From these results, the strong stabilizing effect of density stratification is once again quite evident.

6.3.3 Properties of $\sqrt{\overline{T'^2}}$, $-\overline{v'T'}$ and $\overline{u'T'}$

In this section some of the basic properties of averaged terms involving temperature fluctuations are discussed.

As would be expected, it was found that $\sqrt{\overline{T'^2}}$ was related to the local value of the mean temperature gradient, but it was also found that it was related to the local value of $\sqrt{\overline{v'^2}}$. This can be seen in Figures 6.3.18 and 6.3.19, which show profiles of $\sqrt{\overline{T'^2}}/\Delta T_o$ for the same cases whose mean temperature profiles are shown in Figures 6.3.7 and 6.3.9. Considering Figure 6.3.18 first, it can be seen that, while the temperature gradient was generally smaller in the flow with the smaller initial density difference (Experiment BH14), the values of $\sqrt{\overline{T'^2}}/\Delta T_o$ were generally larger in this flow than in the similar flow

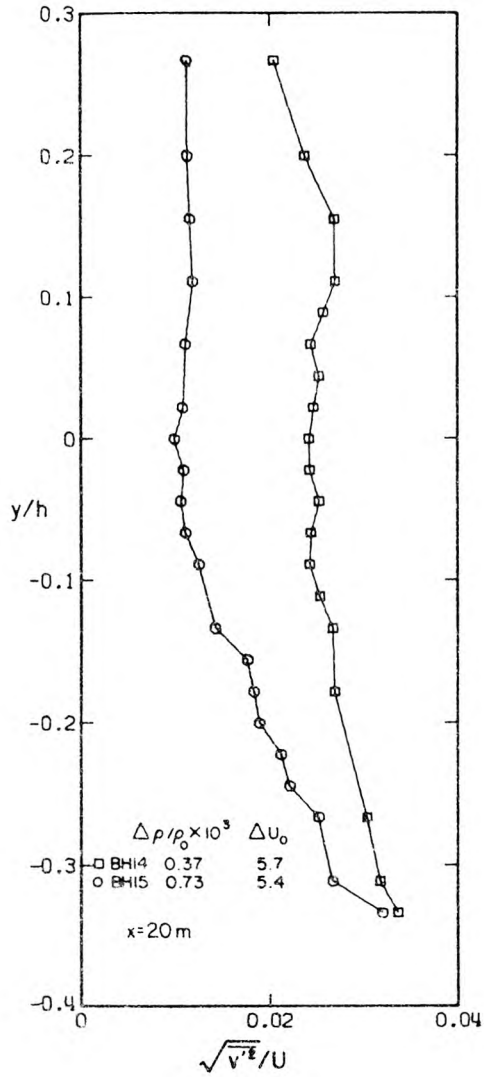

Figure 6.3.16

Profiles of $\sqrt{\overline{v'^2}}/U$ measured at x = 20 m for the same cases considered in Figures 6.3.6 and 6.3.7. Symbol key gives: symbol, experiment number, $\Delta\rho/\rho_o \times 10^3$, ΔU_o (cm/s).

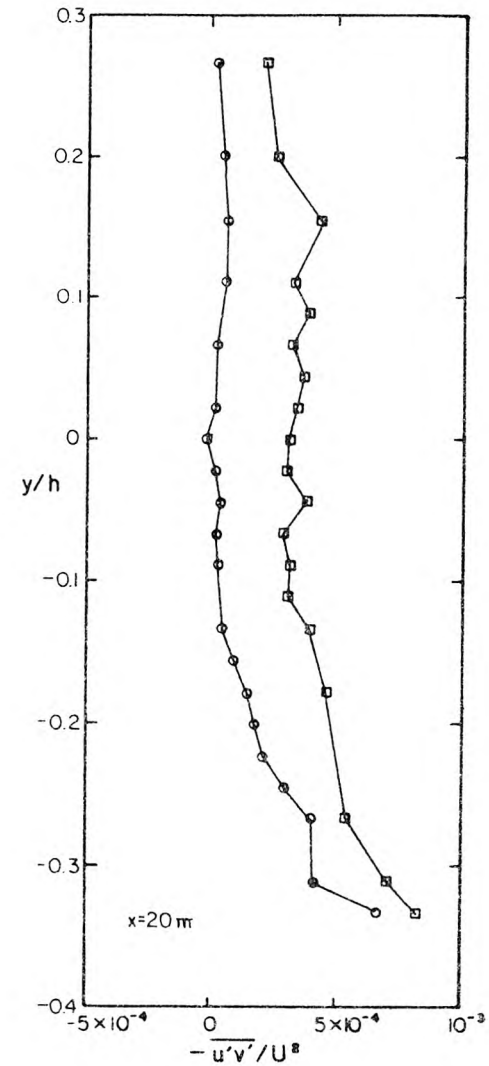

Figure 6.3.17

Profiles of $-\overline{u'v'}/U^2$ measured at x = 20 m for the same cases considered in Figures 6.3.6, 6.3.7 and 6.3.16. Symbols as in Figure 6.3.16.

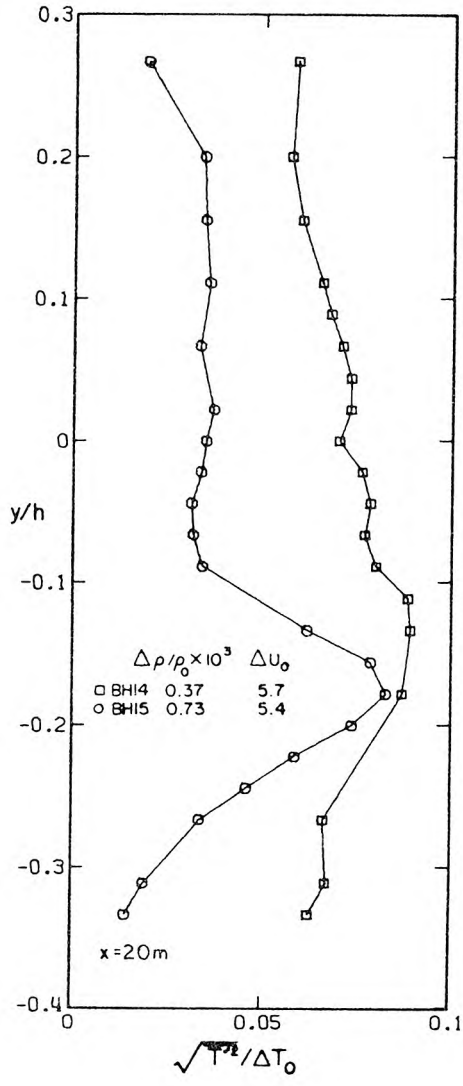

Figure 6.3.18

Profiles of $\sqrt{\overline{T'^2}}/\Delta T_o$, measured at x = 20 m, for the same cases considered in Figures 6.3.6, 6.3.7 and 6.3.16. Symbol key gives: symbol, experiment number, $\Delta\rho/\rho_o \times 10^3$ and ΔU_o (cm/s).

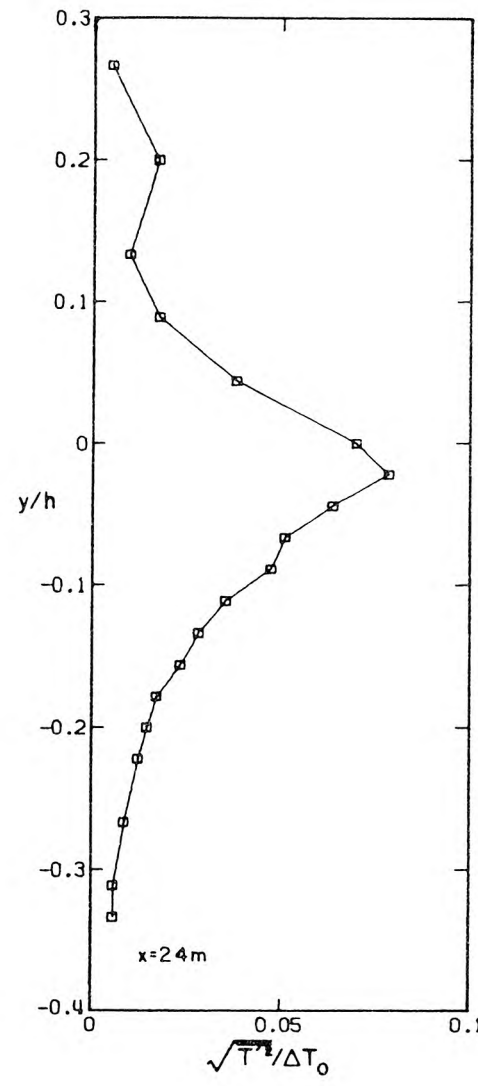

Figure 6.3.19

Profiles of $\sqrt{\overline{T'^2}}/\Delta T_o$, measured at x = 24 m from Experiment BH16, the same flow considered in Figures 6.3.8 and 6.3.9; $\Delta T_o = 3.50°C$.

with the larger initial value of ΔT_o (Experiment BH15). This is attributed in part to the larger values of $\sqrt{\overline{v'^2}}/U$ found in the former case (Figure 6.3.16) since a larger value of $\sqrt{\overline{v'^2}}$ indicates that the vertical excursion of fluid particles from their equilibrium positions is greater, and results in larger values of $\sqrt{\overline{T'^2}}/\Delta T_o$. The sharp increase in $\sqrt{\overline{T'^2}}/\Delta T_o$ near y/h = -0.2 for Experiment BH15 coincides exactly with the increase in the mean temperature gradient for this case (Figure 6.3.7). Below this point, $\sqrt{\overline{v'^2}}/U$ increases (Figure 6.3.7) but the mean temperature gradient becomes very small, resulting in a decrease in $\sqrt{\overline{T'^2}}/\Delta T_o$.

Figure 6.3.19 shows similar features, in that $\sqrt{\overline{T'^2}}/\Delta T_o$ is very small except in the region of the large, mean temperature gradient (Figure 6.3.9). In this strongly stratified flow (Experiment BH16), very little mixing occurred near the sharp temperature gradient, and the flow was essentially laminar in the upper portion. Hence, the fluctuations in temperature and velocity in and above the interface were largely due to internal waves. This was also true for Experiment BH15 (Figure 6.3.18).

This can be seen more clearly in Figures 6.3.20 and 6.3.21, which show profiles of $-\overline{v'T'}/U\Delta T_o$ for the same cases considered in Figures 6.3.18 and 6.3.19. (Figure 6.3.21 also shows the values of $-\overline{v'T'}/U\Delta T_o$ calculated using a digitally low-pass filtered record of v'. Since some of the measurements in this experiment were made in regions with very large values of $\sqrt{\overline{T'^2}}$ and $\frac{\partial \overline{T}}{\partial y}$, there was some noise in the velocity measurements caused by refractive index changes. As can be seen, the

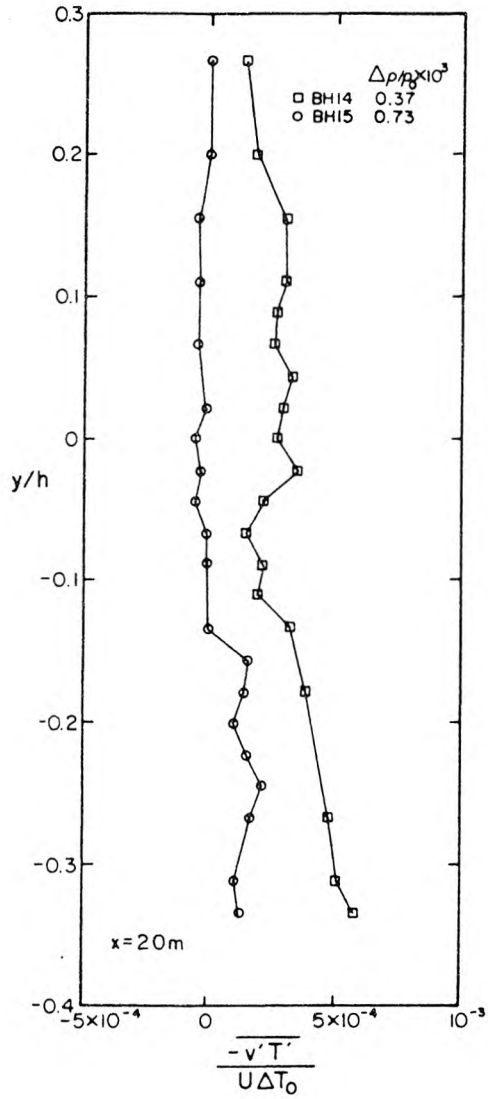

Figure 6.3.20

Profiles $-\overline{v'T'}/U\Delta T_o$, measured at x = 20 m, for the same cases considered in Figures 6.3.6, 6.3.7 and 6.3.18. Symbol key gives: symbol, experiment number, and $\Delta\rho/\rho_o \times 10^3$.

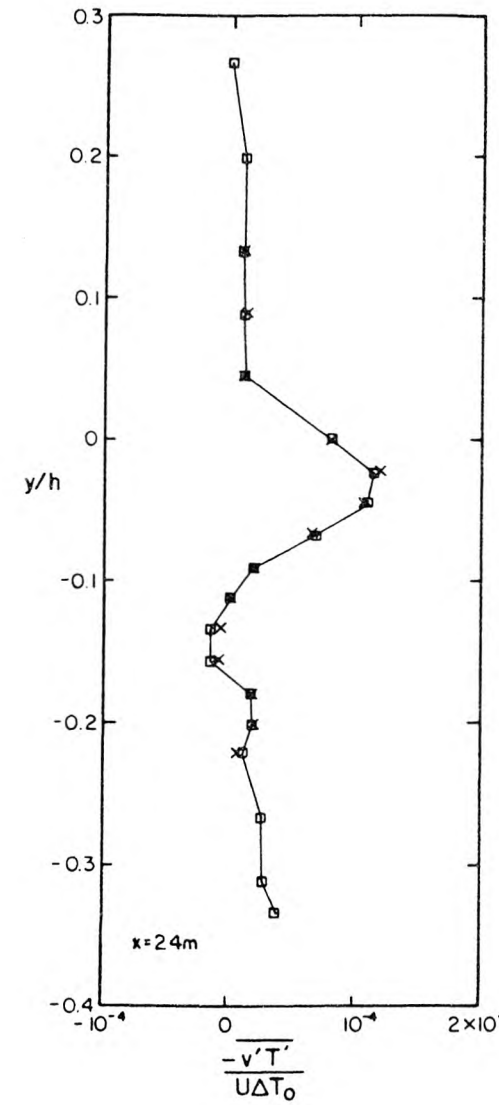

Figure 6.3.21

Profile of $-\overline{v'T'}/U\Delta T_o$, measured at x = 24 m, from Experiment BH16, the same flow considered in Figures 6.3.8, 6.3.9 and 6.3.19. The symbol x denotes values of $-\overline{v'T'}/U\Delta T_o$ computed using low-pass filtered time record of v'.

filtered records of v' yield very nearly the same values of $\overline{v'T'}$ as the unfiltered records. Apparently, the high frequency noise on the signal had little effect on the correlation between v' and T'. This is due to the intermittent nature of the mixing process which is discussed in Section 6.5.) The vertical heat fluxes in both cases with the larger values of ΔT_o (Experiments BH15 and BH16) are near zero above the regions of high mean temperature gradient, as would be expected in laminar flows. The other case (Experiment BH14) exhibits small, but non-negligible positive values of $-\overline{v'T'}/U\Delta T_o$ throughout the flow, as the flow in this case was weakly mixing over the whole reach of the flume.

It is interesting to note that in the lower portion of the regions of highest mean temperature gradient for Experiments BH15 and BH16 (Figures 6.3.20 and 6.3.21), small but still non-zero values of $-\overline{v'T'}/U\Delta T_o$ were measured. These regions were apparently "under attack" by the bed-generated turbulence, which caused a small amount of mixing. As is discussed in Section 6.5, the mixing process in general was found to be highly intermittent, and so it was in this case. In fact, the time histories of u', v', T', u'v' and v'T' in regions such as these indicate that the flow is composed of internal waves which very occasionally break.

The fact that the values of $\overline{u'T'}/\sqrt{\overline{u'^2}}\sqrt{\overline{T'^2}}$ were found to be typically about 0.7 and as high as 0.85 in laminar regions such as these also indicates the existence of internal waves, for linear internal waves imposed on an otherwise steady, stable flow would

result in a value of one for $|\overline{u'T'}/\sqrt{\overline{u'^2}}\sqrt{\overline{T'^2}}|$, with the sign depending on the sign of $\frac{\partial \bar{u}}{\partial y}$.

In fact, the sign of $\overline{u'T'}$ was found to be an extremely sensitive indicator of the sign of $\frac{\partial \bar{u}}{\partial y}$. As an example, consider the velocity profile for Experiment BH6 shown in Figure 6.3.2; the sign of $\overline{u'T'}$ is negative when y/h is between -0.16 and 0.07, corresponding to a region where $\partial\bar{u}/\partial y$ is on the order of $-0.08\ s^{-1}$, while above and below this region $\overline{u'T'}$ is positive, while $\partial\bar{u}/\partial y$ is on the order of $+0.08\ s^{-1}$. It is apparent that the quantity $\overline{u'T'}$ is sensitive to exceedingly small changes in the mean velocity gradient.

For the most part, very little mixing was found to occur in the stratified flows when the flume bed was smooth. The stabilizing effects of the density stratification effectively reduced mixing due to boundary-generated turbulence, and very stable, laminar shear layers were able to persist in many cases over the entire reach of the flume.

6.3.4 Power Spectral Estimates of Fluctuating Quantities

In this section some typical examples of power spectra measured in the downstream flow are presented. The wave number, k, is calculated using Equation 6.2.2 and the spectral estimates, Φ, are calculated using Equation 6.2.3 (Section 6.2.8).

It was usually found that the spectral estimates for u', v' and T' were quite similar, particularly at the higher wave numbers. Exceptions were those instances in which the values of $\sqrt{\overline{u'^2}}$ and $\sqrt{\overline{v'^2}}$ were low, at the same time that $\sqrt{\overline{T'^2}}$ was large; when this was the case, noise caused by refractive index changes was apparent in the high wave

number end of the velocity power spectra. This has been discussed in detail in Section 4.4.

Figure 6.3.22 shows a typical example of the power spectral estimates obtained from measurements in a turbulent region in a stratified flow. The measurements for this case were made 4.7 m from the splitter plate, at y/h = -0.022. (The mean velocity profile in this case is shown in Figure 6.3.5, Experiment BH14.) All three spectra are quite similar in general form, and on a log-log plot exhibit the theoretical (-5/3) slope of the inertial subrange for homogeneous fluids, even though this flow was stratified. These spectra are rather typical of the spectra obtained in the regions of the stratified flows which were turbulent.

Several other spectral forms were found in other flow regions. Figures 6.3.23 - 6.3.25 show power spectra obtained at different elevations in a stratified flow. All these spectral estimates were obtained from measurements made 24 m from the splitter plate; the data are from Experiment BH16, for which mean velocity and temperature profiles are shown in Figures 6.3.8 and 6.3.9. In Figures 6.3.23 - 6.3.25, the values of Φ_u and Φ_v are shown only over the domain of wave numbers in which the velocity measurements were unaffected by refractive index changes. The spectra of T', which were unaffected by refractive index changes, are shown over the entire range of wave numbers measured. Furthermore, the spectra are plotted in the form log $(k^2\ \Phi(k))$ against the log (k), so that the behavior of $\Phi(k)$ can be seen more easily.

The spectra shown in Figures 6.3.23 - 6.3.25 are particularly

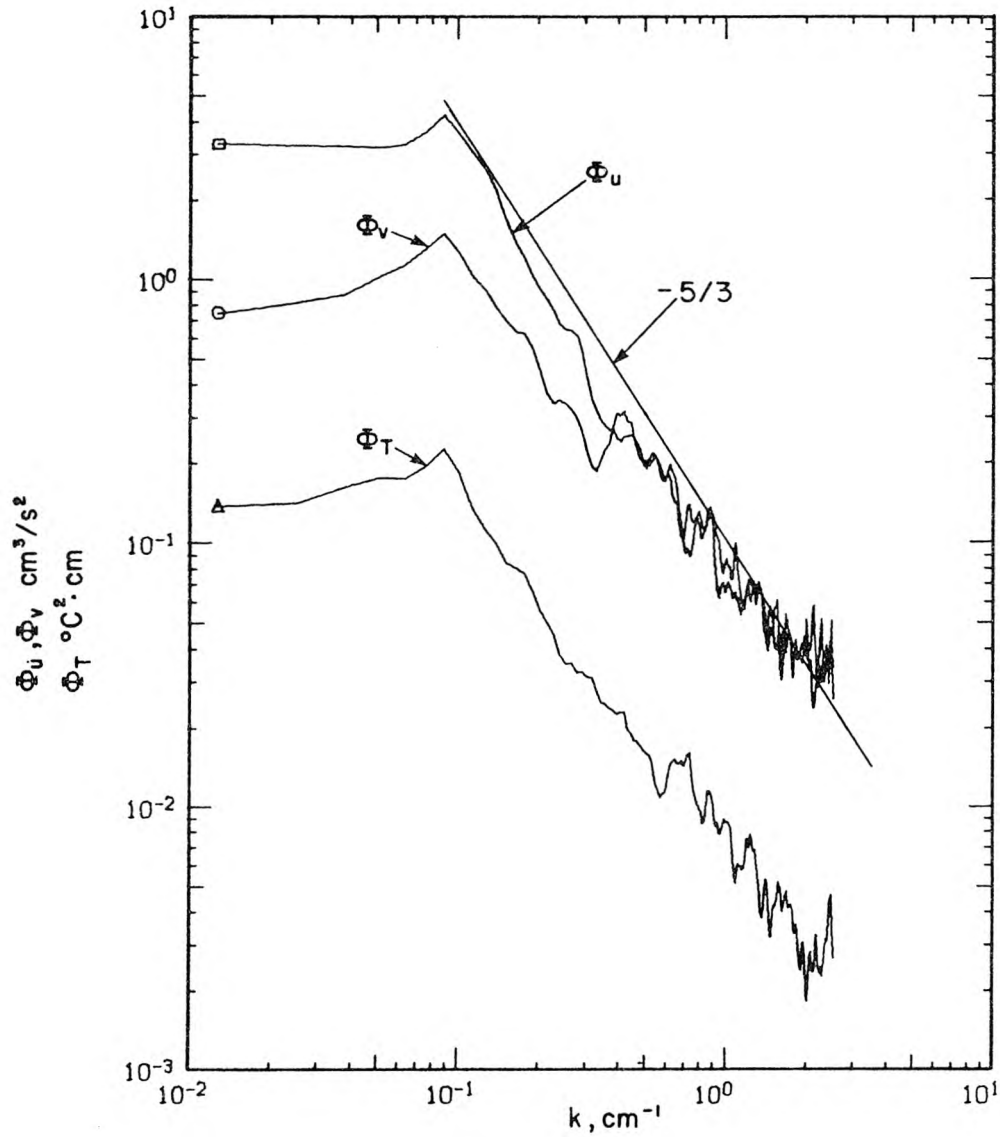

Figure 6.3.22 Power spectral estimates of u', v' and T' in a turbulent region of a stratified flow. Measurements from Experiment BH14, x = 4.7 m, y/h = -0.022. (Refer to Figure 6.3.5 for mean velocity profile at this location)

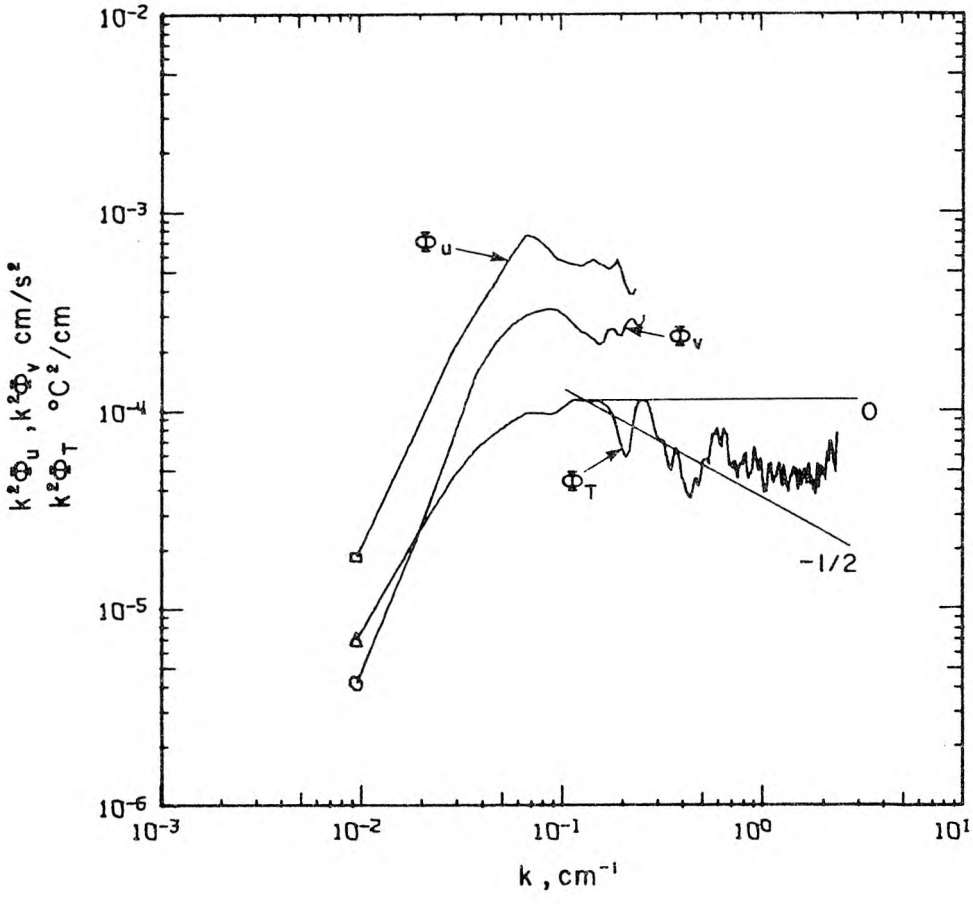

Figure 6.3.23 Power spectral estimates of u', v' and T' in a laminar region of a stratified flow. Measurements from Experiment BH16, x = 24 m, y/h = 0.089, $N^2 = 0.04\ s^{-2}$. (Refer to Figures 6.3.8, 6.3.9, 6.3.19 and 6.3.21 for profiles of mean values at this location)

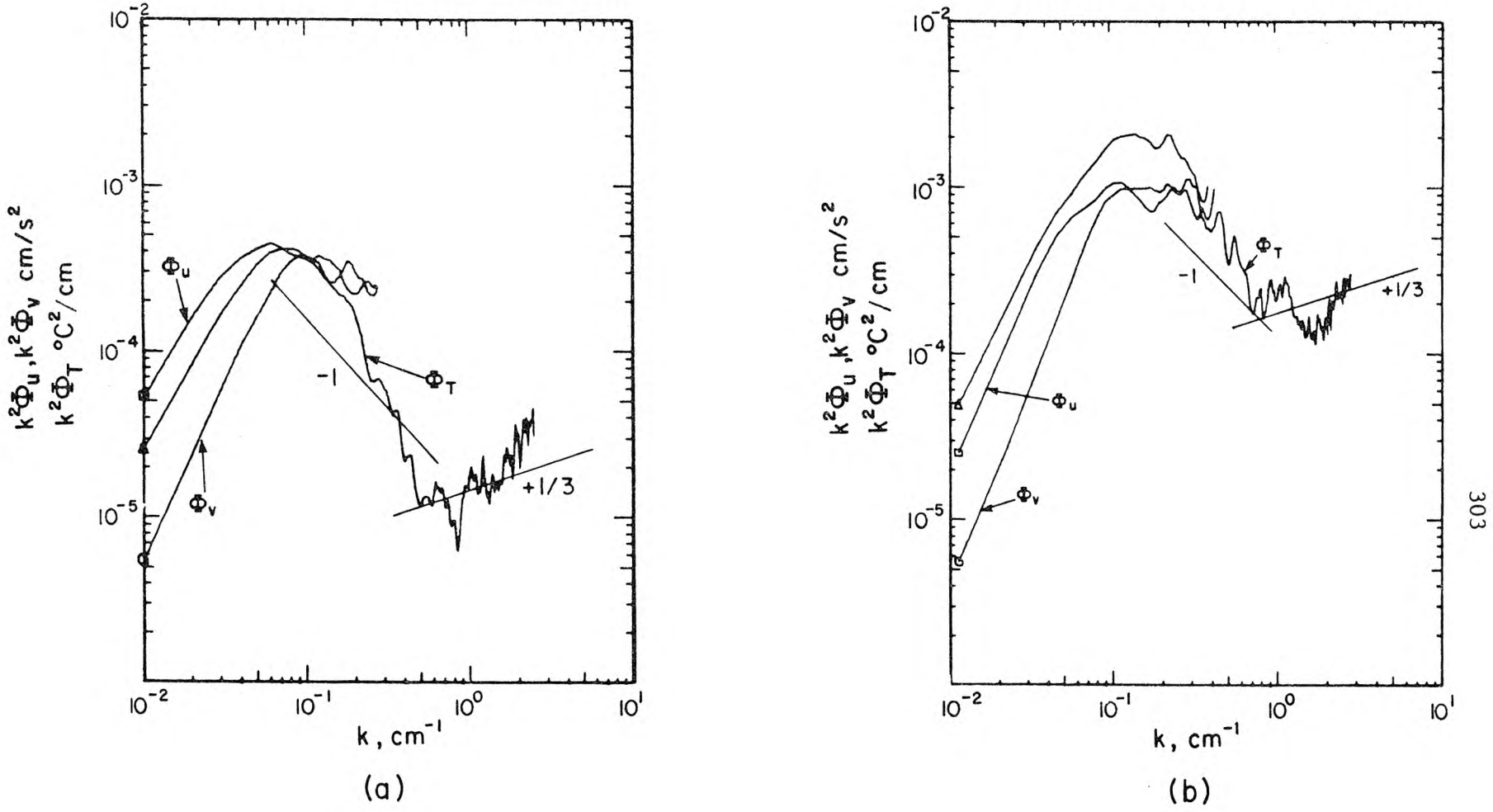

Figure 6.3.24 Power spectral estimates of u', v' and T' in intermittently turbulent regions. Measurements from Experiment BH16, x = 24 m; (a) $N^2 = 0.078\ s^{-2}$, y/h = 0.044, (b) $N^2 = 0.108\ s^{-2}$, y/h = -0.0444. (Refer to Figures 6.3.8, 6.3.9, 6.3.19 and 6.3.21 for profiles of mean values at this location. Refer to Figures 6.3.23 and 6.3.25 for other spectra measured at larger and smaller values of y/h.)

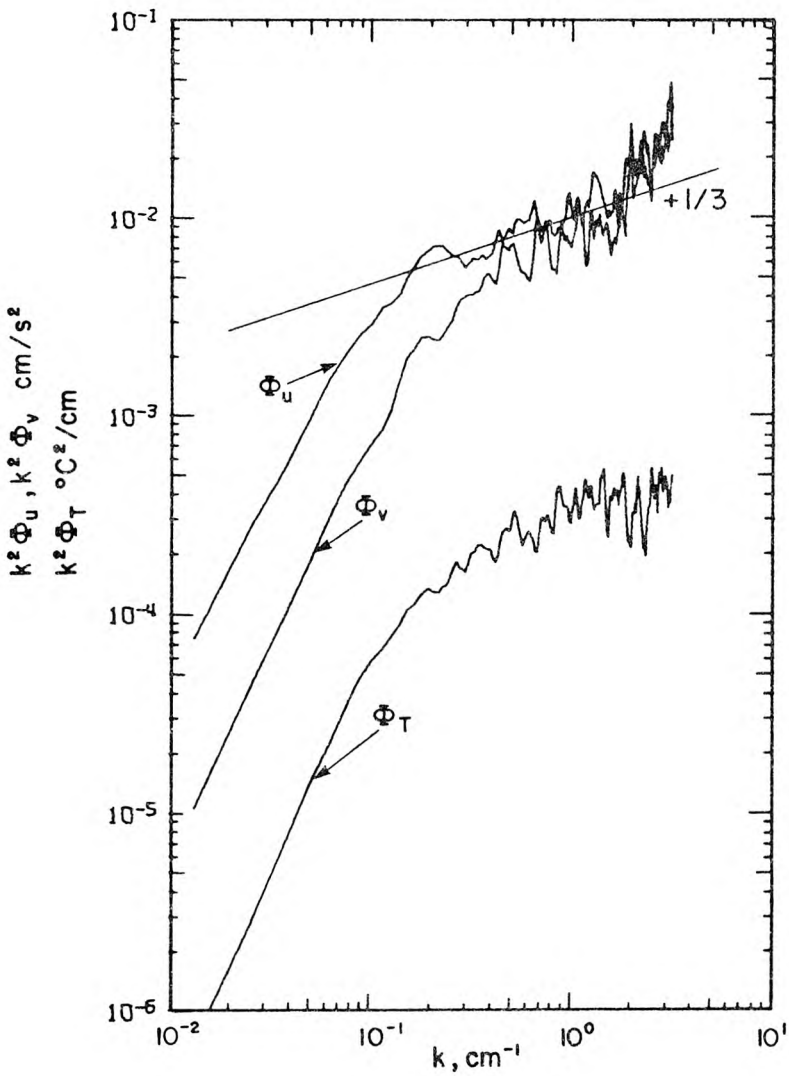

Figure 6.3.25 Power spectral estimates of u', v' and T' in a turbulent region of a stratified flow. Measurements from Experiment BH16, x = 24 m, y/h = -0.0221, $N^2 = 0.005$ s^{-2}. (Refer to Figures 6.3.8, 6.3.9, 6.3.19 and 6.3.21 for profiles of mean values at this location. Refer to Figures 6.3.23 and 6.3.24 for other spectra measured at larger values of y/h.)

interesting since the gross features of the spectra are seen to change as the character of the flow changes. Figure 6.3.23 shows the spectra measured at y/h = 0.089 near the top of the mixed layer. At the higher wave numbers, $\Phi_T(k) \propto k^{-p}$ where p is between 2 and 2.5. As was noted in Section 2.4.1, this type of spectral behavior is typical of internal wave fields; as the flow was observed to be quite laminar in the upper portion of the flow, it is likely that these spectra reflect fluctuations caused by internal waves.

Figures 6.3.24a and 6.3.24b show power spectral estimates measured in the interfacial region. As was mentioned in Section 6.3.3, the profiles of $\overline{v'T'}/U\Delta T_o$ and other evidence indicates that the flow was laminar in this region, with very intermittent wave breaking. The spectra of T' indicate two distinct regions at the higher wave numbers. There is a region in which $\Phi_T(k) \propto k^{-p}$ where p is between three and four, and a region where $\Phi_T(k)$ declines at a slower rate, perhaps as $k^{-5/3}$ at higher wave numbers.

The spectral estimates in Figure 6.3.24a clearly show a decline somewhat faster than k^{-3} for a portion of the wave number domain, so it is not clear that this is the "buoyancy subrange," but the rapid decline of Φ_T with k is indicative of buoyancy effects. Furthermore, the fact that the decline of Φ_T is much more rapid than is typically found in stable regions with internal waves would indicate that totally different processes are involved.

As y/h decreases, the flow eventually becomes fully turbulent and the spectra change character until they become similar to the

spectra shown in Figure 6.3.25. These spectral estimates, measured at y/h = -0.22, indicate that the spectra are fairly constant at the low wave numbers, and then decline approximately as $k^{-5/3}$ at higher wave numbers. Hence, below the interface, the spectra seem not to reflect any effects of the buoyancy forces.

6.3.5 Turbulent Energy Exchange

As a result of the strong stabilizing effects of the density stratification, relatively few data were available which could be used to help establish relationships between useful dimensionless parameters. Consequently, most of the data discussed in this section are from experiments BH7 and BH14, two cases in which the flow did not develop a laminar interface. In the other experiments, which did have laminar interfaces, the mixing was suppressed to such a degree that relatively few data were to be had on turbulent mixing rates.

Figure 6.3.26 shows values of R_f plotted against $\overline{Ri}$ for measurements made in the downstream flow over a smooth bed. Most of the data are bounded by the line $R_f = \overline{Ri}$ (which indicates $K_H/K_m < 1$) and the line $R_f = 0.25$.

Only at the larger values of $\overline{Ri}$ are values of R_f found greater than 0.2. However, as was found in the initial mixing layer, the absolute values of $\overline{B'v'}$ are generally smaller at higher mean-Richardson numbers, so that the higher values of R_f at the higher values of $\overline{Ri}$ do not indicate an increase in mixing compared to the mixing at smaller values of $\overline{Ri}$, but only an increase in the efficiency of mixing (that is, an increase in $\overline{B'v'}$ relative to the turbulent energy production rate

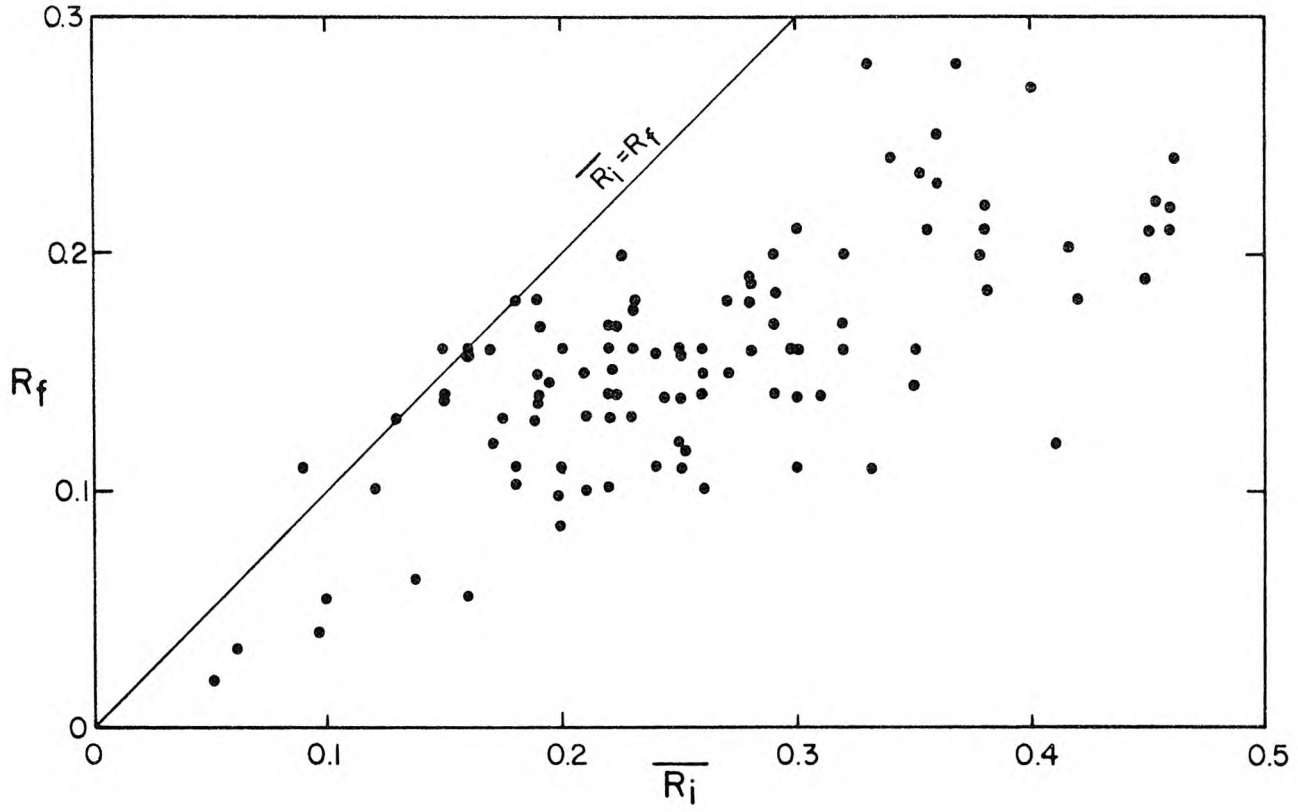

Figure 6.3.26 Values of the flux-Richardson number plotted against the local mean-Richardson number for measurements made in the downstream flow over a smooth bed. Data primarily from Experiments BH7 and BH14.

$-\overline{u'v'}\,\frac{\partial\bar{u}}{\partial y}$). Furthermore, it should be remembered that as $|\overline{B'v'}|$ and $|\overline{u'v'}\,\frac{\partial\bar{u}}{\partial y}|$ decrease, the relative error in R_f will increase, so that the uncertainty of R_f is larger at higher values of $\overline{Ri}$.

While the data in Figure 6.3.26 are scattered, the fact that most of the data have values of R_f less than 0.25 may indicate that a critical value of the flux-Richardson number lies in the neighborhood of this value. Of course, Equations 2.3.7 and 6.2.5 indicate that the critical value of R_f is approached as $\overline{Ri}$ becomes infinite, so that experimental data can only supply a bound for the critical value. However, both Figures 6.3.26 and 6.2.41 indicate that the critical value is probably in the range of 0.2 and 0.3. This is, of course, based on the values of $E^* = \frac{\partial\overline{q^{*2}v'}}{\partial y}\Big/\overline{u'v'}\,\frac{\partial\bar{u}}{\partial y}$ for these experiments.

In the measurements made in the downstream flow over a smooth bed, E^* was generally found between -0.6 and 1.2, while in the mixing layer experiments, E^* was generally found between -0.3 and 0.2. Consequently, the data in Figure 6.3.26 reflect the larger range of values of E^* than the data in Figure 6.2.41.

Figure 6.3.27 shows values of $\overline{B'v'}/\varepsilon^*$ plotted against $\overline{Ri}$. The values of ε^* were calculated using Equation 6.2.6 (Section 6.2.10). The data are very scattered and no general trend was found other than the fact that most of the data lie below the line $\overline{B'v'}/\varepsilon^* = 0.25$, which indicates the inefficiency of the mixing process. It was found that the smaller values of $\overline{B'v'}/\varepsilon^*$ were generally associated with larger values of E^* (that is, $0.4 \leq E^* \leq 1$) while the larger values were generally associated with smaller values of E^*, but the data are

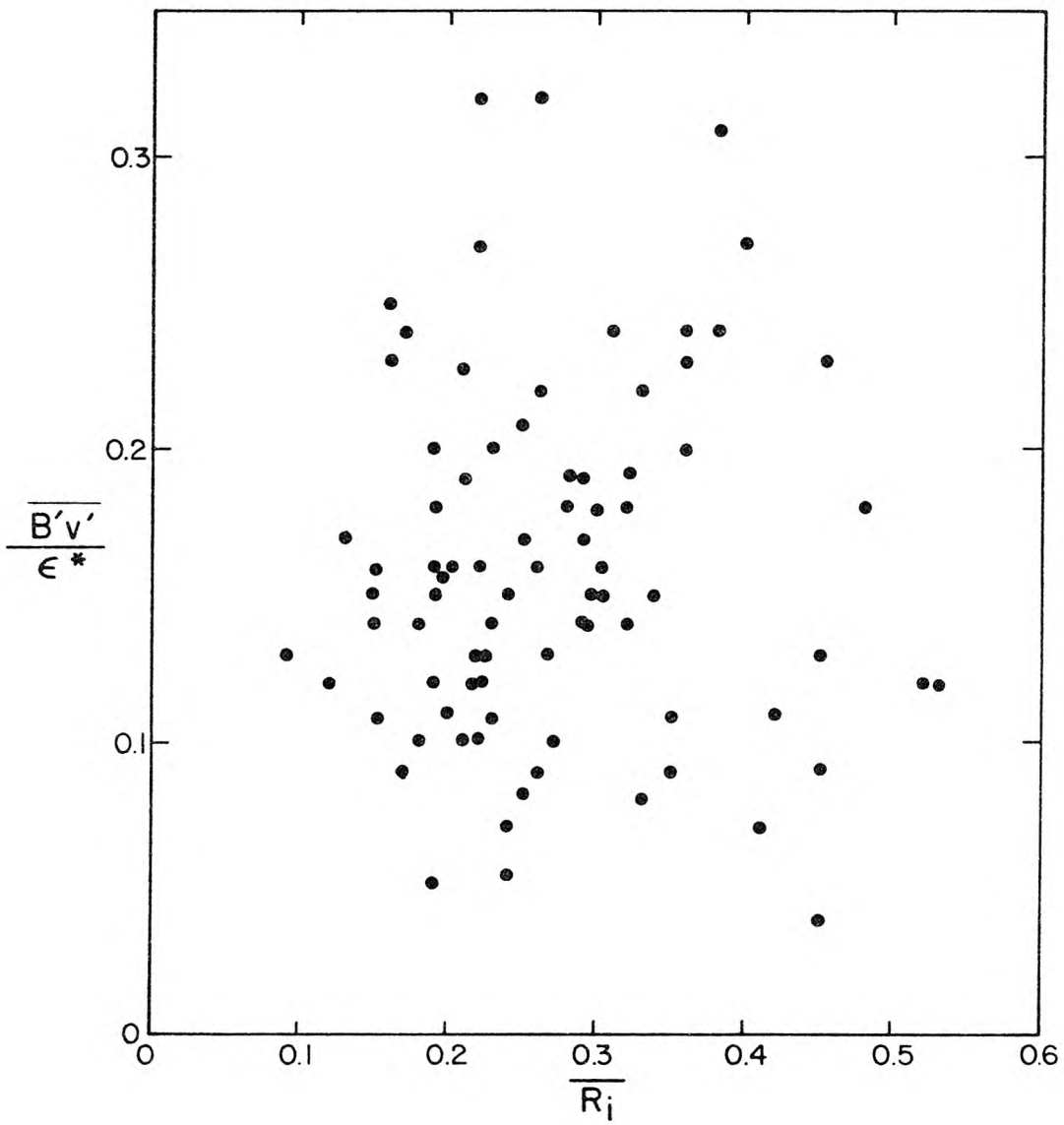

Figure 6.3.27 Values of $\overline{B'v'}/\varepsilon^*$ plotted against the local mean-Richardson number for measurements made in the downstream flow over a smooth bed. Data from Experiment BH14.

so scattered that a firm relationship could not be developed.

The values of ε (for the three-dimensional equation) were calculated as they were in Section 6.2.10, using the measured power spectra and Equation 2.4.1. The ratio $\varepsilon/\varepsilon^*$ was then calculated and found to have a mean value of 1.05 and a standard deviation of 0.4. The correlation coefficient between the calculated values of ε and ε^* was 0.9. Again, as the flow was neither homogeneous nor isotropic, there is no reason to expect the power spectral estimates to conform to the shape of the universal spectrum of Equation 2.4.1, so that the values of ε calculated in this fashion are not necessarily good estimates of the dissipation rate of turbulent kinetic energy. However, as was found in Section 6.2.10, Equations 2.3.3 and 6.2.4 and the assumptions that $\partial\overline{w'^2v'}/\partial y \approx 0$ and $\frac{\partial\overline{w^2}}{\partial x}\Big/\frac{1}{2}\frac{\partial\overline{q^{*2}}}{\partial x} \approx 1$ indicate that $\varepsilon/\varepsilon^* \approx 1.1$. The fact that the values of ε calculated from the power spectra agree so well with this is gratifying, but should be regarded with some caution, since the flow was stratified and Equation 2.4.1 may not be valid for these flows.

6.3.6 Summary of Results for the Downstream Flow Over a Smooth Bed

The most significant result of the measurements in the downstream flow over a smooth bed is the enormous stabilizing effect of a small density gradient on a turbulent flow. This result is typified in all aspects of the measurements, particularly those which are presented in Figures 6.3.26 and 6.3.27. The inefficiency of turbulent mixing process in a density-stratified flow is clearly shown in Figure 6.3.27, in which the ratio of the rate of increase in potential energy,

$\overline{B'v'}$, to the viscous dissipation rate, ε^*, is found to be less than 0.3. The fact that larger values of $\overline{B'v'}$ are generally found only when R_f and $\overline{B'v'}/\varepsilon^*$ are much less than their maximum values further indicates the extreme inefficiency of the mixing process: most of the available turbulent energy is dissipated and only a small fraction works to increase the potential energy of the system.

The fact that laminar shear layers were observed far downstream (Figures 6.3.8, 6.3.9 and 6.3.21) further demonstrates the inhibiting effect that small density gradients have on turbulent mixing processes. This is also seen in cases in which a laminar layer did not develop, yet turbulent intensities were greatly reduced (Figures 6.3.13 - 6.3.15).

Finally, spectral estimates of the fluctuating quantities were obtained, and the spectra were found to change dramatically in different regions of the flow. In particular, the spectra in an internal wave region (Figure 6.3.23) differ substantially from those in a region of intermittent turbulence (Figure 6.3.24). The spectral estimates in fully turbulent regions (Figures 6.3.22 and 6.3.25) generally follow the (-5/3) power law of the inertial subrange over a range of wave numbers, despite the presence of weak density gradients.

6.4 Experimental Results from Measurements Made in the Downstream Flow Over a Roughened Bed

In this section the results from measurements made in the downstream flow over a roughened bed are presented. Details on the initial conditions of these experiments are given in Tables 6.1.1 and 6.1.4.

Vertical profiles of mean quantities which are presented in this

section are shown as a function of y/h, where h is the total flow depth and y is the vertical coordinate, with a zero level arbitrarily defined as the vertical coordinate of the splitter plate (that is, 30 cm above the flume bed). The flow depths shown in Tables 6.1.1 and 6.1.4 are used for normalizations. Therefore, $y/h \approx -0.67$ at the flume bed, while $y/h \approx -0.33$ at the surface. However, it should be noted that when the flume bed was roughened with bricks, the equivalent flow depth over the roughened flume section was 0.5 cm less than the values of h given in Tables 6.1.1 and 6.1.4, and when it was roughened with rocks, the equivalent flow depth was 2.5 cm less.

As in the previous section, the velocity scale used for normalization is U, the overall mean flow speed, and the temperature scale used is ΔT_o, the initial temperature difference between the two layers. The profiles which are presented show the measured values; lines between the points are linearly interpolated.

6.4.1 Profiles of Mean Velocity and Temperature

When the flume bed was roughened, a small density stratification was found to have a substantial effect on the flow, as was the case when the flume bed was smooth. Again, because of the large number of variables involved, the profiles obtained did not lend themselves to simple, similarity descriptions.

Although the flow development over the brick-roughened bed differed in the fine details from the flow over the rock-roughened bed, the basic development was similar in both cases, and the density stratification was found to result in an increase in the mean shear, just as in the

flows over a smooth bed. This can be seen in Figures 6.4.1 and 6.4.2 which show mean velocity profiles for flows over a brick-roughened bed and a rock-roughened bed, respectively.

The profiles shown in Figure 6.4.1 were measured 20 m from the splitter plate. One profile shown is from a homogeneous flow, the other from a flow in which ΔT_o was 0.81°C ($\Delta\rho/\rho_o = 0.24 \times 10^{-3}$); the initial conditions for the two flows were otherwise similar. It is obvious from the figure that the shear is larger in the stratified case.

Figure 6.4.2 shows profiles measured in three flows over the rock-roughened bed. While the inlet speeds for the three cases were similar, the three flows all had different intial temperature differences. Again, these profiles indicate that an increase in the density stratification results in an increase in the mean shear.

Figure 6.4.3 shows two velocity profiles measured 24 m from the splitter plate, one from a stratified flow with a small initial velocity difference, the other from a flow with a similar initial stratification but a larger initial velocity difference. The flow with the larger initial shear exhibits a larger shear 24 m from the splitter plate, even though the flume bed was roughened. It is clear that in these cases the stratification has reduced the vertical momentum flux to such a degree that far downstream the flows are able to retain some features of the initial conditions.

There was one interesting effect which the roughening of the bed had on the flow. It was observed that as the flow progressed down the flume and the fluid speed near the bed decreased because of the bed

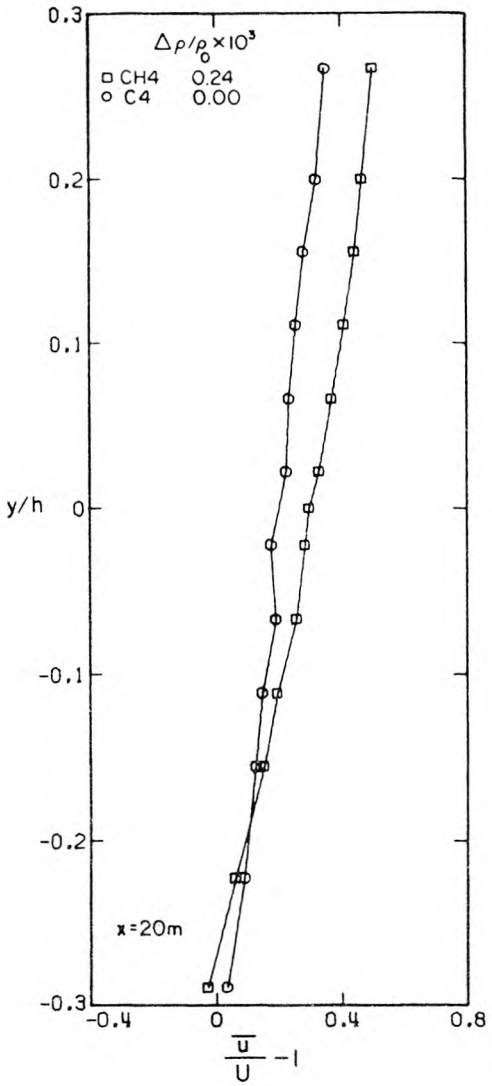

Figure 6.4.1

Mean velocity profiles measured at x = 20 m for two flows over a brick-roughened bed. Symbol key gives: symbol, experiment number, $\Delta\rho/\rho_o \times 10^3$.

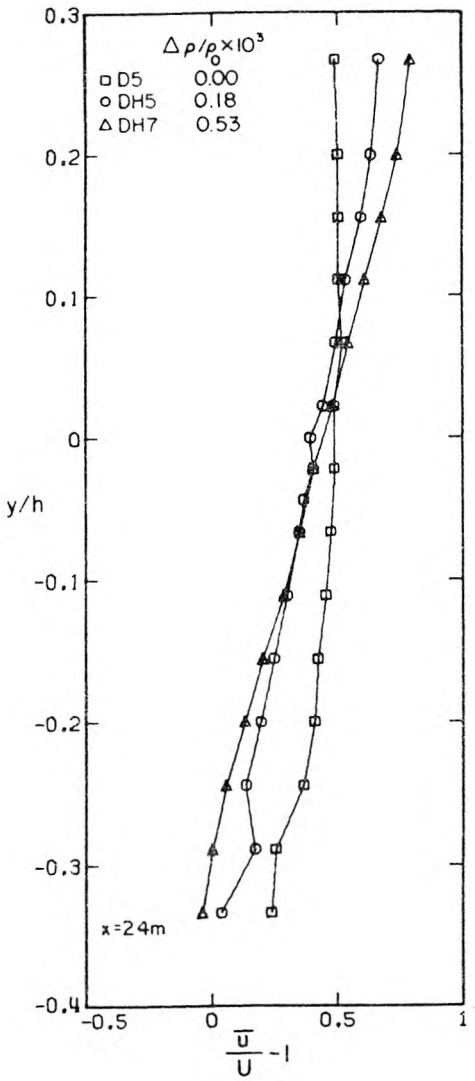

Figure 6.4.2

Mean velocity profiles measured at x = 24 m for flows over a rock-roughened bed. Symbol key gives: symbol, experiment number, $\Delta\rho/\rho_o \times 10^3$.

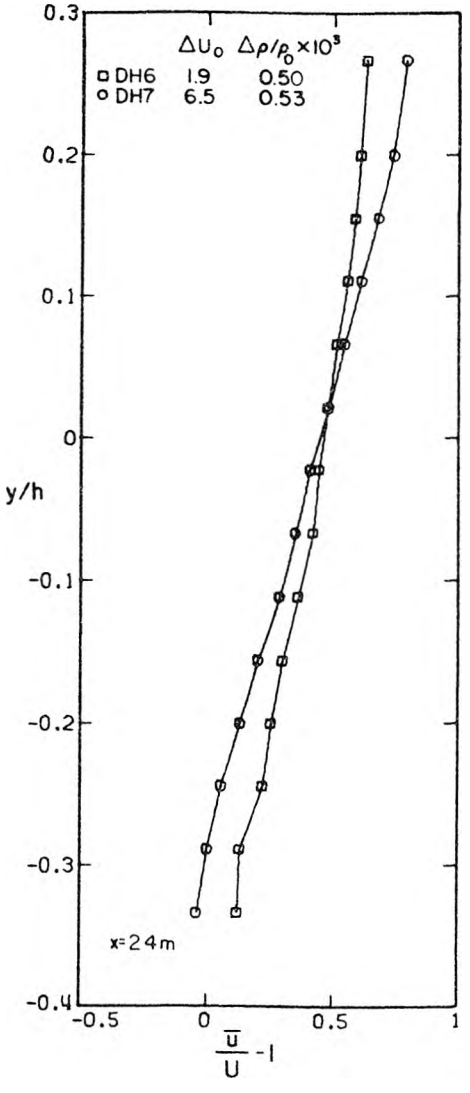

Figure 6.4.3

Profiles of mean velocity, measured 24 m from the splitter plate for two stratified flows with different initial velocity differences. Symbol key gives: symbol, experiment number, ΔU_o (cm/s), $\Delta\rho/\rho_o \times 10^3$.

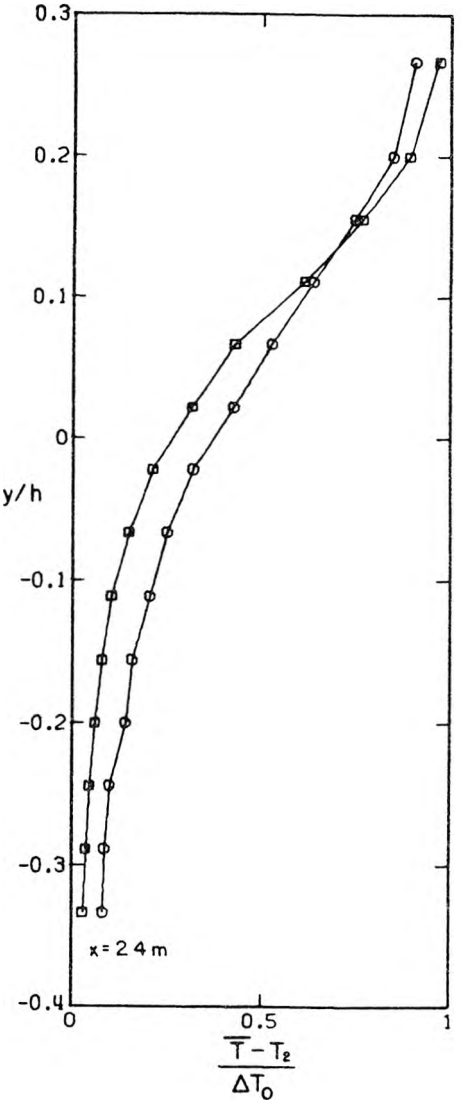

Figure 6.4.4

Profiles of mean temperature measured at x = 24 m for the same flows considered in Figure 6.4.3. Symbols as in Figure 6.4.3.

friction, the fluid near the surface gradually accelerated. If the flow was unstratified, the fluid was able to mix over the depth fairly easily, yielding profiles in the upper portion of the flow with relatively small shear and which changed little with downstream distance. On the other hand, if the flow was stratified, the fluid did not mix easily, and a stronger shear developed; but as the shear increased, the thickness of the upper layer decreased, since the fluid was unable to move freely through the density interface. The thinner upper layers can be seen in Figure 6.4.4, which shows profiles of mean temperature for the same cases considered in Figure 6.4.3. In both the cases shown, the vertical positions of the points at which $(\overline{T} - T_2)/\Delta T_o = 0.5$ were found to rise about 4 cm over the 20 m roughened section. As can be seen in Figure 6.4.4, the interfacial regions of the two flows are well above y/h = 0, the vertical location of the splitter plate.

The fact that the stratification resulted in an increase in shear and a thinning of the upper layer is rather interesting and is considered here in more detail so that general conclusions might be drawn. The integral balances for mass and momentum (Equations 2.5.1 and 2.5.2) were considered for these flows and, in general, the following results were obtained. It was found that while the term $\frac{\partial}{\partial x}\int \overline{u^2}\,dy$ was very significant in the stratified flows, it was negligible in the unstratified flows. Furthermore, $\overline{u}\,\overline{v}$ was found to be small, but not negligible, in the stratified flows, while it was negligible in the unstratified flows. The turbulent momentum flux per unit mass, $-\overline{u'v'}$, was found to be significant in both types of flows. The term $\frac{\partial}{\partial x}\int \overline{p}/\rho_o\,dy$ was

estimated from the measured surface slope of the flow and was found to be able to account for the imbalance. (Since the surface slope was measured over a 31 m section of the flume, and only a 20 m section was roughened, the slope measured over the 31 m section should be scaled up to account for the slope over the roughened section as most of the energy losses occurred over the roughened section (see Section 5.2). In order to balance Equation 2.5.2, it was found that a scale factor of 31/20 was too high while a scale factor of 1.0 was too low, so the correct scaling factor probably lies between 1.0 and 1.5.) The other terms in Equation 2.5.2 were found to be negligible compared to those mentioned above.

The general description of the flows is as follows. In the unstratified case, the fluid can mix relatively freely and the result is a fairly uniform flow in the upper portion. The velocity profile changes very little as the flow progresses downstream, so the time-averaged momentum equation in this case has two dominant terms, the pressure term and the turbulent momentum flux term, which balance each other. All the other terms are relatively small.

The stratified case is much different, however. The shear stress at the bed is nearly the same as the unstratified case (assuming identical inlet conditions in the two cases, with the exception of the initial density difference), so that the surface slope is about the same. This results in a pressure force which is nearly the same as in the unstratified case. The difference lies in the turbulent momentum flux, which is greatly reduced in the stratified case. The

reduction of $-\overline{u'v'}$ which results from the buoyancy effects means that the turbulent shear stress can balance only a portion of the net pressure force. The unbalanced portion of the pressure force accelerates the fluid and the result is an increase in the speed of the upper layer.

One can think of the decrease in $-\overline{u'v'}$ which results from the buoyancy forces as a decrease in the fluid resistance to shear, so that the buoyancy forces allow layers of fluid to slide more easily over each other. With this view in mind, it is easy to understand the reason that the shear increases as the stratification is increased. It is important to remember that the pressure force is responsible for the increase in shear as the flow progresses downstream. There may be other flow situations in which other factors prevent an increase in shear despite the reduction in mixing as the stratification is increased, and the change in the profiles of $\bar{u}$ may not be the same as those found in this study. (An example would be the three-dimensional spread of a buoyant fluid from a point source.) However, one could still expect to find a decrease in the turbulent momentum flux with an increase in stratification, and a possible alteration of the flow as a result.

6.4.2 Profiles of $\sqrt{\overline{u'^2}}$, $\sqrt{\overline{v'^2}}$ and $-\overline{u'v'}$

Just as was found in the downstream flow over a smooth bed, the stabilizing effect of the density stratification was very apparent in the profiles of $\sqrt{\overline{u'^2}}$, $\sqrt{\overline{v'^2}}$ and $-\overline{u'v'}$ measured over the roughened beds. This can be seen very clearly in Figures 6.4.5 and 6.4.6, which

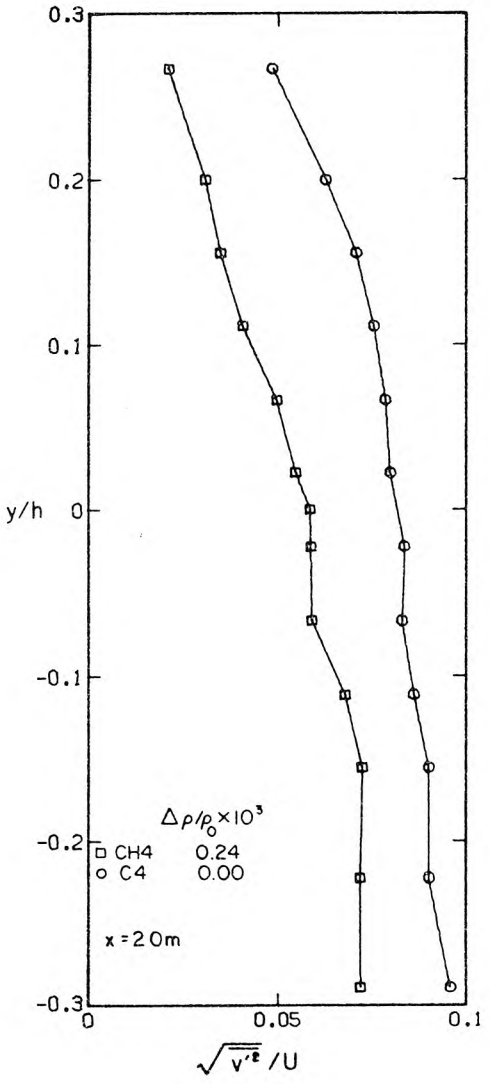

Figure 6.4.5

Profiles of $\sqrt{\overline{v'^2}}/U$ for the same cases shown in Figure 6.4.1 measured at x = 20 m. Symbol key gives: symbol, experiment number, $\Delta\rho/\rho_o \times 10^3$.

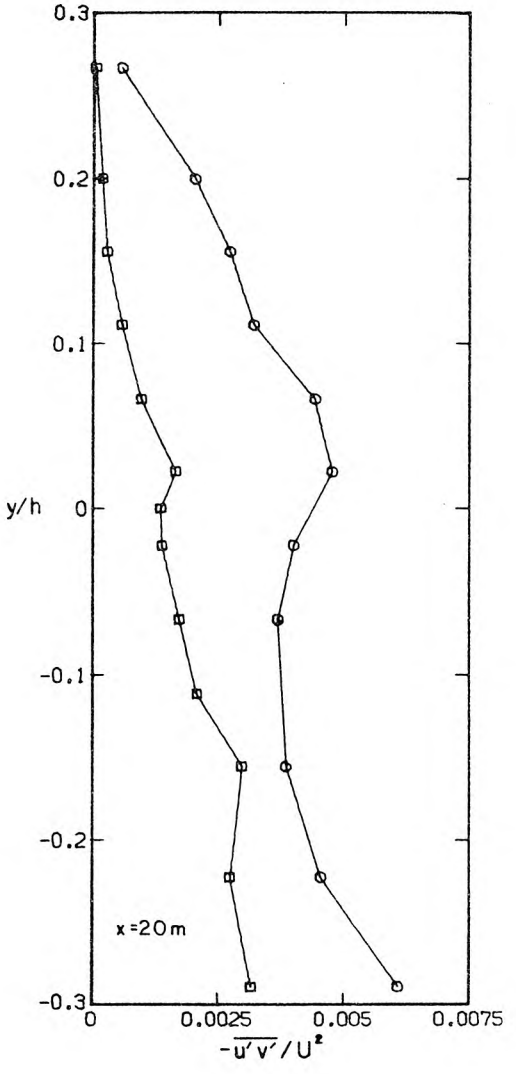

Figure 6.4.6

Profiles of $-\overline{u'v'}/U^2$ for the same cases shown in Figures 6.4.1 and 6.4.5 measured at x = 20 m. Symbols as in Figure 6.4.5.

show profiles of $\sqrt{\overline{v'^2}}/U$ and $-\overline{u'v'}/U^2$ for the same cases considered in Figure 6.4.1. The figures show rather large reductions in the measured values of $\sqrt{\overline{v'^2}}/U$ and $-\overline{u'v'}/U^2$ in the flow in which ΔT_o was only 0.8°C $\left(\frac{\Delta\rho}{\rho_o} = 2.4 \times 10^{-4}\right)$, compared to the unstratified, but otherwise similar, flow. What is more interesting is the fact that because the shear in the unstratified case is less than the stratified case, the turbulent diffusivity of momentum, K_m, is very much smaller in the stratified case. In fact, for the region $-0.3 \leq y/h \leq 0$, the ratio $(K_m)_u/(K_m)_s$ (where the subscripts u and s denote the unstratified and stratified cases, respectively) is about 3.4, which is remarkable when one considers the very small initial density difference in the stratified case.

The fact that it is important to consider the value of K_m when comparing values of $-\overline{u'v'}$ is seen from the profiles of Figures 6.4.7, 6.4.8 and 6.4.9 which show the turbulent intensities and the momentum fluxes for the same flows considered in Figure 6.4.2. The comparison of these three flows is interesting in that they all had similar inlet conditions, with the exception of their initial density differences, and as a result, the flow development was different in each case. It was observed visually that a laminar shear layer developed upon the collapse of the initial mixing layer only in the most stratified case considered here (although far downstream the boundary-generated turbulence caused this laminar layer to break down) and that the flow was always turbulent in the more weakly stratified case. The velocity measurements made 24 m downstream indicate that the turbulent intensities (shown in Figures 6.4.7 and 6.4.8) in the unstratified case

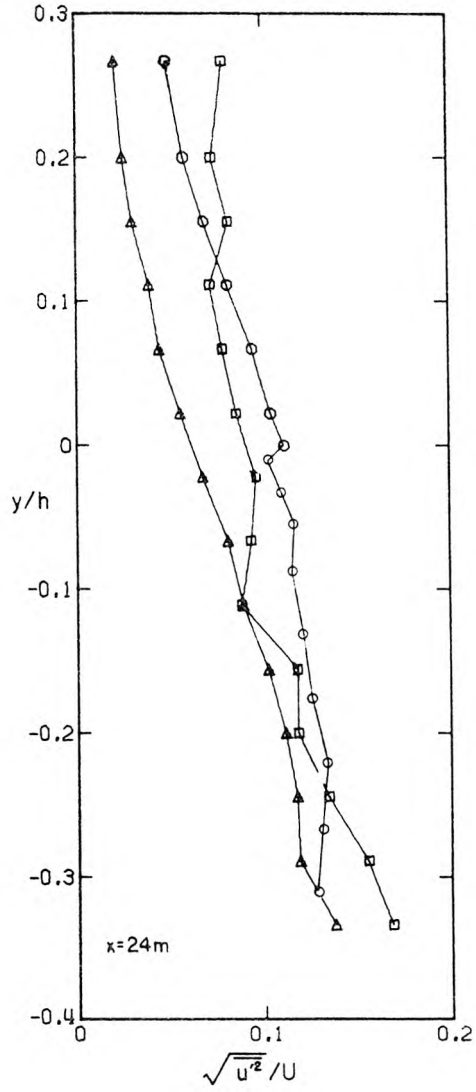

Figure 6.4.7
Profiles of $\sqrt{\overline{u'^2}}/U$ for the same flows considered in Figure 6.4.2. x = 24 m, symbols as in Figure 6.4.9.

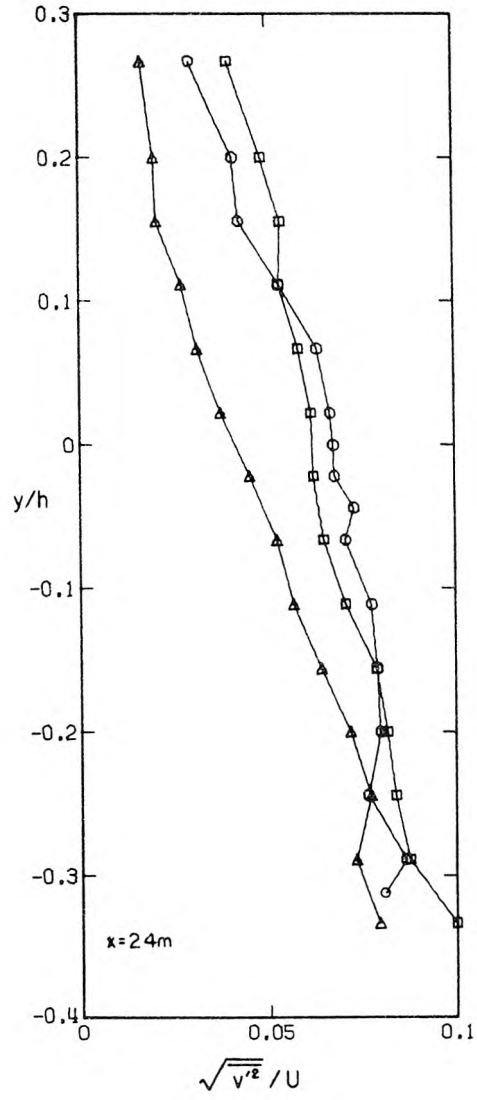

Figure 6.4.8
Profiles of $\sqrt{\overline{v'^2}}/U$ for the same flows considered in Figure 6.4.2. x = 24 m, symbols as in Figure 6.4.9.

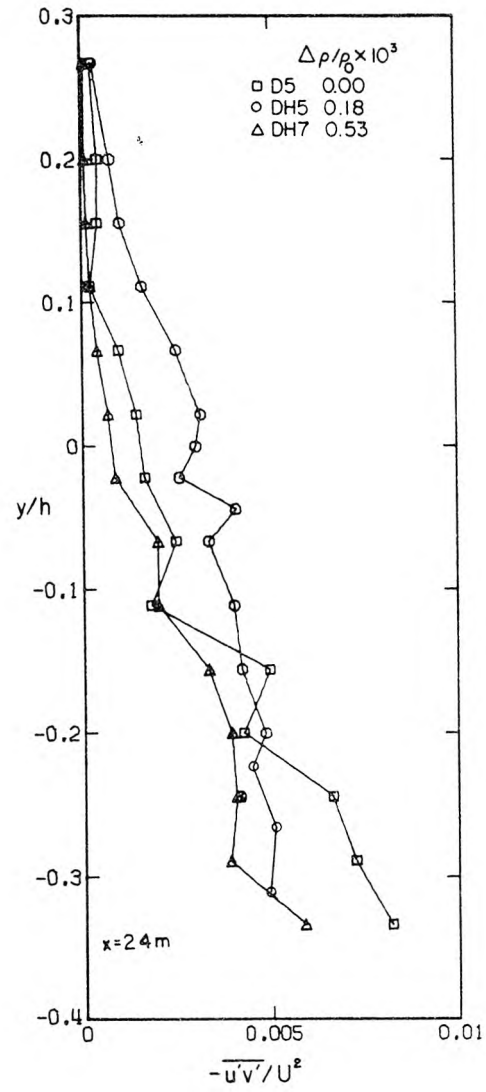

Figure 6.4.9.
Profiles of $-\overline{u'v'}/U^2$ for the same flows considered in Figures 6.4.2, 6.4.7 and 6.4.8. x = 24 m. Symbol key gives: symbol, experiment number, $\Delta\rho/\rho_o \times 10^3$.

(Experiment D5) and the weakly stratified case (Experiment DH5, $\frac{\Delta\rho}{\rho_o} = 1.8 \times 10^{-4}$) were nearly the same throughout the flow, while in the strongly stratified case (Experiment DH7, $\frac{\Delta\rho}{\rho_o} = 5.3 \times 10^{-4}$) they were much lower.

However, when one considers the turbulent momentum flux, it is seen in Figure 6.4.9 that the largest values of $-\overline{u'v'}/U^2$ in the upper portion of the flows belong to the weakly stratified flow; the most stratified case has the smallest values of $-\overline{u'v'}/U^2$ over the range of y/h shown, while the unstratified case has the largest values only at the smaller values of y/h. An examination of Figure 6.4.2 reveals that the unstratified case has a very flat profile for the mean velocity, which accounts for its smaller values of $-\overline{u'v'}/U^2$ at larger values of y/h. The weakly stratified case, which was completely turbulent, has a mean velocity profile which exhibits rather more shear, thus accounting for the larger values of $-\overline{u'v'}/U^2$.

If one considers the values of K_m/ν for these three cases, one finds that K_m/ν ranges from 270 to over 1000 in the unstratified case (with the larger values found in the upper portion of the flow where the shear was small) while K_m/ν ranges from about 50 to 170 in the weakly stratified case (with the smaller values found in the upper portion of the flow), and it ranges from about 4 to 120 in the most stratified case considered here (with the smaller values again found in the upper portion of the flow). Thus, for stably stratified flows, the values of $-\overline{u'v'}/U^2$ may not always be decreased compared to unstratified flows, but K_m/ν definitely is sharply reduced.

From the three cases considered in Figures 6.4.7 - 6.4.9, one can see that an increase in stratification results in a decrease in the mixing rate as measured by the value of K_m, and also that the momentum flux in a weakly stratified flow appears to be related to the mean shear. In more strongly stratified flows, the momentum flux does not seem to be strongly related to small changes in the shear, as is indicated in the profiles of $-\overline{u'v'}/U^2$ and $\bar{u}/U$ for Experiment DH7, which are shown in Figures 6.4.9 and 6.4.2.

Further evidence that the turbulence is not greatly affected by the amount of shear in a strongly stratified flow is shown in Figures 6.4.10 - 6.4.12 which present profiles of $\sqrt{\overline{u'^2}}/U$, $\sqrt{\overline{v'^2}}/U$ and $-\overline{u'v'}/U^2$ for the two cases considered in Figure 6.4.3. The initial temperature differences in these two flows (Experiments DH6 and DH7) were nearly the same, while the initial velocity difference in the flow of Experiment DH7 was much larger than that of Experiment DH6; the result was a much larger amount of shear downstream in flow of Experiment DH7, as can be seen in Figure 6.4.3. The mean temperature profiles, shown in Figure 6.4.4, are similar in some respects, particularly in the vertical gradients in the region of $y/h < 0$. However, the normalized turbulence intensities, shown in Figure 6.4.10 and 6.4.11 are nearly identical in the two cases, as are the measured values of the momentum flux, shown in Figure 6.4.12. It appears that the mechanism of momentum transfer is so completely dominated by buoyancy forces in these cases that the difference in shear that existed between the two flows had a negligible effect.

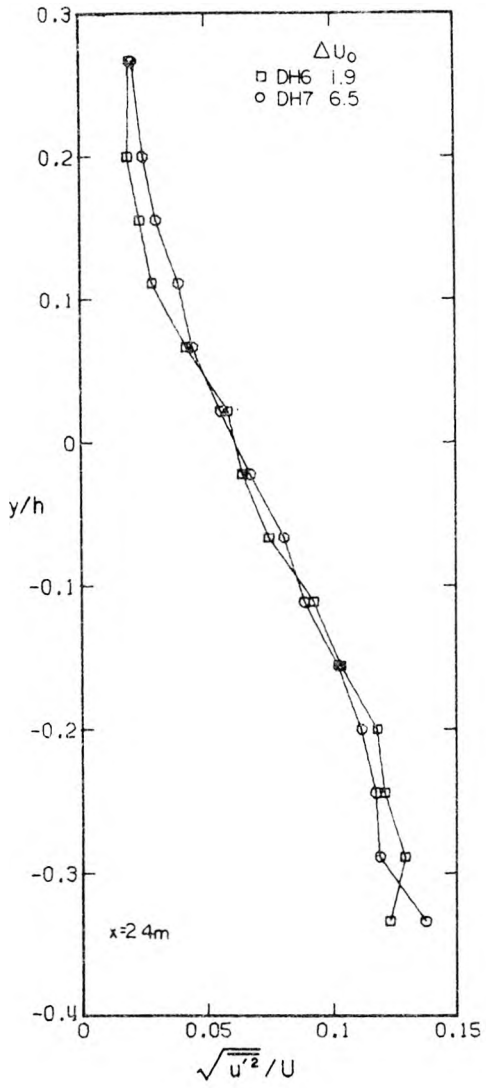

Figure 6.4.10
Profiles of $\sqrt{\overline{u'^2}}/U$ for the same flows shown in Figure 6.4.3. x = 24 m. Symbol key gives: symbol, experiment number, ΔU_o (cm/s).

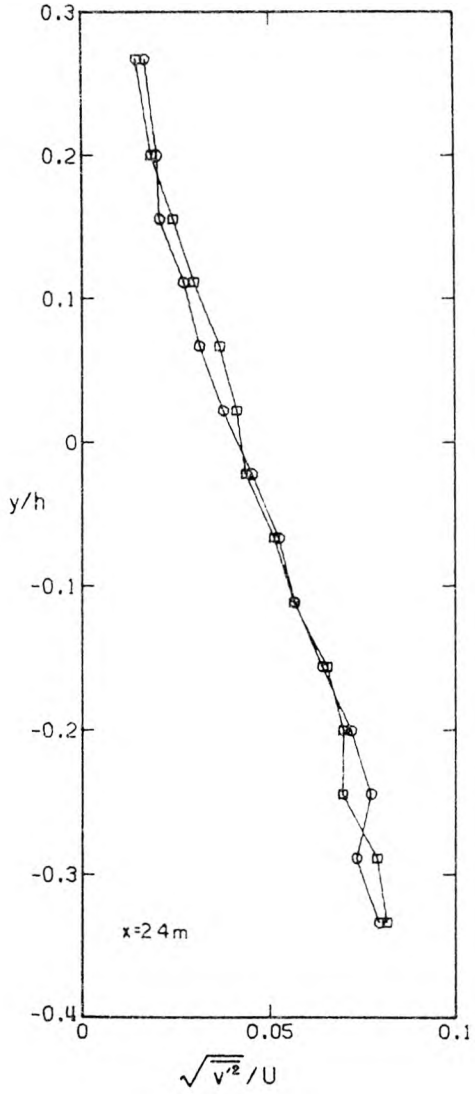

Figure 6.4.11
Profiles of $\sqrt{\overline{v'^2}}/U$ for the same flows shown in Figure 6.4.3. x = 24 m. Symbols as in Figure 6.4.10.

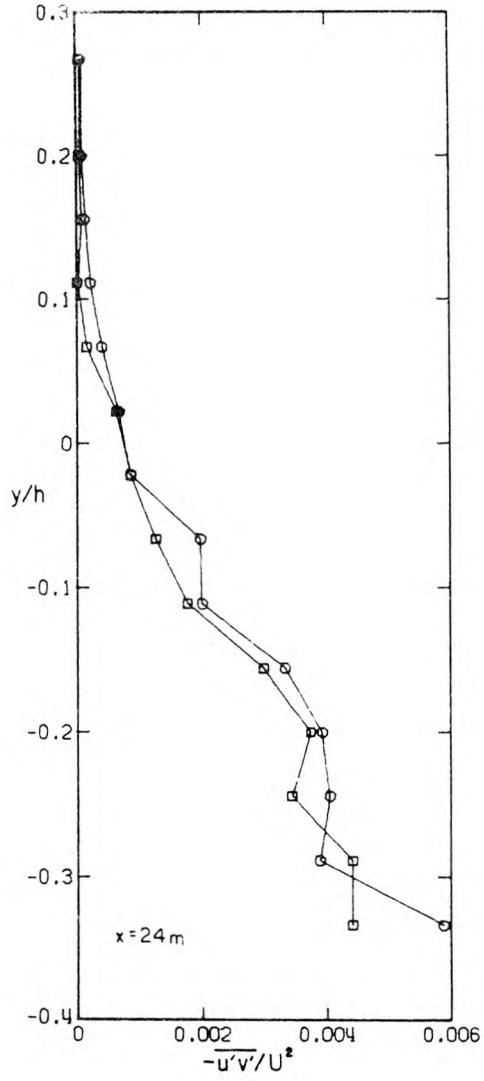

Figure 6.4.12
Profiles of $-\overline{u'v'}/U^2$ for the same flows shown in Figure 6.4.3. x = 24 m. Symbols as in Figure 6.4.10.

It is clear then that a small density stratification can drastically change the character of a turbulent flow. In Section 6.5, evidence is presented which indicates that the turbulence in these flows is dominated by large, turbulent bursts, and it appears that the interaction of these turbulent bursts with the buoyant forces in stratified flows is largely responsible for the effects shown in this section. Further discussion of these ideas is presented in Section 7.3.

6.4.3 Profiles of $\sqrt{\overline{T'^2}}$ and $-\overline{v'T'}$

For the most part, the values of $\sqrt{\overline{T'^2}}/\Delta T_o$ appeared to be related to the local mean temperature gradients. An example is shown in Figure 6.4.13, which presents profiles of $\sqrt{\overline{T'^2}}/\Delta T_o$, measured 24 m from the splitter plate for the same cases considered in Figures 6.4.3 and 6.4.4. In general, the larger values of $\sqrt{\overline{T'^2}}/\Delta T_o$ are found in the regions in which the mean temperature profiles (shown in Figure 6.4.4) have the highest gradients. One should remember, however, that the temperature fluctuations are a function not only of the local temperature gradient, but also the local turbulence intensity; thus, a perfect correlation with temperature gradient should not be expected.

Of somewhat more interest are the profiles of $-\overline{v'T'}/U\Delta T_o$ as these indicate the rate of increase of potential energy in the flow. Figure 6.4.14 shows profiles of $-\overline{v'T'}/U\Delta T_o$ for the two stratified cases which were considered in Figure 6.4.2. It is interesting to note that the more weakly stratified case shown (Experiment DH5) had values of $-\overline{v'T'}/U\Delta T_o$ larger than those for the more stratified case. As was mentioned previously, the flow in Experiment DH5 was always turbulent,

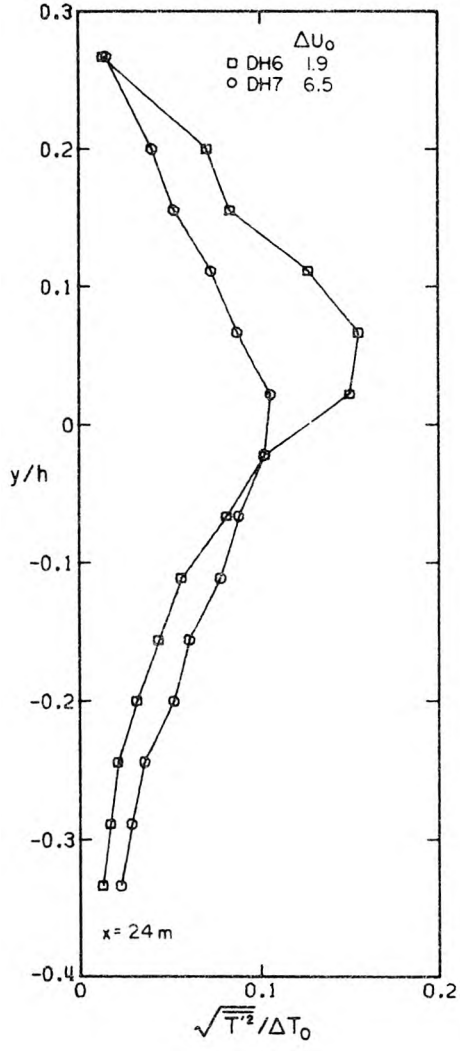

Figure 6.4.13
Profiles of $\sqrt{\overline{T'^2}}/\Delta T_0$ for the same cases considered in Figures 6.4.3 and 6.4.4. Symbol key gives: symbol, experiment number, ΔU_0 (cm/s). x = 24 m.

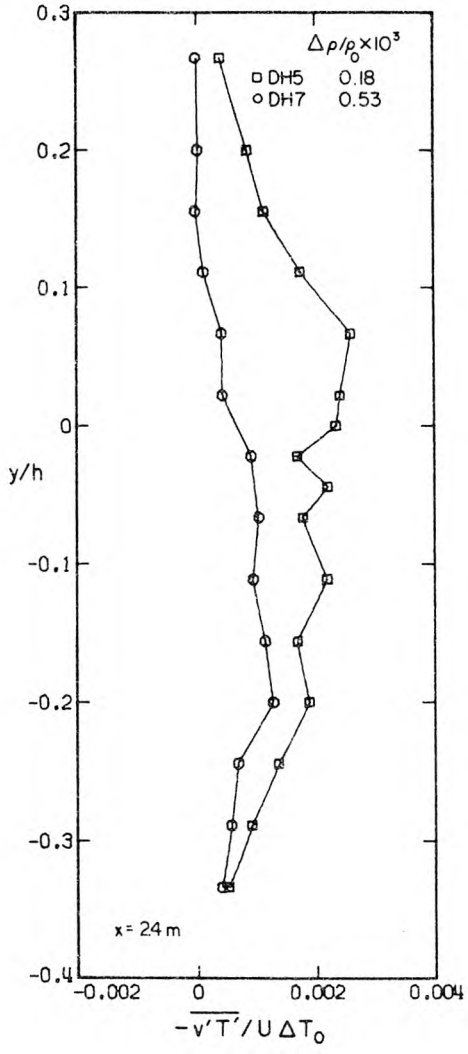

Figure 6.4.14
Profiles of $-\overline{v'T'}/U\Delta T_0$ for the stratified flows considered in Figures 6.4.1 and 6.4.7 - 6.4.9. Symbol key gives: symbol, experiment number, and $\Delta\rho/\rho_0 \times 10^3$. x = 24 m.

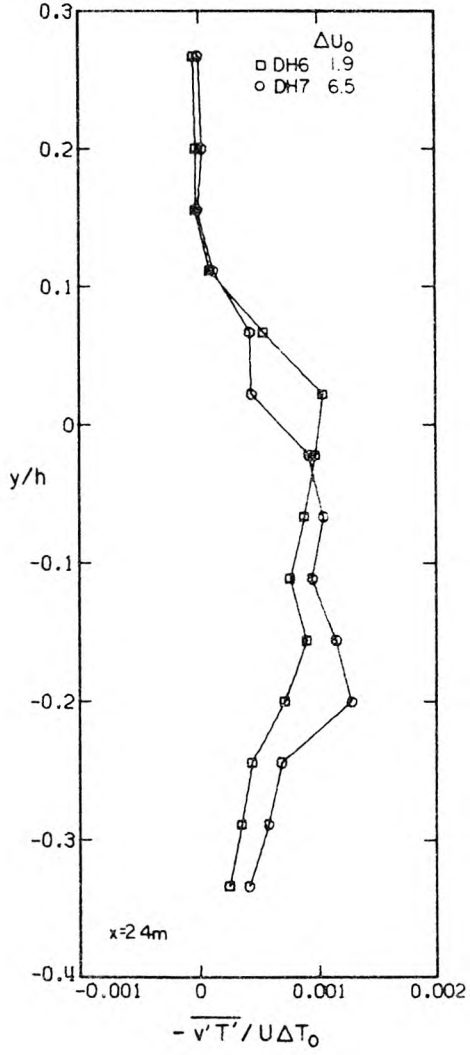

Figure 6.4.15
Profiles of $-\overline{v'T'}/\Delta T_0$ for the same cases considered in Figures 6.4.3, 6.4.4, 6.4.10 - 6.4.12 and 6.4.13. Symbol key gives: symbol, experiment number, ΔU_0 (cm/s).

while the flow in Experiment DH7 had a laminar interface for some distance downstream of the initial mixing layer. At the location at which the profile shown in Figure 6.4.14 was measured, the boundary-generated turbulence had begun to break down the laminar interface. The effects of buoyancy forces are evident in Figures 6.4.14, however, as $-\overline{v'T'}/U\Delta T_o$ was smaller in the more stratified case.

In Section 6.4.2 it was shown that two stratified flows with different mean velocity profiles had nearly identical turbulence levels (Figures 6.4.3, 6.4.4 and 6.4.10 - 6.4.12). The profiles of $-\overline{v'T'}/U\Delta T_o$ for these two cases are shown in Figure 6.4.15 and they are quite similar, even though the profiles of $\sqrt{\overline{T'^2}}$ for these two cases are different, especially in the upper portion of the flow (Figure 6.4.13). The correlation between v' and T' was small in the upper portion of these flows as the boundary-generated turbulence was just beginning to mix through the interface here and the flow was only intermittently turbulent. Thus, while the value of ΔU_o was quite different between the two cases, resulting in different interface thicknesses and velocity profiles downstream (as can be seen in Figures 6.4.3 and 6.4.4), the average turbulence transport properties far downstream were nearly identical in these two flows. Again, the reason that the turbulence properties here seem to be weakly dependent upon the shear is a result of the large effects of the small density stratification and the nature of the boundary-generated turbulence.

6.4.4 Power Spectral Estimates of Fluctuating Quantities

In this section a few examples of power spectra measured

in the downstream flow over roughened beds are presented. The wave number, k, is calculated using Equation 6.2.2 and the spectral estimates, Φ, are calculated using Equation 6.2.3 (Section 6.2.8).

Figure 6.4.16 shows the spectral estimates of u', v' and T' which were measured 12 m from the splitter plate in the lower portion of the density interface. The flume in this case was roughened with bricks, and the initial temperature difference in the flow was 2.67°C (Experiment CH3, $\frac{\Delta\rho}{\rho_o} = 7.9 \times 10^{-4}$). At this distance downstream, the fluid in the interfacial region was largely laminar, but there was some occasional internal wave breaking in the region. The spectral estimates in Figure 6.4.16 indicate that for a range of wave numbers, the power spectra behave as k^{-3} at this location, while at the higher wave numbers, the slope of the power spectrum of T' appears to behave as $k^{-5/3}$. As discussed in Section 2.4.1, one would expect this sort of behavior in the power spectra of a turbulent fluid in which buoyancy effects dominate the energy transfer. Similar behavior was found in very stratified flows over a smooth bed (Section 6.3.4), and these spectral estimates may indicate the existence of the "buoyancy subrange" in some regions of these stratified flows. The fact that it is often difficult to accurately measure the functional behavior of spectral estimates, (it being difficult, for example, to differentiate between a -5/3 slope and a -2 slope) indicates that one should be cautious when interpreting these power spectra. Nevertheless, these spectra do tend to indicate the presence of the "buoyancy subrange."

Figure 6.4.17 shows power spectral estimates measured below the

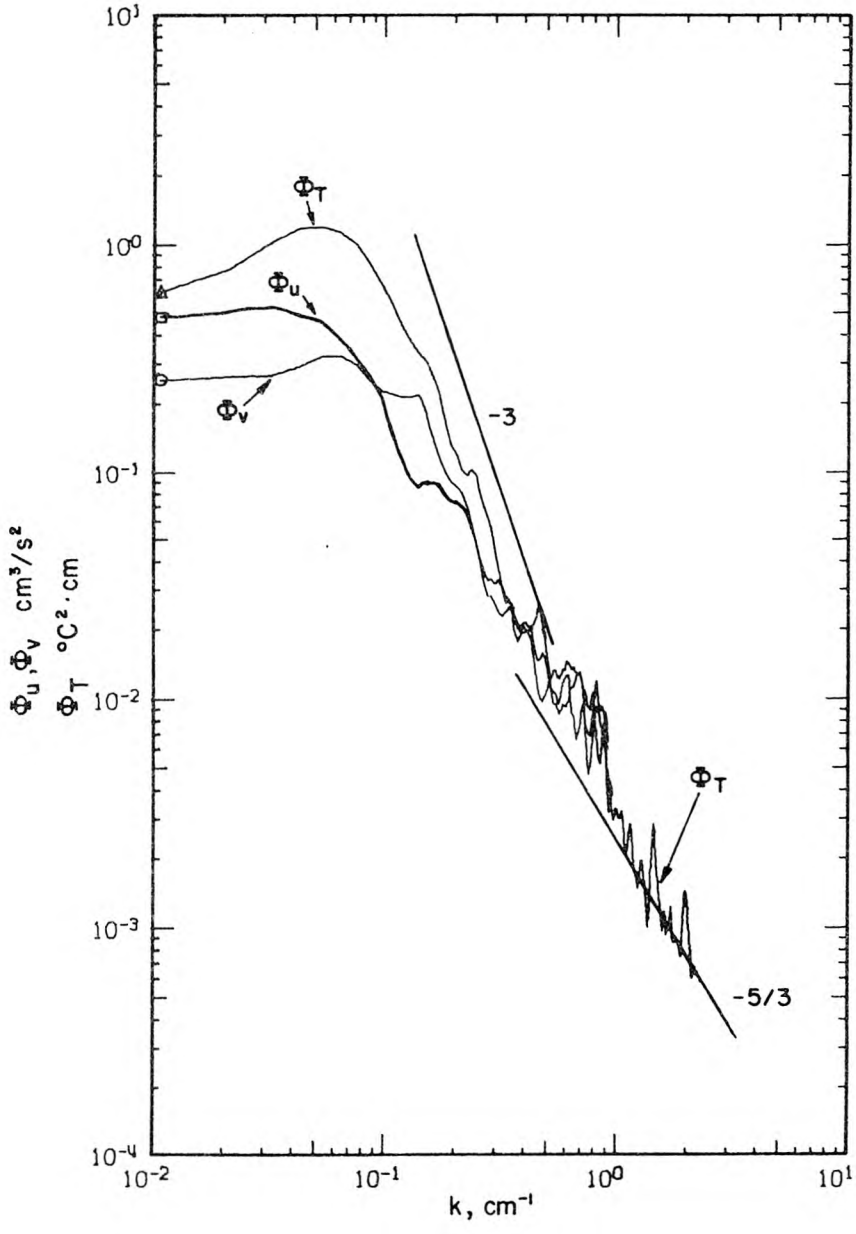

Figure 6.4.16 Power spectral estimates of u', v', and T', measured 12 m from the splitter plate. Data from Experiment CH3, y/h = 0, $N^2 = 0.087\ s^{-2}$.

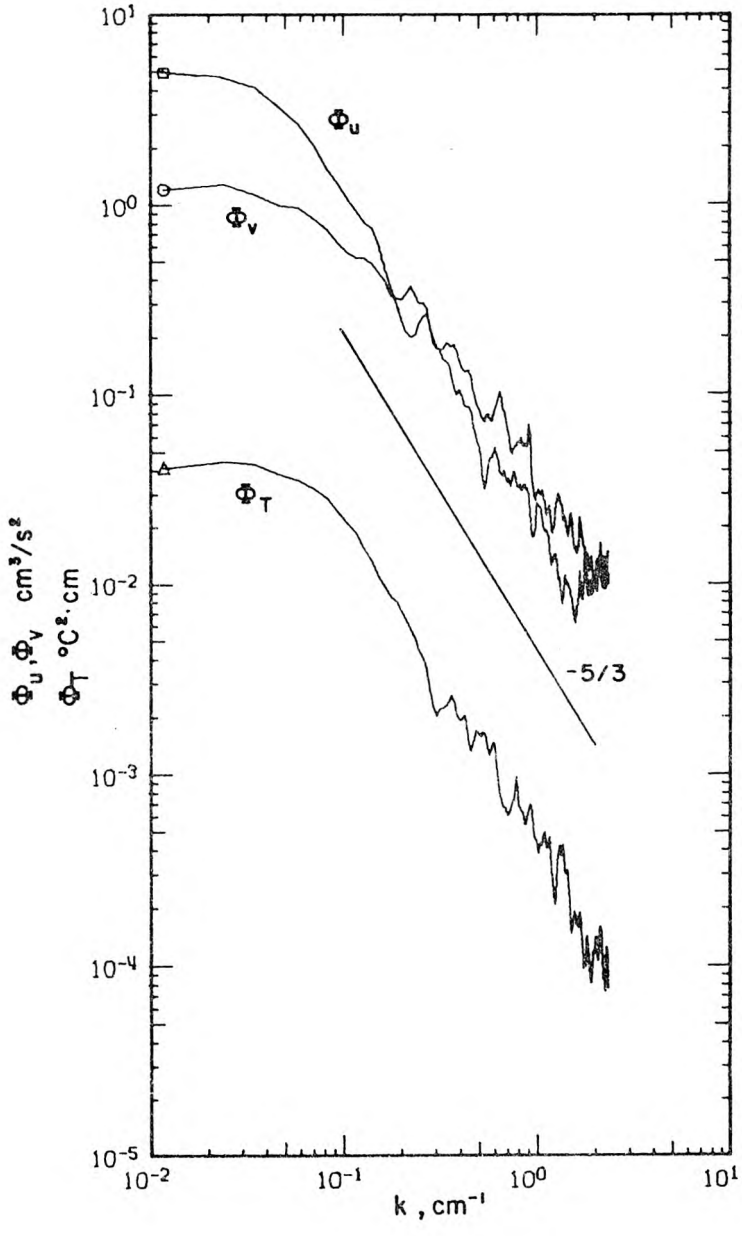

Figure 6.4.17 Power spectral estimates of u', v' and T' measured 12 m from the splitter plate. Data from Experiment CH3, y/h = -0.18, $N^2 = 0.005\ s^{-2}$.

interfacial region of the same flow considered in Figure 6.4.16. In this region of the flow, the power spectra behave as $k^{-5/3}$ at the higher wave numbers, as one would expect to be the case in the inertial subrange. The flow in this region was turbulent although the turbulence was suppressed to some degree by buoyancy forces. The spectral estimates of u', v' and T' shown here are typical of spectra found in turbulent regions, both in their individual behaviors as a function of wave number, and in their similarities in shape.

Finally, Figure 6.4.18 shows the power spectral estimates of u', v' and T' measured 24 m downstream of the splitter plate in the interfacial region of the same flow considered in Figures 6.4.16 and 6.4.17. The interface had begun to break down and slowly mix at this distance, and the "buoyancy subrange" can no longer be seen in the spectral estimates. Thus, it appears that even a moderate amount of turbulence is sufficient to alter the power spectral estimates in such a way that buoyancy effects are not easily discerned from the spectra alone.

6.4.5 Turbulent Energy Exchange

The measurements in the flows over roughened beds provided a large amount of data on the mixing rates in density-stratified shear flows. In this section several interesting results from these measuremeants are presented and discussed.

Figure 6.4.19 shows values of R_f plotted against $\overline{Ri}$ from measurements made in weakly stratified flows over roughened beds (Experiments CH4, $\frac{\Delta\rho}{\rho_o} = 2.4 \times 10^{-4}$, and DH5, $\frac{\Delta\rho}{\rho_o} = 1.8 \times 10^{-4}$). Some of the profiles of mean values measured in the flows under consideration in Figure

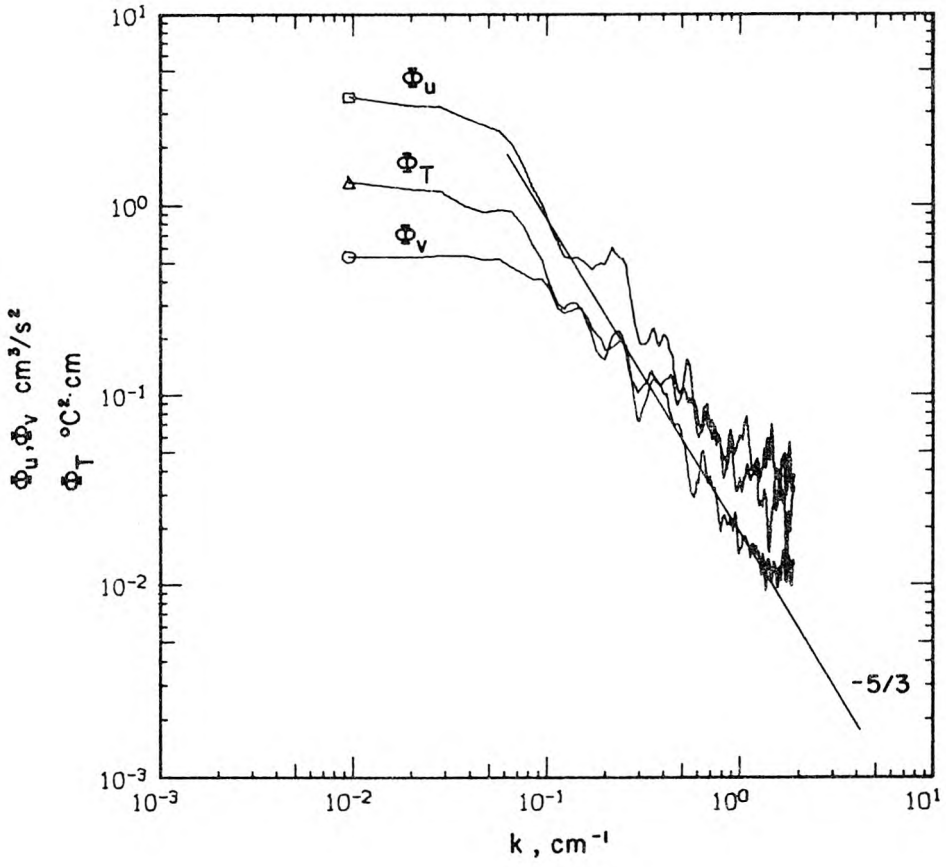

Figure 6.4.18 Power spectral estimates of u', v', and T' measured 24 m from the splitter plate in the interfacial region. Data from Experiment CH3, y/h = 0.02, N^2 = 0.065 s^{-2}.

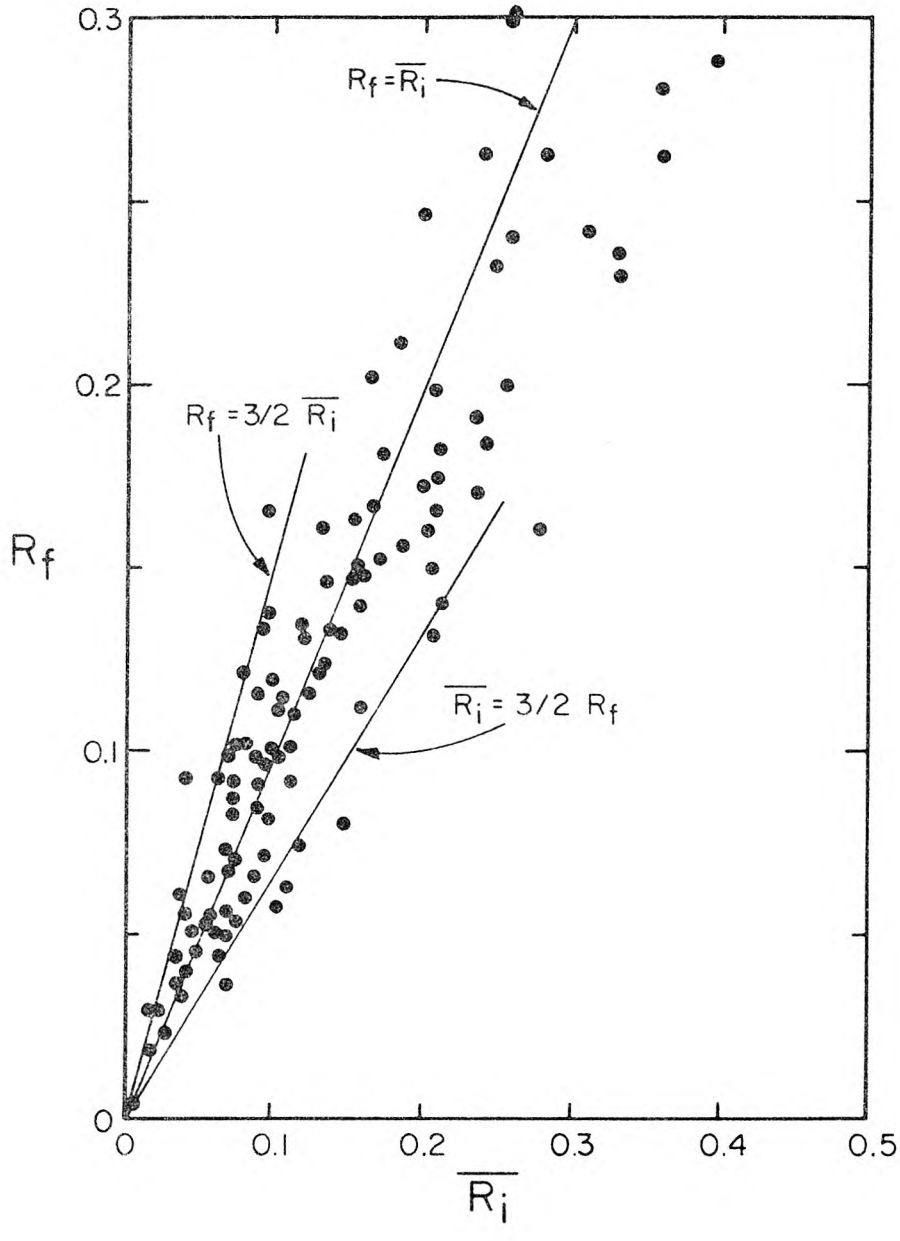

Figure 6.4.19 Values of the flux-Richardson number plotted against the local mean-Richardson number, from measurements made in weakly stratified flows over roughened beds. Data are from Experiment CH4 ($\Delta\rho/\rho_o = 2.4 \times 10^{-4}$, $\Delta U_o = 6.4$ cm/s) and Experiment DH5 ($\Delta\rho/\rho_o = 1.8 \times 10^{-4}$, $\Delta U_o = 6.8$ cm/s).

6.4.19 are shown in Figures 6.4.1, 6.4.2, 6.4.5 - 6.4.8 and 6.4.14. The initial mixing layer never collapsed to a laminar shear layer in these experiments, and as a consequence, few values of $\overline{Ri}$ exceeded 0.3.

The interesting feature in Figure 6.4.19 is the fact that the data cluster around the line $R_f = \overline{Ri}$, indicating that K_H/K_m is near unity for these experiments. (Recall that $R_f = (K_H/K_m)\overline{Ri}$.) As $\overline{Ri}$ increases past 0.2, the data tend to fall slightly below the line $R_f = \overline{Ri}$ (indicating that $K_H/K_m < 1$), but there is some scatter. As $\overline{Ri}$ decreases to zero, R_f decreases to zero, but the data are too scattered to determine an accurate, limiting value of $R_f/\overline{Ri} = K_H/K_m$ as $\overline{Ri}$ approaches zero. A linear least-squares fit of the data for which $\overline{Ri}$ is less than 0.075 indicates that $K_H/K_m \to 0.99$ as $\overline{Ri} \to 0$, but as can be seen in Figure 6.4.19, the data are scattered and the limit of K_H/K_m could easily be greater or less than one.

The other interesting feature is that, again, few data are found above the level $R_f = 0.25$. Since these flows did not collapse, the maximum values of $\overline{Ri}$ encountered were around 0.35; even if K_H/K_m were unity at these large values of $\overline{Ri}$, the maximum value of R_f would be 0.35, so it is not surprising to find a maximum value of R_f between 0.25 and 0.3. The values of $E^* = \dfrac{\partial \overline{q^{*2}v'}}{\partial y} \Big/ \overline{u'v'}\,\dfrac{\partial \overline{u}}{\partial y}$ were largely between -0.2 and 0.3 for these data, so the maximum values of R_f found here are in agreement with the maximum values of R_f found in the mixing layer (Figure 6.2.41 in which E^* was usually between -0.3 and 0.2), and with the maximum values found in the downstream flow over a smooth bed (Figure 6.3.26 in which E^* was usually between -0.6 and 1.2). Thus,

it appears that a bound for the critical value of R_f may be near 0.25, when $|E^*|$ is less than unity.

Figure 6.4.20 shows values of R_f plotted against $\overline{Ri}$, from measurements made in several strongly stratified flows over roughened beds. The data shown in this figure were generally taken far downstream after the laminar interface had begun to break up, but generally below the location of the highest temperature gradient. For the most part, $|E^*|$ was less than 0.5 for these data. The data included in Figure 6.4.20, then, reflect the values of R_f and $\overline{Ri}$ that were found as the interfacial region was approached from below, but do not include the regions in which E^* was large or in which $\overline{Ri}$ was greater than about 0.5. The interesting feature here is that R_f is less than 0.2 for values of $\overline{Ri}$ up to about 0.45.

The flows from which the data in Figure 6.4.20 were obtained all had regions in which the temperature gradient was very large (see, for example, Figure 6.4.4), and the resulting density gradient and buoyancy forces limited the extent to which boundary-generated turbulence could penetrate vertically. In general, the flux-Richardson number and the mean-Richardson number were found to increase with the vertical distance from the bed until the interfacial region was approached. As the temperature gradient increased with distance from the bed, the turbulence levels declined and the rate of increase of R_f declined. Often near the region of the highest temperature gradient, a region was found in which E^* became much larger than unity; the values of R_f, $\overline{Ri}$ and E^* in this region and above it depended upon several factors, including the mean shear, $\partial\overline{u}/\partial y$.

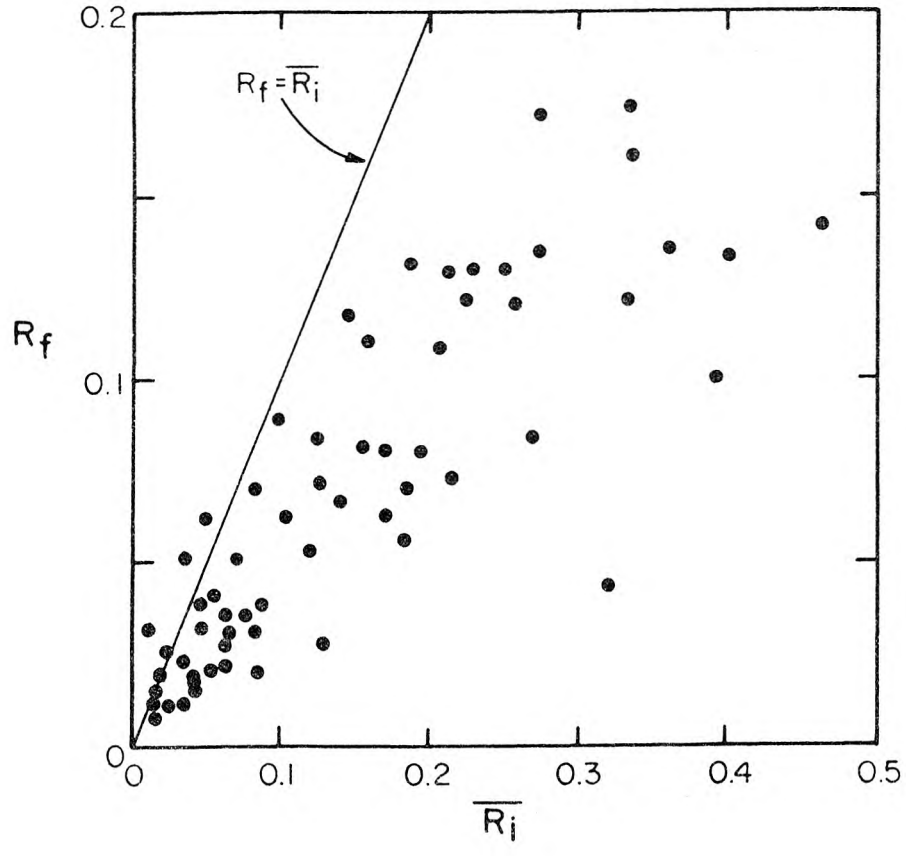

Figure 6.4.20 Values of the flux-Richardson number plotted against the local mean-Richardson number, from measurements made in strongly stratified flows over roughened beds. Measurements shown were made below the interfacial regions where $|E^*| < 0.5$. Data from Experiments CH1, CH2, CH3, DH6, DH7.

To illustrate the change in turbulence properties with depth, Figure 6.4.21 is presented, which shows $-\overline{u'v'}\,\frac{\partial \bar{u}}{\partial y}$, $\overline{B'v'}$, $-\frac{\partial \overline{q^{*2}v'}}{\partial y}$ and $\bar{u}\,\frac{\partial \overline{q^{*2}}}{\partial x}$ as a function of y/h from measurements made 24 m from the splitter plate in a strongly stratified flow (Experiment DH7, see also Figures 6.4.3, 6.4.4, 6.4.10 - 6.4.13, 6.4.15). It can be seen that in the lower portion of the flow, $-\overline{u'v'}\,\frac{\partial \bar{u}}{\partial y}$ is by far the largest term, while in the interfacial region and above, this term no longer dominates the flow.

In this particular case, $\overline{Ri}$ was almost a monotonically increasing function of y/h over the whole depth of flow. Consequently, it is interesting to consider R_f and $\overline{B'v'}/\varepsilon^*$ as functions of $\overline{Ri}$ for this case; these data are shown in Figure 6.4.22, along with the corresponding values of y/h. It can be seen that as y/h increases, $\overline{Ri}$ generally increases, but R_f only increases until y/h = 0.07 and then rapidly decreases. From Figure 6.4.4 one can see that the temperature gradient is large in the region of y/h = 0.07. So, R_f increases until the interface is approached, and then rapidly decreases.

The behavior of $\overline{B'v'}/\varepsilon^*$ is much the same as R_f, increasing until the interfacial region is approached, then rapidly decreasing. (As before, the two-dimensional dissipation rate, ε^*, was calculated using the measured data and Equation 6.2.6 (Section 6.2.10).) Thus, when the interface is crossed, the rate of increase of potential energy ($\overline{B'v'}$) rapidly decreases relative both to the rate of production of turbulent kinetic energy from the mean shear ($-\overline{u'v'}\,\partial\bar{u}/\partial y$) and to the rate of dissipation of turbulent kinetic energy per unit mass (ε^*).

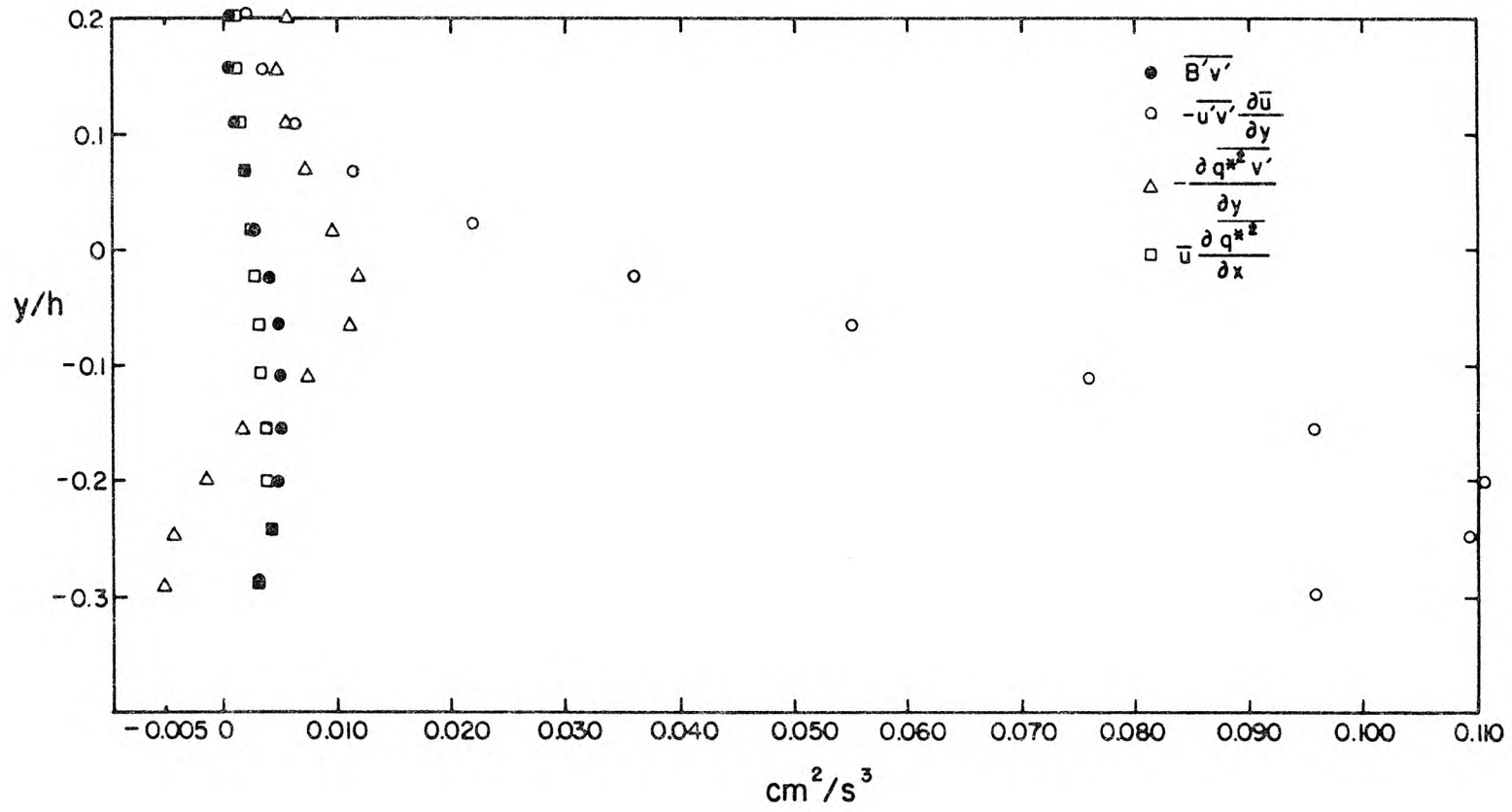

Figure 6.4.21 Values of $\overline{B'v'}$, $-\overline{u'v'}\,\frac{\partial \bar{u}}{\partial y}$, $-\frac{\partial \overline{q^{*2}v'}}{\partial y}$ and $\bar{u}\,\frac{\partial \overline{q^{*2}}}{\partial x}$ plotted against y/h. Measurements from Experiment DH7, x = 24 m.

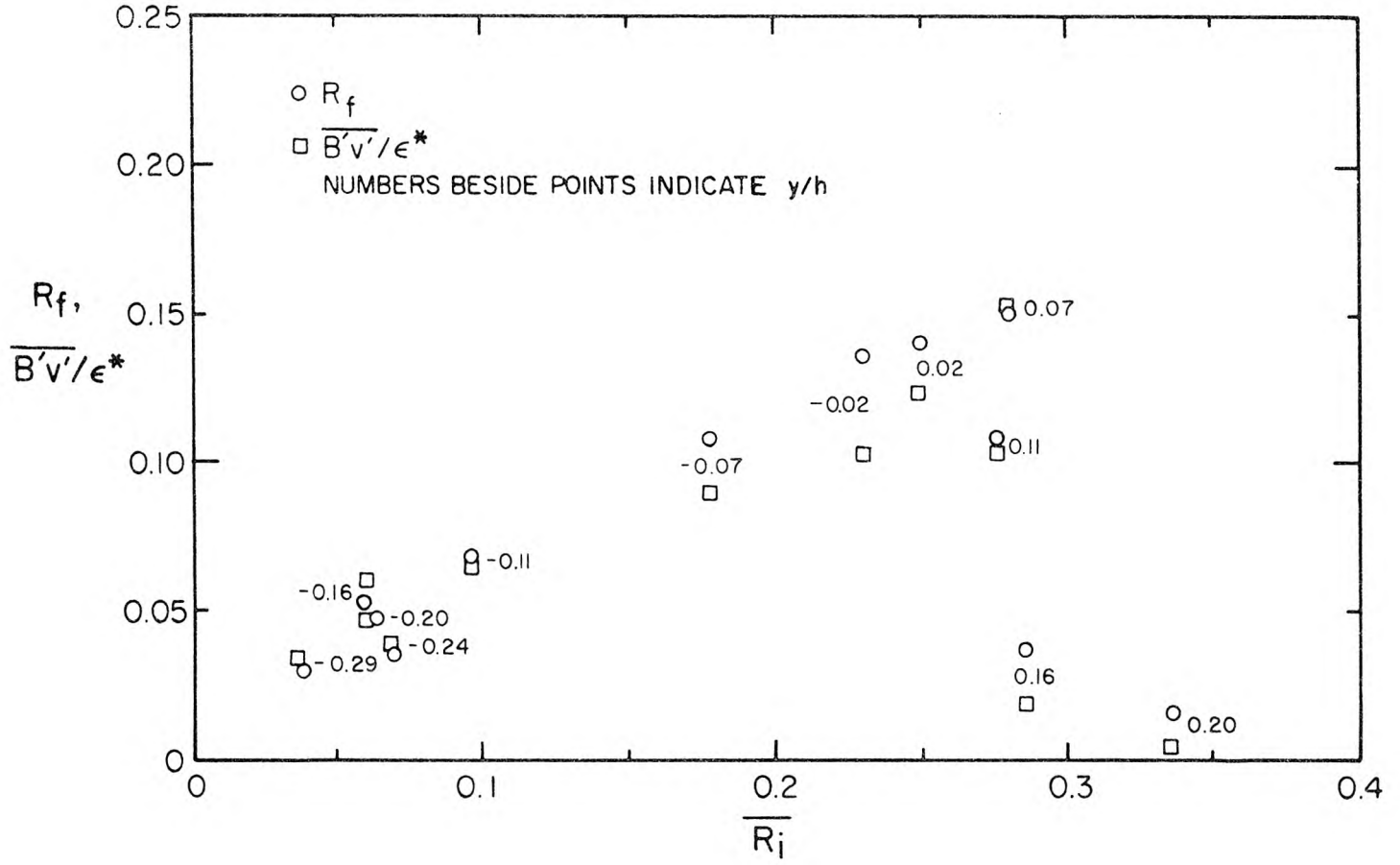

Figure 6.4.22 Values of $R_f = -\overline{B'v'}/\overline{u'v'}\,\frac{\partial \bar{u}}{\partial y}$ and $\overline{B'v'}/\epsilon^*$ plotted against the local mean-Richardson number, from measurements made at x = 24 m in a flow with large initial shear and temperature difference (Experiment DH7). Numbers indicate values of y/h. Refer to Figures 6.4.3, 6.4.4, 6.4.10, 6.4.13, 6.4.15 and 6.4.21 for profiles of mean values for this case.

Furthermore, it is interesting that the maximum values of both R_f and $\overline{B'v'}/\varepsilon^*$ were around 0.15 in this instance.

The behavior of R_f in Figure 6.4.22 is partly attributed to the fact that a large mean shear was present, so that there was always the possibility of significant production of turbulent energy. Other stratified flows in which $\frac{\partial \overline{u}}{\partial y}$ was small did not yield comparable results. In these cases, R_f and $\overline{Ri}$ generally increased as the interface was approached from below, but as the interface was crossed, the relationship between R_f and $\overline{Ri}$ appeared erratic, depending to a large extent on $\frac{\partial \overline{u}}{\partial y}$. If the values of $|\frac{\partial \overline{u}}{\partial y}|$ were very small, both R_f and $\overline{Ri}$ could, and often did, become very large in the interfacial region. The interesting point in these cases is that as the interfacial region was approached from below, E^* generally increased, and large values of E^* were often found in the region of the largest temperature gradients. Furthermore, E^* was invariably found to be very large when R_f was found to be large.

Figure 6.4.23 shows values of R_f plotted against E^* for measurements made within the interfacial regions of several stratified flows. The numbers indicate the local values of $\overline{Ri}$ for the data. As can be seen from the figure, very large values of R_f were often found, the highest values usually corresponding to larger values of $\overline{Ri}$ (as $\frac{\partial \overline{u}}{\partial y}$ was usually very small in these particular instances). As the data in this figure are scattered, no other trend can be easily seen. However, it is obvious from the data in Figure 6.4.23 that one must be cautious when discussing critical values of the flux-Richardson number: if $-\overline{u'v'}\,\frac{\partial \overline{u}}{\partial y}$

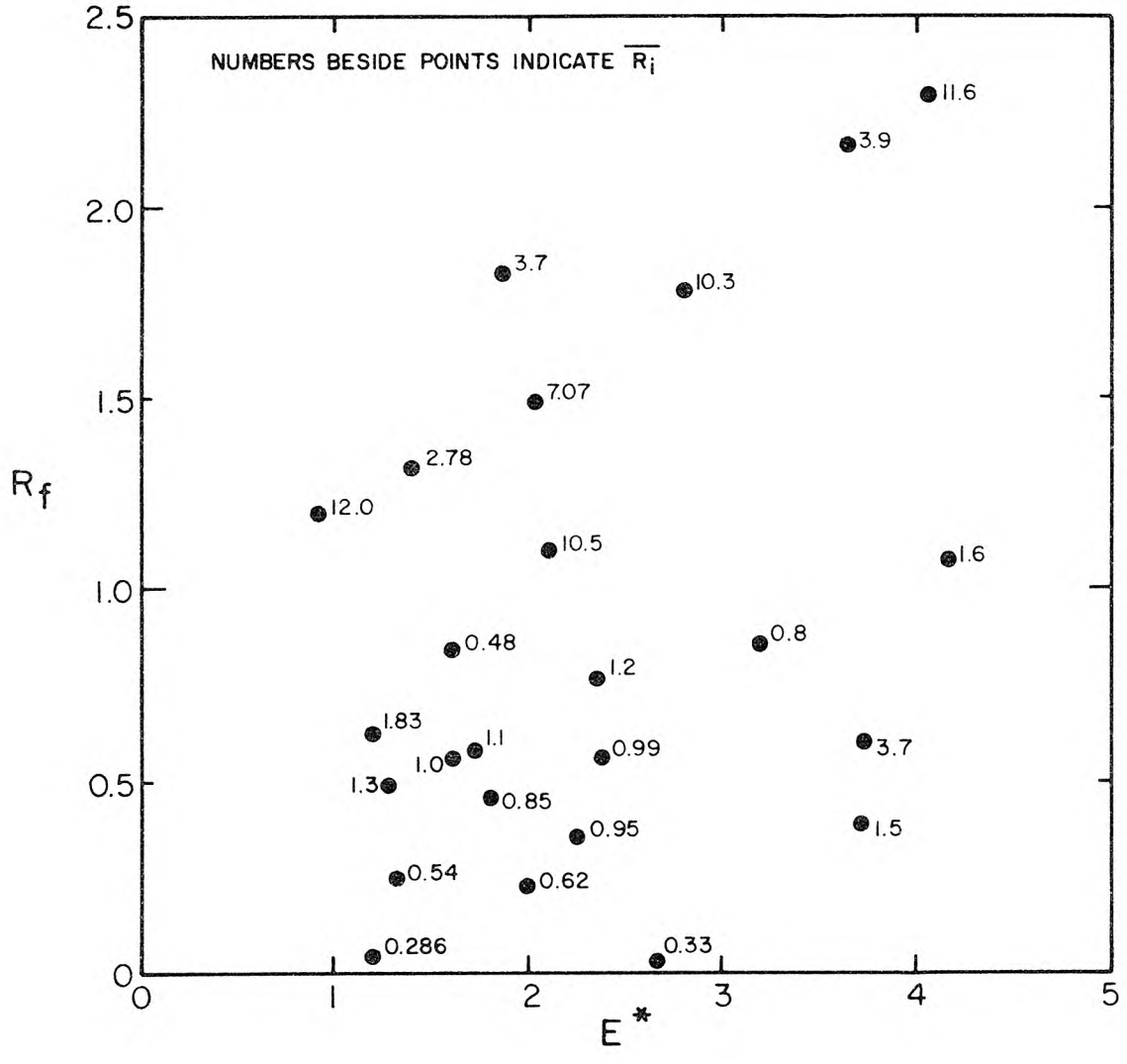

Figure 6.4.23 Values of the flux-Richardson number plotted against $E^* = \overline{\frac{\partial q^{*2} v'}{\partial y}} \Big/ \overline{u'v'} \frac{\partial \bar{u}}{\partial y}$, for measurements made in the interfacial region of stratified flows. Numbers indicate values of $\overline{Ri}$. Data from Experiments CH1, CH2, CH3, DH6 and DH7.

is not the major source of turbulent kinetic energy at a point, then one might expect to find large values of R_f there. A critical value of R_f must be discussed with the explicit assumption that there are no major sources of turbulent energy other than production from the mean shear.

As was pointed out in Section 6.2.1, when E^* is found to be large, one might expect that the quantity $F^* = R_f/E^* = \overline{B'v'} \Big/ \frac{-\partial \overline{q^{*2}v'}}{\partial y}$ to be a more descriptive parameter than R_f. Figure 6.4.24 shows the same data of Figure 6.4.23 plotted in the form of F^* as a function of $\overline{Ri}$. In this figure, F^* is seen to increase with $\overline{Ri}$ over the range $0 < \overline{Ri} < 5$. At the largest values of $\overline{Ri}$ shown, the data are very scattered, but this is not surprising, as $\frac{\partial \overline{u}}{\partial y}$ and $\overline{B'v'}$ are very small in these instances; consequently, the relative errors in $\overline{Ri}$ and F^* are large here.

One interesting feature of Figure 6.4.24 is the fact that F^* attains values larger than one, indicating that other sources of energy may sometimes be important when both E^* and R_f are large. Another feature is that F^* appears to vary approximately in a linear fashion with $\overline{Ri}$ for values of $\overline{Ri}$ less than about 3. This may be indicative of the manner in which a stratified fluid is mixed when the diffusive term $\frac{\partial \overline{q^{*2}v'}}{\partial y}$ is the dominant source of turbulent kinetic energy. However, it is difficult to determine exactly what the mixing mechanisms are without having measured gradient quantities such as $\frac{\partial q^{*2}v'}{\partial y}$ directly, as functions of time and space. As is dramatically demonstrated in Section 6.5, one must be cautious when drawing conclusions about turbulence properties while relying solely on time-averaged quantities.

Values of the two-dimensional dissipation rate, ε^*, were calculated

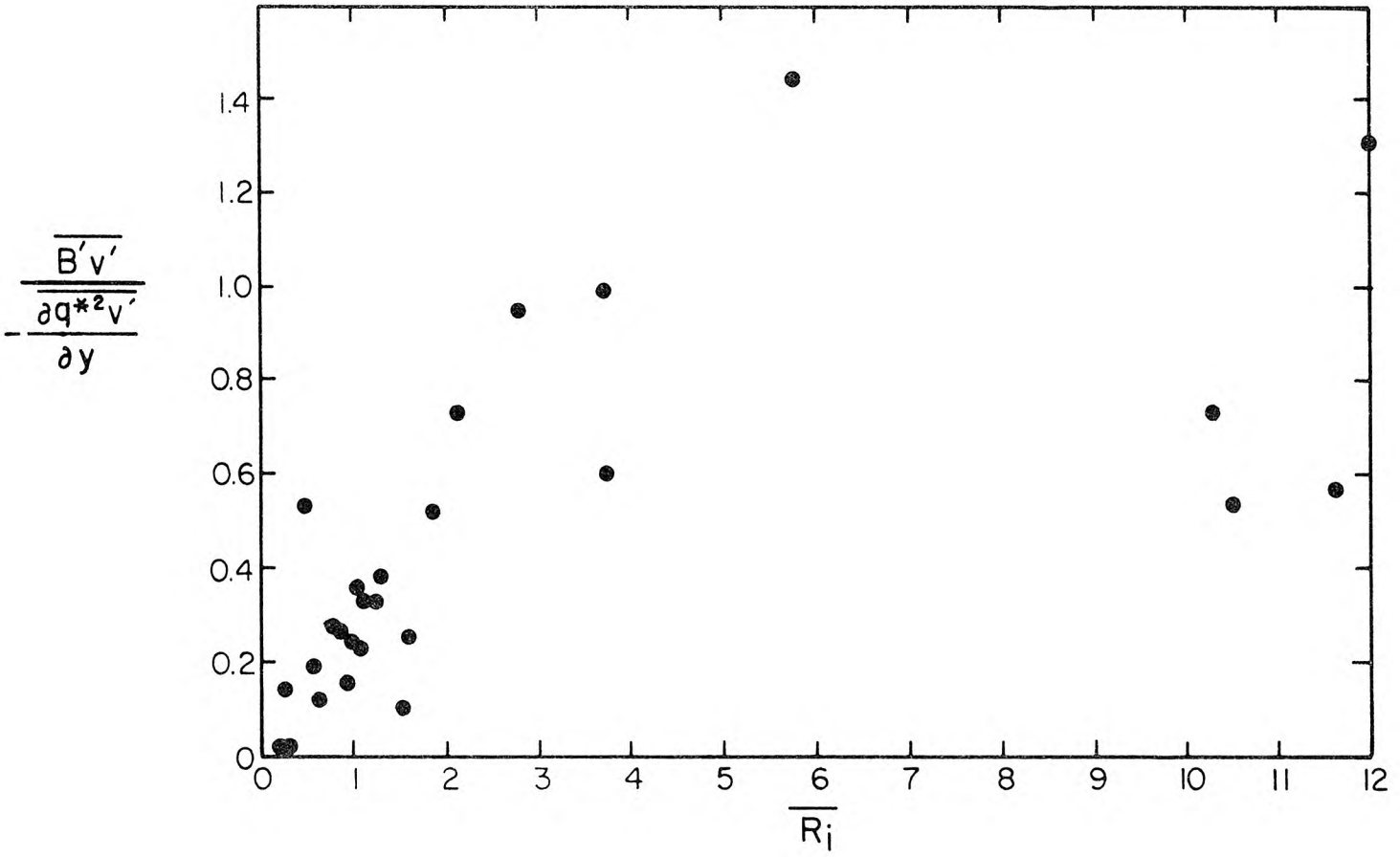

Figure 6.4.24 Values of $F^* = -\overline{B'v'}/\frac{\partial \overline{q^{*2}v'}}{\partial y}$ plotted against the local mean-Richardson number for the same data shown in Figure 6.4.23. Measurements from the interfacial regions in Experiments CH1, CH2, CH3, DH6 and DH7.

for the flows over roughened beds using Equation 6.2.6 (Section 6.2.10) and, as before, compared with the values of ε obtained using the power spectral estimates and Equation 2.4.1. The ratio $\varepsilon/\varepsilon^*$ was found to have a mean value of 1.0 and a standard deviation of 0.6. The reason for the large scatter of values of $\varepsilon/\varepsilon^*$ is not known, but is no doubt partly attributable to the fact that the flows in question were stratified, and there is, therefore, no reason to expect a relationship that is valid for homogeneous, isotropic turbulent flows to be valid for these density-stratified turbulent flows. As was found in Section 6.2.10 and 6.3.5, one might expect $\varepsilon/\varepsilon^*$ to have a value of about 1.1 when measured on the centerline of the flume, and $E^* \approx 0.2$.

The values of ε^*, calculated using the measured data and Equation 6.2.6, were used to produce graphs of the quantity $\overline{B'v'}/\varepsilon^*$ as a function of $\overline{Ri}$. Figure 6.4.25 shows such a graph for data from a weakly stratified flow over a roughened bed (Experiment DH5). The values of $\overline{B'v'}/\varepsilon^*$ rise in a nearly linear fashion with $\overline{Ri}$, with most of the data found slightly above the line $\overline{B'v'}/\varepsilon^* = \overline{Ri}$. Once again, $\overline{B'v'}/\varepsilon^*$ was found to have relative small values, although in this case the mean-Richardson number was always small.

Figures 6.4.26 and 6.4.27 show values of $\overline{B'v'}/\varepsilon^*$ plotted against $\overline{Ri}$, from measurements made in more strongly stratified flows. The data shown in Figure 6.4.26 were taken below the interfacial region where smaller values of E^* were found, while those shown in Figure 6.4.27 were taken in those interfacial regions where E^* was greater than 0.6.

The data in Figure 6.4.26 indicate a definite trend of $\overline{B'v'}/\varepsilon^*$

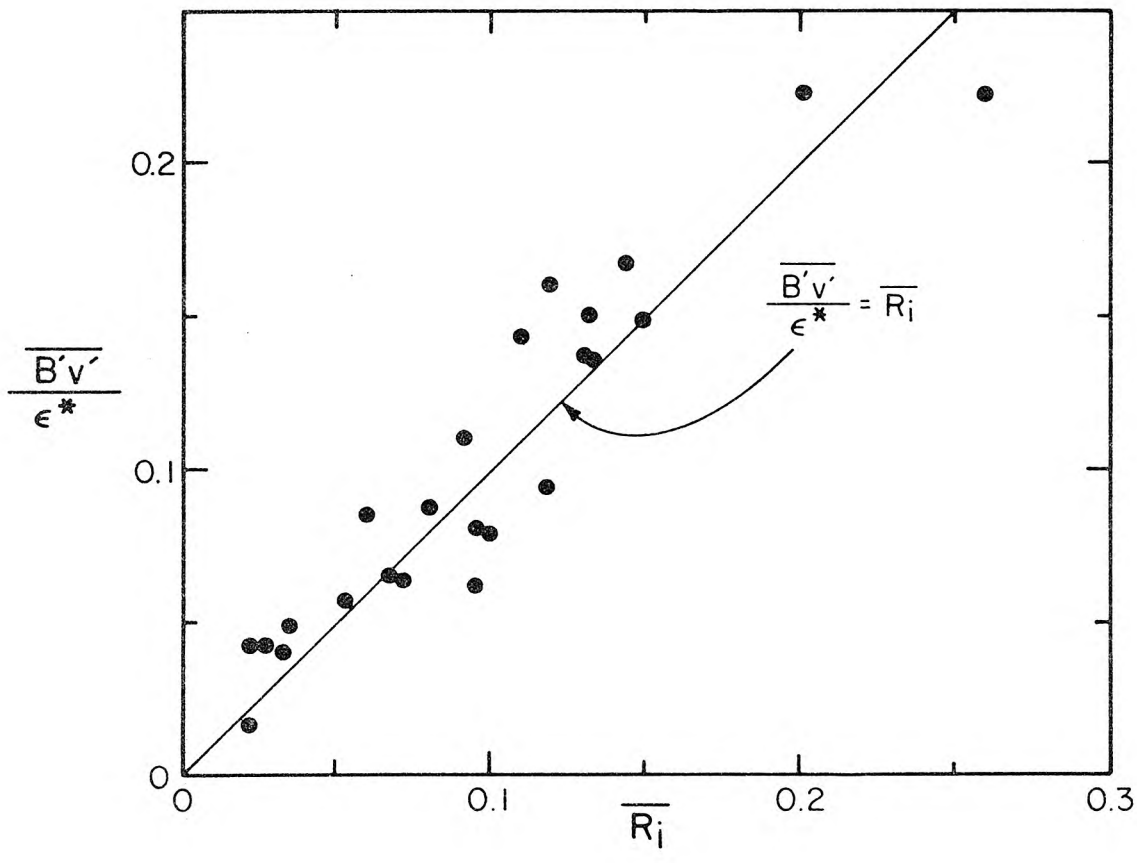

Figure 6.4.25 Values of $\overline{B'v'}/\epsilon^*$ plotted against the local mean Richardson number for measurements made in a weakly stratified flow over a roughened bed. Data from Experiment DH5.

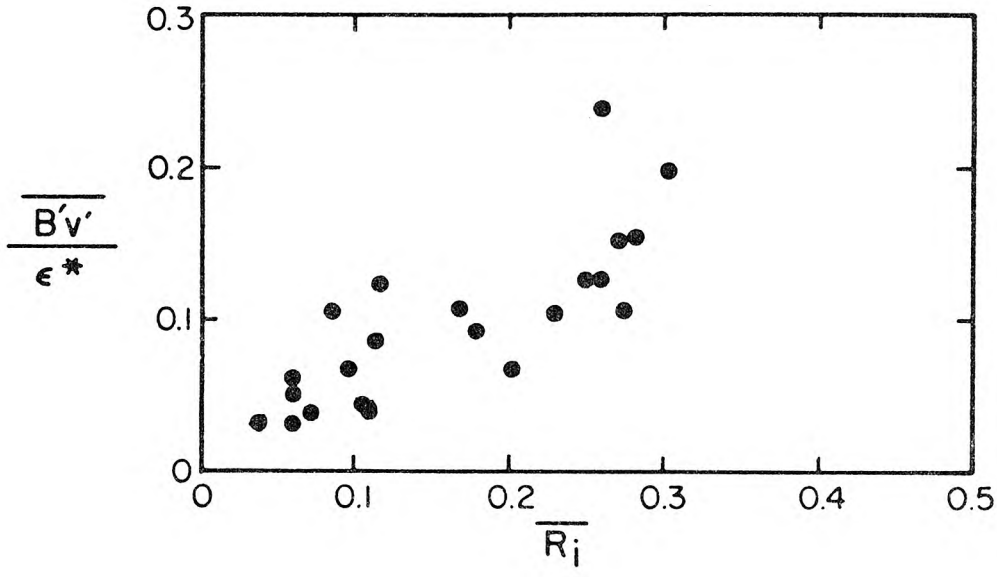

Figure 6.4.26 Values of $\overline{B'v'}/\varepsilon^*$ plotted against $\overline{Ri}$ for measurements made in stratified flows below the interfacial region where $E^* < 0.6$. Data from Experiment CH1, CH3 and DH7.

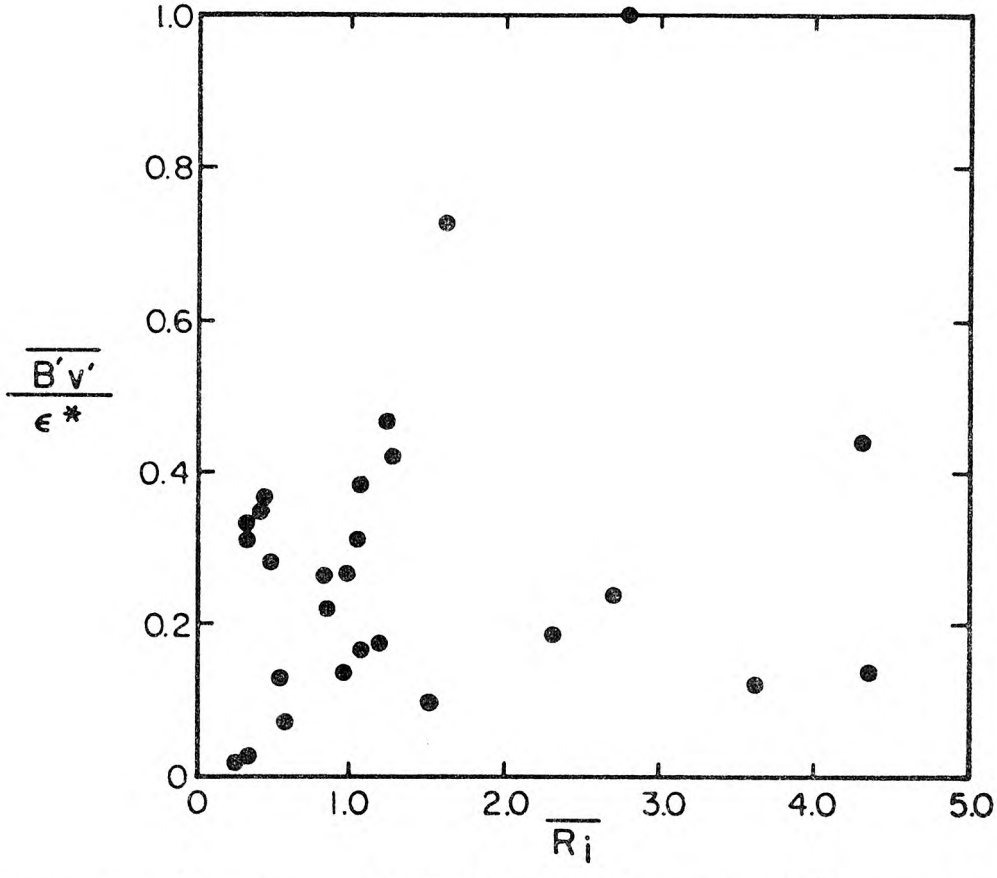

Figure 6.4.27 Values of $\overline{B'v'}/\varepsilon^*$ plotted against $\overline{Ri}$ for measurements made in the interfacial region of stratified flows, where $E^* > 0.6$. Data from Experiments CH1, CH3, DH6, DH7.

with $\overline{Ri}$, while the data in Figure 6.4.27 are so scattered that it is difficult to determine any trend. It is interesting that larger values of $\overline{B'v'}/\varepsilon^*$ are found when E^* is large than when E^* is small; this may indicate that very different mixing processes are involved when $-\frac{\partial \overline{q^{*2}v'}}{\partial y}$ is large compared to $-\overline{u'v'}\frac{\partial \bar{u}}{\partial y}$. Once again, the data indicate the inefficiency of the mixing process and although there are data indicating that $\overline{B'v'}/\varepsilon^*$ is occasionally greater than 0.3, it should be remembered that these values are found in regions in which $\overline{Ri}$ is large, where both $\overline{B'v'}$ and ε^* are relatively small. Consequently, when $\overline{B'v'}/\varepsilon^*$ is found to be greater than 0.3, the actual values of $\overline{B'v'}$ would indicate that the mixing rate is at an extremely low level. Conversely, when $\overline{B'v'}$ is relatively large, $\overline{B'v'}/\varepsilon^*$ is usually found to be less than 0.2, indicating that the dissipation rate is much faster than the rate of increase in potential energy.

6.4.6 Summary of the Results for the Downstream Flow Over a Roughened Bed

The most significant results from the measurements of the downstream flow over a roughened bed are shown in Figures 6.4.19 - 6.4.27. From the data in these figures, it can be seen that when $|E^*| = \left|\frac{\partial \overline{q^{*2}v'}}{\partial y} \Big/ \overline{u'v'}\frac{\partial \bar{u}}{\partial y}\right|$ is relatively small, R_f is almost always found to be less than 0.3. Furthermore, Figure 6.4.20 indicates that when the flow is strongly stratified, the stratification reduces the turbulence to such an extent that $R_f < 0.2$, when $|E^*|$ is small, even at relatively large values of $\overline{Ri}$. When the stratification is very weak, so that the flow is always turbulent, $R_f/\overline{Ri} \equiv K_H/K_m$ is approximately

one, when $\overline{Ri} < 0.2$, as can be seen in Figure 6.4.19. At slightly higher values of $\overline{Ri}$, the data indicate that $R_f/\overline{Ri}$ is slightly less than one, but the trend is not clear because there are too few data at the larger values of $\overline{Ri}$.

In some instances, measured values of E^* were large, and when this was found to be the case, R_f and $\overline{Ri}$ were also usually large (Figure 6.4.23). In these instances, $F^* = -\overline{B'v'} \Big/ \frac{\partial \overline{q^{*2}v'}}{\partial y}$ was found to be a more suitable parameter than R_f, and a relationship between F^* and $\overline{Ri}$ was found (Figure 6.4.24) from the data for which $E^* > 1$.

Figures 6.4.25 - 6.4.27 indicate again that $\overline{B'v'}/\varepsilon^*$ is relatively small in these flows. When $E^* > 0.6$, the data are somewhat scattered (Figure 6.4.27) and indicate that $\overline{B'v'}/\varepsilon^*$ may reach values as large as one, although both $\overline{B'v'}$ and ε^* are quite small when $\overline{B'v'}/\varepsilon^* > 0.3$. When $E^* < 0.6$, the data in Figures 6.4.25 and 6.4.26 indicate that $\overline{B'v'}/\varepsilon^*$ is at most about 0.25, and again the larger values of $\overline{B'v'}/\varepsilon^*$ result when both $\overline{B'v'}$ and ε^* are relatively small. These figures clearly show that turbulent kinetic energy is dissipated at a much greater rate than the rate at which the potential energy of the fluid is increased.

The results in this section also show that density stratification resulted in large reductions of the turbulence levels and in the turbulent fluxes of momentum and heat (Figures 6.4.5 - 6.4.9, 6.4.15), as well as the relative turbulent diffusivity for momentum, K_m/ν. Furthermore, it was found that when the stratification was relatively large (if one considers $\Delta\rho/\rho_o = 5 \times 10^{-4}$ to be large), the mean turbulence

properties such as $\sqrt{\overline{u'^2}}/U$, $\sqrt{\overline{v'^2}}/U$, $-\overline{u'v'}/U^2$ and $-\overline{v'T'}/U\Delta T_o$ appeared to be largely unaffected by small changes in the mean shear (Figures 6.4.3, 6.4.10 - 6.4.12, 6.4.15).

It is believed the pronounced increase in mean shear with the downstream distance in the stratified flows can be explained by the reduction in the turbulent momentum flux. In an unstratified flow, the turbulent shear stress in the flow balances the pressure force, while in a stratified, but otherwise similar flow, the pressure force is nearly the same as in the unstratified flow, but the turbulent momentum flux is much reduced. The unbalanced portion of the pressure force gradually accelerates the flow, which results in the observed increase in shear as the flow progresses downstream.

Finally, it was found that the power spectral estimates obtained from measurements made in the interfacial regions which were intermittently turbulent behave as k^{-3}, which indicates the existence of the "buoyancy subrange" in these flows. The power spectral estimates obtained from moderately turbulent regions show the $k^{-5/3}$ behavior of the inertial subrange, and consequently, it appears that even a moderate amount of turbulence is sufficient to alter the power spectra in such a way that buoyancy effects are not easily discerned from the spectra alone.

6.5 Organized Structures in the Turbulent Regions

As was pointed out in Section 2.4.2, a good deal of attention in the past few years has been focused on large, organized structures in turbulent flows (Lu and Willmarth (1973), Willmarth (1975), Laufer

(1975), Wallace *et al.* (1977)). In the initial mixing layer the structures of interest are the vortices which dominate the flow (Brown and Roshko (1974), Winant and Browand (1974), Koop (1976); see also Figures 5.3.1 - 5.3.3). In boundary layer flows, structures have been identified by the presence of large bursts of turbulent momentum flux (Lu and Willmarth, 1973) and by recognizable patterns in the time history of the velocity fluctuations (Wallace *et al.* (1977), Thomas (1977)).

In this section the results of this study which pertain to the presence of organized structures in the turbulent regions are presented, with the focus on the results from the measurements in the downstream flow. As other investigators have found, the turbulent flow here was found to be dominated by large "bursts" of turbulence; however, as is shown in Sections 6.5.2 and 6.5.3, the time-record of the vertical flux of turbulent energy, $q^{*2}v' = \frac{1}{2}(u'^2 + v'^2)v'$, was found to be useful in the determination of the presence of turbulent bursts, and to provide an excellent means for the conditional sampling of signals.

6.5.1 Probability Density Functions in Turbulent Regions

In this section probability density functions are examined with particular reference to organized structures in the downstream turbulent flow. Typical probability density functions measured in the initial mixing layer are shown in Section 6.2.7, and some reference to them is made in this section, but for the most part, the emphasis here is on the downstream flow.

Figure 6.5.1 shows typical probability density functions of $u'/\sqrt{\overline{u'^2}}$ and $v'/\sqrt{\overline{v'^2}}$, measured 16 m from the splitter plate in a

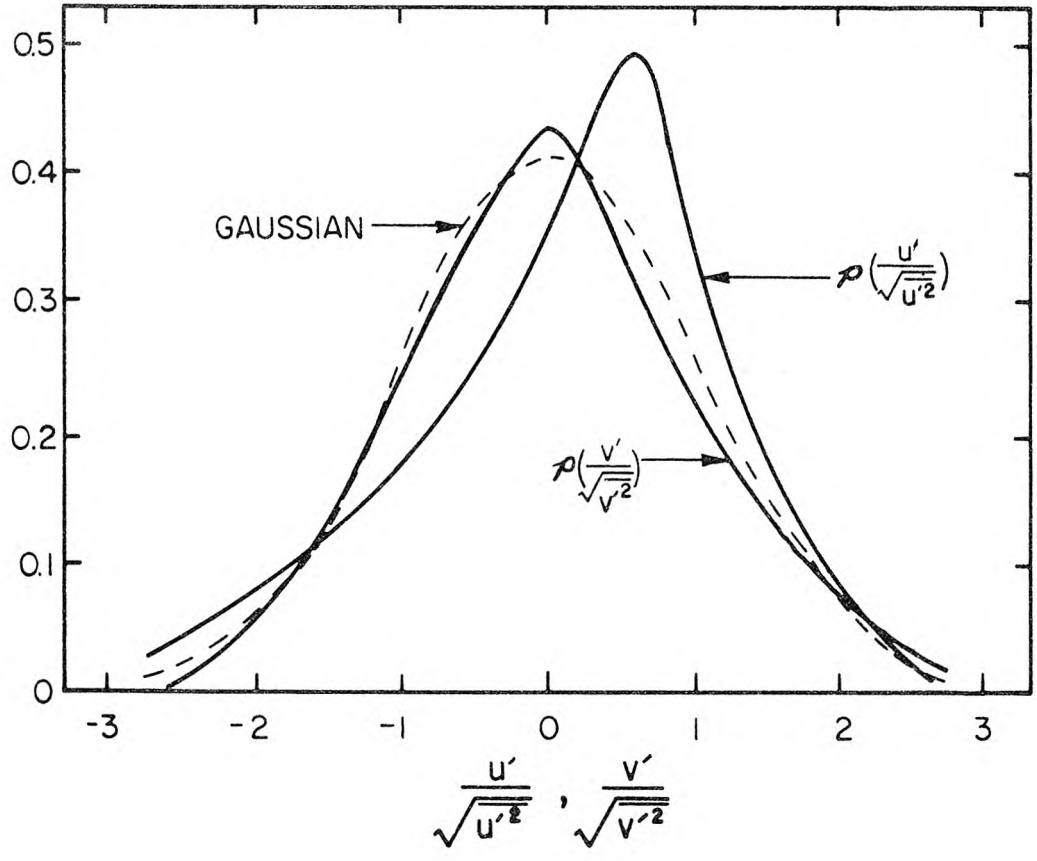

Figure 6.5.1 Probability density functions of $u'/\sqrt{\overline{u'^2}}$ and $v'/\sqrt{\overline{v'^2}}$ measured at x = 16 m, y/h = -0.16. Data from Experiment DH6. Dashed curve indicates Gaussian profile.

stratified flow over a rock-roughened bed (Experiment DH6, y/h = -0.16). A Gaussian distribution is also shown for reference. The probability density function for $u'/\sqrt{\overline{u'^2}}$ is skewed, as seems to be fairly typical in boundary layer flows (e.g. Lu and Willmarth (1973)), while the probability density function for $v'/\sqrt{\overline{v'^2}}$ is fairly symmetric, although not Gaussian in appearance.

The probability density functions of $u'/\sqrt{\overline{u'^2}}$ and $v'/\sqrt{\overline{v'^2}}$ measured downstream are fairly uniform in appearance regardless of y/h. This can be seen in Figures 6.5.2 and 6.5.3 which show the variation of the probability density functions for $u'/\sqrt{\overline{u'^2}}$ and $v'/\sqrt{\overline{v'^2}}$ with depth, again using data measured 16 m from the splitter plate in a stratified flow (Experiment DH6). Profiles of $\sqrt{\overline{u'^2}}/U$, $\sqrt{\overline{v'^2}}/U$ and $-\overline{u'v'}/U^2$ for this case are shown in Figure 6.5.4. At this location there was some mixing at the bottom of the interface (which was located between y/h = 0 and y/h = 0.11), but the boundary-generated turbulence had not caused the interfacial region to break down completely. The probability density functions for $u'/\sqrt{\overline{u'^2}}$ in Figure 6.5.2 are fairly similar, although the probability density functions in the upper portion of the flow (y/h > 0.05) are slightly less skewed than those deeper in the flow. This is very likely due to the nature of the laminar flow above the interfacial region. Likewise, the probability density functions for $v'/\sqrt{\overline{v'^2}}$ also appear to be fairly similar over the depth, except at highest values of y/h shown, where the probability density functions are somewhat "flatter" in the neighborhood of $v'/\sqrt{\overline{v'^2}} = 0$. It is interesting that the probability density functions

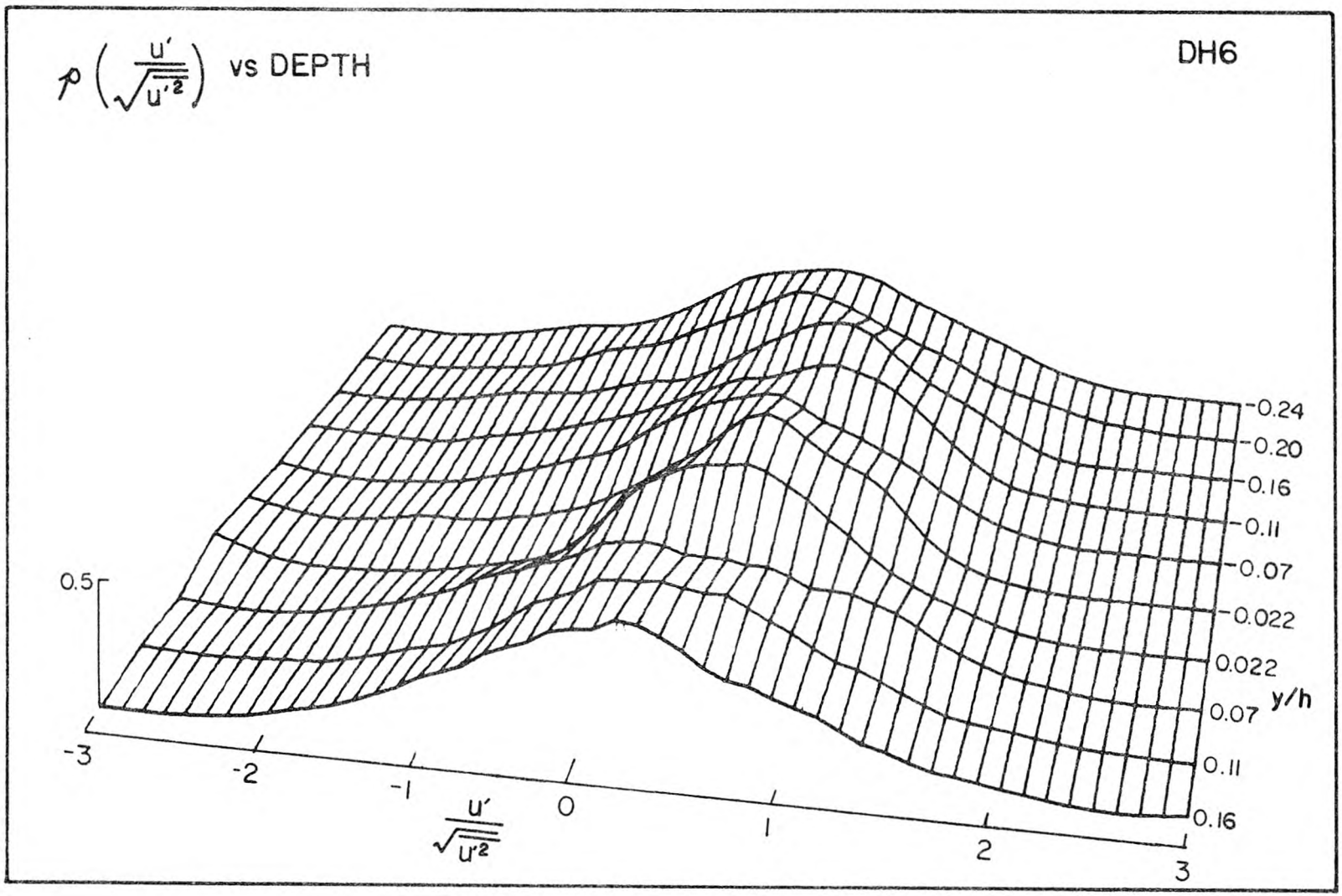

Figure 6.5.2 Variation of the probability density functions for $u'/\sqrt{\overline{u'^2}}$ with depth. Measurements from Experiment DH6, x = 16 m. Profiles of $\sqrt{\overline{u'^2}}/U$ at this location given in Figure 6.5.4.

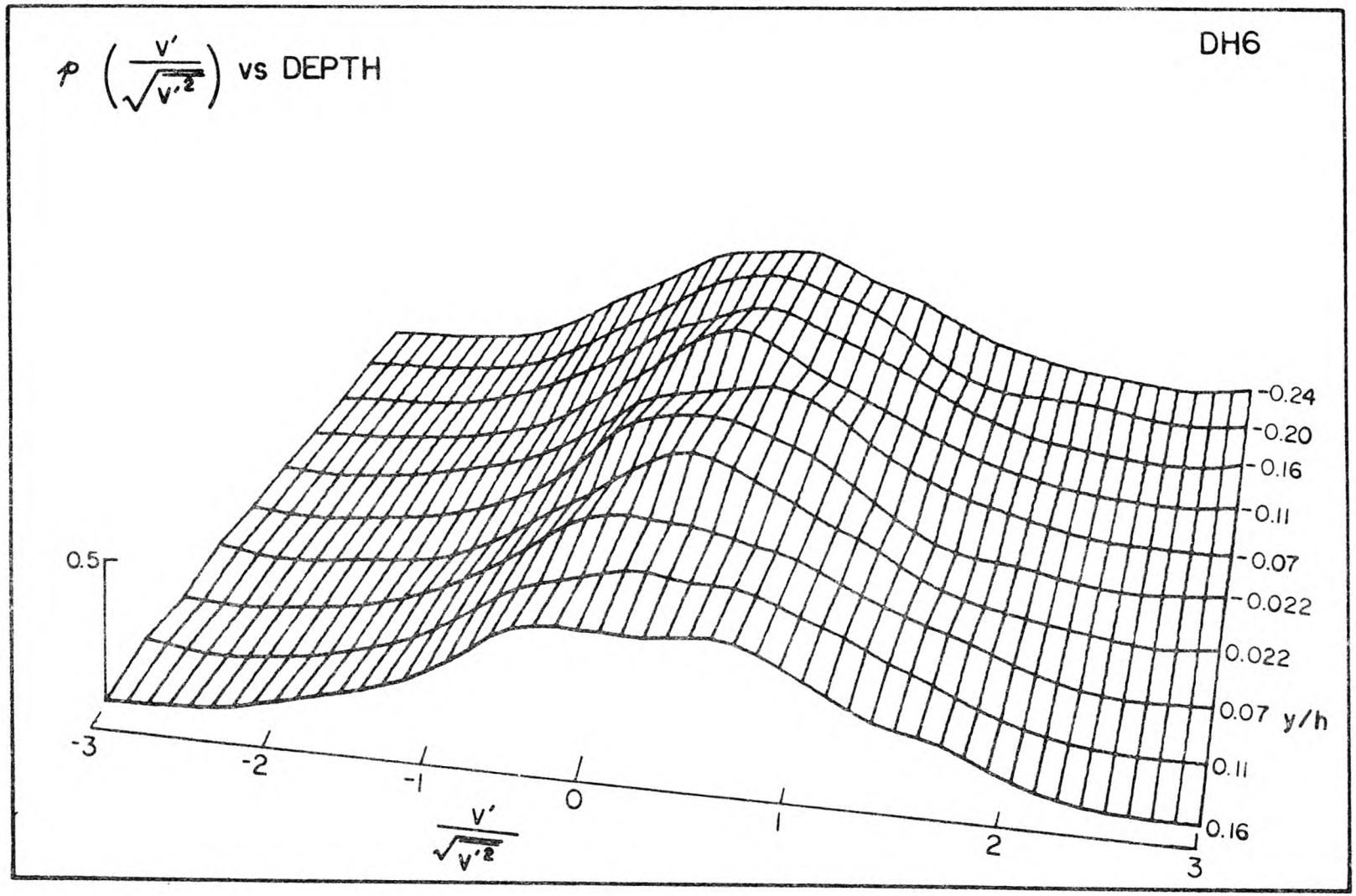

Figure 6.5.3 Variation of the probability density functions for $v'/\sqrt{\overline{v'^2}}$ with depth. Measurements from Experiment DH6, x = 16 m. Profiles of $\sqrt{\overline{v'^2}}/U$ at this location shown in Figure 6.5.4.

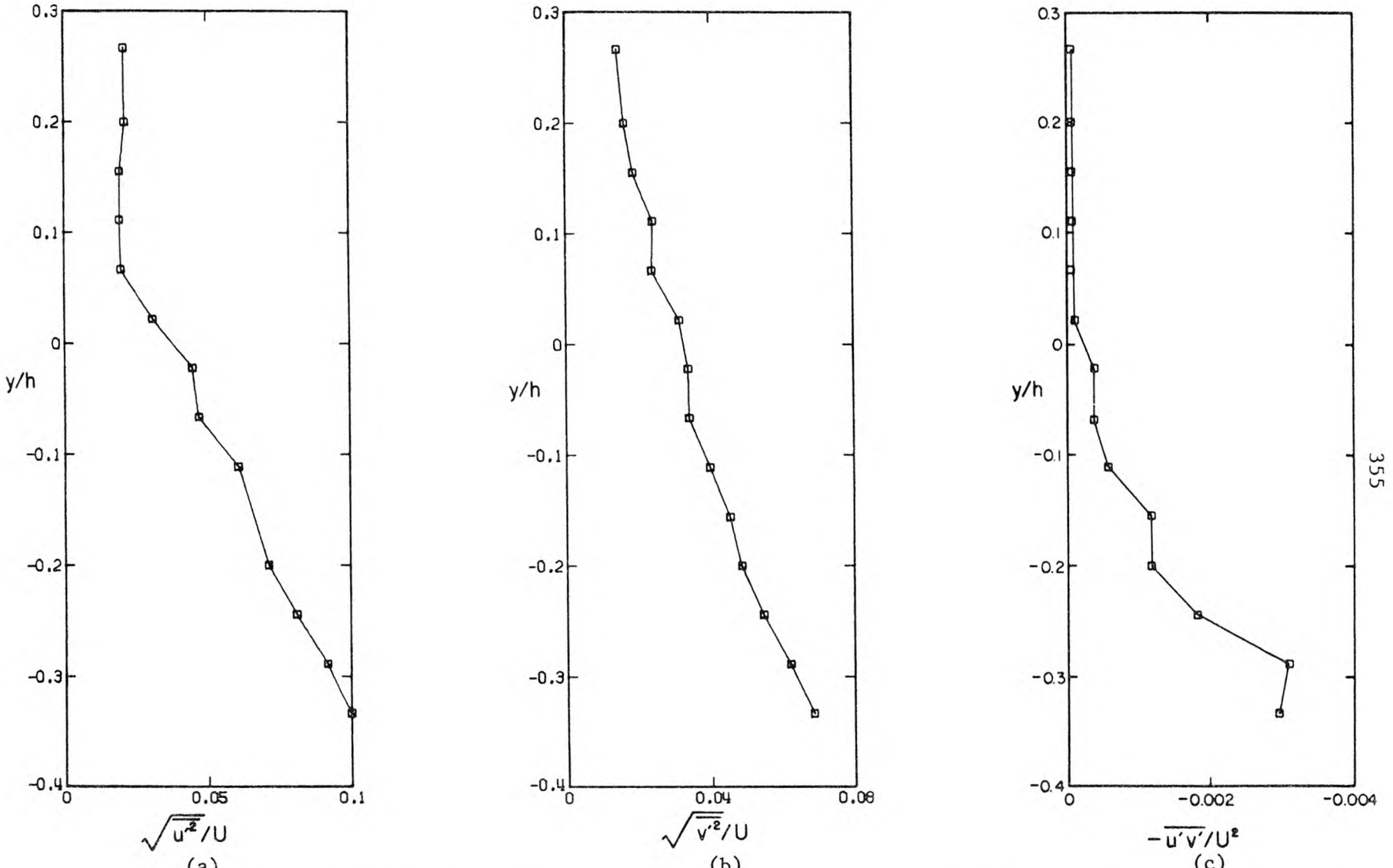

Figure 6.5.4 Profiles of (a) $\sqrt{\overline{u'^2}}/U$, (b) $\sqrt{\overline{v'^2}}/U$ and (c) $-\overline{u'v'}/U^2$, measured at x = 16 m, Experiment DH6. Figures 6.5.1 - 6.5.3, 6.5.5, 6.5.7 - 6.5.11 show probability density functions for this case.

shown in Figures 6.5.2 and 6.5.3 vary little with depth, despite the large variation with depth in the turbulence levels, as seen in Figure 6.5.4. An important feature of the probability density functions shown in Figures 6.5.1 - 6.5.3 is that they all rapidly approach zero at relatively small values of $u'/\sqrt{\overline{u'^2}}$ and $v'/\sqrt{\overline{v'^2}}$. Such is not the case for probability density functions for u'v'.

As was found in the initial mixing layer (see Section 6.2.7), the probability density functions for u'v' in the downstream flow were found to have long tails, indicating that at times the values of u'v' are extremely large. Figure 6.5.5 shows the probability density function of $u'v'/\overline{u'v'}$, calculated from the same data used in Figure 6.5.1. In this instance, the mean value of u'v' was -0.10 cm^2/s^2, while the standard deviation was 0.40 cm^2/s^2. The striking feature of this graph is that the probability density function for $u'v'/\overline{u'v'}$ has not even fallen to zero at $u'v'/\overline{u'v'} = 10$.

The significance of the long, non-zero tail in Figure 6.5.5 can be realized using conditional sampling techniques. The two integrals:

$$\tilde{\Gamma}(L_p) = 1 - \int_{-L_p}^{L_p} p\left(\frac{u'v'}{\overline{u'v'}}\right) \; d\left(\frac{u'v'}{\overline{u'v'}}\right) \tag{6.5.1}$$

and

$$\frac{<u'v'>}{\overline{u'v'}}\,(L_p) = 1 - \int_{-L_p}^{L_p} \frac{u'v'}{\overline{u'v'}}\; p\left(\frac{u'v'}{\overline{u'v'}}\right) \; d\left(\frac{u'v'}{\overline{u'v'}}\right) \tag{6.5.2}$$

yield $\tilde{\Gamma}(L_p)$, the fraction of time for which $|u'v'/\overline{u'v'}| > L_p$ and $<u'v'>/\overline{u'v'}$, the fraction of $\overline{u'v'}$ accounted for by values of

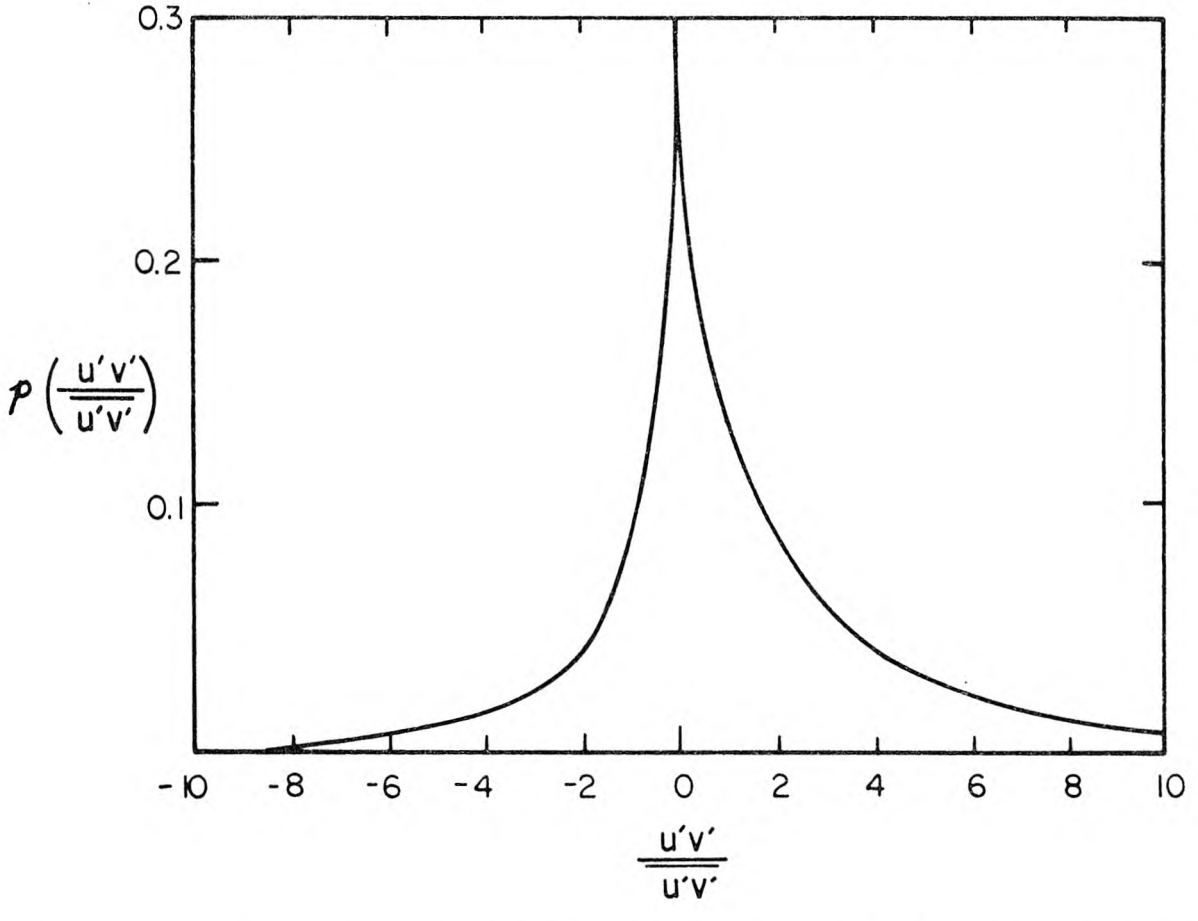

Figure 6.5.5 Probability density function for $u'v'/\overline{u'v'}$, measured at x = 16 m, y/h = -0.16. Data from Experiment DH6.

$|u'v'/\overline{u'v'}| > L_p$. Here $p\left(\frac{u'v'}{\overline{u'v'}}\right)$ denotes the probability density function of $u'v'/\overline{u'v'}$. The functions $\tilde{\Gamma}(L_p)$ and $< u'v' > /\overline{u'v'}$ are plotted against L_p in Figure 6.5.6 using the probability density function shown in Figure 6.5.5. The two curves in Figure 6.5.6 clearly show that the large values of $|u'v'|$ account for most of $\overline{u'v'}$; for example, the values of $|u'v'|$ which are greater than $5|\overline{u'v'}|$ account for almost 67 per cent of $\overline{u'v'}$, yet the periods during which $|u'v'/\overline{u'v'}| > 5$ account for less than 14 per cent of the total time. These data indicate that there are events taking place in the flow during which relatively large amounts of momentum are transferred in relatively short periods of time.

That the probability density functions for u'v' varied little with depth can be seen in Figure 6.5.7, which shows probability density functions of $u'v'/\sqrt{\overline{u'^2}}\sqrt{\overline{v'^2}}$ measured 16 m from the splitter plate in a stratified flow (Experiment DH6; see also Figures 6.4.2 and 6.4.3). Again, values at the extreme ends of the scale ($u'v'/\sqrt{\overline{u'^2}}\sqrt{\overline{v'^2}} = \pm 4$, in this case) indicate the fraction of values outside the range shown. Consequently, the probability density functions in Figure 6.5.7 indicate a significant fraction of values of $u'v'/\sqrt{\overline{u'^2}}\sqrt{\overline{v'^2}}$ are less than -4.0, while almost none are greater than 4.0, and by far the largest fraction are near zero. Again, this is indicative of the turbulent bursts which transport large amounts of momentum.

Figure 6.5.8 is presented to indicate the variation of the probability density function of u'v' with depth. Since $\sqrt{\overline{u'^2}}$, $\sqrt{\overline{v'^2}}$ and $-\overline{u'v'}$ all increased substantially as y/h decreased, the unnormalized

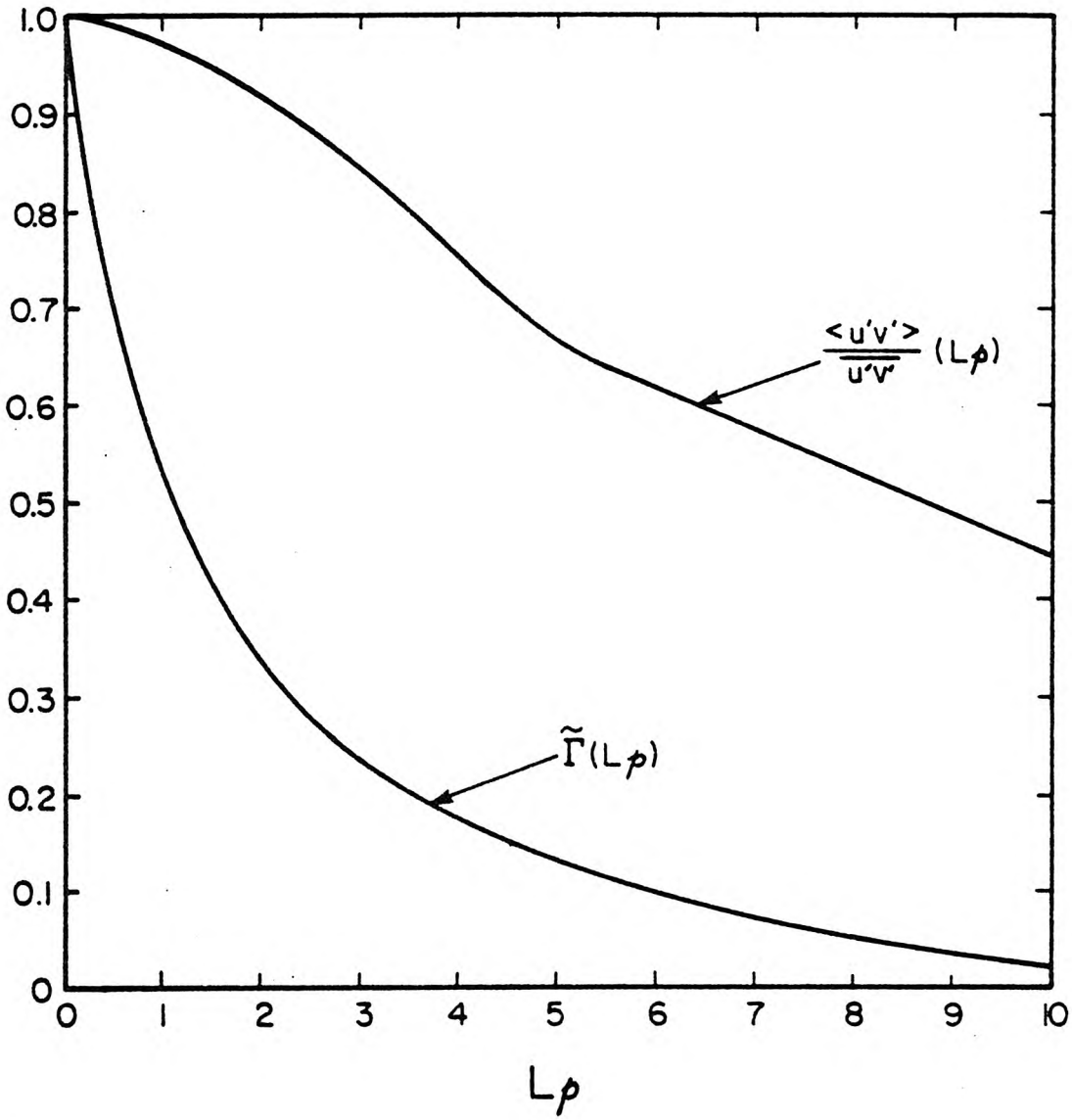

Figure 6.5.6 $\tilde{\Gamma}(L_p)$ and $\frac{\langle u'v' \rangle}{\overline{u'v'}}(L_p)$ (from Equations 6.5.1 and 6.5.2) plotted against L_p. $\tilde{\Gamma}(L_p)$ and $\frac{\langle u'v' \rangle}{\overline{u'v'}}(L_p)$ calculated using the probability density function for $u'v'/\overline{u'v'}$ shown in Figure 6.5.4.

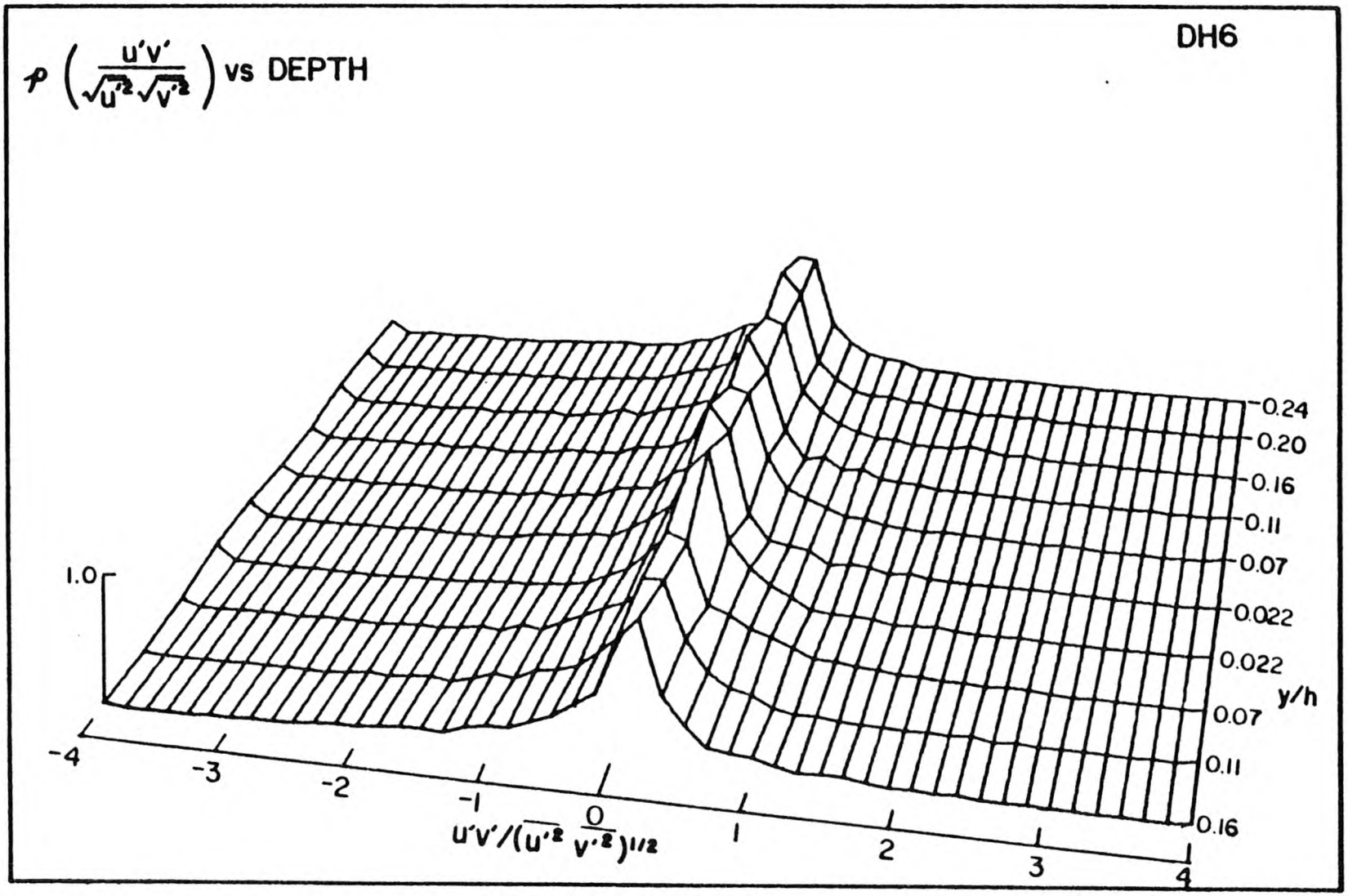

Figure 6.5.7 Variation of the probability density functions for $u'v'/\sqrt{\overline{u'^2}}\sqrt{\overline{v'^2}}$ with depth. Measurements from Experiment DH6, x = 16 m. Profiles of $-\overline{u'v'}/U^2$ shown in Figure 6.5.4.

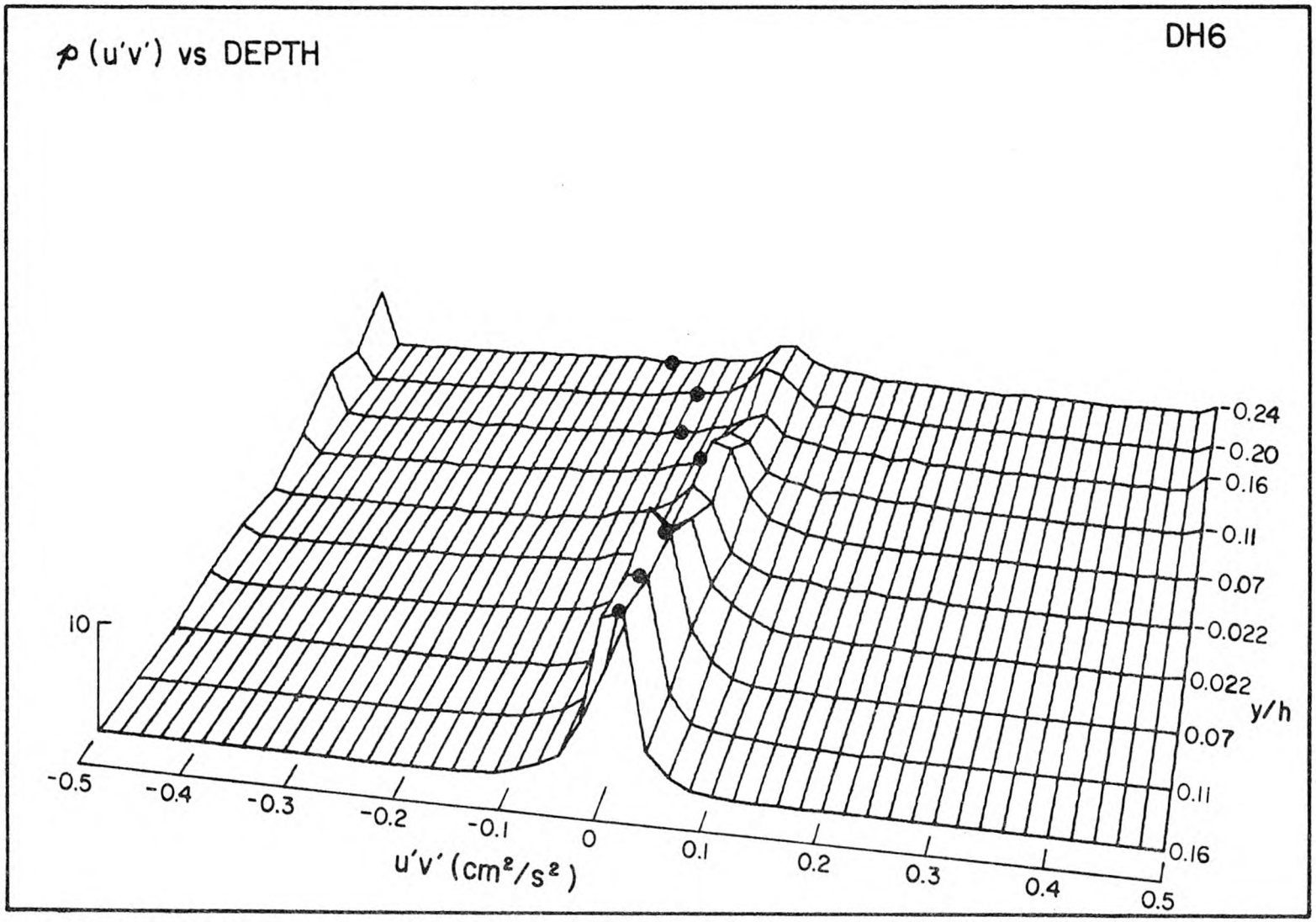

Figure 6.5.8 Unnormalized probability density functions of u'v' (cm^2/s^2) for the same data used in Figure 6.5.7. Points indicate values of $\overline{u'v'}$. Values at u'v' = ± 0.5 cm^2/s^2 indicate the probabilities that u'v' is greater than (or less than) 0.5 cm^2/s^2 (-0.5 cm^2/s^2).

probability density functions of $u'v'$ vary a great deal with depth. The mean values $\overline{u'v'}$ are indicated on the figure, and it is easily seen that as $-\overline{u'v'}$ increases, the probability of finding very large values of $-u'v'$ (in this case, values greater than 0.5 cm^2/s^2) also increases. However, Figure 6.5.8 indicates that the normalized probability density functions for $u'v'/\sqrt{\overline{u'^2}}\sqrt{\overline{v'^2}}$ vary little with depth; this is significant in this instance since the turbulence intensity and the momentum flux, shown in Figure 6.5.4, as well as the stratification, all varied dramatically with depth.

Figure 6.5.9 shows the probability density function of $v'T'/\overline{v'T'}$ measured at the same location as those shown in Figures 6.5.1 and 6.5.5 (x = 16 m, y/h = -0.16, Experiment DH6). As was the case for the probability density functions of $u'v'/\overline{u'v'}$, this graph shows that $v'T'/\overline{v'T'}$ is very large for a significant fraction of time. Furthermore, Figure 6.5.10 indicates that the normalized probability density functions of $v'T'/\sqrt{\overline{v'^2}}\sqrt{\overline{T'^2}}$ show little basic variation with depth except at the largest values of y/h where the flow was laminar. Figure 6.5.11 shows unnormalized probability density functions of $v'T'$ calculated from the same data used in Figure 6.5.10. The mean values, $\overline{v'T'}$, are also shown in Figure 6.5.11 and it is easily seen that the form of the unnormalized probability density functions vary with $\overline{v'T'}$, just as was found to be the case for the unnormalized probability density functions of $u'v'$ (Figure 6.5.8).

Thus, it appears that the mixing in the flow is dominated by events which cover relatively short periods of time, during which

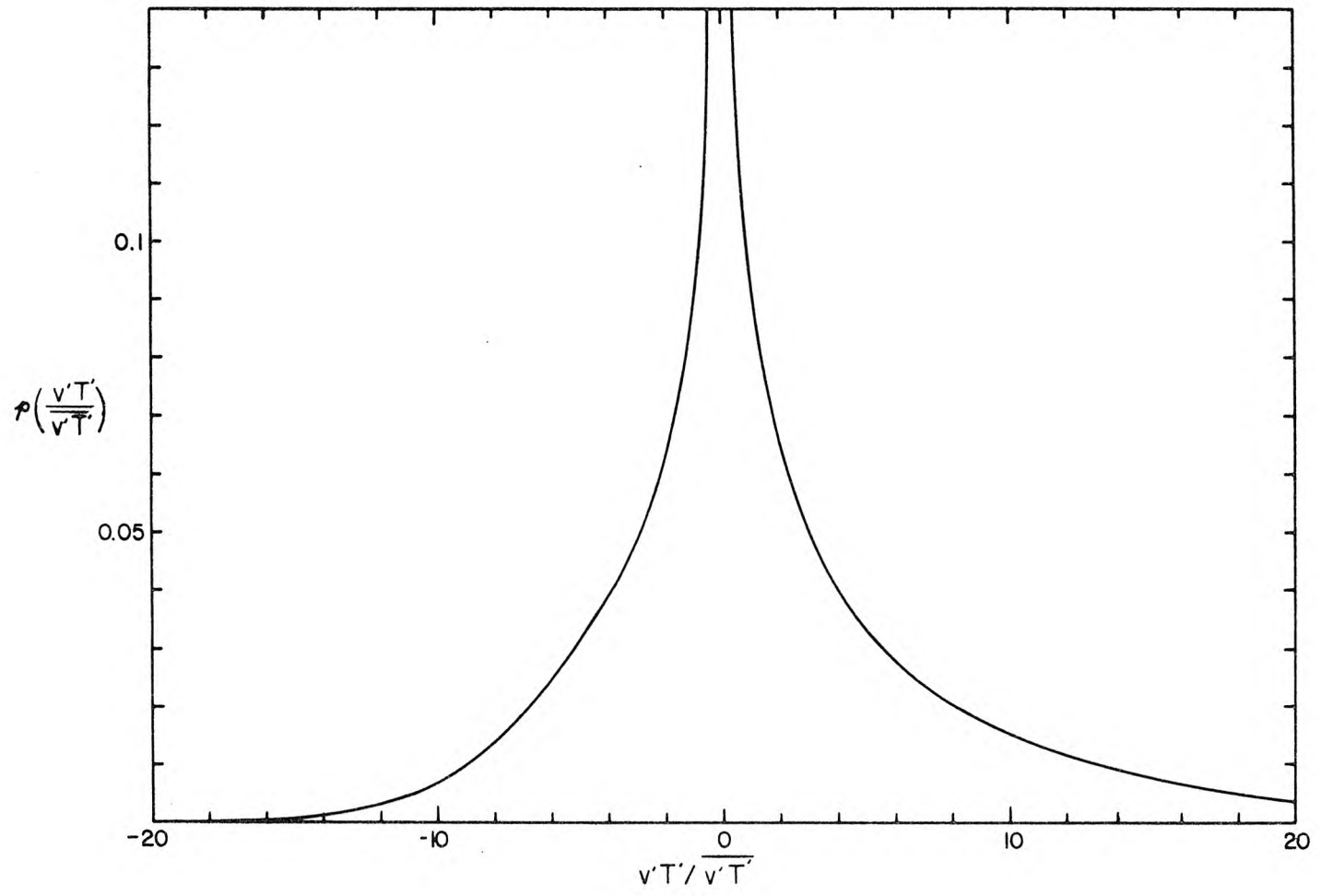

Figure 6.5.9 Probability density function for $v'T'/\overline{v'T'}$, measured at x = 16 m, y/h = -0.16. Data from Experiment DH6.

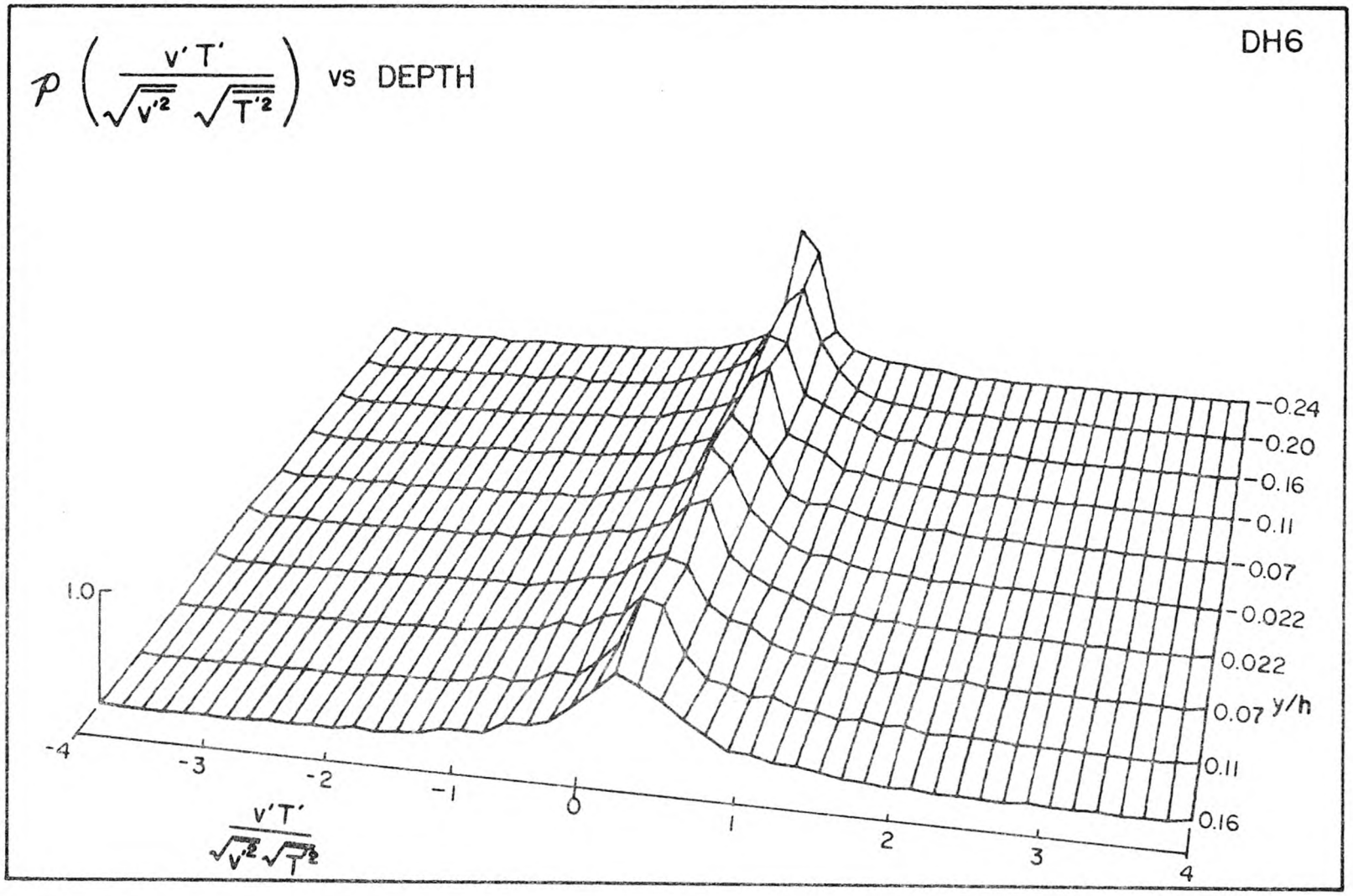

Figure 6.5.10 Variation of the probability density functions for $v'T'/\sqrt{\overline{v'^2}}\sqrt{\overline{T'^2}}$ with depth. Measurements made at x = 16 m, Experiment DH6.

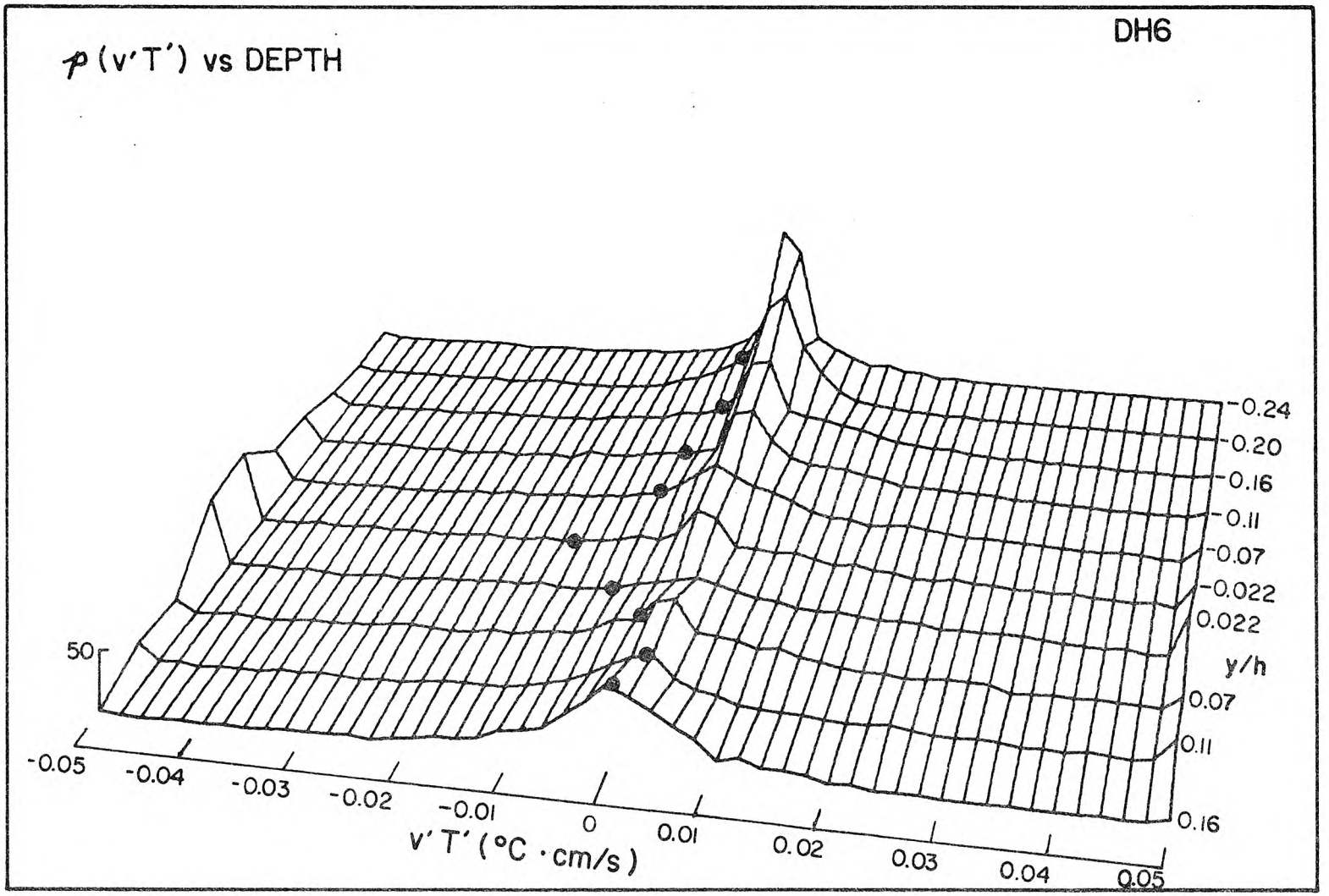

Figure 6.5.11 Unnormalized probability density functions for v'T' (°C.cm/s), for the same data used in Figure 6.5.10. Points indicate measured values of v'T'. Values at v'T' = ±0.05°C.cm/s indicate probabilities that v'T' is greater than (or less than) 0.05°C.cm/s (-0.05°C.cm/s).

quantities such as $-u'v'$ and $-v'T'$ may attain very high values compared to their mean values. This is rather significant, in that the data in this section would indicate that time-averaged quantities may not have the same significance as once thought, especially when one considers that the standard deviation of quantities such as $u'v'$ is often four times the mean value of $u'v'$. One should keep in mind then, when examining data such as $\overline{v'T'}$ and $\overline{u'v'}$, that the fluctuations in the time histories of $v'T'$ and $u'v'$ are large, in fact, very large compared with their respective mean values. The time histories of the fluctuating quantities are explored in more detail in the next section.

6.5.2 Time-Records of Fluctuating Quantities

The nature of the probability density functions prompted an examination of the time records of the turbulent fluctuating quantities to determine whether or not turbulent bursts could be identified. Work by Wallace *et al.* (1977) and Thomas (1977) along similar lines indicates that a pattern in the time-record of u' can be used to recognize turbulent bursts in turbulent boundary layers. This pattern consists of a relatively long period of deceleration in u' followed by a rapid acceleration in u'. The general pattern is often complicated by the fact that the lengths of different turbulent events vary, and more than one event may take place in a given period of time; consequently, one long pattern may have subpatterns superimposed upon it (Wallace *et al.* (1977)). Thomas (1977) found that, in the ensemble averages, the time-record of $u'v'/\overline{u'v'}$ showed a large positive spike during the period of the rapid acceleration of u'.

With the results of these authors in mind, the time-records of fluctuating quantities measured in this study were examined.

Figure 6.5.12 shows time-records of $[u']_N$, $[u'v']_N$ and $[q^*v']_N$, where the symbol $[\quad]_N$ denotes a normalization such that the mean of the quantity is zero and its standard deviation is unity. The data in this figure were measured in a stratified flow over a brick-roughened bed (Experiment CH3), at the bottom of the interfacial region (y/h = -0.11). Each interval on the ordinate indicates one standard deviation, and a dimensional scale for each quantity is also provided. In this instance, the mean values for the three records are $\overline{u'} = 0$, $\overline{u'v'} = -0.17$ cm^2/s^2 and $\overline{q^{*2}v'} = 0.057$ cm^3/s^3. Of course, the laser-Doppler system provides discrete measurements, but in these time-records, straight lines were drawn between adjacent measurements to facilitate the interpretation of the plots.

Upon examining the time-record of u', one can see several patterns (marked with arrows) similar to those described by Thomas (1977) and Wallace *et al.* (1977). Furthermore, the time-record of u'v' usually exhibits a large, negative spike at the same time that the rapid acceleration in the burst pattern occurs. The spikes in u'v' are actually quite large; in this instance, the relative standard deviation of u'v' (that is, $\Sigma_{uv}/|\overline{u'v'}| \equiv \sqrt{\overline{(u'v' - \overline{u'v'})^2}}/|\overline{u'v'}|$) is about 2.7, and the spike in u'v' that occurs near t = 58s reaches almost seven standard deviations below the mean value of u'v' (located at the zero level on this graph). It is easily seen from this graph that the quantity -u'v' often attains values an order of magnitude larger than $-\overline{u'v'}$.

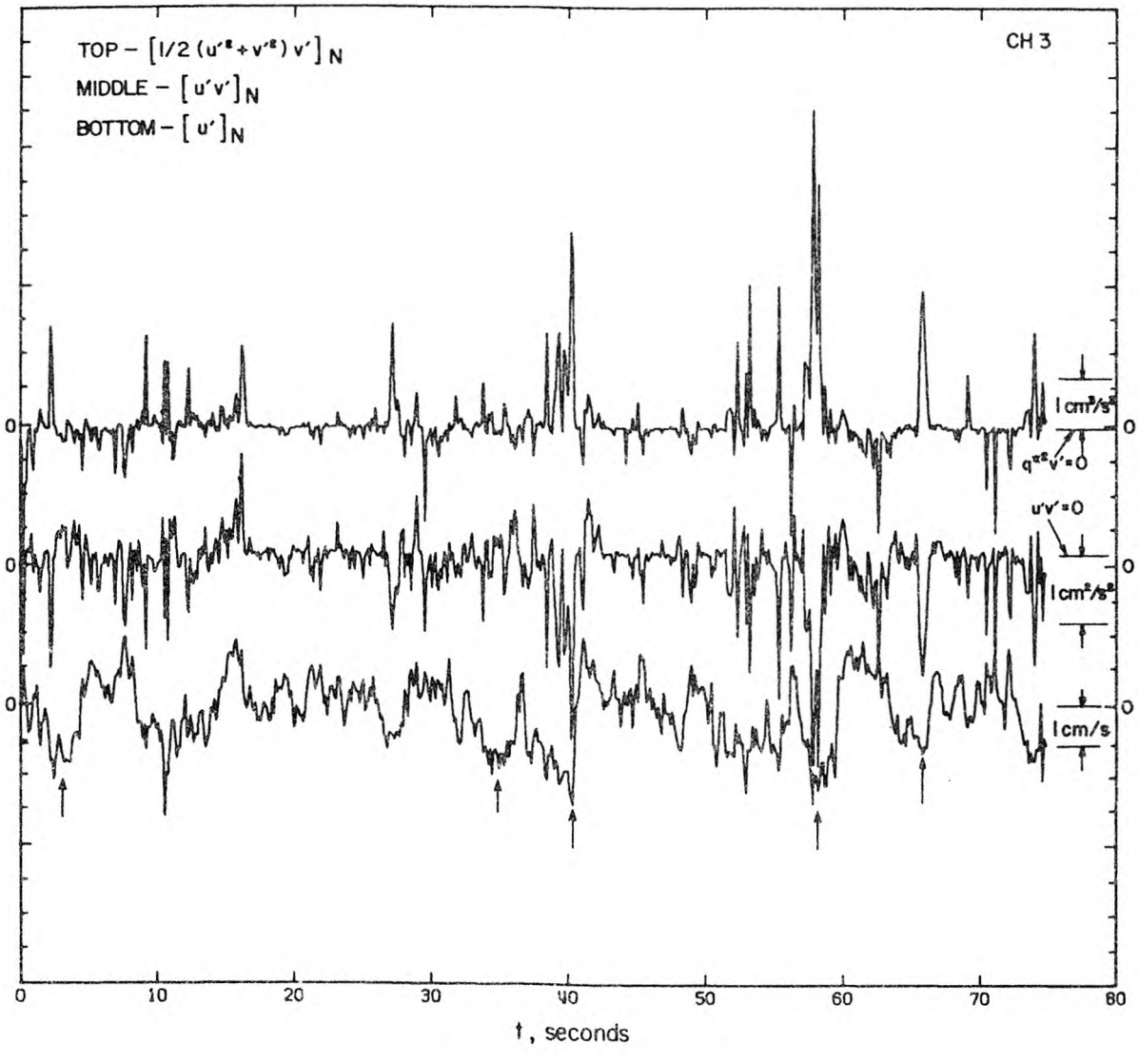

Figure 6.5.12 Time-records of $[q^{*2}v']_N$ (top), $[u'v']_N$ (middle), and $[u']_N$ (bottom). Data measured in a stratified flow over a brick-roughened bed (Experiment CH3, x = 24 m, y/h = -0.11). Records are normalized (denoted by $[\ ]_N$) such that the mean is zero and the standard deviation is one unit. Arrows indicate some turbulent bursts. $-\overline{u'v'} = 0.17$ cm^2/s^2, $q^{*2}v' = 0.057$ cm^3/s^3. Data rate was 8 Hz.

The time-record of $q^{*2}v'$ was also found to be quite interesting. As can be seen in Figure 6.5.12, $q^{*2}v'$ was often very nearly zero (recall that the plot is offset so that the mean value, $\overline{q^{*2}v'}$, which is 0.057 cm^3/s^3 in this case, is at the zero level of the graph), but there are enormous spikes in the record. In fact, the spike at t = 58s is nine standard deviations high, or in this case, 113 times the mean value $\overline{q^{*2}v'}$. Furthermore, it can be seen that the positive spikes in $q^{*2}v'$ are almost always accompanied by large negative spikes in u'v'. This suggests that the turbulent vertical flux of turbulent kinetic energy may be an excellent indicator of the presence of turbulence bursts. Moreover, the fact that the spikes are largely one-sided, almost always positive, indicates that the flux of turbulent kinetic energy is in the positive vertical direction, away from the flume bed as it should be. Relatively few negative spikes of $q^{*2}v'$ are seen, and many of the ones that are present precede large positive spikes by a short period of time.

To demonstrate that the patterns seen in Figure 6.5.12 are typically found in many types of turbulent flows, several other time-records are presented here. All show similar features as seen in Figure 6.5.12.

Figure 6.5.13 shows time-records of $[u']_N$, $[v']_N$, $[u'v']_N$ and $[q^{*2}v']_N$ measured in a homogeneous flow (Experiment D5) over a rock-roughened flume. The measurements were made 24 m from the splitter plate at y/h = -0.16. Again, the same pattern of a long deceleration followed by a relatively rapid acceleration in u' is seen in the flow. Accompanying these patterns in u' are large negative spikes in u'v' and

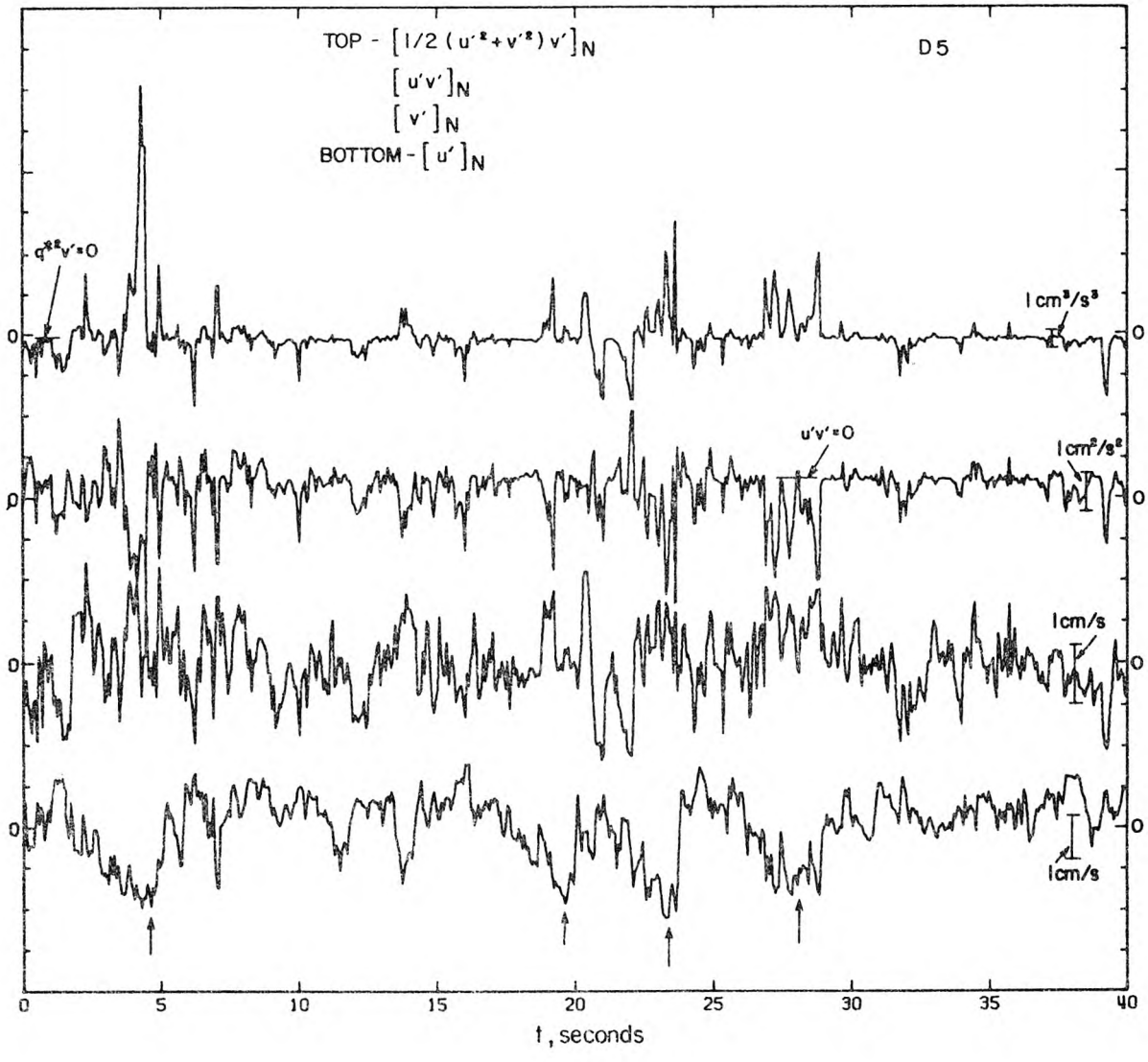

Figure 6.5.13 Time-records of $[q^{*2}v']$ (top), $[u'v']_N$, $[v']_N$ and $[u']_N$ (bottom). Data measured in a homogeneous flow over a rock-roughened bed (Experiment D5, x = 24 m, y/h = -0.16). Arrows indicate turbulent bursts. $-\overline{u'v'} = 0.5$ cm^2/s^2, $\overline{q^{*2}v'} = 0.26$ cm^3/s^3. Data rate was 15 Hz.

large positive spikes in $q^{*2}v'$. Again, it is interesting to note the one-sided nature of the bursts: $u'v'$ is often zero, or very nearly zero, for long periods of time, and the large spikes away from the zero level are almost exclusively negative spikes. On the other hand, the large spikes in $q^{*2}v'$ are almost always positive.

Since the quantity $q^{*2}v'$ includes the term v'^3, it seems necessary to show that the spikes in $q^{*2}v'$ are not merely the result of randomly large values in v' with little correlation to u'. To demonstrate that this is not the case, Figure 6.5.14 is presented which shows time-records of $[q^{*2}u']_N$, $[q^{*2}]_N$, and $[q^{*2}v']_N$ from the same measurements used in Figure 6.4.13. The interesting feature here is that whenever there is a spike in $q^{*2}v'$, there is almost always a spike of opposite sign in $q^{*2}u'$ which would indicate that u' and v' are well correlated during these periods (the correlation being, of course, negative). Furthermore, spikes in q^{*2} are also found when there are spikes in $q^{*2}v'$ (or $q^{*2}u'$), so it seems clear that the spikes in $q^{*2}v'$ (or $q^{*2}u'$) mark highly turbulent events during which the turbulent transport of both momentum and turbulent energy are large.

These general patterns in the time-records of fluctuating quantities were observed over and over, despite differences in the bed roughness and in the flow stratification. Figure 6.5.15, for example, shows time-records of $[u']_N$, $[u'v']_N$ and $[q^{*2}v']_N$ from a stratified flow over a rock-roughened bed (Experiment DH6). Once again it is seen that the record of $q^{*2}v'$ exhibits large spikes and that these spikes are almost always accompanied by large negative spikes in $u'v'$. Furthermore, it

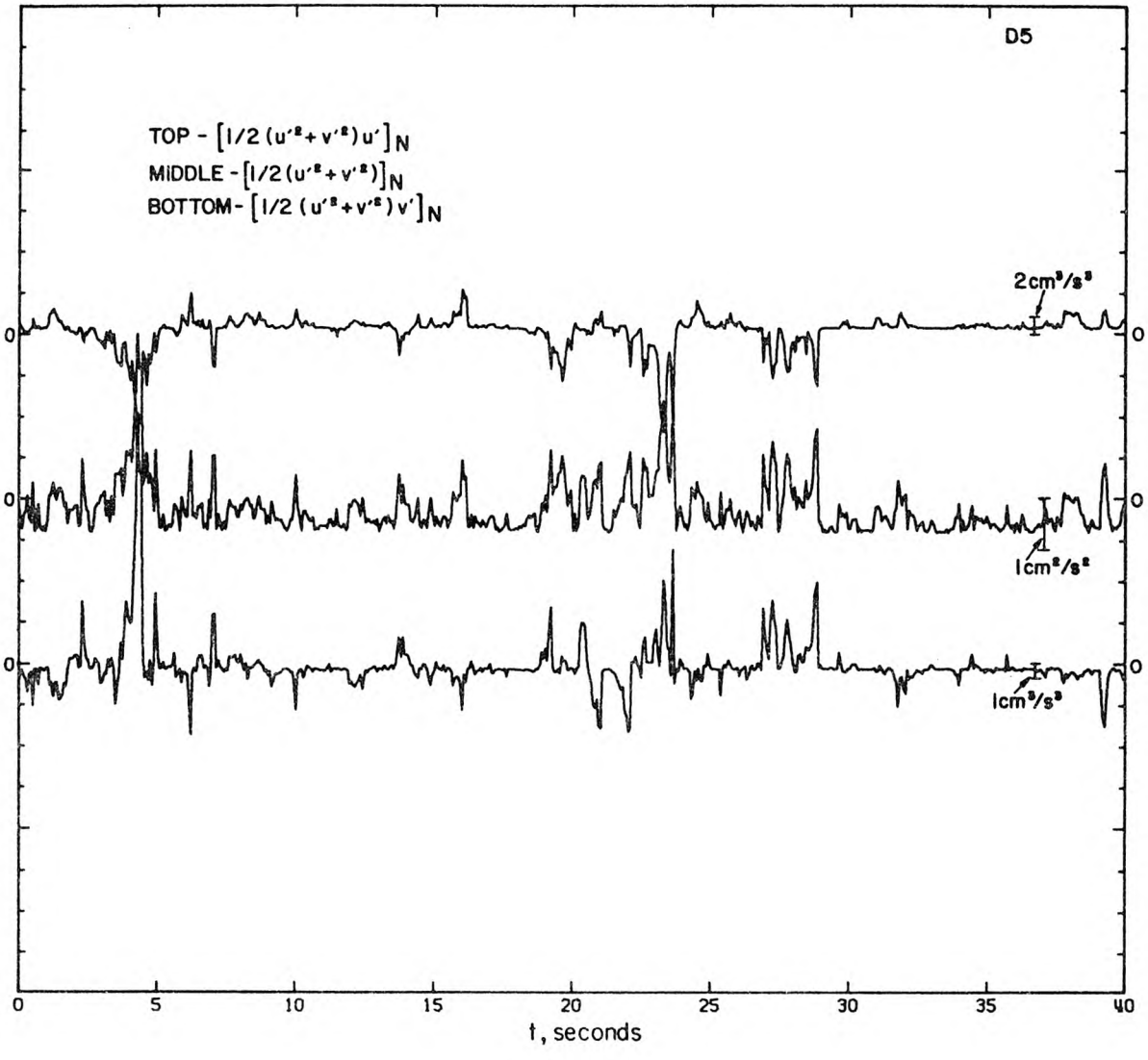

Figure 6.5.14 Time-records of $[q^{*2}u']_N$ (top), $[q^{*2}]_N$ (middle), and $[q^{*2}v']_N$ (bottom) from the same case considered in Figure 6.5.13 (Experiment D5, x = 24 m, y/h = -0.16).

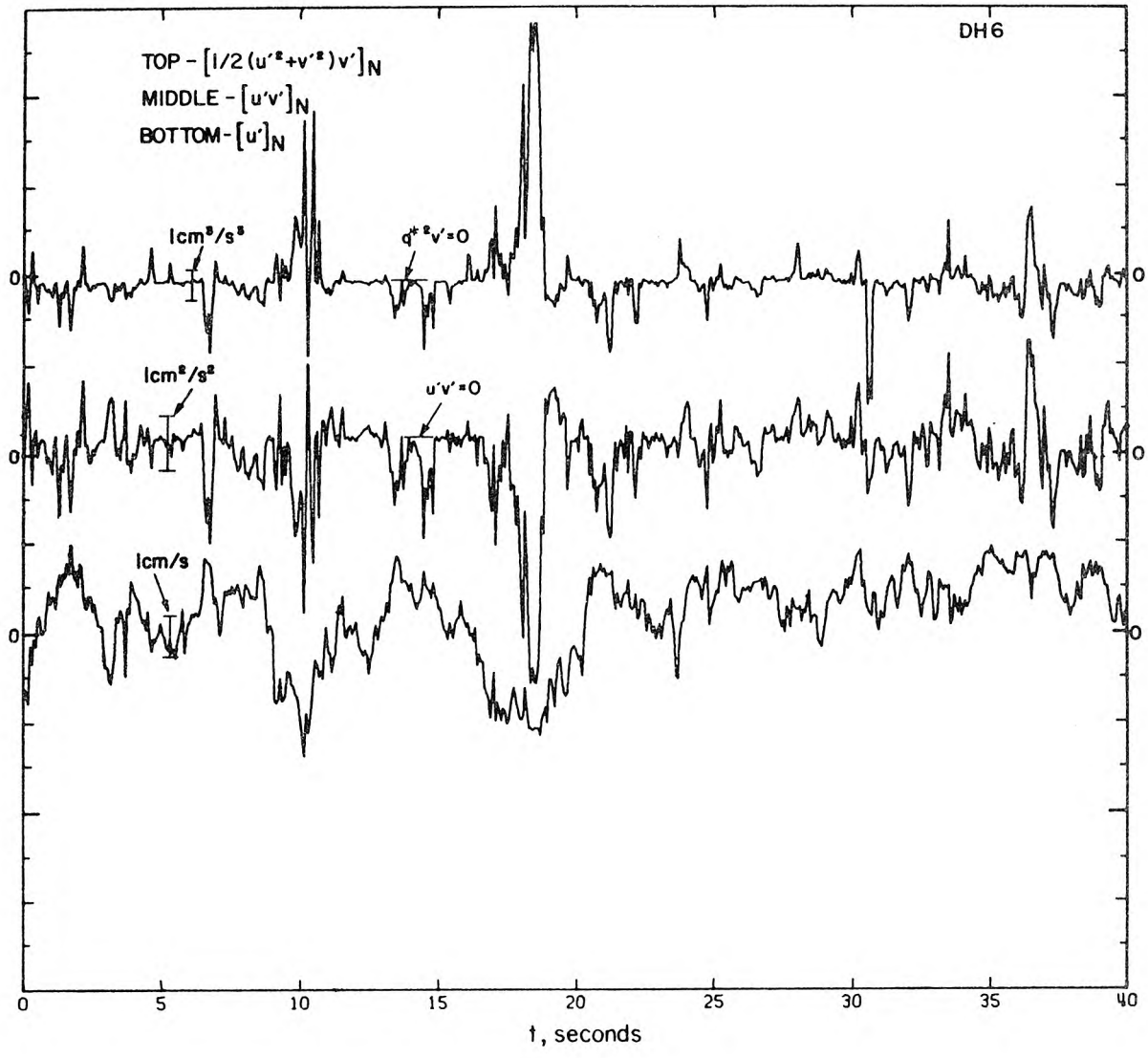

Figure 6.5.15 Time-records of $[q^{*2}v']_N$ (top), $[u'v']_N$ (middle), and $[u']_N$ (bottom). Data from a stratified flow over a rock-roughened bed (Experiment DH6, x = 24 m, y/h = -0.20). $-\overline{u'v'}$ = 0.31 cm^2/s^2, $q^{*2}v'$ = 0.20 cm^3/s^3.

is interesting to note that, while the spikes in $q^{*2}v'$ are largely one-sided, with the largest spikes always positive, both the smaller negative spikes and the large positive spikes are accompanied by negative spikes in $u'v'$. Consequently, it appears that whatever the sign of $q^{*2}v'$, momentum in this flow is largely transferred in the same direction during periods of high turbulent transport of q^{*2}.

Figures 6.5.16 and 6.5.17 show time-records of several normalized fluctuating quantities measured in a density-stratified flow over a rock-roughened bed (Experiment DH7). There are several interesting features in these plots, among them the fact that once again the typical burst patterns are seen in u', and are accompanied by large negative spikes in $u'v'$ and positive spikes in $q^{*2}v'$. Another feature is the fact that the records of $[u']_N$ and $[T']_N$ exhibit many similarities in the large scale structure. The most interesting feature is the fact that the record of $v'T'$ exhibits large negative spikes during the periods in which $q^{*2}v'$ is large (notice in particular the regions around $t = 0s$, $t = 10s$ and $t = 35s$). In contrast to $u'v'$, the record of $v'T'$ shows positive spikes as well as negative, although the latter are generally stronger. Negative spikes indicate that the turbulent transport of heat was large and toward the bed (the expected direction in terms of the temperature gradient).

The time-records of $q^{*2}v'$ did not always exhibit one-sided spikes. Such a case is shown in Figure 6.5.18 which shows time-records of $[u']_N$, $[v']_N$, $[u'v']_N$, and $[q^{*2}v']_N$ measured in a homogeneous flow over a smooth bed (Experiment B4). These measurements were made in

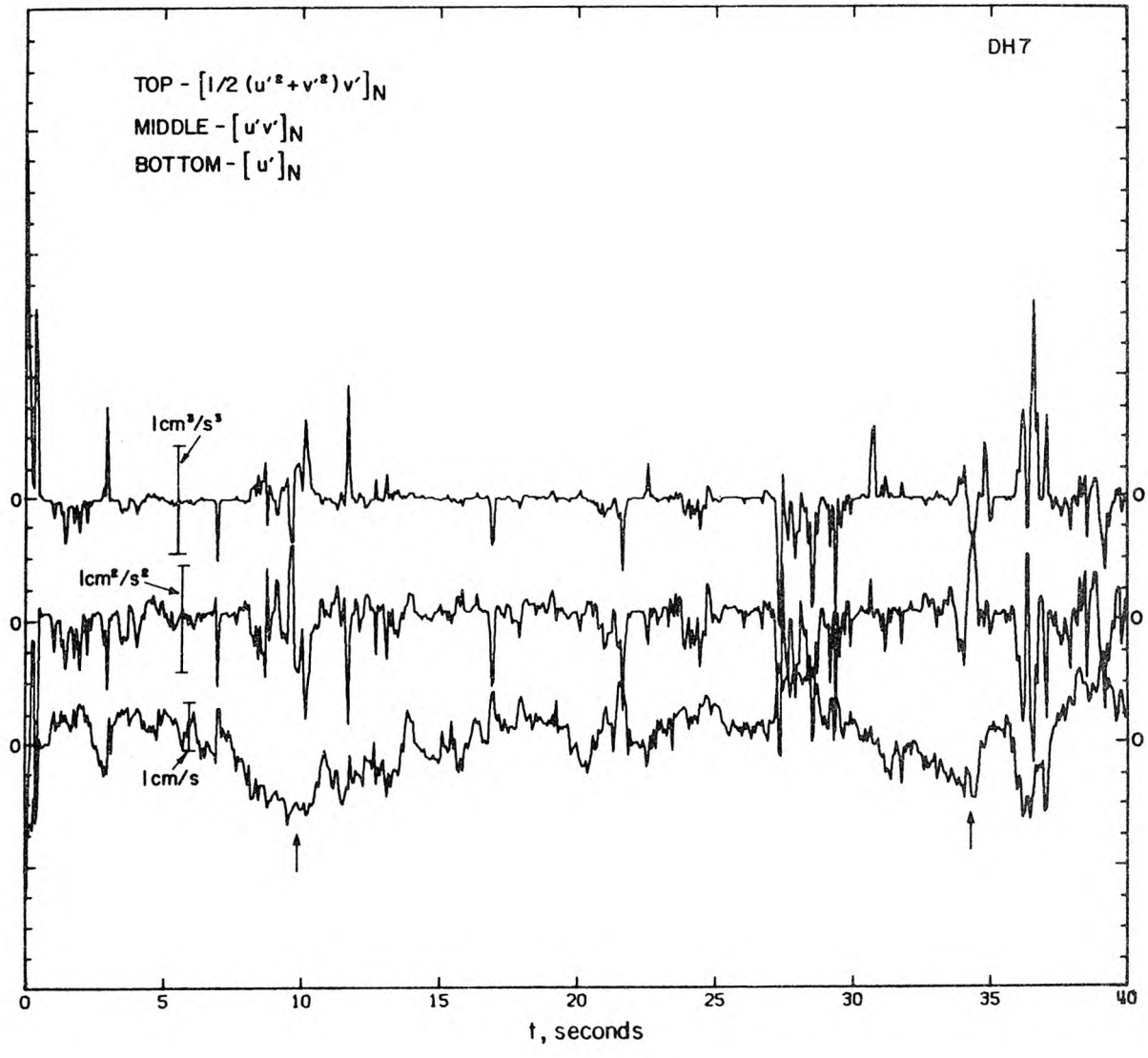

Figure 6.5.16 Time-records of $[q^{*2}v']_N$ (top), $[u'v']_N$ (middle), and $[u']_N$ (bottom). Data measured in a stratified flow over a rock-roughened bed (Experiment DH7, x = 16 m, y/h = -0.11). Arrows indicate turbulent bursts. $-\overline{u'v'}$ = 0.07 cm^2/s^2, $q^{*2}v'$ = 0.017 cm^3/s^3. Data rate was 15 Hz.

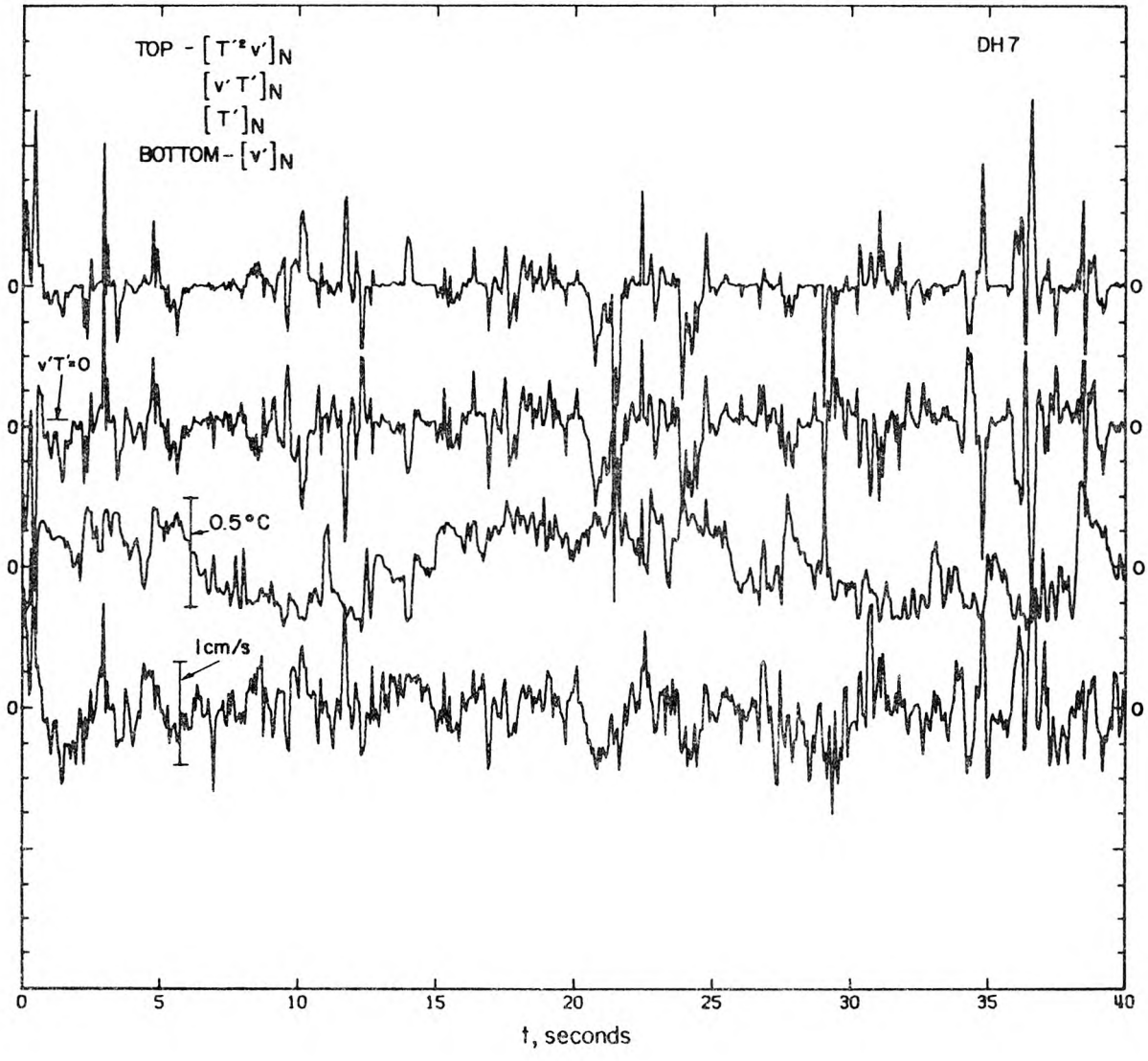

Figure 6.5.17 Time-records of $[T'^2v']_N$ (top), $[v'T']_N$, $[T']_N$, $[v']_N$ (bottom). Measurements made for the same case shown in Figure 6.5.16 (Experiment DH7, x = 16 m, y/h = -0.11). $-\overline{v'T'}$ = 0.0029 °C.cm/s, $\overline{T'^2v'}$ = -1.06×10^{-4} °C^2.cm/s.

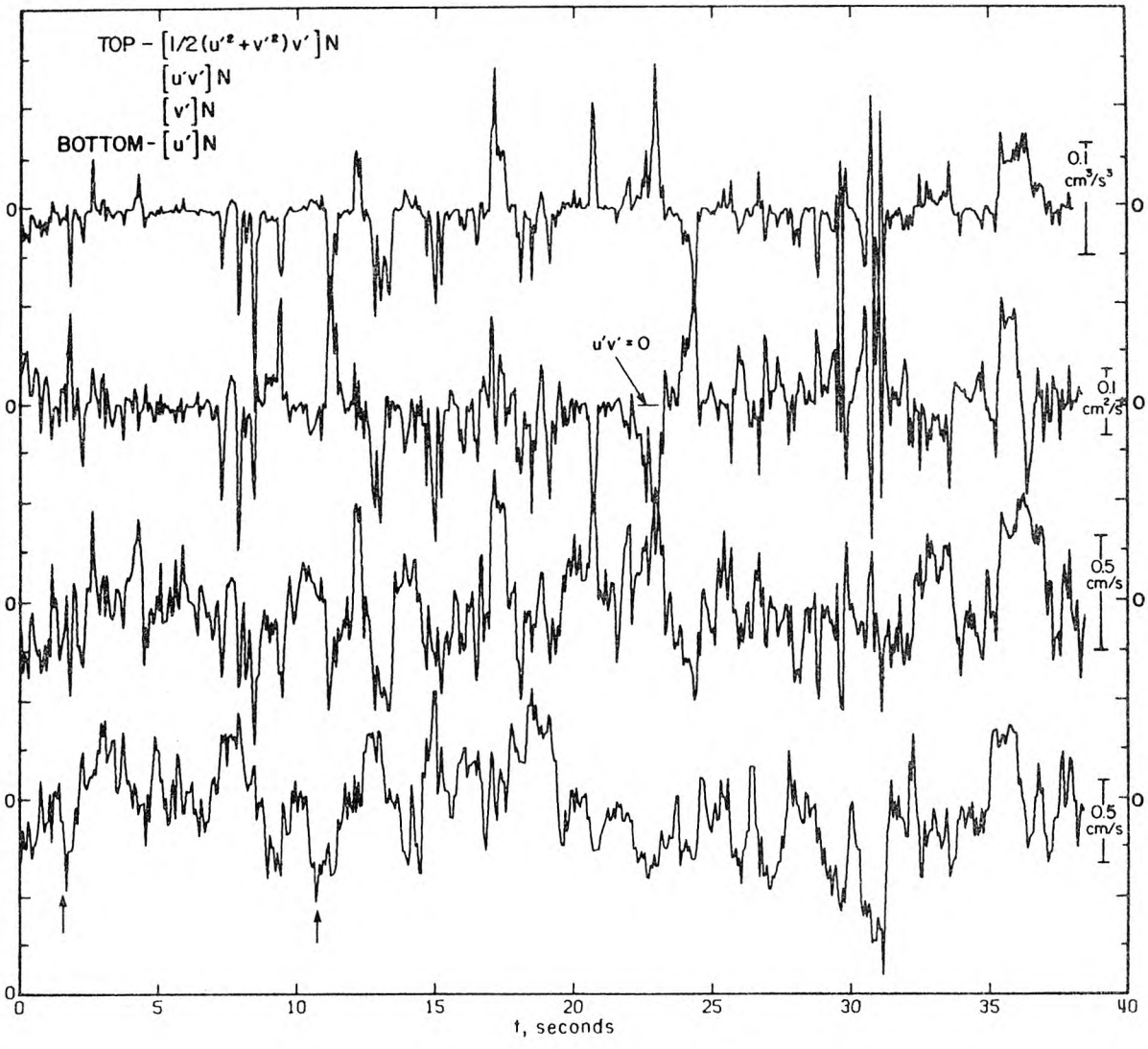

Figure 6.5.18 Time-records of $[q^{*2}v']_N$ (top), $[u'v']_N$, $[v']_N$, and $[u']_N$ (bottom). Data measured in a homogeneous flow over a smooth bed (Experiment B4, x = 21.4 m, y/h = 0.11). $\overline{u'v'}$ = 0.0027 cm^2/s^2, $\overline{q^{*2}v'}$ = 0.0031 cm^3/s^3. Data rate was 15 Hz.

the upper portion of the flow at y/h = 0.11; at this level both the shear and the net momentum flux were very small ($\partial\bar{u}/\partial y$ was $-0.028\ s^{-1}$ and $\overline{u'v'}$ was $0.0027\ cm^2/s^2$).

The most striking feature of these plots is the fact that the quantity $q^{*2}v'$ has both positive and negative spikes of comparable size; moreover, just as the large positive spikes are often preceded by small negative spikes, the large negative spikes are often preceded by small positive spikes. The similarity does not end there, however, for during those periods in which a negative spike in $q^{*2}v'$ is accompanied by a positive spike in u'v', the pattern often found in u' is one of a sudden deceleration followed by a long period of slow acceleration, just the opposite of the pattern seen in the usual boundary layer bursts. (Two such "inverse" patterns are marked with arrows in Figure 6.5.18.) However, there are exceptions to these patterns, as some positive (or negative) spikes in $q^{*2}v'$ are accompanied by positive (or negative spikes in u'v'. Nonetheless, the fact that some of the bursts in the upper portion of this homogeneous flow appear to be "inverses" of typical boundary layer bursts may be suggestive as to the manner in which these bursts interact with the free-surface.

The fact that the u'v' record shows both positive and negative spikes in a region in which both $\left|\frac{\partial\bar{u}}{\partial y}\right|$ and $\left|\overline{u'v'}\right|$ are small is interesting in itself. One might have expected that the unnormalized time-records of turbulent quantities such as u'v' would be similar regardless of location and merely be scaled by, say, $\overline{u'v'}$ or $\partial\bar{u}/\partial y$, but this is clearly not the case. The somewhat peculiar nature of the time-records

shown in Figure 6.5.18 cannot be attributed solely to the fact that this flow was a flow over a smooth bed, for in the deeper portion of this same flow, where $\partial\overline{u}/\partial y$ was larger, the measured time-records are quite similar to those from flows over roughened beds (for example, those in Figure 6.5.13). Furthermore, the time-records from measurements made in flows over roughened beds also exhibited "inverse" bursts in regions near the free surface if both $|\frac{\partial\overline{u}}{\partial y}|$ and $|\overline{u'v'}|$ were small. The influence of the free-surface is not clear, for the presence of "inverse" bursts seems to require a region of low shear (and low turbulent momentum flux), and such regions were only found near the free-surface. Whether these patterns would also be found in a region of low shear which was far from a free-surface cannot be clearly established from these measurements.

One important observation in these time-records is that the burst patterns all possess similar characteristics: neither the stratification nor the roughness of the bed seems to matter. This is particularly evident when one considers the time-records of normalized quantities. In fact, the major difference between the turbulent burst patterns seems not to be in the basic shape of the patterns, but merely in the magnitude and length of the patterns. It is important to note that the shape of the burst patterns measured over the smooth bed were quite similar to those measured over roughened beds.

6.5.3 Mean Quantities from Conditionally Sampled Data Records

In this section the results from the conditional sampling of the data records are presented. Unlike other conditional sampling techniques, the technique used here was based solely on the time-record

of $q^{*2}v'$. Because the spikes in the time-records of $q^{*2}v'$ are good indicators of turbulent bursts, they were used to develop a somewhat crude, but effective, conditional sampling method.

The method used is one which depends solely on the instantaneous, relative magnitude of $q^{*2}v'$. A function, I, is defined such that:

$$I(L_c,t) = \begin{cases} 1, \text{ if } |q^{*2}v'(t)| \Big/ \Sigma_{qv} > L_c \\ 0, \text{ otherwise} \end{cases} \tag{6.5.3}$$

where L_c is the conditional sampling level, and

Σ_{qv} is the standard deviation of $q^{*2}v'$ at the point in question.

Hence, the function I is one if the instantaneous value of $|q^{*2}v'|$ exceeds its standard deviation by a factor L_c. The basis for choosing the quantity Σ_{qv} as the unit of measurement is the fact that the time-records of $q^{*2}v'$ appear to be rather similar when normalized by Σ_{qv}.

Because the records of $q^{*2}v'$ often appear to be one-sided, a second conditional sampling function is defined such that

$$I^*(L_c,t) = \begin{cases} 1, \text{ if } q^{*2}v' \Big/ \Sigma_{qv} > L_c \\ 0, \text{ otherwise} \end{cases} \tag{6.5.4}$$

I^*, then, is one only if $q^{*2}v'$ exceeds Σ_{qv} by a factor of L_c. With these two functions, conditionally sampled averages can be defined by:

$$\langle f \rangle (L_c) = \frac{1}{t} \int_o^t I(L_c,\tau)\ f(\tau)d\tau \tag{6.5.5}$$

and

$$\langle f\rangle^*(L_c) = \frac{1}{t}\int_o^t I^*(L_c,\tau)\ f(\tau)d\tau \qquad (6.5.6)$$

where f is some measured quantity. Note that the averages are normalized with the <u>total</u> length of the record, and also that the brackets, < >, denote different conditionally sampled averages than those used in Section 6.5.1, which were based on the probability density functions.

Finally, the time fractions of the conditionally sampled periods are given by:

$$\Gamma(L_c) = \frac{1}{t}\int_o^t I(L_c,\tau)d\tau \qquad (6.5.7)$$

$$\Gamma^*(L_c) = \frac{1}{t}\int_o^t I^*(L_c,\tau)d\tau \qquad (6.5.8)$$

so that the mean of some quantity f when I (or I^*) is one is given by $\langle f\rangle/\Gamma$ (or $\langle f\rangle^*/\Gamma^*$).

Figure 6.5.19 shows graphs of the conditionally averaged values of u'v' from measurements made in a weakly stratified flow over a roughened bed (Experiment CH4). The figure shows measurements made at two depths (y/h = 0.02 and y/h = -0.16) 20 m from the splitter plate. It is an interesting fact that the plots of $\langle u'v'\rangle/\overline{u'v'}$ as a function of L_c are not dissimilar to the partial integrals of the probability density function of $u'v'/\overline{u'v'}$ (Figure 6.5.6), even though the conditional sampling methods are entirely different. The graphs in Figure 6.5.6 were obtained by integrating the probability density function for $u'v'/\overline{u'v'}$ over specified ranges (Equation 6.5.1 and 6.5.2), whereas

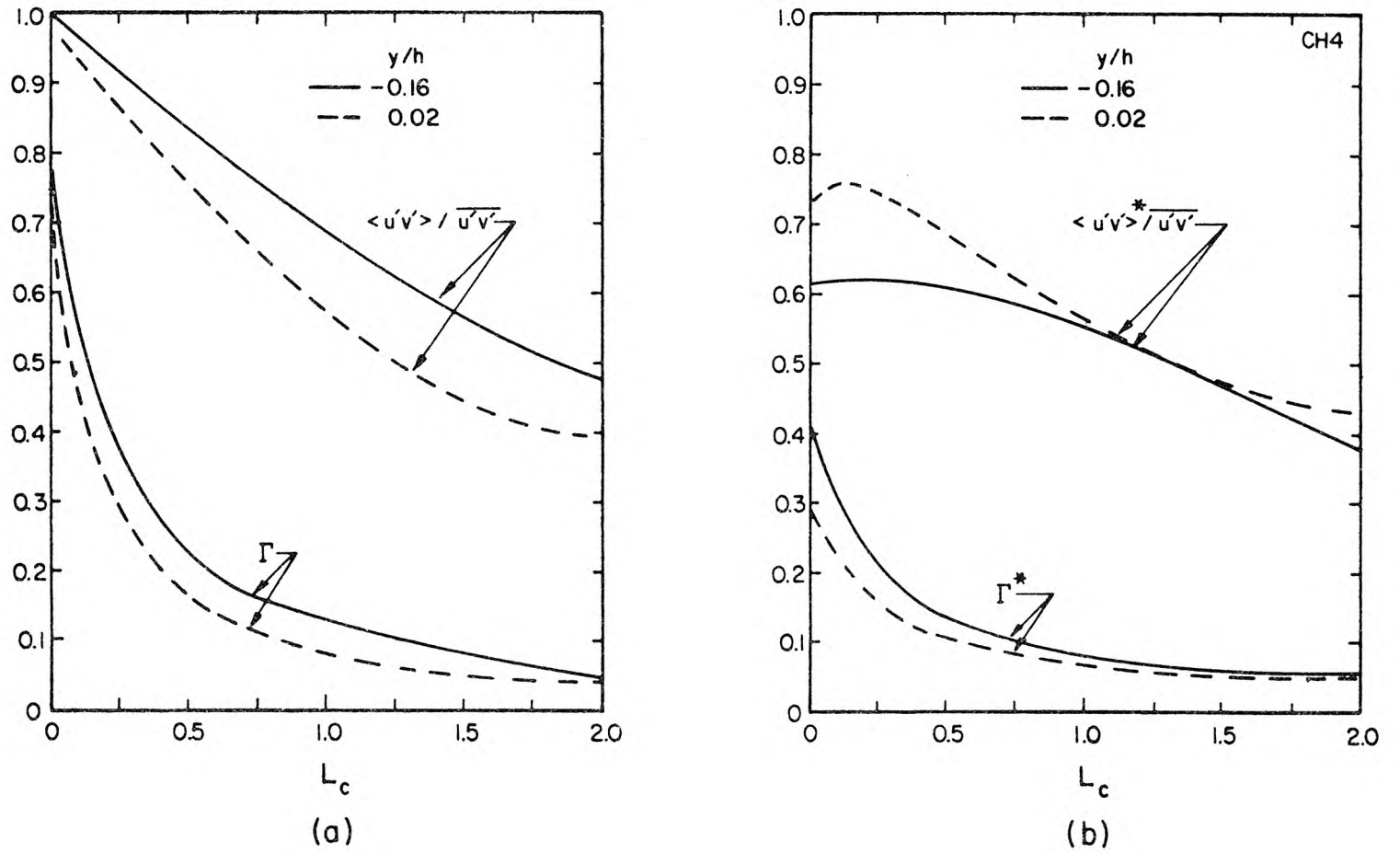

Figure 6.5.19 Conditionally sampled averages (defined by Equations 6.5.3 - 6.5.8) from measurements made at two depths in a weakly stratified flow (Experiment CH4, x = 20 m).

(a) $\langle u'v' \rangle / \overline{u'v'}$ and $\Gamma(L_c)$ plotted against L_c.

(b) $\langle u'v' \rangle^* / \overline{u'v'}$ and $\Gamma^*(L_c)$ plotted against L_c.

the values of $<u'v'>/\overline{u'v'}$ and Γ shown in Figure 6.5.19 were obtained using the time-record of $q^{*2}v'$ (Equations 6.5.3, 6.5.5 and 6.5.7). Despite the fact that Figures 6.5.6 and 6.5.19 show data from two distinct experiments (DH6 and CH4), there is a great similarity between the two sets of data.

Considering Figure 6.5.19 by itself, one can see some rather remarkable properties. Although there is some difference between the data measured at the two depths, the differences are not great, especially when one considers the fact that $-\overline{u'v'}$ was 0.17 cm^2/s^2 at y/h = 0.02, and 0.30 cm^2/s^2 at y/h = -0.16. The similarity in $<u'v'>/\overline{u'v'}$ between the two measurements seems even greater when one observes that for a given value of Γ, the respective values of $<u'v'>/\overline{u'v'}$ for the two cases are nearly the same. (For example, when Γ = 0.2, $<u'v'>/\overline{u'v'}$ is about 0.79 for y/h = 0.02, and $<u'v'>/\overline{u'v'}$ is about 0.81 for y/h = -0.16. Consequently, it appears that at the higher depth where $-\overline{u'v'}$ is small, the time fraction of "large bursts" (in terms of $q^{*2}v'/\Sigma_{qv}$) is smaller than at the lower depth, but for a given time fraction Γ, $<u'v'>/\overline{u'v'}$ is about the same in either case.

When one considers the actual values of $<u'v'>/\overline{u'v'}$ compared to the values of Γ, the results are somewhat astounding; better than 60 per cent of the total turbulent momentum flux can be accounted for in less than 10 per cent of the total time of the data record. These values are obtained for values of $L_c = q^{*2}v'/\Sigma_{qv} < 1.5$.

The one-sidedness of the records is apparent from the curves in Figure 6.5.19b, which show the values of $<u'v'>^*/\overline{u'v'}$ and Γ^* for these

same two cases. When $L_c = 0$, $\langle u'v' \rangle^* / \overline{u'v'}$ is found to be greater than 0.6, while Γ^* is seen to be between 0.3 and 0.45. As L_c increases, Γ^* decreases rapidly, while $\langle u'v' \rangle^* / \overline{u'v'}$ falls off much more slowly: when $L_c = 1$, $\langle u'v' \rangle^* / \overline{u'v'}$ is still greater than 0.55, while Γ^* is less than 0.08. The fact that Γ^* falls off so fast as L_c increases from zero to 0.5, while $\langle u'v' \rangle^* / \overline{u'v'}$ declines much more slowly indicates that the smaller bursts account for a substantial fraction of the total time, but a small fraction of the total momentum flux.

Figure 6.5.20 shows plots of conditionally sampled averages of u'v' measured in a stratified flow over a roughened bed (Experiment CH3). Although the flow in this case was much more strongly stratified than the case shown in Figure 6.5.19 ($\frac{\Delta\rho}{\rho_o} = 7.9 \times 10^{-4}$ compared to 2.4×10^{-4}), the results are quite similar. Once again, Γ and Γ^* decrease rapidly as L_c increases from zero to 0.5, while $\langle u'v' \rangle^* / \overline{u'v'}$ remains nearly constant. Furthermore, when $\Gamma(L_c) = 0.1$, $\langle u'v' \rangle^* / \overline{u'v'}$ is greater than 0.65, again indicating that while the bursts account for a small fraction of time, they are responsible for a large fraction of the total momentum flux.

Figure 6.5.21 shows curves of two other conditionally sampled quantities, calculated from measurements made in the same case considered in Figure 6.5.20. The first of these quantities is a correlation coefficient, $-\langle u'v' \rangle^* / (\langle u'^2 \rangle^* \langle v'^2 \rangle^*)^{1/2}$. The value of this conditionally sampled correlation coefficient has a value of about 0.42 when L_c is zero; the value of $-\overline{u'v'} / (\sqrt{\overline{u'^2}} \sqrt{\overline{v'^2}})$ at this location was 0.39, which is a typical value for the correlation coefficient in this

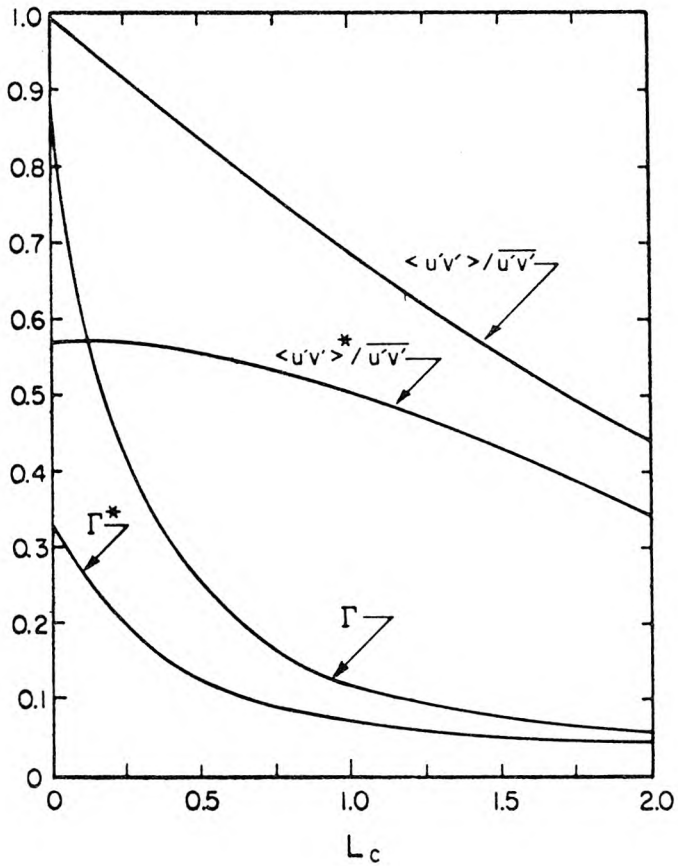

Figure 6.5.20

Conditionally sampled averages (defined by Equations 6.5.3 - 6.5.8), from measurements made in a stratified flow over a roughened bed (Experiment CH3, y/h = -0.11, x = 24 m).

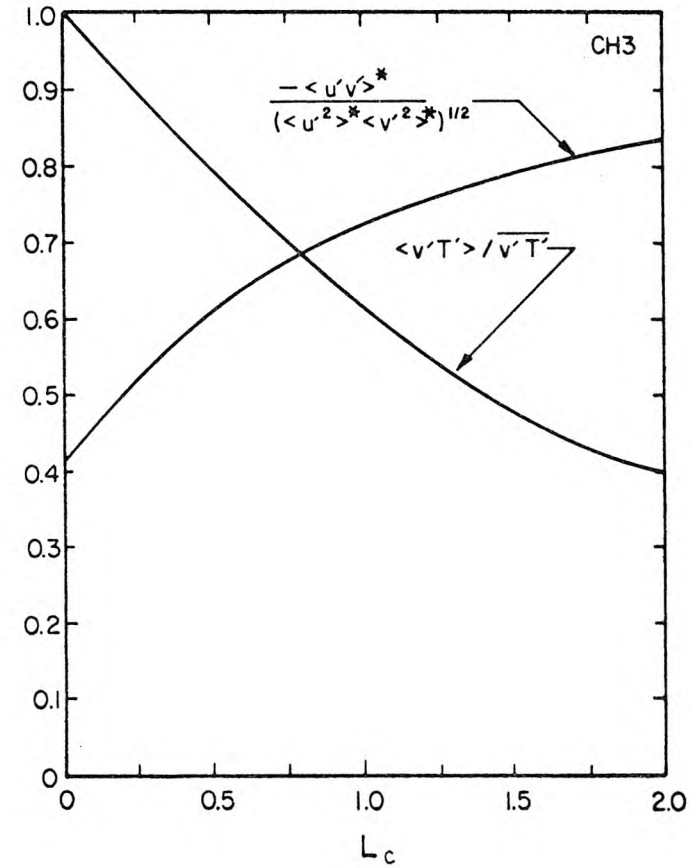

Figure 6.5.21

Conditionally sampled averages (defined by Equations 6.5.3 - 6.5.8), from measurements made in a stratified flow over a roughened bed (Experiment CH3, y/h = -0.11, x = 24 m).

situation. However, as L_c increases, $-\langle u'v'\rangle^*/(\langle u'^2\rangle^*\langle v'^2\rangle^*)^{1/2}$ also increases and, at $L_c = 2$, reaches a value greater than 0.8. This is a remarkably large value for a turbulent flow, and it demonstrates the efficacy of using the spikes in $q^{*2}v'$ to identify turbulent bursts and conditionally sample the data records.

The second quantity shown in Figure 6.5.21 is $\langle v'T'\rangle/\overline{v'T'}$, and this curve is presented to demonstrate that a large fraction of the turbulent flux of heat in this flow also occurred during the same turbulent bursts. The curve of $\langle v'T'\rangle/\overline{v'T'}$ shown in Figure 6.5.21 is not dissimilar to that of $\langle u'v'\rangle/\overline{u'v'}$ shown in Figure 6.5.20; with the curve of $\Gamma(L_c)$ in Figure 6.5.20, one can see that over 55 per cent of the turbulent heat flux occurred in turbulent bursts which accounted for less than 10 per cent of the total time.

Figure 6.5.22 shows conditionally sampled averages of u'v' measured in a homogeneous flow over a smooth bed (Experiment B4). Again, these graphs show that a large fraction of the total momentum flux occurs in a small fraction of the total time. Furthermore, the plots are remarkably similar to those shown in Figures 6.5.19 - 6.5.21 despite the vastly different flow conditions; but this is not really surprising when one considers the similarity in the time records of normalized turbulent quantities, regardless of basic flow conditions (see Section 6.5.2).

Finally, the functions $I(L_c,t)$ and $I^*(L_c,t)$ were used to estimate the mean period between bursts. This was done by counting the number of transitions from zero to one in I (or I^*) over a given period of

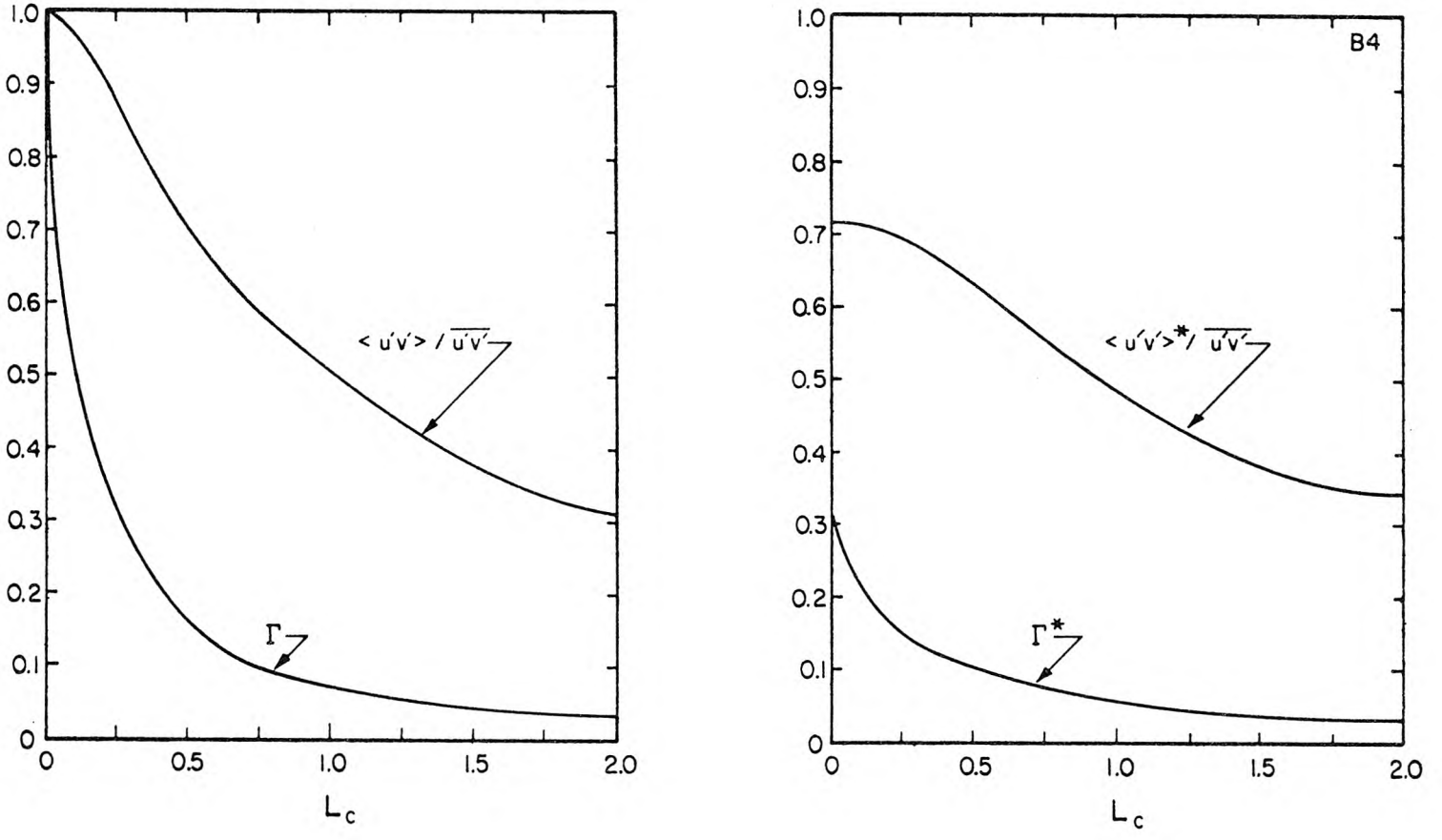

Figure 6.5.22 Conditionally sampled averages (defined by Equations 6.5.3 - 6.5.8) from measurements made in a homogeneous flow over a smooth bed. Data from Experiment B4, x = 21.4 m, y/h = -0.24.

time to get an estimate on the frequency of the bursts. The results from the calculations are shown in Figures 6.5.23 and 6.5.24 which show the scatter-bands of $\overline{Ut_b}/h$ and $\overline{Ut_b^*}/h$ plotted against L_c, where $\overline{t_b}$ is the mean time between the bursts found with $I(L_c,t)$ and t_b^* is the mean time between bursts found with $I^*(L_c,t)$. The data in both cases were scattered, and the bands show the range of the data. As would be expected, the mean period, $\overline{t_b^*}$, found from the "one-sided" positive bursts is generally larger than $\overline{t_b}$.

While the values of $\overline{Ut_b}/h$ and $\overline{Ut_b^*}/h$ were scattered, they did show some general trends. It was found that at a given value of L_c, $\overline{t_b}$ and $\overline{t_b^*}$ were generally larger in more stratified flows than in less stratified or homogeneous flows. Furthermore, it was found that $\overline{t_b}$ and $\overline{t_b^*}$ were larger when the flume bed was smooth than when it was roughened. This would indicate that there are proportionally fewer bursts of a given relative size range (that is, fewer bursts for which $q^{*2}v'/\Sigma_{qv} > L_c$) in a stratified flow or a flow over a smooth bed, and this fact may be suggestive as to the manner in which bursts are produced; in particular, it may be that it takes large turbulent bursts to initiate the development of other large bursts. In a stratified flow, the development of a large burst may be suppressed by buoyancy forces so that fewer similar bursts are produced, resulting in a decrease in the burst frequency. This is, of course, speculative without further data, but it is a plausible explanation of these results.

6.5.4 Summary of the Results on Organized Structures in the Turbulent Regions

The results of this section indicate that the vertical

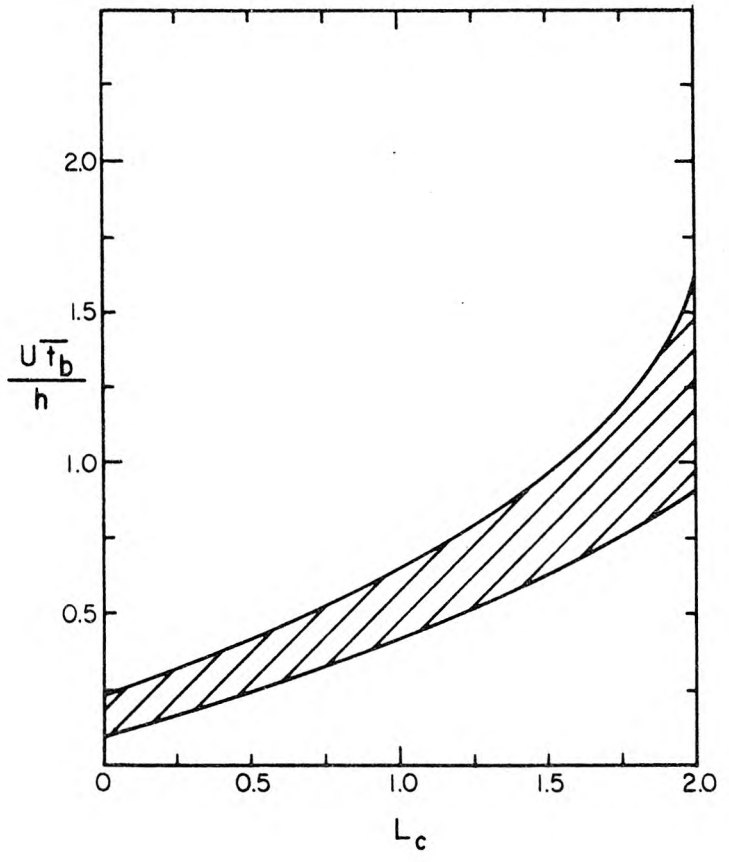

Figure 6.5.23

Average periodicity of bursts $\frac{\overline{Ut}_b}{h}$ plotted against L_c.

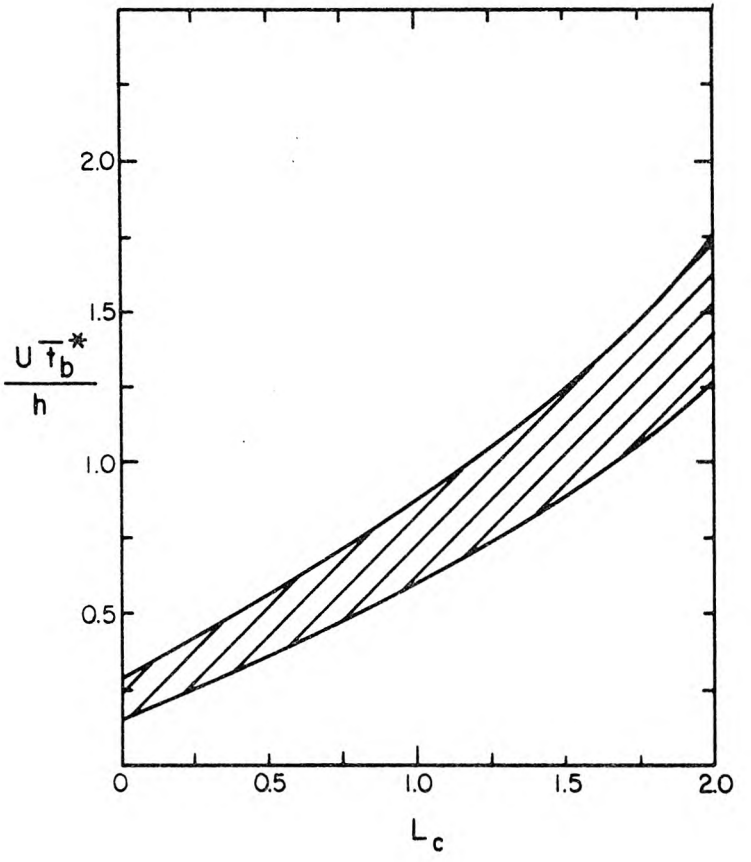

Figure 6.5.24

Average periodicity of "one-sided" bursts plotted against L_c.

turbulent flux of turbulent kinetic energy, $q^{*2}v'$, is a good indicator of the presence of turbulent bursts. During the turbulent bursts, an identifiable pattern in the time-record of u', which consists of a relatively long period of deceleration followed by a sudden acceleration, was often found and the value of u'v' often exceeded $\overline{u'v'}$ by more than a factor of ten. Furthermore, the time-records of $q^{*2}v'$ show that the instantaneous value of $q^{*2}v'$ is very nearly zero for long periods, but during the turbulent bursts, it may exceed $\overline{q^{*2}v'}$ by a factor of over 100.

The general patterns in u', u'v' and $q^{*2}v'$ during highly turbulent events were found to be quite similar whether the flow was stratified or homogeneous, or whether the bed was roughened or smooth. In addition, "inverse" burst patterns were found near the free-surface in homogeneous flows where $|\frac{\partial \overline{u}}{\partial y}|$ was very small. These "inverse" burst patterns consist of a sudden deceleration in u' followed by a relatively long period of slow acceleration, and are accompanied by a large, positive spike in u'v' and a large, negative spike in $q^{*2}v'$.

It was found that the quantity $q^{*2}v'(t)$ can be used effectively to conditionally sample the data records. When the scheme described by Equations 6.5.3 - 6.5.8 is employed, the results indicate that while the turbulent bursts account for a small fraction of the total time, they are responsible for a large fraction of the total turbulent momentum flux and heat flux. Finally, the conditionally sampled records indicate that the time between bursts was generally larger in more stratified flows compared to less stratified flows, and generally smaller in flows over roughened beds compared to flows over smooth beds. These results are discussed in further detail in Section 7.3.

CHAPTER 7

DISCUSSION OF THE EXPERIMENTAL RESULTS

7.0 Introduction

In this chapter a discussion of the results presented in Chapters 5 and 6 is given. Section 7.1 presents a general discussion of the experimental results for the measurements made in the initial mixing layer. Section 7.2 concentrates on the exchange of turbulent kinetic energy in the stratified shear flows examined in this study, while Section 7.3 examines the large, organized structures found in these flows and their relationship to the other results of this study. Finally, Section 7.4 contains a discussion of the implications of these results, particularly those pertaining to the general understanding of the nature of density-stratified, turbulent shear flows.

7.1 Discussion of the Results of the Measurements in the Initial Mixing Layer

In this section a discussion of the results for the initial mixing layer is presented. In Sections 7.1.1 and 7.1.2 some of the present results are compared with those of other investigators. Section 7.1.3 contains a discussion of the turbulent processes which occur during the collapse of the mixing layer, and Section 7.1.4 contains a summary of the discussion on the initial mixing layer.

7.1.1 Comparison of Measured Profiles and the Gross Features of the Initial Mixing Layer

As was discussed in Section 5.1, the inlet turbulence levels were not negligible; in addition, the boundary layers on the splitter

plate produced a wake which had some effect on the initial flow development. Since the primary objective of this study was to examine the flow development downstream, these were not considered to be serious problems. However, the inlet turbulence levels and splitter plate wake did have some effect on the measurements in the initial mixing layer, and these effects are considered in this discussion.

Mean Velocity Profiles

It was found in this study that the profiles of $(\overline{u} - \overline{u}_2)/\Delta\overline{u}_o$ are similar for a given experiment when they are plotted as a function of $(y - y_o)/(x - x_o)$, as is shown in Figure 6.2.1 (see Section 6.2.1). However, it was found that the profiles of the homogeneous flow (Experiment B5) were not the same as the profiles of a stratified, but otherwise similar flow (Experiment BH12), and the difference in the profiles is attributed to buoyancy effects. When one considers the large stabilizing effect of the small density stratifications found in this study, it is perfectly reasonable to conclude that the increased shear (and decreased spreading rate) in the stratified case is due to the influence of buoyancy forces.

Buoyancy effects can also be seen to some degree when one compares the profiles from Experiments BH10 and BH12; the profiles are quite similar even though the respective values of $\lambda_m = \Delta\overline{u}_o/(\overline{u}_1 + \overline{u}_2)$ were 0.15 and 0.20 for these cases. Generally, one finds an increase in the spreading rate (or a decrease in the maximum slope of the normalized profile of $\overline{u}$) with an increase in λ_m (Brown and Roshko (1974)). The fact that the spreading rate, δ_ω', was about the same for the two cases

may be due to the fact that the flow with the larger value of λ_m (Experiment BH12) also had a larger initial density difference. However, as was pointed out by Wygnanski and Fiedler (1970) and Champagne *et al.* (1976), the state of the initial boundary layer of the flow on the splitter plate may have a significant effect on the development of the mixing layer; since the boundary layer thickness and turbulence levels in the inlet streams were larger in this study than in others, it may be difficult to determine the relative influence of the inlet turbulence as opposed to the density differences for these two flows. It seems clear, however, that the buoyancy forces do have some effect on the initial development of the mixing layer, since the spreading rates for Experiments BH12 and B5 were so different, despite the fact that the inlet conditions for the two cases were nearly identical, with the exception of the stratification.

The inlet conditions directly affected the measurements in the initial mixing layer in several other ways. The wake from the splitter plate is slightly apparent near $(y - y_o)/(x - x_o) = -0.025$ in Figure 6.2.1 and the fact that the inlet velocity profiles were not perfectly uniform is apparent in Figure 6.2.1 (and in Figures 5.1.1 - 5.1.4) away from the mixing region. The relatively high turbulence intensities in the inlet flow were also apparent in the measurements (Figures 6.2.11 and 6.2.13). Since the properties of turbulence are of prime importance in this study, the effect of the inlet turbulence on the measurements is discussed in some detail here.

Turbulence Intensities

In this study the maximum values of $\sqrt{\overline{u'^2}}/\Delta\bar{u}_o$ and $\sqrt{\overline{v'^2}}/\Delta\bar{u}_o$ measured in the mixing layer are higher than those reported by other investigators. In the homogeneous flow, $\sqrt{\overline{u'^2}}/\Delta\bar{u}_o$ was found to be as high as 0.25, and $\sqrt{\overline{v'^2}}/\Delta\bar{u}_o$ was found to be as high as 0.19; by contrast Wygnanski and Fiedler (1970) found that the maximum values were 0.176 and 0.138, respectively. Baddour and Chu (1978) found the maximum values of $\sqrt{\overline{u'^2}}/\Delta\bar{u}_o$ to be about 0.15 in a stratified mixing layer, while Koop (1976) found maximum values around 0.164, also in a stratified mixing layer. The discrepancy between the values measured in this study and those measured by others is very likely due to the higher inlet turbulence levels in this study.

As can be seen in Figures 6.2.11 and 6.2.13, the free-stream turbulence levels were as much as 1/3 to 1/2 of the maximum values found in the mixing layer, and the larger values of $\sqrt{\overline{u'^2}}/\Delta\bar{u}_o$ and $\sqrt{\overline{v'^2}}/\Delta\bar{u}_o$ found in the mixing layer are probably due in large part to the high inlet turbulence levels. There are several other factors which support this conclusion. First, it can be seen that while $\sqrt{\overline{u'^2}}/\Delta\bar{u}_o$ (Figure 6.2.11) decreases with x in both the homogeneous and the stratified flows, the change in the maximum value of $\sqrt{\overline{u'^2}}/\bar{u}_o$ with x is <u>much</u> larger in the stratified flows; in fact, the maximum values of $\sqrt{\overline{u'^2}}/\Delta\bar{u}_o$ for $x \geq 1.0$ m are nearly constant in the homogeneous case, while they continue to decrease in the stratified cases (especially for $x/\ell_b > 2$). It is felt that the <u>initial</u> decrease in $(\sqrt{\overline{u'^2}}/\Delta\bar{u}_o)_{max}$ in the homogeneous flows is due to the dissipation of turbulent kinetic energy, particularly that

due to inlet turbulence, while the continual decrease in $\sqrt{\overline{u'^2}}/\Delta\bar{u}_o$ in the stratified flows is due both to dissipation and work by buoyancy forces.

Turbulence Spectra and Inlet Conditions

Figure 6.2.38 shows that a substantial amount of the turbulent energy is in the small scales in the homogeneous flow. The contrasting appearances of the spectral estimates of the homogeneous case (Figure 6.2.38) and the stratified case (Figure 6.2.39) measured close to the splitter plate indicate that buoyancy forces tend to suppress the smaller scales. This is supported by visual observations as well (Section 5.3), for it was found that photographing the two-dimensional vortices downstream was easier when the flow was turbulent than when the flow was stratified, since the dye used for flow visualization did not "smear out" and disperse as much in the stratified flows as in the homogeneous flows; this was clearly the result of a reduction of the smaller turbulence scales in the stratified flows.

The smaller turbulence scales seen in the power spectral estimates of Figure 6.2.38 may be attributed to the inlet turbulence, for the power spectra of u' and v' measured above (or below) the mixing layer also show a substantial amount of power in the small scales, and fall off much less rapidly than $k^{-5/3}$. Champagne *et al.* (1976) found the spectra of u' and v' to clearly follow the (-5/3) power law for moderate wave numbers, and none of their spectra show the behavior seen in Figure 6.2.38. The relative free-stream turbulence levels in their experiments were on the order of 10^{-3}. Furthermore, the fact that the initial

portion of the mixing layer in this study was often three-dimensional, with the large two-dimensional structures developing a little farther downstream (Section 5.3) is in contrast to the observations of mixing layers in which the inlet turbulence levels were low (Koop (1976), Brown and Roshko (1974)). The initial three-dimensionality near the splitter plate may be attributed to the fact that the scales of the turbulence in the initial portion of the developing mixing layer are of the same order as the scales of the inlet turbulence; consequently, the three-dimensional inlet turbulence produced an initially three-dimensional turbulent mixing region.

To check these ideas, the velocity records for the homogeneous flow were digitally low-pass filtered, with a cut-off frequency of 1.5 Hz and the values of $\sqrt{\overline{u'^2}}/\Delta\bar{u}_o$ and $\sqrt{\overline{v'^2}}/\Delta\bar{u}_o$ were then calculated from the filtered records. It was found that for $x \geq 0.5$ m, the mean of the maximum values of $\sqrt{\overline{u'^2}}/\Delta\bar{u}_o$ calculated from the filtered data was 0.176, with a standard deviation of 0.01, and the mean of the maximum values of $\sqrt{\overline{v'^2}}/\Delta\bar{u}_o$ for the filtered data was 0.143, with a standard deviation of 0.01. These values are quite close to those measured by Wygnanski and Fiedler. The maximum values of $\sqrt{\overline{u'^2}}/\Delta U_o$ and $\sqrt{\overline{v'^2}}/\Delta\bar{u}_o$ at $x = 0.2$ m were 0.159 and 0.110, respectively, much lower than the nearly constant values found at larger values of x. The fact that maximum values of $\sqrt{\overline{u'^2}}/\Delta\bar{u}_o$ and $\sqrt{\overline{v'^2}}/\Delta\bar{u}_o$ from the low-pass filtered data increased between $x = 0.2$ m and $x = 0.5$ m, while the unfiltered values decreased, would indicate that the small scales dominated the flow to a larger degree initially, and also that they were, to a large extent, quickly

dissipated. In fact, a comparison of the filtered and unfiltered measurements between x = 0.2 m and x = 1.0 m indicates that the turbulent energy in the smaller scales decreased by almost 50 per cent over this distance. Thus, it seems clear that the increased turbulence intensities, as well as the initially three-dimensional flow in the mixing layer, were in large part due to the high inlet turbulence levels. Furthermore, the dissipation of the inlet turbulence, particularly in the small scales, was certainly responsible for the observed decrease in $\sqrt{\overline{u'^2}}/\Delta\bar{u}_o$ in the homogeneous flow between x = 0.2 m and x = 1.0 m, and was probably responsible for some, but not all, of the observed decrease in $\sqrt{\overline{u'^2}}/\Delta\bar{u}_o$ in the stratified flows.

One other factor in this discussion is the influence of the boundary layers on the splitter plate. The increased turbulence levels in the experiments of Wygnanski and Fiedler (1970) compared to those of Liepmann and Laufer (1947) have been attributed to the fact that Wygnanski and Fiedler used a trip-wire to produce a turbulent boundary layer as the flow left their contraction section (Batt *et al.* (1970)). Thus, it may be that aside from the turbulence intensities, the size of the boundary layers on the splitter plate also contributed to the higher turbulence intensities, and the initial three-dimensionality found in the mixing layers of this study.

It seems clear, then, that the splitter plate wake and inlet turbulence intensities were responsible for the high turbulence levels found in the mixing layer. Although the increased turbulence intensities had some effect on the flow, in many ways the flow was similar

to mixing layers with inlet conditions which approximate the ideal situation more closely. As was discussed in Section 5.3, the large, two-dimensional vortex structures which have been observed in other mixing layers were found here as well, so the basic development of the mixing layer is really no different in this case. However, visual observations indicated that there was more mixing within the vortex structures found in this study, and this was very likely due to the additional turbulence at the flume inlet.

Turbulent Shear-Stress Profiles

That the mixing was enhanced by the inlet turbulence is also seen when the maximum values of $-\overline{u'v'}/\Delta\bar{u}_o^2$ (Figure 6.2.19) are compared with the measurements of other investigators. Wygnanski and Fiedler (1970) found that the maximum value of $-\overline{u'v'}/\Delta\bar{u}_o^2$ in a homogeneous mixing layer was about 0.009, whereas the maximum values in the homogeneous flow shown in Figure 6.2.19 were much higher. When the velocity records were filtered, the maximum value was found to be about 0.013, still higher than the value found by Wygnanski and Fiedler. Again, the larger values of $-\overline{u'v'}/\Delta\bar{u}_o^2$ in this study are attributed to the increased mixing in the large vortex structures which was a result of the higher inlet turbulence levels. It is interesting to note, however, that much smaller maximum values of $-\overline{u'v'}/\Delta\bar{u}_o^2$ were found in the stratified flows than were found in the homogeneous case, again the result of buoyancy forces. However, both the fact that Figure 6.2.20 shows that the basic shape of the profiles of $-\overline{u'v'}$ were similar for all cases, and the fact that Figure 6.2.21

indicates there is little change in the correlation coefficient $-\overline{u'v'}/\sqrt{\overline{u'^2}}\sqrt{\overline{v'^2}}$ either with the downstream distance x or with the stratification would indicate that the basic mixing process itself was similar in all cases. This, of course, is confirmed by the visual observations.

Temperature Profiles

There are several other measurements which indicate the general similarity among the mixing layers examined by others and those examined in this study. Among these are the profiles of the normalized mean temperature (Figure 6.2.3) and the normalized temperature fluctuations (Figure 6.2.15). Of particular interest are the asymmetric shapes of these profiles with respect to $(y - y_o)/(x - x_o)$. The same basic asymmetry of the mean temperature (or density) profiles was also found in the density profiles measured by Brown and Roshko (1974), Koop (1976), and Baddour and Chu (1978). In all these cases, a sharp "corner" in the profile was found on one side of the mixing layer. Furthermore, asymmetric profiles of density fluctuations which are similar to the profiles of temperature fluctuations shown in Figure 6.2.15 were reported by Koop (1976) and Baddour and Chu (1978). Again, the sharp drop in $\sqrt{\overline{\rho'^2}}/\Delta\rho_o$ (or $\sqrt{\overline{T'^2}}/\Delta T_o$) was found on the low-speed side of the mixing layer. Figure 11(a) in the paper by Brown and Roshko (1974) indicates that the density fluctuations in their experiments increased slowly from the high-speed side and suddenly decreased on the low-speed side of the flow when the dense fluid was on the low-speed side. The fact that the basic shapes of all these

profiles are similar would indicate that the asymmetries are not caused by buoyancy effects (which were not a factor in the experiments of Brown and Roshko), but by the manner in which the mixing layer develops.

It is easy to account for the asymmetry in these profiles when one considers the development of the vortex structures in the mixing layer, depicted graphically in Figure 7.1.1 (see also Figures 5.3.1 - 5.3.2; see also Brown and Roshko (1974) and Koop (1976)). One of the more important aspects of the developing mixing layer is that its basic appearance is asymmetric with respect to its centerline; in particular, the vortices initially appear to grow out of the low-speed side and engulf fluid largely from the high-speed side (see, for example, Figures 22-25 in Koop (1976)). There often appears to be a rather sharp boundary between the mixing layer and the fluid on the low-speed side, while there is a rather diffuse boundary on the high-speed side. If one side of the flow is marked with a tracer (such as a slightly different temperature) then the asymmetric profiles of the mean tracer concentrations and fluctuations can be accounted for quite easily. One would expect to find a sudden change both in the mean value of a tracer and in the root-mean-square value of its fluctuations near the low-speed side, but a gradual change on the high-speed side. The fact that the profiles of mean velocity and turbulence intensities do not exhibit the same asymmetries as the temperature (or density profiles) is probably due to the fact that momentum is also transferred directly by pressure forces, whereas heat is not.

As a final point in this discussion, the maximum value of $\sqrt{\overline{T'^2}}/\Delta T_o$ (or $\sqrt{\overline{\rho'^2}}/\Delta\rho_o$) measured in this study (for $x/\ell_b < 2.5$) was just under

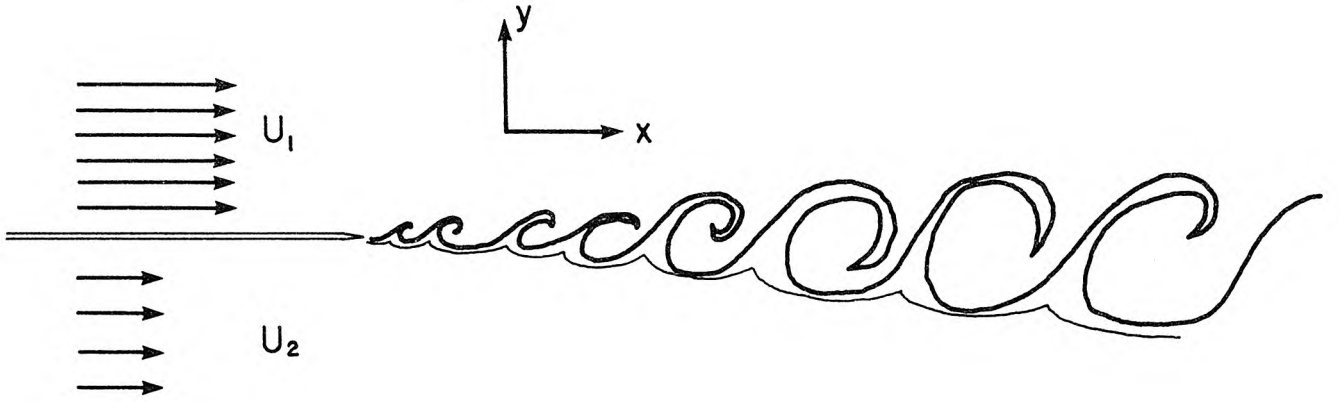

Figure 7.1.1 Graphic depiction of the development of the large vortex structures in the two-dimensional mixing layer.

0.3 while Koop (1976) measured a maximum value of about 0.4. The lower value found in this study was again probably the result of the higher turbulence levels. Koop found that the time-records of his salinity measurements in the mixing layer near the splitter plate often simply flipped back and forth from the maximum value to minimum value; the vortices apparently rolled up fluid, but little mixing initially took place inside the vortices. The result was larger measured root-mean-square values of the fluctuations. In this study the larger inlet turbulence levels resulted in increased mixing in the vortices, which increased the "mixedness" (in the sense used by Koop) and resulted in smoother time-records of the temperature and slightly smaller root-mean-square values of the fluctuations.

7.1.2 Growth and Collapse of the Stratified Mixing Layer--Macroscale Measurements

In this section macroscale properties of the mixing layer are considered. The primary focus is on the measured length scales and Richardson numbers of the stratified mixing layer.

A problem of interest in engineering practice is the determination of the distance (or time) between the initiation of a stratified mixing layer and its subsequent collapse. One method of determining the collapse distance is to examine the behavior of the bulk-Richardson number $\frac{\Delta\rho}{\rho_o} g\ell_T^*/\Delta\bar{u}_o^2$ as a function of $x/\ell_b = 2\frac{\Delta\rho}{\rho_o} gx/\Delta\bar{u}_o(\bar{u}_1 + \bar{u}_2)$. Figure 7.1.2 shows plots of such measurements from several investigations. In general, $\frac{\Delta\rho}{\rho_o} g\ell_T^*/\Delta\bar{u}_o^2$ initially increases with x/ℓ_b, but after some distance, it tends to level off. Here the concern is the

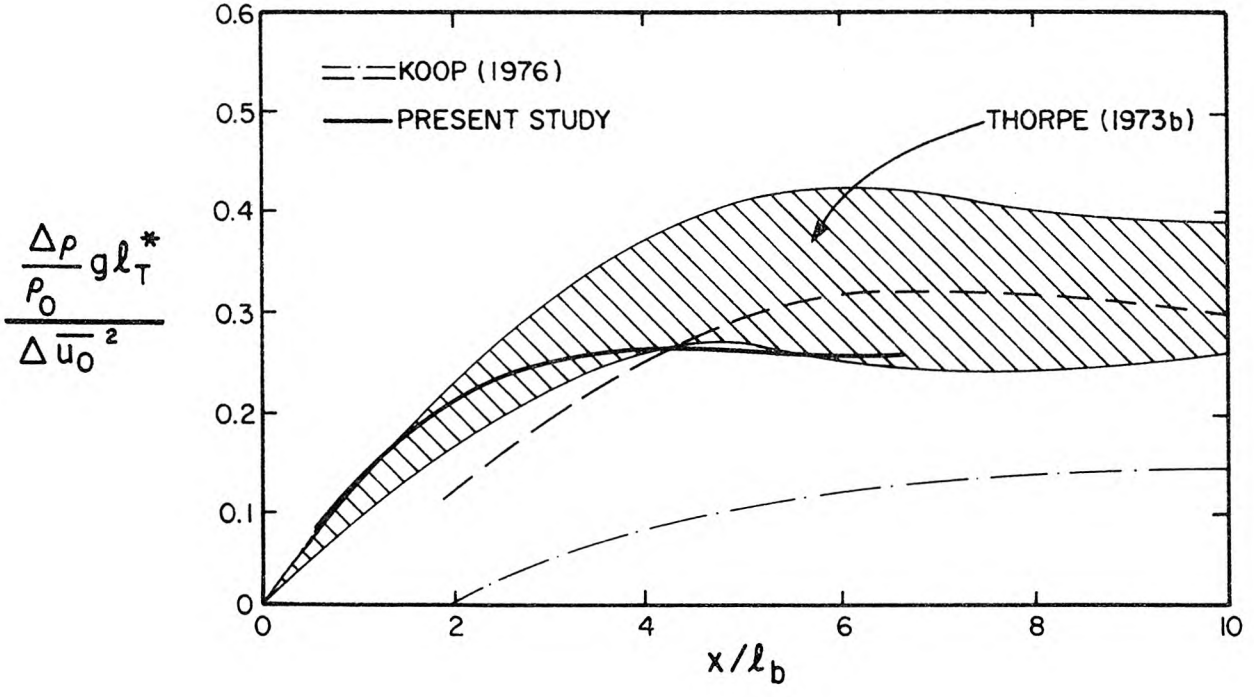

Figure 7.1.2 Measurements of the bulk-Richardson number based on the maximum-slope thickness of the temperature (or density) profile, as a function of x/ℓ_b, from several investigations. Present study curve from Figure 6.2.10.

value of $\frac{x_c}{\ell_b}$, the distance at which the bulk-Richardson number attains its maximum value; the actual maximum value of the bulk-Richardson number will be discussed later.

There appears to be a wide range of values of x_c/ℓ_b depending on the type of experiment. Koop's measurements showed a range of curves between the two lines shown in Figure 7.1.2; the upper curve is from experiments in which $\frac{\Delta\rho}{\rho_o} g\ell_u^*/\Delta\bar{u}_o^2$ was initially less than 0.1, while the lower curve is from two experiments in which $\frac{\Delta\rho}{\rho_o} g\ell_u^*/\Delta\bar{u}_o^2$ was initially 0.15 and 0.20; here, ℓ_u^* denotes the maximum-slope thickness of the velocity profile at the splitter plate. Since the experiments with the larger initial values of $\frac{\Delta\rho}{\rho_o} g\ell_u^*/\Delta\bar{u}_o^2$ were not observed to develop turbulent mixing layers, only the upper curve will be considered here. The data of Thorpe (1973b) are from experiments made in a counter-flowing stratified flow. Both Koop's data and Thorpe's data indicate that x_c/ℓ_b is in the vicinity of 5 to 6, while the data from this study indicate x_c/ℓ_b is about 3.

Visual observations made in this study of the collapse distance indicate that x_c/ℓ_b is about 1.8 (see Section 6.2.4). Although visual observations are a somewhat crude method for determining the collapse distance, they can be helpful when one attempts to interpret more objective data such as those in Figure 7.1.2. The visual collapse distance was found by determining the distance at which the large vortex structures appeared to begin to collapse (see Section 5.3, especially Figure 5.3.3) and flatten; apparently the vortices begin to collapse before the maximum value of $g\frac{\Delta\rho}{\rho_o}\ell_T^*/\Delta\bar{u}_o^2$ is attained,

for x_c/ℓ_b was 1.8 from visual observations, while the data from this study shown in Figure 7.1.2 indicate that $x_c/\ell_b \approx 3$. This is also true for other studies: the data of Koop and Thorpe in Figure 7.1.2 indicate that x_c/ℓ_b is about 5 or 6, while Figure 23 from Koop (1976) indicates that the vortices begin to collapse between $x/\ell_b = 2$ and $x/\ell_b = 3.6$, and Figure 1 from Thorpe (1973b) indicates they begin to collapse between $x/\ell_b = 2.5$ and $x/\ell_b = 4.7$. The vortex structures, therefore, begin to alter their shape and flatten well before the bulk-Richardson number attains its maximum value.

Koop (1976) attempted to relate x_c/ℓ_b to the initial value of $\frac{\Delta\rho}{\rho_o} g\ell_u^*/\Delta\bar{u}_o^2$, but his data show no clear trend. The initial values of $\frac{\Delta\rho}{\rho_o} g\ell_u^*/\Delta\bar{u}_o^2$ for the experiments of this study fall within the range of initial values of his experiments, but x_c/ℓ_b was found to be significantly smaller in this study. (The values of ℓ_u^* at $x = 0$ were obtained here by extrapolating the data in Figure 6.2.5.) It is believed that the higher inlet turbulence levels with the resulting increase in mixing, and the splitter plate wake, are partly responsible for the smaller values of x_c/ℓ_b found in this study.

The data in Figure 7.1.2 tend to support these ideas. Initially, the values of $\frac{\Delta\rho}{\rho_o} g\ell_T^*/\Delta\bar{u}_o^2$ measured in this study are larger at a given value of x/ℓ_b than in the other experiments, which have much lower inlet turbulence levels, but the mixing layer collapses sooner and results in a somewhat smaller final value of $\frac{\Delta\rho}{\rho_o} g\ell_T^*/\Delta\bar{u}_o^2$. Koop (1976) found that when the initial value of $\frac{\Delta\rho}{\rho_o} g\ell_u^*/\Delta\bar{u}_o^2$ was less than 0.1, the final value of $\frac{\Delta\rho}{\rho_o} g\ell_T^*/\Delta\bar{u}_o^2$ was about 0.32; at higher initial

values of $\frac{\Delta\rho}{\rho_o} g\ell_u^*/\Delta\bar{u}_o^2$, the final bulk-Richardson number was smaller. In this study, the initial values of $\frac{\Delta\rho}{\rho_o} g\ell_u^*/\Delta\bar{u}_o^2$ were less than 0.09 (based on values of ℓ_u^* extrapolated from the data in Figure 6.2.5), and the final value of $\frac{\Delta\rho}{\rho_o} g\ell_T^*/\Delta\bar{u}_o^2$ found in this study was about 0.26, somewhat smaller than Koop's data. There does appear to be a wide range of final values, but the data in Figure 7.1.2 do tend to indicate that the final value of $\frac{\Delta\rho}{\rho_o} g\ell_T^*/\Delta\bar{u}_o^2$ in the collapsed mixing layer is between 0.25 and 0.35. (However, the data of Koop indicate that when the stratification is very large, the initial mixing layer may not form at all, and the resulting flow is much different from those encountered in this study; Koop found that $\frac{\Delta\rho}{\rho_o} g\ell_T^*/\Delta\bar{u}_o^2$ did not appear to approach a constant value in these cases, shown by the lower curve in Figure 7.1.2.)

It was found in this study, and in Koop's as well, that ℓ_u^* continued to increase after the mixing layer collapsed, in contrast to the behavior of ℓ_T^* (see Figure 6.2.7). Since the velocity profile continues to change, quantities such as $(\overline{Ri})_{min}$ and $\frac{\Delta\rho}{\rho_o} g\ell_u^{*2}/\ell_T^*\Delta\bar{u}_o^2$ continue to increase with x/ℓ_b after the mixing layer collapses (see, for example, Figure 6.2.8). The variation of ℓ_T^*/ℓ_u^* with x/ℓ_b found in this study is in general agreement with the results of Koop, but both are apparently different from the results of Thorpe (1973b) who found that at $x/\ell_b = 12$, ℓ_T^*/ℓ_u^* varied from 0.9 to 0.72, depending on the initial value of $(\overline{Ri})_{min}$, but that $\frac{\Delta\rho}{\rho_o} g\ell_u^{*2}/\ell_T^*\Delta\bar{u}_o^2$ was 0.32 ± 0.06.

There is, however, a major difference between Thorpe's experiments and those of Koop and this study: Thorpe used a counter-current

stratified flow. This results in the development of symmetric vortex structures in the mixing layer, unlike the spatially developing mixing layer. Consequently, the profiles of $\overline{T}$ are antisymmetric, unlike the asymmetric profiles found in spatially developing mixing layers (see Figure 6.2.3 and Section 7.1.1), and ℓ_u^* and ℓ_T^* are found at the same vertical location in Thorpe's experiments, unlike the situation in a spatially developing mixing layer. Therefore, it seems clear from the profiles of the mean and fluctuating quantities that there is some difference in the turbulent transport processes for scalar quantities in the temporally developing mixing layer compared to the spatially developing mixing layer.

7.1.3 Growth and Collapse of the Stratified Mixing Layer--Energy Exchange

In this section some of the energy exchange processes within the mixing layer are considered. Of particular interest are the processes which occur as the stratified mixing layer collapses to a laminar shear layer.

Figure 7.1.3 shows a log-log plot of several normalized quantities related to turbulent energy; the data shown are from Experiment BH12 and were measured at $(y - y_o)/(x - x_o) = 0$. The quantities in Figure 7.1.3 include $-\overline{u'v'}\,\frac{\partial \overline{u}}{\partial y}$, $\frac{\partial \overline{q^{*2}v'}}{\partial y}$, $-\overline{u}\,\frac{\partial \overline{q^{*2}}}{\partial x}$ and $\overline{B'v'}$, which are all normalized with $\frac{\Delta\rho}{\rho_o} g\Delta\overline{u}_o$ and are all important quantities in the conservation equation for turbulent kinetic energy (Equations 2.1.12, 2.3.3 and 6.2.6). In addition, the quantity $\overline{q^{*2}}/\Delta\overline{u}_o^{\,2}$ is presented.

Figure 7.1.3 shows that at any value of x/ℓ_b, the turbulent energy

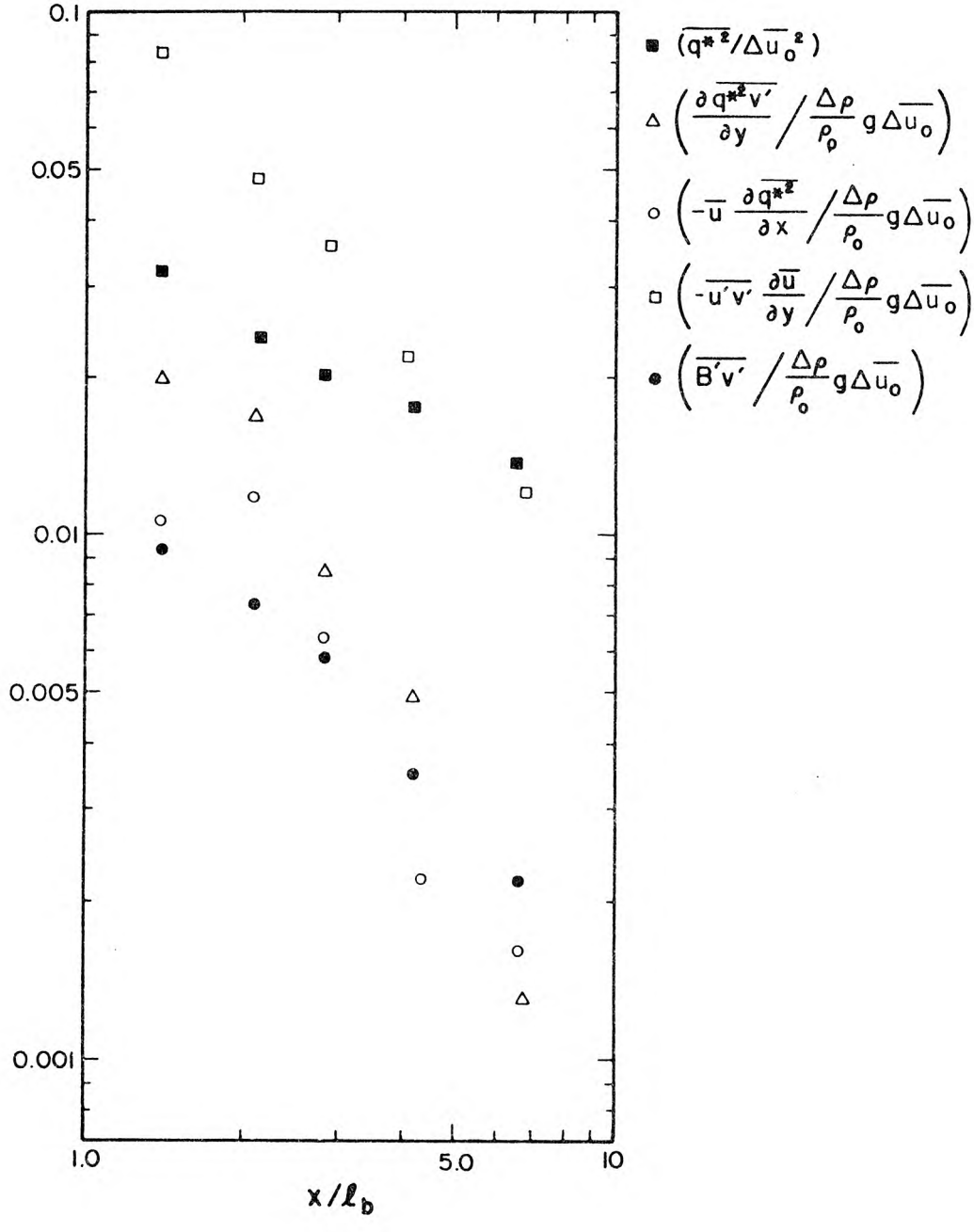

Figure 7.1.3 Variation with x/ℓ_b of quantities related to the turbulent kinetic energy. Measurements made on $(y - y_o)/(x - x_o) = 0$, Experiment BH12.

production term, $-\overline{u'v'}\,\frac{\partial \bar{u}}{\partial y}$, is much larger than the other terms related to the exchange of turbulent kinetic energy. This was found to be the case in all the mixing layers studied. There are several other items of interest in Figure 7.1.3. While both $\log(-\overline{u'v'}\,\frac{\partial \bar{u}}{\partial y})$ and $\log(\overline{q^{*2}})$ appear to have a near linear trend with $\log(x/\ell_b)$, this is not true for the other quantities shown. In fact, the rate of decrease of the other quantities generally appears to increase as x/ℓ_b increases; this is particularly evident for $\frac{\partial \overline{q^{*2}v'}}{\partial y}$ and $-\bar{u}\,\frac{\partial \overline{q^{*2}}}{\partial x}$. It is apparent, then, that the turbulent energy exchange processes markedly change as the mixing layer collapses.

Koop (1976) plotted the net change in the depth-integrated mean potential energy of the mixing layer as a function of x and found that as the layer collapsed, the net change approached a constant value. By contrast, he found that the net change in the depth-integrated value of the kinetic energy of the mean flow (that is, $\frac{1}{2}\,\bar{u}^2$) continued to decrease as the layer collapsed. To account for this continued reduction in the mean kinetic energy, he examined the conservation equation for $\frac{1}{2}\,\bar{u}^2$, and concluded that none of the terms he measured directly (the terms related to $\bar{u}$, $\overline{u'^2}$ and $\overline{\rho'u'}$) were large enough to be responsible for the observed loss of kinetic energy from the mean flow. He concluded that the depth averages of the quantities $\overline{u'v'}\,\frac{\partial \bar{u}}{\partial y}$, $\overline{B'v'}$ and $\frac{\bar{p}\,\bar{u}}{\rho_o}$, none of which he had measured, were responsible for the loss.

Koop noted that the term $\frac{\bar{p}\,\bar{u}}{\rho_o}$ has been found to be a small contributor in homogeneous mixing layers (Spencer and Jones (1971)) and

that it is probably small in the stratified mixing layer as well. He then concluded that $\overline{u'v'}\frac{\partial \bar{u}}{\partial y}$ must also be small for the following reasons. First he noted that $\overline{u'v'}\frac{\partial \bar{u}}{\partial y}$ also appears in the conservation equation for $\overline{u'^2}$ (Equation 2.1.9) as a production term for $\overline{u'^2}$. He then noted that the measured values of $\overline{u'^2}$ decreased approximately as $x^{-3/4}$, a decay rate which is faster than that found in grid-generated turbulence in a stratified flow in which the production term is unimportant (Lin and Veenhuizen (1974)). On the basis of these observations, Koop felt that the production term $-\overline{u'v'}\frac{\partial \bar{u}}{\partial y}$ was also unimportant in the collapsing mixing layer. This left only the term $\overline{B'v'}$, which Koop concluded must be negative in the collapsing region in order to account for the continued reduction in the kinetic energy of the mean flow.

One fault in Koop's argument is that he ignored the effect of the diffusion term, $\frac{\partial \overline{q^{*2}v'}}{\partial y}$, which is not important in a grid-generated turbulence problem but is important in the mixing layer. In fact, the term $\frac{\partial \overline{q^{*2}v'}}{\partial y}$ is generally positive in the middle of the mixing layer (see Figure 6.2.29) which means that turbulent kinetic energy is lost by turbulent diffusion. Furthermore, if $\overline{B'v'}$ is positive, as was usually, but not always, found to be the case in the collapsing mixing layer in this investigation, it is another sink for turbulent kinetic energy. Thus, despite the rate of decay of turbulent kinetic energy, it cannot be presumed that $-\overline{u'v'}\frac{\partial \bar{u}}{\partial y}$ is a negligible quantity in terms of the energy exchange processes of the collapsing mixing layer.

There is a second problem in Koop's analysis that concerns his explanation of the means by which negative values of $\overline{B'v'}$ would result.

Koop correctly noted that the vortex structures roll up fluid from both sides of the mixing layer, but that the fluid is not completely mixed in the vortices. He then observed that as the mixing layer began to collapse, much of the fluid in the vortices is located at statically unstable positions (that is, denser fluid above and less dense fluid below). He concluded that during the collapse, fluid particles would move towards neutrally buoyant positions, and as the denser fluid in the vortices moved down, and the less dense fluid up, one would expect a negative value of $\overline{B'v'}$ to result. The problem with this argument is that Koop attempts to explain a time-averaged phenomenon by examining only a (conditionally sampled) portion of the flow, that is, only the vortex structures, while ignoring the mechanics of the fluid between vortices. It is important to note that *one must be extremely cautious when drawing conclusions about the mean flow from observations made in a portion of the flow.* (This is equally true when one considers turbulent bursts from a boundary layer: while the momentum flux may be very large during the period of a burst, one must remember that there are long periods when the momentum flux is low, and that the mean momentum flux results from both periods.)

Koop was correct in concluding that there is unmixed fluid in the vortices, and that it moves toward neutrally buoyant positions during the collapse process. The probability density functions in Figures 6.2.36 and 6.2.37 clearly show that there is a significant probability of finding positive values of both u'v' and v'T' in the collapsing mixing layer, something not found before the collapse of

the mixing layer. Furthermore, small positive values of $\overline{v'T'}$ (or negative values of $\overline{B'v'}$) were found near the bottom of the collapsing mixing layer (Figure 6.2.27). Since the higher inlet turbulence levels in this investigation resulted in an increase in the vortex structures, it is likely that a flow with lower inlet turbulent levels (such as in Koop's study) could result in a larger region in which $\overline{B'v'}$ is negative as the mixing layer collapses. However, one still could not expect the depth-averaged value of $\overline{B'v'}$ to be negative.

In summary, the results of this study indicate that the production of kinetic energy from the mean flow, $-\overline{u'v'}\,\frac{\partial \bar{u}}{\partial y}$, is much larger than the diffusion term, the convection term and the buoyancy flux term of the turbulent energy equation (Equation 6.2.6). Furthermore, as the mixing layer collapses to a laminar shear layer, both the convection term, $-\bar{u}\,\frac{\partial \overline{q^{*2}}}{\partial x}$, and the diffusion term, $\frac{\partial \overline{q^{*2}v'}}{\partial y}$, decrease with x/ℓ_b at much faster rates than the production term, which indicates that the relative turbulent energy transfer processes change somewhat as the layer collapses.

Examination of both the probability density functions and time-records indicates that when the mixing layer collapses, there are brief periods in which $B'v'$ is negative. Unfortunately, measurements could only be made at one location at a time in this investigation, so real time measurements of such quantities as $u\,\frac{\partial q^{*2}}{\partial x}$, $\frac{\partial q^{*2}v'}{\partial y}$ and $u'v'\,\frac{\partial u}{\partial y}$ could not be made. Without real time measurements of these quantities, it is very difficult to determine the nature of the fine-scale energy transfer processes in the mixing layer, and in particular, it is

difficult to determine accurately the energy transfer process which takes place in the vortex structures as they collapse.

7.1.4 Summary of the Discussion on the Initial Mixing Layer

The higher inlet turbulence levels and the splitter plate wake increased the turbulence intensities and mixing compared to the amounts measured in other studies with more refined inlet conditions. It is believed that the inlet turbulence was suppressed to some extent by buoyancy forces in the stratified flows, but that the larger inlet turbulence levels still resulted in somewhat larger growth rates in the initial mixing layer (in terms of the maximum-slope thickness of the temperature profile) and also resulted in a smaller collapse distance.

The dimensionless collapse distance, defined as the quantity $\frac{x_c}{\ell_b} = 2x_c \frac{\Delta\rho}{\rho_o} g/\Delta\bar{u}_o(\bar{u}_1 + \bar{u}_2)$ (where x_c is the distance at which the bulk-Richardson number, $\frac{\Delta\rho}{\rho_o} g\ell_T^*/\Delta\bar{u}_o^2$, attains its maximum value) was found to be about 3 in this study. Other experiments in which the inlet turbulence levels were much lower, indicate that x_c/ℓ_b is about 6. However, from flow visualization, it appears that the vortex structures begin to collapse at about $x/x_c = 0.6$. The maximum value of the bulk-Richardson number $\frac{\Delta\rho}{\rho_o} g\ell_T^*/\Delta\bar{u}_o^2$ was found to be about 0.26; the data from this study, as well as from Koop's (1976) and Thorpe's (1973b), indicate that $0.25 < \frac{\Delta\rho}{\rho_o} g\ell_T^*/\Delta\bar{u}_o^2 < 0.40$ (Figure 7.1.2).

It was found that the quantity ℓ_T^*/ℓ_u^* continues to decrease after the collapse process begins. The basic appearances of the profiles of velocity and temperature are different, indicating that somewhat

different processes are involved in the transfer of heat and momentum in the spatially developing mixing layer. Furthermore, the asymmetric development of the vortex structures in the mixing layer is believed to be responsible for the asymmetric profiles of the mean temperature and the root-mean-square temperature fluctuations.

It was found that as the mixing layer collapses, $B'v'$ often attains large negative values, indicating that some of the fluid in the vortices is unmixed. During the collapse process unmixed dense fluid that has been elevated sinks (while unmixed, less dense fluid that has been lowered rises), and the result is intermittently negative values of $B'v'$. In the lower portion of the collapsing mixing layer, $\overline{B'v'}$ was found to be negative, although $|\overline{B'v'}|$ was small. Furthermore, the production rate of turbulent kinetic energy, $-\overline{u'v'}\,\frac{\partial \bar{u}}{\partial y}$, was found to be much larger than $\overline{B'v'}$, both in the initial portion of the mixing layer and in the collapsing portion (Figure 7.1.3), so that even when the mixing layer collapses, turbulent energy is produced from the mean shear, although it is produced at a small rate.

Finally, it is believed that further study is needed on the nature of the vortex structures in the initial mixing layer. In particular, it is believed that simultaneous velocity measurements of at least two components at several points are required to obtain a better understanding of the nature of the mixing layer. Multiple point measurements will allow quantities such as $\frac{\partial q^{*2} v'}{\partial y}$, $u'v'\,\frac{\partial u}{\partial y}$ and $u\,\frac{\partial q^{*2}}{\partial x}$ to be measured as functions of time; such measurements, combined with conditional sampling techniques should allow one to draw detailed conclusions on the fine-scale energy transfer processes within the density-stratified mixing layer.

7.2 Turbulent Energy Exchange Processes

In this section the results of this study which pertain to turbulent energy exchange processes are considered. Some aspects of these exchange processes were discussed in Sections 2.3, 6.2.10, 6.3.5 and 6.4.5. In this section the equations derived in Section 2.3 are examined in more detail, and some conclusions on the mixing processes in turbulent density-stratified flows are drawn.

7.2.1 Conservation Equations for Fluctuating Quantities

In this section Equations 2.3.7, 2.3.8 (derived in Section 2.3) and 6.2.5 (derived in Section 6.2.10) are examined as they relate to the results of this study. These equations were derived from the conservation equations for $\overline{q^2}$, $\overline{B'^2}/2$ (or equivalently, $\overline{\rho'^2}/2$), $\overline{B'v'}$ (or equivalently, $\overline{\rho'v'}$) and $\overline{q^{*2}}$ (see Sections 2.1 and 2.3). These equations will be presented again and the terms of the equations will be discussed in light of the results of this study.

The steady-state conservation equation for density-variance (Equation 2.1.10, with $B = g(\rho - \rho_o)/\rho_o$) is given by:

$$\overline{\rho'u'}\frac{\partial\bar{\rho}}{\partial x} + \overline{\rho'v'}\frac{\partial\bar{\rho}}{\partial y} + \bar{u}\frac{\partial\overline{\rho'^2}/2}{\partial x} + \bar{v}\frac{\partial\overline{\rho'^2}/2}{\partial y} + \frac{1}{2}\frac{\partial\overline{\rho'^2u'}}{\partial x} + \frac{1}{2}\frac{\partial\overline{\rho'^2v'}}{\partial y} = -\varepsilon_\rho \tag{7.2.1}$$

where it has been assumed that gradients in the z-direction are zero. All the terms in Equation 7.2.1 were measured except ε_ρ, the dissipation rate for $\overline{\rho'^2}/2$. In general, the measurements made in this study

indicate that the term of largest magnitude in this equation is $\left| \overline{\rho'v'} \frac{\partial \bar{\rho}}{\partial y} \right|$; the next largest is $\left| \frac{1}{2} \frac{\partial \overline{\rho'^2 v'}}{\partial y} \right|$, as $\left| \frac{1}{2} \frac{\partial \overline{\rho'^2 v'}}{\partial y} \Big/ \overline{\rho'v'} \frac{\partial \bar{\rho}}{\partial y} \right|$ is generally found between 0.1 and 0.3. The measurements indicate that the convection term, $\left| \bar{u} \frac{\partial \overline{\rho'^2/2}}{\partial x} \right|$ is usually 0.1 $\left| \overline{\rho'v'} \frac{\partial \bar{\rho}}{\partial y} \right|$ or less, and that the magnitude of the remaining measured terms are generally less than 0.02 $\left| \overline{\rho'v'} \frac{\partial \bar{\rho}}{\partial y} \right|$. Consequently, the most important terms in Equation 7.2.1, which relate to this study, are $\overline{\rho'v'} \frac{\partial \bar{\rho}}{\partial y}$, $\frac{1}{2} \frac{\partial \overline{\rho'^2 v'}}{\partial y}$, $\bar{u} \frac{\partial \overline{\rho'^2/2}}{\partial x}$ and by difference ε_ρ.

The steady-state conservation equation for $\overline{\rho'v'}$ (Equation 2.1.11) is given by:

$$\overline{\rho'u'} \frac{\partial \bar{v}}{\partial x} + \overline{\rho'v'} \frac{\partial \bar{v}}{\partial y} + \overline{u'v'} \frac{\partial \bar{\rho}}{\partial x} + \overline{v'^2} \frac{\partial \bar{\rho}}{\partial y} + \bar{u} \frac{\partial \overline{\rho'v'}}{\partial x}$$

$$+ \bar{v} \frac{\partial \overline{\rho'v'}}{\partial y} + \frac{\partial \overline{\rho'v'u'}}{\partial x} + \frac{\partial \overline{\rho'v'^2}}{\partial y} + \overline{\rho'^2} g =$$

$$- \frac{1}{\rho_o} \overline{\rho' \frac{\partial p'}{\partial y}} - \varepsilon_{\rho v} \quad , \qquad (7.2.2)$$

where, again, gradients in the z-direction have been assumed to be zero. All terms in Equation 7.2.2 were measured except $\varepsilon_{\rho v}$ and $\frac{1}{\rho_o} \overline{\rho' \frac{\partial p'}{\partial y}}$. The measurements indicate that $\left| \overline{\rho'^2} g \right|$ and $\left| \overline{v'^2} \frac{\partial \bar{\rho}}{\partial y} \right|$ are the terms of largest magnitude in this equation, but $\overline{\rho'^2} g$ is always positive, and $\overline{v'^2} \frac{\partial \bar{\rho}}{\partial y}$ is never positive (in a neutral or stable stratification) so the sum of these terms is sometimes much smaller in magnitude than either of them. In general, $\left| \frac{\partial \overline{\rho'v'^2}}{\partial y} \Big/ \overline{v'^2} \frac{\partial \bar{\rho}}{\partial y} \right|$ is about 0.15 or less, but $\left| \frac{\partial \overline{\rho'v'^2}}{\partial y} \Big/ \left(\overline{v'^2} \frac{\partial \bar{\rho}}{\partial y} + \overline{\rho'^2} g \right) \right|$ is sometimes greater than one.

Similarly, $\left| \bar{u} \frac{\partial \overline{\rho' v'}}{\partial x} \Big/ \overline{v'^2} \frac{\partial \bar{\rho}}{\partial y} \right|$ is found to be about 0.1 or less. The other measured terms generally have magnitudes less than 0.02 $\left| \overline{v'^2} \frac{\partial \bar{\rho}}{\partial y} + \overline{\rho'^2} g \right|$. Consequently, the most important terms in Equation 7.2.2 are $\overline{v'^2} \frac{\partial \bar{\rho}}{\partial y}$, $\overline{\rho'^2} g$, $\frac{\partial \overline{\rho' v'^2}}{\partial y}$, $\bar{u} \frac{\partial \overline{\rho' v'}}{\partial x}$ and, by difference, $-\frac{1}{\rho_o} \overline{\rho' \frac{\partial p'}{\partial y}} - \varepsilon_{\rho v}$.

Finally, the steady-state conservation equation for turbulent kinetic energy (Equation 2.1.12) is given by:

$$\bar{u} \frac{\partial \overline{q^{*2}}}{\partial x} + \bar{v} \frac{\partial \overline{q^{*2}}}{\partial y} + \frac{\partial \overline{q^{*2} u'}}{\partial x} + \frac{\partial \overline{q^{*2} v'}}{\partial y} + \overline{B' v'} + \overline{u' v'} \frac{\partial \bar{u}}{\partial y}$$

$$+ \overline{u'^2} \frac{\partial \bar{u}}{\partial x} + \overline{v'^2} \frac{\partial \bar{v}}{\partial y} + \overline{u' v'} \frac{\partial \bar{v}}{\partial x} = -\bar{u} \frac{\partial \overline{w'^2}}{\partial x} - \bar{v} \frac{\partial \overline{w'^2}}{\partial y}$$

$$- \frac{1}{\rho_o} \left(\overline{u' \frac{\partial p'}{\partial x}} + \overline{v' \frac{\partial p'}{\partial y}} + \overline{w' \frac{\partial p'}{\partial z}} \right) - \frac{1}{2} \left(\frac{\partial \overline{w'^2 u'}}{\partial x} + \frac{\partial \overline{w'^2 v'}}{\partial y} \right) - \varepsilon \qquad (7.2.3)$$

where both $\bar{w}$ and gradients in the z-direction have been assumed to be zero. The two-dimensional equivalent of this equation is given by:

$$\bar{u} \frac{\partial \overline{q^{*2}}}{\partial x} + \bar{v} \frac{\partial \overline{q^{*2}}}{\partial y} + \frac{\partial \overline{q^{*2} u'}}{\partial x} + \frac{\partial \overline{q^{*2} v'}}{\partial y} + \overline{B' v'} + \overline{u' v'} \frac{\partial \bar{u}}{\partial y}$$

$$+ \overline{u'^2} \frac{\partial \bar{u}}{\partial x} + \overline{v'^2} \frac{\partial \bar{v}}{\partial y} + \overline{u' v'} \frac{\partial \bar{v}}{\partial y} = -\frac{1}{\rho_o} \left(\overline{u' \frac{\partial p'}{\partial x}} + \overline{v' \frac{\partial p'}{\partial y}} \right) - \varepsilon^* \qquad (7.2.4)$$

which is the relevant equation in this case since w was not measured.

The terms on the left-hand sides of both Equations 7.2.3 and 7.2.4 were measured, while the terms on the right-hand sides were not.

Usually the term $\overline{u'v'}\,\frac{\partial \bar{u}}{\partial y}$ is the largest term in Equation 7.2.4, but as was discussed previously, the terms $\frac{\partial \overline{q^{*2}v'}}{\partial y}$, $\bar{u}\,\frac{\partial \overline{q^{*2}}}{\partial x}$ and $\overline{B'v'}$ are also important terms. The other measured terms usually have magnitudes much smaller than the sum of $\overline{u'v'}\,\frac{\partial \bar{u}}{\partial y}$, $\bar{u}\,\frac{\partial \overline{q^{*2}}}{\partial x}$, $\overline{B'v'}$ and $\frac{\partial \overline{q^{*2}v'}}{\partial y}$. By difference, the term $-\frac{1}{\rho_o}\left(\overline{u'\,\frac{\partial p'}{\partial x}} + \overline{v'\,\frac{\partial p'}{\partial y}}\right) - \varepsilon^*$ is also an important quantity in Equation 7.2.4.

Since the dissipation rates as well as the terms involving pressure fluctuations were not measured, one cannot readily separate the effects of these terms. However, from the work of others, one can speculate on the importance of the pressure transport terms. Wyngaard and Coté (1971) found that the pressure transport term, which they measured by difference, was a negligible term in Equation 7.2.3 in the atmospheric boundary layer in the presence of a stable density stratification. Wyngaard and Coté did not, however, measure gradients in the x-direction, but the measurements were made in a flat area of Kansas, with a 2400 m fetch to windward of the measurement direction, so they felt that the terms involving gradients in the x-direction were probably negligible in their experiments.

Wygnanski and Fiedler (1970) found that in some portions of the homogeneous mixing layer the pressure transport term, again measured by difference, was slightly larger than the dissipation rate in Equation 7.2.3. It is clear then that the pressure transport terms may not always be neglected in comparison with the dissipation rates.

As was discussed in Section 6.2.10, the value of ε was calculated from the power spectral estimates for u' and compared to the values of ε^* calculated using Equation 7.2.3. (When calculating ε^* in this manner, the pressure transport term was neglected; alternatively, one can consider the calculated value of ε^* to represent both the dissipation rate and the pressure transport term.) It was found that in regions of the homogeneous mixing layer where one would expect $\frac{\partial \overline{w'^2 v'}}{\partial y}$, $\frac{\partial \overline{w'^2}}{\partial x}$ and the pressure transport term to be small (based on the work by Wygnanski and Fiedler), $\varepsilon/\varepsilon^* \approx 0.98$, so the values of ε^* do seem to be reasonable when $\frac{1}{\rho_o}\left(\overline{u' \frac{\partial p'}{\partial x}} + \overline{v' \frac{\partial p'}{\partial y}}\right)$ is known to be small. In stratified cases, the mean values of $\varepsilon/\varepsilon^*$ varied from 0.94 to 1.05, and the data are very scattered, but this is to be expected since ε was calculated using Equation 2.4.1 which is not necessarily valid for stratified flows. Furthermore, if the pressure transport term and $\frac{\partial \overline{w'^2 v'}}{\partial y}$ are negligible, and if $\bar{u} \frac{\partial \bar{w}^2}{\partial x} \approx \bar{u} \frac{\partial \bar{u}^2}{\partial x}$, then one might expect $\varepsilon/\varepsilon^* \approx 1.1$ in these flows, so it seems clear that one cannot always neglect the pressure transport term with confidence.

The power spectral estimates for T' and the calculated values of ε_ρ were used to evaluate the constant in Equation 2.4.3, which gives the spectrum for T' in the inertial subrange. The values of ε in Equation 2.4.3 were calculated from the spectral estimates for u', using Equation 2.4.1 with $e_1 = 0.5$. The mean value of e_5 was calculated to be 0.95, with a standard deviation of 0.35. This compared with values of about 0.4 found by Gibson and Schwarz (1963) and Kaimal *et al.* (1972), and with the value of 1.2 found by Gibson *et al.* (1970). There

appears to be a wide range of reported values of e_5; Gibson *et al.* (1970) felt that both anistropy and intermittency in turbulence may result in larger values of e_5, but it is not absolutely clear why the spread in values of e_5 is so large. However, the fact that the mean value of e_5 in this study falls in the middle of the spread indicates that the values of ε_ρ calculated from Equation 7.2.1 are not unreasonable.

With these results in mind, the relationships derived in Sections 2.3 and 6.2.10 will be examined. These relationships, which are similar to those first derived by Ellison (1957), are given by

$$\overline{Ri} = \frac{R_f(1 - R_f + E^*)^2 \dfrac{t_2^*}{t_3} \overline{u'v'}^2}{(1 - R_f/R_c^* + E^*)\ \overline{q^{*2}}\ \overline{v'^2}} \tag{7.2.5}$$

and

$$\frac{\overline{\rho'v'}^2}{\overline{\rho'^2}\ \overline{v'^2}} = \frac{1 - R_f/R_c^* + E^*}{2(1 - R_f + E^*)\dfrac{t_1}{t_3}} \tag{7.2.6}$$

where

$$R_c^* = \left(1 + \frac{2\overline{q^{*2}}}{\overline{v'^2}} \frac{t_1}{t_2^*}\right)^{-1} ,$$

$$E^* = \frac{\overline{\dfrac{\partial q^{*2} v'}{\partial y}}}{\overline{u'v'}\ \dfrac{\partial \bar{u}}{\partial y}} ,$$

$$t_1 = \overline{\rho'^2}/2\varepsilon_\rho ,$$

$$t_2^* = \overline{q^{*2}}/\varepsilon^* ,$$

$$t_3 = \overline{\rho'v'}/\varepsilon_{\rho v} ,$$

and it has been assumed that

$$\overline{\rho'v'}\,\frac{\partial\rho}{\partial y} + \varepsilon_\rho = 0 \quad , \tag{7.2.7}$$

$$\overline{u'v'}\,\frac{\partial\bar{u}}{\partial y} + \frac{\partial\overline{q^{*2}v'}}{\partial y} + \overline{B'v'} + \varepsilon^* = 0 \quad , \tag{7.2.8}$$

and

$$\overline{v'^2}\,\frac{\partial\bar{\rho}}{\partial y} + \frac{\overline{\rho'^2 g}}{\rho_o} + \varepsilon_{\rho v} = 0 \quad . \tag{7.2.9}$$

These equations include the very largest terms, but other terms which are not always negligible have been dropped. These include the convection terms $\frac{\bar{u}}{2}\frac{\partial\overline{\rho'^2}}{\partial x}$, $\bar{u}\frac{\partial\overline{q^{*2}}}{\partial x}$ and $\bar{u}\frac{\partial\overline{\rho'v'}}{\partial x}$, the pressure transport terms, $\frac{1}{\rho_o}\left(\overline{u'\frac{\partial p'}{\partial x}} + \overline{v'\frac{\partial p'}{\partial y}}\right)$ and $\frac{1}{\rho_o}\left(\overline{\rho'\frac{\partial p'}{\partial y}}\right)$ and the diffusion terms $\frac{\partial\overline{\rho'^2v'}}{\partial y}$ and $\frac{\partial\overline{\rho'v'^2}}{\partial y}$.

If these terms are included in Equations 7.2.7 - 7.7.24, then alternate relationships to Equations 7.2.5 and 7.2.6 can be derived, but these relationships are rather cumbersome and do not really add much to the understanding of density-stratified shear flows. One alternative is to consider t_1, t_2^* and t_3 to be general functions which incorporate the combined effects of the dissipation, convection, diffusion (except $\frac{\partial\overline{q^{*2}v'}}{\partial y}$) and pressure transport terms. Since these terms were generally found to be much smaller than the terms included in Equations 7.2.7 - 7.2.9, although not always negligible, this may not be an unreasonable alternative. Then, Equations 7.2.5 and 7.2.6 can be compared with the measurements of this study, although one must keep in mind the fact that t_1/t_2^*, t_2^*/t_3 and t_1/t_3 are general

functions which may vary with flow conditions.

7.2.2 Turbulent Energy Exchange Relationships

In this section the results presented in Sections 6.2.10, 6.3.5 and 6.4.5 are compared with the behavior predicted by Equations 7.2.5 and 7.2.6.

Figure 6.4.19 in Section 6.4.5 shows values of R_f plotted against $\overline{Ri}$ from measurements made in weakly stratified flows over roughened beds. Most of the data in this figure are scattered around the line $R_f = \overline{Ri}$ (which indicates that K_H/K_m is close to one); since $\frac{\Delta\rho}{\rho_o}$ was small, a laminar shear layer did not develop in the flows considered in Figure 6.4.19, and $\overline{Ri}$ was generally small. The results in this figure contrast with those of Figures 6.2.41 and 6.4.20, in which it is seen that $R_f < \overline{Ri}$, even at small values of $\overline{Ri}$. This would indicate that the nature of the mixing processes in strongly stratified flows are different from those in weakly stratified flows.

An examination of Equation 7.2.5 helps clarify this point, as this relationship indicates that $R_f < (1 + E^*)R_c^*$, where $R_c^* = \left(1 + \frac{2\overline{q^{*2}}}{\overline{v'^2}} \frac{t_1}{t_2^*}\right)^{-1}$. As pointed out by Arya (1975), the ratio $\overline{q^{*2}}/\overline{v'^2}$ remains relatively unaffected by buoyancy forces in a turbulent flow. While buoyancy forces result in a reduction in $\overline{v'^2}$, they also result in a reduction of $-\overline{u'v'}$, so that the production rate for $\overline{u'^2}$ is reduced (Equation 2.1.9). Since pressure forces redistribute the turbulent energy from $\overline{u'^2}$ to $\overline{v'^2}$ and $\overline{w'^2}$ (Equation 2.1.9), a suppression of all components results, not just the vertical component. In this study $\overline{q^{*2}}/\overline{v'^2}$ was found to vary from about 1.3 to about 1.7; Laufer

(1950) made measurements in a two-dimensional, homogeneous flow and found that $\overline{q^{*2}}/\overline{v'^2}$ varied from 2.1, near the wall, to 1.2 near the center of the flow. Arya (1975) made measurements in a density-stratified boundary layer and found that $\overline{q^{*2}}/\overline{v'^2}$ varied from about 2.1 to 1.0 with the largest values found near the wall. It seems clear then that $\overline{q^{*2}}/\overline{v'^2}$ does not vary a great deal, so any change in the maximum value of R_f probably results from changes in E^* or $t_1/t_2{}^*$.

The values of E^* for the data shown in Figures 6.2.41, 6.4.19 and 6.4.20 were, for the most part, between -0.3 and 0.5, so the values of E^* for the data of the weakly stratified flows shown in Figure 6.4.19 were not dissimilar to those in the more strongly stratified flows; if anything, they were generally smaller, which would result in a somewhat smaller maximum value of R_f, the opposite of what was observed. It seems then that the variation in $t_1/t_2{}^*$ is responsible for the difference in behavior of R_f in the strongly stratified flows compared to the weakly stratified flows.

Now, $t_1/t_2{}^*$ is approximately equal to $\frac{\overline{\rho'^2}}{2\varepsilon_\rho}\frac{\varepsilon^*}{\overline{q^{*2}}}$, since in this context, t_1 and $t_2{}^*$ are assumed to contain all the neglected terms in Equations 7.2.7 - 7.2.9. The results of the experiments in the initial mixing layer show that an increase in the stratification gives an increase ε^*; initially $\overline{q^{*2}}$ was about the same for both stratified and homogeneous flows, so it is probable that an increase in the stratification results in an increase in $\varepsilon^*/\overline{q^{*2}}$, that is, an increase in the dissipation rate relative to the turbulent energy. Increasing the stratification generally resulted in an increase in $\overline{\rho'^2}$ also, although

$\overline{\rho'^2}$ depends on the turbulence intensity as well as the stratification. The behavior of ε_ρ is not as simple as the other terms. To a first approximation $\varepsilon_\rho = -\overline{\rho'v'} \frac{\partial \bar{\rho}}{\partial y}$ (Equation 7.2.7); as the stratification increases from zero, $-\frac{\partial \bar{\rho}}{\partial y}$ increases, while $\overline{\rho'v'}$ increases at first, then decreases as the stratification becomes strong. Thus, it is not unreasonable to expect that ε_ρ would decrease as the density stratification becomes strong. Consequently, it is reasonable to expect that $t_1/t_2^* \approx \frac{\overline{\rho'^2}}{2\varepsilon_\rho} \frac{\varepsilon^*}{q^{*2}}$ would increase with increasing stratification, and that, as a result, both R_c^* and the maximum value of R_f would decrease.

From Equation 7.2.5, then, one can obtain a plausible explanation of the difference in the relationship between R_f and $\overline{Ri}$ when the stratification is small (Figure 6.4.19) and when the stratification is large (Figures 6.2.41 and 6.4.20). What constitutes large or small stratification is an interesting point, for the data of Figure 6.3.26 show R_f behaving in a manner that would lead one to believe the data came from strongly stratified flows, but the values of $\Delta\rho/\rho_o$ for the data in Figure 6.3.26 were nearly the same as those for the data shown in Figure 6.4.19. The difference is that the data shown in Figures 6.4.19, 6.4.20 and 6.2.41 were all measured in highly turbulent regions, either in the initial mixing layer or over roughened beds, while the data shown in Figure 6.3.26 were measured in regions with very low turbulence intensities. It seems, then, that it is not the magnitude of $\Delta\rho/\rho_o$ that is important, but the stratification relative to the available turbulent energy: the tiniest stratification will appear strong if little or no turbulent energy is produced to mix the fluid.

Further evidence that shows Equations 7.2.5 and 7.2.6 are valid approximations is found when one considers the limit as $R_f \to 0$, when $|E^*|$ is small. In this case, $\overline{Ri} \approx 2 \dfrac{\overline{u'v'}^2}{\overline{u'^2}\,\overline{v'^2}} \dfrac{t_2^*/t_3}{1+\overline{v'^2}/\overline{u'^2}} R_f$. Typically $-\overline{u'v'}/\sqrt{\overline{u'^2}}\sqrt{\overline{v'^2}}$ was about 0.4 when R_f was small and the flow turbulent, while $\overline{v'^2}/\overline{u'^2}$ was about 0.5. With these values and with the assumption that $R_f/\overline{Ri} \to 1$ as $R_f \to 0$ (Figure 6.4.19), one finds that t_2^*/t_3 is about 4.7. If one next assumes that $R_c^* \approx 0.3$ then one finds that t_1/t_2^* is about 0.78, so that t_1/t_3 is about 3.7. An examination of Equation 7.2.6 shows that if $t_1/t_3 = 3.7$, then when R_f is small, $\dfrac{\overline{\rho'v'}}{\sqrt{\overline{\rho'^2}}\sqrt{\overline{v'^2}}}$ is about 0.37; in fact, the measured values of $\dfrac{\overline{\rho'v'}}{\sqrt{\overline{\rho'^2}}\sqrt{\overline{v'^2}}}$ were found to be in the range of 0.34 to 0.39 when R_f was small and the flow turbulent. So, it appears that Equations 7.2.5 and 7.2.6 are in many respects reasonable approximations.

Equation 7.2.5 can be rewritten in the form

$$\overline{Ri} = \frac{\left(\dfrac{\partial\overline{q^{*2}v'}}{\partial y}\right)^2 \dfrac{t_2^*}{t_3} F^*(1 - F^* + 1/E^*)^2}{\overline{q^{*2}}\;\overline{v'^2}\left(\dfrac{\partial\overline{u}}{\partial y}\right)^2 (1 - F^*/Ri^* + 1/E^*)} \qquad (7.2.10)$$

where $F^* = R_f/E^* = -\overline{B'v'}\Big/\dfrac{\partial\overline{q^{*2}v'}}{\partial y}$. Then, when E^* is large, this relationship is approximated by

$$\overline{Ri} \approx \frac{\left(\dfrac{\partial\overline{q^{*2}v'}}{\partial y}\right)^2 \dfrac{t_2^*}{t_3} F^*(1 - F^*)^2}{\overline{q^{*2}}\;\overline{v'^2}\left(\dfrac{\partial\overline{u}}{\partial y}\right)^2 (1 - F^*/R_c)}, \quad E^* \gg 1 . \qquad (7.2.11)$$

When F^* is small, Equation 7.2.11 implies that

$$\overline{Ri} \approx \frac{\left(\frac{\partial \overline{q^{*2}v'}}{\partial y}\right)^2 \frac{t_2^*}{t_3}}{\overline{q^{*2}}\ \overline{v'^2}\left(\frac{\partial \bar{u}}{\partial y}\right)^2} F^*, \quad F^* \ll 1, \quad E^* \ll 1 \ . \tag{7.2.12}$$

Figure 6.4.24 shows values of F^* plotted against $\overline{Ri}$. As can be seen in Figure 6.4.23, the data shown in Figure 6.4.24 were associated with large values of E^*. Although the data are scattered in Figure 6.4.24, they do show an approximately linear relationship between F^* and $\overline{Ri}$ when F^* is small; of course, the leading factor in Equation 7.2.12 precludes the possibility of an exact linear relationship between F^* and $\overline{Ri}$, as it is unreasonable to believe that this factor would ever be constant in a turbulent flow. However, the trend in Figure 6.4.24 does suggest that Equation 7.2.5 at least qualitatively predicts the correct behavior here.

7.2.3 Summary of the Discussion on Turbulent Energy Exchange Processes

In this section the conservation equations for $\overline{\rho'^2}/2$, $\overline{\rho'v'}$ and $\overline{q^{*2}}$ (Equations 7.2.1, 7.2.2 and 7.2.4) were examined in light of the results of this study. In general, the diffusive terms (such as $\frac{\partial \overline{\rho'^2 v'}}{\partial y}$, $\frac{\partial \overline{\rho' v'^2}}{\partial y}$ and $\frac{\partial \overline{q^{*2} v'}}{\partial y}$) are not negligible compared to the other terms, and in some instances they may be large compared to other terms. Likewise, the convective terms (such as $\bar{u}\frac{\partial \overline{\rho'^2}}{\partial x}$, $\bar{u}\frac{\partial \overline{\rho' v'}}{\partial x}$ and $\bar{u}\frac{\partial \overline{q^{*2}}}{\partial x}$) are important terms which may not always be neglected.

Equation 7.2.5 was examined with respect to the measurements of

the flux-Richardson number (Figures 6.2.41, 6.3.26, 6.4.19, 6.4.20, 6.4.23 and 6.4.24). The qualitative behavior predicted by Equation 7.2.5 was found in the results. In particular, the critical value of the flux-Richardson number has a weak dependence on the stratification and the turbulence levels (when $|E^*| = \left| \frac{\partial \overline{q^{*2}v'}}{\partial y} \Big/ \overline{u'v'} \frac{\partial \bar{u}}{\partial y} \right|$ is small): when $\Delta\rho/\rho_o$ is small and the flow highly turbulent, R_f is found to be as high as 0.3 (Figure 6.4.19); when the stratification is larger and the turbulence more suppressed, R_f is seldom found to be as high as 0.2. When E^* was large, the quantity $F^* = R_f/E^* = -\overline{B'v'} \Big/ \frac{\partial \overline{q^{*2}v'}}{\partial y}$ was found to be a more useful parameter than R_f. This is seen both in Equations 7.2.10 - 7.2.12 as well as in Figures 6.4.23 and 6.4.24.

It should be remembered when considering these results that when R_f was found to be greater than about 0.2, both $\overline{B'v'}$ and $\overline{u'v'} \frac{\partial \bar{u}}{\partial y}$ were relatively small, so while the efficiency may seem large (that is, the rate of increase of potential energy relative to the rate of production of turbulent kinetic energy) the actual mixing rates were small. By contrast, when $\overline{B'v'}$ was found to be relatively large, R_f was usually quite small, so in general, the mixing processes in a density-stratified fluid are very inefficient processes.

7.3 Discussion on Coherent Structures in the Turbulent Flow

In this section a discussion on some aspects of the large, turbulent structures in the flow is presented. In Section 7.3.1 the results of this study are compared with others, and in Section 7.3.2 there is a discussion on the interaction of the turbulent structures with buoyancy forces.

7.3.1 Comparison With the Findings in Other Studies

The main point of the discussion in this section is that the large, turbulent structures found in the turbulent flows in this study are not dissimilar to those found in other flows. It has been adequately demonstrated that the initial mixing layer observed in this study was similar to those found in other studies; in particular, the large vortex structures which make up the mixing layer were observed here (see Section 5.3, 6.2 and 7.1). Consequently, the discussion in this section concentrates on the turbulent bursts found in the downstream flow.

An examination of the mean turbulence properties measured in this study quickly leads one to the conclusion that, on the average, the turbulence found in the stratified and homogeneous flows of this study appears to be fairly typical boundary-generated turbulence. Turbulence intensities in the homogeneous cases, as well as the shear stresses at the bed and the measured values of quantities such as $\overline{q^{*2}}/\overline{v'^2}$ and $\overline{u'v'}\Big/\sqrt{\overline{u'^2}}\sqrt{\overline{v'^2}}$ were all found to be rather typical values. Even the finer details of the flow properties show rather typical features.

The probability density functions for u' and v' (Figures 6.5.1 - 6.5.3) found in this study are quite similar to those found by Lu and Willmarth (1973) in a turbulent boundary layer. In particular, the probability density functions for u' are skewed in both cases, with the maximum value found between $u'/\sqrt{\overline{u'^2}} = 0$ and $u'/\sqrt{\overline{u'^2}} = 1$; furthermore, the probability density functions for v' are symmetric about $v'/\sqrt{\overline{v'^2}} = 0$, but they are narrower in shape than a Gaussian profile

(see Figure 6.5.1). More importantly, though, the probability density functions for u'v' found in this study are very similar to the one measured by Lu and Willmarth (1973) in the turbulent boundary layer: all have a sharp peak near u'v' = 0, and a long tail for $u'v'/\overline{u'v'} > 0$ (see Figure 6.5.5). The fact that the flow was stratified seems to make little difference in these comparisons as long as the flow is fully turbulent.

The similarities with the measurements of Lu and Willmarth (1973) do not end there, however. Lu and Willmarth examined the fractional contributions to $\overline{u'v'}$ from the extreme values of u'v', and their results are quite similar to those shown in Figure 6.5.6. (Lu and Willmarth used the value of $u'v'/\sqrt{\overline{u'^2}}\sqrt{\overline{v'^2}}$ as the criterion in Equations 6.5.1 and 6.5.2, rather than $u'v'/\overline{u'v'}$ as in this study, so that the "hole" size" H, used by Lu and Willmarth is equal to $L_p \overline{u'v'}/\sqrt{\overline{u'^2}}\sqrt{\overline{v'^2}}$. Otherwise the results are quite similar.) In particular, the results of both studies show that a large fraction of $\overline{u'v'}$ occurs during bursts which account for a small fraction of the total time.

The time-records of u', v', and u'v' (Figures 6.5.12 - 6.5.15) are also similar to those found in other turbulent flows. In particular, patterns in the u', v' and u'v' signals found by Thomas (1977) and Wallace *et al.* (1977) during turbulent bursts in boundary layer flows were found in this study. The fact that a repeated pattern in u' (that of a long period of slow deceleration followed by a rapid sudden acceleration), which is accompanied by a large, negative spike in u'v', is found in many types of flows, both stratified and homogeneous, and over many

types of boundaries, both roughened and unroughened, suggests that these turbulent bursts are a rather fundamental part of boundary-generated turbulence. Furthermore, the results of this study indicate that not only is the vertical turbulent momentum flux very large during the bursts, but the vertical turbulent transport of turbulent kinetic energy is large as well, and that most of the vertical transport of turbulent kinetic energy takes place during these bursts.

Finally, the average time between bursts found in this study is similar to those found in other studies. Lu and Willmarth found that when $L_p \left| \overline{u'v'} \Big/ \sqrt{\overline{u'^2}}\sqrt{\overline{v'^2}} \right|$ (see Equations 6.5.1 and 6.5.2) was about 4, then $U_{max}\ \overline{t_b}/\ell$ was about 4, where U_{max} is the free stream speed of the flow, and ℓ was the boundary layer thickness. The same level L_p was used to detect bursts in the time-records of $u'v'$ in this study, and it was found that $U_{max}\ \overline{t_b}/h$ was 2 to 3 in this study, where U_{max} was the maximum flow speed on the flume centerline. Similar values are found when one uses the time-record of $q^{*2}v'$ to detect bursts, if the level L_c is about 2 (Equation 6.5.3). (Interestingly enough, the values of $< u'v' > / \overline{u'v'}$ and Γ found at $L_c = 2$ are quite close to the values of $< u'v' > / \overline{u'v'}$ and Γ found by Lu and Willmarth when $L_p\ \overline{u'v'} \Big/ \sqrt{\overline{u'^2}}\sqrt{\overline{v'^2}}$ is about 4.) The average period between bursts does seem to vary with stratification and the boundary roughness (see Section 6.5.3), but the values obtained in this study are not dissimilar to those found by others.

7.3.2 Coherent Structures and Buoyancy Effects

The effect of buoyancy forces on the vortex structures in the mixing layer was easily observed with dye streaks: even very

small density differences resulted in buoyancy forces which were eventually able to destroy the structures, and the mixing layer collapsed to a laminar layer. This has been discussed in Section 5.3, and in a more quantitative fashion in Sections 6.2 and 7.1. The effect of buoyancy forces on the turbulence in the downstream flow is also quite evident in measurements of mean turbulence properties (such as $\sqrt{\overline{u'^2}}$ and $\overline{u'v'}$). However, the turbulent bursts in the downstream flow are not easily visualized with dye, so it is somewhat more difficult to assess the direct effects of buoyancy forces on the turbulent bursts.

Although the turbulent bursts were not easily visualized, their effects often were, as can be seen in Figure 5.4.8b, which shows a large amplitude internal wave at the density interface. Such waves were often observed to develop quite suddenly in the downstream flow, especially when the flume bed was roughened. Since waves on the interface were always observed to bulge suddenly upward, away from the bed, it is strongly believed that these waves are the direct result of turbulent bursts rising up and hitting the interface. This is obviously one way in which buoyancy forces and turbulent bursts interact, for if a turbulent burst finds a density interface impenetrable, no mixing will take place above the interface until the interface breaks down. This point is, of course, verified by the measurements of such quantities as $\overline{u'v'}$ (see Sections 6.4.2 and 6.4.3, for examples).

There are apparently more subtle effects of buoyant forces on the turbulent bursts, however, for it was found that even very small

density gradients caused large reductions in the mixing rates. It is believed that the density gradients, even though slight, exert sufficient forces on the turbulent bursts to suppress substantially their development and growth. This can be argued by analogy with the vertical discharge of a turbulent puff of fluid into an ambient fluid. When the ambient fluid is homogeneous and of the same density as the puff, then the fluid in the puff will travel some distance, slowing down rather slowly. If, on the other hand, the ambient fluid is stratified, buoyancy forces slow down the puff much more quickly, and it travels a much shorter distance. It is believed that the turbulent bursts are affected in much the same manner: the slight density gradients slow them down and inhibit their development. Most of the vertical turbulent transport of momentum and turbulent kinetic energy is a result of the bursts; consequently, when the density gradients inhibit the bursts, the result is seen dramatically in the reduced mixing rates.

As an aside, it seems likely that similar processes are involved in sediment-laden flows. It has long been known that in a sediment-laden flow, the mean shear in the flow increases as the suspended load increases, which results in a smaller von Kármán constant for the velocity profile (see, for example, Vanoni and Brooks (1957)). But as the suspended load increases, the bulk density of the flow increases, so that the suspension of sediment causes slight density gradients, which inhibit the turbulent bursts. (One can also view this in terms of energy, as work must be done by the bursts to lift the sediment and

carry it away from the bed, just as work must be done by the bursts to move through and mix a stratified fluid.) So, just as density stratification inhibits turbulent bursts, and results in reduced mixing and an increase in shear, the suspension of sediment also inhibits the turbulent bursts with similar consequences.

As a final note in this discussion, it is important to note that while the stratification resulted in reduced mixing, many other turbulence properties were not strongly affected. In particular, the spectral estimates for u' and v' seemed to be unaffected by stratification, as long as the flow was completely turbulent. (This is, of course, not true when the flow was largely laminar, and only intermittently turbulent.) Furthermore, the character of the normalized time-records of u', v', u'v' and $q^{*2}v'$ was quite similar in turbulent regions, whether or not the flow was stratified. Although density stratification appears to cause a reduction in the intensity of the bursts, and in the frequency of occurrence, the basic character of the turbulent bursts appears to be similar whether the flow is density-stratified or homogeneous.

7.4 General Discussion of the Results

The most obvious result from this study is the fact that a small density stratification can cause an enormous reduction in turbulent mixing. This became very apparent when it was found that even small temperature differences between the two layers could result in the development of a laminar shear layer in the flow. If the flume bed was smooth, this laminar layer would persist over the thirty meter

reach of the flume, even though the overall Reynolds number of the flow was on the order of 10^5. In fact, it was found that the depth-averaged value of the turbulent diffusivity for heat was often thirty to one hundred times lower in the stratified flows than the value one would expect to find in similar, homogeneous flows.

The strong stabilizing effects of density stratification have some interesting implications. For example, one cannot expect much mixing in power plant cooling water which has been discharged to the ocean (after it has risen to the surface and begins to drift away) unless there is a substantial source of turbulent energy present. One such source could be wind stress on the ocean surface, but the results of this study clearly indicate that turbulent mixing processes are highly inefficient in the presence of density stratification. At any single point, one cannot expect the flux-Richardson number to be much greater than about 0.2 (assuming, of course, that $-\overline{u'v'}\,\frac{\partial \bar{u}}{\partial y}$ is the dominant source of turbulent kinetic energy) so that a large amount of energy would have to be supplied at the surface in order to do a small amount of mixing some distance below the surface.

There are other effects as well, for it was found that the reduced vertical momentum flux, which was caused by density stratification, resulted in an increase in the mean shear. Thus, one might expect a layer of warm water on the ocean surface to spread somewhat faster than it would if there were no density effects.

The results of this study show that the mixing processes in density-stratified flows are not simple ones. Several types of distinct mixing

processes were observed visually, including the breaking of large internal waves (Figure 5.4.7), the "chipping away" at the bottom of an interface (Figure 5.4.8) and the local breakdown to turbulence as small instabilities developed on a large wave (Figure 5.4.6). The quantitative measurements clearly indicate that turbulence is greatly inhibited by stratification, and that the local mixing rates depend on a number of factors, including the local mean-Richardson number and local turbulence properties (such as $-\overline{u'v'}\,\frac{\partial \bar{u}}{\partial y}$ and $\frac{\partial \overline{q^{*2}v'}}{\partial y}$). Consequently, it is believed that it would be a very difficult task to attempt to relate turbulent diffusivities directly to bulk flow quantities (such as h, U, u_* and $\frac{\Delta\rho}{\rho_o}$ g) without taking into consideration some of the dynamics of turbulence.

The results of this study should be very helpful in modeling turbulent mixing processes involving density stratification. However, it is firmly believed that an important key to the general understanding of turbulence lies in the understanding of the nature of the large coherent structures found both in the flows examined in this study, as well as in those studied by others. The mixing processes found in this study appear to be intimately connected to these coherent structures, and it is believed that these structures must be examined in more detail in order that mixing processes in stratified flows, as well as homogeneous flows, might be finally understood.

CHAPTER 8

SUMMARY AND CONCLUSIONS

The objective of this study was to examine in a fundamental way the mixing processes in a stably stratified shear flow. An experimental study was conducted in which detailed measurements were made in a two-layered, density-stratified flow in an open channel. In addition, the results of this study have been considered in terms of several dimensionless parameters including the flux-Richardson number and the local, mean-Richardson number.

A wide range of experiments was conducted, and the parameters which were varied include the temperature (or density) difference between the two layers, the velocity difference between the layers and the roughness of the flume bed. Detailed measurements of the temperature and two velocity components were made, recorded and later analyzed both in the initial mixing layer and the downstream flow. From the measurements, a large amount of new information on turbulent mixing processes in density-stratified flows has been obtained.

The basic conclusions from this study are summarized as follows:

1. The initial mixing layer was found to be dominated by large, two-dimensional vortex structures (Section 5.3). These structures would grow until the dimensionless distance $2xg\frac{\Delta\rho}{\rho_o}\Big/\Delta\bar{u}_o(\bar{u}_1 + \bar{u}_2)$ was about 2, and would then collapse to a laminar shear layer. (In some cases, the initial stratification was so small that the mixing layer would grow until it was clearly influenced by the water surface and

flume bed before the collapse process had begun. In these instances, no laminar layer developed.)

2. When the initial mixing layer collapsed, the bulk-Richardson number, $g\frac{\Delta\rho}{\rho_o}\ell_T^*/\Delta\bar{u}_o^2$ (where ℓ_T^* is the maximum-slope thickness of the temperature profile), attained a maximum value between 0.25 and 0.3 (Figure 6.2.10). This value agrees with those found by other investigators.

3. Just as the flow in the initial mixing region was found to be dominated by the large, two-dimensional vortex structures, the flow downstream was found to be dominated by large, organized turbulent bursts. During these bursts, the turbulent fluxes of heat and momentum were found to be much larger than the time-averaged values. In addition, most of the total vertical fluxes of heat and momentum could be accounted for during these bursts (Figure 6.5.6). The general characteristics of the bursts were found to be very similar to those found in turbulent boundary layers.

4. The turbulent bursts in the downstream flow can be detected by the large flux of turbulent kinetic energy which occurs during the bursts. Figures 6.5.12 - 6.5.18 show that $q^{*2}v'(t)$ is usually near zero, except during short periods in which $q^{*2}v'/\overline{q^{*2}v'}$ is often greater than one hundred. These spikes often coincide with large negative spikes in $u'v'$ and with a repeating pattern in u' (that of a long, slow deceleration followed by a sudden acceleration) which is characteristic of turbulent bursts in a boundary layer.

5. Conditional averages of $u'v'$ and $v'T'$ were made (Section 6.5.3)

and it was found that large fractions of $\overline{u'v'}$ and $\overline{v'T'}$ occurred during small fractions of the total time (Figures 6.5.19 - 6.5.22). The conditional averages were based on the level of $q^{*2}v'$ (Equations 6.5.3 - 6.5.8).

6. The flux-Richardson number measured in the flows was examined in detail, and its behavior was found to be described at least qualitatively by Equation 7.2.5. In particular, it was found that if the stratification was relatively strong then R_f was generally found to be less than 0.2 as $\overline{Ri}$ increased (Figures 6.2.41, 6.3.26 and 6.4.20) but only if $-\overline{u'v'}\,\frac{\partial \overline{u}}{\partial y}$ was the dominant source of turbulent kinetic energy. If the stratification was relatively weak, it was found that the measured values of $R_f(\overline{Ri})$ were scattered around the line $R_f = \overline{Ri}$ (Figure 6.4.19) up to $R_f = 0.3$.

7. It was found that when $E^* = \frac{\partial \overline{q^{*2}v'}}{\partial y} \Big/ \overline{u'v'}\,\frac{\partial \overline{u}}{\partial y}$ was large, R_f often attained large values, and that the quantity $F^* = R_f/E^* = -\overline{B'v'} \Big/ \frac{\partial \overline{q^{*2}v'}}{\partial y}$ was a more useful parameter than R_f (Figures 6.4.23 and 6.4.24). Furthermore, Equation 7.2.10 was found to describe the behavior of F^* in a qualitative manner.

8. It was found that, when E^* was less than one, the ratio of $\overline{B'v'}$ to the estimated value of the dissipation rate for turbulent kinetic energy, ε^*, was less than 0.3 (Figures 6.4.42, 6.3.27, 6.4.25 and 6.4.26). Furthermore, when $\overline{B'v'}$ was relatively large, $\overline{B'v'}/\varepsilon^*$ was much less than 0.3. This would indicate that turbulent energy is dissipated at a much faster rate than the potential energy is increased in a turbulent, density-stratified flow.

9. Power spectral estimates were made for u', v' and T', and it was found that in laminar regions with internal waves, the spectra behaved as k^{-p}, where p was between 2 and 2.5 (Figure 6.3.23). In intermittently turbulent regions of a strongly stratified flow, the spectra often followed a k^{-3} behavior (Figures 6.3.24 and 6.4.16). When the flow was completely turbulent, the spectra behaved as $k^{-5/3}$ even if there was a strong stratification (Figures 6.3.22, 6.3.25, 6.4.17 and 6.4.18).

10. It was found that small amounts of stratification resulted in large reductions of the turbulent diffusivities for heat and momentum. The fact that K_m was reduced by the density stratification resulted in large increases in the mean shear in the downstream flow compared to what was found in homogeneous flows (see Sections 6.3 and 6.4.1).

11. The depth-averaged values of the turbulent diffusivities for heat and momentum were found to be as much as thirty to one hundred times lower in the stratified flows than the values one would expect to find in similar, but unstratified flows. The local mixing rates as well as average mixing rates vary in a complex manner in the flow, and it appears that it is very difficult to relate bulk mixing rates to bulk flow properties (such as $\frac{\Delta\rho}{\rho_o}$, h, U and u_*) without taking into account fine-scale turbulent processes.

REFERENCES

Arya, S. P. S. (1972) "Critical Condition for Maintenance of Turbulence in Stratified Flows," Q. J. Roy. Met. Soc., 98:264-273.

Arya, S. P. S. (1975) "Buoyancy Effects in a Horizontal Flat-Plate Boundary Layer," J. Fluid Mech., 68:321-343.

Arya, S. P. S. and Plate, E. J. (1969) "Modeling of the Stably Stratified Atmospheric Boundary Layer," J. Atmos. Sci., 26:656-665.

Baddour, R. E. and Chu, V. H. (1977) "Development of Turbulent Mixing Layers at High Exit Reynolds Number," Proc., 17th Cong. IAHR, Hydraulic Engineering for Improved Water Management, Baden-Baden, Germany, No. A41.

Baddour, R. E. and Chu, V. H. (1978) "Turbulent Gravity-Stratified Shear Flows," Tech. Report 78-3, Dept. of Civil Eng. & Appl. Mech., McGill University, Montreal, Canada.

Batchelor, G. K. (1959) "Small-Scale Variation of Convected Quantities Like Temperature in Turbulent Fluid. Part 1. General Discussion and the Case of Small Conductivity," J. Fluid Mech., 5:113-133.

Batt, R. G., Kubota, T. and Laufer, J. (1970) AIAA Reacting Turbulent Flows Conference, San Diego.

Browand, F. K. and Winant, C. D. (1973) "Laboratory Observations of Shear-Layer Instability in a Stratified Fluid," Boundary-Layer Meteorology, 5:67-77.

Brown, G. L. and Roshko, A. (1971) "The Effect of Density Difference on the Turbulent Mixing Layer," Shear Flows AGARD Current Paper No. 93, §§23.1-23.12.

Brown, G. L. and Roshko, A. (1974) "On Density Effects and Large Structure in Turbulent Mixing Layers," J. Fluid Mech., 64:775-816.

Buchhave, P., George, W. K. and Lumley, J. L. (1979) "The Measurement of Turbulence With the Laser-Doppler Anemometer," Ann. Rev. Fluid Mech., 11:443-503.

Businger, J. A., Wyngaard, J. C., Izumi, Y. and Bradley, E. F. (1971) "Flux-Profile Relationships in the Atmospheric Surface Layer," J. Atmos. Sci., 28:181-189.

Champagne, F. H., Pao, Y. H. and Wygnanski, I. J. (1976) "On the Two-Dimensional Mixing Region," J. Fluid Mech., 74:209-250.

Chandrsuda, C., Mehta, R. D., Weir, A. D. and Bradshaw, P. (1978) "Effect of Free-Stream Turbulence on Large Structure in Turbulent Mixing Layers," J. Fluid Mech., 85:693-704.

Chu, V. H. and Vanvari, M. R. (1976) "Experimental Study of Turbulent Stratified Shearing Flow," J. Hyd. Div., ASCE, 102(HY6):691-706.

Corrsin, S. (1951) "On the Spectrum of Isotropic Temperature Fluctuations in an Isotropic Turbulence," J. Appl. Phys., 22:469-473.

Csanady, G. T. (1978) "Turbulent Interface Layers," J. Geophys. Res., 83(HC5):2329-2342.

Davis, C. V. and Sorensen, K. E. (ed.) (1969) Handbook of Applied Hydraulics, McGraw-Hill Book Company, New York, pp. 2-14.

Dimotakis, P. E. (1976) "Single Scattering Particle Laser-Doppler Measurements of Turbulence," AGARD Symposium on Nonintrusive Instrumentation in Fluid Flow Research, Saint-Louis, France, Paper No. 10.

Dimotakis, P. E. and Brown, G. L. (1976) "The Mixing Layer at High Reynolds Number: Large-Structure Dynamics and Entrainment," J. Fluid Mech., 78:535-560.

Drazin, P. G. and Howard, L. N. (1966) "Hydrodynamic Stability of Parallel Flow of Inviscid Fluid," Adv. Appl. Mech., 9:1-89.

Durst, F., Melling, A. and Whitelaw, J. H. (1976) Principles and Practice of Laser-Doppler Anemometry, Academic Press, London.

Ellison, T. H. (1957) "Turbulent Transfer of Heat and Momentum from an Infinite Rough Plane," J. Fluid Mech., 2:456-466.

Ellison, T. H. and Turner, J. S. (1959) "Turbulent Entrainment in Stratified Flows," J. Fluid Mech., 6:423-448.

Ellison, T. H. and Turner, J. S. (1960) "Mixing of a Dense Fluid in a Turbulent Pipe Flow, Part 2," J. Fluid Mech., 8:529-544.

Eriksen, C. C. (1978) "Measurements and Models of Fine Structure, Internal Gravity Waves and Wave Breaking in the Deep Ocean," J. Geophys. Res., 83(C6):2989-3009.

French, R. H. (1978) "Stratification and Open-Channel Flow," J. Hyd. Div., ASCE, 104(HY1), Proc. Paper 13458.

Garrett, C. and Munk, W. (1972) "Space-Time Scales of Internal Waves," Geophys. Fluid Dynam., 2:225-264.

Gartrell, G. Jr. (1977) "Wave-Breakdown in a Simple Model of a Density-Stratified Flow," in Notes on the 1977 Summer Study Program in Geophysical Fluid Dynamics at the Woods Hole Oceanographic Institution, pp. 118-132.

Gibson, C. H. and Schwarz, W. H. (1963) "The Universal Equilibrium Spectra of Turbulent Velocity and Scalar Fields," J. Fluid Mech., 16:357.

Gibson, C. H., Stegan, G. R. and Williams, R. B. (1970) "Statistics of the Fine Structure of Turbulent Velocity and Temperature Fields at High Reynolds Number," J. Fluid Mech., 41:153-167.

Gibson, C. H., Vega, L. A. and Williams, R. B. (1974) "Turbulent Diffusion of Heat and Momentum in the Ocean," Adv. in Geophys., 18A, Academic Press.

Goldstein, S. (1931) "On the Stability of Superposed Streams of Fluids of Different Densities," Proc. Roy. Soc., A, 132:524-548.

Hinze, J. O. (1959) Turbulence, McGraw-Hill, Inc., New York.

Hopfinger, E. J. and Toly, J.-A. (1976) "Spatially Decaying Turbulence and Its Relation to Mixing Across Density Interfaces," J. Fluid Mech., 78:155-175.

Howard, L. N. (1961) "A Note on a Paper of John W. Miles," J. Fluid Mech., 10:509-512.

Howard, L. N. (1963) "Neutral Curves and Stability Boundaries in Stratified Flow," J. Fluid Mech., 16:333.

Hunt, J. (1978) Private communication.

Johnson, J. W. (1942) "The Importance of Considering Side-Wall Friction in Bed-Load Investigations," Civil Engineering, 12:329-331.

Kaimal, J. C., Wyngaard, J. C., Izumi, Y. and Coté, O. R. (1972) "Spectral Characteristics of Surface Layer Turbulence," Q. J. Roy. Met. Soc., 98:563-589.

Kantha, L. H. (1975) "Turbulent Entrainment at the Density Interface of a Two-Layered Stably Stratified Fluid System," Ph.D. Thesis, Geophysical Fluid Dynamics Tech Lab Report 75-1, Johns Hopkins Univ., Baltimore, MD.

Kantha, L. H., Phillips, O. M. and Azad, R. S. (1977) "On the Turbulent Entrainment at a Stable Density Interface," J. Fluid Mech., 79:753-768.

Kato, H. and Phillips, O. M. (1969) "On the Penetration of a Turbulent Layer into a Stratified Fluid," J. Fluid Mech., 37:643-655.

Keulegan, G. H. (1949) "Interfacial Instability and Mixing in a Stratified Fluid," Nat. Bureau of Standards, 43, RP2040 Nov. 1949: 487-500.

Kline, S. J., Reynolds, W. C., Schraub, F. A. and Runstadler, P. V. (1967) "The Structure of Turbulent Boundary Layers," J. Fluid Mech., 30:741.

Kolmogoroff, A. N. (1941) C.R. Acad. Sci. U.R.S.S., 30:301.

Koloseus, H. J. and Davidian, J. (1966) "Roughness-Concentration Effects on Flow Over Hydrodynamically Rough Surfaces," Geol. Survey Water-Supply Paper 1592-D, USGS.

Koop, C. G. (1976) "Instability and Turbulence in a Stratified Shear Flow," Ph.D. Thesis, Dept. of Aerospace Eng., Univ. of Southern California.

Kullenberg, G. (1977) "Entrainment Velocity in Natural Stratified Vertical Shear Flow," Estuarine and Marine Sci., 5:329-338.

Landahl, M. T. (1972) "Wave Mechanics of Breakdown," J. Fluid Mech., 56:775-802.

Landahl, M. T. and Criminale, W. O. (1977) "Wave Breakdown in Stratified Shear Flows," J. Fluid Mech., 79:481-497.

Laufer, J. (1950) "Some Recent Measurements in a Two-Dimensional Turbulent Channel," J. Aero Sci., 17:277=287.

Laufer, J. (1975) "New Trends in Experimental Research," Ann. Rev. Fluid Mech., 7:307.

Liepmann, H. W. and Laufer, J. (1947) "Investigations of Free Turbulent Mixing," NACA Tech. Note 1257.

Lin, J. T. and Veenhuizen, S. (1974) "Measurements of the Decay of Grid-Generated Turbulence in a Stably Stratified Fluid," Bull. Am. Phys. Soc., 19:1142.

Linden, P. F. (1975) "The Deepening of a Mixed Layer in a Stratified Fluid," J. Fluid Mech., 71:385-401.

List, E. J. (1978) Private communication.

Lofquist, K. (1960) "Flow and Stress Near and Interface Between Stratified Liquids," Phys. of Fluids, 3:158-175.

Long, R. R. (1975) "The Influence of Shear on Mixing Across Density Interfaces," J. Fluid Mech., 70:305-320.

Lu, S. S. and Willmarth, W. W. (1973) "Measurements of the Structure of the Reynolds Stress in a Turbulent Boundary Layer," J. Fluid Mech., 60:481-511.

Lumley, J. L. (1964) "Spectrum of Nearly Inertial Turbulence in a Stably Stratified Fluid," J. Atmos. Sci., 21:99.

Miles, J. W. (1961) "On the Stability of Heterogeneous Shear Flows," J. Fluid Mech., 10:496-508.

Moore, M. J. and Long, R. R. (1971) "An Experimental Investigation of Turbulent Stratified Shearing Flow," J. Fluid Mech., 49:635-655.

Nychas, S. G., Hershey, H. C. and Brodkey, R. S. (1973) "A Visual Study of Turbulent Shear Flow," J. Fluid Mech., 61:513-540.

Obukhov, A. M. (1949) Izv. Akad. Nauk SSSR Geogor Geofiz, 12:58.

Okoye, J. K. (1970) "Characteristics of Transverse Mixing in Open-Channel Flows," W. M. Keck Lab of Hyd. and Water Res. Tech. Report No. KH-R-23, Calif. Inst. of Tech., Pasadena, CA.

Okoye, J. K. and Raichlen, F. (1969) "Description and Operation of Analog-to-Digital Data Acquisition System," Tech. Memo. 69-9, W. M. Keck Lab. of Hyd. and Water Res., Calif. Inst. of Tech., Pasadena, CA.

Pedersen, Fl. B. (1974) "Interfacial Mixing in a Two-Layered Stratified Flow," Danish Center for Applied Math. and Mech. Report No. 74.

Phillips, O. M. (1966) The Dynamics of the Upper Ocean, Cambridge Univ. Press.

Praturi, A. K. and Brookey, R. S. (1978) "A Stereoscopic Visual Study of Coherent Structures in Turbulent Shear Flow," J. Fluid Mech., 89:251-272.

Pui, N. K. and Gartshore, I. S. (1977) Paper presented at 6th Canadian Congress on Applied Mechanics.

Raichlen, F. (1967) "Some Turbulence Measurements in Water," J. Eng. Mech. Div., ASCE, 93(EM2):73-97.

Schiller, E. J. and Sayre, W. W. (1973) "Vertical Mixing of Heated Effluents in Open Channel Flow," IIHR Report No. 148, Iowa Inst. of Hyd. Res., Univ. of Iowa, Iowa City, IA.

Spencer, B. W. and Jones, B. G. (1971) "Statistical Investigation of Pressure and Velocity Fields in the Turbulent Two-Stream Mixing Layer," AIAA 4th Fluid and Plasma Dynamics Conference, Paper No. 71-613, Palo Alto, CA.

Stevenson, W. (1970) "Optical Frequency Shifting by Means of a Rotating Diffraction Grating," Appl. Optics, 9:649-652.

Sunyach, M. (1971) "Contribution à l'étude des frontières d'écoulements turbulents libres," Ph.D. Thesis, Ecole Centrale de Lyon.

Taylor, G. I. (1931) "Effect of Variation in Density on the Stability of Superposed Streams of Fluid," Proc. Roy. Soc., A, 132:499-523.

Tennekes, H. and Lumley, J. L. (1972) A First Course in Turbulence, MIT Press, Cambridge, MA.

Thomas, A. S. W. (1977) "Organized Structures in the Turbulent Boundary Layer," Ph.D. Thesis, Univ. of Adelaide.

Thompson, S. M. and Turner, J. S. (1975) "Mixing Across an Interface Due to Turbulence Generated by an Oscillating Grid," J. Fluid Mech., 67:349-371.

Thorpe, S. A. (1971) "Experiments on the Instability of Stratified Shear Flows: Miscible Fluids," J. Fluid Mech., 46:299-319.

Thorpe, S. A. (1973a) "Turbulence in Stably Stratified Fluids: A Review of Laboratory Experiments," Boundary Layer Meteorology, 5:95.

Thorpe, S. A. (1973b) "Experiments on Instabilities and Turbulence in a Stratified Shear Flow," J. Fluid Mech., 61:731-751.

Thorpe, S. A. (1978a) "On the Shape and Breaking of Finite Amplitude Internal Gravity Waves in a Shear Flow," J. Fluid Mech., 85:7-32.

Thorpe, S. A. (1978b) "The Near Surface Ocean Mixing Layer in Stable Heating Conditions," J. Geophys. Res., 83(C6):2875-2885.

Turner, J. S. (1968) "The Influence of Molecular Diffusivity on Turbulent Entrainment Across a Density Interface," J. Fluid Mech., 33:639-656.

Turner, J. S. (1973) Buoyancy Effects in Fluids, Cambridge Univ. Press.

Vanoni, V. A. and Brooks, N. H. (1957) "Laboratory Studies of the Roughness and Suspended Load of Alluvial Streams, Report E-68 Sedimentation Laboratory, Calif. Inst. of Tech., Pasadena, CA.

Vanoni, V. A., Brooks, N. H. and Raichlen, F. (1967) "A 40-Meter Precision Tilting Flume," Tech. Memo. 67-3, W. M. Keck Lab. of Hyd. and Water Res., Calif. Inst. of Tech., Pasadena, CA.

Wallace, J. M., Brodkey, R. S. and Eckelmann, H. (1977) "Pattern-Recognized Structures in Bounded Turbulent Shear Flows," J. Fluid Mech., 83:673-693.

Watrasiewicz, B. M. and Rudd, M. J. (1976) Laser Doppler Measurements, Butterworth, London.

Webb, E. K. (1977) "Convection Mechanisms of Atmospheric Heat Transfer From Surface to Global Scale," Second Australasian Conference on Heat and Mass Transfer, Univ. of Sydney, Feb. 1977:523-539.

Williams, R. B. and Gibson, C. H. (1974) "Direct Measurements of Turbulence in the Pacific Equitorial Undercurrent," J. Phys. Oceanography, 4:104-108.

Willmarth, W. W. (1975) "Structure of Turbulence in Boundary Layers," Adv. in Appl. Mech., 15:159.

Winant, C. D. and Browand, G. L. (1974) "Vortex Pairing: The Mechanism of Turbulent Mixing-Layer Growth at Moderate Reynolds Number," J. Fluid Mech., 63:237-255.

Woods, J. D. (1968) "Wave Induced Shear in the Summer Thermocline," J. Fluid Mech., 37:791.

Woods, J. D. (1969) "On Richardson's Number as a Criterion for Laminar-Turbulent-Laminar Transition in the Ocean and Atmosphere," Radio Science, 4:1289.

Wyatt, L. R. (1978) "The Entrainment Interface in a Stratified Fluid," J. Fluid Mech., 86:293-311.

Wygnanski, I. and Fiedler, H. E. (1970) "The Two-Dimensional Mixing Region," J. Fluid Mech., 41:327-361.

Wyngaard, J. C. and Coté, O. R. (1971) "The Budgets of Turbulent Kinetic Energy and Temperature Variance in the Atmospheric Surface Layer," J. Atmos. Sci., 28:190-201.

_____ Weast, R. C. (ed.) (1975) Handbook of Chemistry and Physics, CRC Press: F-5.